

nagra.

ARBEITSBERICHT NAB 24-25

Model Based Performance Assessment in Support of the Safety Assessment for a Geological Repository

October 2024

Nagra | National Cooperative for the Disposal of Radioactive Waste
Hardstrasse 73 | 5430 Wettingen | Switzerland
+41 56 437 11 11 | info@nagra.ch | nagra.ch

nagra.

ARBEITSBERICHT NAB 24-25

Model Based Performance Assessment in Support of the Safety Assessment for a Geological Repository

October 2024

KEYWORDS
Repository-induced effects, performance assessment, modelling, L/ILW, HLW, THM, total system

Nagra | National Cooperative for the Disposal of Radioactive Waste
Hardstrasse 73 | 5430 Wettingen | Switzerland
+41 56 437 11 11 | info@nagra.ch | nagra.ch

Nagra Arbeitsberichte ("Working Reports") present the results of work in progress that have not necessarily been subject to a comprehensive review. They are intended to provide rapid dissemination of current information.

This report has been elaborated by a project team consisting of A. Papafotiou[1], T. Guillemot[1], U. Lengler[2], K. Luu[2], M. Hayek[2], C. Li[2] & P. Marschall[1]

[1] Nagra

[2] Intera

An earlier version of the report has been reviewed and commented on by Mikey Hannon (Hannon Clean Energy). The authors would like to thank him for his valuable contributions.

Copyright © 2024 by Nagra, Wettingen (Switzerland) / All rights reserved. All parts of this work are protected by copyright. Any utilisation outwith the remit of the copyright law is unlawful and liable to prosecution. This applies in particular to translations, storage and processing in electronic systems and programs, microfilms, reproductions, etc.

Abstract

This report documents the development of a robust modelling workflow and delivers the associated model-based analyses for the performance assessments of an exemplary repository implementation at the Haberstal site. The modelling tools and analyses are implemented on the level of the total barrier system, as well focused on the high-level waste and low-/intermediate-level waste disposal areas, respectively.

In particular, a comprehensive description of numerical models used in the performance assessment is provided with all input data, technical specifications, and links within the performance assessment model chain. The abstraction methodology is elaborated in detail, including a discussion on the treatment of conceptual uncertainty, the assumptions and justifications of choices made in model implementations, as well as the extensive model benchmarking performed within the performance assessment model chain. The implementation of the model chain for the model-based assessments and the role and usage of each model is explained. The modelling performed for the total system assessments is described in detail for the expected barrier performance as well as several deterministic scenarios representing deviations therefrom. In addition, probabilistic simulations considering parametric uncertainty are presented for high-level waste and low-/intermediate-level waste, for the expected performance and several scenarios that address individual barriers of the repository system.

The analysis of modelling results confirms on the one hand the confidence in the performance assessment model chain and on the other hand the robustness of the barrier system in the exemplary repository implementation. The latter is demonstrated comprehensively from the perspectives of the total system as well as of barrier components, gained by the multitude of modelling tools for a broad range of uncertainties and scenarios associated with the evolution of the repository system.

The modelling results presented here are used in the synthesis of the performance assessment for quantitative assessment with regards to safety functions of the barrier system and the associated performance margins. The latter is not addressed in the present report.

Table of Contents

Abstract I

Table of Contents III

List of Tables VII

List of Figures IX

List of Acronyms XVIII

1 Introduction 1
1.1 Background and scope 1
1.2 Objectives 3
1.3 Report outline 4

2 Repository concept and performance assessment 5
2.1 Repository concept and provisional design 5
2.1.1 Safety and repository concept 5
2.1.2 Provisional design 5
2.1.3 HLW disposal area 6
2.1.4 L/ILW disposal area 6
2.1.5 Sealing and backfill system 7
2.1.6 Implementation timeline for performance assessment 8
2.1.7 Waste inventory and source terms 9
2.2 Performance assessment 10
2.2.1 General approach 10
2.2.2 Performance assessment of the total system 11
2.2.3 Performance assessment at component level 11
2.2.4 Uncertainty assessment and quantification 12

3 Modelling tools and approaches 13
3.1 Model portfolio – overview 13
3.1.1 Codes 13
3.1.2 Scales of interest 13
3.1.3 Intended use of model portfolio 14
3.2 Site models (3D) 15
3.3 Deterministic repository and component models (3D) 22
3.3.1 Model of the geological repository 22
3.3.2 Models of components of the repository 23
3.4 Probabilistic component models HLW 25
3.4.1 Mesh generation 25
3.4.2 Model parameters 26
3.4.3 Boundary and initial conditions 27
3.4.4 Source terms 27
3.4.5 Reference case 29
3.4.6 Monte Carlo simulations 29

3.5 Probabilistic component models L/ILW ... 35
3.5.1 Mesh generation ... 35
3.5.2 Model parameters ... 37
3.5.3 Boundary and initial conditions ... 38
3.5.4 Source terms ... 38
3.5.5 Reference case ... 39
3.5.6 Monte Carlo simulations ... 39
3.6 Process models (2D) ... 42
3.7 Model outputs ... 43

4 Model abstraction ... 51
4.1 Basic principles ... 51
4.2 Geometric abstractions ... 51
4.2.1 Simplifications in model geometries ... 51
4.2.2 Simplification of quasi-symmetric geometries ... 55
4.2.3 Transport paths ... 57
4.3 Simplified representation of phenomena and processes ... 58
4.3.1 Basic principles ... 58
4.3.2 Flow and transport of mass and energy (TH) ... 58
4.3.3 Extension to two-phase flow (TH^2) ... 59
4.3.4 $TH^2M \rightarrow TH^2$ abstraction ... 59
4.3.5 $TH^2C \rightarrow TH^2$ Abstraction ... 60
4.4 Homogenisation / scaling of parameters ... 61
4.4.1 Basic principles ... 61
4.4.2 Parametric uncertainties associated with the inaccuracy of the model form ... 61
4.4.3 Inherent variability of the modelled material properties ... 62
4.4.4 Anisotropic and isotropic properties ... 63
4.5 Simplified formulation of boundary conditions, initial conditions and source terms ... 64
4.6 Verification of codes and validation of models ... 65
4.7 Selected examples ... 65
4.8 Concluding remarks on model chain abstractions ... 74

5 Modelling workflow for performance assessment ... 79
5.1 Performance screening - Evaluation workflow ... 79
5.2 Modelling of expected barrier performance ... 81
5.2.1 Key features ... 81
5.2.2 Models and indicators ... 81
5.3 Modelling of deviations from expected performance ... 82
5.3.1 Approach ... 82
5.3.2 Models and performance metrics/indicators ... 83

6 Deterministic model-based analyses – total system ... 85
6.1 Expected performance ... 85
6.1.1 Phenomenology ... 85

6.1.2 Quantitative analysis ... 86
6.1.3 Summary of key processes ... 98
6.2 Deviations – total system ... 99
6.2.1 Thermal interactions ... 100
6.2.2 Hydraulic interactions ... 106

7 Probabilistic model-based analyses – HLW ... 141
7.1 Expected performance ... 141
7.2 Deviations ... 145
7.2.1 Instant release fraction and congruent release of activity (CONGRUENT) ... 146
7.2.2 Instant release of activity entire activity (IRMAX) ... 146
7.2.3 Canister failure at time of repository closure (WPFAIL) ... 147
7.2.4 Pessimistic heat source term (UBHEAT) ... 151
7.2.5 Pessimistic gas source term (UBGAS) ... 151
7.2.6 Upflow with artesian pressure in Keuper (UPFLOW) ... 154
7.2.7 Downflow with artesian pressure in Malm (DOWNFLOW) ... 154
7.2.8 Hardbeds as release path (HRDBDS) ... 154
7.2.9 Herrenwis as release path (HERWIS) ... 158
7.2.10 Fault normal to HLW drifts (FLTHLWN) ... 158
7.2.11 Fault parallel to HLW drifts (FLTHLWP) ... 161
7.2.12 Thermally or gas induced fracture (RIEHLW) ... 161
7.2.13 Loss of overburden (LOSSOB) ... 161

8 Probabilistic model-based analyses – L/ILW ... 167
8.1 Expected performance ... 167
8.2 Deviations ... 170
8.2.1 Permeable V3 (V3PERM) ... 171
8.2.2 No gas generation (ZEROGAS) ... 173
8.2.3 Pessimistic gas generation (PESSGAS) ... 173
8.2.4 Fault through L/ILW caverns (FLTILW) ... 177

9 Summary and conclusions ... 179

10 References ... 189

App. A Complementary information on model conceptualisation ... A-1
A.1 Two phase flow and transport - mathematical formulations ... A-1
A.2 Geometric abstractions in repository modelling ... A-4
A.2.1 Model geometry of entire repository ... A-4
A.2.2 Model geometry of a L/ILW emplacement cavern ... A-8
A.2.3 Model geometry of a HLW emplacement drift ... A-9
A.2.4 3D component model of a V2-L/ILW seal ... A-10
A.2.5 3D component model of a V3 seal ... A-11

App. B **Complementary results: total system analysis** **B-1**
B.1 Expected performance B-1
B.2 Expected performance with H_2 molecular diffusion B-7
B.3 Deviation: no V1 seals *[TSD14]* B-16
B.4 Deviation: no V2 seals *[TSD15]* B-24
B.5 Deviation: impermeable V3 seals *[TSD16]* B-31
B.6 Deviation: impermeable V2-L/ILW seals *[TSD21]* B-40
B.7 Deviation: low-permeable V1-L/ILW seals *[TSD20]* B-48
B.8 Deviation: instant repository resaturation *[TSD4]* B-56
B.9 Deviation: fault through L/ILW caverns B-64

App. C **Complementary results: HLW** **C-1**
C.1 Expected performance C-1
C.2 Expected performance with H_2 molecular diffusion C-9
C.3 Expected performance with H_2O consumption C-11

App. D **Complementary results: L/ILW** **D-1**
D.1 Expected performance D-1
D.2 Expected evolution with H_2 molecular diffusion and H_2O consumption D-7
D.3 Expected evolution with H_2 molecular diffusion (probabilistic) D-10
D.4 Expected evolution with H_2O consumption (probabilistic) D-11

App. E **Benchmarking between PA and safety analysis** **E-1**

List of Tables

Tab. 2-1: Generic timeline for the implementation of a combined repository, as assumed in model-based analyses of repository performance 8

Tab. 3-1: Stratigraphic units respectively formations in the siting region, from Nagra (2024c), and their representation in the site model 17

Tab. 3-2: Porosity of stratigraphic units respectively formations, from Nagra (2024c), and their representation in the PA 18

Tab. 3-3: Hydraulic conductivity of stratigraphic units respectively formations, from Nagra (2024c), and their representation in the PA 19

Tab. 3-4: Effective diffusion coefficient of stratigraphic units respectively formations (from Glaus et al. 2024) and their representation in the PA 20

Tab. 3-5: Additional parameters assigned to formations considered in the PA models 21

Tab. 3-6: Reference hydraulic and thermal parameters assigned to the HLW drifts in 2D 26

Tab. 3-7: Distributions of parameter values used for Monte Carlo gas-heat simulations for HLW 31

Tab. 3-8: Means and standard deviations of the lognormal distributions fitted to the effective diffusion coefficients used for tracer simulations for HLW 33

Tab. 3-9: Volumes and thicknesses of sections 36

Tab. 3-10: Reference hydraulic parameters assigned to the L/ILW caverns in 2.5D 38

Tab. 3-11: Distributions of of parameter values used in the Monte Carlo gas simulations for L/ILW 40

Tab. 3-12: Means and standard deviations of the lognormal distributions fitted to the effective diffusion coefficients used for tracer simulations for L/LW 42

Tab. 4-1: Model abstraction chain – L/ILW: comparison between models used in the PA in terms of key metrics relevant to the model-supported analysis 76

Tab. 4-2: Model abstraction chain – HLW: comparison between models used in the PA in terms of key metrics relevant to the model-supported analysis 77

Tab. 6-1: Deviations from expected performance total system – by interaction 99

Tab. 6-2: Simulated scenarios for deviations by hydraulic interactions[1] 106

Tab. 7-1: Deviations from expected performance HLW at level of components 146

Tab. 8-1: Deviations from expected performance L/ILW – by barrier (component level) 170

Tab. 9-1: Overview of chain of numerical models used in the model-based assessments 180

Tab. 9-2: Selected examples of benchmarking within the PA model chain 181

Tab. A-1: Geometric data of repository sections A-4

Tab. A-2: Geometry of repository components in the L/ILW section and central area implemented in the 3D repository model grid and scaling of effective porosity to adjust void space volumes A-6

Tab. A-3: Geometry of repository components in the HLW section implemented in the 3D repository model grid and scaling of effective porosity to adjust void space volumes A-7

Tab. A-4: Geometric data of L/ILW section A-8

Tab. A-5: Geometry of L/ILW emplacement cavern and adjacent tunnels implemented in the 3D component model grid A-8

Tab. A-6: Geometric data of HLW section A-9

Tab. A-7: Geometry of HLW emplacement drift implemented in the 3D component model grid A-9

Tab. A-8: Geometric data of a V2-L/ILW sealing section A-10

Tab. A-9: Geometry of V2-L/ILW seal implemented in the 3D component model grid A-10

Tab. A-10: Geometric data of a V3 seal and access shaft A-11

Tab. A-11: Geometry of V3 seal and shaft implemented in the 3D component model grid A-11

Tab. B-1: Two-phase molecular diffusion coefficients B-7

List of Figures

Fig. 1-1: Structure of reports covering post-closure safety aspects of the site comparison and the post-closure safety case 2

Fig. 2-1: Schematic view of the provisional repository design with the L/ILW emplacement caverns (left) and the HLW emplacement drifts (right) 7

Fig. 2-2: Location of the closure structures in the current concept of a combined repository 9

Fig. 3-1: Illustration of the 3D site model 16

Fig. 3-2: Illustration of the 3D repository model 22

Fig. 3-3: Illustration of the 3D component models 24

Fig. 3-4: Close-up view of the detailed representation of a HLW emplacement drift in 2D 25

Fig. 3-5: 2-D hybrid mesh with twenty HLW emplacement drifts 26

Fig. 3-6: Gas generation rates per HLW emplacement drifts, from HLW disposal canisters and from tunnel support materials (F10) 28

Fig. 3-7: Representative average heat generation rates per SF canister type (PWR-MOX, PWR-UO_2, BWR) and average used for repository-scale modelling (Kombi) 29

Fig. 3-8: Scatter-plot matrix of the 100 Latin Hypercube samples used for gas-heat simulations for HLW 32

Fig. 3-9: Scatter-plot matrix of the 100 Latin Hypercube samples used for tracer simulations for HLW 34

Fig. 3-10: Close-up view of the detailed representation of a L/ILW cavern in 2D, consisting of three sections 36

Fig. 3-11: 2.5D hybrid mesh with seven L/ILW emplacement caverns 37

Fig. 3-12: Total gas generation rates per L/ILW emplacement cavern 39

Fig. 3-13: Scatter-plot matrix of the 100 Latin Hypercube samples used for gas simulations for L/ILW 41

Fig. 3-14: Example of a 2D process model of a cross-section through an HLW tunnel with surrounding EDZ, OPA, and the over- and underlying stratigraphic units 43

Fig. 3-15: Observation points used for simulated transients 50

Fig. 4-1: Example model geometries implemented in PA modelling 52

Fig. 4-2: Example representations of the L/ILW disposal area in the PA 54

Fig. 4-3: Example representations of the HLW disposal area in the PA 56

Fig. 4-4: Homogenisation of emplaced materials in the L/ILW nearfield 62

Fig. 4-5: Exemplary effective diffusion coefficient (left) and porosity fields (right) derived from geostatistical models of clay content in the OPA 63

Fig. 4-6: Comparison of gas saturation and gas pressure simulated with different levels of geometric abstraction for L/ILW 67

Fig. 4-7: Comparison of gas saturation and gas pressure simulated with different levels of geometric abstraction for HLW 67

Fig. 4-8: Comparison of gas pressure simulated with different levels of geometric abstraction in L/ILW and HLW 68

Fig. 4-9: Comparison of gas saturation after 5,000 years in an HLW emplacement drift (top) and in an L/ILW emplacement cavern (bottom) 69

Fig. 4-10: Comparison of three variants of the 3D model of the V3 seal 71

Fig. 4-11: Comparison between three variants of breaching times assigned to 10 canisters in the 3D model of an HLW emplacement drift 73

Fig. 4-12: Comparison between four variants of heat source assigned to the canisters of the 3D model of an HLW emplacement drift 74

Fig. 4-13: Comparison between 3D repository model, 3D component model of a single cavern, and 2.5D component model of a single cavern 75

Fig. 5-1: Funnel-shaped event horizon, dividing the space of state of the multi-barrier system in domains of possible and hypothetical states 80

Fig. 6-1: Expected performance total system: transients of temperature 89

Fig. 6-2: Expected performance total system: transients of gas saturation 91

Fig. 6-3: Expected performance total system: transients of pressure 93

Fig. 6-4: Expected performance total system: transients of gas flow rate through the sealing sections of the repository (towards shafts) 94

Fig. 6-5: Expected performance total system: transients of liquid flow rate through the sealing sections of the combined repository (towards shafts) 95

Fig. 6-6: Expected performance total system: transients of normalised flow rates 96

Fig. 6-7: Expected performance total system: spatial distribution of partial gas saturation of H_2 generated 97

Fig. 6-8: Deviations scenario *"no heat source in the HLW repository"*: transients of (a) pressure and (b) gas saturation in the central area of the repository 101

Fig. 6-9: Deviations scenario *"no heat source in the HLW repository"*: comparison of absolute temperature increase from initial temperature 102

Fig. 6-10: Deviations scenario *"conservative heat source and high thermal conductivity of host rock"*: transients of (a) pressure and (b) gas saturation in the central area of the repository 104

Fig. 6-11: Deviations scenario *"conservative heat source and high thermal conductivity of host rock"*: comparison of absolute temperature increase from initial temperature (a) in the L/ILW section and (b) in the central area. 105

Fig. 6-12: Deviations scenario *"lower bound gas generation"*: transients of (a) pressure and (b) gas saturation in the central area of the repository 108

Fig. 6-13: Deviations scenario *"lower bound gas generation"*: normalised cumulative flows of (a) gas and (b) liquid 109

Fig. 6-14: Deviations scenario *"upper bound gas generation"*: (a) pressure and (b) gas saturation in the central area of the repository 111

Fig. 6-15: Deviations scenario *"upper bound gas generation"*: normalised cumulative flows of (a) gas and (b) liquid 112

Fig. 6-16: Implementation of fault in scenarios (a) *"fault through L/ILW"* and (b) *"fault through central area"* 114

Fig. 6-17: Deviations scenario *"fault through L/ILW"*: (a) pressure and (b) gas saturation in the L/ILW section of the repository, and (c) pressure and (d) gas saturation in the central area of the repository 115

Fig. 6-18: Deviations scenario *"fault through L/ILW"*: normalised cumulative flows of (a) gas and (b) liquid 117

Fig. 6-19: Deviations scenario *"fault through central area"*: (a) pressure and (b) gas saturation in the central area of the repository 119

Fig. 6-20: Deviations scenario *"fault through central area"*: normalised cumulative flows of (a) gas and (b) liquid 120

Fig. 6-21: Deviations scenario *"low-permeable V2-L/ILW seal"*: (a) pressure and (b) gas saturation in the L/ILW section of the repository, and (c) pressure and (d) gas saturation in the central area of the repository 123

Fig. 6-22: Deviations scenario *"low-permeable V2-L/ILW seal"*: normalised cumulative flows of (a) gas and (b) liquid 124

Fig. 6-23: Deviations scenario *"high-permeable V3 seal (variant 1)"*: (a) pressure and (b) gas saturation in the central area of the repository 126

Fig. 6-24: Deviations scenario *"high-permeable V3 seal (variant 1)"*: normalised cumulative flows of (a) gas and (b) liquid 127

Fig. 6-25: Deviations scenario *"high-permeable V3 seal (variant 2)"*: (a) pressure and (b) gas saturation in the central area of the repository 129

Fig. 6-26: Deviations scenario *"high-permeable V3 seal (variant 2)"*: normalised cumulative flows of (a) gas and (b) liquid 130

Fig. 6-27: Deviations scenario *"high-permeable V3 and V2-L/ILW seals"*: (a) pressure and (b) gas saturation in the central area of the repository 132

Fig. 6-28: Deviations scenario *"high-permeable V3 and V2-L/ILW seals"*: normalised cumulative flows of (a) gas and (b) liquid 133

Fig. 6-29: Deviations scenario *"high-permeable V2 seals"*: (a) pressure and (b) gas saturation in the central area of the repository 135

Fig. 6-30: Deviations scenario *"high-permeable V2 seals"*: normalised cumulative flows of (a) gas and (b) liquid 136

Fig. 6-31: Deviations scenario *"high-permeable V2 and V1 seals"*: (a) pressure and (b) gas saturation in the central area of the repository 138

Fig. 6-32: Deviations scenario *"high-permeable V2 and V1 seals"*: normalised cumulative flows of (a) gas and (b) liquid 139

Fig. 7-1: Expected barrier performance HLW: best estimate and uncertainty ranges 143

Fig. 7-2: Expected barrier performance HLW: best estimate and uncertainty ranges of solute tracer (I-129) release 144
Fig. 7-3: CONGRUENT scenario: best estimate and uncertainty ranges of solute tracer (I-129) release 148
Fig. 7-4: IRMAX scenario: best estimate and uncertainty ranges of solute tracer (I-129) release 149
Fig. 7-5: WPFAIL scenario: best estimate and uncertainty ranges of solute tracer (I-129) release 150
Fig. 7-6: UBHEAT scenario: best estimate and uncertainty ranges 152
Fig. 7-7: UBGAS scenario: best estimate and uncertainty ranges 153
Fig. 7-8: UPFLOW scenario: best estimate and uncertainty ranges of solute tracer (I-129) release 155
Fig. 7-9: DOWNFLOW scenario: best estimate and uncertainty ranges of solute tracer (I-129) release 156
Fig. 7-10: HRDBDS scenario: best estimate and uncertainty ranges of solute tracer (I-129) release 157
Fig. 7-11: HERWIS scenario: best estimate and uncertainty ranges of solute tracer (I-129) release 159
Fig. 7-12: FLTHLWN scenario: best estimate and uncertainty ranges of solute tracer (I-129) release 160
Fig. 7-13: FLTHLWP scenario (var. 1): best estimate and uncertainty ranges of solute tracer (I-129) release 162
Fig. 7-14: FLTHLWP scenario (var. 2): best estimate and uncertainty ranges of solute tracer (I-129) release 163
Fig. 7-15: RIEHLW scenario: best estimate and uncertainty ranges of solute tracer (I-129) release 164
Fig. 7-16: LOSSOB scenario: best estimate and uncertainty ranges of solute tracer (I-129) release 165
Fig. 8-1: Expected barrier performance L/ILW: best estimate and uncertainty ranges 168
Fig. 8-2: Expected barrier performance L/ILW: best estimate and uncertainty ranges of solute tracer (Cl-36) release 169
Fig. 8-3: V3PERM scenario: best estimate and uncertainty ranges 172
Fig. 8-4: ZEROGAS scenario: best estimate and uncertainty ranges of solute tracer (Cl-36) release 174
Fig. 8-5: PESSGAS scenario: best estimate and uncertainty ranges of gas induced pressures in the L/ILW nearfield 175
Fig. 8-6: PESSGAS scenario: best estimate and uncertainty ranges of solute tracer (Cl-36) release 176
Fig. 8-7: FLTLILW scenario: best estimate and uncertainty ranges of solute tracer (Cl-36) release 178

Fig. 9-1: Total system, expected evolution: distribution of gas generated from HLW (left) and from L/ILW (right) at different times 183

Fig. 9-2: Total system, expected evolution: storage of waste-generated gas mass after 100,000 years..... 184

Fig. 9-3: Total system, deviation scenarios: correlation between maximum overpressure (calculated as peak pressure minus hydrostatic pressure) and permeability of V2-L/ILW seals (blue) and V3 seals (green)..... 186

Fig. 9-4: PA scenarios HLW: percentage of tracer mass (I-129) retained in the CRZ compared to that in the expected performance (EXPERF)..... 188

Fig. B-1: Expected performance total system (3D repository model): Spatial distribution of temperature after (a) 100 years, (b) 500 years, (c) 1,000 years, (d) 5,000 years, (e) 10,000 years, (f) 20,000 years, (g) 50,000 years, and (h) 100,000 years B-2

Fig. B-2: Expected performance total system (3D repository model): Spatial distribution of gas saturation after (a) 100 years, (b) 500 years, (c) 1,000 years, (d) 5,000 years, (e) 10,000 years, (f) 20,000 years, (g) 50,000 years, and (h) 100,000 years B-3

Fig. B-3: Expected performance total system (3D repository model): Spatial distribution of pressure after (a) 100 years, (b) 500 years, (c) 1,000 years, (d) 5,000 years, (e) 10,000 years, (f) 20,000 years, (g) 50,000 years, and (h) 100,000 years B-4

Fig. B-4: Expected performance total system (3D repository model): Spatial distribution of H_2 mass fraction in liquid after (a) 100 years, (b) 500 years, (c) 1,000 years, (d) 5,000 years, (e) 10,000 years, (f) 20,000 years, (g) 50,000 years, and (h) 100,000 years B-5

Fig. B-5: Expected performance total system (3D repository model): Spatial distribution of partial gas saturation of H_2 released in the HLW drifts (left) and in the L/ILW caverns (right) after (a) 1,000 years, (b) 10,000 years, (c) 20,000 years, and (d) 100,000 years..... B-6

Fig. B-6: Expected performance total system with H_2 molecular diffusion: Transients of temperature B-9

Fig. B-7: Expected performance total system with H_2 molecular diffusion: Transients of gas saturation B-11

Fig. B-8: Expected performance total system with H_2 molecular diffusion: Transients of pressure..... B-13

Fig. B-9: Expected performance total system with H_2 molecular diffusion: Transients of gas flow rate through the sealing sections of the repository (towards shafts)..... B-14

Fig. B-10: Expected performance total system with H_2 molecular diffusion: Transients of liquid flow rate through the sealing sections of the repository (towards shafts)..... B-14

Fig. B-11: Expected performance total system with H_2 molecular diffusion: Transients of normalised flow rates of (a) gas and (b) liquid through the sealing sections of the repository (towards disposal areas) B-15

Fig. B-12: Deviations scenario *"no V1 seals"*: Transients of temperature..... B-17

Fig. B-13: Deviations scenario *"no V1 seals"*: Transients of gas saturation B-19
Fig. B-14: Deviations scenario "no V1 seals": Transients of pressure B-21
Fig. B-15: Deviations scenario *"no V1 seals"*: Transients of gas flow rate through the sealing sections of the repository (towards shafts) B-22
Fig. B-16: Deviations scenario *"no V1 seals"*: Transients of liquid flow rate through the sealing sections of the repository (towards shafts) B-22
Fig. B-17: Deviations scenario *"no V1 seals"*: Transients of normalised flow rates of (a) gas and (b) liquid through the sealing sections of the repository (towards disposal areas) B-23
Fig. B-18: Deviations scenario *"no V2 seals"*: Transients of temperature B-25
Fig. B-19: Deviations scenario *"no V2 seals"*: Transients of gas saturation B-27
Fig. B-20: Deviations scenario *"no V2 seals"*: Transients of pressure B-29
Fig. B-21: Deviations scenario *"no V2 seals"*: Transients of gas flow rate through the sealing sections of the repository (towards shafts) B-30
Fig. B-22: Deviations scenario *"no V2 seals"*: Transients of liquid flow rate through the sealing sections of the repository (towards shafts) B-30
Fig. B-23: Deviations scenario *"no V2 seals"*: Transients of normalised flow rates of (a) gas and (b) liquid through the sealing sections of the repository (towards disposal areas) B-31
Fig. B-24: Deviations scenario *"impermeable V3 seals"*: Transients of temperature B-33
Fig. B-25: Deviations scenario *"impermeable V3 seals"*: Transients of gas saturation B-35
Fig. B-26: Deviations scenario *"impermeable V3 seals"*: Transients of pressure B-37
Fig. B-27: Deviations scenario *"impermeable V3 seals"*: Transients of gas flow rate through the sealing sections of the repository (towards shafts) B-38
Fig. B-28: Deviations scenario *"impermeable V3 seals"*: Transients of liquid flow rate through the sealing sections of the repository (towards shafts) B-38
Fig. B-29: Deviations scenario *"impermeable V3 seals"*: Transients of normalised flow rates of (a) gas and (b) liquid through the sealing sections of the repository (towards disposal areas) B-39
Fig. B-30: Deviations scenario *"impermeable V2-L/ILW seals"*: Transients of temperature B-41
Fig. B-31: Deviations scenario *"impermeable V2-L/ILW seals"*: Transients of gas saturation B-43
Fig. B-32: Deviations scenario *"impermeable V2-L/ILW seals"*: Transients of pressure B-45
Fig. B-33: Deviations scenario *"impermeable V2-L/ILW seals"*: Transients of gas flow rate through the sealing sections of the repository (towards shafts) B-46
Fig. B-34: Deviations scenario *"impermeable V2-L/ILW seals"*: Transients of liquid flow rate through the sealing sections of the repository (towards shafts) B-46
Fig. B-35: Deviations scenario *"impermeable V2-L/ILW seals"*: Transients of normalised flow rates of (a) gas and (b) liquid through the sealing sections of the repository (towards disposal areas) B-47

Fig. B-36: Deviations scenario *"low-permeable V1-L/ILW seals"*: Transients of temperature B-49

Fig. B-37: Deviations scenario *"low-permeable V1-L/ILW seals"*: Transients of gas saturation B-51

Fig. B-38: Deviations scenario *"low-permeable V1-L/ILW seals"*: Transients of pressure B-53

Fig. B-39: Deviations scenario *"low-permeable V1-L/ILW seals"*: Transients of gas flow rate through the sealing sections of the repository (towards shafts)..... B-54

Fig. B-40: Deviations scenario *"low-permeable V1-L/ILW seals"*: Transients of liquid flow rate through the sealing sections of the repository (towards shafts)..... B-54

Fig. B-41: Deviations scenario *"low-permeable V1-L/ILW seals"*: Transients of normalised flow rates of (a) gas and (b) liquid through the sealing sections of the repository (towards disposal areas) B-55

Fig. B-42: Deviations scenario *"instant repository resaturation"*: Transients of temperature B-57

Fig. B-43: Deviations scenario *"instant repository resaturation"*: Transients of gas saturation B-59

Fig. B-44: Deviations scenario *"instant repository resaturation"*: Transients of pressure B-61

Fig. B-45: Deviations scenario *"instant repository resaturation"*: Transients of gas flow rate through the sealing sections of the repository (towards shafts)..... B-62

Fig. B-46: Deviations scenario *"instant repository resaturation"*: Transients of liquid flow rate through the sealing sections of the repository (towards shafts)..... B-62

Fig. B-47: Deviations scenario *"instant repository resaturation"*: Transients of normalised flow rates of (a) gas and (b) liquid through the sealing sections of the repository (towards disposal areas) B-63

Fig. B-48: Deviations scenario *"fault through L/ILW"*: Spatial distribution of gas saturation in the repository and the fault after (a) 100 years, (b) 500 years, (c) 1,000 years, (d) 5,000 years, (e) 10,000 years, (f) 20,000 years, (g) 50,000 years, and (h) 100,000 years B-65

Fig. B-49: Deviations scenario *"fault through L/ILW"*: Transients of (a) gas flow rate and (b) cumulative gas flow through the sealing sections of the repository (towards shafts) and through the fault B-66

Fig. B-50: Deviations scenario *"fault through L/ILW"*: Transients of liquid flow rate through the sealing sections of the repository (towards shafts) and through the fault B-67

Fig. C-1: Expected performance HLW (3D component model): Spatial distribution of temperature after (a) 100 years, (b) 200 years, (c) 500 years, and (d) 1,000 years C-2

Fig. C-2: Expected performance HLW (3D component model): Spatial distribution of gas saturation after (a) 100 years, (b) 200 years, (c) 500 years, and (d) 1,000 years C-3

Fig. C-3: Expected performance HLW (3D component model): Spatial distribution of pressure after (a) 100 years, (b) 200 years, (c) 500 years, and (d) 1,000 years C-4

Fig. C-4: Expected performance HLW (2D component model): Spatial distribution of temperature after (a) 50 years, (b) 100 years, (c) 200 years, (d) 500 years, (e) 1,000 years, (f) 10,000 years, (g) 20,000 years, and (h) 100,000 years C-5

Fig. C-5: Expected performance HLW (2D component model): Spatial distribution of gas saturation after (a) 50 years, (b) 100 years, (c) 200 years, (d) 500 years, (e) 1,000 years, (f) 10,000 years, (g) 20,000 years, and (h) 100,000 years C-6

Fig. C-6: Expected performance HLW (2D component model): Spatial distribution of pressure after (a) 50 years, (b) 100 years, (c) 200 years, (d) 500 years, (e) 1,000 years, (f) 10,000 years, (g) 20,000 years, and (h) 100,000 years..... C-7

Fig. C-7: Expected performance HLW (2D component model): Spatial distribution of I-129 liquid saturation after (a) 100,000 years, (b) 200,000 years, (c) 500,000 years, and (d) 1,000,000 years..... C-8

Fig. C-8: Expected performance HLW with H_2 molecular diffusion (2D component model): best estimate and uncertainty ranges C-10

Fig. C-9: Expected performance HLW with water consumption (2D component model): best estimate and uncertainty ranges C-12

Fig. D-1: Expected performance L/ILW (3D component model up to V2-L/ILW): Spatial distribution of gas saturation after (a) 1,000 years, (b) 10,000 years, (c) 50,000 years, and (d) 100,000 years..... D-2

Fig. D-2: Expected performance L/ILW (3D component model up to V2-L/ILW): Spatial distribution of pressure after (a) 1,000 years, (b) 10,000 years, (c) 50,000 years, and (d) 100,000 years..... D-3

Fig. D-3: Expected performance L/ILW (2.5D component model up to V2-L/ILW): Spatial distribution of gas saturation after (a) 1,000 years, (b) 10,000 years, (c) 50,000 years, and (d) 100,000 years..... D-4

Fig. D-4: Expected performance L/ILW (2.5D component model up to V2-L/ILW): Spatial distribution of pressure after (a) 1,000 years, (b) 10,000 years, (c) 50,000 years, and (d) 100,000 years..... D-5

Fig. D-5: Expected performance L/ILW (2.5D component model up to V2-L/ILW): Spatial distribution of Cl-36 liquid saturation after (a) 100,000 years, (b) 200,000 years, (c) 500,000 years, and (d) 1,000,000 years..... D-6

Fig. D-6: Expected performance L/ILW with water consumption and H_2 molecular diffusion (3D component model): Spatial distribution of gas saturation after (a) 1,000 years, (b) 10,000 years, (c) 50,000 years, and (d) 100,000 years..... D-8

Fig. D-7: Expected performance L/ILW with water consumption and H_2 molecular diffusion (3D component model): Spatial distribution of pressure after (a) 1,000 years, (b) 10,000 years, (c) 50,000 years, and (d) 100,000 years..... D-9

Fig. D-8: Expected barrier performance L/ILW with H_2 molecular diffusion (2.5D component model): best estimate and uncertainty range of gas induced overpressures in the L/ILW nearfield..... D-10

Fig. D-9: Expected barrier performance L/ILW with water consumption (2.5D component model): Best estimate and uncertainty range of gas induced overpressures in the L/ILW nearfield..... D-11

Fig. E-1: Comparison between (a) tracer mass fluxes and (b) normalised tracer mass fluxes at top-OPA obtained in 1D with PICNIC and in 2D with TOUGH2, for the case of tracer transport by diffusion only.....E-2

Fig. E-2: Comparison between (a) tracer mass fluxes and (b) normalised tracer mass fluxes (right) at top-OPA obtained in 1D with PICNIC and in 2D with TOUGH2, for the case of tracer transport by diffusion and advection with vf = 2E-14 m/s (Pe = 0.344).....E-3

List of Acronyms

AAK	Anhydritic-argillaceous Keuper
AD	Argillaceous Dogger
AL	Argillaceous Lias
ATW	Alpha-toxic waste
BD	Brauner Dogger
BLOCK	Bentonite pedestal
BOTBC	Bottom boundary
BWR	Boiling-water reactor
CAN	Canister (elements)
CD	Calcareous Dogger
CL	Calcareous Lias
CM	Calcareous Malm
CPM	Continuous porous media (model)
CRZ	Containment-providing rock zone
DAK	Dolomitic-anhydritic Keuper
DFN	Discrete-fracture network (model)
DK	Dolomitic Keuper
DM	Dolomitic Malm
EBS	Engineered barrier system
EDZ	Excavation damaged zone
ENSI	Swiss Federal Nuclear Safety Inspectorate
EUU	Pilot facility for underground geological investigations (*erdwissenschaftlichen Untersuchungen untertag*)
FCONC	Concrete fillings
FPG	Failure potential (of intact rock), gas-induced
FPH	Failure potential (of intact rock), heat-induced
FPI	Failure potential of intact rock
HERRE/HERW	Herrenwis unit
HLW	High-level waste (spent fuel assemblies and high-level waste from reprocessing)
IRF	Instantaneous release fraction
JO	Jura Ost proposed siting region

KEG	Nuclear Energy Act
KEV	Nuclear Energy Ordinance
LCU	Lower confining unit
L/ILW	Low- and intermediate-level waste
MAK	Massive anhydritic Keuper
MIRAM	Model Inventory of Radioactive Materials
ML	Marly Lias
MM	Marly Malm
MORT1	Mortar
MUSCH	Muschelkalk
NAB	Nagra Work Report
NBT	Normalised buffer temperature
NL	Nördlich Lägern proposed siting region
NTB	Nagra Technical Report
(N)TF	(Normalised) tracer flux
OPA	Opalinus Clay
PA	Performance assessment
PELL	Bentonite buffer
PERM	Permo Carboniferous
PWR	Pressurised-water reactor
QUART	Quaternary
RBG	General licence application (*Rahmenbewilligungsgesuch*)
REV	Representative elementary volume
RP-HLW	(Vitrified) reprocessing high-level waste
SA	Safety assessment
SCAD	Sandy-calcareous argillaceous Dogger
S/B	Sand/bentonite mixture
SCD	Sandy-calcareous Dogger
SF	Spent fuel
SGT	Sectoral Plan for Deep Geological Repositories
SK	Sandy Keuper
TERT	Tertiary
THM-C	Thermal, hydraulic, mechanical and chemical (interactions)

TOPBC	Top boundary
UPU	Upper confining unit
V&V	Verification and (model) validation
WP	Waste package
ZNO	Zürich Nord Ost proposed siting region

1 Introduction

1.1 Background and scope

In Switzerland, legal regulations (Nuclear Energy Act (KEG 2003) and Nuclear Energy Ordinance (KEV 2004)) and guidelines are in place for the management of radioactive waste. The Nuclear Energy Ordinance (KEV) classifies Switzerland's radioactive waste into low- and intermediate-level waste (L/ILW), alpha-toxic waste[1] (ATW) and high-level waste (HLW), the latter comprising spent fuel (SF) and vitrified HLW from reprocessing (RP-HLW). The Nuclear Energy Act (KEG) requires the disposal of all these types of radioactive waste in deep geological repositories. The feasibility of this disposal solution has been demonstrated for L/ILW in Nagra (1985) and for long-lived intermediate-level waste and HLW in Nagra (2002).

The Sectoral Plan for Deep Geological Repositories (SGT) regulates the search for suitable siting regions for deep geological repositories in Switzerland. This site selection process is conducted in three stages (BFE 2008). Stages 1 and 2 have already been completed and Nagra is currently in Stage 3 (SGT-E3). Clarifications on the safety-related specifications for this stage are provided in ENSI 33/649 (ENSI 2018), while ENSI Guideline G03 and the corresponding explanatory report (ENSI 2023, ENSI 2020) specify the protection objective, protection criteria and design principles for deep geological repositories.

In SGT-E3, three siting regions located in Northern Switzerland have been considered – Jura Ost (JO), Nördlich Lägern (NL) and Zürich Nordost (ZNO) – with the objective of selecting one siting region for an HLW repository, one for an L/ILW repository, or one for a combined repository for all waste types.

Following a comparison of these siting regions, Nagra concluded that NL is the safest and most flexible siting region. Therefore, it is applying for a general licence for a repository for both HLW and L/ILW, with surface facilities at the Haberstal site (municipality of Stadel, ZH).

The justification for this selection and the safety demonstration for a repository at the site are submitted as part of the general licence application (RBG[2]). The reports relating to post-closure safety, shown in Fig. 1-1, are structured as follows:

- The overall safety-related argumentation, including post-closure and operational safety, is summarised in an overarching safety report ("*Sicherheitsbericht"*) NTB 24-01 (Nagra 2025b) shown at the top of Fig. 1-1.
- The upper left side of Fig. 1-1 shows the reports supporting Nagra's site comparison. The available options are compared with respect to safety and technical feasibility and the results are synthesised in NTB 24-03 (Nagra 2025a) («B*ericht zur Begründung der Standortwahl»*).
- The upper right side of Fig. 1-1 shows the reports documenting the post-closure safety case for the combined repository at the site, including its synthesis in the post-closure safety report NTB 24-10 (Nagra 2024f).
- The lower part of Fig. 1-1 shows a report that presents the safety and repository concept, including the provisional design, and reports providing the assessment basis.

The present report is bordered in red in Fig. 1-1.

---

[1] According to Nagra (2024a), ATW can coexist with L/ILW within the same emplacement caverns. As a result, for the sake of simplicity, the term L/ILW encompasses ATW without explicit mention.

[2] From the German *Rahmenbewilligungsgesuch*.

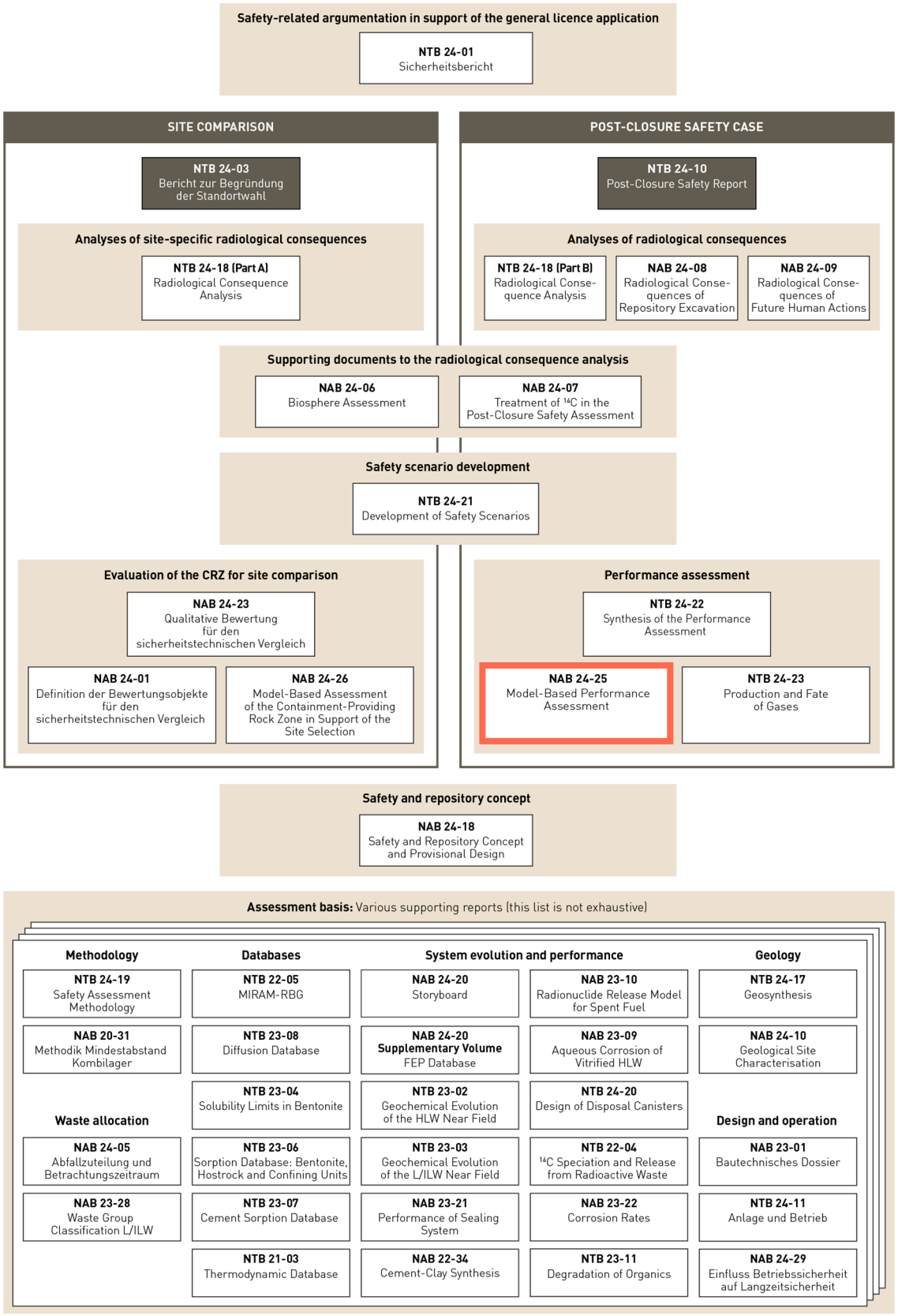

Fig. 1-1: Structure of reports covering post-closure safety aspects of the site comparison and the post-closure safety case

The post-closure protection objective for a deep geological repository is the permanent protection of humans and the environment (KEG 2003, ENSI 2023). The protection objective, design principles, protection criteria and the safety and repository concept inform the iterative design development process. This process leads to a provisional design and implementation plan for a combined repository at the Haberstal site, to serve as the basis for the post-closure safety case and underlying safety assessment (SA) (as documented in the reports shown on the upper right side of Fig. 1-1). The SA consists of four main processes:

- **performance assessment** (PA), in which the thermal, hydraulic, mechanical, and chemical (THM-C) evolution of the repository system is analysed;
- **safety scenario development**, which entails the identification and description of a set of safety scenarios that capture uncertainty in initial state and subsequent evolution of the repository system over time;
- **analysis of radiological consequences**, which consists of an evaluation of radionuclide release rates to the surface environment as a function of time; and
- **demonstration of post-closure safety**, in which evidence, arguments and results from the three previous steps are brought together in the post-closure safety report (cf. Fig. 1-1).

1.2 Objectives

The first step of the PA, elaborated in Nagra (2024g), is the comprehensive, quantitative understanding of the thermo-hydraulic evolution of the repository associated with the production and fate of gases in the underground structures. This is done on the scale of the entire repository as well as on the scale of individual components (Nagra 2024g). The present report builds upon that understanding to take the next step in the PA: the implementation of a robust modelling workflow and the delivery of model-based analyses to the PA of the repository as a total system, which includes the disposal areas, access structures and sealing sections, as well as focused on HLW and L/ILW, respectively. The outcomes of this step feed into the synthesis of the PA (Nagra 2024j) which constitutes the first stage of the safety assessment as described in Section 1.1.

To achieve this goal, the objectives set forth in the present report are to provide:

- *Obj1*: a comprehensive outline of numerical models used in the PA, including the input data, the configuration of each model, the model outputs evaluated in each model, and the links between models in the modelling chain;
- *Obj2*: a comprehensive description of the abstraction methodology that encompasses the treatment of conceptual uncertainty, the justification of choices and conservatism in model implementations, and model benchmarking;
- *Obj3*: an overview of the modelling workflow implemented for the model-based assessments including the role of each model;
- *Obj4*: documentation and comprehensive overview of the deterministic modelling performed for the total system as well as the probabilistic modelling performed for HLW and L/ILW, respectively.

1.3 Report outline

The chapters of this report are structured as follows. Chapter 2 describes the background, includeing an outline of the current, exemplified repository project and an overview of the PA methodology. Chapter 3 provides a comprehensive description of the model portfolio used in the PA. Chapter 4 is dedicated to the abstraction methodology used for the development of the model chain. Chapter 5 gives an overview of the modelling workflow that is implemented using the model chain. Chapter 6 describes the total system analysis, with a detailed description of the assessment cases and the respective modelling results. In a similar fashion, Chapters 7 and 8 describe the probabilistic simulations performed for HLW and L/ILW, respectively. Finally, Chapter 9 provides a synthesis and main conclusions of the report.

The objectives stated in Section 1.2 are addressed as follows. Objective *Obj1* is addressed in Chapter 3. Objective *Obj2* is addressed in Chapter 4. Objective *Obj3* is addressed in Chapter 5. Objective *Obj4* are addressed in Chapters 6, 7, and 8.

2 Repository concept and performance assessment

2.1 Repository concept and provisional design

2.1.1 Safety and repository concept

The safety concept explains how, through the safety barriers and the safety functions they perform, the geological deep repository ensures the protection of humans and the environment. The current repository concept describes the safety barriers and their properties, including their interactions. The safety concept and repository concept are thus closely intertwined and are collectively referred to as the safety and repository concept. The current safety and repository concept as described below is exemplified for the purpose of safety demonstration in the framework of the RBG. Further details can be found in detail in Nagra (2024h). The current Swiss safety concept for deep geological disposal of radioactive waste is based on a system of staggered passive barriers, termed the *multi-barrier system*, that operates passively such that after closure of the repository no further measures are required to ensure long-term safety. The repository is provisionally designed in such a way that it is largely insensitive to the remaining uncertainties associated with the long-term evolution of the backfilled repository structures (including the repository induced effects) and the geological environment, providing additional confidence in the robustness and reliability of the safety concept.

The geological barrier is of primary importance in the long term, mainly due to the excellent safety-related properties and long-term stability of the containment-providing rock zone (CRZ). The CRZ includes the Opalinus Clay (OPA), as well as the geological units above or below the host rock that also contribute to radionuclide immobilisation and retardation of release. The geological barrier is at sufficient depth to limit any possible impact of events and processes at the surface on the safety-related properties of the OPA as well as its confining geological units.

The geological barrier is complemented by a mutually compatible set of engineered barriers, implemented in the provisional design as described in the next section.

2.1.2 Provisional design

The provisional design for the exemplified repository used as a basis for the model-based analyses discussed in the present report, i.e., the current implementation of the safety and repository concept, is summarised in the following text. More details can be found in Nagra (2024h) and Nagra (2025b).

The provisional repository design for the exemplified repository envisages two repository sections, one for HLW (including both RP-HLW and SF) and one for L/ILW (including ATW) co-located at the same site (Fig. 2-1) and in the same host rock, yet spatially separated with a distance of nearly 2 km. The underground facilities of the repository in the provisional layout described here for the purpose of the RBG are located roughly in the middle of the OPA, at a depth between 800 and 900 m below ground level (b.g.l.) at the Haberstal site. Waste disposal takes place in parallel dead-end emplacement rooms (HLW emplacement drifts and L/ILW emplacement caverns). The HLW disposal canisters with the SF assemblies and vitrified RP-HLW flasks comprise the innermost engineered barriers. The canisters are emplaced in drifts that are subsequently backfilled with a compacted bentonite buffer and sealed, forming an additional engineered barrier for the HLW. For L/ILW disposal, an engineered barrier is put in place with the cementitious nearfield. This is established with cementitious material used to fill voids between L/ILW waste packages inside waste containers and with cement-based mortar surrounding the containers, respectively. In addition to the main HLW and L/ILW disposal areas, each disposal section includes a pilot facility (Fig. 2-1), where the behaviour of the wastes, the backfill,

the seals and the host rock is monitored until the end of a monitoring phase. The spatial separation between the HLW emplacement drifts and the L/ILW emplacement caverns is such that interactions between the two disposal areas are minimised. The repository is connected to the surface via three shafts: an access shaft, an operation shaft and a ventilation shaft (Fig. 2-1). In this provisional design, elements of the surface infrastructure and some of the access structures are shared between the two repository sections. The waste emplacement rooms are backfilled in parallel with the emplacement of the waste, and a sealing system is currently planned to be installed to close the repository.

2.1.3 HLW disposal area

According to the provisional design, HLW are encapsulated in carbon steel disposal canisters, placed coaxially along the emplacement drifts, with the surrounding space filled with the bentonite buffer (Fig. 2-1). The ~800 m long drifts have a diameter of about 3.2 to 3.9 m, including prefabricated concrete liner segments (tubbing) to provide support. The gap between the tubbing and the rock is filled with mortar material. The disposal canisters are emplaced every 3 m on pedestals made of compacted bentonite blocks. The remaining space between the disposal canisters and the tubbing are backfilled with granular bentonite material. The emplacement drifts are accessed from the operations tunnel through branching tunnels with an area for transferring the waste into the drifts.

2.1.4 L/ILW disposal area

The L/ILW emplacement caverns are ~240 m long and have a cross-section of approximately 12.5 m × 13.5 m, supported by rock bolts and a two-shell lining made of sprayed reinforced shotcrete and unreinforced concrete. The disposal containers are stacked in arrays and the void spaces between the cavern walls and the containers as well as gaps between containers are filled with a porous cementitious mortar (Fig. 2-1). In the model-based assessments presented in this report, it is assumed that disposal containers correspond to type LC-86H (Nagra 2023b). The emplacement caverns are accessed from the operations tunnel through branching tunnels with an area for unloading and receiving disposal containers at the mouth of the cavern. Most of the L/ILW is assumed to be compacted, embedded in a cement/mortar matrix and placed in standardised 200 L drums, MOSAIK-II-type casks made of cast iron, or steel flasks. These waste packages are placed inside containers made of reinforced concrete and infilled with a cement-based mortar. The L/ILW containers are emplaced in the caverns, which are then backfilled with a cement-based mortar.

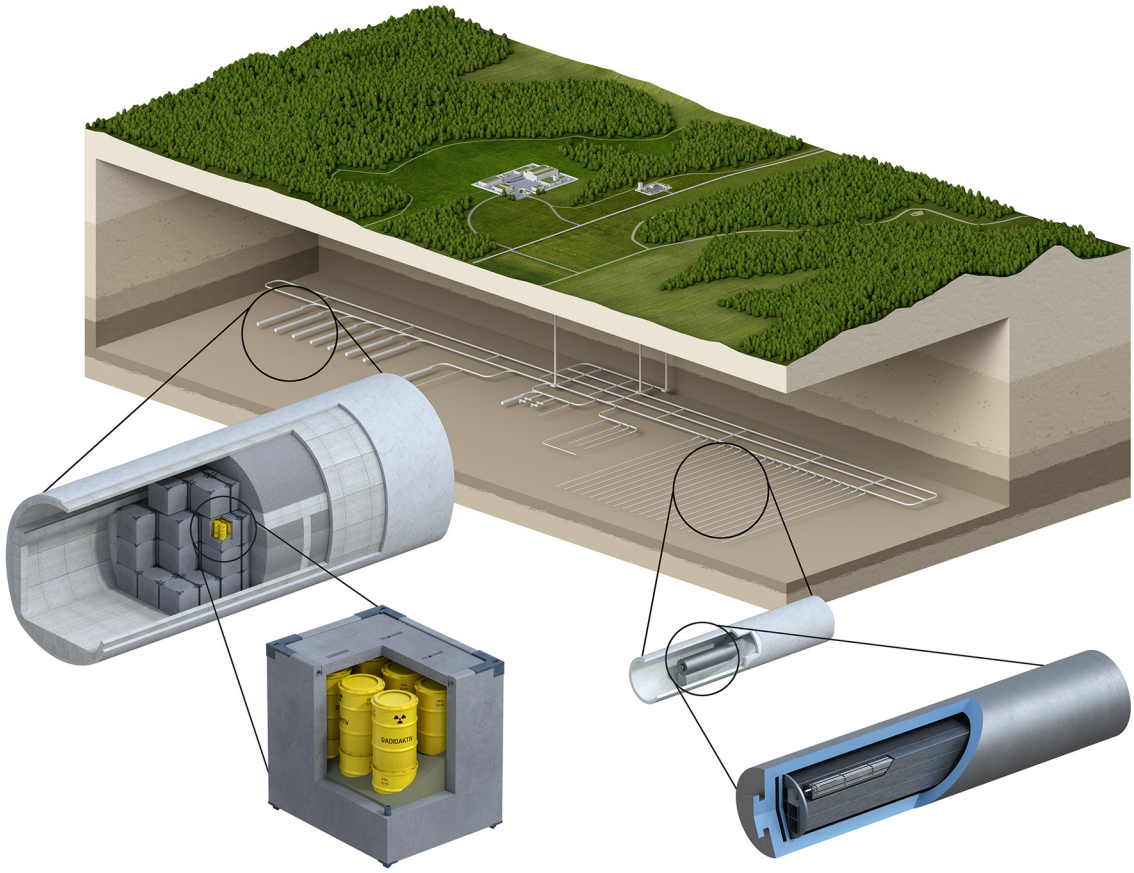

Fig. 2-1: Schematic view of the provisional repository design with the L/ILW emplacement caverns (left) and the HLW emplacement drifts (right)

2.1.5 Sealing and backfill system

According to the provisional design, the sealing and backfill system includes multiple individual seals as well as the backfilling of all underground openings. The provisional repository design foresees the following types of seals:

- V1-HLW and V1-L/ILW seals (emplacement room seals) located at the mouth of the HLW emplacement drifts and L/ILW emplacement caverns, respectively (Fig. 2-2). These seals are installed immediately after emplacement of the waste and the complete backfilling of the emplacement rooms.
- V2-HLW and V2-L/ILW seals (disposal area access seals) located at the mouth of the disposal area accessways (in the construction, operations and ventilation tunnels) of the HLW repository section and the L/ILW repository section (in the ventilation and operations tunnel), respectively (Fig. 2-2).
- V3 seals are placed in the access, ventilation and operation shafts up to the top of the OPA host rock to seal the repository from the surface environment and protect it from external impacts. These are the outermost seals (Fig. 2-2).

Backfill material is emplaced in the underground openings between these seals: VF1 between the V1 and V2 seals and VF2 between the V2 and V3 seals (Fig. 2-2). Further information on these materials and the provisional engineering design and functions of the sealing system are given in Martin et al. (2023) and Nagra (2024g).

2.1.6 Implementation timeline for performance assessment

A total of five main operational phases are defined for the implementation of a combined repository in the model-based PA analyses. These phases and sub-phases are described in Tab. 2-1.

Tab. 2-1: Generic timeline for the implementation of a combined repository, as assumed in model-based analyses of repository performance

(Modified after Nagra 2021 and Nagra 2024b).

Phase	**Description**
Operations phase 1	Construction and operation of central and test area (**0 – 21 years**).
Operations phase 1b	Construction of main repository L/ILW (**21 – 34 years**).
Operations phase 2a	Construction and waste emplacement RP-HLW (**34 – 36 years**).
Operations phase 2b	Construction and waste emplacement SF (**36 – 46 years**).
Operations phase 3	First monitoring phase (**46 – 56 years**): Backfilling of HLW emplacement rooms and L/ILW caverns.s
Operations phase 4	Second monitoring phase (**56 – 96 years**): Backfilling of all underground structures except access tunnels to pilot repository.
Post closure phase	All repository components backfilled and sealed (>**96 years**).

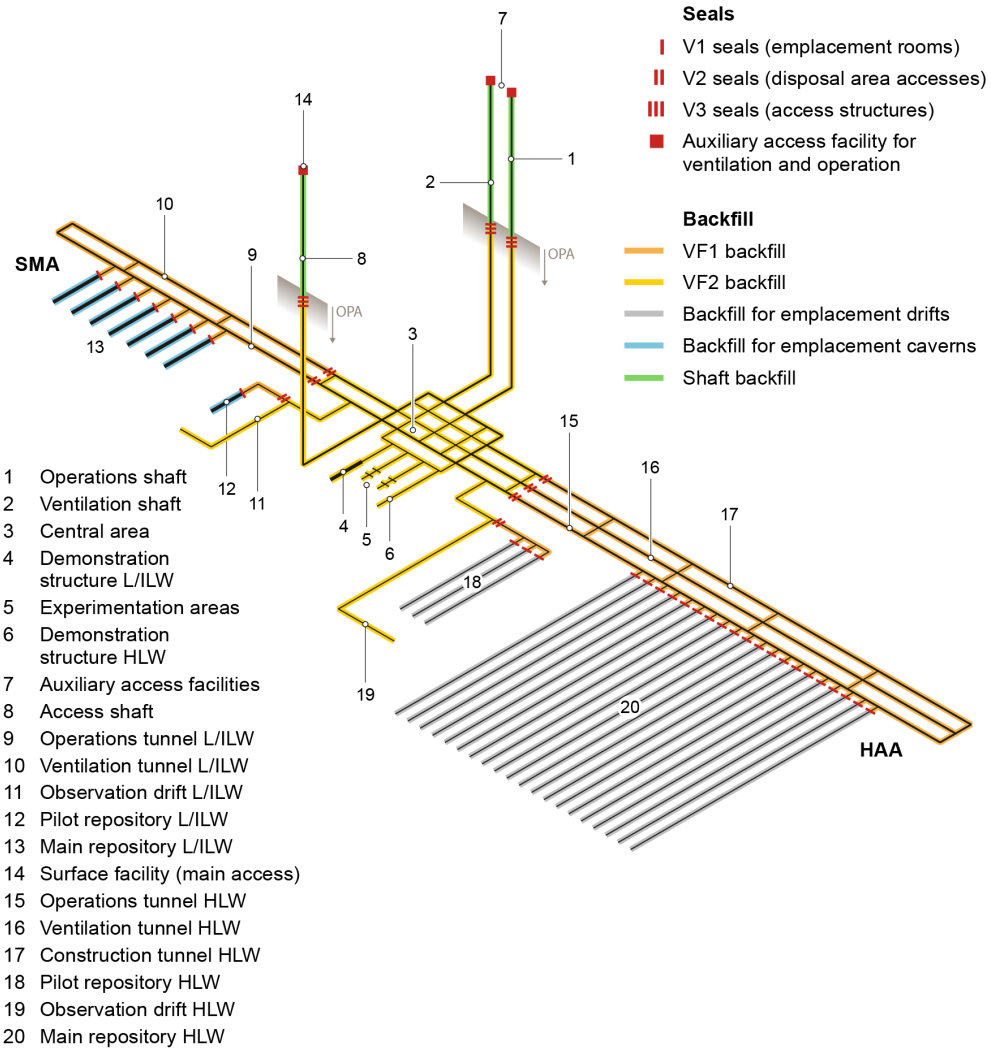

Fig. 2-2: Location of the closure structures in the current concept of a combined repository

This provisional design may be refined and modified.

2.1.7 Waste inventory and source terms

This section provides a brief summary of the materials generating gas, based on the waste inventory. Further information can be found in Nagra (2024g), Diomidis et al. (2023), Guillemot et al. (2023), and Nagra (2023b).

The inventory of all of Switzerland's radioactive waste that exists today and will be produced in the future has been compiled specifically for the RBG in the database called MIRAM-RBG (Model Inventory of Radioactive Materials), documented in Nagra (2023b).

L/ILW (including ATW) arises during the operation and decommissioning of nuclear power plants and also as a result of medical, industrial and research activities. It includes inorganics, metals and organic materials within the waste matrix, containers and backfill (Nagra 2023b). The metals and alloys present in L/ILW correspond to the majority of the L/ILW materials generating gas. Iron and carbon steel, followed by stainless steel and Ni alloys, are especially the two largest corrosion groups of L/ILW metals (Nagra 2023b). Organic materials present in L/ILW also

generate gas. They are almost exclusively part of the waste form and mainly present as ion-exchange resins (including polystyrene and styrene), polyvinyl chloride and bitumen (Nagra 2023b).

In HLW (including SF and RP-HLW), metals are the materials largely contributing to gas generation. Only a negligeable amount of organics are inventoried (Nagra 2023b). Iron and carbon steel form by far the largest corrosion group of HLW metals, mainly because of the disposal canisters (Nagra 2023b).

In the provisional design for the exemplified repository, iron and carbon steel is expected to be used as building materials for tunnel support, concrete reinforcement and shaft lining. It should be noted that metals used for the construction of the deep geological repository currently correspond to half of the total metal mass foreseen (including L/ILW and HLW matrices, backfilling, containers and canisters) (Nagra 2024g).

2.2 Performance assessment

2.2.1 General approach

A shot summary of key aspects of the PA is given in the following text. More details are provided in Nagra (2024j).

Assessment basis

The quality of the PA, and of the SA overall, rests on a sound assessment basis. The assessment basis is defined as the evidence, knowledge, assessment tools, and methodologies developed or acquired by Nagra in support of the SA. Key inputs from the assessment basis needed for the assessment of repository performance on the scale of components and on the scale of the total system are as follows:

- the radionuclide inventory and a description of the waste forms, masses and volumes provided by the MIRAM-RBG database (Nagra 2023b);
- the interpretation of the geoscientific databases gathered during site-specific investigation programmes and the synthesis of the geoscientific interpretations in the context of the regional geological setting (Nagra 2024c);
- a comprehensive description of the phenomenological evolution of the geological repository in the OPA formation from the perspective of long-term safety (Nagra 2024e);
- the models and codes that support the present model-based PA calculations (Nagra 2024i).

Claims, arguments and evidence

The need for an auditable assessment framework calls for a traceable method of proof with quantitative performance targets whenever possible. For this, claims are formulated to describe how the individual repository components, and the repository system as a whole, contribute to the different safety functions. A suite of arguments, backed up by evidence, is developed to substantiate each claim. A claim can be said to be robust if it is well substantiated by sound arguments and convincing evidence. In line with the assessment principles, the robustness of a claim is strengthened by seeking multiple lines of arguments. Claims, arguments and evidence used by the PA are fully listed and described in Nagra (2024j).

As part of their substantiation, and in accordance with the assessment principles (i.e., rigour in consideration and treatment of uncertainty; validation and verification of models and databases; multiple lines of arguments for safety; and assurance of completeness; cf. Nagra 2024f), claims need to be tested for their robustness with respect to uncertainties. This includes, for example, uncertainties in the occurrence of processes, the spatial extent of features and the timing of events. Specific arguments may be developed for robustness with respect to some uncertain phenomena. In addition, model-supported quantitative assessments, including sensitivity and uncertainty analyses, support the assessment of robustness in the synthesis of the PA as described in Nagra (2024j).

Indicator approach

Model-supported quantitative assessments apply, wherever possible, a so-called indicator approach, similar to the criteria-based indicator approach applied in the context of the site comparison (Nagra 2024d). The approach involves the use of numerical models to evaluate a set of performance indicators or indices, which are compared with a set of performance targets. A detailed discussion of the indicator approach used in the PA is provided in Nagra (2024j). In the present report, a set of model outputs is defined in Chapter 3 to be delivered by numerical modeling as input to Nagra (2024j).

2.2.2 Performance assessment of the total system

The construction and operation of a deep geological repository changes the conditions in the vicinity of the underground structures, creating thermal, hydraulic, geomechanical and geochemical disequilibria in the repository nearfield over an extended period of time. These perturbations of the physico-chemical state conditions could give rise to THM-C interactions between the repository components, which may also trigger microbiological activities. Nagra (2024j) addresses the impact of THM-C interactions on the overall performance of the repository system with the aid of the modelling analyses delivered with the present report.

The main drivers for such interactions are phenomena and processes that occur along the backfilled and sealed underground structures. Accordingly, modelling to identify these needs to be done on the scale of the entire repository, which is computationally intensive. Computationally intensive simulations allow only a limited number of numerical analyses, addressing deterministic cases of expected repository performance and possible deviations thereof. State variables such as temperature, pore pressure and gas saturation in the repository nearfield obtained with repository-scale modelling are delivered as input to Nagra (2024j).

2.2.3 Performance assessment at component level

Specific properties of, or actions to be performed by, one or more system features, including features of the system that contribute directly or indirectly to safety functions are termed *component-specific functions* and are fully described in Nagra (2024h). Specific claims inherent in these component-specific functions are examined in Nagra (2024j) at the component level. The claims are statements that express the ways in which the components (i.e., SF/RP-HLW, HLW disposal canister, bentonite backfill, cementitious nearfield, closure system and backfill, and geological barrier system) contribute to the repository safety functions. If the barrier component consists of sub-components which contribute separately to the safety functions, the claims are assigned specifically to the sub-components. For instance, the seals of the closure system in the HLW repository section (V1-HLW, V2-HLW) are considered separately from those of the L/ILW

disposal section (V1-L/ILW, V2-L/ILW), because they perform different safety functions. To support the synthesis of the PA in Nagra (2024j), the present report delivers modelling results also on the component level in addition to the level of the total system.

2.2.4 Uncertainty assessment and quantification

Traceable handling of uncertainty is an indispensable element in the confidence building process contributing to the assessment of post-closure performance and safety of deep geological repositories (Nagra 2024i). It is common practice to categorise uncertainty as *scenario uncertainty*, *model uncertainty* (also termed *conceptual uncertainty*) and data uncertainty (also termed *parameter uncertainty*). Thacker et al. (2004) define uncertainty as a potential deficiency to describe the exact state of a physical system or numerical model that is due to inherent variability (*irreducible uncertainty*) or lack of knowledge (*reducible uncertainty*). The effect, when uncertainties of input parameters of a physical system or numerical model give rise to uncertainties in the system response, is termed *propagation of uncertainty*. The systematic characterisation of all input and model uncertainties and the analysis of their effects on the (computed) model response is called *uncertainty quantification*, aimed at bracketing the confidence bounds on the expected system response.

Uncertainty quantification in PA is embedded in the general SA uncertainty management framework (Nagra 2024i). According to Nagra (2024j), the process of uncertainty quantification can be decomposed in two key steps:

- *Identification and quantification of uncertainties associated with model abstractions:* Conceptual uncertainties associated with the model abstraction process are identified and quantified in numerical benchmarks as part of a model validation procedure to ensure readiness of the simplified PA models to be used for quantitative analyses.
- *Probabilistic PA - quantification of confidence ranges:* Parametric uncertainty of PA model inputs is used to calculate the confidence ranges of the PA model outputs.

The assessment workflows are embedded in a long-term code verification and model validation process in the framework of Nagra's RD&D Programme (Nagra 2024j).

3 Modelling tools and approaches

3.1 Model portfolio – overview

3.1.1 Codes

The model-based assessments require flow and transport modelling under two-phase conditions associated with the ventilation and backfilling of the repository with partially saturated materials, followed by resaturation with porewater and generation of gas from corrosion of metals and degradation of organics in the post-closure phase. In the HLW repository, these effects are further coupled with thermal effects from heat generated by the waste. As stipulated in Nagra (2024g), it is assumed that gases generated in the repository have the properties of hydrogen. Based on this, two-phase modelling is predominantly performed using the EOS5 Equation-of-State module of the TOUGH3 code (Jung et al. 2018) for simulating the isothermal or non-isothermal, fully coupled flow and transport of hydrogen and water in porous media. In addition, EOS7R is used to simulate two-phase flow with one soluble radionuclide in the liquid phase and/or one volatile radionuclide in the gas phase (Jung et al. 2018). Modelling of solute transport under single-phase conditions is performed with EOS1 for water and tracer (Jung et al. 2018).

Probabilistic simulations are performed either with TOUGH3 or, in case of inverse modelling, the iTOUGH2 simulation-optimisation framework (Finsterle 2007) which integrates the non-isothermal single- and multi-phase flow and transport modules used in the TOUGH3 simulations.

Fully coupled THM modelling is performed with the Code_Aster® finite element simulator for multi-physical analysis and modelling (EDF 2016). In particular, the THM module (EDF 2021) is used for non-isothermal, fully coupled flow and transport of hydrogen and water in deformable porous media that is relevant to thermally- and gas-induced effects in the HLW nearfield.

3.1.2 Scales of interest

The tools integrated in the modelling workflow are implemented based on the principles described in Chapter 2. In general, the level of abstraction of a model depends on the model purpose. For assessment models this corresponds to the performance indicators for which the assessment requires quantitative estimates. Particularly in problems of two-phase flow and transport in materials that exhibit property contrasts, the computational demand limits the model size that allows for efficient and robust implementation. The model abstraction chain therefore encompasses models with different levels of detail that are implemented on different spatial scales of interest.

Site models (3D)

The largest models used in the modelling workflow comprise the stack of geological formations in the primary investigation perimeter in the siting region, thus extending to several kilometres from the repository location. The combined repository is not represented explicitly but, if needed, through source terms assigned directly to the OPA at the corresponding locations of the HLW and L/ILW disposal areas, respectively.

Repository and component models for deterministic assessments (3D)

Assessments on the total system level can be performed with a so-called *repository model* that represents in 3D and in an explicit manner the entire geological repository for disposal of HLW and L/ILW in the siting region. The geometric representation of the repository structures is not exact but stylised and approximated through appropriate volumetric scaling. Accordingly, materials within the repository structures are represented by homogenised equivalent media with effective properties.

Analyses on the level of components can be carried out with so-called *component models* that represent in 3D selected parts of the repository that are relevant to safety, namely the emplacement rooms for HLW and L/ILW and the V1, V2, and V3 sealing sections. The geometric representations on this scale become more accurate, and materials explicitly represented in the models are, at least to some extent, as foreseen in the provisional design of the respective component.

An overview of the 3D repository and component models are provided in Section 3.3.

Component models for probabilistic assessments (2D)

Sampling-based probabilistic assessments gain robustness with decreasing dimensionality respectively model mesh size. To achieve this, additional models are implemented in 2D representing cross-sections through the HLW and L/ILW emplacement rooms with the host rock and over- and underlying formations, respectively. The level of discretisation allows to discern the main safety-relevant features of the emplacement rooms. Detailed descriptions of the 2D component models for HLW and L/ILW are given in Sections 3.4 and 3.5, respectively.

Process models (2D)

Emplacement rooms are represented in greater detail in so-called *process models* that aim to reduce dimensionality but at the same time minimise geometric approximations. This approach helps to isolate effects that are strictly relevant to the physical processes and their mathematical and numerical formulation. Examples of process models used in the present analysis are given in Section 3.6.

3.1.3 Intended use of model portfolio

The 3D site model, and variants thereof, essentially represents the upper-level PA abstraction of the site descriptive model developed for the siting region. The intended use of the 3D site model is twofold. The first task of this model is to deliver simulations that need to incorporate information on the scale of the entire primary investigation area in the siting region, such as regional aquifers or data from investigation boreholes. For example, the 3D site model is used for inverse modelling of formation thermal conductivities to temperature profiles measured in deep boreholes in the siting region, and to provide estimates of in-situ temperature distributions in the area of the repository (Nagra 2024k). The second task of the 3D site model is to provide the basis to extract base geometries, either in 3D or 2D, used to subsequently implement other assessment models at various degrees of detail. The present report focuses on the second task, whereas simulations performed with the 3D site model are described in Nagra (2024k).

The 3D repository and component models for deterministic assessments set the basis for the PA as follows. Firstly, the 3D appraisal provides a comprehensive picture of flow and transport of fluid phases, constituents and energy through the repository structures and surrounding rock. Accordingly, these models provide the underpinning assessment of the hydraulic evolution of the repository under consideration of production and fate of gas in Nagra (2024g). Moreover, the 3D repository and component models are the part of the model abstraction chain and are used to

evaluate model performance each time abstractions are applied, e.g., from 3D to 2D, as discussed in Chapter 4. Lastly, these models provide results that feed directly into the PA either on the level of total system or the level of components, discussed in Chapters 6, 7, and 8.

As offspring of the abstraction process, the 2D component models for probabilistic assessments are used to provide confidence ranges around the best estimates for the expected performance and for additional scenarios of the PA. The model outcomes are accordingly evaluated in terms of quantitative outputs, discussed in Section 3.7, and feed into the assessments of Chapters 7 and 8.

The process models are an integral part of the model chain as they essentially provide the fundament of process abstraction. As discussed in Chapter 4, benchmarking and validation exercises between assessment models and process models allow the abstraction of fully coupled $TH^2M(C)$ considerations into more robust TH^2 formulations and subsequently to simpler hydraulic / transport problems used at the highest level of abstraction.

3.2 Site models (3D)

An illustration of the 3D site model is shown in Fig. 3-1. Details on the model implementation and the simulations performed in support of the PA are documented in Nagra (2024k).

In the horizontal direction, the model covers an area of ~9 × 4 km^2 discretised with a regular grid of 100 × 100 m^2. The primary model axes are rotated counterclockwise so that the Y axis deviates 15.6° from the N-S line. The coordinates of the bottom left (SW) corner of the model are (675,300; 263,800). In the vertical direction, the model extends from the top of the Permo-Carboniferous to ground surface. The vertical extent varies depending on the formation thicknesses, respectively the elevations of formation top and bottom surfaces that come from the seismic interpretation (Nagra 2024 *in prep.*). The formations are accordingly inclined in space as shown in Nagra (2024). The variable elevations are assigned to the site model layers representing stratigraphic units respectively listed in Tab. 3-1. Sublayers are assigned in different site model versions depending on purpose, e.g., for finer discretisation or further subdivision of specific formations. Note that not all stratigraphic units distinguished in the seismic interpretation are explicitly accounted for in the model representation. The PA modelling is based on the simplified representation into major formations as shown in Tab. 3-1. No faults are explicitly accounted for in the modelled area (hypothetical faults are implemented in exemplified model calculations for the purpose of scenario analysis, see Chapters 6, 7, and 8).

A set of baseline properties, namely hydraulic conductivity and porosity, is taken from the geosynthesis (Nagra 2024c, Nagra 2024f) and assigned to the modelled formations as shown in Tab. 3-2 and Tab. 3-3. When stratigraphic units are combined in the model representation, arithmetic averages weighted by a representative formation thickness are used for porosity and horizontal hydraulic conductivity, whereas harmonic averages weighted by representative formation thickness are used for vertical hydraulic conductivity. In addition, simulations of diffusion of solutes require input parameters for diffusivity. For this, tortuosity values (used by TOUGH3, see App. A) are calibrated based on the porosities and effective diffusion coefficients summarised in Tab. 3-2 and Tab. 3-4, respectively.

The baseline properties of the site model (Tab. 3-2, Tab. 3-3, and Tab. 3-4) are complemented with two-phase and TH parameters for the geologic formations. These parameters, summarised in Tab. 3-5, are required input for modelling gas and heat transport problems. Capillary strength is calculated from hydraulic conductivity through Leverett scaling using the values for OPA as reference (Nagra 2024g). Similarly, pore compressibility is scaled for each formation using the corresponding porosity value. Thermal conductivity is calculated as described in Nagra (2024k). Grain density corresponds to the best estimates from Nagra (2024c). Additional, less sensitive parameters are assumed constant across all formations as given in Tab. 3-5.

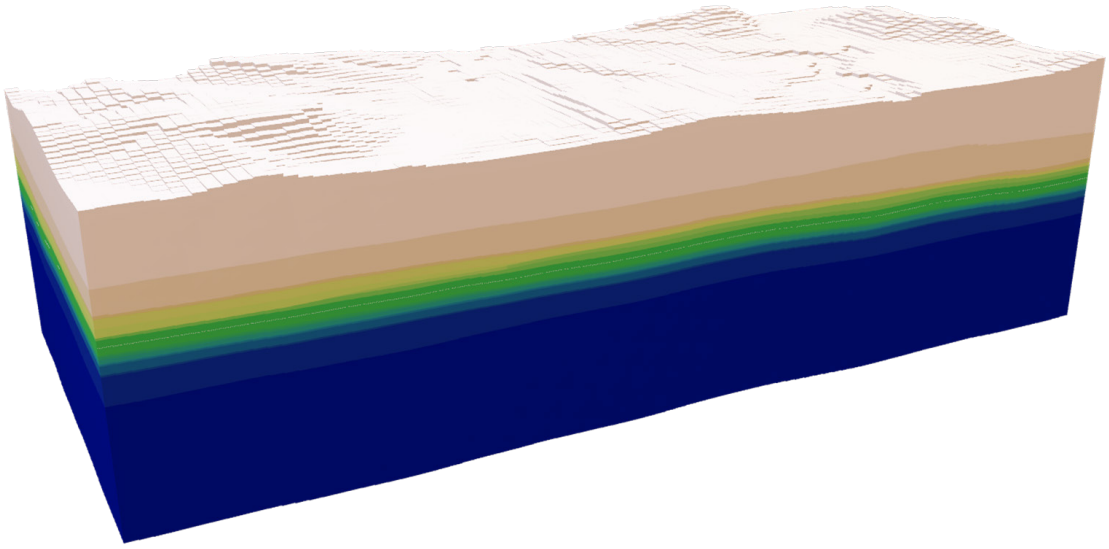

Fig. 3-1: Illustration of the 3D site model
With the stratigraphic units respectively formations from Permo-Carboniferous (dark blue) to Tertiary (beige).

Tab. 3-1: Stratigraphic units respectively formations in the siting region, from Nagra (2024c), and their representation in the site model

Stratigraphic units / formation	**PA material code**
Top Boundary (TOP-BC)	TOPBC
Tertiary (TERT) / Quarternary (QUAT)	TERT
Malm	MALM
Marly Malm (NL-MM2)	MM2
Calcareous Malm (NL-CM - Gerstenhübel Beds)	CM
Marly Malm (NL-MM1)	MM1
Argillaceous Dogger (AD)	AD
Herrenwis unit: in the eastern part (boreholes Stadel-3-1 and Bülach-1-1) Calcareous Dogger (NLE-CD), towards the west (boreholes Stadel-2-1, Weiach) the NLE-CD is neighbored by the stratigraphic unit Calcareous Dogger (NLW-CD)	HERRE/HERRW
Sandy-Calcareous Argillaceous Dogger (SCAD) & Sandy-Calcareous Dogger (SCD) of Wildegg Formation	DOGG
Opalinus Clay (OPA)	OPA/OPAM
Marly Lias (ML) of Staffelegg Formation	ML
Argillaceous Lias (AL) of the Staffelegg Formation	AL
Argillaceous Keuper (JO-AK2/3 - of Klettgau and Staffegg Formation) & Calcareous Lias (CL) of Staffelegg Formation	KEUK
Argillaceous Keuper (NL-AK2 – “lower” Gruhalde Member) & Dolomitic Keuper (NL-DK2 - Seebi Member)	KAU
Argillaceous Keuper (AK1) & Sandy Keuper (SK) & Dolomitic Keuper (JO-DK) of Klettgau Formation	KAL
Anhydritic-Argillaceous Keuper (AAK) of Bänkerjoch Formation	GIPSK
Dolomitic-Anhydritic Keuper (DAK) & Massive Anhydritic Keuper (MAK) of Bänkerjoch Formation	MAK
Muschelkalk	MUSCH
Permo-Carboniferous	PERM
Bottom Boundary	BOTBC

Tab. 3-2: Porosity of stratigraphic units respectively formations, from Nagra (2024c), and their representation in the PA

Porosity n								Thickness for averaging [m]
Unit	**NL (East and West)**			**PA modelling**			**PA material code**	
	Min.	**Best**	**Max.**	**Min.**	**Best**	**Max.**		
	[-]	[-]	[-]	[-]	[-]	[-]		
CM (Malm aquifer)	-	-	-	-	0.09	-	MALM	-
MM2	0.031	0.063	0.109	0.031	0.063	0.109	MM2	25.30
NL-CM	0.024	0.030	0.043	0.024	0.030	0.043	CM	4.79
MM1	0.044	0.074	0.104	0.044	0.074	0.104	MM1	42.61
AD	0.084	0.120	0.154	0.084	0.120	0.154	AD	5.67
E/W-CD (Herrenwis Unit)	0.012/ 0.021	0.026/ 0.043	0.085/ 0.067	0.012/ 0.021	0.026/ 0.043	0.085/ 0.067	HERRE/ HERRW	40.33
NL-ARD	0.117	0.130	0.147	0.071	0.123	0.165	DOGG	-
SCD	-	-	-					28
SCAD	0.071	0.123	0.165					12
OPA	0.078	0.115	0.136	0.078	0.115	0.136	OPA	108.56
ML	0.037	0.075	0.161	0.037	0.075	0.161	ML	13.68
AL	0.071	0.083	0.096	0.071	0.083	0.096	AL	11.80
CL	0.028	0.054	0.141	0.072	0.108	0.166	KEUK	2.70
AK3 and JO-AK2/3	0.078	0.115	0.169					19.70
NL-DK2	0.041	0.082	0.106	0.047	0.087	0.116	KAU	6.40
AK2	0.068	0.103	0.150					1.90
NL-DK1	0.020	0.079	0.127	0.077	0.121	0.182	KAL	1.80
AK1	0.095	0.134	0.199					5.87
SK	0.116	0.144	0.170					
AAK	0.038	0.091	0.149	0.038	0.091	0.149	GIPSK	67.73
MAK	0.009	0.009	0.024	0.009	0.017	0.052	MAK	4.10
DAK	0.008	0.026	0.086					3.40
DM	-	-	-	-	0.120	-	MUSCH	-

Tab. 3-3: Hydraulic conductivity of stratigraphic units respectively formations, from Nagra (2024c), and their representation in the PA

Horizontal hydraulic conductivity K_h								Estimated K_h/K_v
Unit	**NL (East and West)**			**PA modelling**			**PA material code**	
	Min.	**Best**	**Max.**	**Min.**	**Best**	**Max.**		
	[m/s]	[m/s]	[m/s]	[m/s]	[m/s]	[m/s]		[-]
CM (Malm aquifer)	1.E-10	1.E-09	1.E-07	1.E-10	1.E-09	1.E-07	MALM	1
MM2	1.E-14	1.E-12	5.E-10	1.E-14	1.E-12	5.E-10	MM2	1 to 10
NL-CM	1.E-14	1.E-12	1.E-08	1.E-14	1.E-12	1.E-08	CM	1
MM1	1.E-14	1.E-12	5.E-10	1.E-14	1.E-12	5.E-10	MM1	1 to 10
AD	1.E-14	1.E-13	1.E-11	1.E-14	1.E-13	1.E-11	AD	5 (1 to 10)
E/W-CD (Herrenwis Unit)	1.E-14	1.E-12	1.E-07	1.E-14	1.E-12	1.E-07	HERRE/ HERRW	1
NL-ARD	1.E-14	1.E-13	1.E-11	1.0E-14	8.5E-14	1.5E-10	DOGG/ SADHB	5 (1 to 10)
SCD	1.E-14	5.E-14	5.E-10					1
SCAD	1.E-14	1.E-13	1.E-12					5 (1 to 10)
OPA	1.E-14	5.E-14	5.E-13	1.E-14	5.E-14	5.E-13	OPA	5 (1 to 10)
ML	1.E-14	5.E-14	5.E-13	1.E-14	5.E-14	5.E-13	ML	1
AL	1.E-14	1.E-13	1.E-12	1.E-14	1.E-13	1.E-12	AL	5 (1 to 10)
CL	1.E-14	1.E-12	5.E-10	1.0E-14	2.1E-13	6.9E-11	KEUK	1
AK3 and JO-AK2/3	1.E-14	1.E-13	1.E-11					5 (1 to 10)
NL-DK2	1.E-14	1.E-12	5.E-10	1.0E-14	7.9E-13	3.9E-10	KAU	1
AK2	1.E-14	1.E-13	1.E-11					5 (1 to 10)
NL-DK1	1.E-14	1.E-12	5.E-10	1.0E-14	1.0E-12	8.8E-10	KAL	1
AK1	1.E-14	1.E-12	1.E-09					5 (1 to 10)
SK	1.E-09	1.E-07	1.E-05					1
AAK	1.E-14	1.E-13	1.E-11	1.0E-14	1.0E-13	1.0E-11	GIPSK	1
MAK							MAK	
DAK								
DM	1.E-08	5.E-07	1.E-06	1.0E-08	5.E-07	1.E-06	MUSCH	1

Tab. 3-4: Effective diffusion coefficient of stratigraphic units respectively formations (from Glaus et al. 2024) and their representation in the PA

Effective diffusion coefficient D_{eff} (Iodine)							
Unit	**NL (East and West)**			**PA modelling**			**PA material code**
	Min.	**Best**	**Max.**	**Min.**	**Best**	**Max.**	
	[-]	[-]	[-]	[-]	[-]	[-]	
CM (Malm aquifer)	-	-	-	-	-	-	MALM
MM2	1.81E-12	6.05E-12	1.59E-11	1.81E-12	6.05E-12	1.59E-11	MM2
NL-CM	1.24E-12	4.72E-12	1.33E-11	1.24E-12	4.72E-12	1.33E-11	CM
MM1	1.96E-12	6.15E-12	1.58E-11	1.96E-12	6.15E-12	1.58E-11	MM1
AD	1.58E-12	3.66E-12	8.27E-12	1.58E-12	3.66E-12	8.27E-12	AD
E/W-CD (Herrenwis Unit)	9.00E-13/ 1.53E-12	3.40E-12/ 5.57E-12	9.76E-12/ 1.52E-11	9.00E-13/ 1.53E-12	3.40E-12/ 5.57E-12	9.76E-12/ 1.52E-11	HERRE/ HERRW
NL-ARD	1.43E-12	3.14E-12	6.93E-12	1.43E-12	3.35E-12	7.25E-12	DOGG
SCD	1.86E-12	6.47E-12	1.72E-11				
SCAD	1.43E-12	3.35E-12	7.25E-12				
OPA	1.22E-12	2.65E-12	5.48E-12	1.22E-12	2.65E-12	5.48E-12	OPA
ML	1.96E-12	5.76E-12	1.45E-11	1.96E-12	5.76E-12	1.45E-11	ML
AL	1.80E-12	4.28E-12	1.05E-11	1.80E-12	4.28E-12	1.05E-11	AL
CL	1.66E-12	5.02E-12	1.24E-11	1.54E-12	3.87E-12	8.59E-12	KEUK
AK3 and JO-AK2/3	1.53E-12	3.72E-12	8.16E-12				
NL-DK2	1.46E-12	5.20E-12	1.42E-11	1.56E-12	5.32E-12	1.42E-11	KAU
AK2	1.81E-12	5.61E-12	1.44E-11				
NL-DK1	1.05E-12	3.85E-12	1.08E-11	1.23E-12	2.97E-12	6.51E-12	KAL
AK1	1.12E-12	2.45E-12	5.10E-12				
SK	1.97E-12	5.36E-12	1.34E-11				
AAK	1.63E-12	5.17E-12	1.35E-11	1.63E-12	5.17E-12	1.35E-11	GIPSK
MAK	3.48E-13	1.33E-12	3.94E-12	3.48E-13	1.33E-12	3.94E-12	MAK
DAK	4.84E-13	1.83E-12	5.37E-12				
DM	-	-	-	-	-	-	MUSCH

Tab. 3-5: Additional parameters assigned to formations considered in the PA models

Material	**Capillary strength** P_0 [Pa]	**Pore compressibility** C_p [1/Pa]	**Thermal conductivity** λ [W/m K]	**Rock grain density** ρ_s [g/cm^3]
TERT	1.45E05	1.67E-09	4.27	2,700
MALM	1.52E05	1.67E-09	2.74	2,700
MM2	1.08E07	2.38E-09	2.74	2,707
CM	4.81E06	5.00E-09	2.74	2,706
MM1	1.08E07	2.03E-09	2.74	2,708
AD	3.40E07	1.25E-09	2.74	2,708
HERRE/ HERRW	4.81E06	5.77E-09/ 3.49E-09	2.74	2,704/ 2,715
DOGG	3.08E07	1.22E-09	2.53	2,715
OPA	4.81E07	2.10E-09	wet: 2.10 dry: 1.40	2,700
ML	2.15E07	2.00E-09	1.98	2,689
AL	3.40E07	1.81E-09	1.98	2,684
KEUK	3.19E07	1.39E-09	1.98	2,774
KAU	1.68E07	1.73E-09	1.98	2,799
KAL	1.52E04	1.24E-09	1.98	2,810
GIPSK	1.52E07	1.65E-09	1.98	2,808
MAK	1.52E07	9.00E-09	6.26	2,920
MUSCH	6.81E03	1.25E-09	6.26	2,700
PERM	1.45E06	1.25E-09	2.58	2,700

Additional parameters (same value for all formations):

- specific heat capacity (J/kg K): 995.0
- thermal expansion coefficient (1/K): 1.70E-05
- residual water saturation in water retention curve (-): 0.01
- residual water saturation in relative permeability (-): 0.50
- residual gas saturation (-): 0.0
- van Genuchten shape parameter n (-): 1.67

3.3 Deterministic repository and component models (3D)

3.3.1 Model of the geological repository

An illustration of the 3D repository model is shown in Fig. 3-2. This model is used in Nagra (2024g) as part of the description of the hydraulic evolution of the repository, and also in the present report as part of the model-based assessment on the level of the total system, described in Chapter 6.

The repository model is implemented in 3D with a nested rectangular mesh based on a stylised representation of the repository structures with the surrounding host rock and over- and underlying formations. The geological formations considered in this model correspond to those represented in the site model described in Section 3.2. Accordingly, the model layers represent lithostratigraphic units as shown in Tab. 3-1, and are implemented with the thicknesses and inclinations as described in Section 3.2. In the horizontal direction, the model covers an area of 6.7 × 3.24 km^2 with the X axis oriented along the operation tunnels which corresponds to ~10° counterclockwise rotation from the NS line. The coordinates of the bottom left (SW) corner of the model are (675,460; 264,370). The model explicitly represents the emplacement rooms (7 caverns for L/ILW and 20 drifts for HLW), branching tunnels, operations/ventilation/construction tunnels, access tunnels, pilot repositories (separate for L/ILW and HLW, including emplacement rooms, branching/operations and control tunnels), tunnels of the central area and EUU, and operations / ventilation / construction shafts. Each tunnel type is represented with a single, homogenised material. In general, the discretisation is finer within the repository structures and coarsens away towards the model boundaries. More details on the model implementation are provided in Nagra (2024g). Additional information on the model geometry, including the volumes and scaling assigned to different components of the modelled repository, is given in App. A.

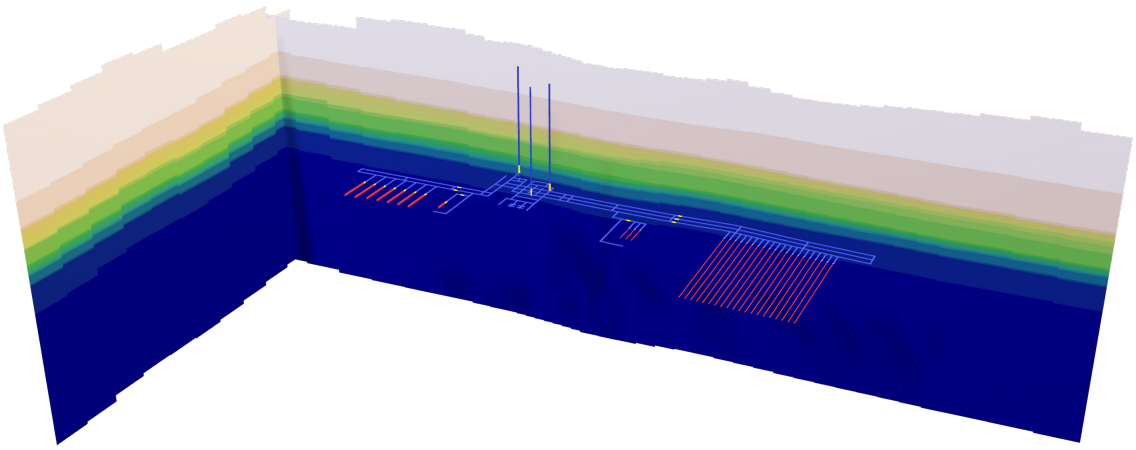

Fig. 3-2: Illustration of the 3D repository model

With the same stratigraphic units from Permo-Carboniferous (dark blue) to Tertiary (beige) as the larger site model. The main repository structures including emplacement rooms (red), sealing sections (yellow) and the rest of the tunnels, galleries, and shafts (blue).

3.3.2 Models of components of the repository

The following models of repository components are implemented in 3D, shown in Fig. 3-3:

- the HLW component model with an HLW emplacement drift and adjacent V1-HLW seal;
- the L/ILW component model with an L/ILW emplacement cavern and adjacent V1-L/ILW seal;
- the V2 seal model; and
- the V3 seal model.

These models are used predominantly in Nagra (2024g) as part of the description of the hydraulic evolution of the repository. Accordingly, the detailed description of their implementation and material input parameters is given in Nagra (2024g). Additional information on the modelled geometries is given in App. A. To complement analyses in the present report, some of the results obtained with the 3D component models are shown in App. C and App. D for HLW and L/ILW, respectively. A short overview of the model implementations is provided in the following.

The HLW 3D component model represents half (width-wise) of an emplacement drift assuming symmetry across the tunnel axis. As explained in Chapter 4, this representation implies super-position of parallel tunnels at specified distance. Accordingly, the model extends laterally to 20 m, in other words the half distance between neighbouring HLW emplacement drifts. This lateral model boundary is assumed to be a no-flow boundary. The model is implemented with a hybrid radial-rectangular mesh reaching the top and bottom of the OPA with the thickness taken at the centre of the HLW disposal area. The mesh is additionally connected to 1D elements extending the model to ground surface and to the base of the Muschelkalk, respectively the base of the site model geometry (Section 3.2). The HLW tunnel has a total length of 887 m including 23 m of the V1-HLW seal. All canisters have length of 5 m with 3 m spacing between them. The branching and operations tunnels are not accounted for.

The L/ILW 3D component model represents half (width-wise) of an emplacement cavern assuming symmetry across the cavern axis and, similarly to the HLW component model, super-position of neighbouring caverns at specified distance. Accordingly, the model extends laterally to 40 m, which is half of the distance between neighbouring caverns. The lateral boundary is assumed to be a no-flow boundary. The L/ILW model is implemented with a nested rectangular mesh reaching the top and bottom of the OPA with the thickness taken at the centre of the L/ILW disposal area. The L/ILW cavern has a length of 230 m emplaced with LC-86H containers and mortar backfill, connected to the waste transfer area, unloading area, V1-L/ILW seal, branching tunnel and part of the operations tunnel. The length of the operations tunnel equals the length up to the V2-L/ILW seal in the repository layout or can be extended to the total length up to the V2-HLW seal. In both cases, the storage volume of the operations tunnel is scaled down accordingly to account for 7 caverns contributing gas and water flux through their branch tunnels.

The V2 seal 3D model is implemented with a hybrid radial-rectangular mesh representing part of the operations tunnel including the respective V2 sealing section with the surrounding host rock and confining units (bottom of AL to top of MM2, see Tab. 3-1). The V2 seal has a length of 40 m including abutments, transition layers and the sealing element. On each side of the seal 30 m of operations tunnel are accounted for in the direction of emplacement area and pilot repository, respectively. The model can be adapted to reflect either V2-L/ILW or V2-HLW configurations. In the present analyses, only the V2-L/ILW configuration is modelled as the V2-HLW seal, comprising of compacted bentonite, evolves similar to the V1-HLW seal that is part of the HLW 3D component model.

The V3 seal 3D model is implemented with a hybrid radial-rectangular mesh representing part of the central area connecting to the access shaft, and the access shaft itself. The shaft section included in the model extends from the shaft sump in the OPA to the bottom of the Malm formation which also corresponds to the top boundary of the model. Below the repository respectively below the shaft the model extends to the bottom of the AL unit some 30 m below the base of the OPA.

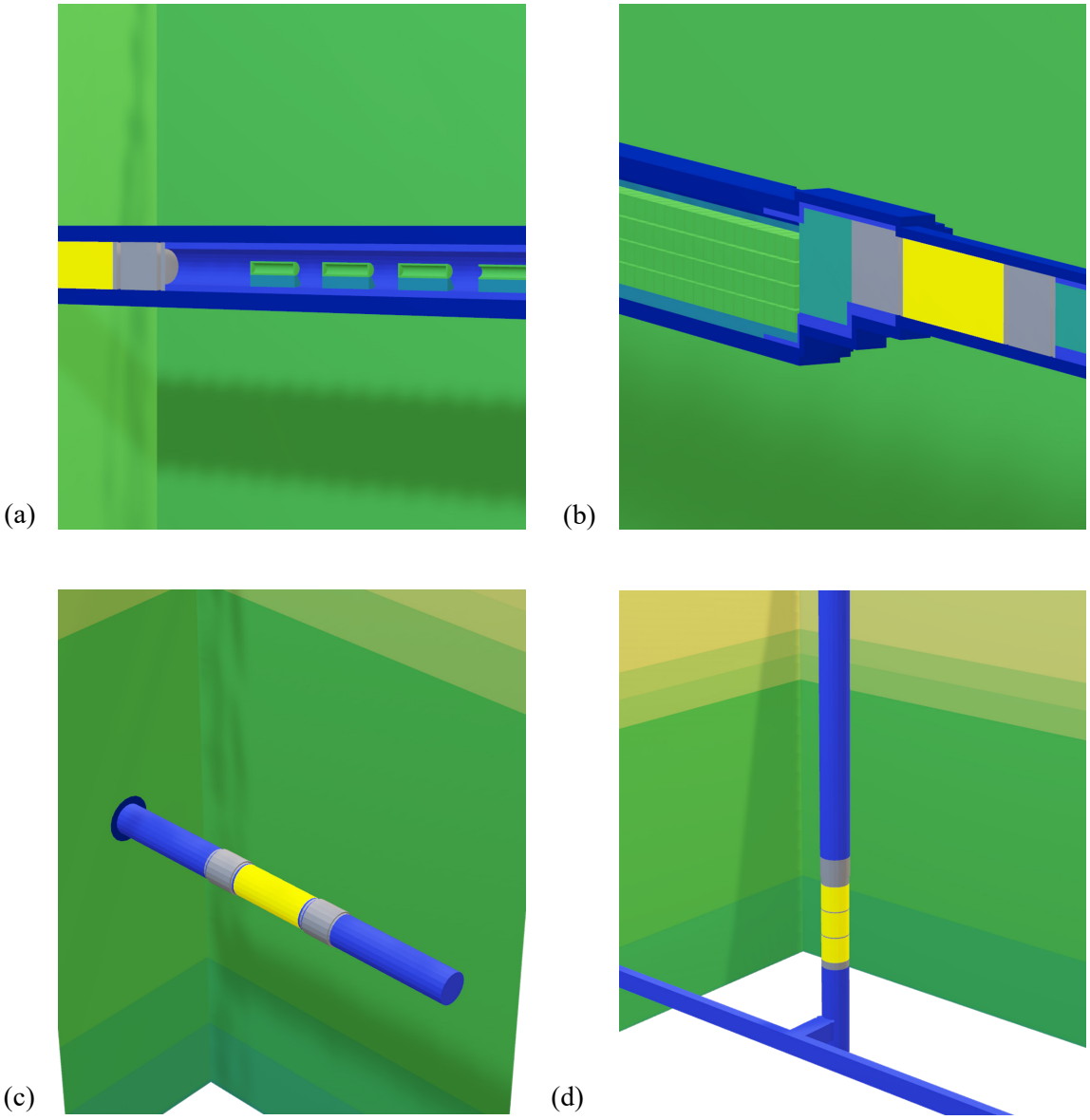

Fig. 3-3: Illustration of the 3D component models

(a) HLW drift; (b) L/ILW cavern; (c) V2 seal; (d) V3 seal and shaft. The repository tunnels (EDZ/liner) are shown in blue, the emplaced waste canisters and packages in green, the sealing elements in yellow and the adjacent abutments in grey.

3.4 Probabilistic component models HLW

The models for probabilistic analysis are implemented for the current provisional HLW configuration. These models are used extensively in Chapter 7 of the present report. The following section presents the development workflow starting with the generation of the computational mesh, followed by a short description of the model parameters, the prescribed initial and boundary conditions, the source terms, and an overview of the reference case with the corresponding probabilistic distributions.

3.4.1 Mesh generation

The geometries are extracted from the 3D site model constructed from the surface data as described in Section 3.2. A preliminary mesh corresponding to a 2 km long 2-D vertical slice cutting the middle of the emplacement drifts is extracted from the site model. The 2-D slice is then re-meshed using Gmsh (Geuzaine et al. 2009) by extracting the top and bottom horizons of each layer. Twenty detailed drifts spaced every 40 m are finally added to the mesh in the middle of the OPA. Each drift comprises an HLW disposal canister, bentonite elements (pedestal and buffer), a liner (tubbing), and an EDZ. The HLW disposal canister has a diameter of 1.05 m, surrounded by a 0.9 m thick bentonite buffer, while the liner and the EDZ are 0.5 m and 1.33 m thick, respectively. The thickness of the mesh along the drift axes (Y axis) is fixed to 4 m, corresponding to half of the lengths of a canister (5 m) and the spacing between adjacent canisters (3 m) to account for symmetry along that axis. Interface areas of the canister elements are also reduced by 1.6, corresponding to the ratio of the HLW disposal canister to spacing lengths. The 2D model with twenty HLW tunnels is referred to as *2D-HLW×20*. To account for the entire length of the tunnels, required by some of the assessments, the 2-D mesh is extruded along the Y axis to a 2.5-D mesh with thickness of 425 m. This model variant is referred to as *2.5D-HLW×20.* The produced finite-element meshes are finally converted into their dual-graph representations as required by TOUGH using the Python package toughio (Luu 2020).

Fig. 3-4 provides a close-up view of the detailed HLW disposal canister and its surrounding bentonite buffer materials. Note that the canisters are modelled as simple shells (i.e., the inner core elements are removed from the mesh) to account for the impermeability of the canister.

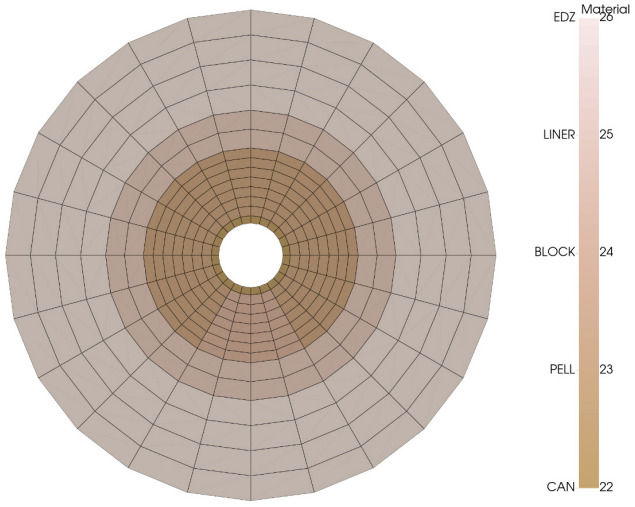

Fig. 3-4: Close-up view of the detailed representation of a HLW emplacement drift in 2D

It consists of a hollow canister (CAN) on a bentonite pedestal (BLOCK), surrounded by a bentonite buffer (PELL), a liner (LINER), and an EDZ (EDZ).

Fig. 3-5 shows the 2-D hybrid grid (i.e., with triangle and quad cells) generated by Gmsh for the slice through the centre of the disposal area. The horizontal and vertical resolution increases at the vicinity of the cells representing the emplacement drifts (near the centre of the OPA).

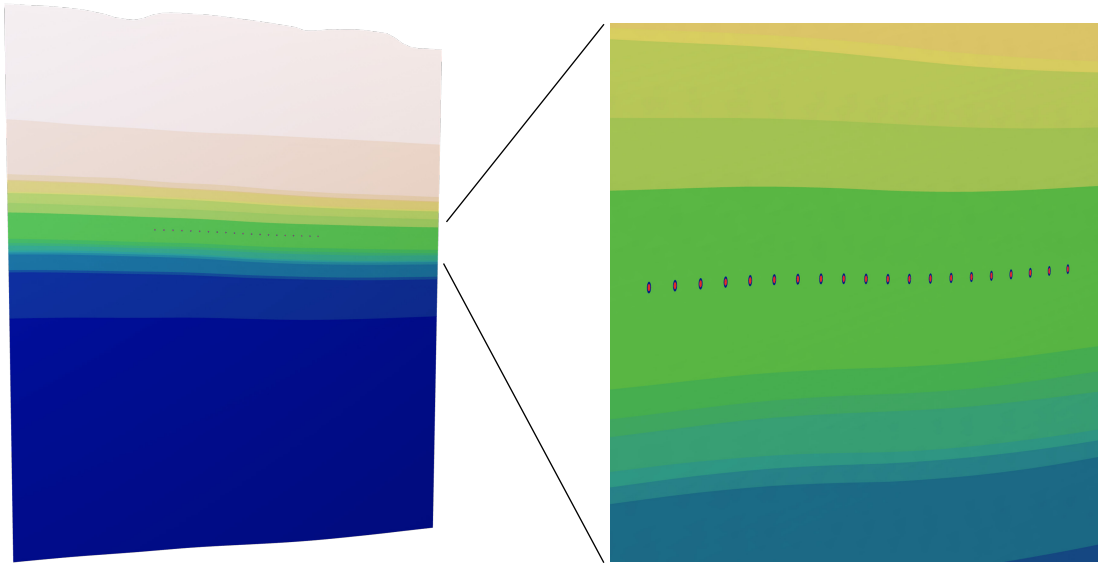

Fig. 3-5: 2-D hybrid mesh with twenty HLW emplacement drifts

3.4.2 Model parameters

The thermo-hydraulic two-phase properties described in Section 3.2 are complemented by parameters assigned to repository materials explicitly represented in the model. The reference values assigned to each material in the modelled HLW drifts are taken from Nagra (2024g) as shown in Tab. 3-6. These are applied in the same way to the *2D-HLW×20* and *2.5D-HLW×20* model variants.

Tab. 3-6: Reference hydraulic and thermal parameters assigned to the HLW drifts in 2D

ρ is the density, $T_{c,dry}$ and $T_{c,wet}$ are the thermal conductivity in unsaturated and saturated conditions, respectively, T_x is the thermal expansivity, K_h and K_v are the horizontal and vertical permeabilities, respectively, ϕ is the porosity, and C_p is the pore compressibility.

Material	$\boldsymbol{\rho}$ [kg/m^3]	$\boldsymbol{T_{c,dry}}$ [W/m/ ºC]	$\boldsymbol{T_{c,wet}}$ [W/m/ ºC]	$\boldsymbol{T_x}$ [1/ ºC]	$\boldsymbol{K_h}$ [m^2]	$\boldsymbol{K_v}$ [m^2]	$\boldsymbol{\phi}$ [-]	$\boldsymbol{C_p}$ [1/Pa]
CAN	7,850	52.5	52.5	1.5E-5	1E-20	1E-20	0.001	0
PELL	2,699	0.35	1.3	2.5E-5	3.5E-20	3.5E-20	0.33	3E-9
BLOCK					2.5E-21	2.5E-21	0.33	
LINER	2,650	1.4	2.3	1.5E-5	1E-18	1E-18	0.1	7E-10
EDZ	2,700	1.36	1.7	1.7E-5	4.54E-20	9.08E-21	0.12	1.7E-9

3.4.3 Boundary and initial conditions

Boundary and initial conditions typically correspond to near hydrostatic pressure conditions with constant pressure at the top of the model (resp. ground surface) equal to atmospheric pressure. Temperature is fixed to 10 ºC at the top and basal heat flux of 120 mW/m^2 is imposed at the bottom of the Permo-Carboniferous layer. Thus, top boundary is opened to flow, and bottom boundary is closed to flow where the constant heat flux is imposed. All lateral boundaries are also assumed to be closed to flow.

The model domain is assumed to be initially fully saturated with water. The initial pressure assigned to the model elements (including boundary elements) are calculated based on the elevation respectively depth b.g.l. of each element assuming a vertical gradient of 9.81 kPa/m. The initial temperature is calculated assuming a geothermal gradient of 0.043 ºC/m. For all simulations, a steady-state run is carried out prior to gas and heat transport modelling until pressure and temperature reach equilibrium (corresponding to undisturbed rock prior to repository construction).

In simulations of gas and heat transport, a 2-year long ventilation run is also performed where atmospheric pressure and a temperature of 28 ºC are prescribed in the open tunnels i.e., canister elements (CAN), bentonite buffer (PELL), bentonite pedestal (BLOCK). For this ventilation phase, the initial water saturation of the emplacement tunnel elements is assumed to be 50%, except for the liner which is assumed to be instantaneously emplaced at the start of the ventilation phase and is prescribed a 70% initial water saturation (Nagra 2024g).

The transition from ventilation to emplaced tunnels is assumed instantaneous. At emplacement the canister elements are assumed to be fully saturated with gas, while the PELL and BLOCK elements are prescribed an initial water saturation of 20% and 50%, respectively (Nagra 2024g).

3.4.4 Source terms

Fig. 3-6 shows the gas generation rates per HLW emplacement drift used in best estimate, lower bound and upper bound gas generation scenarios (Nagra 2024g). Gas generation rates are calculated using the gas generation tool (Nagra 2024g) for HLW components. Heat generation rates per SF canister are shown in Fig. 3-7. These correspond to the "representative average" rates per canister type (PWR-MOX, PWR-UO_2 and BWR) and an average heat rate used for repository-scale modelling as reported in Nagra (2024g). Heat and gas generated by wastes are volumetrically distributed to CAN, and gas generated by tunnel support materials, essentially the tubbing, ("tunnel F10" in Fig. 3-6) to LINER elements. Source terms are scaled for half of a single canister or half-length of the HLW emplacement drifts in the *2D-HLW×20* and *2.5D-HLW×20* model variants, respectively. A discussion of the source term evolution for heat and gas is given in Nagra (2024g).

The tracer source term used in the tracer simulations corresponds to an instantaneous release fraction ($IRF_{I\text{-}129}$) equal to 10% of initial activity of I-129 in the HLW inventory (Nagra 2024j), released at the canister.

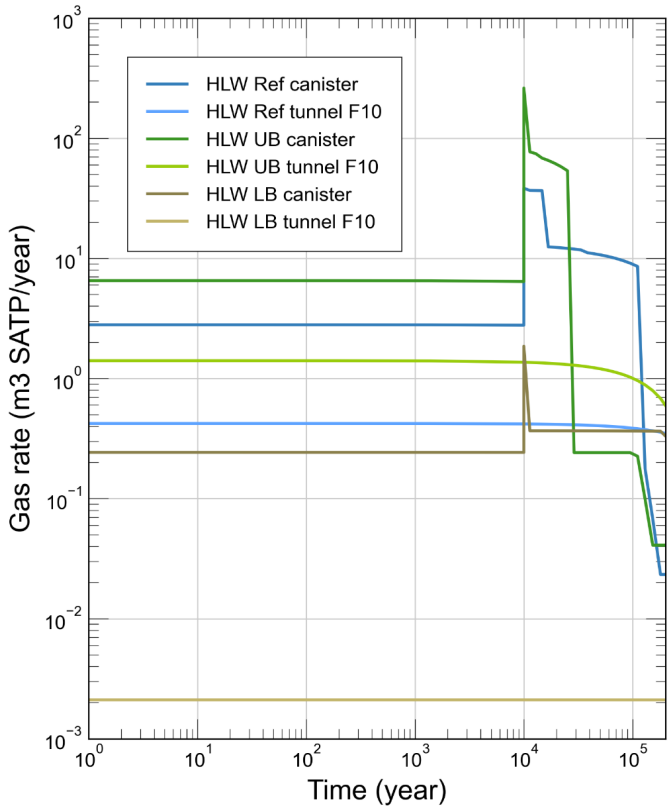

Fig. 3-6: Gas generation rates per HLW emplacement drifts, from HLW disposal canisters and from tunnel support materials (F10)

Best estimates (blue lines), upper bound (green lines) and lower bound (brown lines) values.

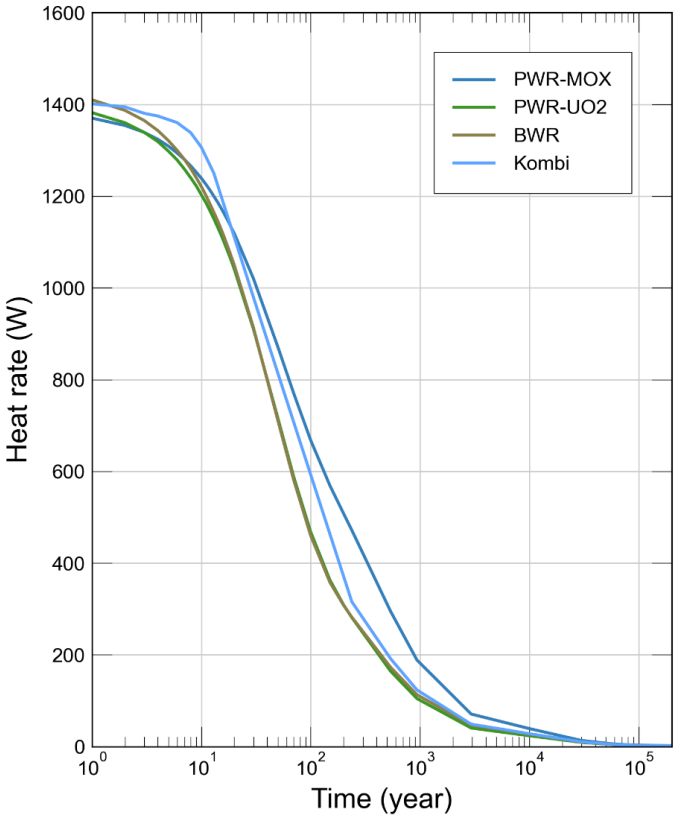

Fig. 3-7: Representative average heat generation rates per SF canister type (PWR-MOX, PWR-UO_2, BWR) and average used for repository-scale modelling (Kombi)

3.4.5 Reference case

The reference simulation corresponds to a case with the reference model parameters and reference gas generation rates ("HLW ref" lines in Fig. 3-6) and average heat generation rates ("Kombi" line in Fig. 3-7). Note that additional scenarios are run with the upper bound and lower bound gas generation rates ("UB" and "LB" lines, respectively in Fig. 3-6), and the upper bound heat generation rates ("PWR-MOX" line in Fig. 3-7). The base case simulates 1 million years of heat and gas generation, preceded by the steady-state ventilation runs as described in Section 3.4.3.

3.4.6 Monte Carlo simulations

Monte Carlo simulations are performed to evaluate the influence of uncertainty of key parameters on performance indicators and estimate the confidence intervals around the best estimate. For gas and heat simulations, parameters are selected based on their sensitivity to maximum pressures and temperatures in the OPA and inside the drifts (Papafotiou et al. 2016). These are the permeability, porosity, pore compressibility, saturated thermal conductivity of the OPA, and the saturated thermal conductivity of the EDZ. The distributions of the parameters considered are given in Tab. 3-7, and are used to generate a set of 100 Latin Hypercube samples, as shown in Fig. 3-8.

Note that other model parameters linked to the ones sampled are further calculated, namely:

- Vertical permeability of the OPA:
  $$K_v(\mathrm{OPA}) = K_h(\mathrm{OPA})/5 \quad (1)$$

- Thermal conductivity in unsaturated condition of the OPA:
  $$k_{dry}(\mathrm{OPA}) = k_{wet}(\mathrm{OPA}) \times \frac{1.4}{2.1} \quad (2)$$

- Horizontal permeability of the EDZ:
  $$K_h(\mathrm{EDZ}) = 10 \times K_h(\mathrm{OPA}) \quad (3)$$

- Vertical permeability of the EDZ:
  $$K_v(\mathrm{EDZ}) = 10 \times K_v(\mathrm{OPA}) \quad (4)$$

- Porosity of the EDZ:
  $$\phi(\mathrm{EDZ}) = \phi(\mathrm{OPA}) \quad (5)$$

- Pore compressibility of the EDZ:
  $$C_p(\mathrm{EDZ}) = C_p(\mathrm{OPA}) \quad (6)$$

- Thermal conductivity in unsaturated condition of the EDZ:
  $$k_{dry}(\mathrm{EDZ}) = k_{wet}(\mathrm{EDZ}) \times \frac{1.4}{1.7} \quad (7)$$

Similarly, diffusion coefficients used in tracer simulations (for I-129) are perturbed to evaluate confidence intervals around the estimated tracer breakthroughs. The respective distributions are given in Tab. 3-8 with the resulting samples shown in Fig. 3-9. Note that the reference values are the best estimates and differ from the means of the lognormal distributions.

Tab. 3-7: Distributions of parameter values used for Monte Carlo gas-heat simulations for HLW

K_h is the horizontal permeability, ϕ the porosity, C_p the pore compressibility, and k_{wet} the thermal conductivity in fully saturated condition. $\mathcal{U}(a, b)$ corresponds to a uniform distribution sampled between a and b, and $\mathcal{N}(\mu, \sigma)$ represents a normal distribution with mean μ and standard deviation σ.

Material	**Parameter**	**Distribution**
OPA	$\log_{10}(K_h)$ [m^2]	$\mathcal{U}(-21.04, -19.34)$
	ϕ [-]	$\mathcal{N}(0.115, 0.0128)$
	C_p [1/Pa^{-1}]	$\mathcal{U}(1.19, 4.167) \times 10^{-9}$
	k_{wet} [W/m/°C]	$\mathcal{N}(2.1, 0.255)$
EDZ	k_{wet} [W/m/°C]	$\mathcal{N}(1.7, 0.207)$

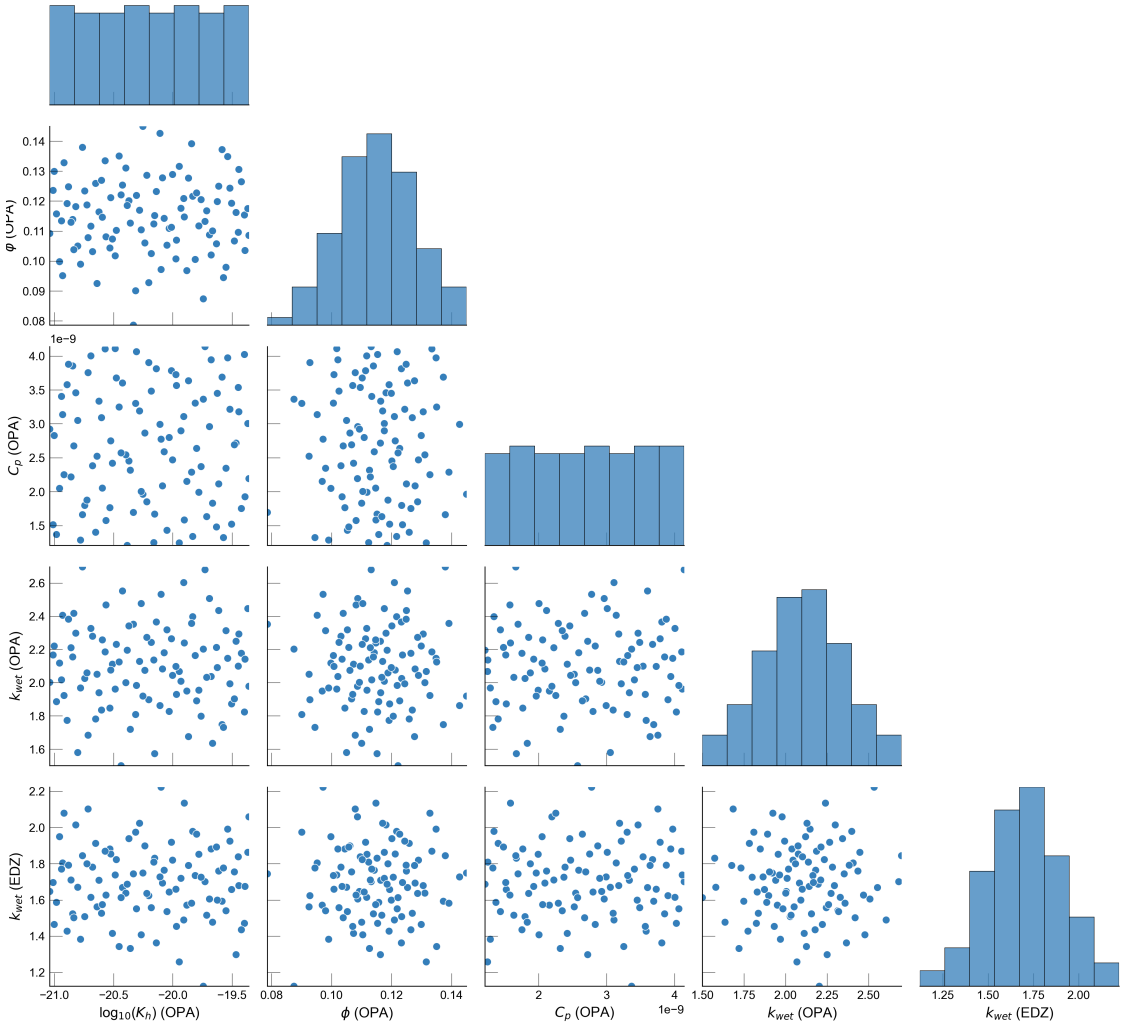

Fig. 3-8: Scatter-plot matrix of the 100 Latin Hypercube samples used for gas-heat simulations for HLW

The subplots along the diagonal show the marginal distributions (as a histogram) of the samples, while the off-diagonal subplots of the matrix represent a pairwise scatter plot between the different model parameters.

Tab. 3-8: Means and standard deviations of the lognormal distributions fitted to the effective diffusion coefficients used for tracer simulations for HLW

(From Glaus et al. 2024).

The last column represents the best estimates used as reference values.

Material	$\log(D_e)$ [mean]	$\log(D_e)$ [std.]	D_e [m^2/s]
TERT	-25.82	0.12	6.05E-12
MALM	-25.82	0.12	6.05E-12
MM2	-25.82	0.12	6.05E-12
CM	-26.07	0.11	4.72E-12
MM1	-25.81	0.09	6.15E-12
AD	-26.28	0.31	3.66E-12
HERRE	-26.33	0.39	3.40E-12
SADHB / DOGG	-26.30	0.48	3.35E-12
OPA	-26.61	0.31	2.65E-12
ML	-25.87	0.14	5.76E-12
AL	-26.16	0.17	4.28E-12
KEUK	-26.15	0.47	3.87E-12
KAU	-25.91	0.27	5.32E-12
KAL	-26.40	0.50	2.97E-12
GIPSK	-25.93	0.29	5.17E-12
MAK	-27.09	0.59	1.52E-12
MUSCH	-27.09	0.59	1.52E-12
PERM	-27.09	0.59	1.52E-12

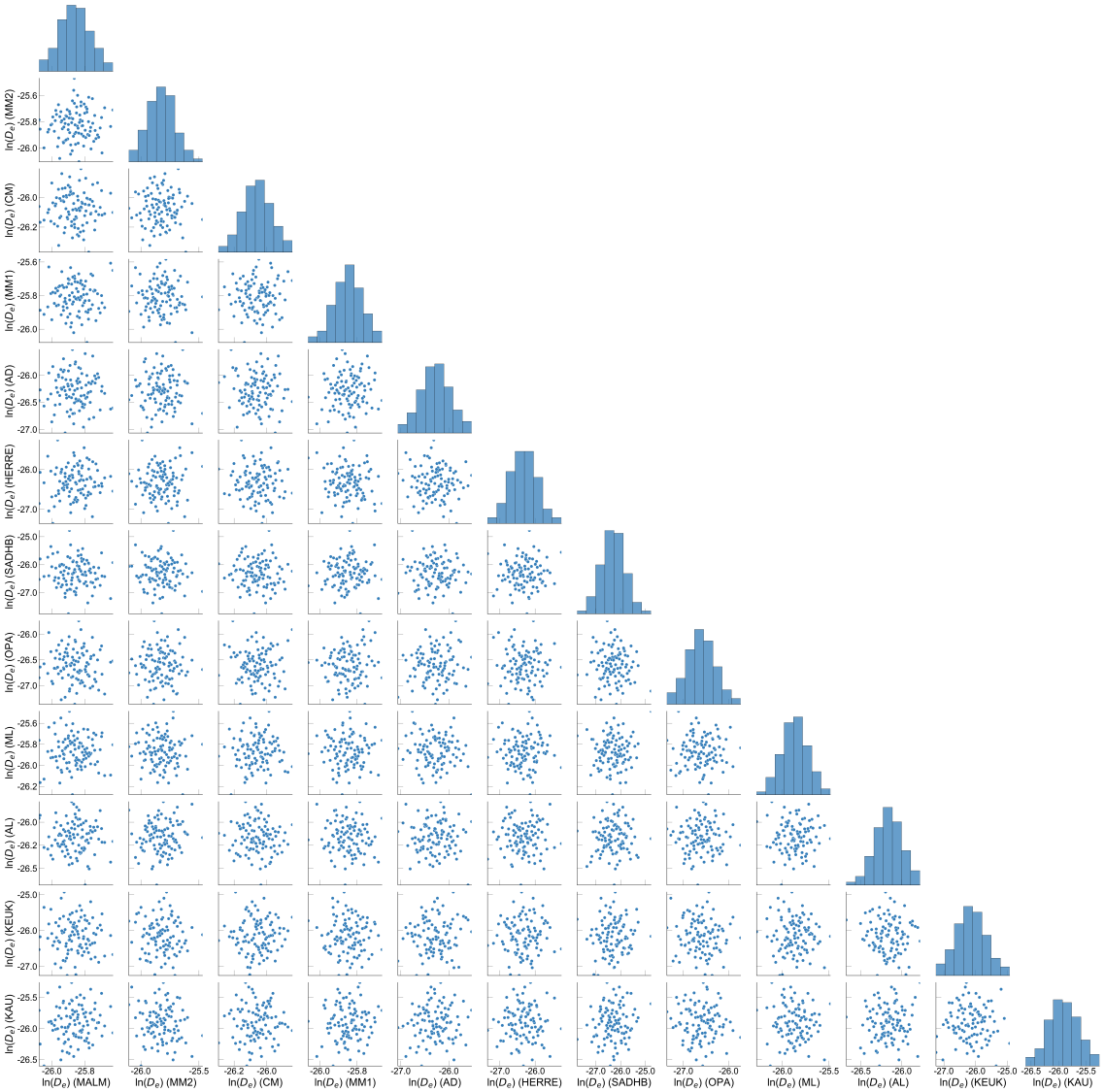

Fig. 3-9: Scatter-plot matrix of the 100 Latin Hypercube samples used for tracer simulations for HLW

The subplots along the diagonal show the marginal distributions (as a histogram) of the samples, while the off-diagonal subplots of the matrix represent a pairwise scatter plot between the different model parameters.

3.5 Probabilistic component models L/ILW

The models for probabilistic analysis are implemented for the current provisional L/ILW configuration. These models are used extensively in Chapter 8 of the present report. The following section presents the development workflow starting with the generation of the computational mesh, followed by a short description of the model parameters, the prescribed initial and boundary conditions, the source terms, and an overview of the reference case with the corresponding probabilistic distributions.

3.5.1 Mesh generation

The geometries are extracted from the 3D site model constructed from the surface data as described in Section 3.2. A preliminary mesh corresponding to a 2 km long 2D vertical slice cutting the middle of the caverns is extracted from the site model. The 2D slice is then re-meshed using Gmsh (Geuzaine et al. 2009) by extracting the top and bottom horizons of each layer. Seven detailed caverns spaced every 85 m are finally added to the mesh in the middle of the OPA. Each cavern comprises waste packages (WP), mortar (MORT1) and concrete fillings (FCONC), a liner (LINER), and an EDZ (EDZ). The waste packages are simplified by a single waste package geometry composed of 11 smaller rectangular containers (corresponding to the LC-86H containers), whereas the caverns are modelled as oval shapes with the liner and the EDZ being 0.5 m and 1 m thick, respectively (Nagra 2024g).

To account for the gas dissipating through the tunnels, the 2D mesh is extruded along the cavern axis (Y axis) to a 2.5D mesh consisting of three sections. The first section corresponds to the initial 2D mesh with the waste packages where the gas is generated, the second section corresponds to the V1-L/ILW seal (PLUG), and the third section corresponds to the branching tunnel and operation tunnels up to V2-HLW (SMABR). In selected variants the operations tunnel reaches only up to V2-L/ILW. The thickness of the first section is fixed to 235 m, corresponding to the average lengths of the seven caverns (five 230-m long caverns and two 250-m long caverns), whereas the thicknesses of the two other sections are scaled based on the total volume of the corresponding tunnels in the 3D repository model, assuming a cross section of 113.4 m^2 for each cavern. The thicknesses of the three sections are summarised in Tab. 3-9. To reduce the total number of elements in the 2.5D mesh, all the geological layers except for the OPA are removed from the sections 2 and 3, as pressure changes are expected to be negligible in these layers. The 2.5D model with seven L/ILW caverns is referred to as *2.5D-L/ILW×7*. An additional variant of this model with a single L/ILW half-cavern is generated in the same manner and referred to as *2.5D-L/ILW×1*. The volumes of the L/ILW half-cavern and adjacent tunnels are scaled down accordingly. The single-cavern model is also used to generate a further variant where a vertical shaft is added in the operations tunnel, including a V3 seal, at distance from the emplacement cavern equal to the average distance of the 3 shafts from the emplacement caverns in the 3D repository model. The latter is used for selected cases aiming to evaluate gas release rates from the V3 seal to the shaft in a probabilistic manner. The produced finite-element meshes are finally converted into their dual-graph representations as required by TOUGH using the Python package toughio (Luu 2020).

Fig. 3-10 provides a close-up view of the detailed L/ILW caverns in each section. Fig. 3-11 shows the 2D hybrid grid (i.e., with triangle and quad cells) generated by Gmsh through the centre of the disposal area. The horizontal and vertical resolutions increase at the vicinity of the cells representing the emplacement caverns (near the centre of the OPA). Fig. 3-11 shows a close-up view of the conceptual 2.5D model with its three sections.

Tab. 3-9: Volumes and thicknesses of sections

The volume represents the total volume of the seven caverns in a given section.

Section	**Volume** [m^3]	**Thickness** [m]
1	186,590	235
2	10,500	13.224
3	141,500	178.212

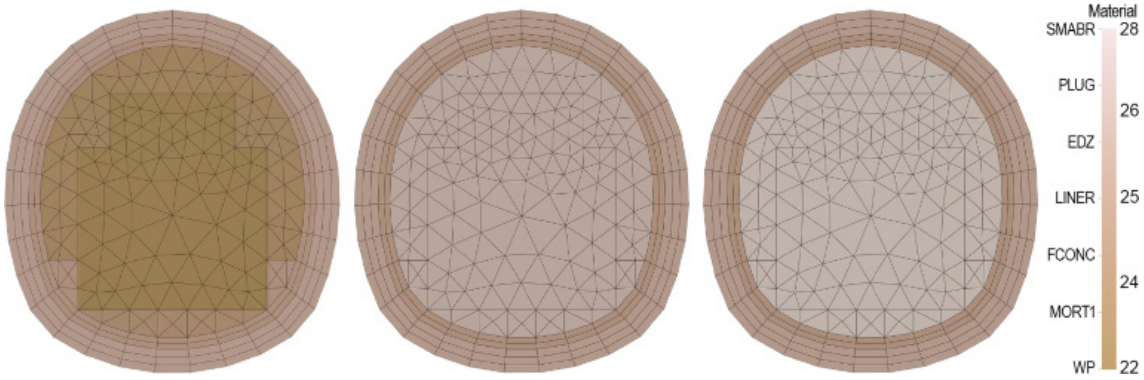

Fig. 3-10: Close-up view of the detailed representation of a L/ILW cavern in 2D, consisting of three sections

From left to right, the section 1 consists of WP, MORT1 and FCONC. Sections 2 and 3 are filled with PLUG and SMABR materials, respectively. For all sections, the caverns are surrounded by a liner and an EDZ.

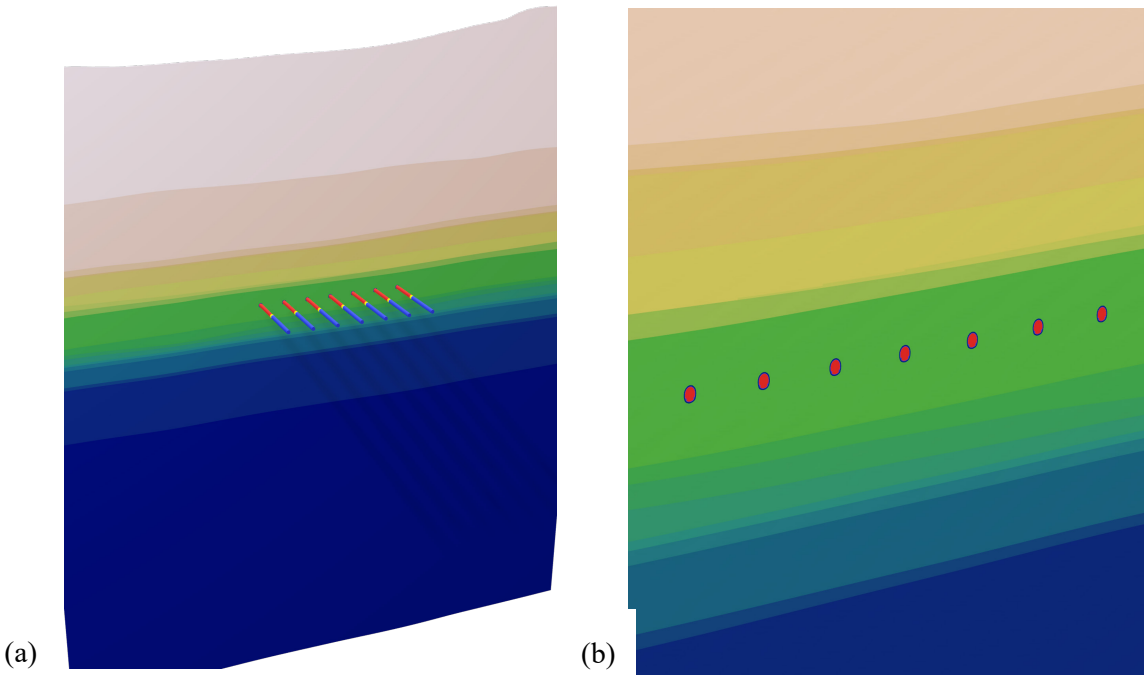

Fig. 3-11: 2.5D hybrid mesh with seven L/ILW emplacement caverns
(a) 2.5D view; (b) Zoom-in and 2D view.

3.5.2 Model parameters

The thermo-hydraulic, two-phase and transport properties described in Section 3.2 are complemented by parameters assigned to repository materials explicitly represented in the model. The reference values assigned to each material in the modelled L/ILW caverns are taken from Nagra (2024g) and summarised in Tab. 3-10. Note that, conservatively for gas pressure, the permeability of MORT1 has been decreased from 1.0E-10 m^2 (Nagra 2024g) to 1.0E-15 m^2 to improve model convergence. These parameters are used both in the *2.5D-L/ILW×7* and the *2.5D-L/ILW×1* model variants.

Tab. 3-10: Reference hydraulic parameters assigned to the L/ILW caverns in 2.5D

ρ is the density, K_h and K_v are the horizontal and vertical permeabilities, respectively, ϕ is the porosity, and C_p is the pore compressibility.

Material	$\boldsymbol{\rho}$ [kg/m^3]	$\boldsymbol{K_h}$ [m^2]	$\boldsymbol{K_v}$ [m^2]	$\boldsymbol{\phi}$ [-]	$\boldsymbol{C_p}$ [1/Pa]
WP	2,650	1E-15	1E-15	0.35	5E-10
MORT1	2,650	1E-15	1E-15	0.2	3E-10
FCONC	2,650	3E-16	3E-16	0.1	7E-10
LINER	2,650	3E-16	3E-16	0.1	7E-10
EDZ	2,700	4.54E-20	9.08E-21	0.12	2.1E-9
PLUG	2,650	1E-15	1E-15	0.35	1E-9
SMABR	2,650	1E-15	1E-15	0.35	1E-9

3.5.3 Boundary and initial conditions

Boundary and initial conditions typically correspond to near hydrostatic pressure conditions with constant pressure at the top of the model (resp. ground surface) equal to atmospheric pressure. As temperature effects are assumed to be negligible, temperature is set to 10 ºC at the top and fixed at the bottom. Thus, both top and bottom boundaries are opened to flow, and temperatures are fixed in all geological layers except in OPA, by setting a large specific heat value (e.g., 1E50 J/kg/ºC) in these layers. All lateral boundaries are assumed to be closed to flow.

The model domain is assumed to be initially fully saturated with water. The initial pressure assigned to the model elements (including boundary elements) are calculated on the elevation respectively depth b.g.l. of each element assuming a vertical gradient of 9.81 kPa/m. The initial temperature is calculated assuming a geothermal gradient of 0.043 ºC/m. For all simulations, a steady-state run is carried out prior to gas modelling until pressure and temperature reach equilibrium (corresponding to undisturbed rock prior to repository construction).

A subsequent 15-year long ventilation run is also performed where atmospheric pressure and a temperature of 28 ºC are prescribed in the open tunnels (i.e., materials WP, MORT1, FCONC, PLUG, and SMABR). For this ventilation phase, the initial water saturation of the emplacement tunnel elements is assumed to be 50%.

The transition from ventilation to emplaced tunnels is assumed instantaneous. At emplacement the WP, FCONC, and SMABR elements are assumed to be initially 30% saturated with gas, while the MORT1 and PLUG elements are prescribed an initial water saturation of 50% (Nagra 2024g).

3.5.4 Source terms

Fig. 3-12 shows the total gas generation rates from L/ILW per emplacement cavern used in the gas simulations for both best estimate, lower bound and upper bound gas generation scenarios (Nagra 2024g). The gas generation rates are calculated using the gas generation tool (Nagra 2024g) for L/ILW components and are then volumetrically distributed to WP elements. Gas generation rates are accordingly scaled for 7 caverns or half a cavern in the *2.5D-L/ILW×7* and *2.5D-L/ILW×1* model variants, accordingly.

The tracer source term used in the L/ILW simulations corresponds to an instantaneous release fraction ($IRF_{Cl\text{-}36}$) equal to the entire initial activity of Cl-36 in the L/ILW inventory (Nagra 2024j), released at the WP.

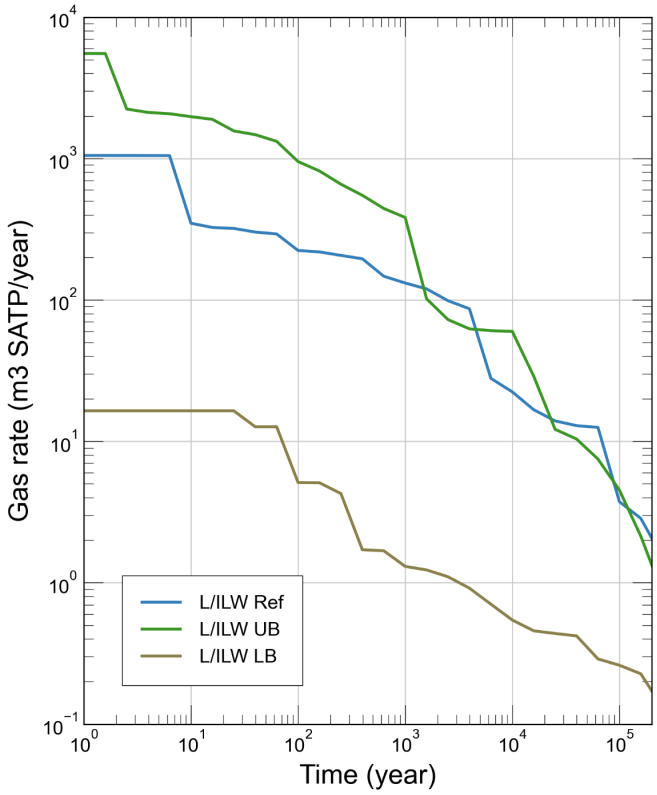

Fig. 3-12: Total gas generation rates per L/ILW emplacement cavern

Best estimates (blue line), upper bound (green line) and lower bound (brown line) values.

3.5.5 Reference case

The reference simulation corresponds to a case with the reference model parameters and reference gas generation rates (blue line in Fig. 3-12). Note that additional scenarios are run with the upper bound and lower bound gas generation rates ("UB" and "LB" lines, respectively in Fig. 3-12). The base case simulates 1,000,000 years of gas generation, preceded by the steady-state ventilation runs as described in Section 3.5.3.

3.5.6 Monte Carlo simulations

Monte Carlo simulations are performed to evaluate the influence of uncertainty of key parameters on the maximum pressures in the OPA and inside the caverns, in particular the permeability, porosity, and pore compressibility of the OPA. The distributions of the parameters considered are given in Tab. 3-11, and are used to generate a set of 100 Latin Hypercube samples, as depicted in Fig. 3-13.

Note that other model parameters linked to the ones sampled are further calculated, namely:

- Vertical permeability of the OPA:
  $K_v(\mathrm{OPA}) = K_h(\mathrm{OPA})/5$ (8)

- Horizontal permeability of the EDZ:
  $K_h(\mathrm{EDZ}) = 10 \times K_h(\mathrm{OPA})$ (9)

- Vertical permeability of the EDZ:
  $K_v(\mathrm{EDZ}) = 10 \times K_v(\mathrm{OPA})$ (10)

- Porosity of the EDZ:
  $\phi(\mathrm{EDZ}) = \phi(\mathrm{OPA})$ (11)

- Pore compressibility of the EDZ:
  $C_p(\mathrm{EDZ}) = C_p(\mathrm{OPA})$ (12)

Similarly, diffusion coefficients used in tracer simulations (for Cl-36) are perturbed to evaluate confidence intervals around the estimated tracer breakthroughs. The respective distributions are given in Tab. 3-12. Note that the reference values are the best estimates and differ from the means of the lognormal distributions.

Tab. 3-11: Distributions of of parameter values used in the Monte Carlo gas simulations for L/ILW

K_h is the horizontal permeability, ϕ the porosity, and C_p the pore compressibility. $\mathcal{U}(a, b)$ corresponds to a uniform distribution sampled between a and b, and $\mathcal{N}(\mu, \sigma)$ represents a normal distribution with mean μ and standard deviation σ.

Material	Parameter	Distribution
OPA	$\log_{10}(K_h)$ [m^2]	$\mathcal{U}(-21.04, -19.34)$
	ϕ [-]	$\mathcal{N}(0.115, 0.0128)$
	C_p [1/Pa^{-1}]	$\mathcal{U}(1.19, 4.167) \times 10^{-9}$

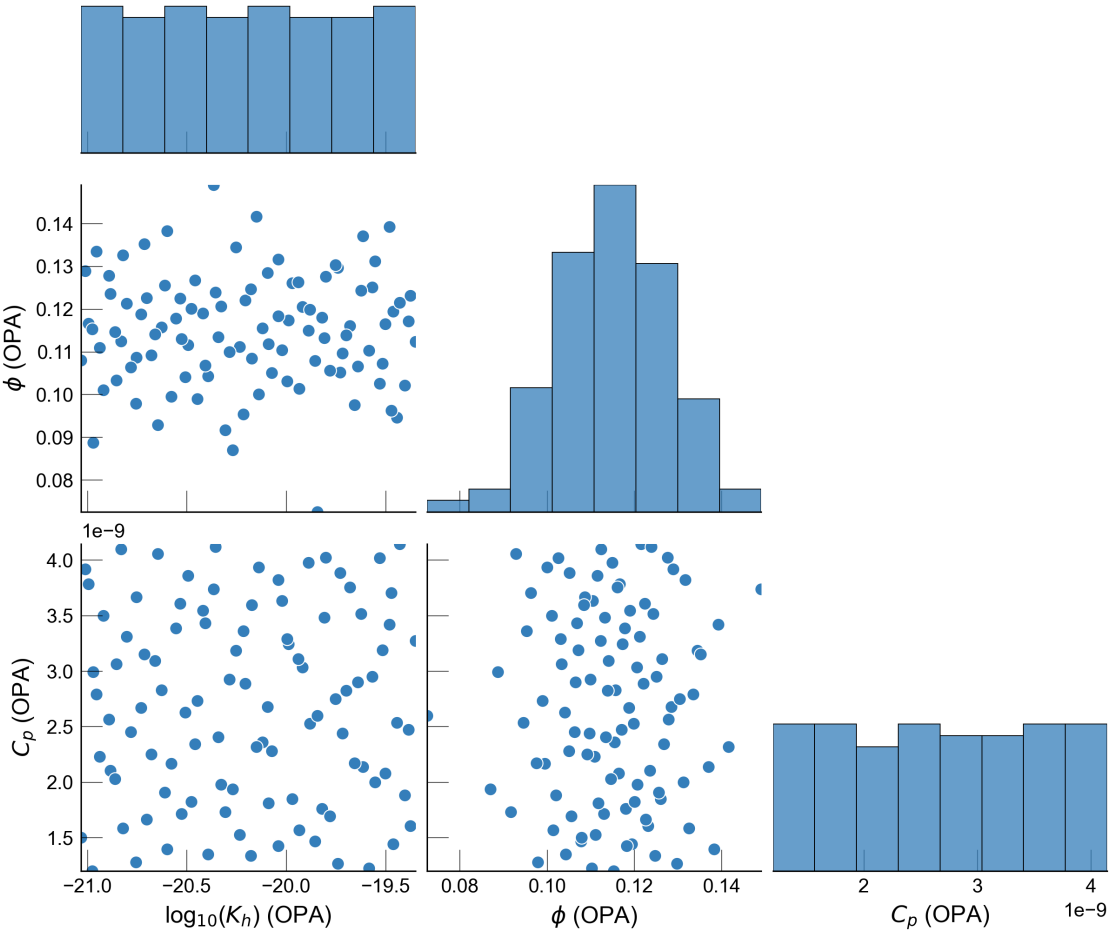

Fig. 3-13: Scatter-plot matrix of the 100 Latin Hypercube samples used for gas simulations for L/ILW

The subplots along the diagonal show the marginal distributions (as a histogram) of the samples, while the off-diagonal subplots of the matrix represent a pairwise scatter plot between the different model parameters.

Tab. 3-12: Means and standard deviations of the lognormal distributions fitted to the effective diffusion coefficients used for tracer simulations for L/LW

(From Glaus et al. 2024).

The last column represents the best estimates used as reference values.

Material	$\log(D_e)$ [mean]	$\log(D_e)$ [std.]	D_e [m^2/s]
TERT	-25.81	0.12	6.14E-12
MALM	-25.81	0.12	6.14E-12
MM2	-25.81	0.12	6.14E-12
CM	-26.10	0.11	4.79E-12
MM1	-25.80	0.09	6.25E-12
AD	-26.26	0.31	3.72E-12
HERRE	-25.89	0.15	5.65E-12
SADHB / DOGG	-26.29	0.48	3.40E-12
OPA	-26.66	0.31	2.69E-12
ML	-25.85	0.14	5.84E-12
AL	-26.18	0.17	4.35E-12
KEUK	-26.13	0.47	3.93E-12
KAU	-25.90	0.28	5.40E-12
KAL	-26.39	0.50	3.02E-12
GIPSK	-25.92	0.29	5.25E-12
MAK	-27.07	0.59	1.35E-12
MUSCH	-27.07	0.59	1.35E-12
PERM	-27.07	0.59	1.35E-12

3.6 Process models (2D)

As discussed in more detail in Chapter 4, the evolution of the nearfield around the disposal areas depends on complex coupled THM-C processes. However, the computationally expensive PA calculations are conducted using simplified conceptual models that in most cases account only for TH processes in an explicit manner (see also Chapter 5). These simplifications require process abstraction steps that are supported by so-called process models. Process models account for fully coupled processes and are used on the one hand to test the validity of the more abstracted assessment models, and on the other hand to derive effective parameters to be used in the abstracted conceptualisations. An example is shown in Fig. 3-14 with a 2D model of the HLW nearfield used to simulate the fully coupled THM evolution with Code_Aster. The results are used as synthetic THM data for data inversion using a TH model with iTOUGH2. The verified TH concept is subsequently used for the model-based assessments with TOUGH3. More details are available in Chapter 4 and in Nagra (2024j). The present report does not discuss process models any further as it focuses on the assessment models (total system and component models for HLW and L/ILW).

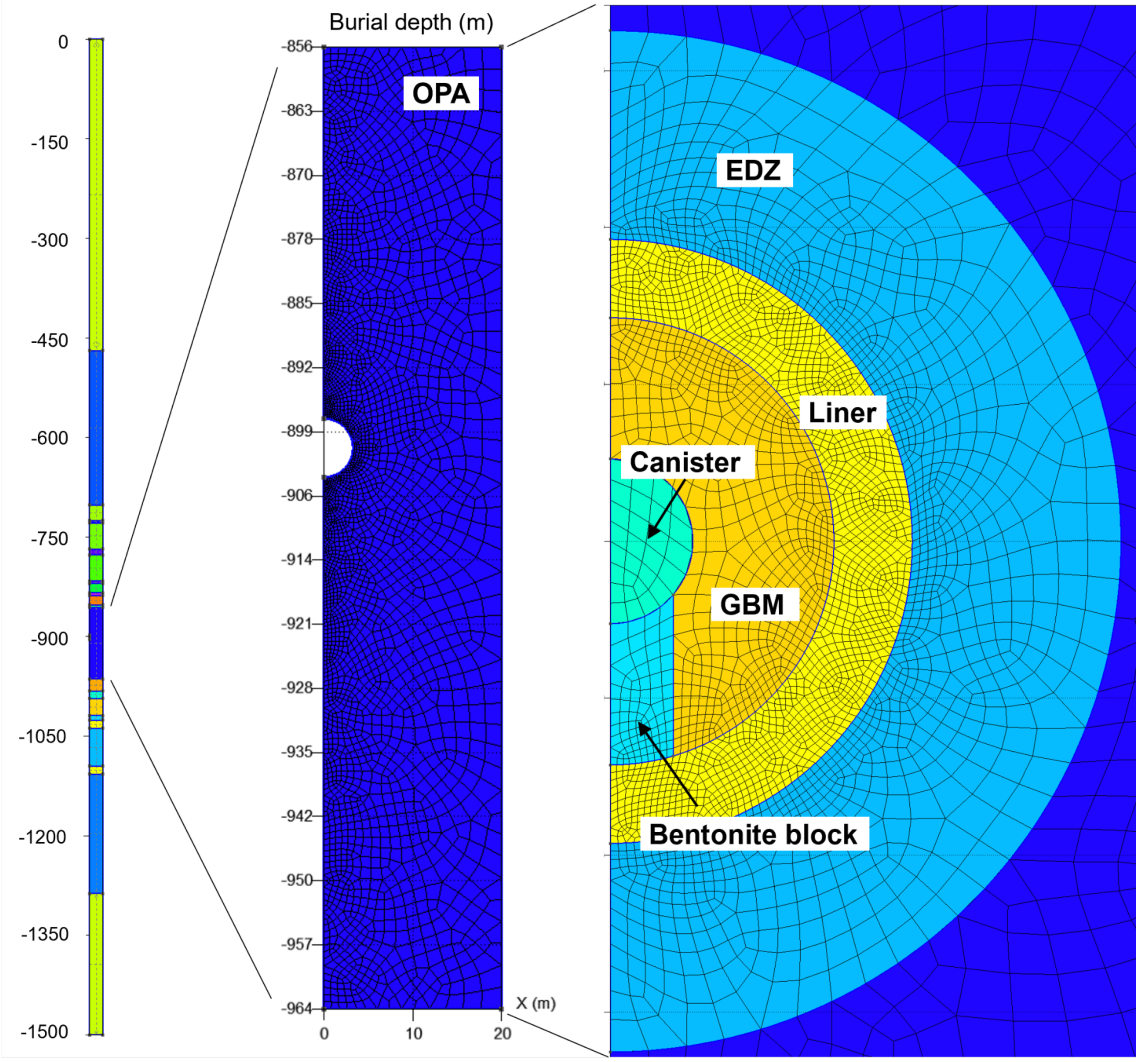

Fig. 3-14: Example of a 2D process model of a cross-section through an HLW tunnel with surrounding EDZ, OPA, and the over- and underlying stratigraphic units

3.7 Model outputs

In general, the assessment models can provide user-defined output of state variables (e.g., saturation, pressure, temperature) in space and time. The following types of quantitative outputs are used in the system analysis:

- spatial plots of distribution of state variables at selected timesteps;
- transients of state variables (pressure, saturation, temperature, mass fractions) at selected locations (Nagra 2024j);
- transients of flow rates (gas, water) at selected cross-sections;
- transients of normalised tracer flux (I-129 for HLW and Cl-36 for L/ILW, respectively; for normalisation method see Sections 7.1 and 8.1, respectively).

Note that pressure corresponds to gas pressure when a gas phase is present, and liquid pressure when only water is present, respectively.

The spatial plots essentially provide isolated snapshots of the hydraulic evolution. In that sense, their use in this report is limited, with the primary aim of helping the reader to visualise the problem under consideration rather than deriving quantitative conclusions. They complement the quantitative analysis which is predominantly based on the assessment metrics, namely the transients of state variables, flow rates and fluxes. A selected subset of these metrics is subsequently used in the PA synthesis as performance indicators to derive performance indices (Nagra 2024j).

The assessment metrics are evaluated at multiple observation points in the models that are deemed relevant to deliver key model outcomes to the assessment. The selection of these observation points is based on the phenomenological understanding of the repository evolution (Nagra 2024e). The rationale behind the PA modelling chain, which is designed to capture the repository evolution in an abstracted yet sufficiently representative manner for the purposes of the safety assessment (see also Nagra 2024j), is tied to each model's performance with regards to these metrics. This process is described in detail in Chapter 4. The observation points, shown in Fig. 3-15, are the following:

3D repository model

L/ILW cav: in the central L/ILW emplacement cavern (fourth cavern);

V1 L/ILW: in the V1 seal of the central L/ILW emplacement cavern;

OT L/ILW: in the operations tunnel directly connected to the L/ILW emplacement caverns, before the V2 seal;

V2 L/ILW: in the V2 seal of the L/ILW repository section;

L/ILW cav pilot: in the pilot L/ILW emplacement cavern in the pilot repository;

OT central (L/ILW): in the operations tunnel between the V2-L/ILW seal and the central area;

HLW can: in the central HLW emplacement drift, within an element containing a heat source;

HLW bent: in the central HLW emplacement drift, within an element not containing a heat source;

V1 HLW: in the V1 seal of the central HLW emplacement drift;

OT HLW: in the operations tunnel directly connected to the HLW emplacement drifts, before the V2 seal;

V2 HLW: in the V2 seal of the HLW repository section;

HLW can pilot: in the emplacement drift of the HLW pilot repository, within an element containing a heat source;

HLW bent pilot: in the emplacement drift of the HLW pilot repository, within an element not containing a heat source;

OT central: in the operations tunnel between the V2-HLW seal and the central area;

OPA above HLW: in the OPA, 30 m directly above the centre of the HLW disposal area;

V2 L/ILW model outlet: in the operations tunnel directly after the V2-L/ILW seal towards the central area;

V3 model outlet: in the access tunnel that leads to the access shaft from the HLW section;

Central area: in the tunnel at the middle of the central area;

EUU: in the facilities of the EUU;

Access tunnel: in the access tunnel that connects to the access shaft;

Access shaft V3: in lower part of the V3 seal of the access shaft;

Access shaft (DOGG): in the shaft directly above the V3 seal (section in DOGG layer).

All observation points in the repository model are taken from the same model layer. This corresponds to the third layer (bottom to top) out of four layers in the L/ILW emplacement caverns, and the second layer (top layer) out of two layers in the operations tunnels, access tunnels, and sealing sections.

3D model of L/ILW emplacement cavern & V1-L/ILW seal

M1, waste top: in the M1 mortar, halfway between the top of the top disposal container and the roof of the emplacement cavern, between the seventh and eighth stacks of disposal containers (counting from mouth of the cavern);

M1, waste bot: in the M1 mortar, between the bottom disposal containers of the seventh and eighth stacks;

M1, mouth top: same as *M1, waste top* but between the first and second stacks of disposal containers (counting from mouth of the cavern);

M1, mouth bot: same as *M1, waste bot* but between the first and second stacks of disposal containers (counting from mouth of the cavern);

S/B top: in the sand/bentonite (S/B) sealing element of the V1 seal, top element at tunnel roof;

S/B bot: in the S/B sealing element of the V1 seal, bottom element at tunnel invert;

Trans. top: in the middle transition layer between sealing element and abutment, top element at tunnel roof;

Trans. top: in the middle transition layer between sealing element and abutment, top element at tunnel roof;

Abut. top: in the abutment, top element at tunnel roof;

Abut. bot: in the abutment, bottom element at tunnel invert.

All observation points are located axially or at the centre of the tunnel, respectively.

3D model of HLW emplacement drift & V1-HLW seal

CAN 2 top: at the second canister (counting from mouth of the emplacement drift);

PELL above CAN 2: in the bentonite directly adjacent to the second canister (5 cm from canister);

PELL mid: in the bentonite halfway between the second canister and the liner wall;

PELL top: in the bentonite directly adjacent to the liner wall;

PELL btw. CAN 2&3: in the bentonite between second and third canister, middle of emplacement drift;

LINER: in the liner above the second canister;

V1 branch side: in the bentonite of the V1 adjacent to the outer transition layer, middle of emplacement drift;

CAN 10 top: same as CAN 2 top, but at the tenth canister (counting from mouth of the emplacement drift);

OPA 20 m lateral: in the OPA, at 20 m laterally from the tenth canister;

OPA 20 m above: in the OPA, at 20 m directly above the tenth canister;

OPA 50 m above: in the OPA, at 50 m directly above the tenth canister.

All observation points are located axially or at the centre of the tunnel, respectively.

3D model of V2-L/LW seal

S/B top: in the S/B sealing element of the V2 seal, top element at cavern roof;

S/B bot: in the S/B sealing element of the V2 seal, bottom element at cavern invert;

EDZ: in the EDZ above *S/B top;*

VF1 top: in the VF1 backfill towards the disposal area, top element at cavern roof;

VF1 bot: in the VF1 backfill towards the disposal area, bottom element at cavern invert;

Liner: in the liner above *VF1 top*;

VF2 top: in the VF2 backfill towards the central area, top element at cavern roof;

VF2 bot: in the VF2 backfill towards the central area, bottom element at cavern invert;

Trans t.: in the transition layer between abutment and VF2 backfill, top element at cavern roof;

Trans b.: in the transition layer between abutment and VF2 backfill, bottom element at cavern invert.

All observation points are located axially or at the centre of the tunnel, respectively.

3D model of V3 seal

Seal: in the middle compartment of the bentonite sealing element of the V3;

EDZ at seal: in the EDZ next to the seal;

Abutment: in the middle of the abutment above the sealing element;

Shaft above seal: at the bottom of the shaft directly above the abutment;

Trans. below seal: in the transition layer below the sealing element;

Shaft bot: in the shaft sump;

Access tunnel: in the access tunnel leading to the base of the shaft.

All observation points are located axially respectively at the centre of the shaft and access tunnel.

2D model of 20 HLW tunnels (*2D-HLW×20),*
2.5D model of 20 HLW tunnels *(2.5D-HLW×20)*

Nearfield: in bentonite directly adjacent to the canister;

Bentonite: at the middle of the bentonite; (for temperature in the 2D representation also referred to as "Average temperature bentonite");

20 m above HLW: in the OPA, at 20 m directly above the tenth drift;

Release from OPA: interface OPA top/bottom to over- and underlying confining units;

Release into Keuper-Malm: interface between KAU and KAL, and between MM2 and Malm (not shown in figure);

Release into Muschelkalk-Malm: interface between MAK and MUSCH, and between MM2 and Malm.

2.5D model of 7 L/ILW caverns *(2.5D-L/ILW×7),*
2.5D model of 1 L/ILW cavern *(2.5D-L/ILW×1),*
2.5D model of 1 L/ILW cavern & V3 (*2.5D V3*)

Mortar: in the L/ILW cavern at the middle of the disposal area;

EDZ: in the EDZ above the L/ILW cavern at the middle of the disposal area;

V1: in the V1-L/ILW seal connected to the cavern at the middle of the disposal area;

Branch: in branching tunnel connected to the V1 seal at the middle of the disposal area;

Release from OPA: interface OPA top/bottom to over- and underlying confining units;

Release into Keuper-Malm: interface between KAU and KAL, and between MM2 and Malm (not shown in figure);

Release into Muschelkalk-Malm: interface between MAK and MUSCH, and between MM2 and Malm;

From V3 to shaft: interface between V3 seal and overlying shaft, in upwards direction (not shown in figure).

(a)

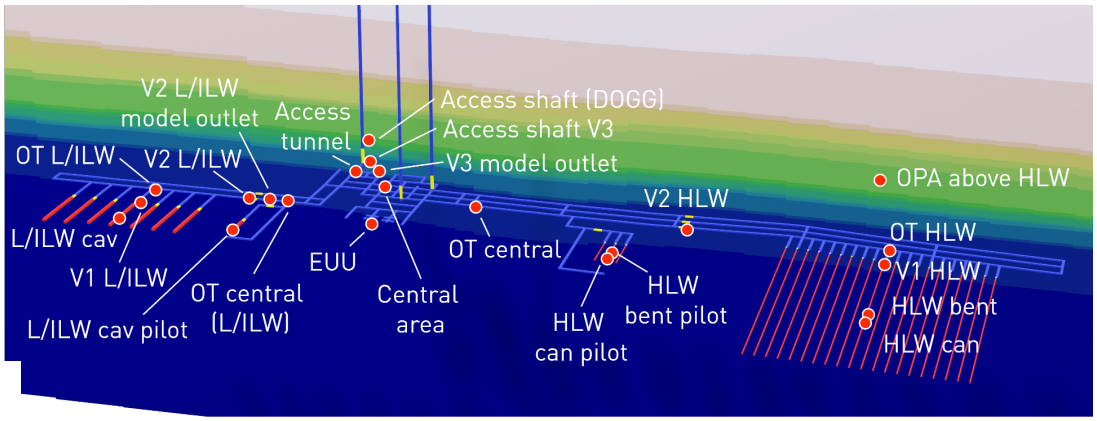

(b)

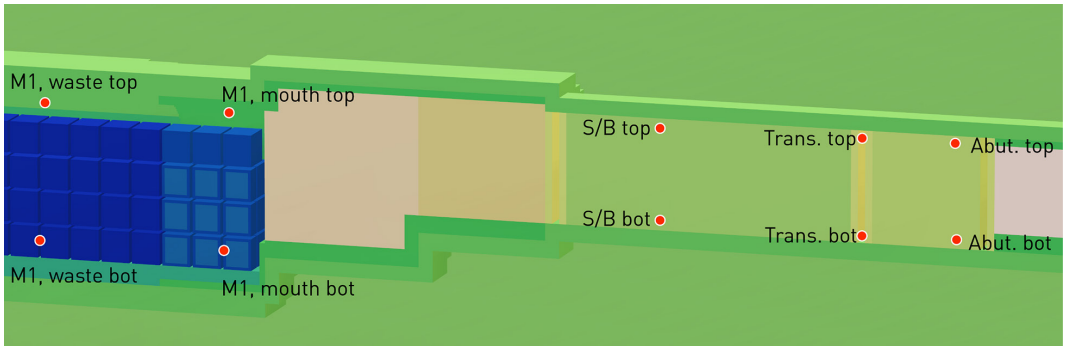

(c)

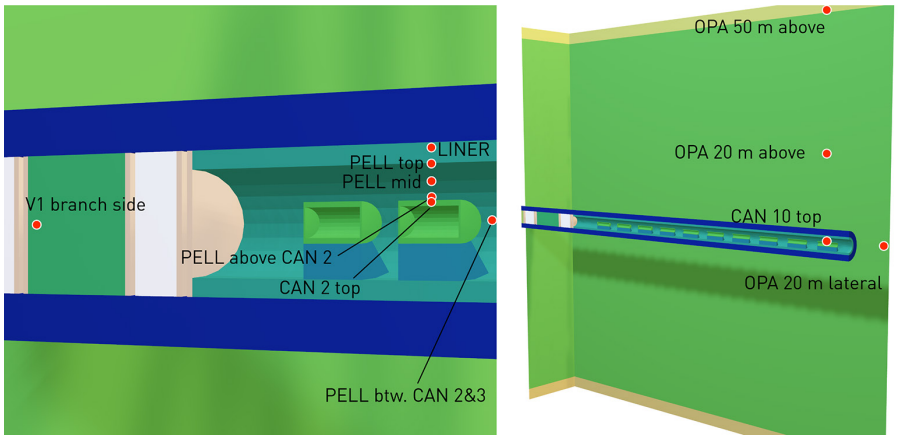

(a) 3D repository model, (b) 3D model of L/ILW cavern, (c) 3D model of HLW drift.

(d)

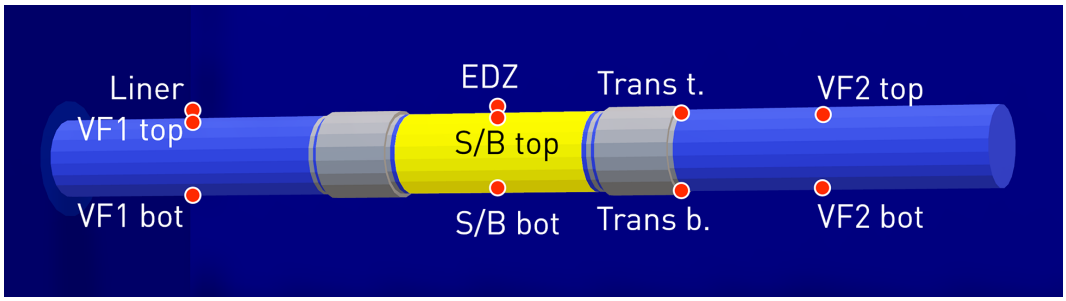

(e)

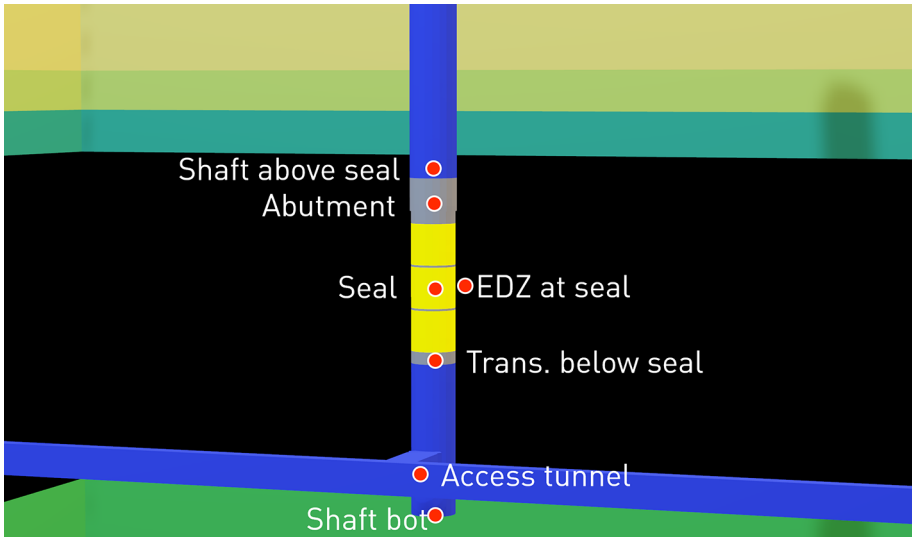

(f)

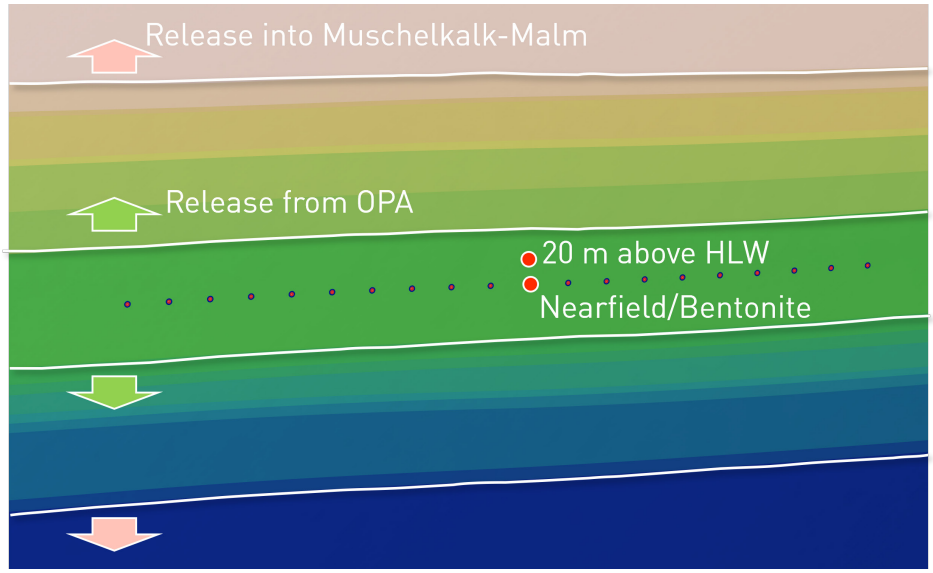

d) 3D model of V2-L/ILW seal, (e) 3D model of V3 seal, (f) 2D model of 20 HLW drifts.

(g)

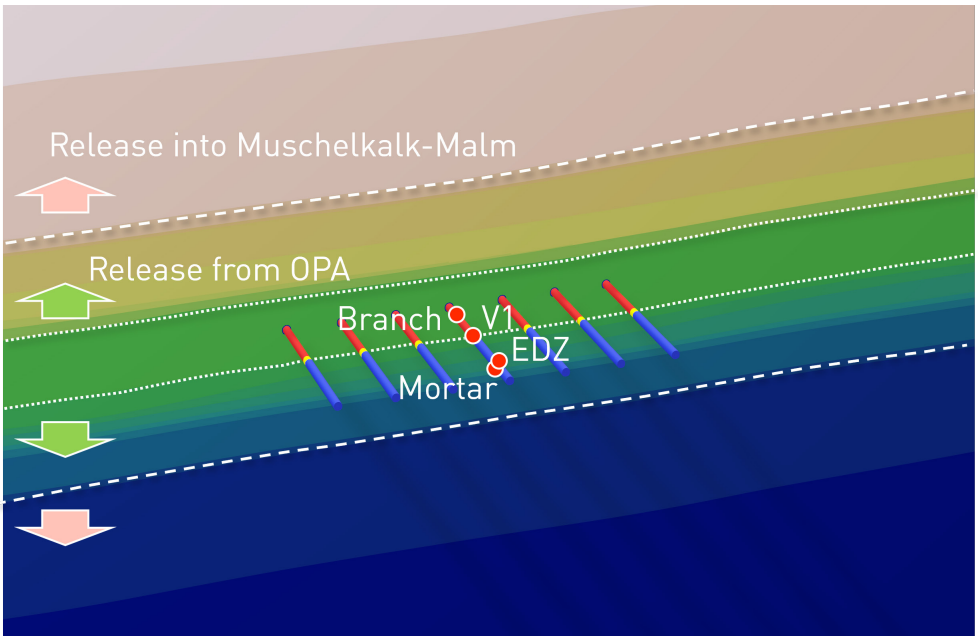

Fig. 3-15: Observation points used for simulated transients
(g) 2.5D model of 7 L/ILW caverns.

4 Model abstraction

4.1 Basic principles

By definition, a model is an abstraction of a real-world system, gained by eliminating unnecessary detail. Consequently, any type of model abstraction (in other terms "conceptualisation") introduces some level of inaccuracy and uncertainty, in that it involves a reduction of the degrees of freedom of the real-world system. In PA and SA workflows, the "elimination of unnecessary detail" is a required and desirable feature, as it improves the traceability of the system behaviour. At the same time, it must be proven that the "elimination of unnecessary detail" does not impair the intended use of the model as a tool for an unbiased assessment of repository safety. This calls for modelling frameworks with a traceable procedure for uncertainty propagation along the model abstraction chain.

Tracking uncertainty propagation is a complex process, which starts with the model-supported interpretation of uncertain field observations, site characterisation data and laboratory experiments, respectively. On the other end of the abstraction chain, focus of the assessment is on the performance of the entire repository system, or components thereof, with respect to predefined safety targets. The abstraction process must bridge the gap and provide the framework to trace the uncertainty ranges of model outputs back to the uncertain input parameters in a quantitative manner. Sources of conceptual uncertainty introduced with the abstraction process (see also Section 2.2.4) are associated with the following:

- geometric abstractions (Section 4.2): simplifications in the representation of geometries;
- process abstractions (Section 4.3): simplifications in the formulation of phenomena and processes;
- homogenisation / scaling of parameters (Section 4.4): spatial and temporal averaging of effective material properties;
- Simplified formulations of boundary conditions, initial conditions and source terms (Section 4.5).

These types of abstractions are accordingly specified in the following sections for the PA models with the outlook of estimating the uncertainty ranges of the corresponding safety indicators.

4.2 Geometric abstractions

4.2.1 Simplifications in model geometries

Model-based assessments rely on model geometries that represent repository structures in the subsurface environment. The first geometric simplification lies in the approximation of the subsurface as an ensemble of discrete geological units and tectonic features (e.g., faults). An example is shown in Fig. 4-1. Sharp interfaces are therein assumed between geological units so that formation- or facies-specific properties can be assigned to different model domains (or formation-specific distributions, see Section 4.4.3). Similarly, interfaces between faults and intact rock are discrete, wherein fault properties can differ from those of the background intact rock (Fig. 4-1). In 3D model geometries, formation interfaces correspond to 3D isosurfaces whereas, in most cases, faults can be assumed to be planar. In 2D geometries, formation interfaces correspond to their trace on the modelled cross-section, whereas fault planes are projected as 1D lines. Accordingly, representative conceptualisations are feasible in 2D to capture possible intersections of faults with the repository structures, as shown exemplarily in Fig. 4-1, instead of explicit representations of all possible configurations ("unnecessary detail", see Section 4.1).

(a)

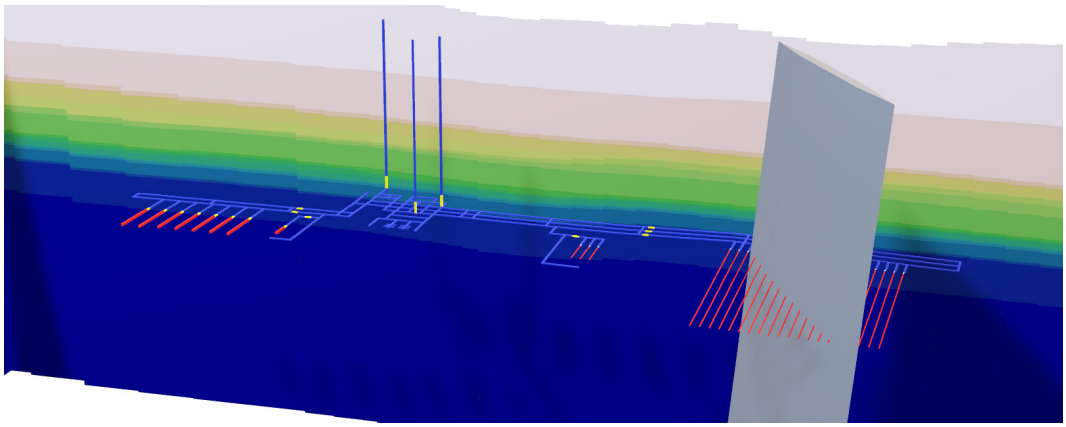

(b)

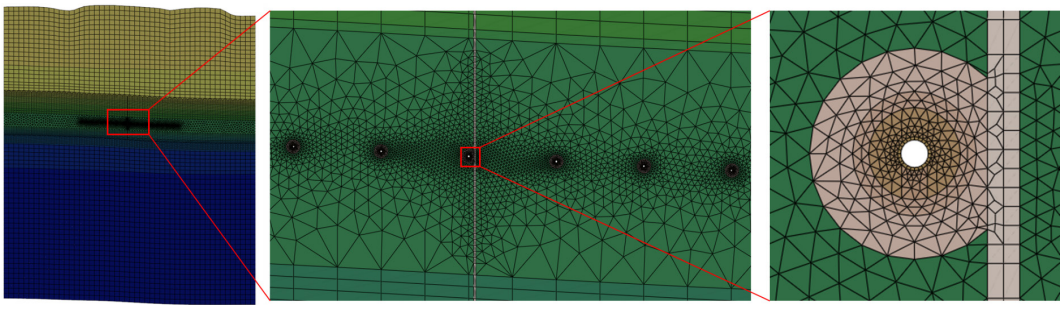

(c)

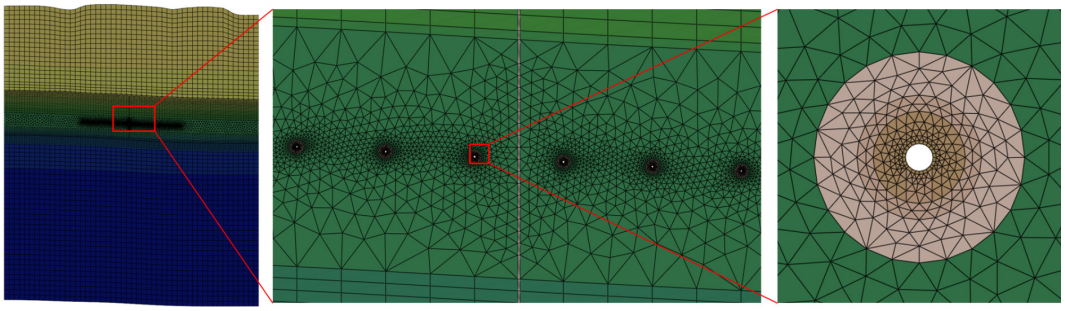

Fig. 4-1: Example model geometries implemented in PA modelling

(a) 3D model representation of the geological repository with the stack of discrete geological units and a hypothetical sub-vertical fault crossing the HLW disposal area; (b) 2D model representation of a cross-section perpendicular to the emplacement drifts approximating the fault as vertical and intersecting with the EDZ of one emplacement drift; (c) 2D representation of a cross-section perpendicular to the emplacement drifts approximating the fault as vertical at the midpoint between two emplacement drifts.

Geometric simplifications are also introduced in the approximation of the real-world repository structures. Like designs, model conceptualisations represent structures using conventional shapes and assuming perfect implementation of these shapes. For example, an emplacement drift for HLW is conceptualised as a perfectly cylindrical tunnel with all waste canisters located exactly in the middle along the central axis. In addition, model geometries may deviate for practical reasons from that design in terms of shapes, lengths, slopes, volumes, and layout.

For the purposes of model-based assessments on the scale of the entire repository, it is possible to reduce the level of detail in the repository layout implemented in model geometries as shown exemplarily in Fig. 4-2a. Accordingly, the main components of the repository, such as emplacement rooms and access tunnels, are approximated in 3D with rectangular cross-sections by scaling volumes and cross-sectional areas of the respective designs. Such geometries are used for deterministic assessments of the total system (see Section 3.3.1, “3D deterministic repository model”).

The abstraction inherent in this approach is controlled through comparison to models that are likewise implemented in 3D but on the scale of individual components that introduce greater level of detail (Fig. 4-2b). The comparison is carried out in terms of key metrics relevant to indicators used in the PA and aims to confirm that the abstracted representation on the repository scale captures the essence of component-scale effects in a representative and, to a reasonable degree, conservative manner. These detailed geometries are further used for deterministic assessments on the level of components (see Section 3.3.2, “3D deterministic component models”).

In the next step, 2D or 2.5D geometries are implemented at selected locations combining repository components and their respective volumes with cross-sections through the geological environment (Fig. 4-2c). The implementation is achieved through benchmarking and validation with the 3D models. These geometries are used for probabilistic assessments to address parametric uncertainty (see Sections 3.4 and 3.5, “Probabilistic component models HLW” and “Probabilistic component models L/ILW”, respectively).

(a)

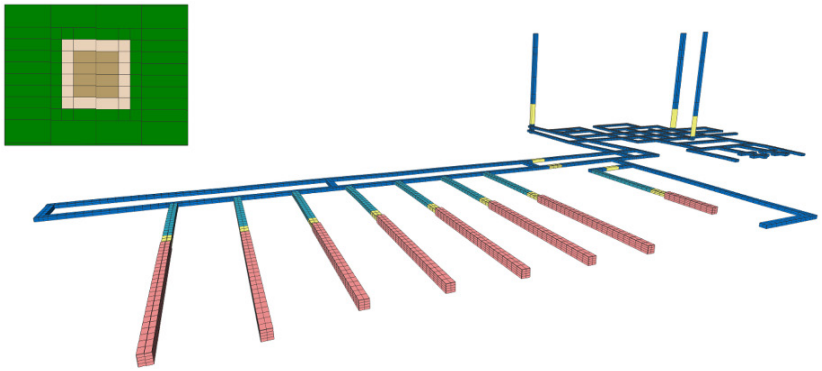

(b)

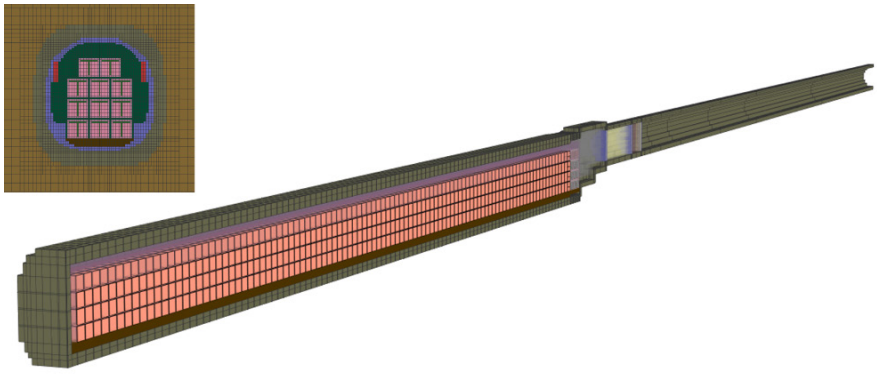

(c)

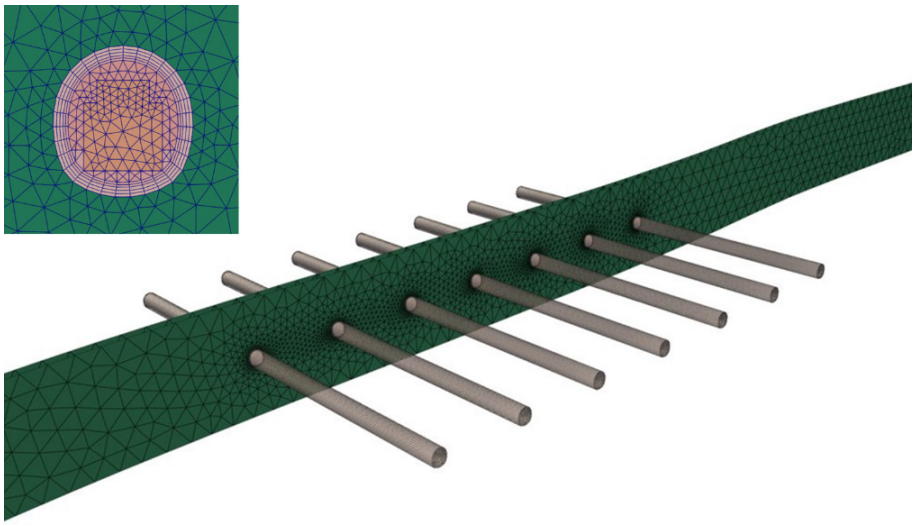

Fig. 4-2: Example representations of the L/ILW disposal area in the PA

(a) 3D representation of entire L/ILW section; (b) 3D representation of a single emplacement cavern; (c) 2.5D representation of disposal area.

4.2.2 Simplification of quasi-symmetric geometries

The decision between detailed or simplified geometries for a given intended use is closely related to the topic of superposition. Model conceptualisations often make use of the principle of superposition to minimise model size and therewith reduce computational effort. The superposition principle is a fundamental concept in physics and engineering, stating that *for all linear systems the net response caused by two or more stimuli is the sum of the responses that would have been caused by each stimulus individually*. An example is the emplacement drift for HLW, where the emplaced materials and their properties are assumed symmetric across the vertical plane along the central axis of the drift. Accordingly, source terms in this model conceptualisation are distributed evenly between both sides of this plane (see also Section 4.5). If the environment surrounding the tunnel is also symmetric, both in terms of geometry and in terms of properties, the functionality of a half-tunnel model with a no-flow boundary condition at the plane of symmetry is the same as that of a full-tunnel model, albeit with half the mesh size. An extension of that principle is the assumption of no-flow conditions at the opposite lateral boundary, e.g., in the host rock away from the tunnel, which implies superposition of multiple tunnels at distance that is equal twice the distance between the two no-flow boundaries in the model. In principle, this conceptualisation corresponds to an ensemble of an infinite number of identical, equidistant tunnels. The assumption of linearity of responses may therefore deviate from reality due to boundary condition effects, as the real-world system corresponds to a finite number of tunnels surrounded by geological formations that are typically inclined in space.

This example is illustrated in Fig. 4-3. The 3D representation (Fig. 4-3a) allows to explicitly account for 20 tunnels with the rock mass surrounding the disposal area in all three directions. The 2D representation of 20 tunnels (Fig. 4-3b) accounts for the rock mass in two directions and essentially corresponds to a finite number of tunnels with infinite length. Finally, the 2D representation of half tunnel (Fig. 4-3c) is the abstracted representation of an infinite number of emplacement drifts next to each other.

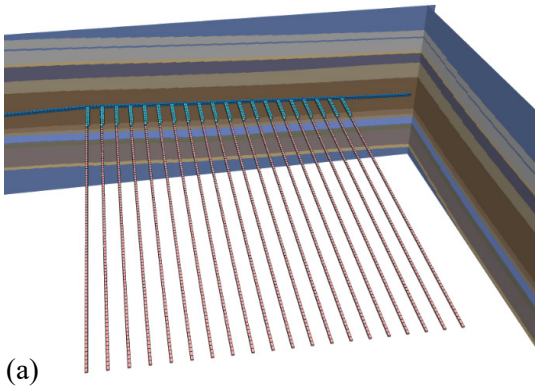

(a)

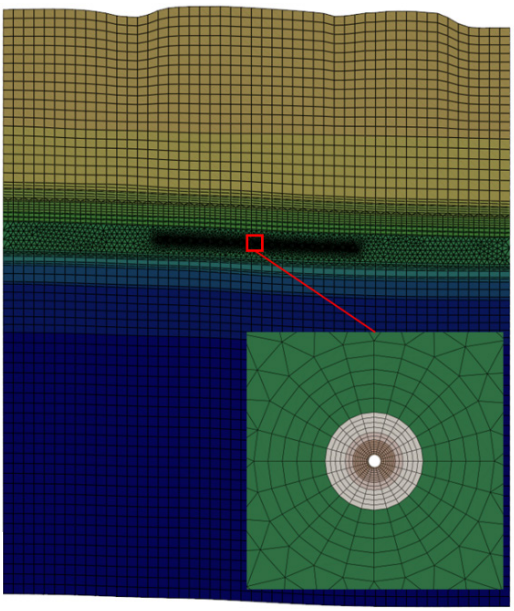

(b)

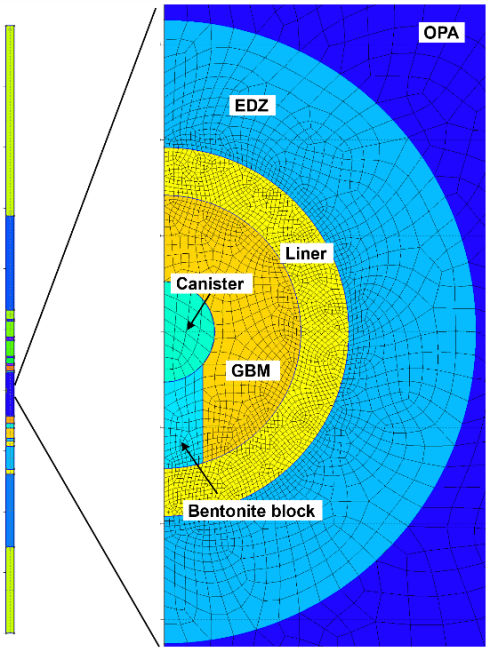

(c)

Fig. 4-3: Example representations of the HLW disposal area in the PA

(a) 3D representation of 20 HLW drifts with surrounding rock mass; (b) 2D representation with 20 HLW drifts and rock mass outside the disposal area; (c) 2D representation of half HLW drift with 20-m of rock mass laterally and no-flow boundaries (entire lateral extent not shown in figure).

4.2.3 Transport paths

Transport of fluid phases and energy will take place in the repository structures and surrounding rock mass during construction and ventilation of the repository as well as after emplacement of the waste and of the backfill and sealing materials (Nagra 2024g). Transport is driven by gradients in state variables, e.g., temperature gradients result in heat transport, concentration gradients in solute transport, and pressure gradients in fluid transport. In general, transport in porous media with low conductivity is mostly diffusive, and capillary-driven in case of partially saturated media, whereas transport in materials with high conductivity can be advective (see also Section 4.3.2). Similarly, fluid pressures increase with compression and accordingly decrease when more volume is available for the same amount of fluid mass. Transport paths in the repository system can be therefore deduced and conceptualised from general principles of physics applied to emplaced materials and surrounding rock formations, and consequently verified through inductive testing as part of the PA (see also Nagra 2024g).

Heat transport in the HLW nearfield takes place through bentonite materials and surrounding clay rock. Owing to the limited hydraulic conductivity of these media, convection of heat is relatively negligible compared to conduction. Heat transport around the HLW canister is therefore predominantly radial and skewed by any anisotropy or heterogeneity in thermal properties of the (partially saturated) media, notably thermal conductivity and heat capacity. Similarly, mass transport in the HLW nearfield is driven by diffusion especially after the saturation of bentonite with water and the dissipation of thermal effects in the early post-closure phase (Nagra 2024g). Heat and solute transport from HLW is therefore a predominantly radial diffusive problem and, depending on purpose, can be accordingly abstracted to 2D (perpendicular to tunnel axis) or even to 1D (vertical paths from emplacement drifts to aquifers).

On the other hand, mass transport in the operation and access tunnels of the repository takes place predominantly in permeable backfill materials. Pressure gradients generated initially from the excavation and ventilation of the repository and later from gas generation from corrosion and degradation of organic materials, can result in advective flows of gas and water along the repository tunnels. This axial transport needs to be considered in addition to any mass exchange, whether advective or diffusive, with the surrounding clay rock. Water and gas transport from the L/ILW caverns therefore combines a radial diffusive with an axial advective problem, and, depending on purpose, may require additional considerations for axial transport when abstracting to 2D or 1D.

The potential for reducing dimensionality is tied to a model's ability to capture adequately transport paths and is therefore a key element of geometric abstractions. Exemplary demonstrations are provided as part of the model verification process in Section 4.7.

4.3 Simplified representation of phenomena and processes

4.3.1 Basic principles

Modelling of physical phenomena is most useful when it is based on a description of the underlying processes rather than purely on correlations of observed data, as it offers the possibility to assess how the system will react when subjected to a new or different stress that is beyond the range of data used in the correlation (Pinder & Gray 2008). Modelling adopted in the PA is therefore based on fundamental principles of continuum mechanics, namely the conservation of mass, the conservation of momentum, and the conservation of energy. However, as explained in the following, modelling real-world systems based on purely physical expressions is unfeasible. The following sections outline the principles governing the systems of interest and the associated assumptions and simplifications adopted in the PA. The resulting mathematical formulations implemented for the purposes of modelling are provided in App. A.

4.3.2 Flow and transport of mass and energy (TH)

In fluid mechanics, the conservation of mass states that mass in a closed system may change chemical composition, due to chemical or biological reactions, but is neither destroyed nor created. A direct consequence of that is the principle of mass balance of a species:

$$\begin{bmatrix}\text{rate of change}\\ \text{of species mass}\\ \text{in volume}\\ (A)\end{bmatrix} + \begin{bmatrix}\text{net rate of loss of}\\ \text{species mass due to flow}\\ \text{across the volume boundary}\\ (B)\end{bmatrix} + \begin{bmatrix}\text{rate of decrease of species}\\ \text{mass due to transformation}\\ \text{to other species}\\ (C)\end{bmatrix} = 0 \qquad (13)$$

applied to a *control volume* of interest. In the case of flow and transport in porous media, the control volume is defined as the so-called *Representative Elementary Volume* (REV), the principles of which are elaborated in Section 4.4. The expression of mass balance in the REV sets the basis for mathematical modelling of flow and transport in porous media, that defines state variables to describe the state of the system at any time (e.g., pressure), and their time derivatives to describe changes in the system. The time derivatives consist of a volume integral for the control volume (terms *A* and *C* in Eq. 13) and a surface integral over its boundaries (term *B* in Eq. 13). The mass that leaves the control volume across its boundaries due to flow moving at the barycentric velocity of the fluid (e.g., the mass fraction weighted velocity of all species within this fluid) is referred to as *advection*. The mass that leaves the control volume across its boundaries due to random collisions between molecules causing spreading of the mass is referred to as *diffusion*. The diffusive flux relates to the gradient of concentration based on Fick's first law.

In a similar fashion, conservation of momentum is expressed with the Navier-Stokes equations, derived directly from the material law of Newtonian fluids (e.g., water, air, hydrogen), expressing shear stress as a function of viscosity and derivative of velocity. The momentum conservation is essentially the relationship between fluid pressure and advective velocity. In the case of flow in porous media, Darcy's law is used in lieu of a direct derivation of momentum conservation. Darcy's law was originally established experimentally in 1-D but has since been derived from the Navier-Stokes equations using averaging (Whitaker 1986, Quintard & Whitaker 1994a, Quintard & Whitaker 1994b) or homogenisation theory (Hornung 1997).

Energy conservation is expressed in a very similar way to mass conservation. Transfer of heat due to the barycentric fluid velocity (in other words, heat transported along with advective mass flow) is referred to as *convection*. Transfer of heat mediated by the combination of vibrations, collisions, and diffusion of molecules is referred to as *conduction*. Fourier's law provides the relationship between conductive flux and gradient of temperature.

Flow and transport problems in porous media can be thus expressed as mathematical formulations of conservation laws. However, it is already apparent from the previous that these equations alone are not sufficient to describe the system behaviour. Even the assumption of a rigid control volume that is available to fluids introduces the material-specific parameters like porosity and specific heat capacity. Moreover, the laws for mass advection, mass diffusion, and heat conduction introduce material-dependent parameters, namely hydraulic conductivity, diffusion coefficient, and thermal conductivity, respectively. Even with such material parameters, the number of unknown state variables that arise is greater than the number of conservation equations, so the equations must be complemented by correlations, or constitutive relationships, that describe some system dynamics in terms of other variables (e.g., dependency of viscosity on temperature, etc.). The need for constitutive relationships complicates efforts to model real-world systems, especially in porous media where constitutive relationships may be scale- and time-dependent.

4.3.3 Extension to two-phase flow (TH^2)

In the case of multiple fluids and species present in the system, conservation laws are formulated in a similar way for each phase and each species. Two additional state variables are introduced when two fluids are present in a porous medium: fluid saturation, defined as the fraction of the pore space occupied by the fluid, and capillary pressure, defined with the Laplace equation as the difference between non-wetting (e.g., gas) and wetting (e.g., liquid) fluid pressure. An additional constitutive relationship is formulated between capillary pressure and fluid saturation, introducing the so-called capillary threshold pressure, also known as entry pressure, and a shape parameter. In gas-water problems, the threshold pressure practically represents the difference between gas and water pressure required to displace porewater from the medium when it is initially fully water-saturated. In theory, the capillary strength corresponds to the capillary pressure of the largest-radius pores that the gas pressure needs to overcome so that gas enters these pores, whereas the shape parameter is a proxy for the pore size distribution and variability of the pore network. Moreover, Darcy's law is extended with the so-called relative permeabilities for each fluid, expressed as constitutive functions of fluid saturation, to account for the fact that the presence of the other fluid decreases the pore space available for flow.

In summary, in visco-capillary flow systems, fluid transport is controlled by the interaction of viscous, capillary and gravity/buoyancy forces, the solubility and diffusion of species, and the connectivity and variability of the pore network. The integral form of the mass and energy conservation equations expressing this problem, complemented with the extended Darcy's law and the constitutive relationships required to close the system of equations, is subsequently discretised and solved by means of numerical modelling.

4.3.4 $TH^2M \rightarrow TH^2$ abstraction

By definition, a phase is a liquid, gas or solid that is separated from another liquid, gas or solid by an identifiable boundary. Although the definition of a porous medium requires that the solid be relatively immobile, a precise specification of the degree of solid mobility or deformation that is allowable by this definition is not possible. The inherent assumption in the formulations discussed in Sections 4.3.2 and 4.3.3 is that the rock mass is either rigid or behaves like an elastic medium that deforms very slowly relative to the fluid motion so that velocity components of the solid phase can be set to zero in the derivatives (Pinder & Gray 2008).

In extension of a TH^2 system to a deformable porous medium, an additional state vector variable, the displacement vector, is introduced. This variable captures the deformation state of the REV to account for elastic or plastic change in the solid phase. Solid mass conservation is maintained under the assumption of negligible velocity components of the solid phase of a deformable REV. Momentum balance and accordingly material laws are derived for solid phase to define the stress equilibrium (e.g., equilibrium between gravitational forces, external mechanical forces, and pore pressures). In the case of hydromechanical coupling, phenomenological material laws are often used in lieu of direct derivations, which introduces additional constitutive relationships. Furthermore, coupling to energy transport requires additional parameters for the transformation of heat to mechanical energy and vice versa.

The accumulation of uncertain material parameters and constitutive relationships required as input when mathematical formulations are extended to include further processes poses a major challenge in modelling. In addition, the number of highly non-linear coupled equations with several unknown state variables significantly increases the problem size and associated computation time even for simplified geometries and decreased dimensionality. This calls for pragmatic approaches that can capture the essence of mechanical effects in the TH^2 consideration a simplified manner. The abstraction follows two main assumptions, elaborated in Nagra (2024j):

- Deformation from the hydromechanical coupling can be approximated as volumetric change as a function of pore pressure change.
- Deformation from the thermomechanical coupling can be approximated as volumetric change as a function of temperature change.

For this, a simple parametric model is adopted, scaling porosity with pressure and temperature change through the pore compressibility and heat expansion coefficient, respectively. In turn, changes in porosity can be coupled to changes in permeability and capillary strength through semi-empirical or scaling relationships (e.g., Kozeny-Carman and Leverett scaling, respectively). Key to the validity of these principles is the intended use of the model. The TH^2 model aims at capturing hydraulics and transport, without introducing bias through the abstraction of mechanics. In the TH^2M consideration, the effect of the mechanical coupling is linked to hydraulics only through changes in porosity. In that sense, using porosity as proxy for the effect of hydromechanics on transport is not against the philosophy of the fully coupled consideration, as long as the parametric model captures sufficiently the result of the underlying mechanisms.

4.3.5 $TH^2C \rightarrow TH^2$ Abstraction

Similarly, modelling the fully coupled geochemical evolution of a TH^2 system on the scale of a repository is practically unfeasible. The spatial and temporal scales associated with all processes relevant to chemical (biological) and transport couplings in heterogeneous media span several orders of magnitude. A common approach adopted in geochemical models to overcome this challenge is to use abstracted representations of the two-phase flow transport problem, postulating that chemical reactions predominantly depend on the availability of water. Hydraulics are therewith approximated, e.g., assuming stationary conditions or using proxy state variables, mainly fluid saturation and/or flows, in the form of boundary conditions or source terms.

Accordingly, the essence of geochemical effects in the TH^2 consideration is captured in a simplified manner. The abstraction follows two main assumptions:

- Chemical reactions that result in changes the chemical composition of fluids can be approximated as species source and sink terms that are variable in time and space.
- Chemical reactions that result in mineral precipitation/dissolution can be approximated as porosity changes that is variable in space and time.

In turn, variants of source / sink terms and porosity are assigned to specified sections of the repository in PA modelling, e.g., in the waste emplacement rooms. These feed directly into the mass conservation formulations adopted for the TH^2 problem. The TH^2 model outcomes feed back into the geochemical analyses to check assumptions and inform variants related to the hydraulic evolution of repository components.

4.4 Homogenisation / scaling of parameters

4.4.1 Basic principles

The properties of a fluid or solid substance at a given "point" are essentially the average effect from a large number of molecules comprising the substance in the vicinity of that point. In a similar way, "point" values for porous media correspond to an averaging region on a spatial scale referred to as the *macroscale*. As discussed in Section 4.3.2, in the formulation of macroscale conservation laws for porous media, the averaging region is the REV. The basic principle of the REV is that it must produce averages that are insensitive to small changes in its size. Essentially that means that the REV is large enough so that no fluctuations are observed in its averaged properties, allowing to represent the porous medium as a continuum (Bear 1972). At each point of the continuum, solid and fluid phases are simultaneously present at a ratio expressed through the state variable of water content (or saturation). On the other hand, extending the size of the region of interest can result in sub-regions with different average properties. The implementation of REVs with different properties constitutes the continuum conceptualisation of macroscale heterogeneity.

When different materials, with different properties, are assigned to regions of a model, parametric uncertainty arises. As discussed in Section 2.2.4, this uncertainty is discerned into two categories. The lack of knowledge of the fabric of a modelled material assigned to a given region can be remedied through material characterisation studies and is therefore classified as reducible uncertainty. Similarly, if geometry simplifications in a model (Section 4.2) result in distinct regions with different properties being represented as one region, the introduced uncertainty can be evaluated and reduced through model benchmarking. To the other end, the inherent variability and randomness in properties even within one material is considered irreducible. Whether of reducible or irreducible origin, heterogeneity can be homogenised and effective material properties can be derived such that the modelled phenomena and processes remain unbiased. The validity of such modelling results needs, however, to be demonstrated. The subsequent paragraphs show examples of such validation exercises for uncertainties from homogenisation as part of geometric simplifications (Section 4.4.2) and from inherent variability in modelled properties (Section 4.4.3).

4.4.2 Parametric uncertainties associated with the inaccuracy of the model form

Homogenisation of material properties is common and inherent in the implementation of simplified representations of components of the multi-barrier system. These representations, and accordingly the homogenisation approach, are tailored to the phenomena and processes under consideration.

Fig. 4-4 displays three cross-sections of a modelled L/ILW cavern, extracted from the deterministic 3D models (Section 3.3). The first one (Fig. 4-4a) is taken from the component model and corresponds to a section with a "detailed" representation of the stack of waste containers assuming a matrix of 3 × 3 containers with 2 containers placed on top. This representation is tailored to support analyses on nearfield saturation related to pathways for gas release and water

uptake. Waste packages and their contents are not explicit but simplified as 4 homogenised packages per LC-86H container (respectively 2 packages in the cross-section) with the grout filling a T-shaped space between the waste packages and the lid of the container. Similarly, the contacts between the LC-86H containers are not exact but approximated so that gaps between containers are accounted for in gas transport. The second cross-section (Fig. 4-4b) is implemented with a coarser mesh and, accordingly, additional homogenisation applied to the emplaced materials. All materials in the containers (LC-86H, grout, waste packages) are lumped into a single material with properties similar to concrete. The gaps between the containers are still discretised and assigned a high-porosity material to represent the effect of gas pathways. Porosity of the mortar backfill is scaled accordingly to correct for volume differences introduced by the coarser mesh. The third cross-section (Fig. 4-4c) is implemented in the repository model with a single material representing the waste containers and surrounding backfill mortar. Volumetric averaging is used for porosity, and geometric averages for permeability and capillary strength (for averaging approaches see also Section 4.4.4). In all three cases, the EDZ surrounding the repository structures is also homogenised and represented in a stylised fashion.

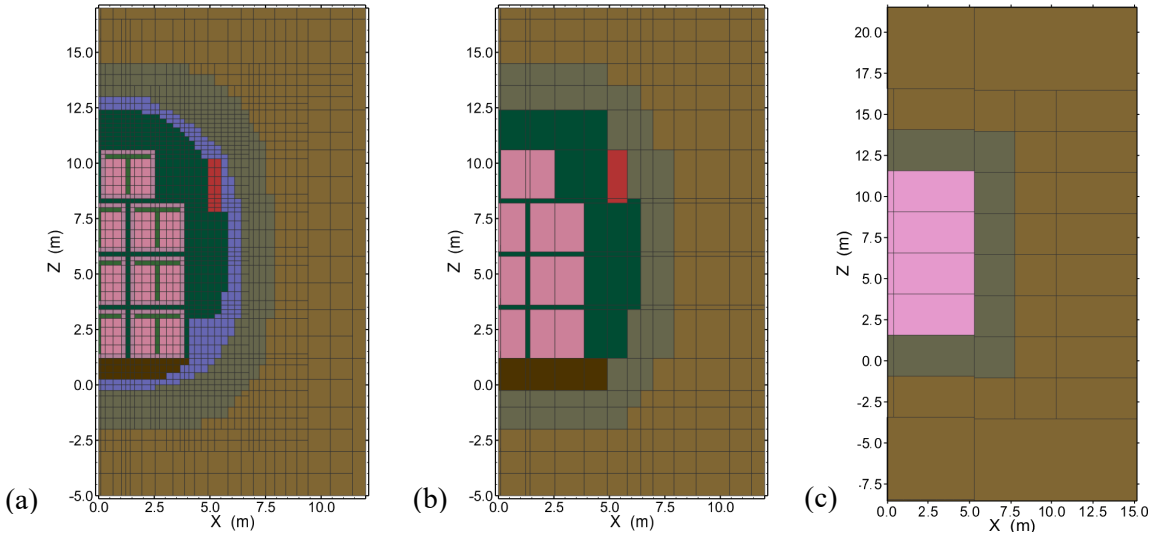

Fig. 4-4: Homogenisation of emplaced materials in the L/ILW nearfield

(a) Cross-section from detailed representation of L/ILW cavern extracted from the 3D component model. (b) Cross-section from simplified representation of L/ILW cavern extracted from the 3D component model. (c) Cross-section from homogenised representation of L/ILW cavern extracted from the 3D repository model.

4.4.3 Inherent variability of the modelled material properties

In a similar way, the homogenised properties adopted for a geological formation (e.g., as shown in Section 3.2) should be representative of the variability it exhibits on the macroscale. In the context of the site investigation programme, a comprehensive database was collected to characterise the flow and transport properties of the OPA in the siting regions. The interpretations of the field data suggest a distinct correlation of the flow and transport properties with the clay mineral content of the host rock. Accordingly, variability of clay content has been inferred from geophysical logs and laboratory analyses of cores retrieved from the investigation boreholes. Two approaches are commonly used to generate spatial distributions of clay content in the OPA: geo-

statistical modelling and facies modelling. Consequently, parametric relationships have been implemented for correlations between clay content and key transport properties, namely porosity and effective diffusion coefficients.

Examples of spatial distributions of effective diffusion coefficient and porosity derived by means of geostatistical modelling are shown in Fig. 4-5. The inherent assumption in this approach is that the OPA comprises one single facies and properties are distributed on a local scale that depends on the correlation length. Although geophysical logs from investigation boreholes allow induction of vertical correlation lengths, the same cannot be said with confidence for horizontal correlation lengths. Variants of geostatistical spatial distributions are therefore generated for different correlation lengths in the horizontal direction.

In a similar way, facies models implemented for the OPA can be integrated into the PA modelling workflow. In the PA, a base case comprises for each facies the best estimates of porosity and effective diffusion coefficient, based on the respective best estimates of clay content. Accordingly, variants are bracketed by sampling for each facies values of the respective clay content range.

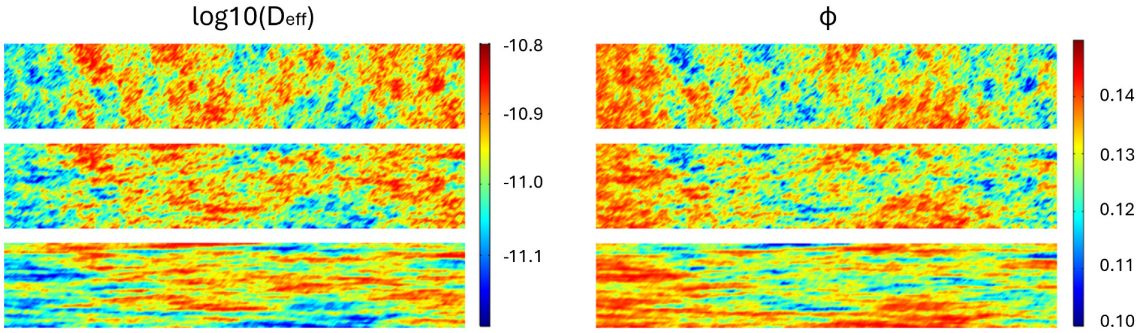

Fig. 4-5: Exemplary effective diffusion coefficient (left) and porosity fields (right) derived from geostatistical models of clay content in the OPA

From top to bottom, correlation ranges a_x = 3.7, 15 and 100 m. The lateral extent of the model is L_x = 500 m.

4.4.4 Anisotropic and isotropic properties

Different pore structure of a porous medium in the horizontal and vertical directions can result in directional dependency of flow and transport properties. From a macroscale perspective, the same principle applies with properties that exhibit different spatial correlations depending on direction (example shown in Fig. 4-5) and therefore must be homogenised accordingly. The concept of anisotropy allows the representation of homogenised, direction-dependent properties in the transport conceptualisations introduced in Section 4.3.

The examples shown in Fig. 4-5 can be used to illustrate this concept. With increasing correlation length, it is expected that the connectivity of high- or low-value regions for a given parameter may have an impact on the pattern of a transport process that is sensitive to that parameter. For example, interconnected lenses with high hydraulic conductivity embedded in a low-permeable background will result in a flow field following predominantly the lensed pattern in the horizontal direction. Accordingly, a homogenised hydraulic conductivity derived to represent this type of

heterogeneity may make distinction between a horizontal and a vertical value. The ratio between the horizontal and vertical value is termed *anisotropy factor* and can be understood as a measure of the degree of anisotropy of the porous medium.

The derivation of isotropic effective properties when a porous medium has a preferred direction of transport requires mathematical formulations tailored to the dimensionality of the problem under consideration and the associated structural pattern in the medium. In the example of the lensed structure described above, a 3D or 2D consideration of transport requires anisotropic hydraulic conductivity to account for the uneven spread of solute in case of advective transport in the horizontal and vertical direction. On the other hand, in a 1D consideration it suffices to select the hydraulic conductivity component corresponding to the model axis (e.g., vertical component of anisotropic conductivity for a 1D transport problem from an emplacement room to the overlying aquifers).

Alternatively, the geometric mean of the horizontal and vertical value can be used as a proxy when modelling in 3D or 2D, resulting in the averaged effect of both directions. Similar averaging approaches are applied also for engineered materials with interfaces that affect flow and transport in the repository structures, e.g., harmonic mean is representative when material interfaces are perpendicular to the dominant direction of transport whereas arithmetic mean is more appropriate when material interfaces are oriented along the transport path.

4.5 Simplified formulation of boundary conditions, initial conditions and source terms

Model abstractions are also introduced in the representation of the physical state of real-world systems. This applies to natural systems considered in the PA, e.g., the broader hydrogeological system in which the repository is introduced, as well as engineered systems, e.g., the repository itself during its construction, operation, and post-closure phases.

The initial state of the geological environment prior to repository construction needs to be approximated through simplifying assumptions. The host rock, confining units, and deep aquifers are assumed to be initially fully saturated with water and in a steady-state condition. The pressure distribution in the stack of geological formations corresponds to hydrostatic equilibrium assuming constant pressure respectively fixed hydraulic heads at the top and bottom of the stack. Similarly, temperature distribution corresponds to the equilibrium between temperature at ground surface and basal heat flow at the bottom of the stack (see also Chapter 3). The formulation of such boundary conditions introduces additional simplifications in the model representation. For example, constant atmospheric pressure and yearly average temperature is typically assumed at the ground surface. Depending on the model purpose, aquifers may be explicitly represented in the model geometry or replaced with constant pressure conditions, under the assumption that these aquifers exhibit sufficient conductivity and spatial extent. Similarly, horizontal or vertical hydraulic gradients can be implemented in the model representation through appropriate pressure boundaries imposed at the lateral or top and bottom boundaries of the model, respectively.

The physical state of the repository structures while these are accessible and operated is also simplified in the model conceptualisations. The ventilation of tunnels is not explicitly modelled with air circulation but represented with internal boundary conditions of constant temperature and relative humidity assigned to the open tunnels. The successive, staged opening and backfilling of tunnels during repository construction is simplified through stylised, discrete operational phases wherein entire sections of the repository (e.g., comprising different tunnels) are opened or backfilled instantaneously.

Simplifying assumptions are also introduced with the source terms assigned to the different sections of the repository. Source terms are implemented to account for the generation of gas from corrosion of metals and degradation of organics in the post-closure phase, the generation of heat from the radioactive decay of SF and HLW, and the release of radionuclides from the waste. The inherent assumption in this approach is that the underlying processes are not directly coupled to state variables calculated in the PA. For example, the corrosion and degradation of organic materials are decoupled from the availability of water for the reactions. This assumption is conservative with respect to pressure buildup in the repository. Similarly, it is conservatively assumed that gas generation from L/ILW starts immediately after emplacement despite the highly alkaline nearfield conditions decreasing corrosion rates and inhibiting microbial activities. The weak links between the underlying mass and energy transformation processes and the mass balance formulations adopted in the PA is compensated with model variants addressing uncertainty in the source terms. Abstraction is also required to discard granularity from the waste inventory in the PA workflow and implement representative waste groups. It is therein assumed that source terms, including their temporal evolution, are distributed evenly within each waste group.

4.6 Verification of codes and validation of models

The abstraction steps described in Sections 4.2 to 4.5 call for verification and model validation (V&V) exercises aimed at justifying choices made in the model conceptualisations and the associated uncertainties. The development of benchmarking workflows for V&V on international modelling platforms has been embedded in Nagra's long-term RD&D programme and is not addressed here in further detail. In particular with regards to process abstraction, recent modelling activities have been associated with Nagra's FE Task Force (Alcolea et al. 2021, Buchwald et al. in prep., Wojnarowicz et al. 2024), EURAD-HITEC, EURAD-GAS (Jacops & Kolditz 2024, Marschall et al. 2024, Wendling et al. 2024) and with EBS-Task Force (Romero & Gonzalez-Blanco 2019, Madaschi & Laloui 2019). In the following section, selected examples are shown from the model benchmarking performed within the chain of assessment models used in the PA.

4.7 Selected examples

The impact of abstractions on key state variables used in the PA is shown exemplarily in the following.

Geometric abstractions and homogenisation

The process of abstracting geometries (for example, Fig. 4-2) typically comes hand in hand with implementing homogenised properties (for example, Fig. 4-4) with the objective of reproducing state variables in an abstracted manner without impairing the intended use of the model.

Transients of gas saturation and pressure calculated with the 3-D component model for L/ILW and the respective L/ILW section of the 3D repository model are shown exemplarily in Fig. 4-6 (note that these two models are also illustrated in Fig. 4-2 and Fig. 4-4). Gas saturation simulated with the 3D component model is shown in Fig. 4-6a. The observation points correspond to these shown in Fig. 3-15. These are located in the M1 mortar at different locations of the L/ILW cavern, namely near the roof of the cavern ("top") and near the bottom between the LC-86H containers ("bot"). Moreover, observation points are selected in the model section with the detailed container representation as shown in Fig. 4-4a ("detail") and the simplified container representation as shown in Fig. 4-4b ("avg"). Overall, the simplified representation reproduces in the first 100,000 years of the post-closure phase the hydraulic evolution related to gas. That includes the gas accumulation at the roof of the cavern, the early increase of gas saturation in the lower parts of the cavern due to water update from the surrounding rock, the subsequent temporary resaturation of the bottom of the cavern with porewater, and then once more the increase of gas

saturation due to the accumulation of waste-generated gas. These results are also compared to the 3D repository model where all emplaced materials (including the M1 and cement containers with higher capillary strength) are replaced with a single, homogenised cavern material as illustrated in Fig. 4-4c. Accordingly, gas saturation shown in Fig. 4-6a ("Kombi @ L/ILW") corresponds to the average saturation in the cavern and represents accordingly the alternating desaturation and resaturation throughout the post-closure phase. Note that in the repository model the L/ILW cavern comprises four model layers – the saturation shown here is taken from the third layer counting from cavern bottom to top. Furthermore, gas pressure simulated with the 3D repository model is based on the pore volumes available for gas storage in the connected repository structures, scaled to correct for geometry approximations (see also Section 4.2.1). In Fig. 4-6b it is compared to two variants of the 3-D cavern model for L/ILW, namely assuming that the adjacent operations tunnel extends to the V2-L/ILW and the V2-HLW seal, respectively. In a general sense, the first version represents an impermeable V2 seal of the L/ILW repository, whereas the second version represents fully permeable repository structures throughout the L/ILW repository and the central area, implemented in a straight line and up to an impermeable V2 seal of the HLW repository (Nagra 2024g). On the other hand, the superposition assumed in the model (see also next section), effectively implies a higher interface area between the operations gallery to the surrounding rock (and accordingly, more depressurisation during the ventilation phase, and more gas dissolution during the post-closure phase) compared to that in the representation of the full repository model. The comparison shows overall similar pressure evolution between the three models, with more conservative estimates of peak pressure produced with the component model extending only to the V2-L/ILW, owing on the one hand to the lower pore volume available for gas storage and on the other hand to the assumption of no-flow lateral boundaries (see also Section 4.2.2).

A similar comparison is illustrated for HLW in Fig. 4-7. Transients of gas saturation from the 3D component model are shown at different locations in the buffer in Fig. 4-7a, namely directly at the canister ("PELL abv can#51"), the middle of the bentonite between canister and liner ("PELL mid"), the bentonite next to the liner ("PELL top") and the bentonite at the midpoint between two canisters ("PELL btw can"). These show minor differences with the bentonite reaching full water saturation after ~200 years. On the other hand, the 3D repository model reproduces a similar evolution however using a single homogenised material (lumping bentonite and the tunnel tubing) that has lower porosity and gas saturation at emplacement compared to granular bentonite (Fig. 4-7a). Pressure simulated with the two models is compared at two locations, namely in the HLW tunnel and in the OPA at 20-m above the tunnel (Fig. 4-7b). The comparison shows overall higher thermally induced pressures produced by the component model that is laterally limited to thickness of 20 m. As explained in Section 4.2.2, this implementation assumes an ensemble of an infinite number of emplacement tunnels and essentially prevents any lateral dissipation of heat and pressure through the rock. The comparison highlights that this approach is overly conservative for estimating pressure associated with the differential thermal expansion of porewater in the rock mass surrounding the tunnel. The 3D component model for HLW is therefore limited to assessments of nearfield saturation and temperature, as discussed in Nagra (2024g).

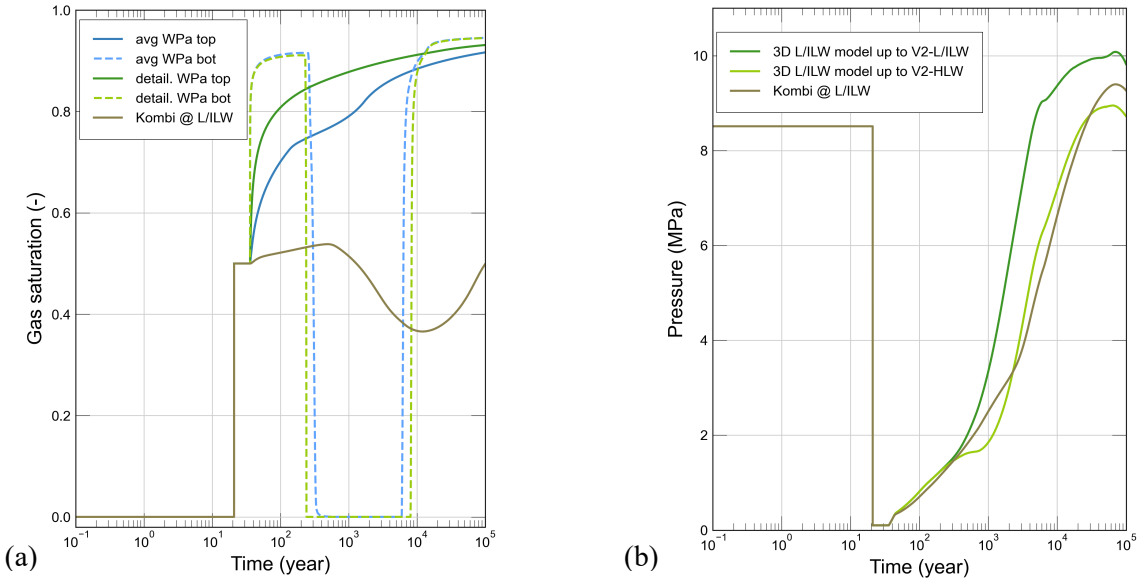

Fig. 4-6: Comparison of gas saturation and gas pressure simulated with different levels of geometric abstraction for L/ILW

(a) Gas saturation simulated with the 3D component model for L/ILW in the M1 at the top and bottom of containers using detailed and averaged representations and with the 3D repository model in the respective L/ILW cavern representation. (b) Gas pressure simulated with the 3D repository model in the L/ILW cavern and with two variants of the 3D component model for L/ILW, namely with operations tunnel extending to the V2-L/ILW and to the V2-HLW seal, respectively.

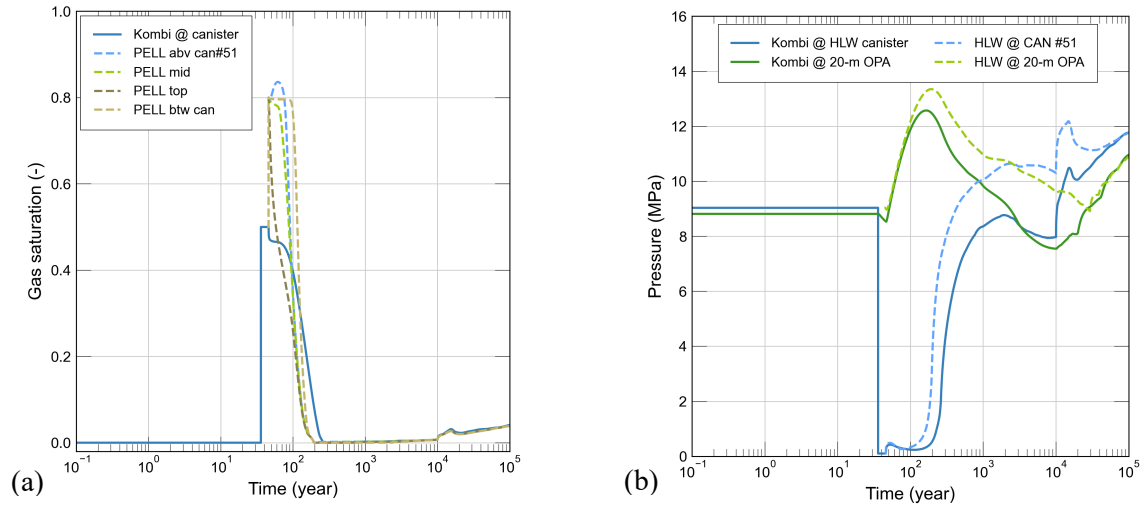

Fig. 4-7: Comparison of gas saturation and gas pressure simulated with different levels of geometric abstraction for HLW

(a) Gas saturation simulated with the 3D component model for HLW in the bentonite at the canister, at the midpoint between canister and liner, at the liner, and at the midpoint between two canisters and with the 3D repository model in the respective HLW drift representation. (b) Gas pressure simulated with the 3D repository model in the HLW drift and in the OPA at 20 m above the tunnel, and with the 3D component model for HLW at the respective locations.

Simplification of symmetric geometries

As introduced in Section 4.2.2, the issue of boundary effects in symmetric geometries is compensated by adapting representations to take into account the rock mass surrounding the repository. In Fig. 4-8a, the pressure comparison in the HLW nearfield is repeated between the 3D repository model and the 2D component model for probabilistic assessments that comprises a cross-section through all emplacement rooms and surrounding rock (Section 3.4; see also Fig. 4-3b). The peak pressure owing to thermal expansion after ~200 years is similar in both models, whereas at later times, the 2D result is more conservative owing to the lack of heat dissipation through the surrounding rock in the direction of the tunnel axes. Accordingly, the pressure recovery after the heating phase (e.g., after 10,000 years) is slower and the subsequent gas-induced pressure peak is approximately 0.5 MPa higher compared to the repository model.

As indicated in Fig. 4-6b, gas pressure in the L/ILW caverns depends strongly on the pore volume accessible for gas storage (see also Nagra 2024g). Accordingly, the 2.5D component model for probabilistic assessments represents a cross-section through all emplacement caverns and surrounding rock combined with volumes representing the adjacent branch and operations tunnels and scaled to match those of the 3D repository model up to the V2-L/ILW seal or up to the V2-HLW seal (Section 3.5; see also Fig. 4-2c). The comparison between the 3D and 2.5D models is shown in Fig. 4-8b. The gas pressure simulated in the L/ILW cavern with the 2.5D model when it includes the volumes up to the V2-HLW seal is similar to that simulated with the 3D repository model. On the other hand, when the volume in the 2.5D consideration is reduced (and corresponds to the volume up to the V2-L/ILW seal), the resulting gas pressure is overall higher than in the 3D model (Fig. 4-8a). Notably, the peak pressure in the 2.5D component model with volume up to the V2-L/ILW seal (Fig. 4-8b) is higher than that in the 3D component model with the same assumption (Fig. 4-6b), showing the increasing conservatism with the reduction of dimensionality.

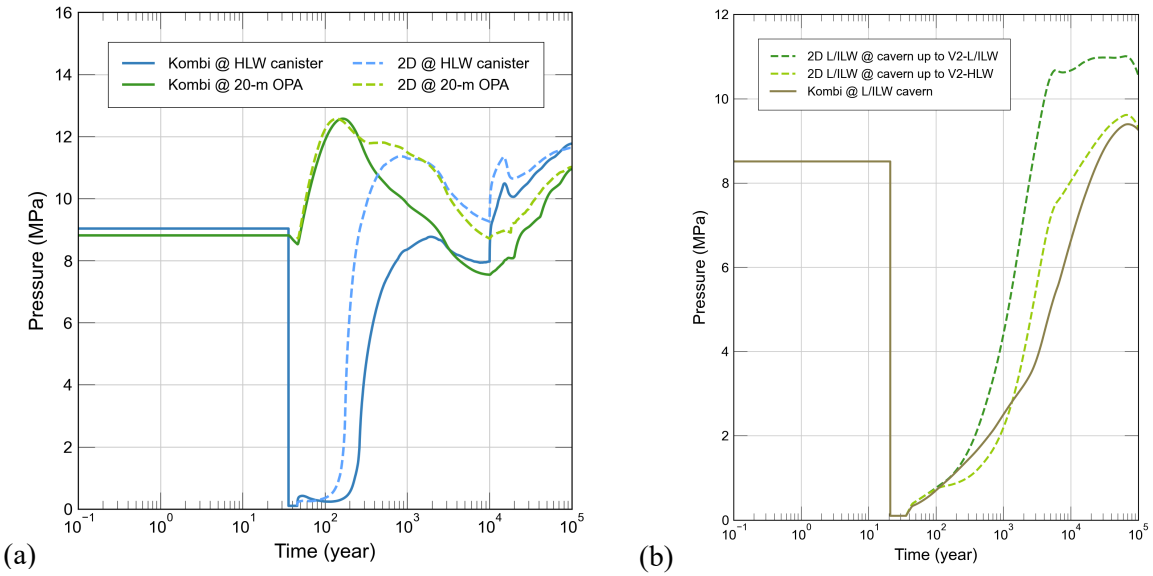

Fig. 4-8: Comparison of gas pressure simulated with different levels of geometric abstraction in L/ILW and HLW

(a) Gas pressure simulated with the 3D repository model in the HLW drift and in the OPA at 20 m above the drift, and with the 2D component model for HLW at the respective locations. (b) Gas pressure simulated with the 3D repository model in the L/ILW cavern and with two variants of the 2D component model for L/ILW, namely with operations gallery extending to the V2-L/ILW and to the V2-HLW seal, respectively.

Transport paths

As discussed in Section 4.2.3, model design depends on the transport paths expected in the component under evaluation, which in turn depend on the type of transport characteristic to different sections of the repository. Fig. 4-9 shows a comparison of spatial distribution of gas saturation after 5,000 years in the HLW and L/ILW emplacement rooms, respectively. In the HLW nearfield gas spreads radially at low saturation values (~1 – 2%) owing to the low permeability and high suction of the bentonite buffer (note that saturation in the buffer is not shown to allow visualisation of the canisters and tunnel wall). The V1-HLW seal remains fully saturated as gas does not form a preferential flow path along the backfill. On the other hand, gas in the L/ILW cavern flows through the high-porosity M1 axially into the adjacent branch tunnel so that gas saturation is in the order of ~60% (note that saturation in the M1 is not shown to allow visualisation of the waste containers and cavern wall). These transport paths justify the 2D and 2.5D approach adopted in the HLW and L/ILW component models for probabilistic assessments, respectively.

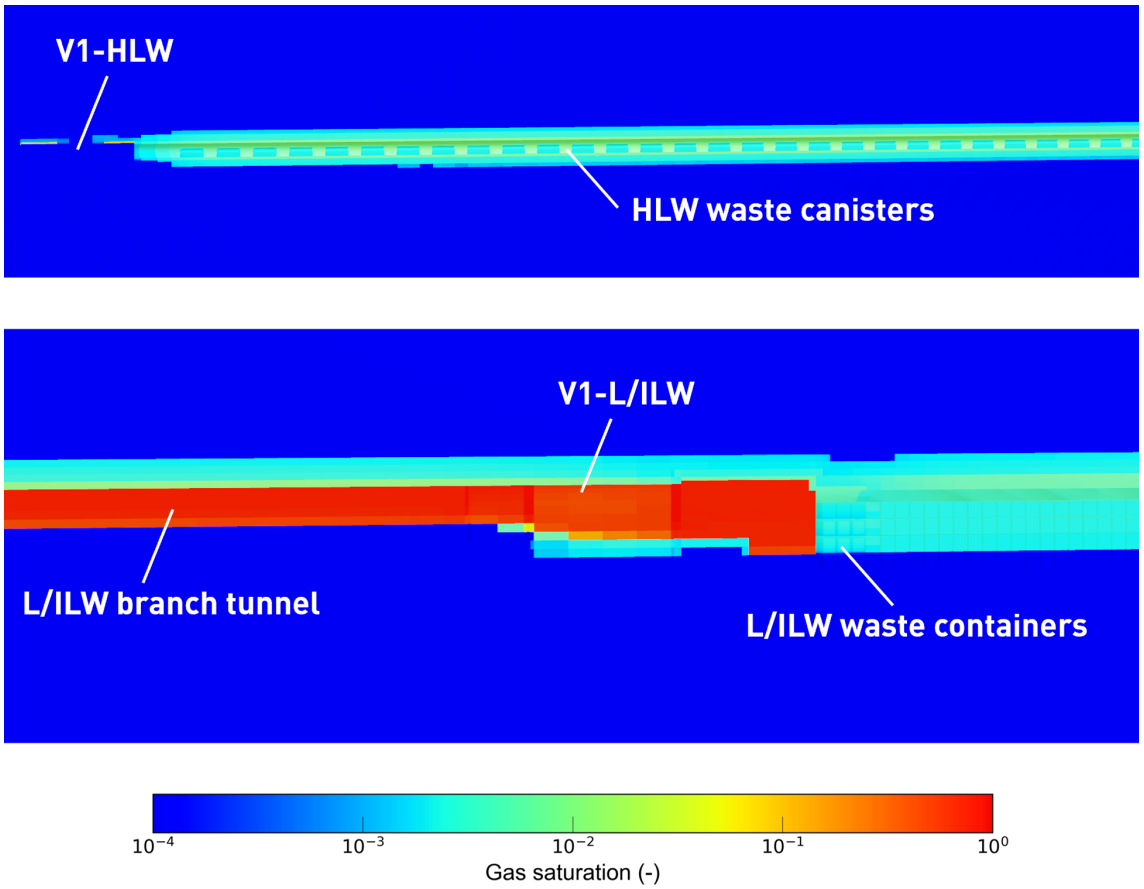

Fig. 4-9: Comparison of gas saturation after 5,000 years in an HLW emplacement drift (top) and in an L/ILW emplacement cavern (bottom)

The results are extracted from the respective 3D component models.

Boundary conditions

As discussed in Section 4.5, constant pressure boundary conditions can be used to represent permeable units acting as aquifers in the stack of geological formations. An example is shown in Fig. 4-10a that compares three variants of the 3D component model of a V3 seal. As described in Section 3.3.2, this model represents a shaft extending from the middle of the OPA to the top boundary of the model, which is set at the bottom of the Malm. This corresponds to variant 3 of the model, shown in Fig. 4-10a, right. In variant 1 (Fig. 4-10a, left), the vertical extent of the model is limited so that the top boundary is fixed at the bottom of the Herrenwis instead of the Malm. Similarly, in variant 2 (Fig. 4-10a, middle), the model top boundary is fixed at the bottom of the MM1+CM+MM2 sequence (Fig. 4-10). Conceptually, the three variants correspond to the three units acting as water reservoirs with their respective hydraulic conductivity (Herrenwis in variant 1, KBA/KMA in variant 2, Malm in variant 3). The resulting gas saturation and pressure transients after backfilling the shaft (including the V3 seal) are shown in Fig. 4-10b. It is shown that the shaft above the seal ("Shaft (BD)") reaches full water saturation ~100 years faster in variant 3 compared to variant 1. This is due to the higher conductivity of the Malm that delivers water to the shaft in variant 3. On the other hand, the saturation of the bentonite seal with pore-water is practically identical in all cases, indicating that this process is less sensitive to the distance to the boundary condition at the top.

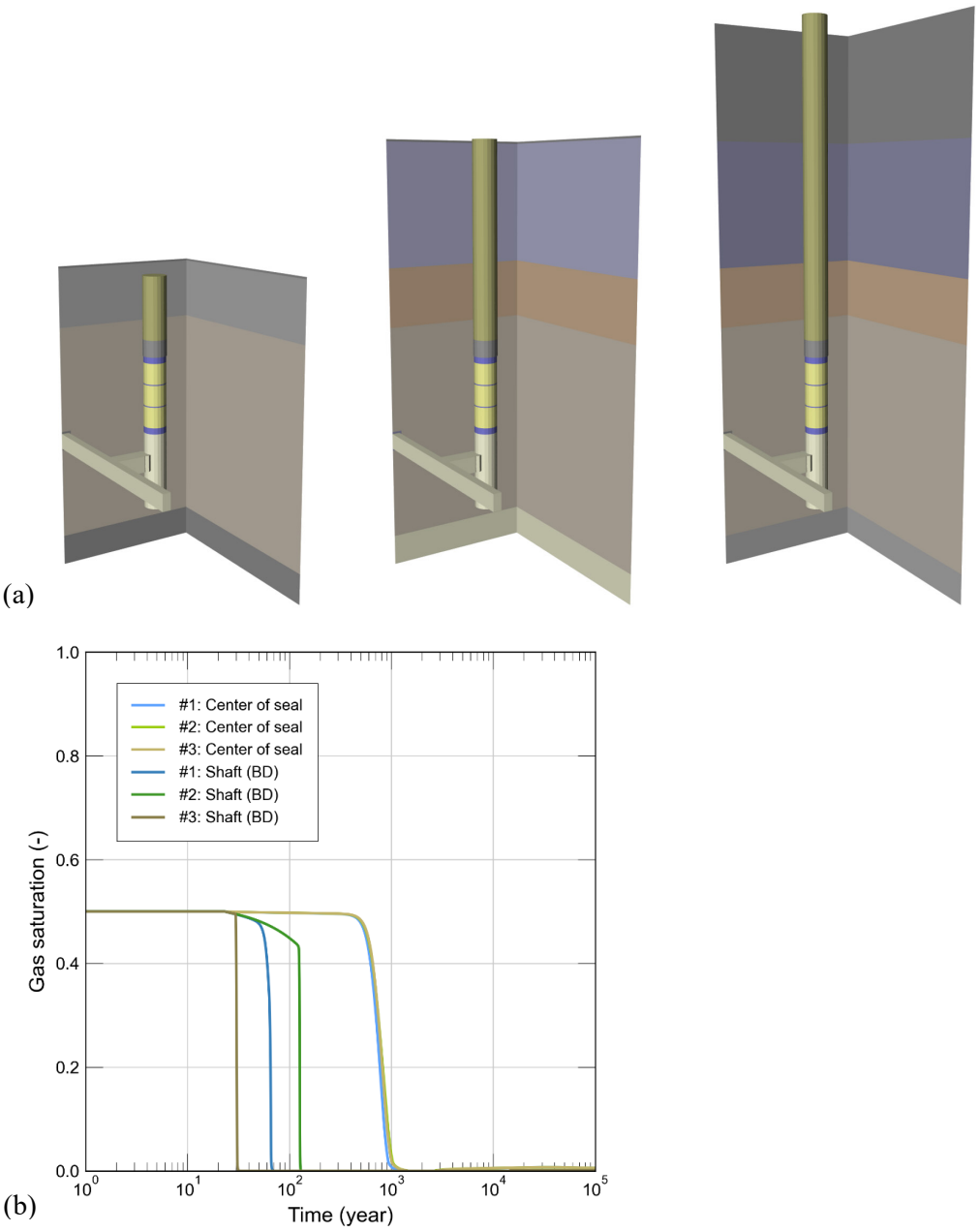

Fig. 4-10: Comparison of three variants of the 3D model of the V3 seal

(a) Variant 1 (left) extends to the bottom of the Herrenwis; variant 2 (middle) extends to the bottom of the KBA/KMA sequence; variant 3 (right) extends to the bottom of the Malm aquifer. (b) Water resaturation of the shaft above the seal and the centre of the bentonite seal when using the three model variants.

Source terms

The representative waste groups and their respective source terms may require different implementations in the PA models depending on the scale and purpose of each model. For example, the time of the HLW disposal canister breaching in the PA models is assumed to be 10,000 years. Accordingly, gas generation rates are derived based on the assumption that additional corrosion of the waste and of the canister from inside (not in contact with bentonite) begins at that time, resulting in a "spike" of gas generation. This results in significant conservatism in repository-scale modelling as it is implied that all canisters in the repository breach at the same time. A demonstrative example is shown in Fig. 4-11 using 10 canisters in three variants of the 3D component model in which different canisters are assumed to breach at various breaching times. The canisters are numbered from 1 to 10 starting from the mouth of the emplacement drift. In variant 1, canister 5 breaches at 10,000 years whereas all other canisters breach at 50,000 years. In variant 2, canister #5 breaches at 50,000 years whereas all other canisters breach at 10,000 years. In variant 3, canisters #1, 3, 5, 7, and 9 breach at 10,000 years whereas canisters #2, 4, 6, 8, and 10 breach at 50,000 years. All canisters are conservatively assigned the upper bound gas generation rates. Based on the earlier discussion on boundary effects, pressure calculated with these three cases are only used for comparison to each other as shown in Fig. 4-11. The comparison between variants 1 and 2 indicate that earlier breaching times (e.g., 10,000 years instead of 50,000 years) result in higher peak pressure. On the other hand, alternating between two discrete breaching times in variant 3 results in approximately 1 MPa lower peak pressure.

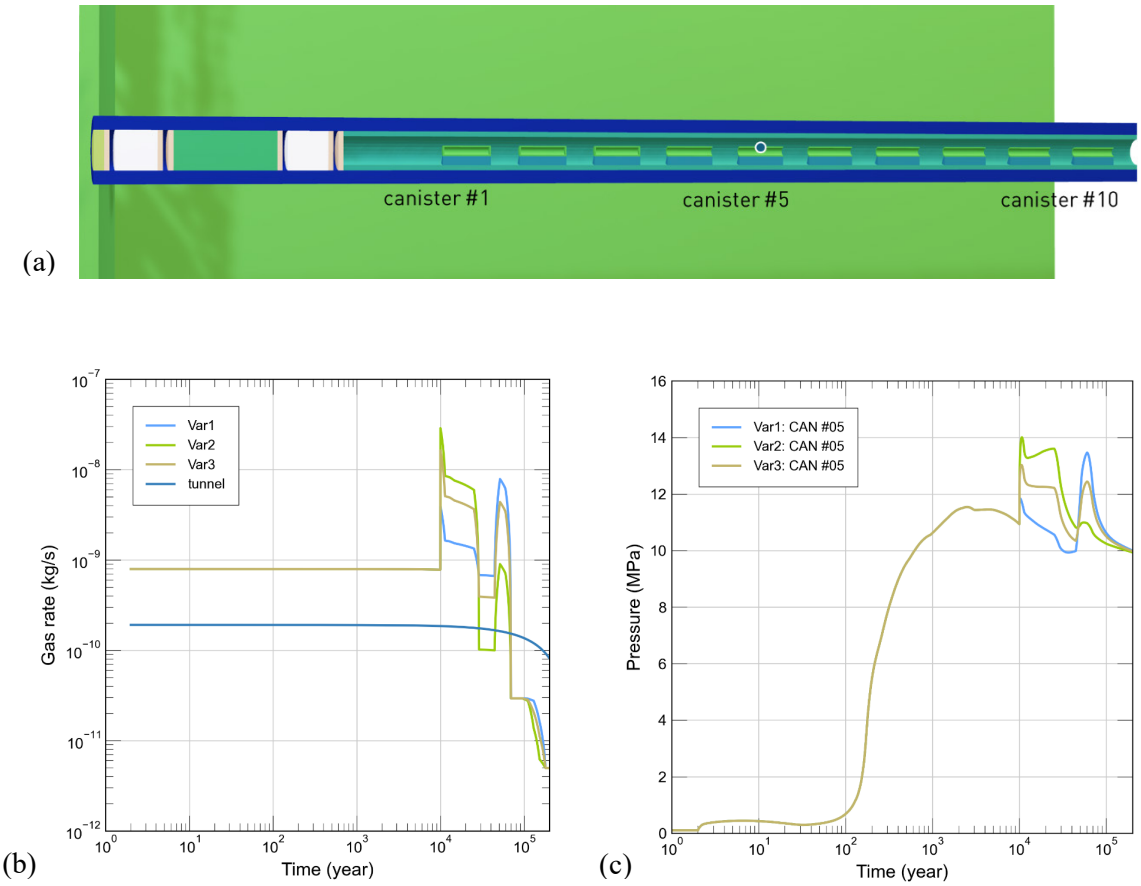

Fig. 4-11: Comparison between three variants of breaching times assigned to 10 canisters in the 3D model of an HLW emplacement drift

(a) Model geometry showing canisters 1, 5, and 10. (b) Gas generation rate corresponding to model variants 1, 2, 3. (c) Gas pressure simulated at the surface of canister 5 in the three model variants.

A similar logic applies to the thermal source terms assigned to the HLW drifts. In repository-scale geometries that do not explicitly model each individual canister (e.g., 3D repository model), it is reasonable to adopt an average heat source assigned to the entire HLW inventory and distribute it across the heat-generating elements in the model. For comparison, the 3D component model can provide nearfield temperatures for the three types of SF, namely PWR-MOX, PWR-UO_2, and BWR, assigned their respective representative single-canister heat output (Nagra 2024g). The comparison is shown in Fig. 4-12. Due to assumptions related to the emplacement schedule, the source term used on the repository scale in the first 20 years is higher than the representative values for individual canisters (Fig. 4-12a). After that time, the repository source term lies between the source terms for the three SF types. Peak temperatures at the canister are reached shortly after emplacement and are similar for the three SF types and the repository representation (Nagra 2024g). After ~2,000 years temperatures from the component model are overall higher due to the lateral boundary that limits heat dissipation to the surrounding rock (Fig. 4-12b).

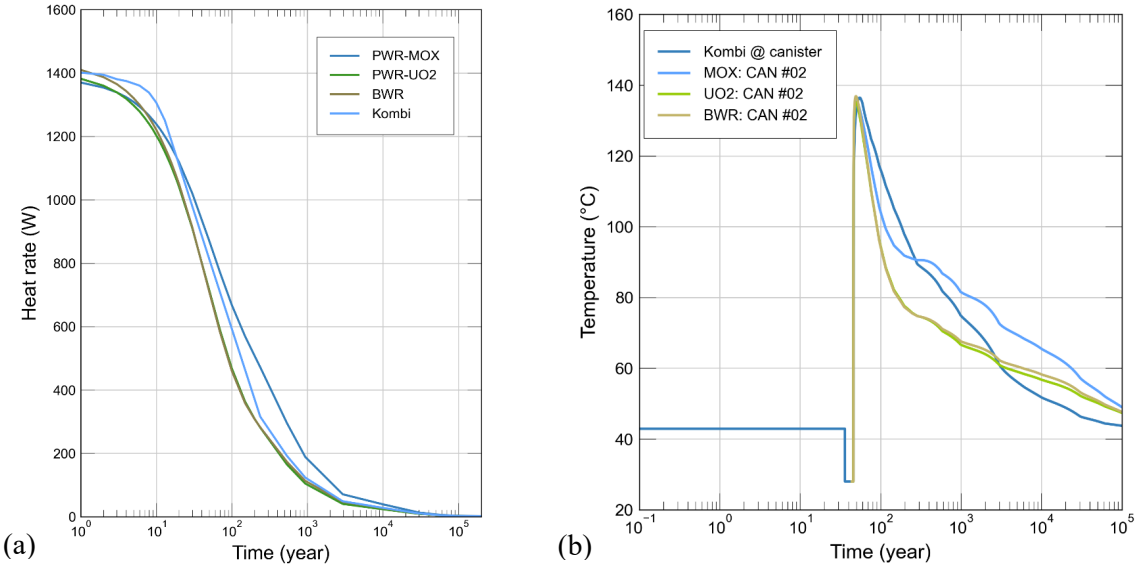

Fig. 4-12: Comparison between four variants of heat source assigned to the canisters of the 3D model of an HLW emplacement drift

(a) Heat output per canister. (b) Simulated temperature at the surface of the canister.

4.8 Concluding remarks on model chain abstractions

The model abstraction workflow described in this chapter is embedded in the model implementations used in the PA. As shown in the examples presented in Section 4.7, model comparisons in terms of key metrics that are relevant to the purposed analysis are essential in understanding the origin of deviations between models and making justified choices in the model-supported assessments. In general, model abstraction of any type is likely to introduce some uncertainty that needs to be accounted for in the analysis in a conservative fashion so as not to introduce bias (see also Section 4.1).

Some outcomes of benchmarking between models used in the PA for the L/ILW are summarised in Tab. 4-1. The model chain comprises models for 3D total system deterministic assessment (entire repository), 3D component deterministic assessment (single L/ILW cavern) and finally 2.5D component probabilistic assessment (half or seven L/ILW caverns). From the latter only, best estimate is shown here for the comparison. Three metrics are selected for the comparison, namely the time when hydrostatic pressure is reached ($t_{hydrost.}$), the time of peak gas-induced pressure (t_{peak}), and the magnitude of the peak pressure at that time (P_{peak}). The model chain shows overall good agreement between the different tools and scales, with some added conservatism in the abstracted 2.5D implementations. In Fig. 4-13 a direct comparison is shown in terms of pressure simulated with the 3D repository model, the 3D component model, and the 2.5D component model when the V2-L/ILW is assumed to be impermeable.

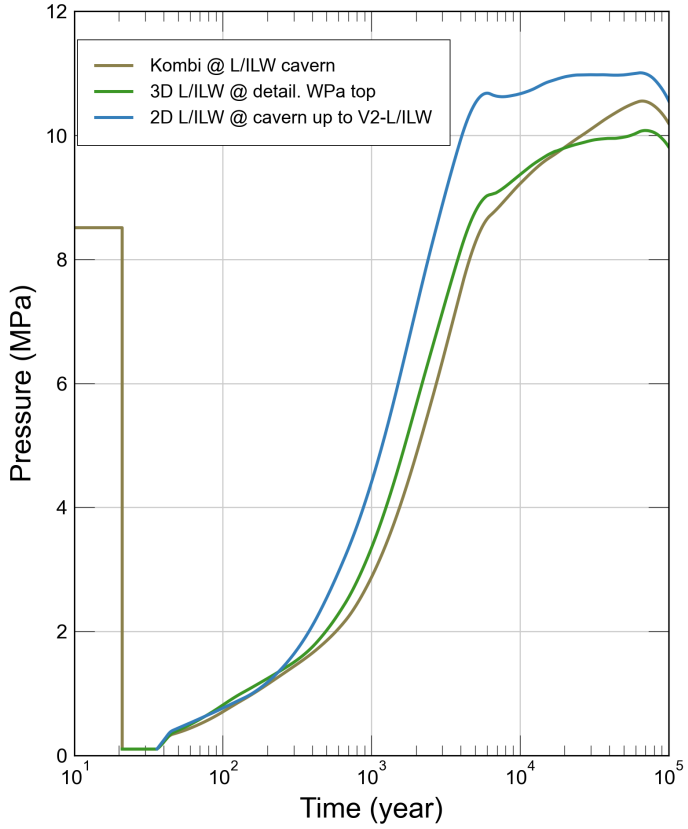

Fig. 4-13: Comparison between 3D repository model, 3D component model of a single cavern, and 2.5D component model of a single cavern

3D repository model corresponding to case TSD21 in Chapter 6. 3D and 2.5D component models corresponding to model variants with operations tunnel extending only up to V2-L/ILW.

A similar comparison between models used in the PA for the HLW is shown in Tab. 4-2. The model chain comprises accordingly the models for assessments of 3D total system (entire repository), 3D component (single HLW drift) and 2D component (twenty HLW drifts). From the latter only best estimate is shown here for the comparison. Three metrics are selected for the comparison, namely the average maximum temperature reached in the bentonite ($T_{bent,max\ avg}$), the peak heat-induced pressure reached at 20 m above the repository ($P_{heat,peak}$), and the peak gas-induced pressure reached in the tunnels ($P_{gas,peak}$). Note that in the component analyses, one of three SF types are considered, namely BWR, MOX, or UO_2, whereas the total system analyses adopt a mix of these as discussed in Section 3.4.4. Taking into account these differences the comparison overall shows good agreement between the different tools and scales considered in the assessments.

Tab. 4-1: Model abstraction chain – L/ILW: comparison between models used in the PA in terms of key metrics relevant to the model-supported analysis

Model	$t_{hydrost.}$ [ka]	t_{peak} [ka]	P_{peak} [MPa]	**Results documented in**
Expected evolution / as designed				
3D repository	20	70	9.5	Chapter 6, Nagra (2024g)
Scenario impermeable V2-L/ILW				
3D repository	4	70	10.5	App. B, Nagra (2024g)
3D L/ILW cavern[1]	4	70	10.1	Nagra (2024g)
2.5D L/ILW caverns	3	70	11.0	Chapter 4
Scenario high-permeable V2-L/ILW				
3D repository	20	70	9.3	Chapter 6
3D L/ILW cavern[2]	20	70	8.9	Nagra (2024g)
2.5D L/ILW caverns	20	70	9.6	Chapter 8

[1] Conservatively adopted as base case in the component analyses in Nagra (2024g).
[2] Assuming "straight-line" tunnel without V2-L/ILW with length and volume of all repository structures until the V2-HLW.

Tab. 4-2: Model abstraction chain – HLW: comparison between models used in the PA in terms of key metrics relevant to the model-supported analysis

Model	**$T_{bent.\ max\ avg}$** [°C]	**$P_{heat,peak}$** [MPa]	**$P_{gas,peak}$** [MPa]	**Results in**
Expected evolution / as designed				
3D repository (SF mix)	106	13.0	11.9	Chapter 6, Nagra (2024g)
3D HLW tunnel (all rep. BWR/MOX/UO_2)	93	12.3/13.5/12.3	12.0/12.2/11.9	Nagra (2024g)
2D HLW tunnels (SF mix)	96	12.6	11.6	Chapter 7
Scenario max heat				
3D repository	-	-	-	-
3D HLW tunnel (all max. of BWR/MOX/UO_2)	95	12.5/14.0/12.6	-	Nagra (2024g)
2D HLW tunnels (all rep. MOX)	94	13.5	11.7	Chapter 7
Scenario max gas				
3D repository (SF mix)	106	13.0	14.4	Chapter 6, Nagra (2024g)
3D HLW tunnel (all rep. MOX)	93	13.5	15.0	Nagra (2024g)
2D HLW tunnels (SF mix)	96	12.6	14.2	Chapter 7

5 Modelling workflow for performance assessment

The role of PA is to classify the possible paths of repository evolution in terms of a so-called *expected performance* of the multi-barrier systems and *deviations* thereof (Nagra 2024j). Deviations from expected performance are analysed at the component level and at the level of the entire repository system with emphasis on the likelihood of occurrence and their relevance for safety (Nagra 2024j). This process feeds into safety scenarios that describe the possible paths for the evolution of the disposal system and its environment for assumed geological scenarios and other assumed features, events and processes (Nagra 2024i). The development of safety scenarios as input for the analysis of radiological consequences requires a traceable and transparent simplification of the evolution of the real-world repository system from the perspective of long-term safety. Unnecessary features, events and processes that could distract from the intended use are eliminated. Accordingly, the PA modelling workflow that leads to that screening needs to balance between the necessary level of detail and the spatial and temporal scales that need to be considered for the appropriate representation of the expected performance and the deviations therefrom.

5.1 Performance screening - Evaluation workflow

By design, the multi-barrier system of the geological repository complies with all required long-term safety functions over the entire period of assessment, both on the scale of components and of the total system. The performance of the multi-barrier system is tied to the evolution of the geological repository. Fig. 5-1 illustrates the relevant paths of repository evolution in the PA framework, explained in the following.

The initial state of the repository system is well-constrained by the assessment basis (see Section 2.2). The schematic drawing in Fig. 5-1 exhibits the repository evolution during the entire period of assessment. The well-constrained initial state is characterised by a narrow opening of the funnel-shaped *event horizon*, dividing the space of state of the multi-barrier system in domains of possible and hypothetical states. Throughout the *period of assessment*, the state of the repository system evolves with time under the impact of internal and external perturbations (*"prevailing regimes"* in Fig. 5-1), encompassing repository induced effects and the impacts of geological long-term evolution. The evolution of the repository system is entailed by a loss of determinism of the associated state variables. At the end of the assessment period, the safety relevant state variables of the system can be inferred within an uncertainty range, expressed in terms of *probability density functions*.

The expected performance combines all paths of repository evolution which are related to the exemplified repository as currently designed. On the other hand, deviations from expected performance may occur if one or several barrier components do not perform according to the safety functions assigned to them. In such cases, the inherent redundancy of the multi-barrier system foresees that the remaining, properly functioning barrier components ensure the overall performance of the repository system. Furthermore, detrimental impacts associated with an unfavourable evolution of internal and / or external perturbations may impair the performance of the entire repository system. The paths of repository evolution, related to deviations from expected performance can be merged for each barrier component and for all safety-related interactions between the repository components, to form their own category of PA scenarios.

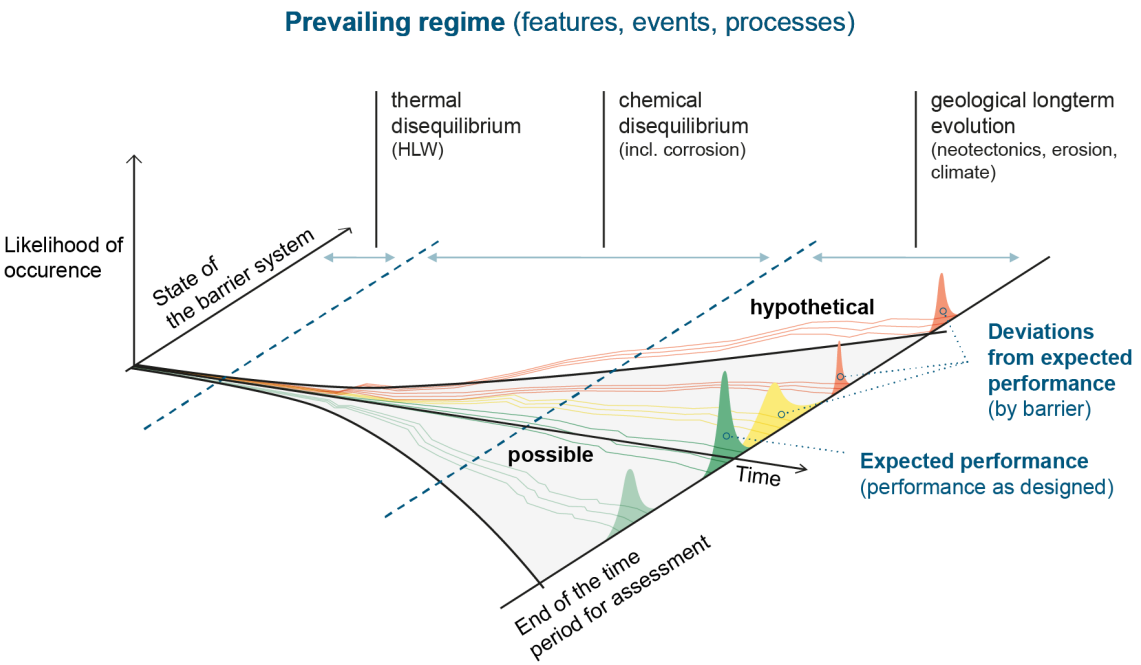

Fig. 5-1: Funnel-shaped event horizon, dividing the space of state of the multi-barrier system in domains of possible and hypothetical states

Illustration of the relevant paths of repository evolution in the PA framework, encompassing expected performance and deviations thereof.

From Nagra (2024j).

The general workflow of performance screening thus encompasses:

(1) The expected performance of the repository system is evaluated with performance indicators. The modelling workflow used to achieve this is outlined in Section 5.2.

(2) Deviations from expected performance - by barrier component and by interaction - are modelled under consideration of parametric, conceptual, and scenario uncertainties and evaluated with performance indicators. The modelling workflow to achieve this is outlined in Section 5.3.

Consequently, screening of performance is applied by barrier wherein an evaluation of likelihood of deviations allows to assign the possible paths of repository evolution in terms of likelihood of occurrence and their relevance to safety (Nagra 2024j). The latter is not addressed in the present report.

The results of modelling performed for the expected performance are described in Chapters 6.1, 7.1, and 8.1 for the total system, the HLW, and the L/ILW, respectively. The results of modelling performed for deviations from the expected performance are described in Chapters 6.2, 7.2, and 8.2 for the total system, the HLW, and the L/ILW, respectively.

5.2 Modelling of expected barrier performance

5.2.1 Key features

The exemplified project for a geological repository for HLW and L/ILW, which has been elaborated for the RBG, complies by design with the assigned functionality of the multi-barrier repository system both on the component scale and on the scale of the entire repository. Its expected performance is deduced from a well-constrained assessment basis using the PA methodology (Section 2.2). The latter comprises numerical simulations of the evolution of the repository providing quantitative outputs that feed into the indicator workflow (Section 3.7). The following key features of the geological repository (HLW and L/ILW) as currently designed are implemented in the PA model set-ups representing the scenario of expected repository performance:

- All elements of the multi-barrier system perform are according to provisional design requirements.
- The source terms for radionuclide release correspond to the reference values specified in MIRAM-RBG (Nagra 2023b).
- Thermal (HLW only) and gas related source terms (HLW and L/ILW) correspond to the reference values specified in the gas synthesis report (Nagra 2024g).
- The lithostratigraphic units of the CRZ and their mineralogical composition are consistent with the geological setting described in the geosynthesis report (Nagra 2024c).
- Hydrogeological and geomechanical conditions in the subsurface correspond to present-day conditions as described in the geosynthesis report (Nagra 2024c).
- Diffusion is the prevailing radionuclide transport mechanism in the CRZ. Advective transport along steeply dipping faults does not represent a relevant vertical release path. Sedimentary features such as hardbeds in the upper and lower confining units do not act as lateral release paths.
- Expected flow and transport properties of the geological layer stack and their uncertainty ranges are well constrained according to the geological datasets given in Chapter 3.

The overarching PA model portfolio has been described in detail in Chapter 3. The next section elaborates the implementation of selected models and associated performance indicators for demonstrating the expected performance based on the current design.

5.2.2 Models and indicators

As described in Chapter 3, the PA models span a wide range of scales of interest and levels of detail associated with their intended use. In general, computationally demanding models are used for deterministic assessments and for benchmarking more moderate-sized models that implement simplified representations. The simulations on the scale of the entire repository are performed with the 3D repository model (see also model description in Section 3.3.1) and target the assessment of the total system performance. The TH evolution of the repository is complemented in Nagra (2024g) with more refined, deterministic 3D simulations on the scale of components, namely emplacement rooms and sealing sections (see also model descriptions in Section 3.3.2). The results confirm that the HLW and the L/ILW disposal areas are hydraulically and thermally decoupled from each other, which means that the two sections of the geological repository can be analysed accordingly. A key aspect of the PA screening methodology is the assessment of parametric uncertainty in a probabilistic framework with Monte Carlo simulations. Accordingly, the PA screening workflow relies heavily on the 2D and 2.5D representations of the HLW and

L/ILW repository fields, respectively, for calculating their respective performance metrics and associated confidence ranges elaborated in Nagra (2024j) (see also model descriptions in Sections 3.4 and 3.5 and definition of model outputs in Section 3.7). The overall abstraction process applied to the model chain has been described in Chapter 4. In particular, all model-based analyses in the screening workflow are carried out with the TH^2 representation in lieu of the complex TH^2MC processes as described in Chapter 4.3. The expected performance is first addressed on the level of total system analysis (Chapter 6.1) and then separately for the HLW and L/ILW disposal areas (Chapters 7.1 and 8.1, respectively).

5.3 Modelling of deviations from expected performance

5.3.1 Approach

Deviations from expected performance occur over time if a barrier component fails to perform the safety functions assigned to it or if detrimental impacts (e.g., repository induced effects, effects of geological long-term evolution) impair the performance of the entire repository system. According to the current design principles of redundancy and diversity, underperformance of a single barrier component will not result in failure of the entire multi-barrier system. Rather, the motivation for the quantitative assessment of deviations from expected performance lies in the estimation of the resulting effect on the global safety margins of the barrier system. A complete list of deviations and associated PA scenarios examined in the PA is given in Nagra (2024j). The scenarios implemented in terms of numerical modelling at the level of the total system and then at the component level for HLW and L/ILW are listed in Tab. 6-1, Tab. 7-1, and Tab. 8-1, respectively.

Impacts from deviations are first addressed on the total system level by interaction (Chapter 6.2), and then on the component level by barrier. In the total system, interactions can be classified based on the type of physical processes by which they take place:

- *Thermal interactions* take place through transport of heat in the repository.
- *Hydraulic interactions* take place through transport of fluid mass from one section of the repository to another.
- *Mechanical interactions* are a consequence of TH effects introduced in one section and affecting another section (including heat and mass transport).
- *Chemical interactions* are a consequence of species transported along with fluids from one section to another.

On the other hand, on the component level, deviations are addressed by means of conceivable and hypothetical PA scenarios representing the reduced performance of an addressed barrier component as compared to its expected performance.

The models and indicators used to address the deviations from expected performance are discussed in the next section.

5.3.2 Models and performance metrics/indicators

Two sets of metrics are used for the analysis of deviations on the total system level (Section 6.2).

The first set corresponds to state variables that give insight into the total system evolution for the given deviation scenario. Pressure and gas saturation in the central area are selected for that purpose. Pressure is the indicator for thermally- and gas-induced effects; any significant perturbation in one disposal area of the repository that may be relevant to the other disposal area should first have an impact on the central area due to proximity. Accordingly, mechanical interactions introduced by overpressures in either disposal area can be excluded if significant overpressures are not present in the central area. Gas saturation is the indicator for the saturation state in the central area that facilitates any mass transfer from or towards the disposal areas. Complementary metrics, such as mass fractions of gas in liquid, or pressures and saturations in the disposal areas of the repository complete the assessment when deemed necessary.

The second set of indicators aims to identify heat and mass transport across sections of the repository. Heat transport will have a direct impact on temperature; therefore, the increase of absolute temperature in the disposal areas and in the central area is the indicator for heat transport. Mass transport can be identified at the sealing sections by extracting gas and liquid flows in the direction of the disposal areas and the shaft. In some cases, flow rates are normalised and accumulated as described in Section 6.1. If heat and mass exchange between the disposal areas is negligible, it can also be assumed that any resulting mechanical and chemical interactions can be excluded.

The models and indicators used for the assessment of deviations by barrier (Sections 7.2 and 8.2) are essentially the same as those used in the assessment of expected performance for HLW and L/ILW (Sections 7.1 and 8.1, respectively). Each deviation on the component level is assessed with probabilistic simulations using the 2D and 2.5D models with the respective component(s) of the multi-barrier system. Gas- and thermally-induced overpressures, temperatures, normalised solute tracer fluxes, and gas flow rates are evaluated where applicable with their respective uncertainty ranges for each deviation.

6 Deterministic model-based analyses – total system

6.1 Expected performance

The expected performance of the total system is tied to an expected TH^2 evolution of the repository based on the features described in Section 5.2.1. The model-based analysis of the TH^2 evolution comprises the 3D repository model encompassed by the 3D component models as documented in greater detail with focus on gas in Nagra (2024g). Selected results from the 3D component models elaborated in Nagra (2024g) for HLW and L/ILW are provided in App. C and App. D, respectively. In the following, the focus is on key outcomes relevant to the total system performance.

6.1.1 Phenomenology

The "storyboard" report (Nagra 2024e) provides a general phenomenological description of the expected evolution of the deep geological repository over the entire assessment period. This includes coupled processes that may be relevant to safety and take place during construction and ventilation of the repository as well as after emplacement of the waste, the backfill and the sealing materials. The quantitative assessment of the hydraulic evolution of the repository is provided in Nagra (2024g). A brief overview is given in the following.

The excavation of the repository structures introduces pore pressure changes in the rock and creates an EDZ where hydraulic properties of the OPA are altered. The subsequent ventilation of the underground structures at prescribed temperature and relative humidity causes depressurisation and partial desaturation of the EDZ and surrounding rock. After emplacement and backfilling of the repository, the EDZ will start to resaturate, and pressure in the host rock will gradually recover. In the HLW repository section, thermal effects will be induced due to heat generated by the waste. At the same time, gas will be generated in both HLW and L/ILW sections of the repository (see Nagra 2024g), increasing the gas pressure. Porewater will migrate between the host rock and the backfill materials depending on the balance of capillary, viscous and gravity forces over time in different sections of the repository. In general, gas and water transport in the low-permeable host rock is diffusion-dominated, whereas transport in some parts of the repository, comprising materials with higher porosity and permeability, can be driven by advection if sufficient pressure gradient develops.

Accordingly, two distinct phases can be discerned with regards to system analysis after closure of the repository (see also Nagra 2024g). The first phase coincides with the early post-closure phase (hundreds of years) and is marked by the development of a thermal pulse extending radially (or taking an ellipsoid shape) around the HLW disposal area from the heat released by the waste. The increasing temperature in the HLW emplacement drifts and surrounding rock results in a porewater pressure increase caused by the difference between the expansivity of porewater and of the pores, referred to as *differential thermal expansion*. The second phase of the evolution coincides with the late post-closure phase (thousands to tens of thousands of years) and is marked by the accumulation of gas in the L/ILW and HLW repository sections. The increasing mass of gas in the repository structures also increases the pressure as gas compresses in the available pore volume, referred to as *gas pressure buildup*. Note that the pore volume available to gas is also coupled to porewater exchange with the surrounding rock. In general, gas pressure buildup is mitigated when the generated gas can transport into sufficient pore volume and when it dissolves into the porewater of the host rock. As shown in Fig. 3-6 and Fig. 3-12, the rate of gas generated in the L/ILW caverns is orders of magnitude higher than that in the HLW drifts of the repository. The materials in the L/ILW and HLW repository sections of the provisional design are tailored accordingly. In the L/ILW section, materials are chosen so that gas generated in the emplacement

caverns can be transported along the network of repository tunnels and in this way stored over larger volumes. In the HLW section, the gas generation rate is lower, and gas dissipates by radial transport and dissolution through the nearfield and surrounding OPA.

6.1.2 Quantitative analysis

Transients of temperature simulated with the 3D repository model at selected observation points (see Fig. 3-15) are shown in Fig. 6-1. In addition, spatial distributions of temperature at selected times are given in Fig. B-1.

The simulation time spans the stepwise implementation of construction and ventilation phases of the repository followed by the post-closure phase up to 1 million years. The sharp temperature drops from ambient rock temperature (~43 °C) to ventilation temperature (28 °C) during the first decades correspond to the successive and instantaneous opening of the respective repository structures at these times. In the HLW emplacement drifts (Fig. 6-1a), temperature increases sharply directly after emplacement (t = 46 years) due to waste-generated heat and then gradually decreases back to the ambient rock temperature. The operations tunnels connected to the disposal area show some temperature increase that depends on the distance of the respective observation point to the disposal area. For example, temperature in the V1-HLW seals increases by ~12 °C compared to ambient rock temperature, whereas the corresponding temperature increase in the V2-HLW seals is only ~2 °C. In the L/ILW repository structures (Fig. 6-1b), temperature recovers from the ventilation to the ambient rock temperature within ~3,000 years. Temperature in the L/ILW caverns does not exceed the ambient rock temperature at any time. Similarly, the temperature transients simulated in the central area of the repository (Fig. 6-1c) do not indicate any appreciable perturbation from the heat emitted in the HLW disposal area.

Transients of gas saturation from the same simulation are shown in Fig. 6-2. In addition, spatial distributions of gas saturation at selected times are given in Fig. B-2.

Gas saturation in the HLW repository structures (Fig. 6-2a) depends on the material used to backfill the respective sections. The operations tunnels, backfilled with high-porosity and permeable material, accumulate gas that is generated in the repository and therefore show increasing gas saturation with time. Note that the observation points shown for operations tunnels in Fig. 6-2 correspond to the upper part of the tunnel that accumulates more gas than the lower part due to buoyancy. On the other hand, the sections backfilled with bentonite fully saturate with water due to suction. The HLW emplacement drifts saturate with water between 200 and 300 years after emplacement. The V1-HLW and V2-HLW seals fully saturate after ~500 and ~3,000 years, respectively. After that, gas permeability effectively reduces to zero at the respective sealing sections. The bentonite buffer and the V1-HLW seals remain fully water saturated until 10,000 years when the associated increase in gas generation results in formation of gas phase with gas saturations of up to 4% and 2% in the emplacement drifts and in the seal, respectively (Nagra 2024g). In the L/ILW caverns (Fig. 6-2b), gas saturation decreases temporarily as porewater flows into the cavern until ~10,000 years and then increases with the accumulation of gas from the corrosion of metals and degradation of the organics. Note that the detailed spatial and temporal distribution of gas saturation in the cavern also depends on the exchange of water and gas between the emplaced materials and surrounding rock as described in Nagra (2024g). In the operations tunnels of the L/ILW repository section (Fig. 6-2b), gas saturation increases continuously after backfilling and until the end of the simulation due to gas migrating from the L/ILW emplacement caverns and accumulating at the roof of the tunnels. The same effect with increasing gas saturation during the post-closure phase is observed in the central area of the repository (Fig. 6-2c). Overall, a continuous gas path is maintained along the emplacement caverns, the operations tunnels, the V1-L/ILW and V2-L/ILW sealing sections and the central area of the repository during the simulated time of 1 million years. On the other hand, the lower part of the V3 seal of the access shaft, made of compacted bentonite, fully saturates with porewater after ~4,000 years (Fig. 6-2c).

After ~25,000 years, a gas phase develops once more in the V3 with gas saturations in the order of 1 – 2 %.

Transients of pressure from the same simulation are shown in Fig. 6-3. In addition, spatial distributions of pressure at selected times are given in Fig. B-3. Note that pressure shown in the figures corresponds to gas pressure when gas phase is present, and water pressure when only water is present.

In the early post-closure phase (~1,000 years), pressure increases in the OPA surrounding the HLW disposal area due to differential thermal expansion caused by the heat emitted from the waste (Fig. 6-3a, Fig. B-3a;b;c), reaching a peak of ~13 MPa after 200 years at 30 m above the centre of the HLW disposal area. In comparison, thermally induced pressures within the HLW emplacement drifts do not exceed the hydrostatic value. After the thermal pulse has dissipated, pressure in the HLW drifts begins to increase due to gas accumulation from the corrosion of the canisters. As the canisters are assumed to breach at 10,000 years, corrosion rate and gas generation increases, and gas pressure reaches a first peak of ~10.5 MPa after 15,000 years followed by a peak of ~11.8 MPa after ~115,000 years when the canister corrodes entirely (Nagra 2024g). Consequently, gas pressure gradually decreases back to hydrostatic at the end of the simulation. In the L/ILW caverns, pressure starts to increase after emplacement (t = 36 years) due the accumulation of waste-generated gas, reaching the hydrostatic value after ~20,000 years and a peak pressure of ~9.3 MPa after ~70,000 years (Fig. 6-3b). Pressure in the operation tunnels and sealing sections of the L/ILW section of the repository follows the same evolution, indicating the hydraulic connection through the continuous gas pathway in these repository structures (Nagra 2024g). The same is observed in the pressure evolution in the central area of the repository (Fig. 6-3c). On the other hand, the fast restoration of hydrostatic pressure in the shaft above the V3 seal points to the hydraulic separation of the shaft from the repository, introduced by the seal (Nagra 2024g).

(a)

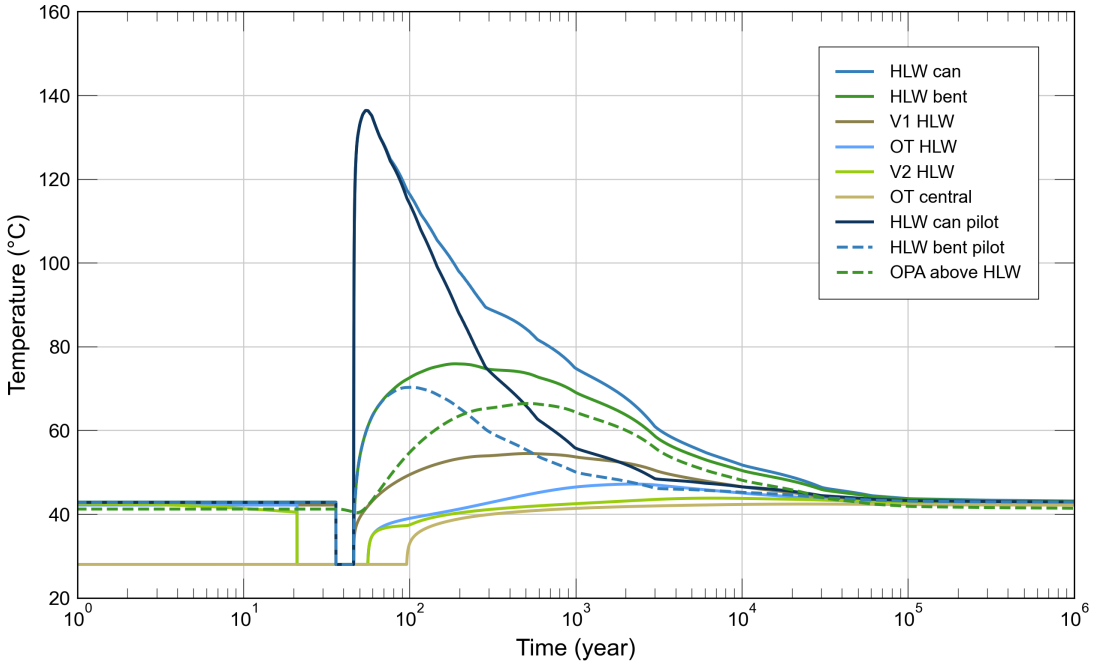
Temperature (°C)
Time (year)
HLW can
HLW bent
V1 HLW
OT HLW
V2 HLW
OT central
HLW can pilot
HLW bent pilot
OPA above HLW

(b)

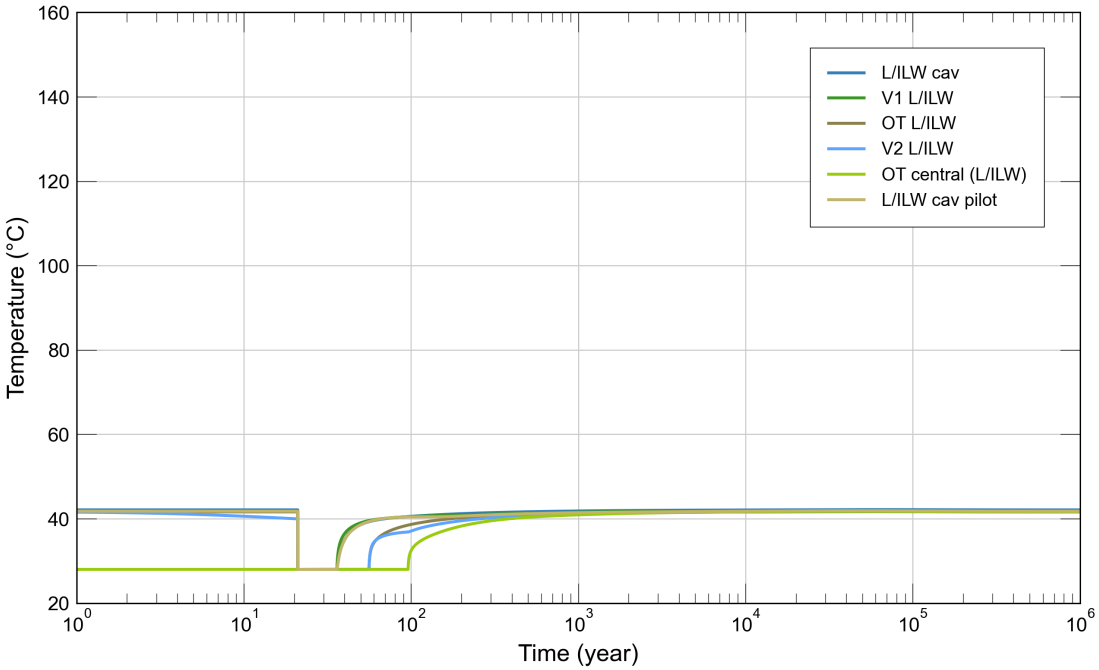
Temperature (°C)
Time (year)
L/ILW cav
V1 L/ILW
OT L/ILW
V2 L/ILW
OT central (L/ILW)
L/ILW cav pilot

(c)

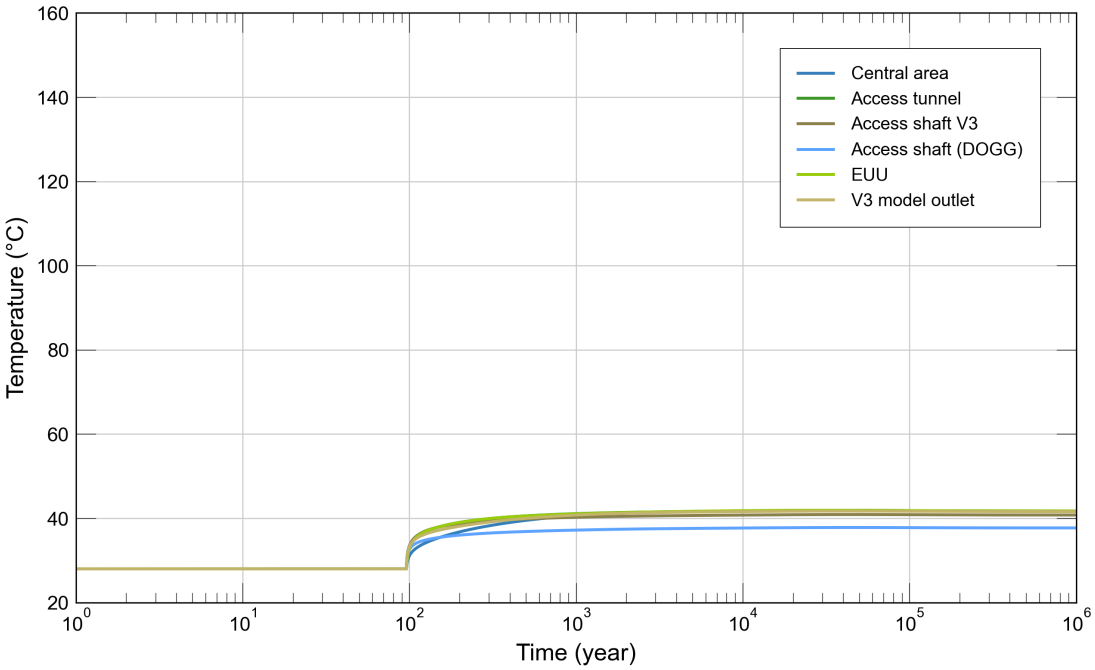

Fig. 6-1: Expected performance total system: transients of temperature
(a) HLW section, (b) L/ILW section and (c) Central area.

(a)

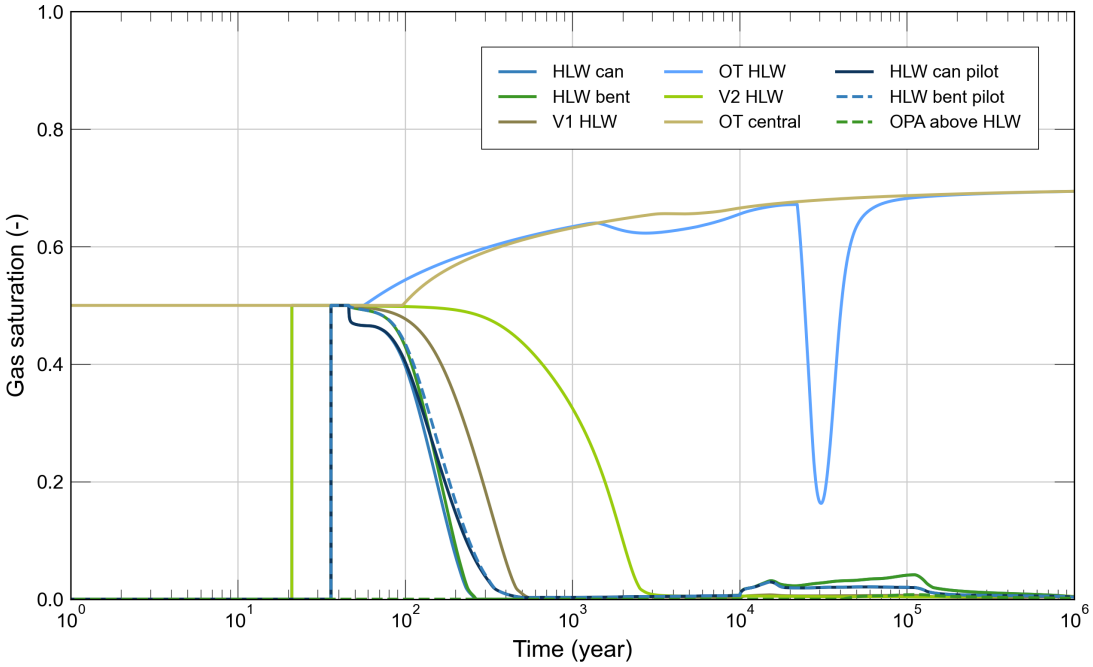
HLW can
HLW bent
V1 HLW
OT HLW
V2 HLW
OT central
HLW can pilot
HLW bent pilot
OPA above HLW
Gas saturation (-)
Time (year)

(b)

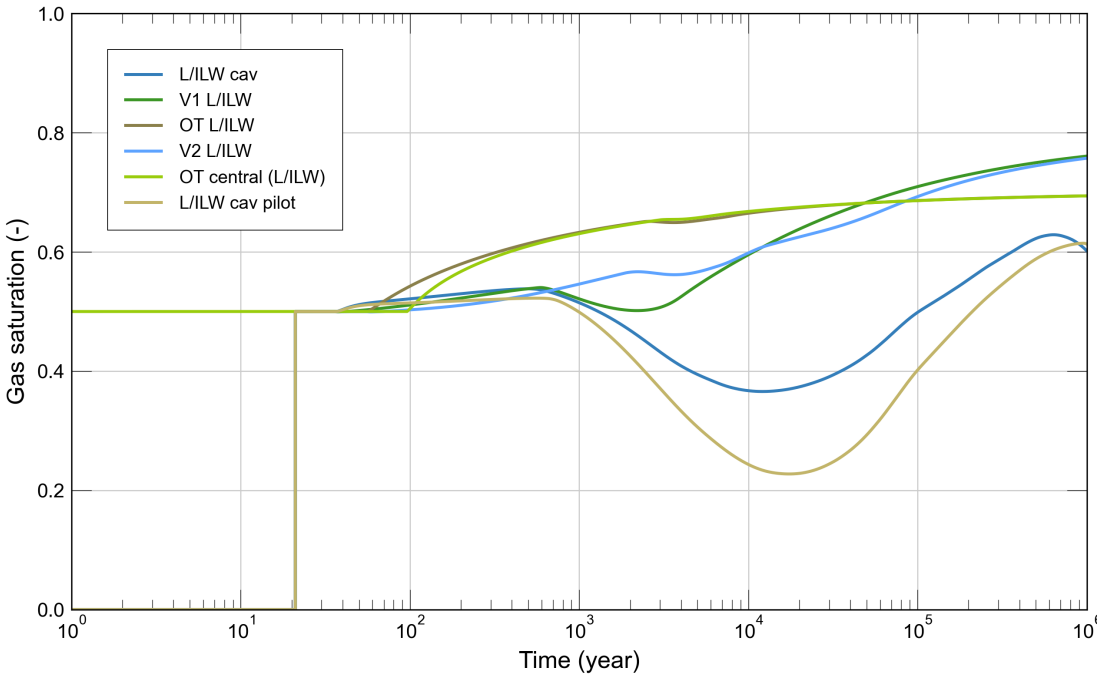
L/ILW cav
V1 L/ILW
OT L/ILW
V2 L/ILW
OT central (L/ILW)
L/ILW cav pilot
Gas saturation (-)
Time (year)

(c)

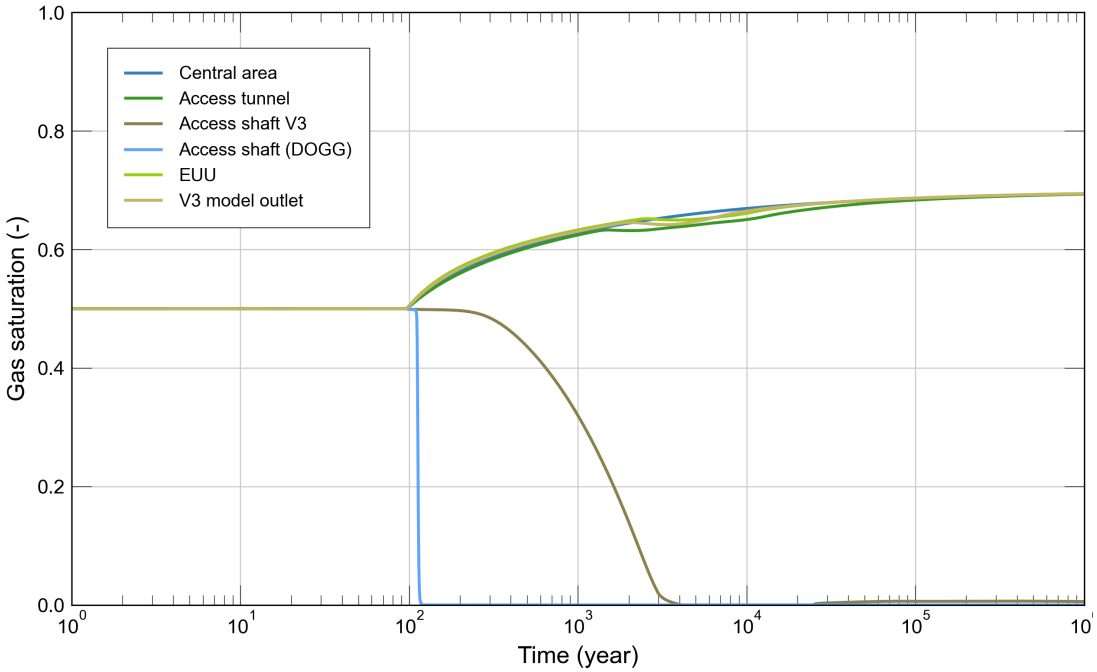

Fig. 6-2: Expected performance total system: transients of gas saturation
(a) HLW section, (b) L/ILW section and (c) Central area.

(a)

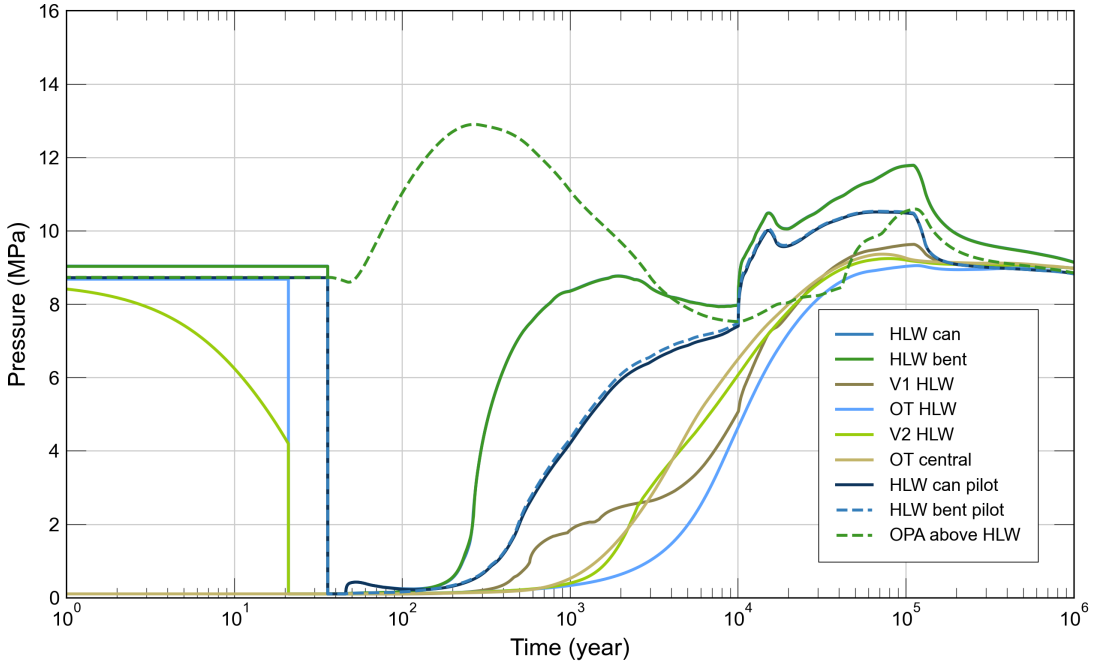
Pressure (MPa)
Time (year)
HLW can
HLW bent
V1 HLW
OT HLW
V2 HLW
OT central
HLW can pilot
HLW bent pilot
OPA above HLW

(b)

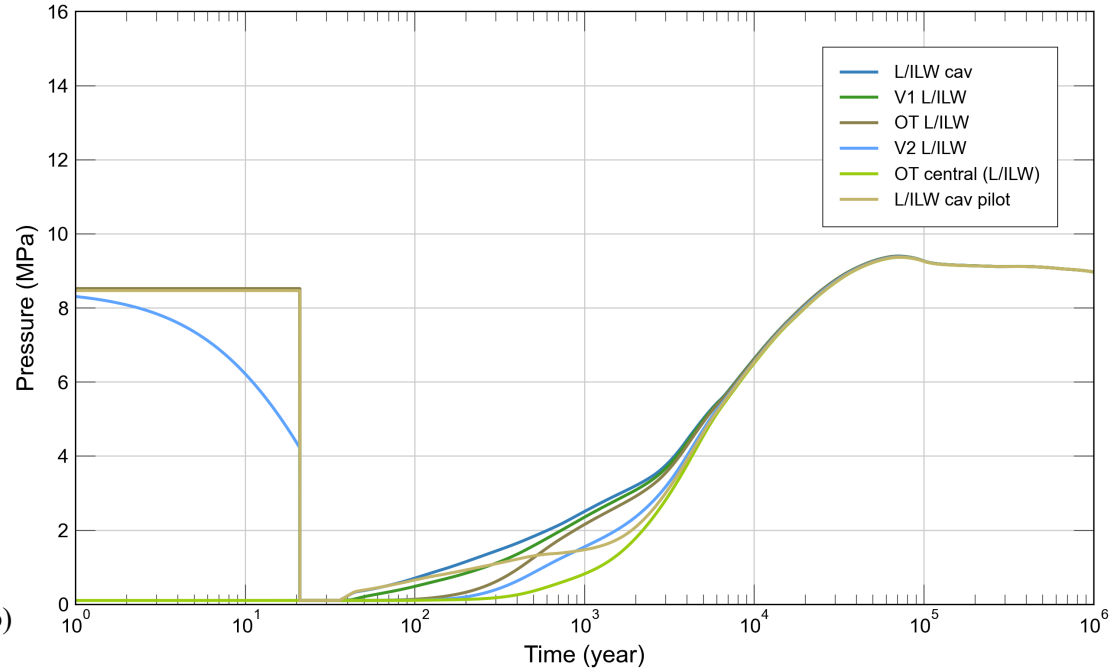
Pressure (MPa)
Time (year)
L/ILW cav
V1 L/ILW
OT L/ILW
V2 L/ILW
OT central (L/ILW)
L/ILW cav pilot

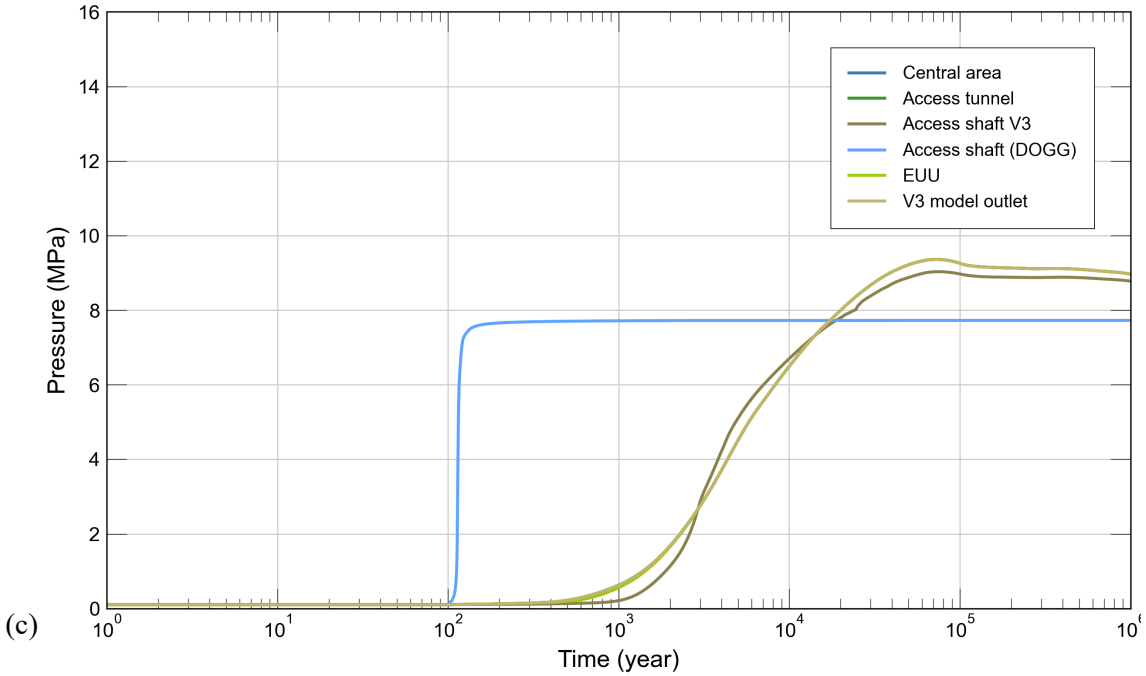

(c)

Fig. 6-3: Expected performance total system: transients of pressure

(a) HLW section, (b) L/ILW section and (c) Central area.

Flow rates of gas released through the sealing sections of the repository are shown in Fig. 6-4. These are compared to rates of gas generation from the L/ILW, from the HLW, and the combined total rate. After emplacement of the L/ILW caverns (t = 36 years), gas flows through the V1-L/ILW seals into the adjacent ventilated branching tunnels. Similarly, gas flow is observed through the V2-L/ILW seals shortly after their emplacement into the adjacent ventilated operations tunnels (t = 56 years). After backfilling of the central area and closure of the repository (t = 96 years), gas flow rate through the L/ILW seals towards the central area of the repository increases in the first few hundreds of years and reaches the rate of gas generation from the L/ILW after ~2,000 years. After that, the rates of gas flows through the L/ILW seals follow those of gas generation, indicating the effective gas transport path through the L/ILW repository structures. At later times (e.g., after 10,000 years), the rate of gas released through the seals becomes lower than the rate of gas generation, owing to the increasing dissolution and diffusion of gas as it spreads through the repository. In comparison, gas flows through the sealing sections of the HLW repository section are orders of magnitude lower. In general, gas flow through the HLW seals changes direction as it is determined by pressure disequilibria developing across each seal. These are subject to the thermal pulse in the HLW disposal area, that may result in displacement of water and gas, the depressurisation of the operation tunnels during their ventilation, and the gas pressure buildup in the disposal areas and in the repository central area, respectively. Between 10,000 and ~500,000 years after closure, gas flow from the V1-HLW seals to the adjacent branch tunnel is ~2 – 3 orders of magnitude below the rate of gas generation in the HLW disposal area. Throughout the simulation, gas flows from the V2-HLW in the direction of the central area are negligible, indicating that HLW-generated gas remains within the HLW section during that time. Gas break-through through the V3 seal occurs after ~42,000 years. Gas release into the shaft continues until the end of the simulation.

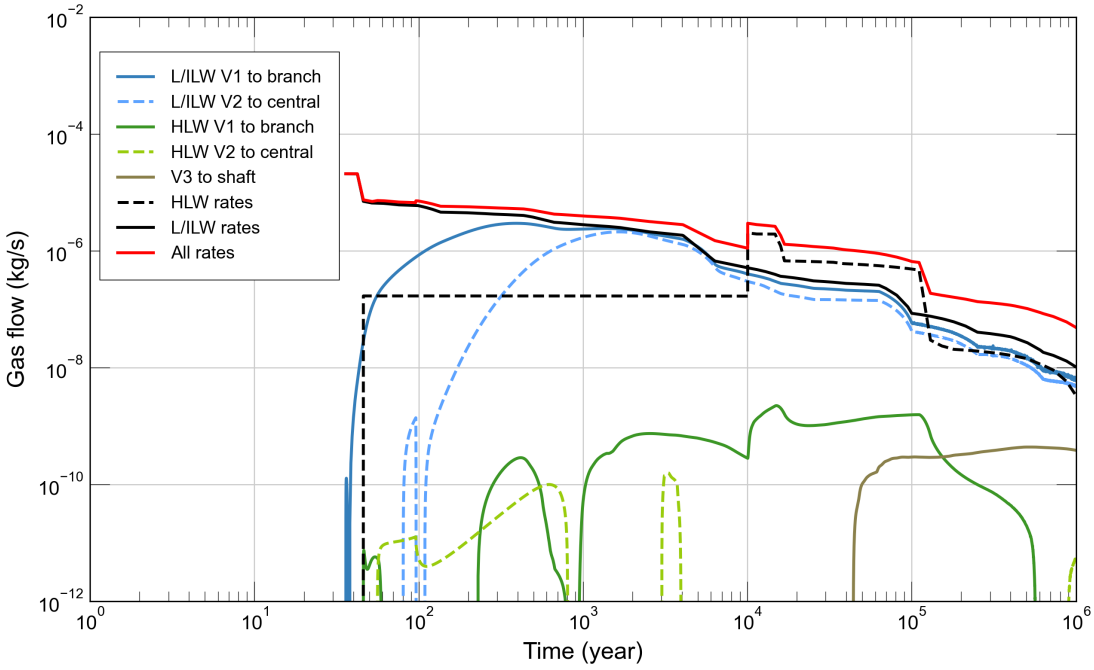

Fig. 6-4: Expected performance total system: transients of gas flow rate through the sealing sections of the repository (towards shafts)

Flow rates of displaced liquid passing through the same sealing sections are shown in Fig. 6-5. With the emplacement of the L/ILW caverns (t = 36 years), water is displaced into the ventilated branching tunnels through the V1-L/ILW seals. After emplacement of the operations tunnel and adjacent V2-L/ILW seal (t = 56 years), water is displaced into the adjacent ventilated central area until it is also backfilled (t = 96 years). After backfilling of the central area and closure of the repository, water displacement from the L/ILW repository section towards the operation tunnels and central area continues until ~150,000 years. The maximum liquid flow rate is observed through the V2-L/ILW seal after ~20,000 years and corresponds to less than 100 litres per year. In comparison, liquid flows through the sealing sections of the HLW section are overall lower. Water displacement from the V1-HLW seals into the adjacent branching tunnels stops after ~20,000 years. The maximum total liquid flow rate through all V1-HLW seals corresponds to less than ~100 litres per year, respectively. Liquid flow from the V3 seal to the shaft above the seal occurs after ~39,000 years. Liquid flow into the shaft continues until the end of the simulation.

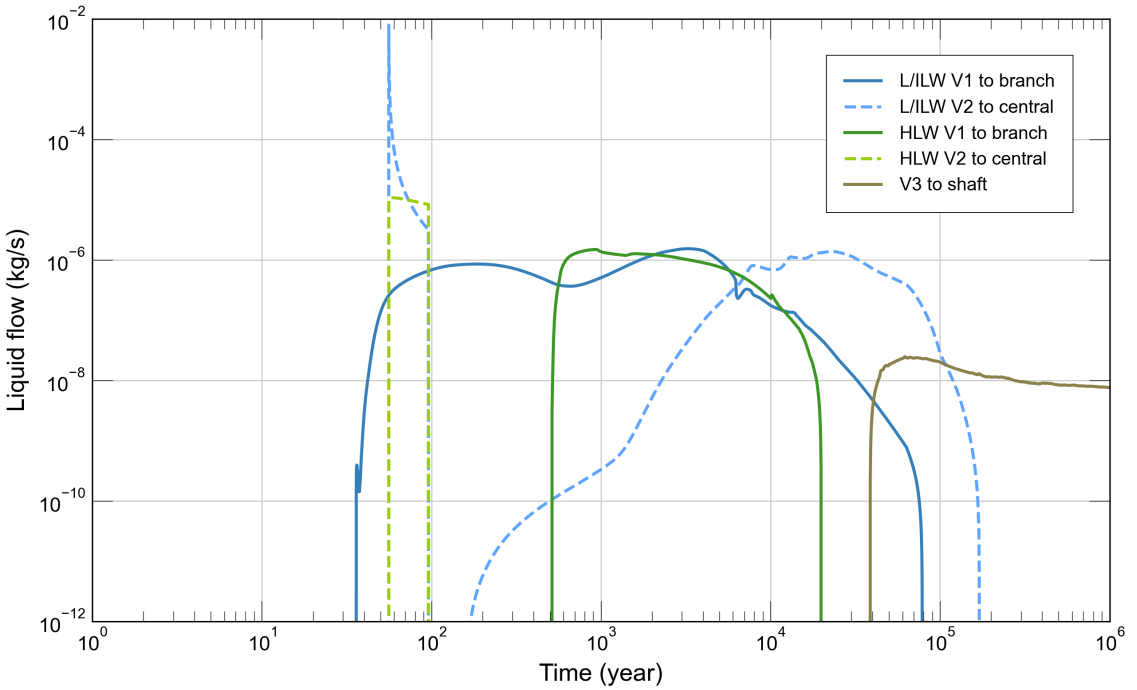

Fig. 6-5: Expected performance total system: transients of liquid flow rate through the sealing sections of the combined repository (towards shafts)

Gas and water mass flow rates (unit M/T) in the opposite direction, e.g., from the central area into the V2 seals are normalised and accumulated. Gas flow rates are normalised by the total gas production in the repository in the simulated period (e.g., 1 million years). The resulting normalised rate (unit 1/T) is then accumulated over the simulated period (unit -). Only values down to 1E-07 are considered (respectively 0.1 millionth of generated gas). Liquid flow rates are normalised by the total water mass that can be stored in the pore volumes of the repository tunnels assuming hydrostatic pressure and ambient rock temperature (e.g., assuming a fully water-saturated repository). The resulting normalised rate (unit 1/T) is then accumulated over the simulated period (unit -).

The normalised cumulative gas and liquid flows are shown in Fig. 6-6. Gas flows towards the L/ILW repository section are negligible over the entire simulated period of 1 million years (Fig. 6-6a). In the HLW section, some gas flows through the V2-HLW seal starting from 1,000 years until the end of the simulation (Fig. 6-6a). The cumulative amount after 1 million years reaches a mass that corresponds to approximately 1E-03 of the gas generated in the repository. During this entire period, no gas reaches the HLW emplacement drifts through the V1-HLW seals. After gas breakthrough from the V3 seal, the cumulative amount of gas released to the shaft corresponds to 1E-04 and 3E-03 after 100,000 and 1,000,000 years, respectively (Fig. 6-6a). The normalised liquid flows show only negligible amount of water taken up by the V2-HLW seal from the adjacent central area between 20,000 and 80,000 years (Fig. 6-6b).

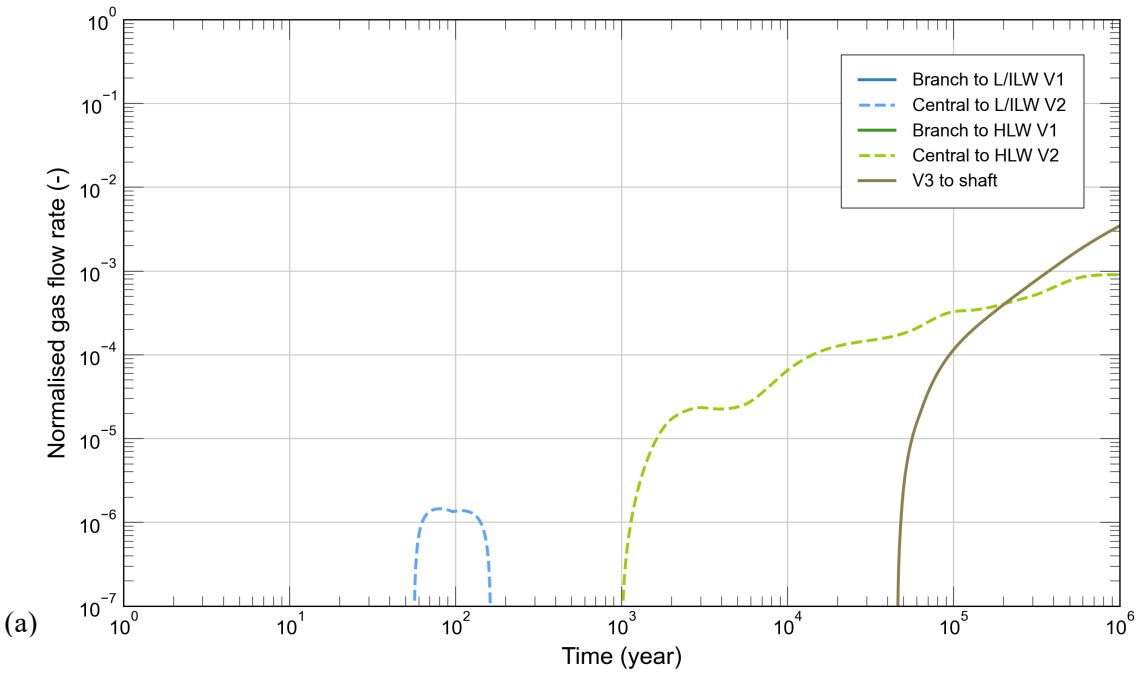

(a)

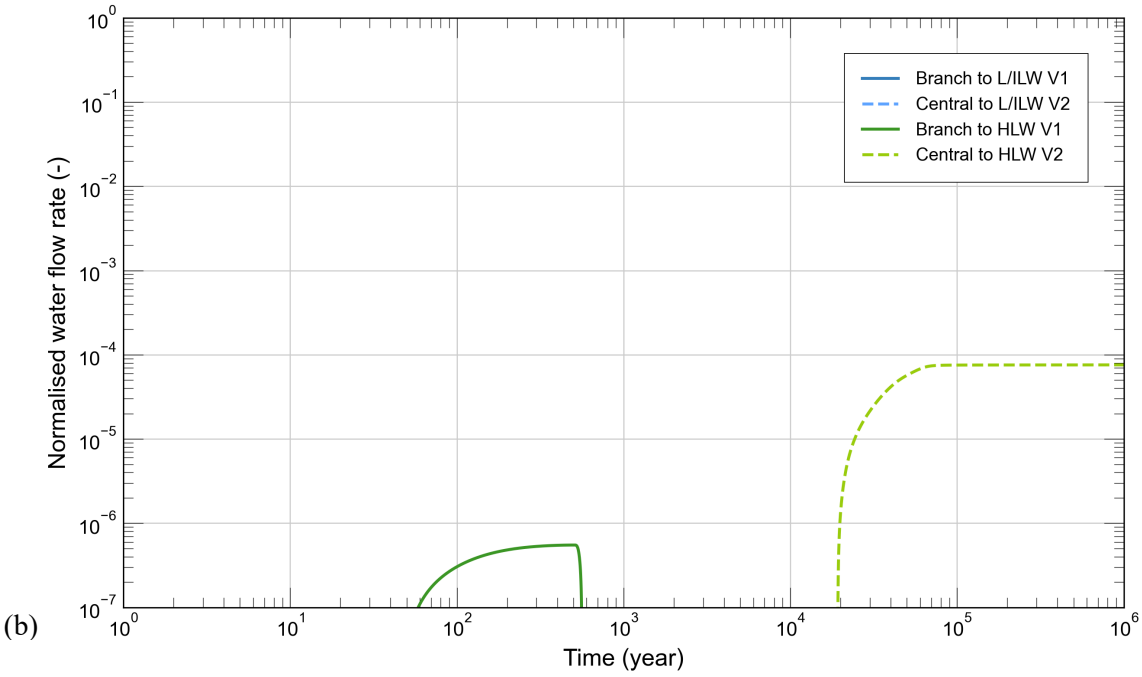

(b)

Fig. 6-6: Expected performance total system: transients of normalised flow rates

(a) Gas and (b) liquid through the sealing sections of the repository (towards disposal areas).

Further insight into the distribution of gas in the repository is given with the spatial plots of H_2 tracer partial gas saturation as shown in Fig. 6-7. The partial gas saturations in Fig. 6-7 show H_2 gas in the repository after 50,000 years, originating from the HLW emplacement drifts (Fig. 6-7a) and originating from the L/ILW emplacement caverns (Fig. 6-7b), respectively. Similar plots at additional times of the post-closure phase are provided in Fig. B-5. It is shown that H_2 gas generated in the HLW emplacement drifts remains contained within the HLW section of the repository for at least 100,000 years. On the other hand, gas originating from the L/ILW emplacement caverns spreads through the L/ILW section and the central area of the repository where it remains contained for tens of thousands of years.

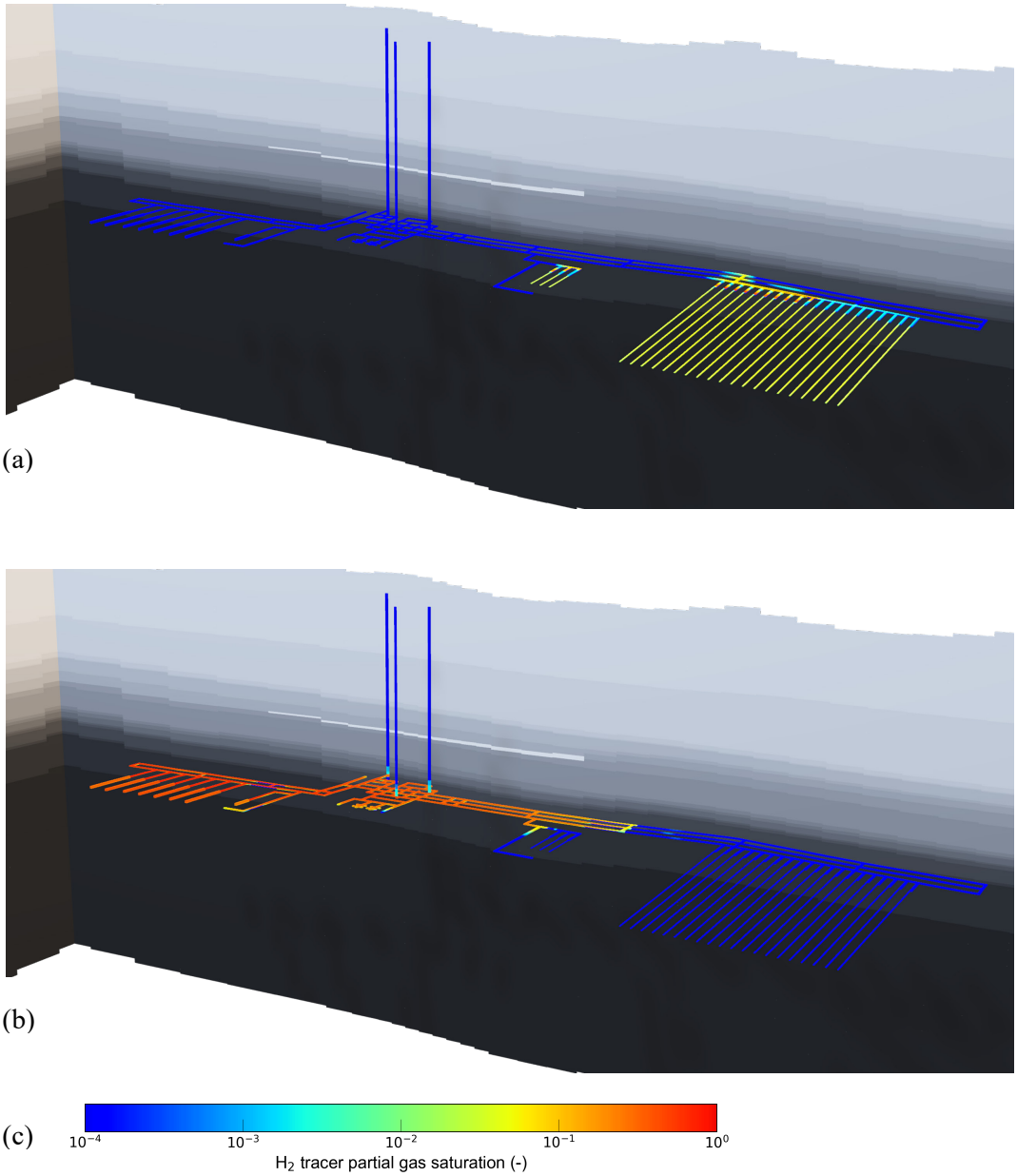

Fig. 6-7: Expected performance total system: spatial distribution of partial gas saturation of H_2 generated

(a) In the HLW emplacement drifts, and (b) in the L/ILW emplacement caverns. After 50,000 years.

6.1.3 Summary of key processes

The excavation and ventilation of the repository structures causes depressurisation and partial desaturation of the EDZ and the surrounding rock. After emplacement and backfilling of the repository structures, heat is generated by the radioactive decay of the HLW, and gas is generated from the corrosion of metals (HLW and L/ILW) and degradation of organics (L/ILW only) in the repository. The rate of gas generated in a L/ILW emplacement cavern is orders of magnitude higher than that in a HLW emplacement drift.

The early post-closure phase of the HLW section of the repository is marked by heat induced effects. The heat output and temperature increase in the nearfield is highest directly after emplacement and decreases with time (see Fig. 6-1, Nagra 2024g, Fig. C-1 and Fig. C-2). The thermal pulse results in pressure increase caused by thermal expansion of porewater in the rock surrounding the HLW disposal area, that dissipates after few hundreds of years (see Fig. 6-3 and Fig. B-3). The maximum pressure reached in the OPA approximately 30 m above the HLW disposal area is 13 MPa. During that period, the bentonite of the HLW drifts and adjacent V1-HLW seals takes up porewater, reaching full water saturation after few hundreds of years (Fig. 6-2, see also Nagra 2024g and Fig. C-2). Combined with the OPA, this creates a low-permeable barrier in the HLW section of the repository where gas dissipates through radial transport and dissolution (Nagra 2024g). Gas transport axially through the tunnels in the HLW section is very limited so that gas that is generated from the HLW remains within that section and the surrounding rock (see Fig. 6-6 and Fig. B-5). Similarly, water expulsion to the adjacent operations tunnels due to thermally- and gas-induced overpressures in the HLW nearfield is very limited (see Fig. 6-5 and Fig. 6-6). The maximum gas-induced overpressure corresponds to less than 3 MPa.

Gas generation from L/ILW is highest directly after emplacement and decreases with time. Backfill and sealing materials in the L/ILW section of the repository are currently designed such that they allow axial transport through the repository structures (Nagra 2024g). Pressure gradients generated from gas accumulation therefore result in advective gas flow along the network of tunnels in the repository so that eventually most of the gas generated in the L/ILW emplacement caverns transports through the V1-L/ILW seals (Fig. 6-4). At the same time, gas is also transported radially from the tunnels into the surrounding rock by dissolution and diffusion in porewater (Fig. B-4). Through the advective spreading of gas along the repository tunnels, the interface area for gas dissolution in porewater also increases (Fig. B-4). Gas saturations in the repository tunnels are overall high, forming a connected pathway for gas that facilitates the transport of gas through the L/ILW section of the repository and the central area (Fig. 6-2, see also Nagra 2024g, Fig. B-2 and Fig. D-1). Gas remains contained within these tunnels and gradually dissolves into the surrounding rock or, to a much lesser extent, flows to the shafts through the V3 seals (Fig. 6-6 and Fig. B-5, see also Nagra 2024g). Hydrostatic pressure is reached after 20,000 years, whereas maximum gas-induced overpressure is reached after 70,000 years and corresponds to less than 1 MPa.

After backfilling, the shafts saturate with porewater from the surrounding rock formations. Full saturation of the shaft sections in the Wildegg Formation is reached almost immediately (Fig. 6-2, see also Nagra 2024g and Fig. B-2). The bentonite of the V3 seal also saturates with porewater, albeit slower, creating a hydraulic barrier to gas release from the repository tunnels to the overlying shaft. Gas and liquid flows from the V3 seal to the shaft occur only after hydrostatic pressures are exceeded in the repository (see Fig. 6-4 and Fig. 6-5) after some 42,000 years. If molecular diffusion is included in the calculations, gas pressures in the repository are lower (Fig. B-8) and breakthrough of gas to the shaft is delayed to after 100,000 years (Fig. B-9).

6.2 Deviations – total system

Performance scenarios are formulated to account for deviations in the total system analysis associated with possible interactions in the repository. These are summarised in Tab. 6-1 and discussed in the following paragraphs. The scenarios are simulated with the 3D repository model. Note that some of these simulations are also discussed in Nagra (2024g), as outlined in Tab. 6-1.

Tab. 6-1: Deviations from expected performance total system – by interaction

PA scenario - total system (simulation code)	Metrics: state variables	Metrics: transport
Deviations by thermal interactions		
No heat source in the HLW repository [TS1]	Pressure and saturation in central area.	Temperature change from ambient temperature: • in L/ILW repository; • in central area.
Conservative heat source and high thermal conductivity of host rock [TSD12]		
Deviations by hydraulic interactions		
Lower bound gas generation[1] [TSD2]	Pressure and saturation in central area.	Normalised cumulative gas and liquid flows: • through V2-L/ILW and V1-L/ILW seals towards L/ILW caverns; • through V2-HLW and V1-HLW seals towards HLW repository; • through V3 seal towards overlying shaft.
Upper bound gas generation[1] [TSD3]		
Fault through L/ILW caverns [TSD13]		
Fault through central area [TSD9]		
Low-permeable V2-L/ILW seal[1] [TSD6]		
High-permeable V3 seal (var. 1)[1] [TSD5]		
High-permeable V3 seal (var. 2) [TSD7]		
High-permeable V3 and V2-L/ILW seals [TSD8]		
High-permeable V2 seals [TSD10]		
High-permeable V2 and V1 seals [TSD11]		
No V1 seals[2] [TSD14]	Temperature, pressure and saturation in HLW section, in L/ILW section, and in central area.	Gas and liquid flows: • through V1 and V2 sealing sections towards central area; • through V3 seal towards overlying shaft. Normalised cumulative gas and liquid flows: • through V2-L/ILW and V1-L/ILW seals towards L/ILW caverns; • through V2-HLW and V1-HLW seals towards HLW repository; • through V3 seal towards overlying shaft.
No V2 seals[2] [TSD15]		
Impermeable V3 seals[2] [TSD16]		
Impermeable V2-L/ILW seals[2] [TSD21]		
Low-permeable V1-L/ILW seals[2] [TSD20]		
Instant repository resaturation[2] [TSD4]		
Mechanical & chemical interactions – Implicit in variants for TH interactions.		

[1] Also discussed in Nagra (2024g).
[2] Results from these scenarios are given in App. B.

6.2.1 Thermal interactions

To identify potential thermal interactions in the repository, two scenarios are implemented in the repository model:

1. *No heat source in the HLW repository:* The heat source term is entirely removed from the HLW disposal area.
2. *Conservative heat source and high thermal conductivity of host rock:* The maximum heat output from PWR-MOX is assinged to all heat source terms in the HLW disposal area and the thermal conductivity of the OPA is set equal to the horizontal value (2.8 W/m K).

The analysis of thermal interactions with these two variants is based on the comparison to the expected evolution of the total system (Section 6.1). This is carried out in terms of pressure, saturation, and temperature evolution in the L/ILW section and in the central area of the repository.

No heat source in HLW repository *[TS1]*

In this scenario, the simulation of the total system expected evolution (Section 6.1) is modified by setting to zero all heat sources in the HLW emplacement rooms. This simulation is used to assess the thermal evolution in the L/ILW disposal area without thermal impact from the HLW and, with regards to thermal effects, can be understood as a proxy of a separate L/ILW repository at the same location.

The simulated transients of pressure and saturation in the central area of the repository are shown in Fig. 6-8. Similar to the simulation of the expected evolution, pressure in the central area increases gradually until it reaches a peak of ~9.3 MPa after ~70,000 years associated with the generation of gas in the L/ILW disposal area (Fig. 6-8a). The pressure transients in the V3 seal and the shaft above are also identical to the expected evolution. Similarly, the saturation transients do not indicate any change in the saturation state in the central area (Fig. 6-8b).

The transients of temperature change from ventilation temperature (28 °C) in the L/ILW disposal area and in the central area are shown in Fig. 6-9. The results are compared to corresponding temperature change in the expected evolution (e.g., including the heat source term in the HLW). In the L/ILW disposal area (Fig. 6-9a), the increase of temperature after backfilling (36 years for L/ILW caverns, 46 years for adjacent operations tunnel and V2-L/ILW seal) is identical to the expected evolution. Based on a similar comparison, Fig. 6-9b shows that thermal effects are not of relevance already in central area between the disposal areas. Note that the central area is back-filled later (96 years).

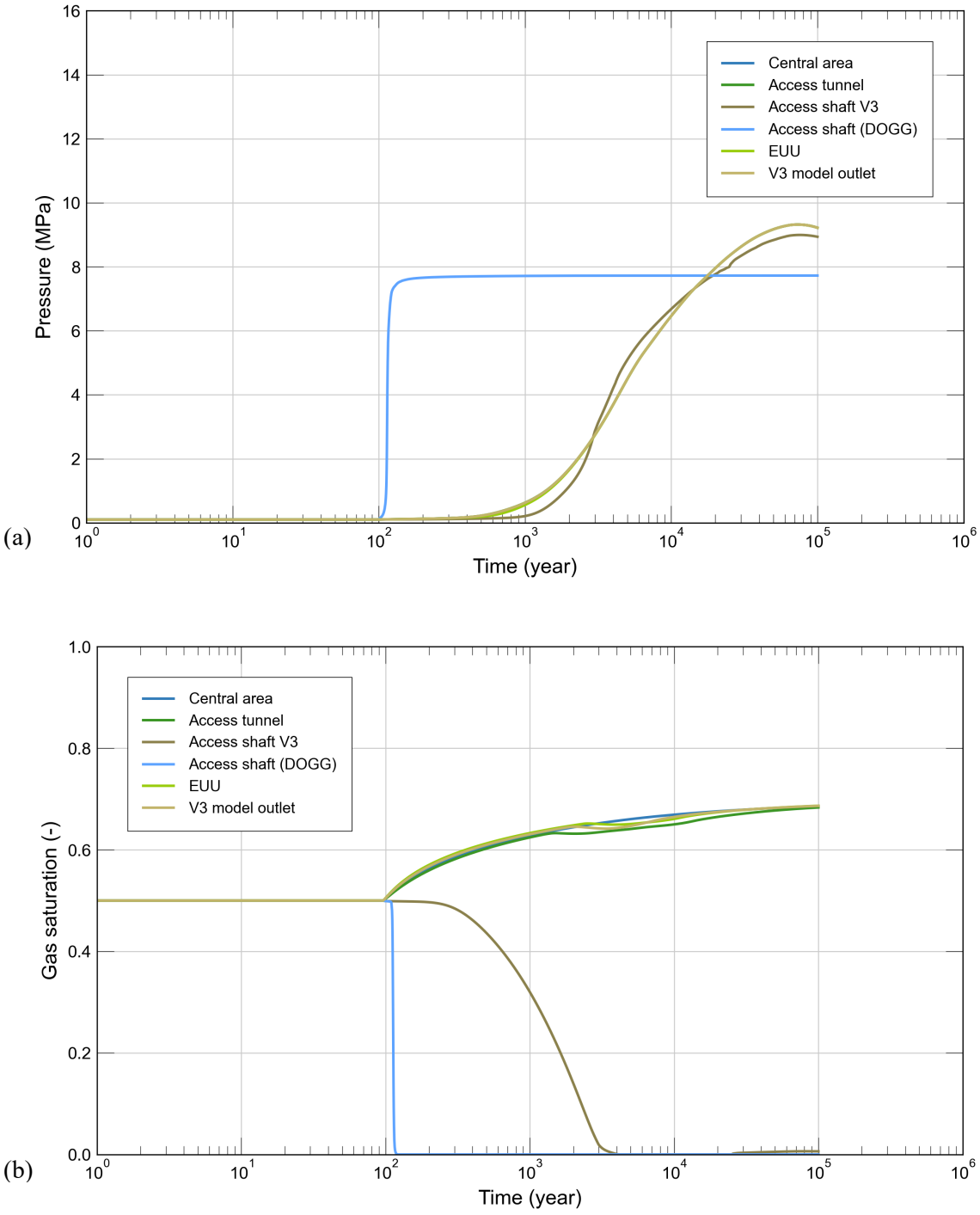

Fig. 6-8: Deviations scenario *"no heat source in the HLW repository"*: transients of (a) pressure and (b) gas saturation in the central area of the repository

(a)

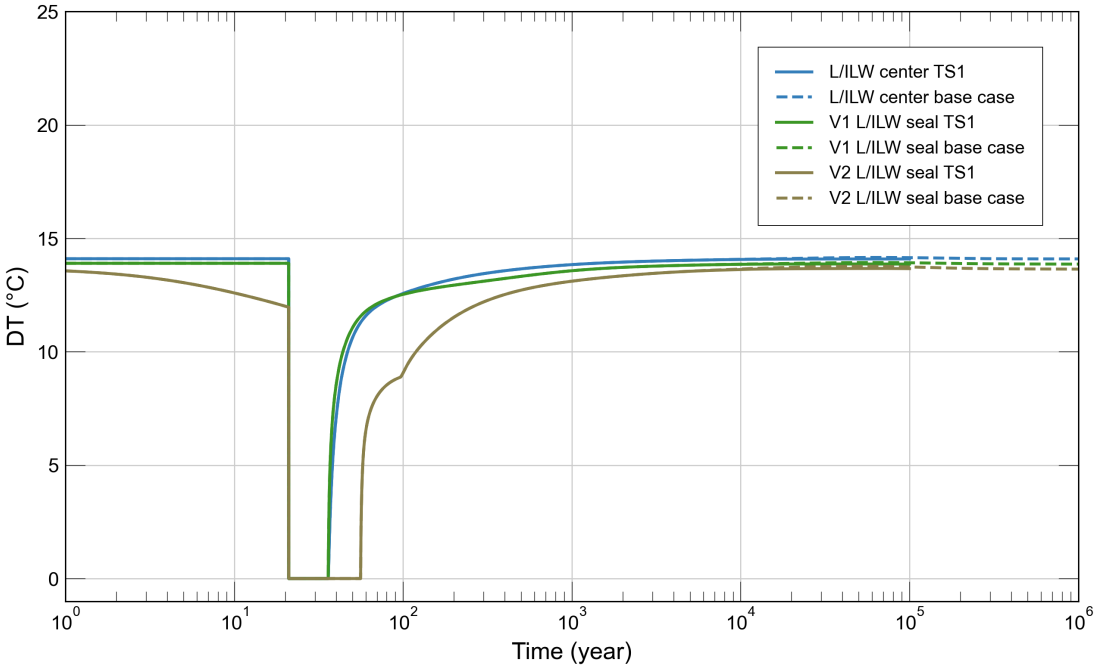

(b)

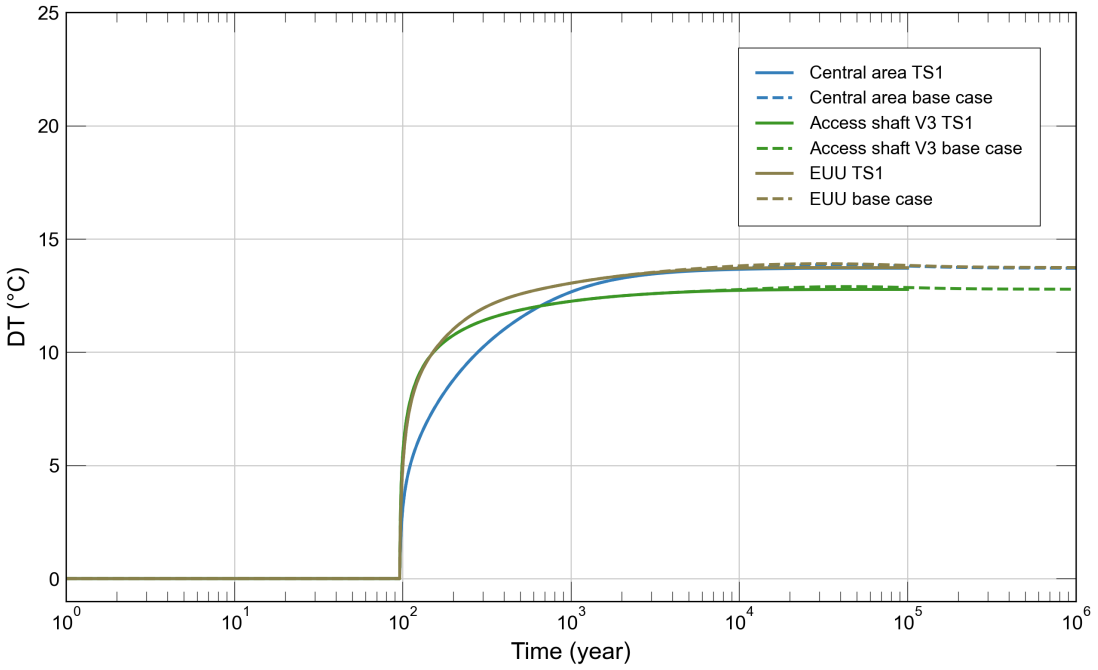

Fig. 6-9: Deviations scenario *"no heat source in the HLW repository"*: comparison of absolute temperature increase from initial temperature

(a) In the L/ILW section; (b) in the central area.

Conservative heat source and high thermal conductivity of host rock *[TSD12]*

In this variant it is assumed that the entire inventory of SF generates heat at the same rate as the maximum heat output of PWR-MOX canisters, corresponding to "representative maximum heat rates" reported in in Nagra (2024g). Note that these heat rates are higher than the representative average heat output from PWR-MOX shown in Fig. 3-7. This unrealistically high heat source is used here to preclude any thermal impacts on the L/ILW disposal area for all possible heat outputs in the repository. This conservative assumption is combined with the horizontal value for thermal conductivity of the OPA to allow faster transport of heat from the HLW to the farfield (and towards the central area and the L/ILW section).

The simulated transients of pressure and saturation in the central area of the repository are shown in Fig. 6-10 a and b, respectively. The differences to the expected evolution are negligible.

The transients of temperature change from ventilation temperature (28 °C) in the L/ILW disposal area and in the central area are shown in Fig. 6-11. The transients are compared in the same figure to those simulated for the expected evolution (e.g., with the expected heat source term in the HLW). In the L/ILW disposal area (Fig. 6-11a), the increase of temperature after backfilling is practically the same as in the expected evolution (differences of less than 1 °C). The outcome of the comparison is similar in the observation points of the central area (Fig. 6-11b), indicating that even for the conservative assumptions adopted in this scenario thermal interactions can be excluded.

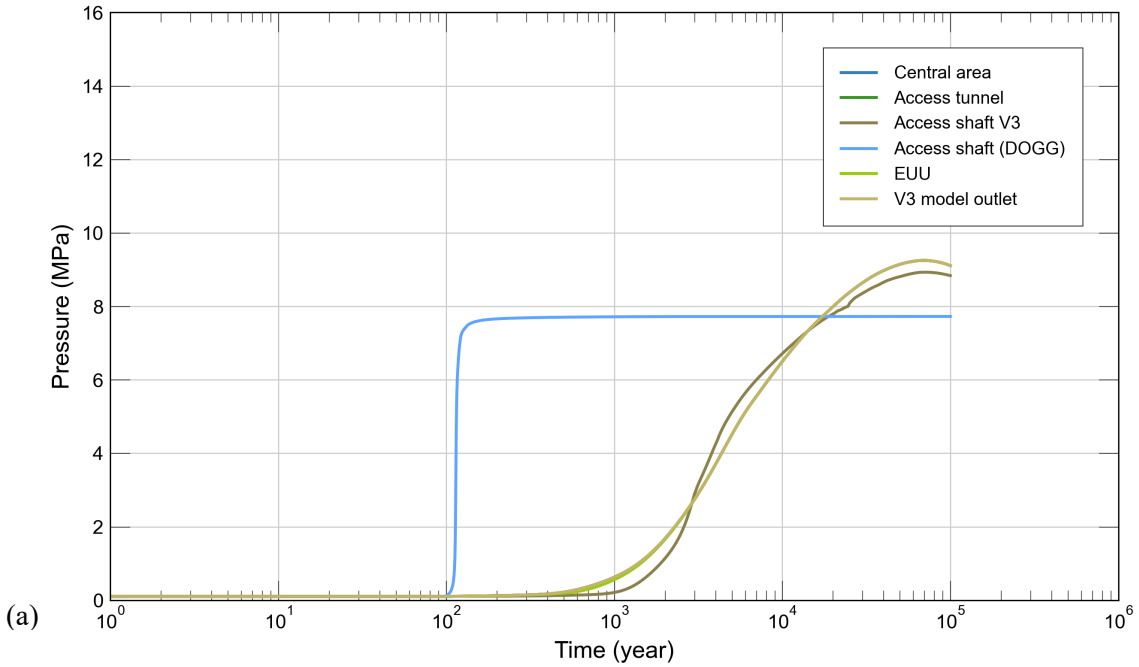

(a)

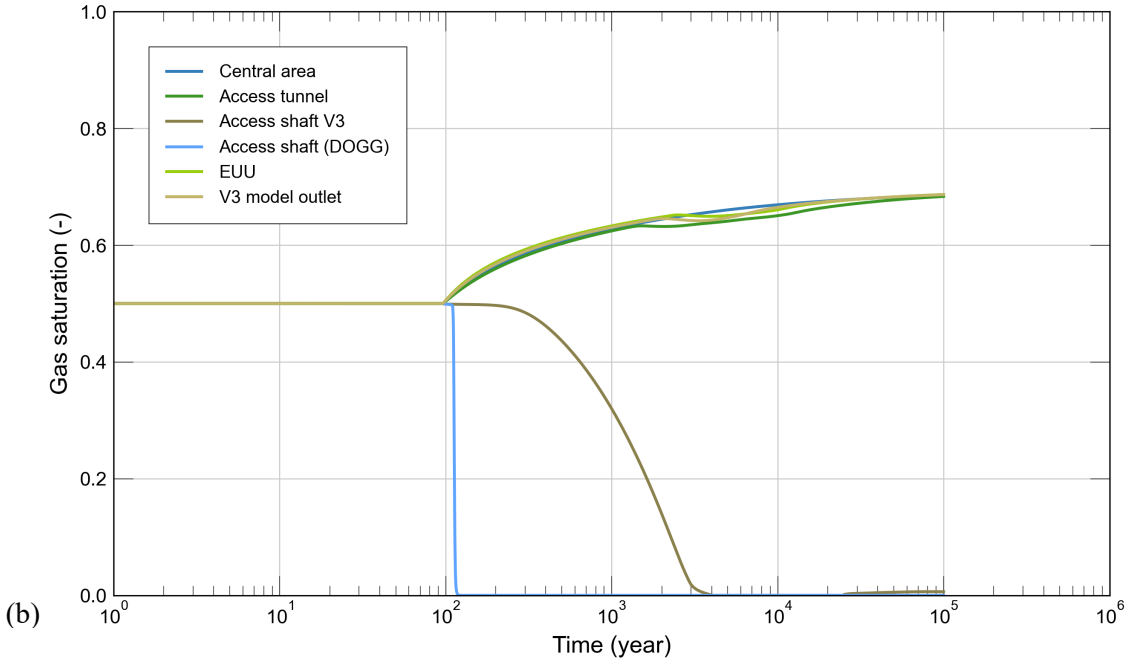

(b)

Fig. 6-10: Deviations scenario *"conservative heat source and high thermal conductivity of host rock"*: transients of (a) pressure and (b) gas saturation in the central area of the repository

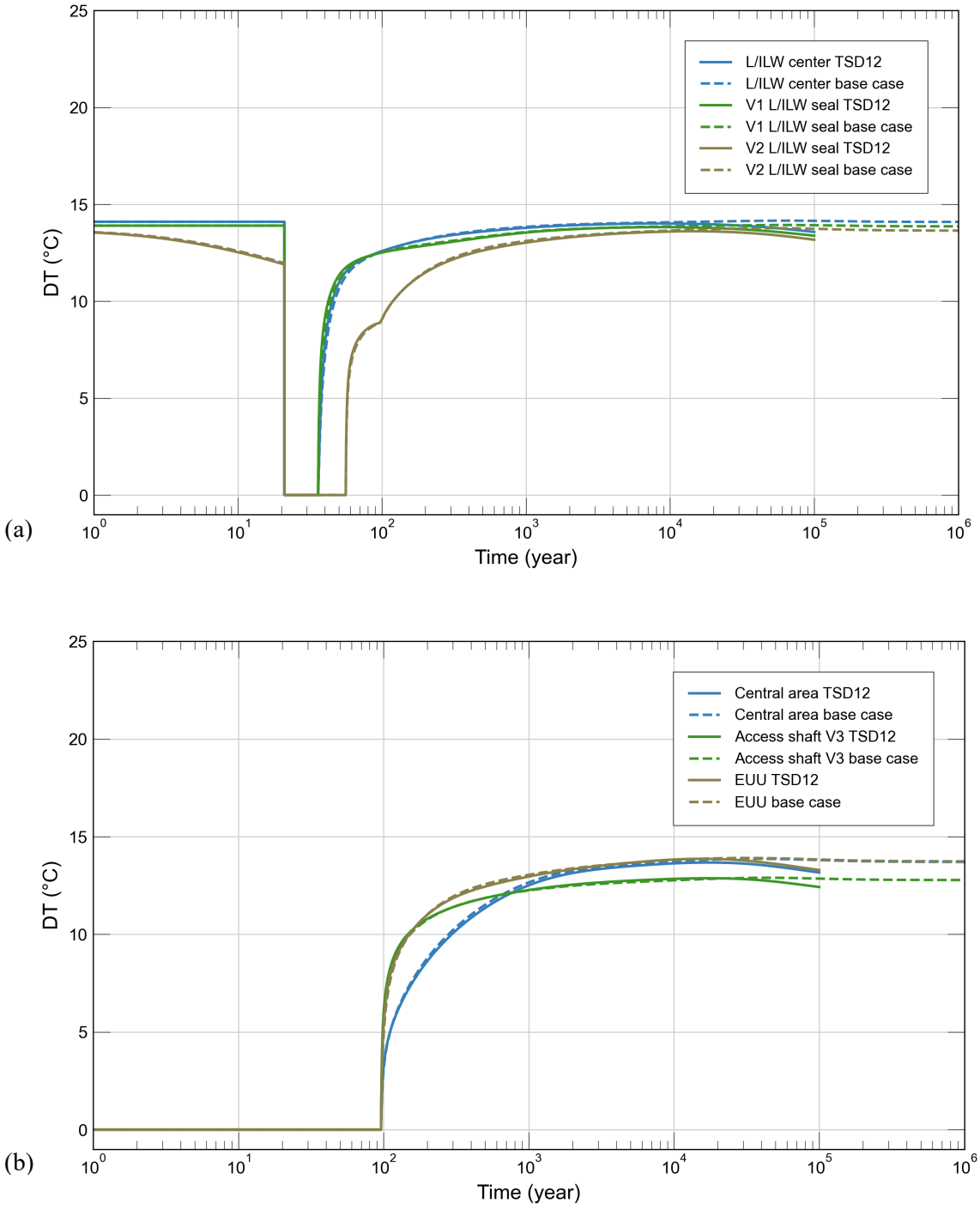

Fig. 6-11: Deviations scenario *"conservative heat source and high thermal conductivity of host rock"*: comparison of absolute temperature increase from initial temperature (a) in the L/ILW section and (b) in the central area.

6.2.2 Hydraulic interactions

Deviations by hydraulic interactions are formulated with the scenarios listed in Tab. 6-2.

Tab. 6-2: Simulated scenarios for deviations by hydraulic interactions[1]

	Gas generation	V1-L/ILW	V2-L/ILW	V1-HLW	V2-HLW	V3
TSD2[2]	**LB**	5E-18	5E-18	1E-20	1E-20	1E-20
TSD3[2]	**UB**	5E-18	5E-18	1E-20	1E-20	1E-20
TSD4[3], TSD9[3], TSD13[4]	BE	5E-18	5E-18	1E-20	1E-20	1E-20
TSD5	BE	5E-18	5E-18	1E-20	1E-20	**1E-19**
TSD6	BE	5E-18	**1E-19**	1E-20	1E-20	1E-20
TSD7	BE	5E-18	5E-18	1E-20	1E-20	**1E-17**
TSD8	BE	5E-18	**1E-17**	1E-20	1E-20	**1E-17**
TSD10	BE	5E-18	**1E-17**	1E-20	**1E-19**	1E-20
TSD11	BE	**1E-17**	**1E-17**	**1E-19**	**1E-19**	1E-20
TSD14	BE	**(1E-16)**	5E-18	**(1E-16)**	1E-20	1E-20
TSD15	BE	5E-18	**(1E-16)**	1E-20	**(1E-16)**	1E-20
TSD16	BE	5E-18	5E-18	1E-20	1E-20	**1E-22**
TSD20	BE	**1E-19**	5E-18	1E-20	1E-20	1E-20
TSD21	BE	5E-18	**1E-22**	1E-20	1E-20	1E-20

[1] Absolute permeability values given for the sealing sections (in m^2).
[2] Seal permeabilities equal to those in expected performance, combined with scenarios of gas generation.
[3] Seal permeabilities equal to those in expected performance, combined with scenarios of hypothetical faults.
[4] Seal permeabilities equal to those in expected performance, combined with scenario of instant resaturation.

Scenarios TSD2 and TSD3 are related to the rate of gas generation in the repository. Scenarios TSD3 and TSD9 represent highly transmissive faults intersecting the repository at the L/ILW disposal area and at the central area, respectively. Scenario TSD13 assumes instant resaturation of the repository after closure. The rest of the scenarios relate to the permeability of the sealing sections.

Lower bound gas generation *[TSD2]*

The first scenario of gas generation is based on the lower bound gas generation rates in the L/ILW and in the HLW disposal areas (Fig. 3-6 and Fig. 3-12, respectively). A comprehensive description of the TH^2 evolution under this assumption, including modelling in 3D for individual repository components, is documented in Nagra (2024g). The transients of pressure and gas saturation in the central area with this simulation are shown in Fig. 6-12. In comparison to the expected evolution, the pressure increase after repository closure is slower due to the slower accumulation of gas in the repository (Fig. 6-12a). The maximum pressure is reached after ~80,000 years and is approximately equal to the hydrostatic pressure, which is ~0.8 MPa lower

than in the expected performance. The gas saturation transients at the same locations (Fig. 6-12b) show the resaturation of the central area with porewater after ~10,000 years with the exception of the EUU that retains some gas until the end of the simulation after 100,000 years.

The normalised gas and liquid flows through the V2 and V1 sealing sections are shown in Fig. 6-13. In the first ~400 years, a small amount of gas flow takes place from the central area through the V2 seals into the adjacent operations tunnels for L/ILW and for HLW, respectively (Fig. 6-13a). Consequently, gas flow through the sealing sections is negligible. No gas breakthrough through the V3 is observed in the first 100,000 years. Similarly, liquid flows through the sealing sections in the direction of the disposal areas are negligible (Fig. 6-13b).

(a)

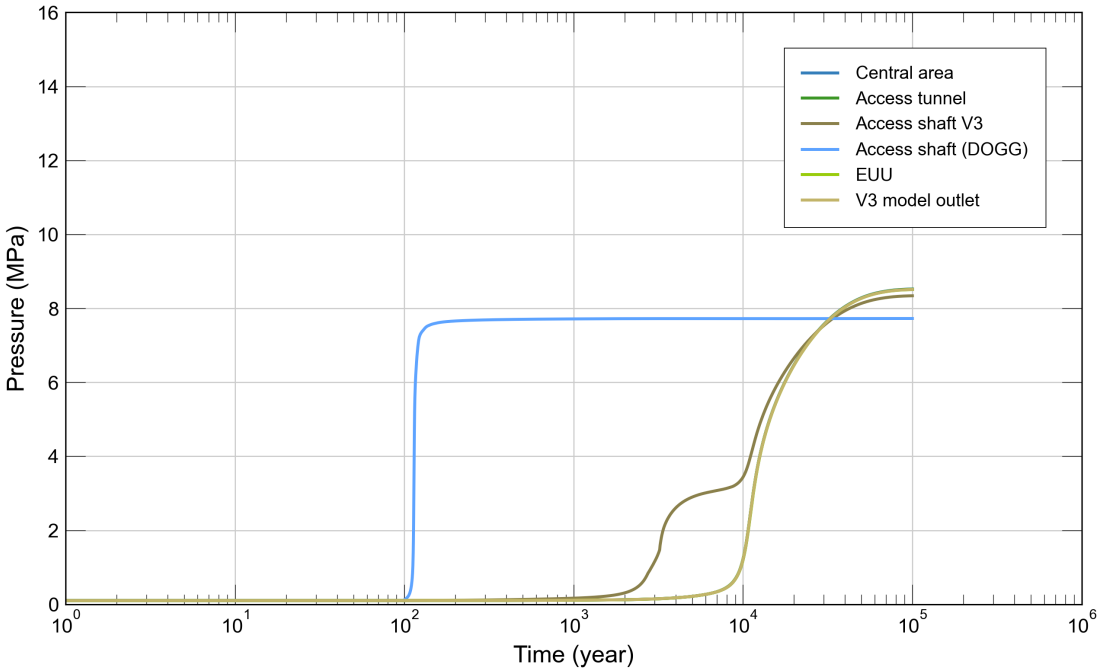

(b)

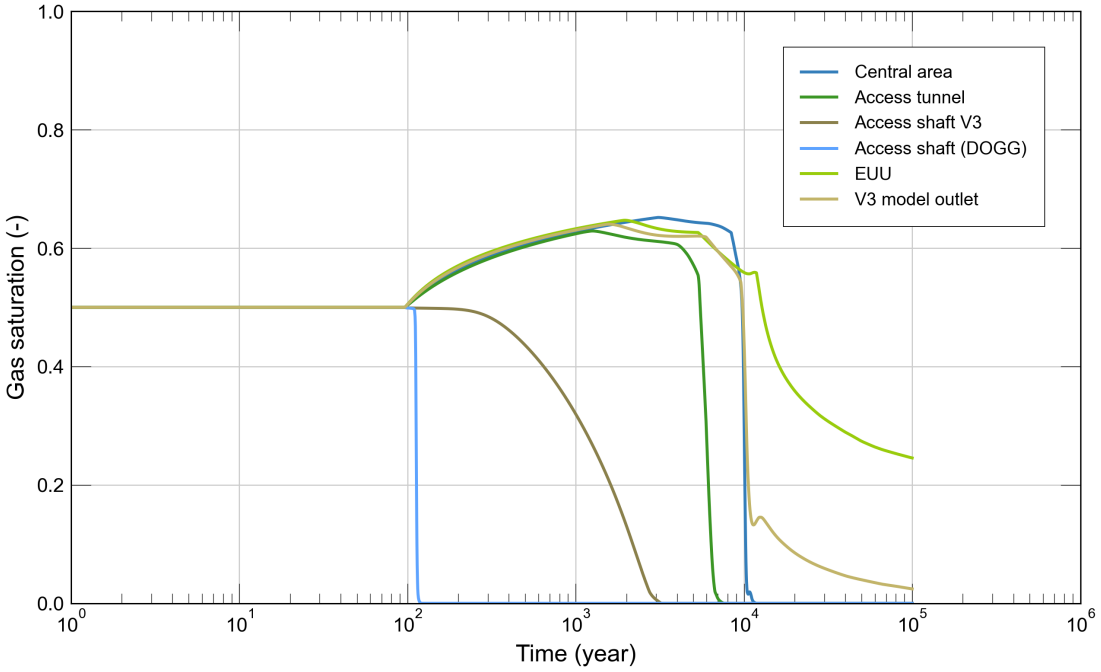

Fig. 6-12: Deviations scenario *"lower bound gas generation"*: transients of (a) pressure and (b) gas saturation in the central area of the repository

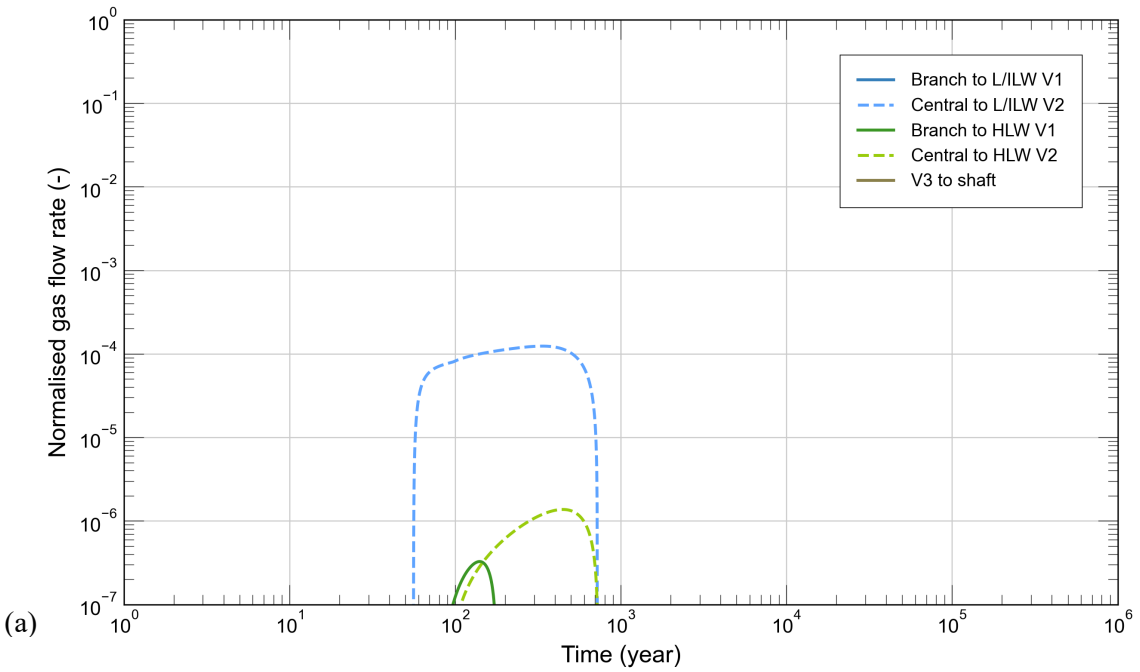

(a)

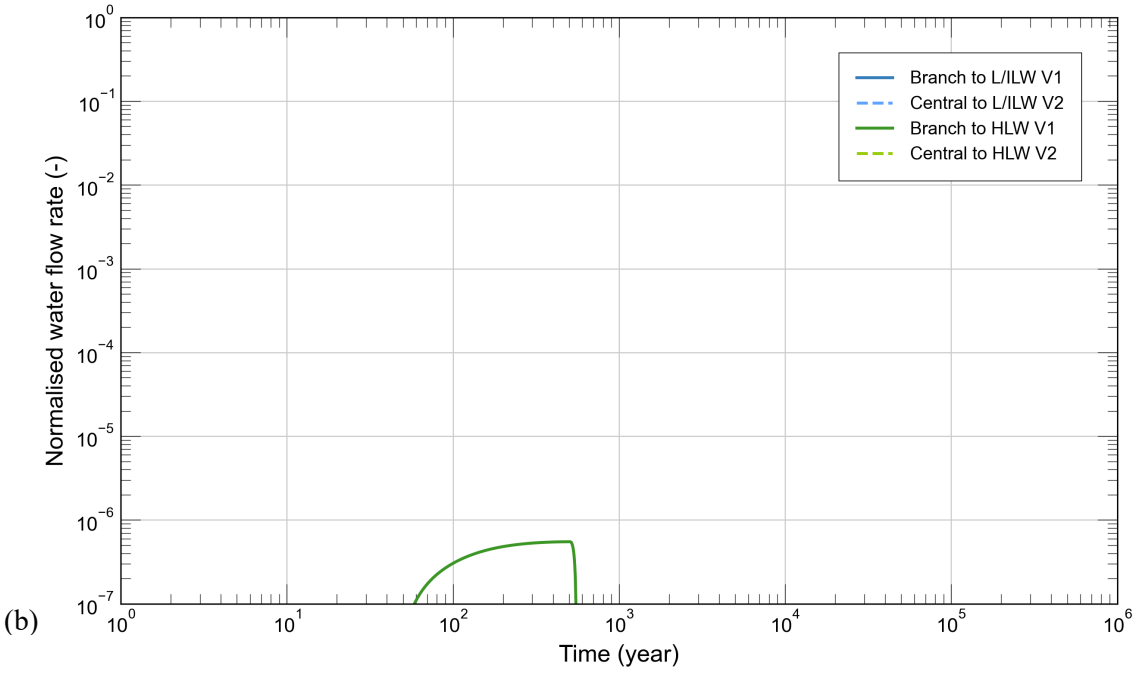

(b)

Fig. 6-13: Deviations scenario *"lower bound gas generation"*: normalised cumulative flows of (a) gas and (b) liquid

Upper bound gas generation *[TSD3]*

The second scenario of gas generation adopts the upper bound gas generation rates in the L/ILW and HLW disposal areas (Fig. 3-6 and Fig. 3-12, respectively). The corresponding TH^2 evolution under this assumption, including modelling in 3D for the repository components, is described in detail in Nagra (2024g). Simulated transients of pressure and gas saturation in the central area of the repository are shown in Fig. 6-14. Peak pressure is reached after ~70,000 years and lies slightly below 10 MPa (Fig. 6-14a), which is ~0.6 MPa higher than in the expected evolution (Fig. 6-3). The transients of saturation (Fig. 6-14b) point to similar gas saturation state throughout the central area compared to the expected evolution (Fig. 6-2), except the slower resaturation of the V3 seal when the upper bound gas generation rates are used.

The normalised gas and liquid flows through the sealing sections are shown in Fig. 6-15. Between 100 and 300 years, some gas flow into the V1-HLW seals is associated with redistribution of phases locally within the HLW section (Fig. 6-15a). Flow from the central area into the V2-HLW reaches a cumulative mass that is equivalent to ~1E-3 (-) of the gas mass generated in the repository after 100,000 years. During this period there is no gas flow through the V1-HLW. Gas breakthrough from the V3 to the shaft is observed shortly before 20,000 years, and the cumulative amount of gas released from the V3 after 40,000 years and 100,000 years corresponds to 5.E-05 (-) and 3.E-04 (-) of the gas mass generated in the repository, respectively. Liquid flows through the sealing sections in the direction of the disposal areas are negligible (Fig. 6-15b).

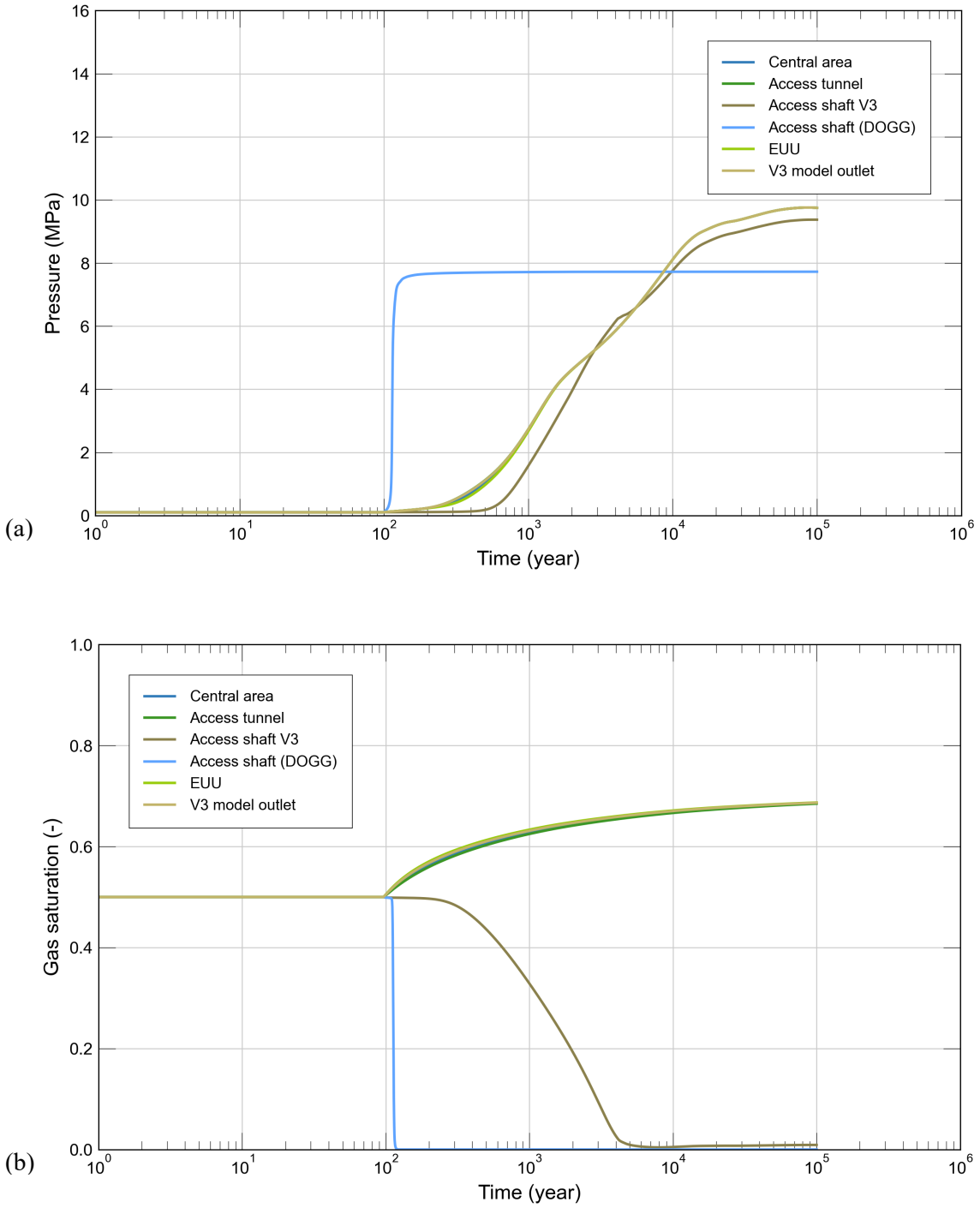

Fig. 6-14: Deviations scenario *"upper bound gas generation"*: (a) pressure and (b) gas saturation in the central area of the repository

(a)

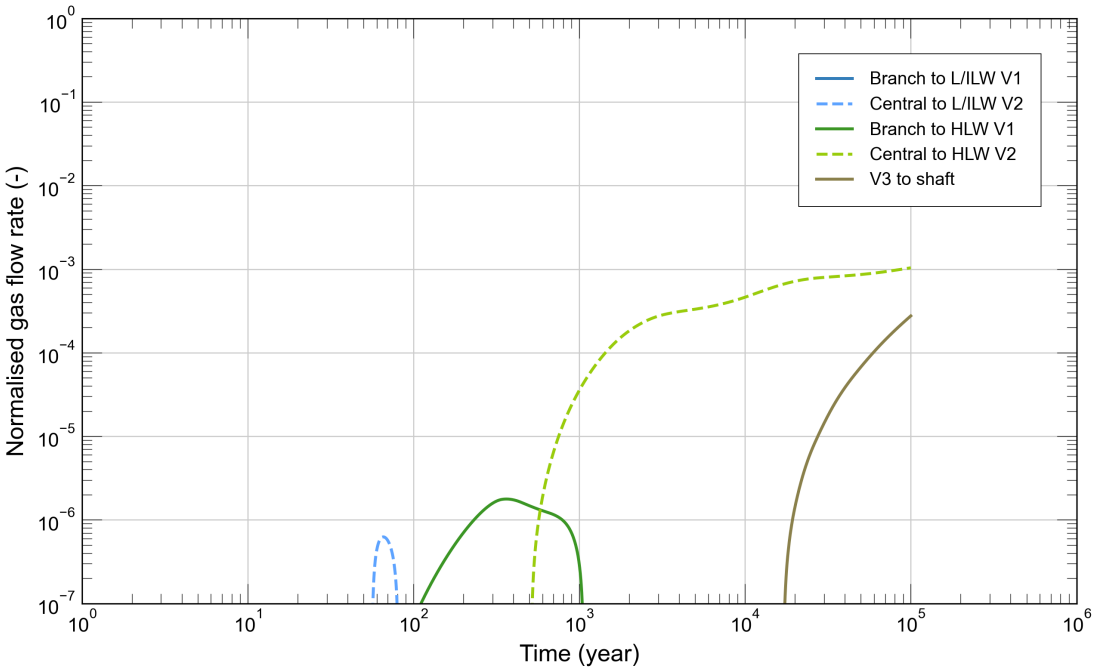

(b)

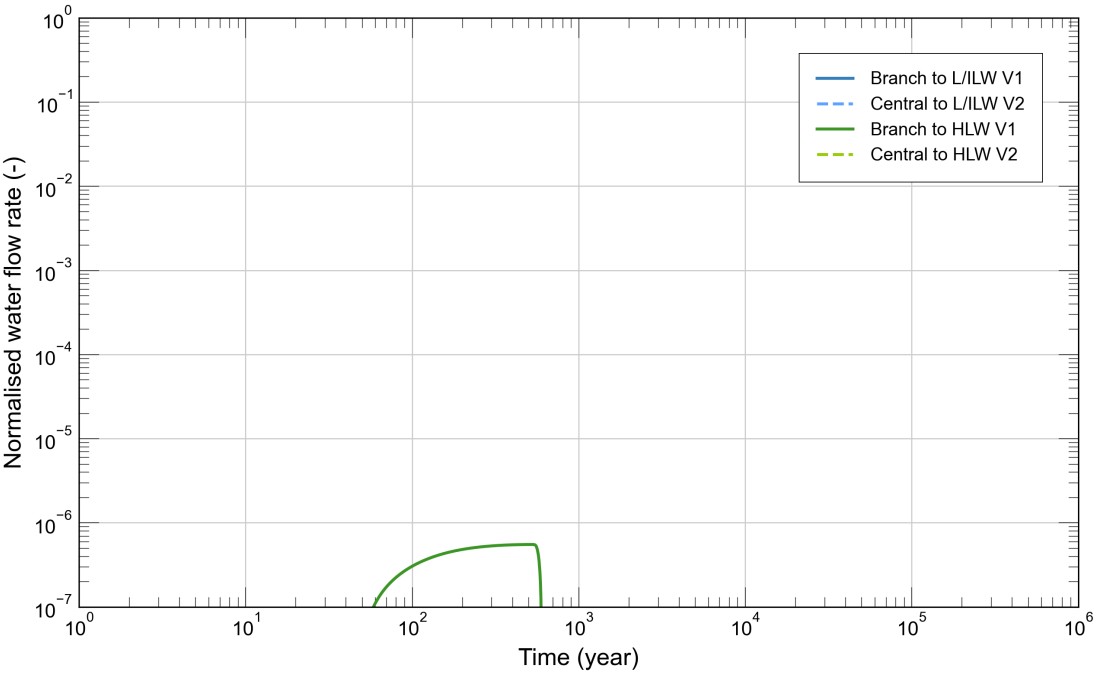

Fig. 6-15: Deviations scenario *"upper bound gas generation"*: normalised cumulative flows of (a) gas and (b) liquid

Fault through L/ILW caverns *[TSD13]*

This simulation represents the scenario of a highly transmissive (T_{fault} = 1E-10 m^2/s), vertical fault intersecting with all L/ILW caverns as shown in Fig. 6-16a. The fault is conceptualised as a 10 m thick zone with an intrinsic permeability of 1E-18 m^2. In the vertical direction, the fault extends from the top of the Muschelkalk to the base of the Malm (see also Tab. 3-1). Essentially, the fault constitutes a transmissive pathway between the two aquifers and through the CRZ and repository. Despite the empirical evidence for rapid self-sealing in OPA, the transmissivity is maintained at the initial value. Note that this scenario is discussed here to evaluate the relevance to hydraulic interactions (i.e., interruption of gas pathways in the repository, liquid flows across sealing sections) rather than the relevance to safety analysis, which is addressed in Nagra (2024j). In addition to the discussion provided below, transients of gas and water flow through the fault, as well as spatial plots of gas saturation in the repository and in the fault, are given in App. B.9. These indicate that water flows through the fault take place predominantly in the direction from the Malm into the repository until the end of the simulation. Accordingly, advective flow of solutes from the repository to the Malm through the transmissive fault is not expected. On the other hand, some of the gas generated in the L/ILW caverns reaches the Malm through the fault once hydrostatic pressure conditions are established in the caverns (~10,000 years). The assessment with regards to transport of volatiles and the relevance to safety is addressed in detail in Nagra (2024j).

Transients of pressure and saturation in the L/ILW section and in the central area are shown in Fig. 6-17. In addition, spatial plots of gas saturation in the fault and the L/ILW section are provided in App. B. Pressure in the L/ILW caverns increases faster compared to the expected evolution (Fig. 6-3) due to the earlier resaturation of the caverns with porewater from the transmissive fault. In the first 10,000 years after backfilling, pressures along the operations tunnels (i.e., in the V1 and V2 sealing sections) decrease with increasing distance from the emplacement caverns. The L/ILW emplacement caverns reach hydrostatic pressure after ~10,000 years. After ~20,000 years, pressures equilibrate across the L/ILW section and in the central area of the repository (Fig. 6-17a;c). The maximum pressures reached after 20,000 years do not exceed appreciably the hydrostatic values, and a slight decrease in pressure is observed between 20,000 and 100,000 years due to the depressurisation of the repository tunnels by the transmissive fault. The early resaturation of the repository tunnels due to porewater inflow from the transmissive fault is also depicted in the gas saturations (Fig. 6-17b;d). The normalised gas and liquid flows through the sealing sections are shown in Fig. 6-18. Some gas flow from the central area into the V2-HLW is observed between ~900 and ~20,000 years corresponding to gas displaced by the inflow of porewater. Similar to the previous scenarios, there is no gas flow into the V1-HLW seals. Gas flow from the V3 to the shaft is decreased to approximately half of that in the expected evolution (shown in Fig. 6-6). As indicated in the saturation and pressure transients, water flow occurs mainly from the L/ILW caverns towards the operations tunnels.

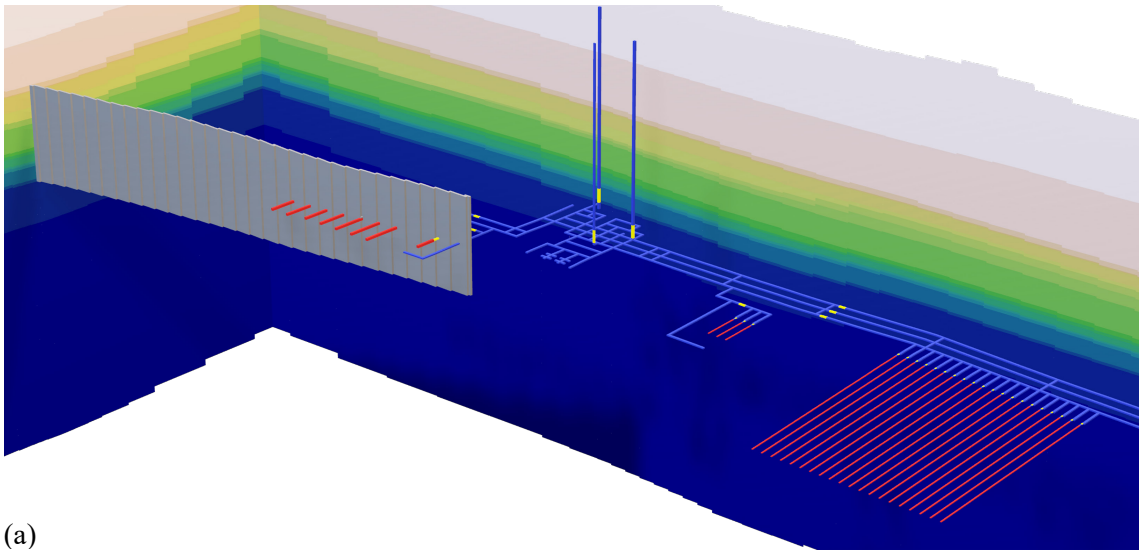

(a)

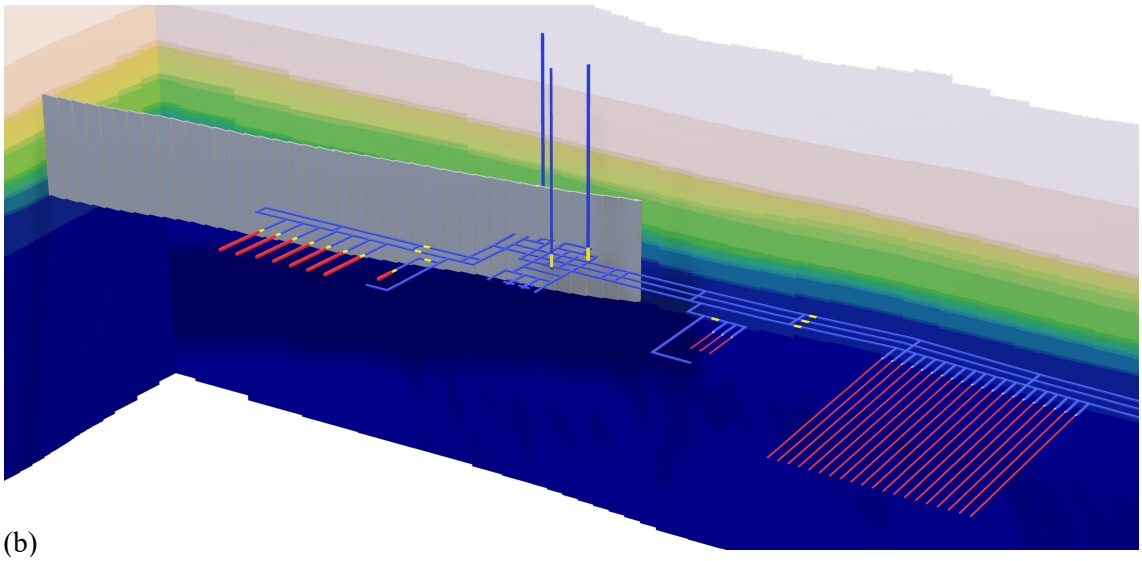

(b)

Fig. 6-16: Implementation of fault in scenarios (a) *"fault through L/ILW"* and (b) *"fault through central area"*

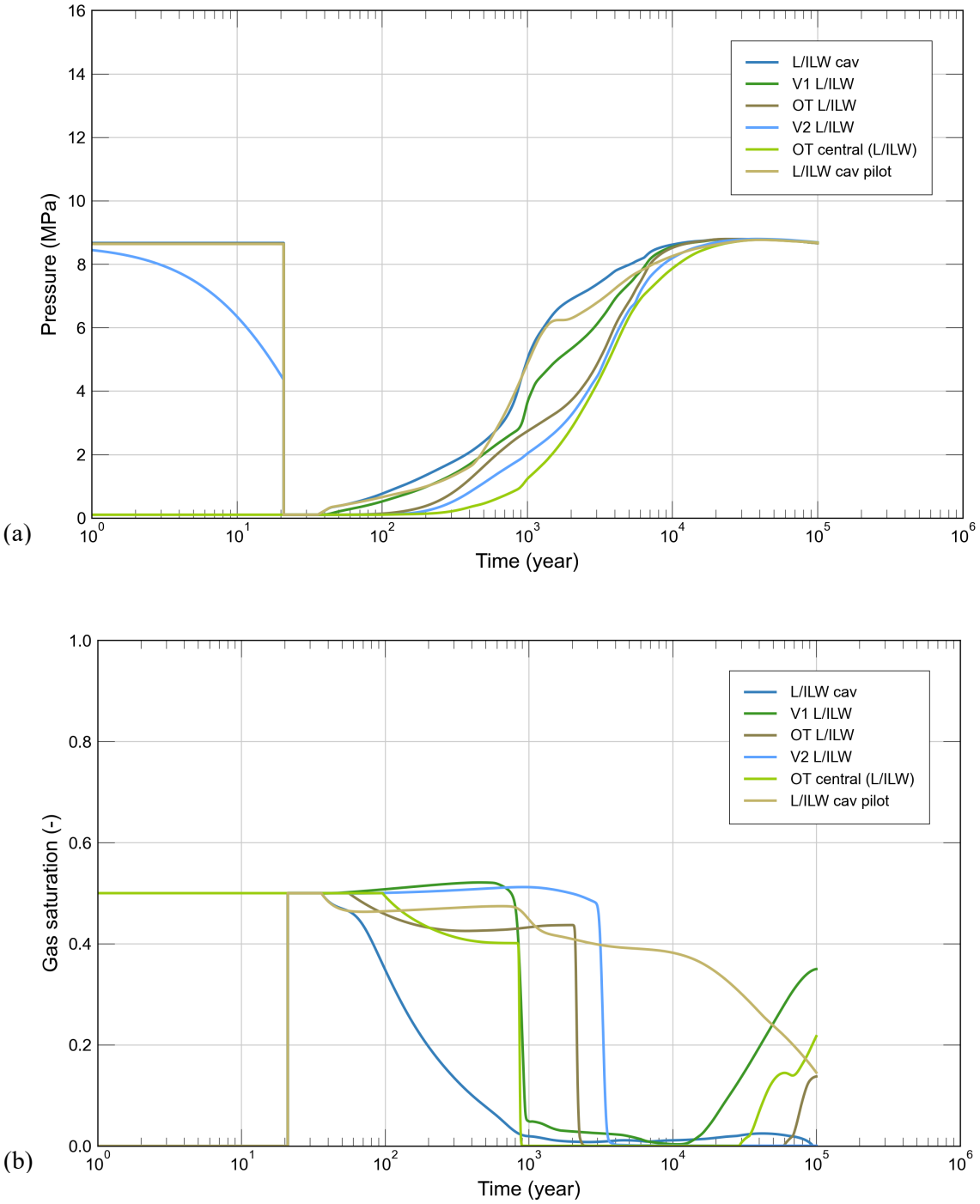

Fig. 6-17: Deviations scenario *"fault through L/ILW"*: (a) pressure and (b) gas saturation in the L/ILW section of the repository

(c)

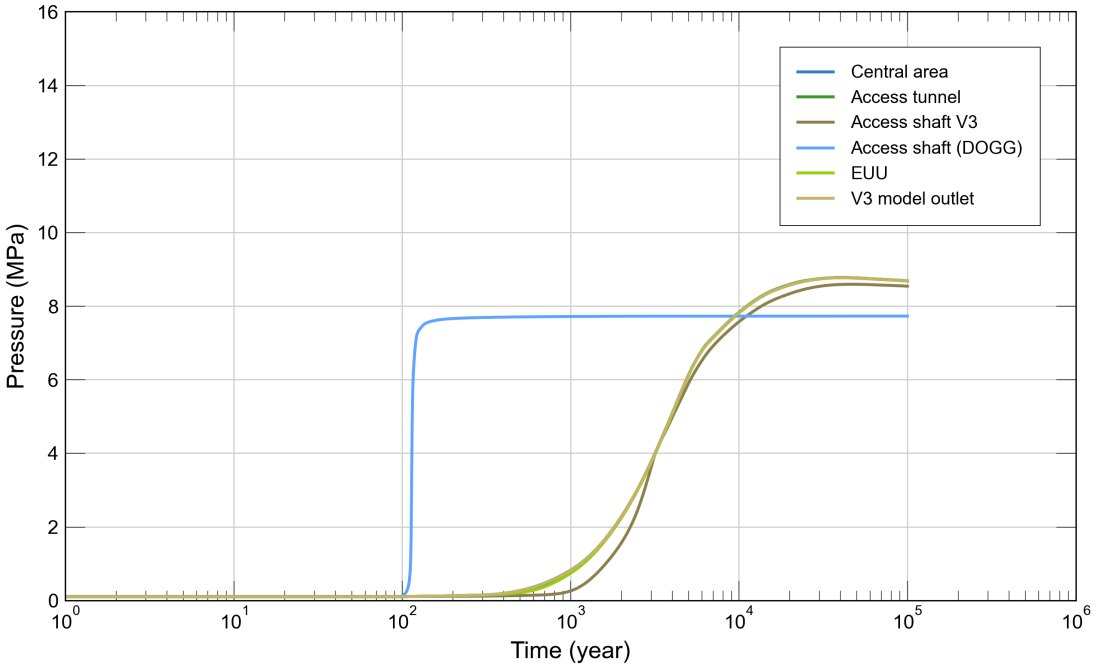

(d)

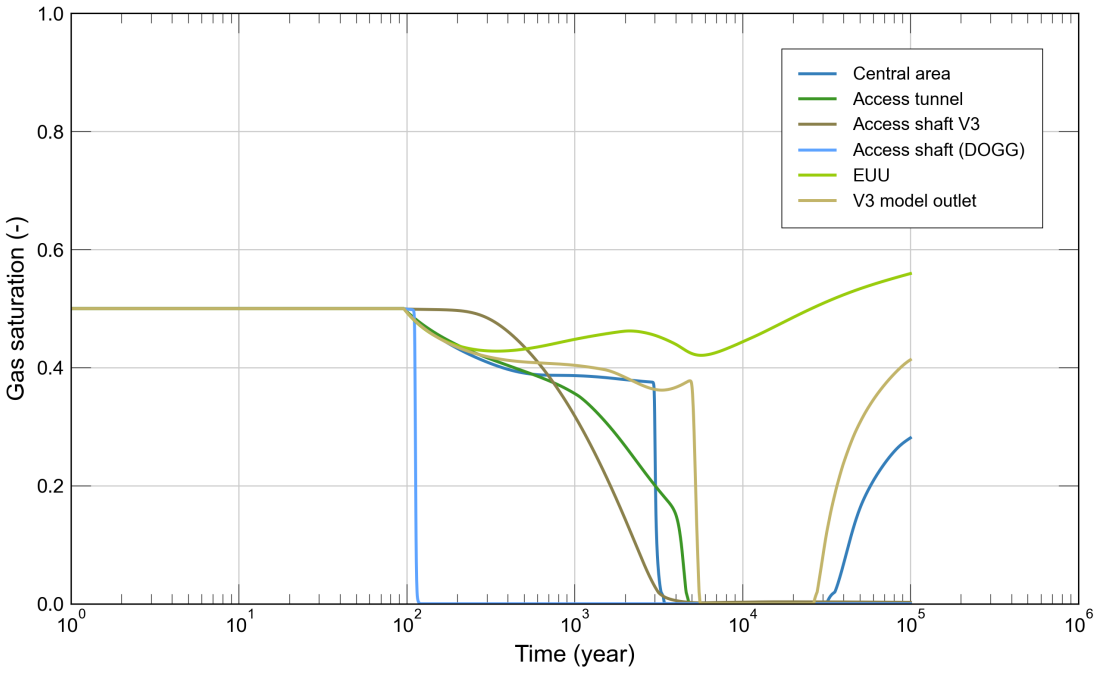

Fig. 6-17: Cont. (c) pressure and (d) gas saturation in the central area of the repository

(a)

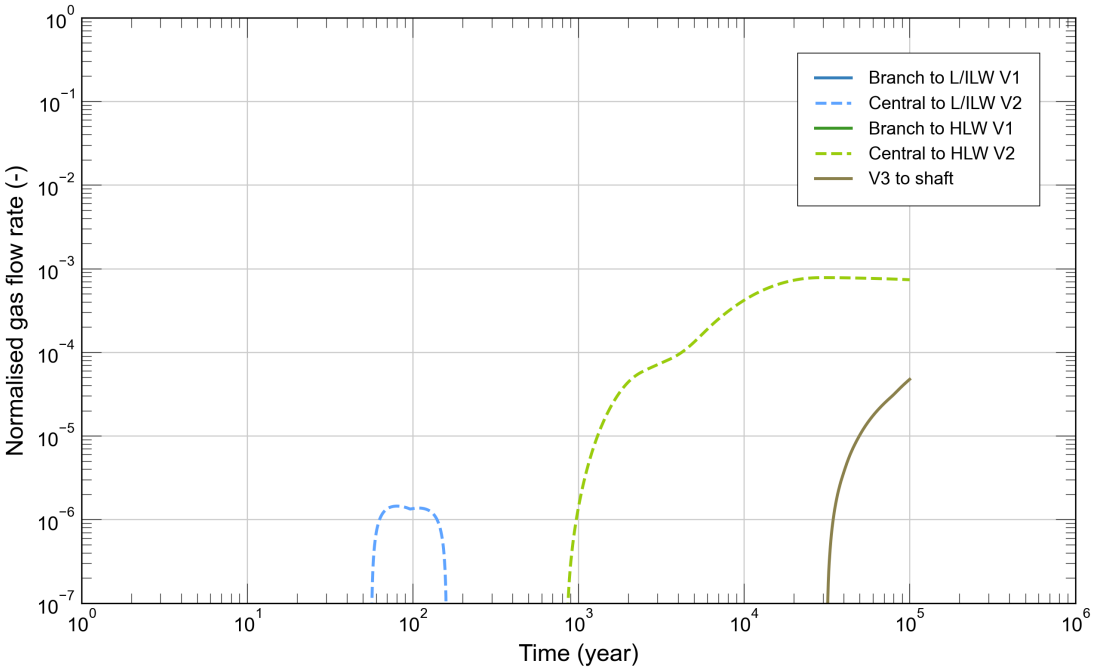

(d)

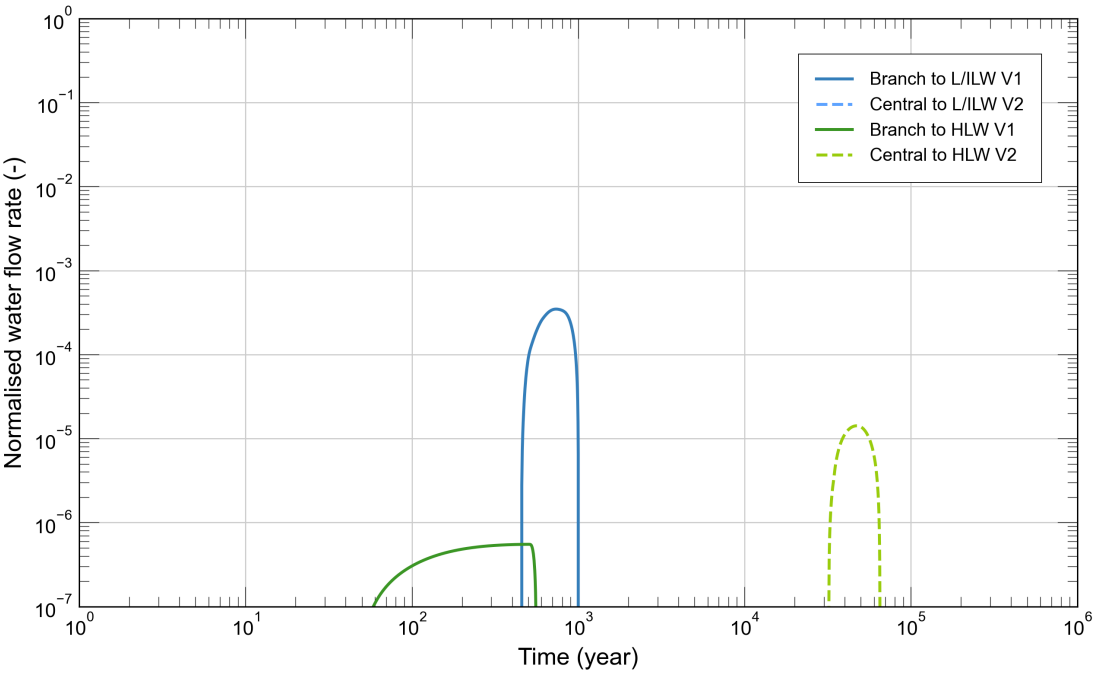

Fig. 6-18: Deviations scenario *"fault through L/ILW"*: normalised cumulative flows of (a) gas and (b) liquid

Fault through central area *[TSD9]*

In this model variant a high-transmissive fault (T_{fault} = 1E-10 m^2/s) is assumed to intersect with the access tunnels near the base of the access shaft as shown in Fig. 6-16b. Similar to the previous scenario, the fault extends from the top of the Muschelkalk to the base of the Malm (see also Tab. 3-1), forming a transmissive pathway between the two aquifers and through the CRZ and repository. As in the previous scenario, this simulation is used to evaluate the relevance of the transmissive fault to potential hydraulic interactions in the repository.

The transients of pressure and gas saturation simulated in the central area are shown in Fig. 6-19. The increase of pressure after backfilling of the repository tunnels (Fig. 6-19a) is faster than in the expected evolution (Fig. 6-3) due to the faster resaturation of the tunnels with porewater delivered from the Malm into the repository through the transmissive fault. Hydrostatic pressure is reached between 10,000 and to 20,000 years, whereas peak pressure only slightly exceeds the hydrostatic value after ~20,000 years (compared to 70,000 years in the expected evolution). Accordingly, the saturation evolution of the repository tunnels in the vicinity of the fault is affected by the inflow of porewater from the Malm. The transient at "access tunnel", that is the closest to the intersection of the repository with the fault, shows that the tunnels leading to the access shaft resaturate with water within few hundreds of years (Fig. 6-19b). In comparison, the transient at "central area", which is further away, shows resaturation with water after 1,000 years. The transient at "EUU" does not indicate any porewater flow reaching there, as saturation is practically identical to the one in the expected evolution (Fig. 6-2). At later times (~8,000 to 20,000 years), the results indicate that gas saturation increases again in the tunnels of the central area due to gas generation and the associated buildup of gas pressure in the repository (Fig. 6-19b). Overall, the results show that despite the change in the saturation evolution of the repository due to porewater inflow from the Malm through the fault, there is no compromising impact on the gas transport mechanisms within the repository and the associated buildup of gas pressure.

The normalised gas and liquid flows through the sealing sections are shown in Fig. 6-20. Gas displacement from the central area into the V2-HLW occurs between ~900 and ~20,000 years (Fig. 6-20a), but no gas flow takes place into the V1-HLW seals. Gas breakthrough from the V3 seal to the shaft occurs after ~50,000 years, and the cumulative mass of gas released to the shaft reaches 3.E-05 (-) after 100,000 years. Liquid flow in the direction of the disposal areas is observed only through the V2-HLW seal between ~12,000 and 50,000 years (Fig. 6-20b). The cumulative water mass is equivalent to ~9E-04 (-) of the water mass that can be stored in the repository. In comparison to the expected performance, gas flow from the V3 to the shaft is somewhat decreased, whereas liquid flow through the V2-HLW seal is only slightly increased.

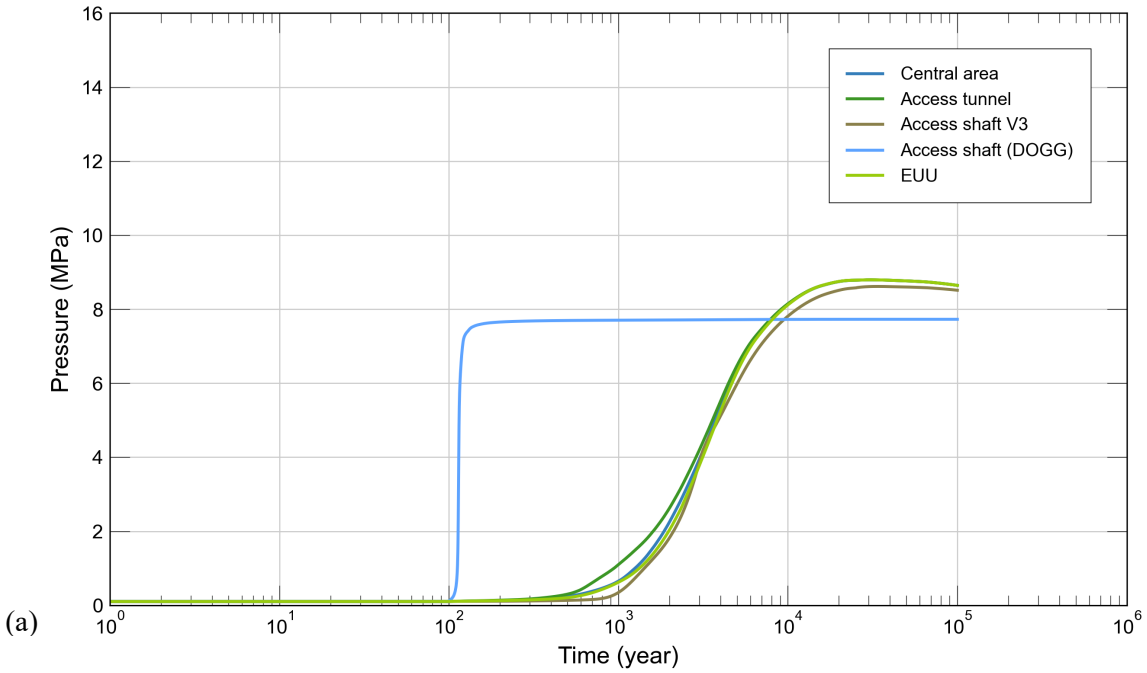

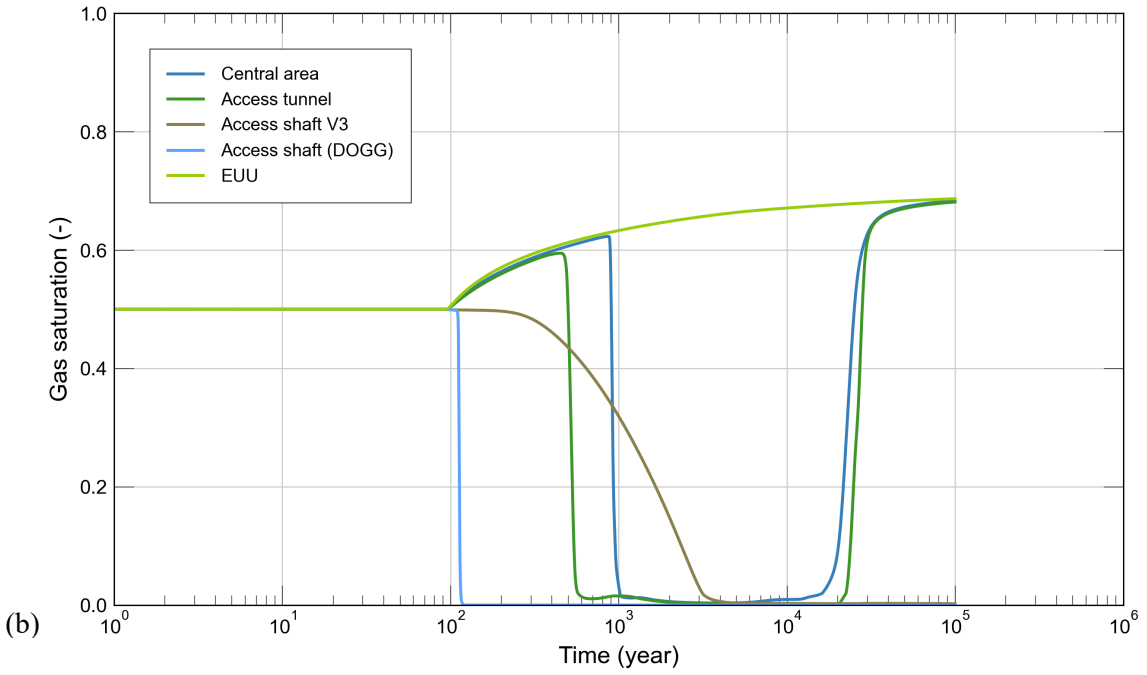

Fig. 6-19: Deviations scenario *"fault through central area"*: (a) pressure and (b) gas saturation in the central area of the repository

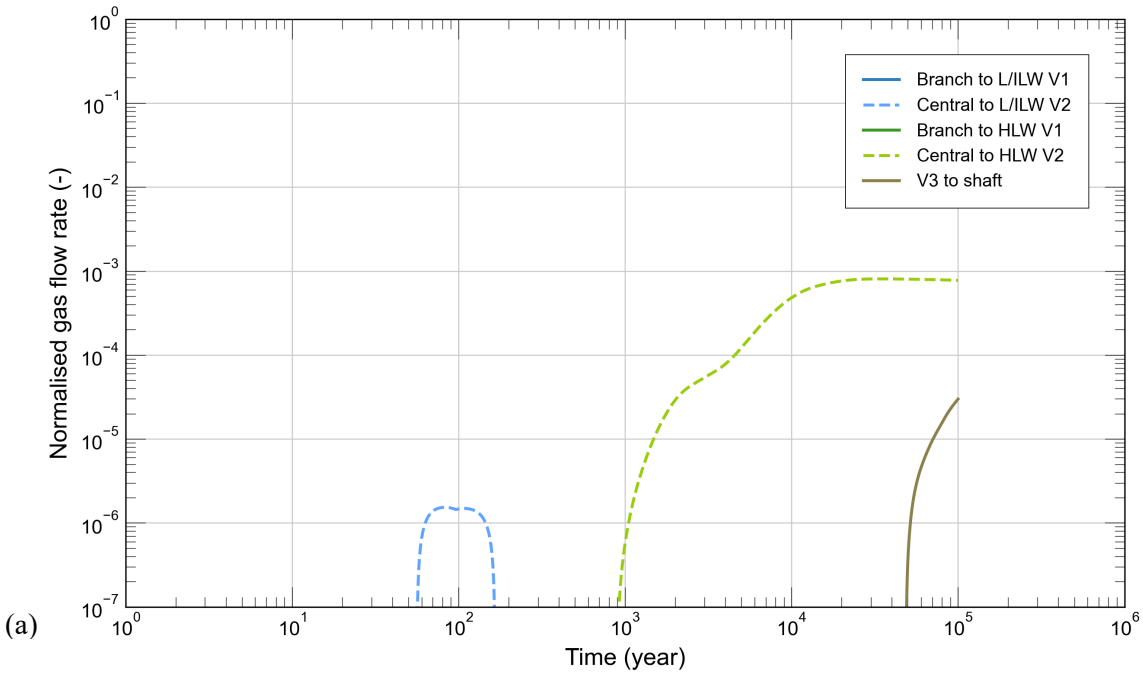

(a)

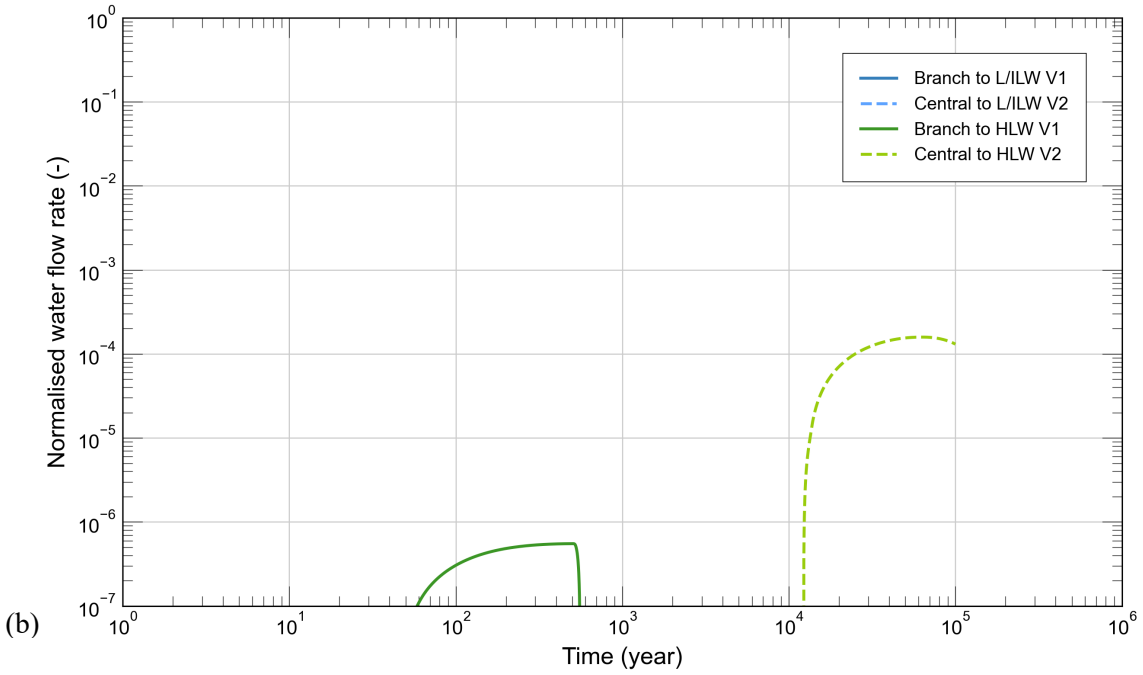

(b)

Fig. 6-20: Deviations scenario *"fault through central area"*: normalised cumulative flows of (a) gas and (b) liquid

Low-permeable V2-L/ILW seal *[TSD6]*

The first scenario related to the sealing system adopts a lower permeability of the V2-L/ILW seal than in the base case (1.E-19 m^2 instead of 5.E-18 m^2). A similar assessment is performed on the component level with the 3D model of the V2-L/ILW seal in Nagra (2024g). Here, the pressure and saturation transients simulated with the 3D repository model in the L/ILW disposal area are shown in addition to the central area to facilitate the interpretation of the results (Fig. 6-21). The transients of pressure in the L/ILW disposal area (Fig. 6-21a) show some hydraulic separation of the disposal area (e.g., at "L/ILW cav") from the rest of the repository (e.g., at "OT central") imposed by the low-permeable V2 seal (Fig. 6-21c). After ~60,000 years pressure reaches a peak of ~9.8 MPa and ~9.2 MPa in the L/ILW emplacement caverns and in the central area, respectively (Fig. 6-21a;c). Accordingly, gas saturations in the L/ILW disposal area (Fig. 6-21b) are overall higher compared to the expected evolution (Fig. 6-2) due to the increased accumulation of gas. However, the central area maintains a connected gas pathway through the tunnels, as indicated in the saturation transients (Fig. 6-21d).

The normalised gas and liquid flows through the sealing sections are shown in Fig. 6-22. As a result of gas accumulation and pressure buildup mostly in the L/ILW disposal area, there is practically no gas flow through the V2 and V1 seals in the direction of the emplacement rooms (Fig. 6-22a). Gas breaks through the V3 seal after ~60,000 years, and the cumulative amount of gas released after 100,000 years corresponds to 6E-05 (-) of the total gas mass generated in the repository. Liquid flows through the sealing sections in the direction of the disposal areas are not significant (Fig. 6-22b).

(a)

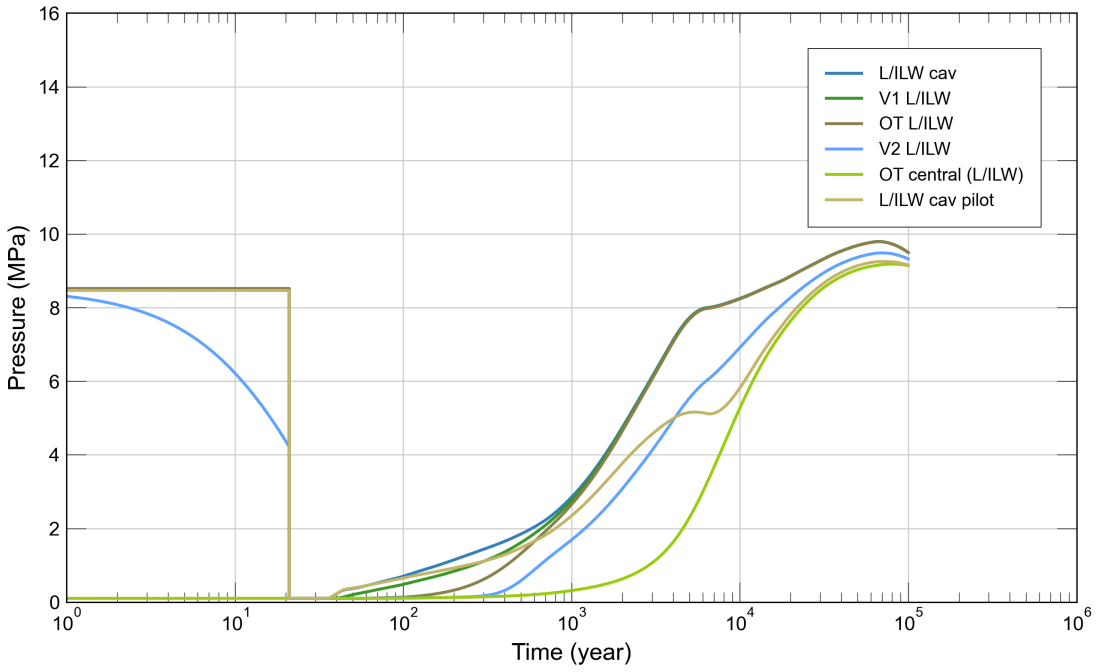
Pressure (MPa)
Time (year)
L/ILW cav
V1 L/ILW
OT L/ILW
V2 L/ILW
OT central (L/ILW)
L/ILW cav pilot

(b)

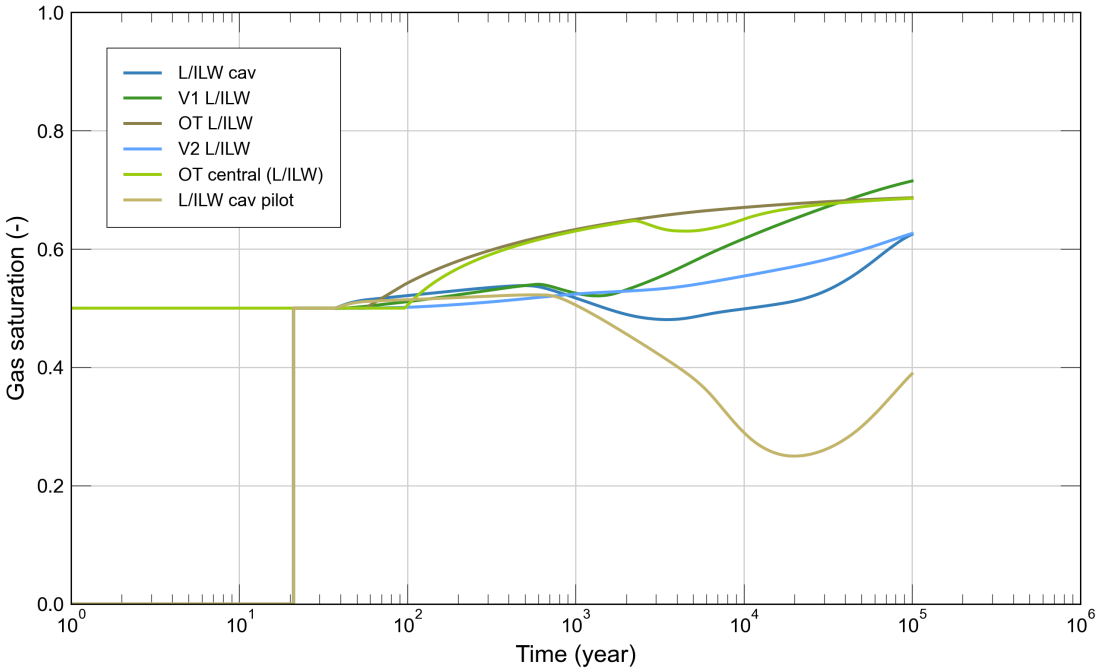
Gas saturation (-)
Time (year)
L/ILW cav
V1 L/ILW
OT L/ILW
V2 L/ILW
OT central (L/ILW)
L/ILW cav pilot

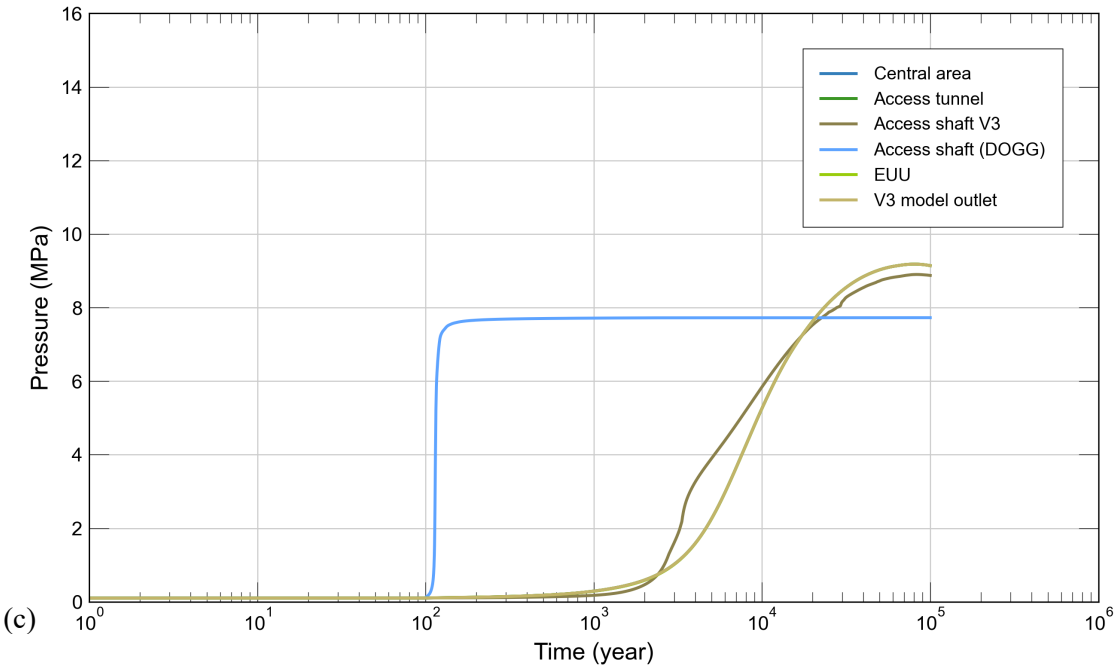

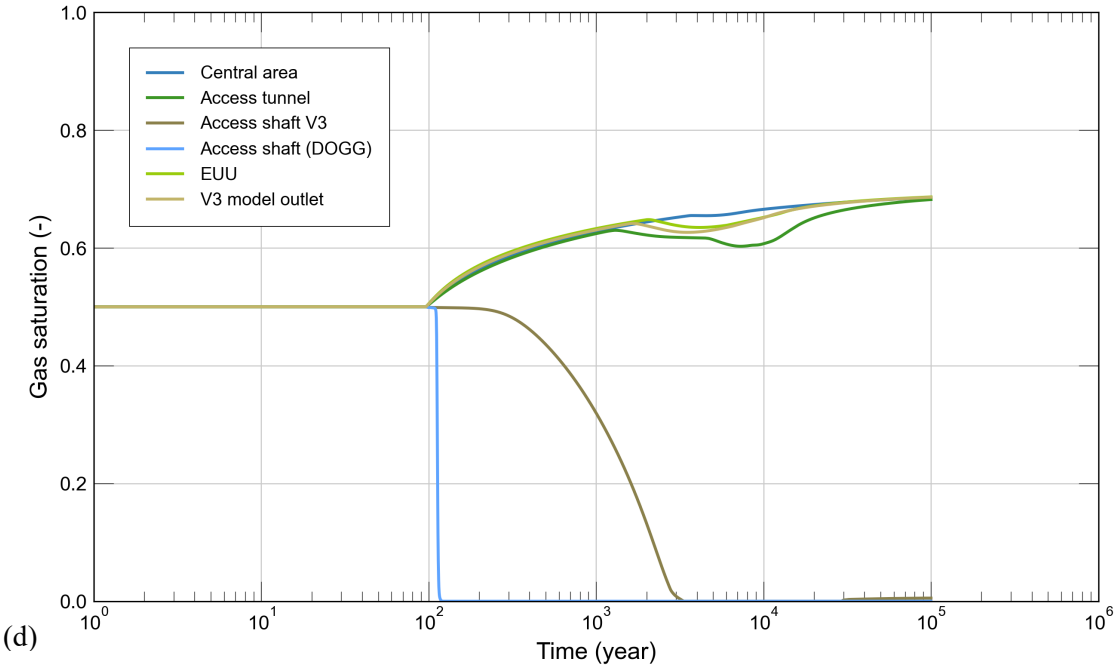

Fig. 6-21: Deviations scenario *"low-permeable V2-L/ILW seal"*: (a) pressure and (b) gas saturation in the L/ILW section of the repository (c) pressure and (d) gas saturation in the central area of the repository

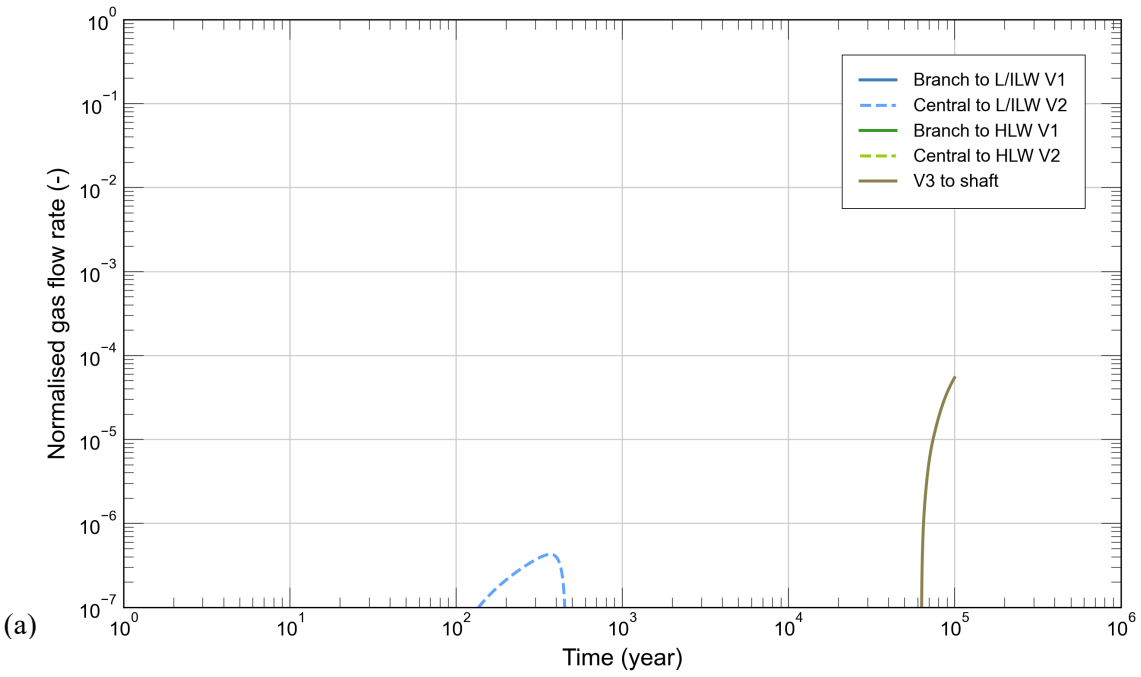

(a)

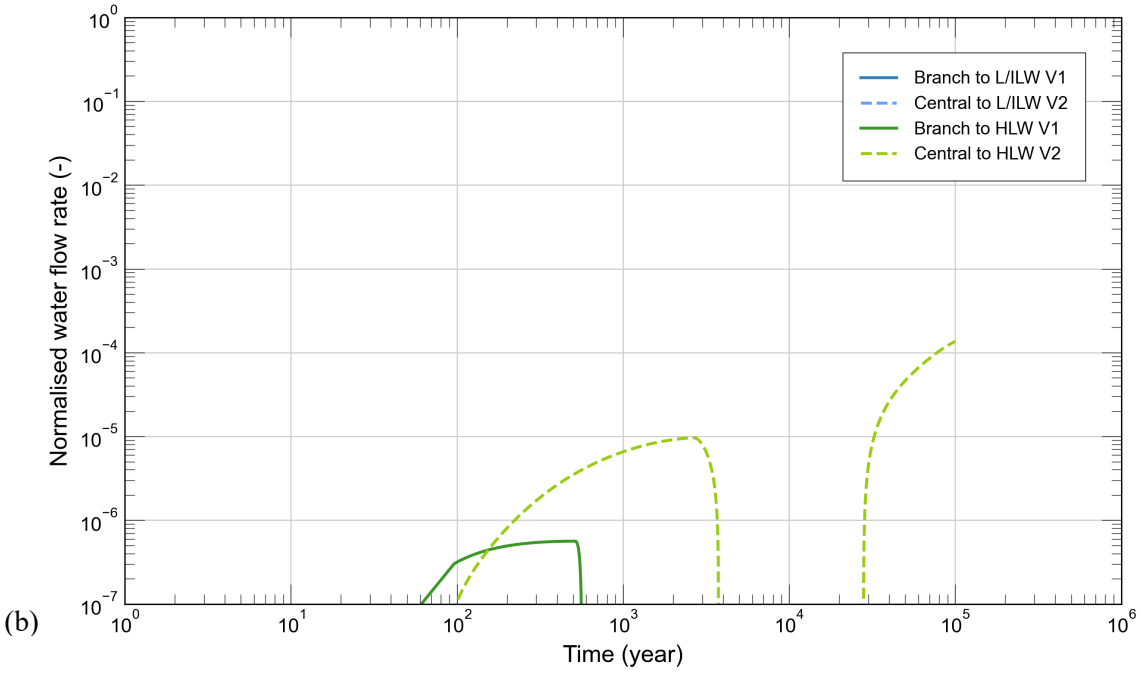

(b)

Fig. 6-22: Deviations scenario *"low-permeable V2-L/ILW seal"*: normalised cumulative flows of (a) gas and (b) liquid

High-permeable V3 seal (variant 1) *[TSD5]*

The second scenario related to the sealing system adopts a higher permeability of the V3 seal than in the base case (1.E-19 m^2 instead of 1.E-20 m^2). This scenario has also been evaluated on the component level with the 3D model of the V3 seal in Nagra (2024g). Pressure and saturation transients simulated with the 3D repository model in the central area are shown in Fig. 6-23. Peak pressure is reached after ~70,000 years (Fig. 6-23a) and is practically identical to the expected evolution (Fig. 6-3). The pressure difference between V3 seal and the central area below it is somewhat reduced in this scenario due to the increase in permeability of the seal. Accordingly, the saturation transients in Fig. 6-23b point to faster saturation of the V3 seal with porewater, in less than 3,000 years, and somewhat higher gas saturations at later times after gas entry into the seal (e.g., gas saturation increase after 15,000 years, reaching up to 2% after 50,000 years).

The normalised gas and liquid flows through the sealing sections are shown in Fig. 6-24. Some gas flow is observed from the central area into the V2-HLW seal (Fig. 6-24a), but no gas flow takes place through the V1-HLW. Gas breaks through the V3 seal after ~25,000 years, and the cumulative amount of gas released after 30,000 years and 100,000 years corresponds to 1E-04 (-) and 7E-03 (-) of the total gas mass generated in the repository, respectively. Liquid flows through the sealing sections in the direction of the disposal areas remain negligible (Fig. 6-24b).

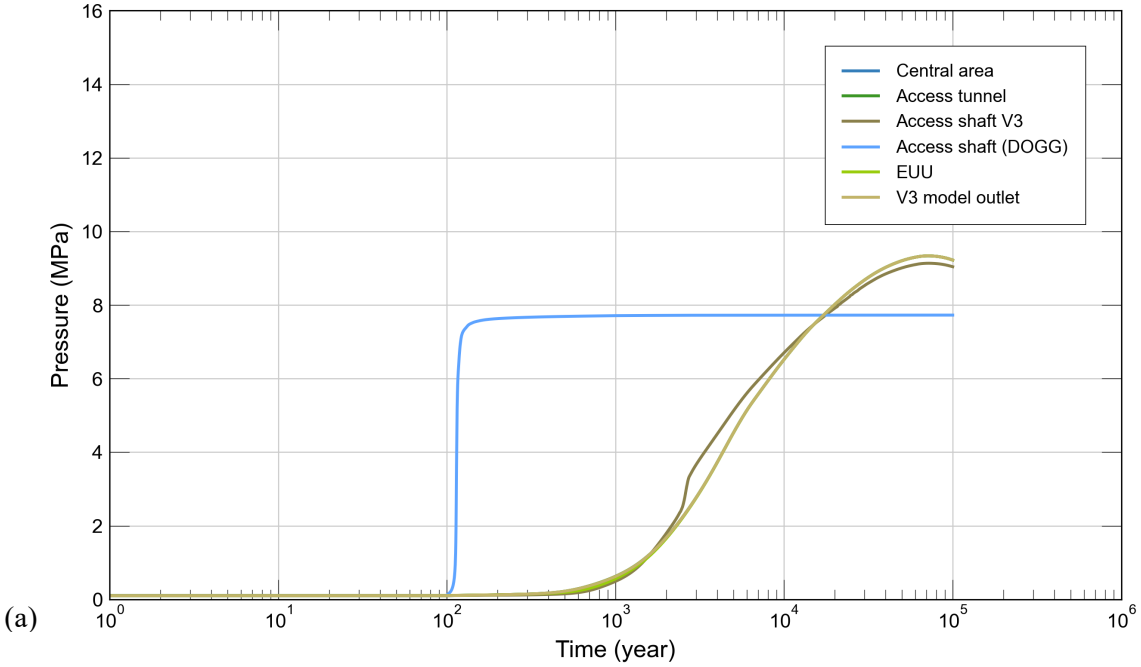

(a)

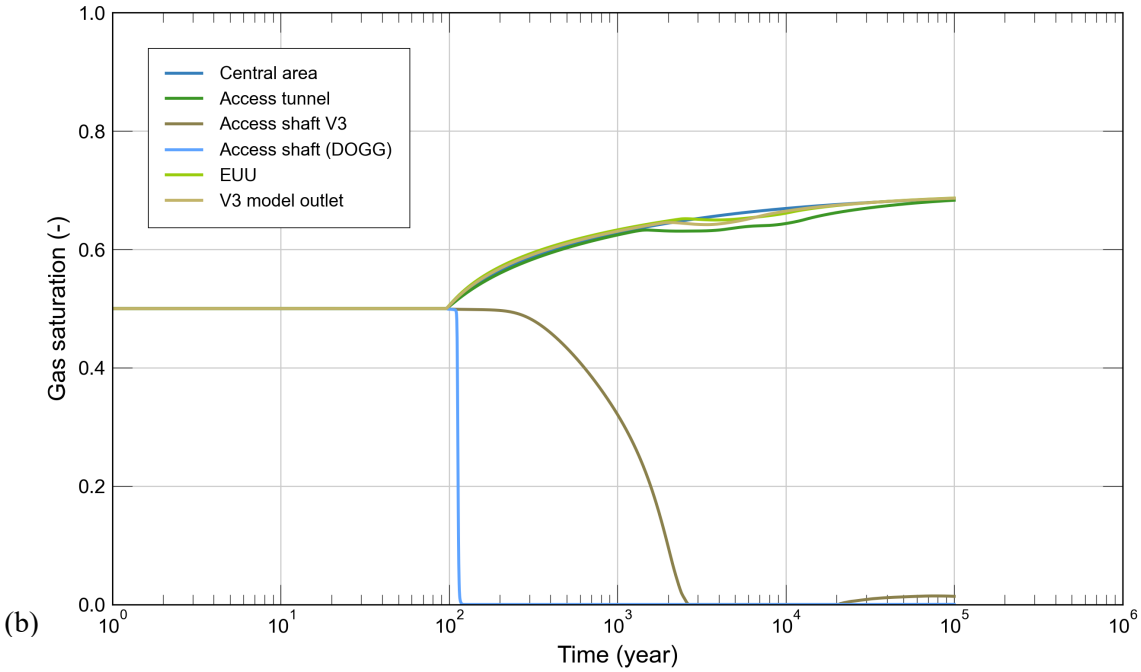

(b)

Fig. 6-23: Deviations scenario *"high-permeable V3 seal (variant 1)"*: (a) pressure and (b) gas saturation in the central area of the repository

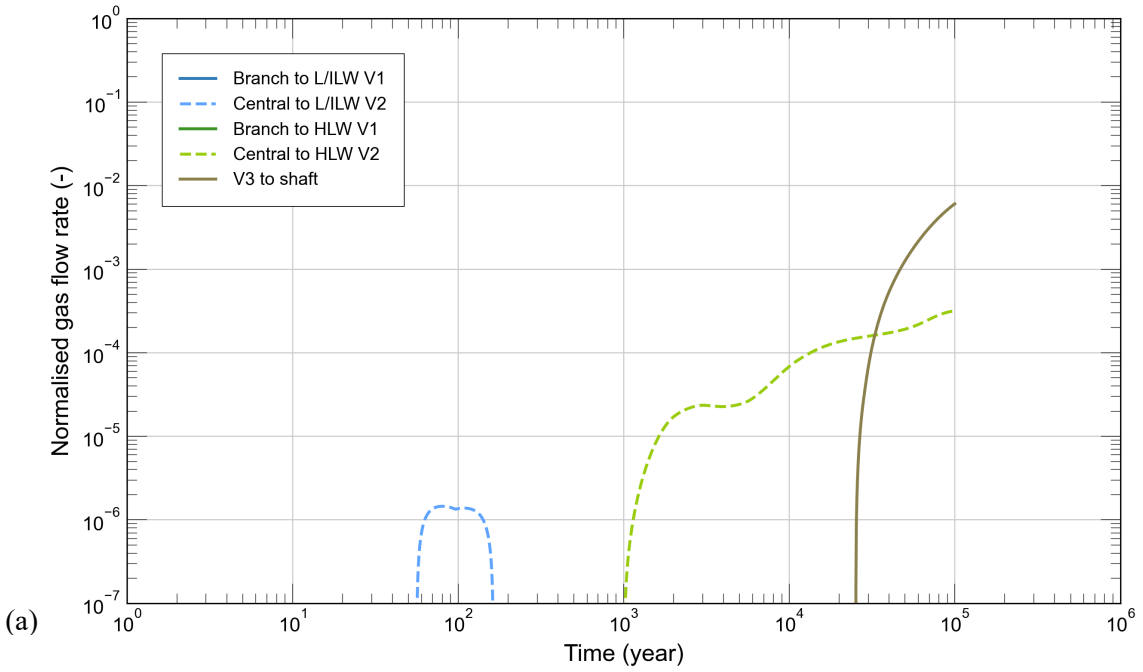

(a)

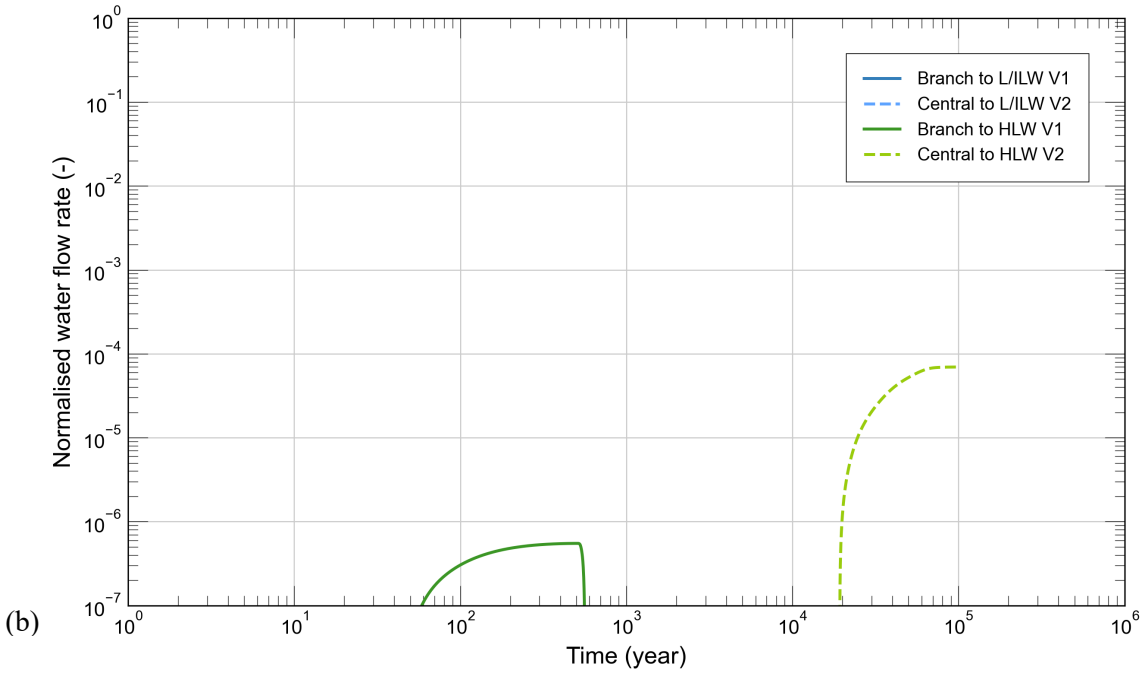

(b)

Fig. 6-24: Deviations scenario *"high-permeable V3 seal (variant 1)"*: normalised cumulative flows of (a) gas and (b) liquid

High-permeable V3 seal (variant 2) *[TSD7]*

In this scenario, the permeability of the V3 seal is increased to 1.E-17 m^2. Combined with the capillary strength value that is scaled accordingly (Leverett scaling), this extreme value essentially corresponds to a seal that is open for gas and liquid flow across it. Transients of pressure and saturation simulated in the central area are shown in Fig. 6-25. After the tunnels are backfilled, pressure (Fig. 6-25a) increases faster compared to the expected evolution (Fig. 6-3) due to the faster resaturation with porewater delivered by the shaft. Hydrostatic pressure is reached after ~15,000 years which is also the maximum pressure reached in the repository central area. The water inflow from the shaft has a marked impact on the saturation state of the central area as shown in Fig. 6-25b. The access tunnel leading to the access shaft is water saturated between ~400 and 20,000 years. Other sections of the central area (e.g., "central area" and "V3 model outlet") point to shorter periods of full water saturation depending on the distance from the shafts. The V3 seal saturates with porewater already after 200 years, which is much faster than the expected evolution (~4,000 years) and the previous scenario with a high-permeable V3 (~3,000 years). After 15,000 years gas enters the seal and gas saturations in the seal remain below ~1% until the end of the simulation.

The normalised gas and liquid flows through the sealing sections are shown in Fig. 6-26. Gas flow from the central area into the V2-HLW seal begins after ~1,000 years and continues until ~15,000 years (Fig. 6-26a). During that time and until 100,000 years there is no gas flow through the V1-HLW seals. Gas breaks through the V3 seal after ~13,000 years, and the cumulative amount of gas released after 20,000 years and 100,000 years corresponds to 2E-02 and 3E-01 of the total gas generated in the repository, respectively. Liquid flow in the direction of the disposal areas is observed only through the V2-HLW seal between 10,000 and 50,000 years but at negligible amounts (Fig. 6-26b).

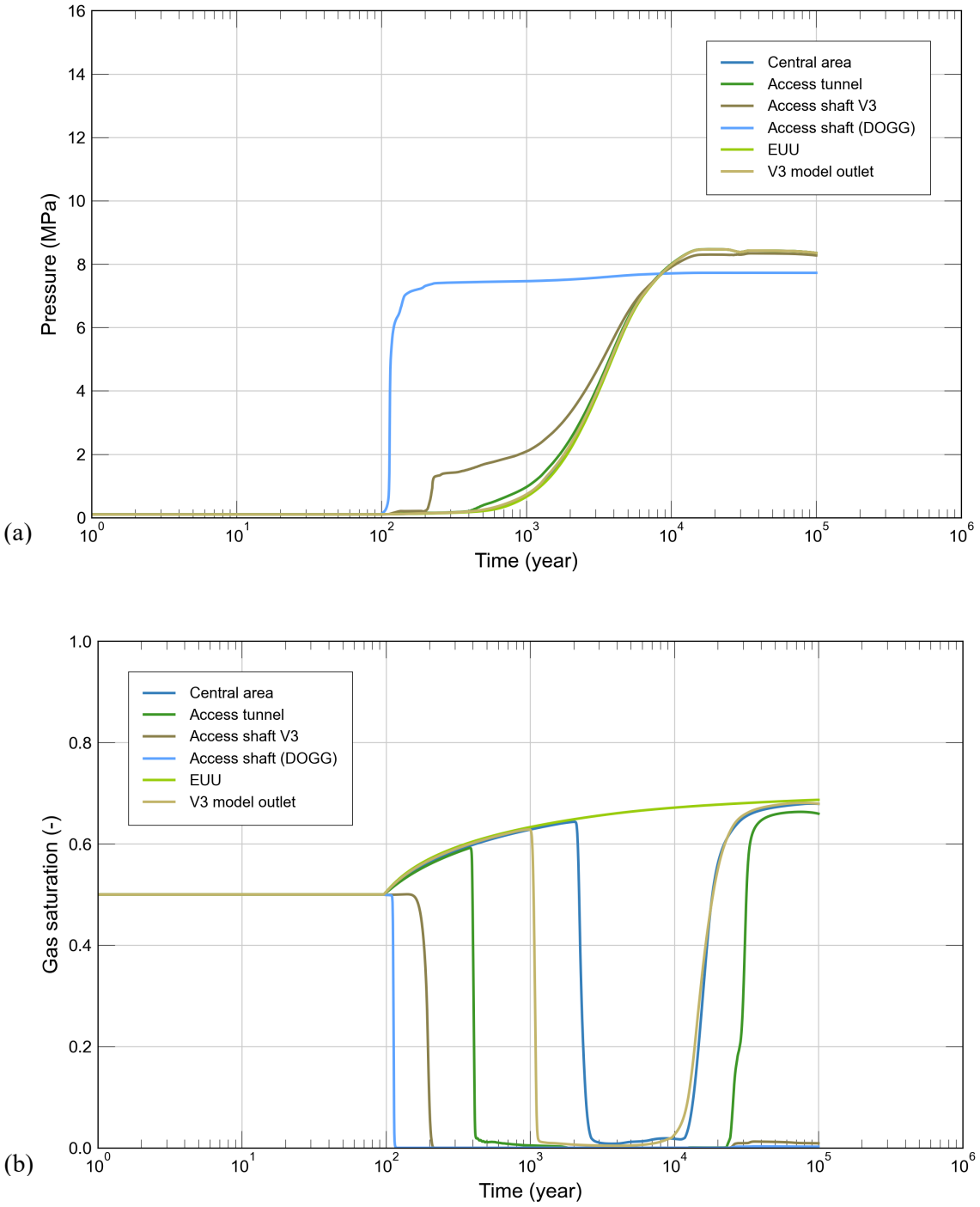

Fig. 6-25: Deviations scenario *"high-permeable V3 seal (variant 2)"*: (a) pressure and (b) gas saturation in the central area of the repository

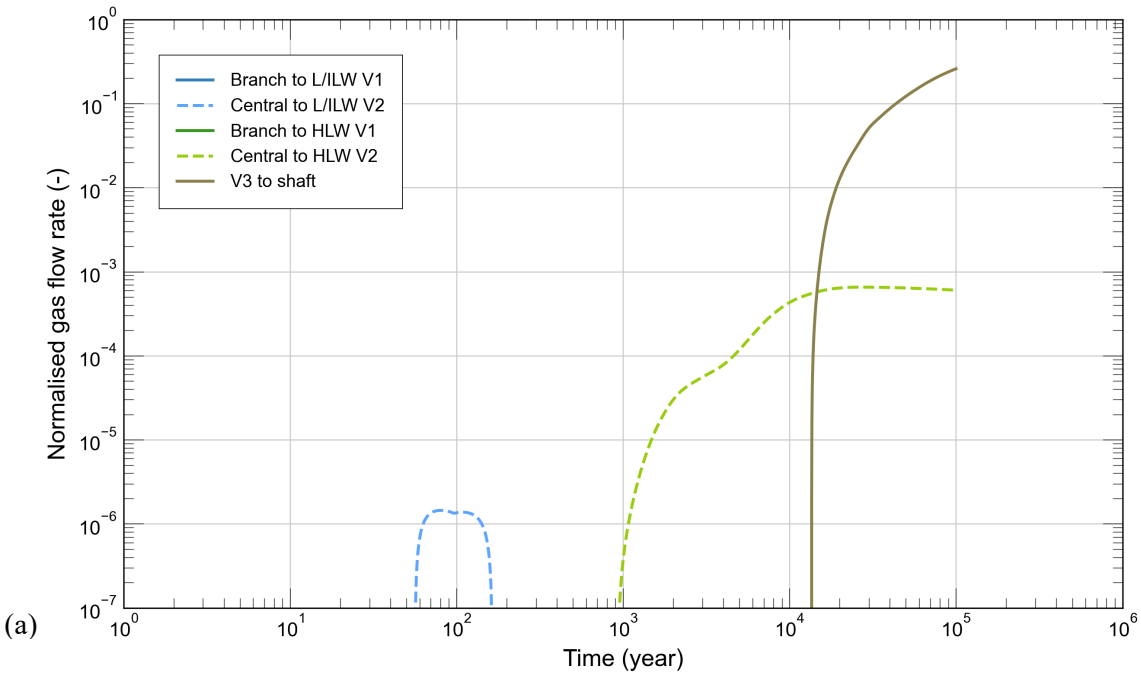

(a)

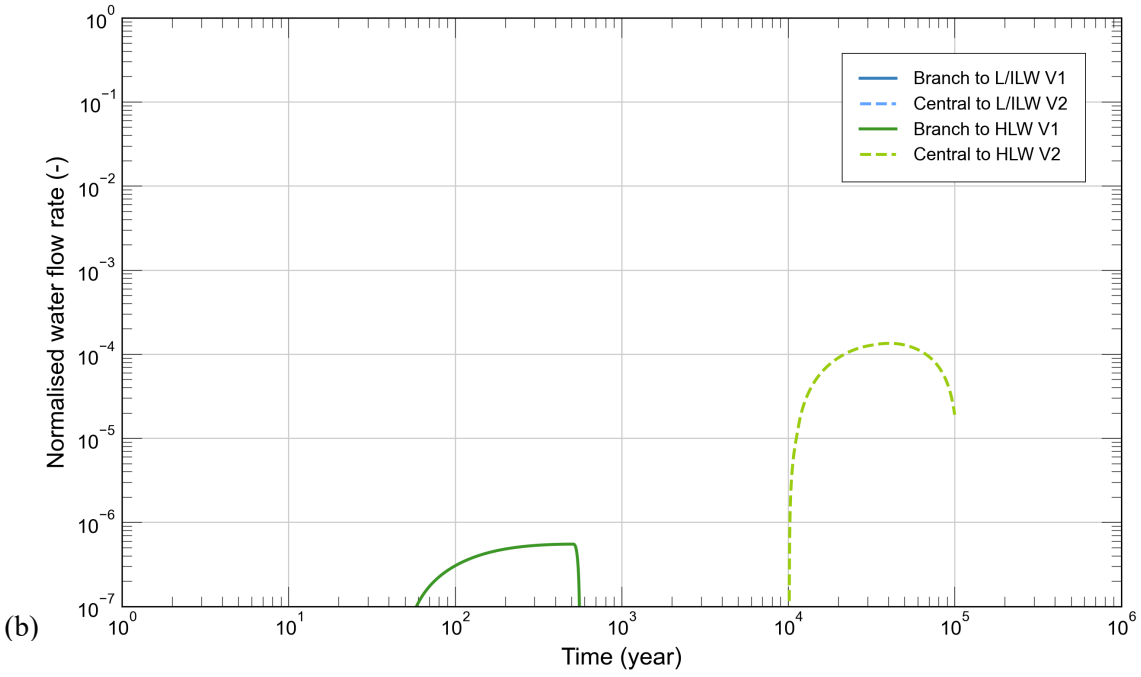

(b)

Fig. 6-26: Deviations scenario *"high-permeable V3 seal (variant 2)"*: normalised cumulative flows of (a) gas and (b) liquid

High-permeable V3 and V2-L/ILW seals *[TSD8]*

This scenario combines the high permeability of the V3 seal with high permeability also for the V2-L/ILW seal (both equal to 1.E-17 m^2). This scenario effectively translates to an "open" pathway for gas and liquid transport from the L/ILW emplacement caverns to the shaft. The resulting transients of pressure and saturation in the central area are shown in Fig. 6-27. These are overall very similar to those in the previous scenario with high permeability assigned to the V3 only (Fig. 6-25). Pressure reaches the hydrostatic value after ~15,000 years which is also the maximum pressure in the repository (Fig. 6-27a). Tunnels in the central area saturate with porewater depending on the distance from the shaft (Fig. 6-27b). The V3 seal itself saturates already after ~200 years and remains nearly fully saturated until the end of the simulation (gas saturations of 1 – 2% observed after 20,000 years).

The normalised gas and liquid flows through the sealing sections are shown in Fig. 6-28. Gas flow from the central area into the V2-HLW begins after ~900 years and continues until ~15,000 years, reaching a total mass equivalent to ~7.E-04 (-) of the total mass of gas generated in the repository (Fig. 6-28a). During that time and until 100,000 years there is no gas flow reaching the V1-HLW seals. Gas breaks through the V3 seal after ~13,000 years, with the cumulative mass of gas released after 20,000 years and 100,000 years equivalent to 2E-02 (-) and 3E-01 (-) of the total gas generated in the repository, respectively. Similar to the previous scenario, liquid flow from the central area into the V2-HLW seal takes place between ~10,000 and 40,000 years, reaching a cumulative mass that is less than ~2E-04 (-) of the water mass that can be stored in the repository (Fig. 6-28b).

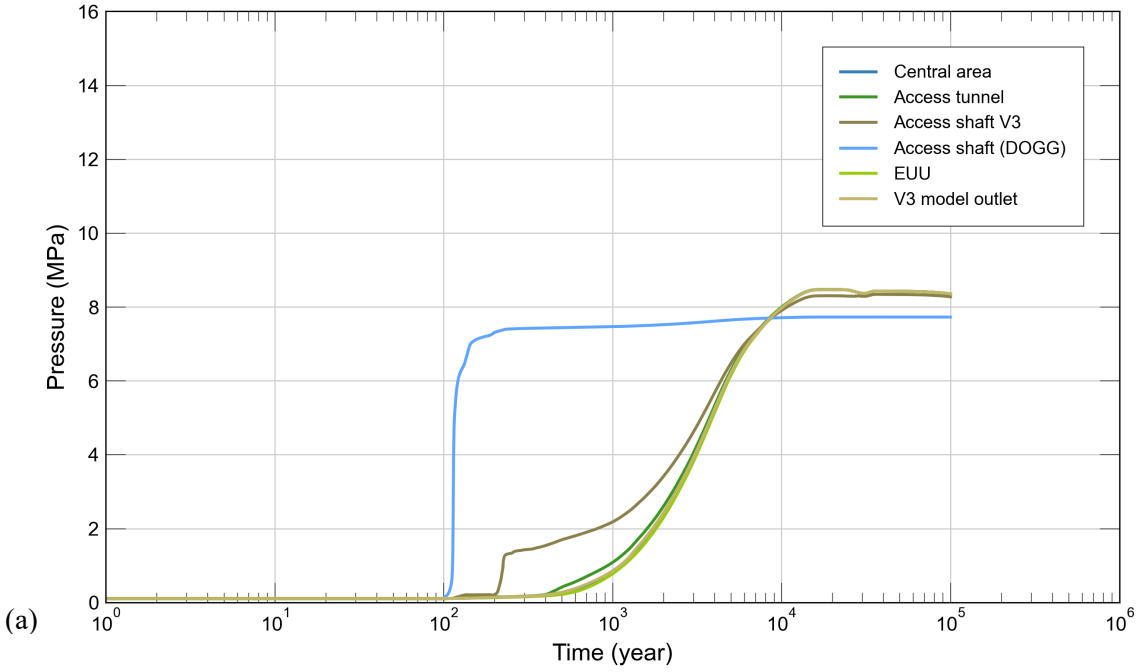

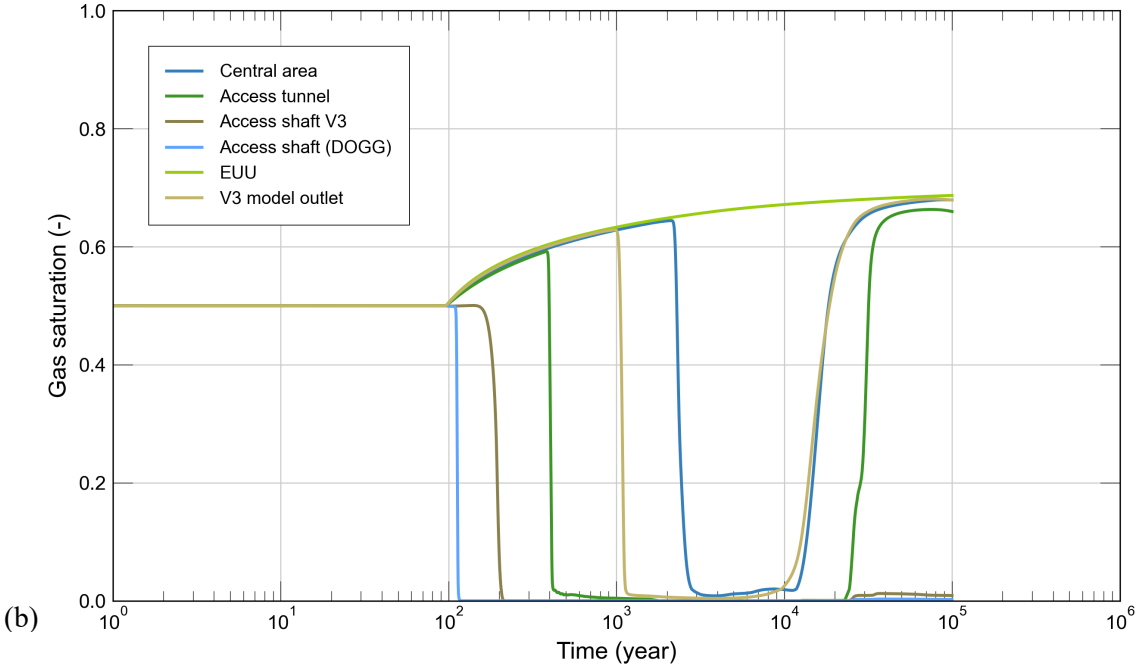

Fig. 6-27: Deviations scenario *"high-permeable V3 and V2-L/ILW seals"*: (a) pressure and (b) gas saturation in the central area of the repository

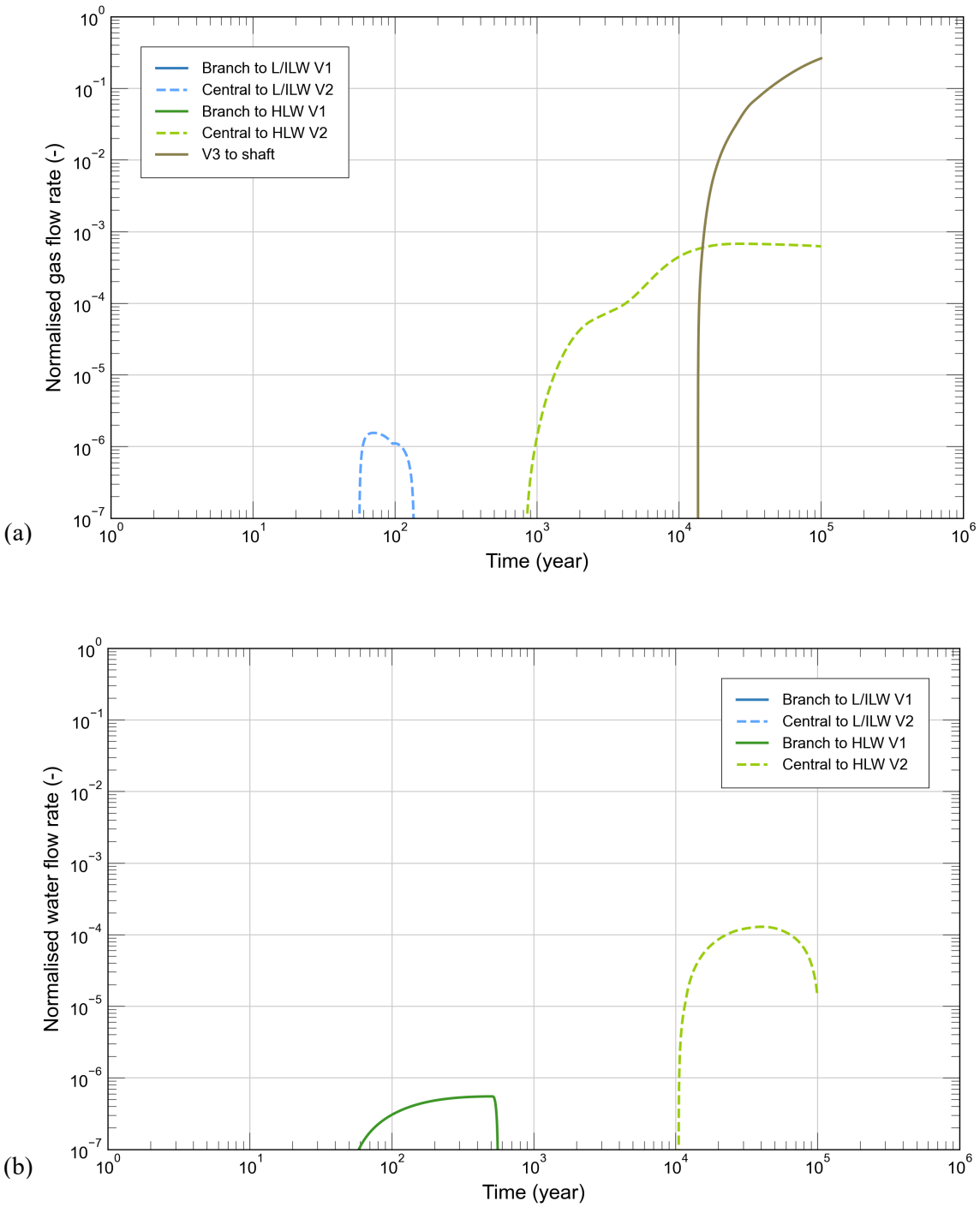

Fig. 6-28: Deviations scenario *"high-permeable V3 and V2-L/ILW seals"*: normalised cumulative flows of (a) gas and (b) liquid

High-permeable V2 seals *[TSD10]*

This scenario modifies the expected evolution by increasing the permeability of the V2-L/ILW seals and the V2-HLW seals to 1.E-17 and 1.E-19 m^2, respectively (from 5.E-18 m^2 and 1.E-20 m^2, respectively). The permeability of the V3 remains equal to 1.E-20 m^2, as in the expected evolution. The resulting transients of pressure and saturation in the central area are shown in Fig. 6-29. The pressure evolution (Fig. 6-29a) is practically identical to the expected evolution (Fig. 6-3). This demonstrates that the increase applied to the V2-L/ILW permeability does not result in additional gas flow from the L/ILW disposal area to the central area – as already indicated by the identical peak gas pressures throughout the corresponding observation points (Section 6.1). Moreover, the increase in V2-HLW permeability does not result in any additional release of gas from the HLW disposal area to the central area. This is also depicted in the gas saturation transients in Fig. 6-29b.

The normalised gas and liquid flows through the sealing sections are shown in Fig. 6-30. Gas flow from the central area into the V2-HLW begins after few hundred years and continues until the end of the simulation with a cumulative mass that is equivalent to 3E-3 (-) of the gas mass generated in the repository (Fig. 6-30a). Gas breakthrough from the V3 seal to the shaft takes place after ~45,000 years, reaching a cumulative normalised mass of 1E-4 (-) after 100,000 years. Some liquid flow from the central area into the V2-HLW seals is observed between ~15,000 and ~60,000 years without any liquid flow into the V1-HLW seals (Fig. 6-30b).

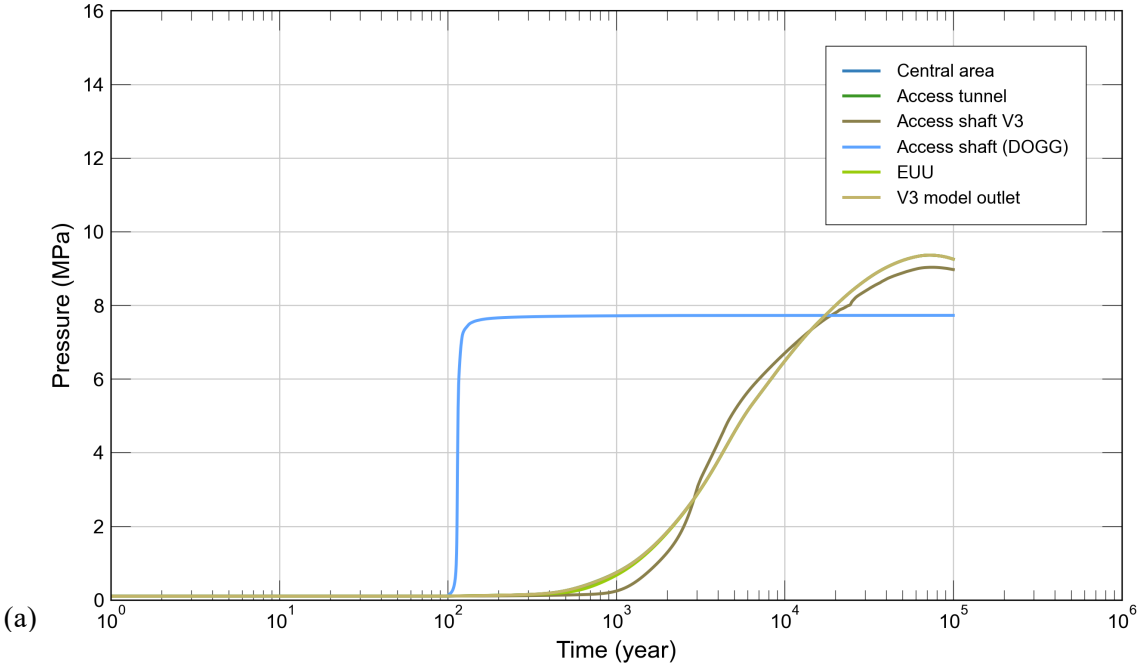

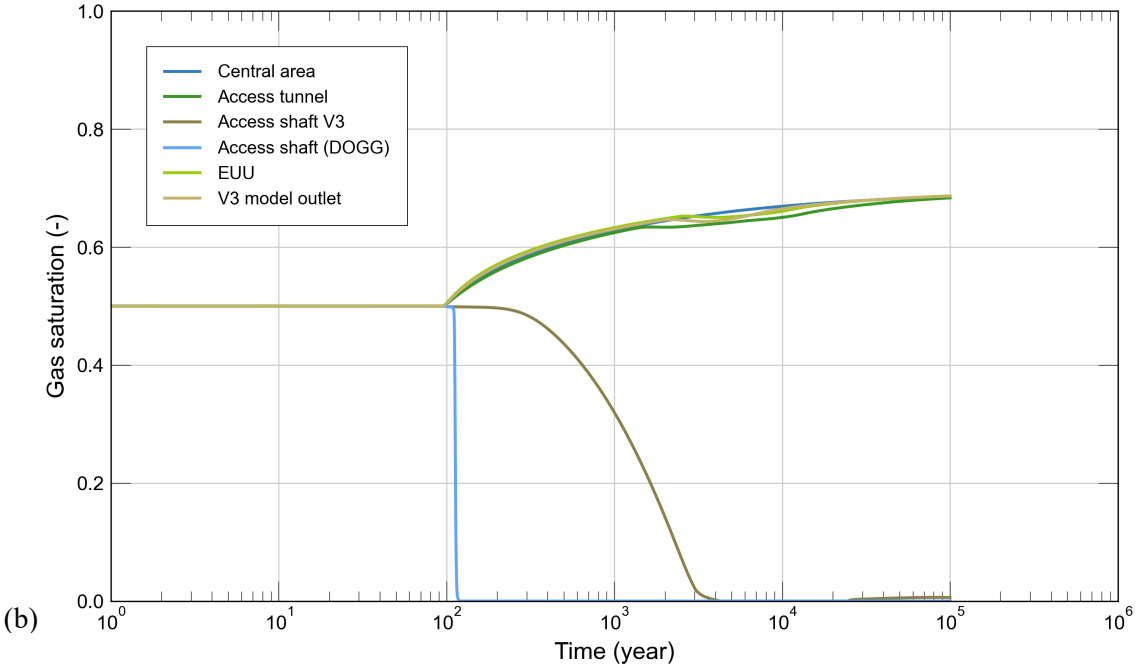

Fig. 6-29: Deviations scenario *"high-permeable V2 seals"*: (a) pressure and (b) gas saturation in the central area of the repository

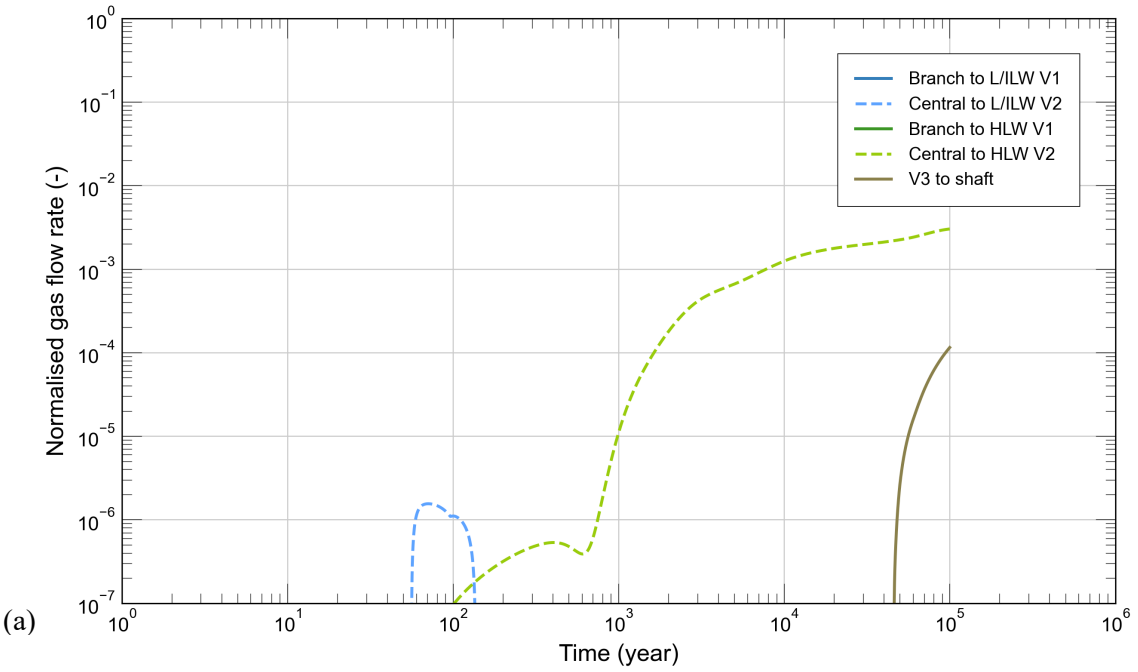

(a)

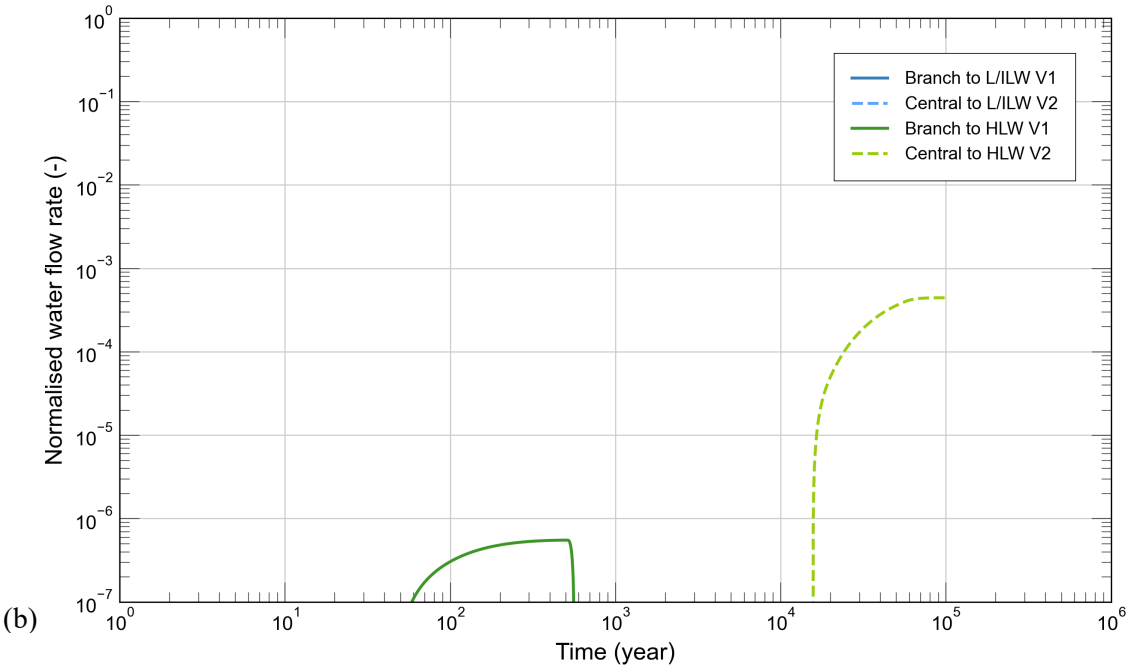

(b)

Fig. 6-30: Deviations scenario *"high-permeable V2 seals"*: normalised cumulative flows of (a) gas and (b) liquid

High-permeable V2 and V1 seals *[TSD11]*

In addition to the increased permeability of the V2 seals adopted in the previous scenario, this scenario also assumes a higher permeability of the V1 seals, namely 1.E-17 m^2 for V1-L/ILW and 1.E-19 m^2 for V1-HLW, respectively. The corresponding transients of pressure and saturation are shown in Fig. 6-31a and b, respectively. These are practically identical to the previous scenario. This confirms on the one hand the effectiveness of the gas path from the L/ILW caverns to the central area and, on the other hand, the diffusion-dominated transport in the buffer surrounding the HLW. The normalised gas and liquid flows, shown in Fig. 6-32, confirm the low sensitivity to the increased permeability in V1-L/ILW and V1-HLW, respectively.

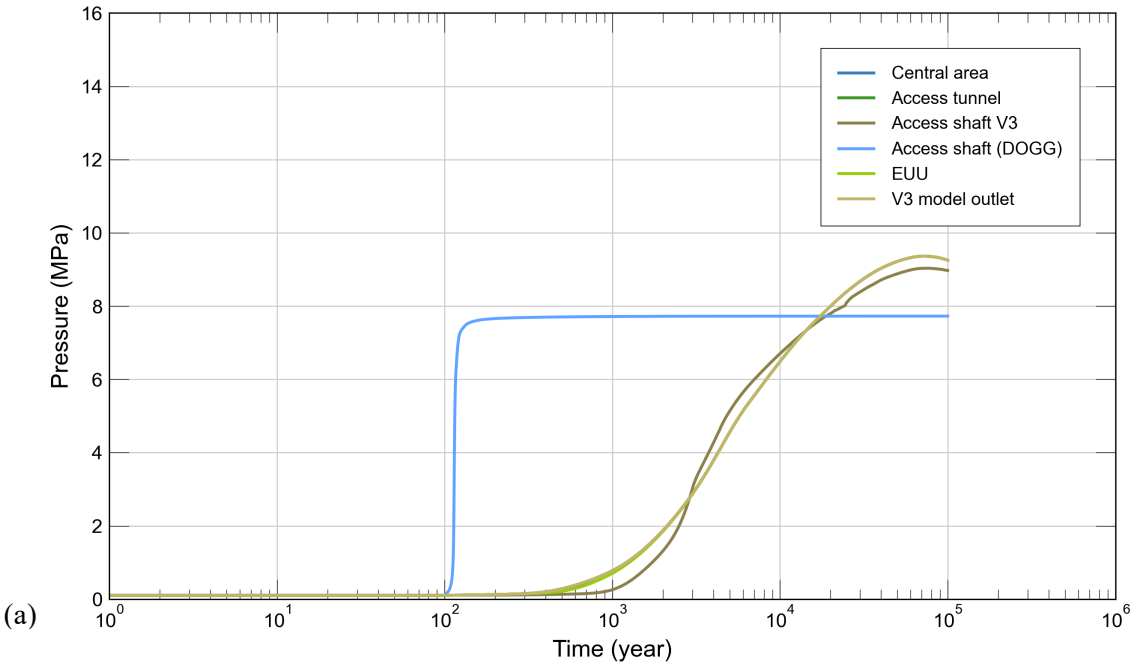

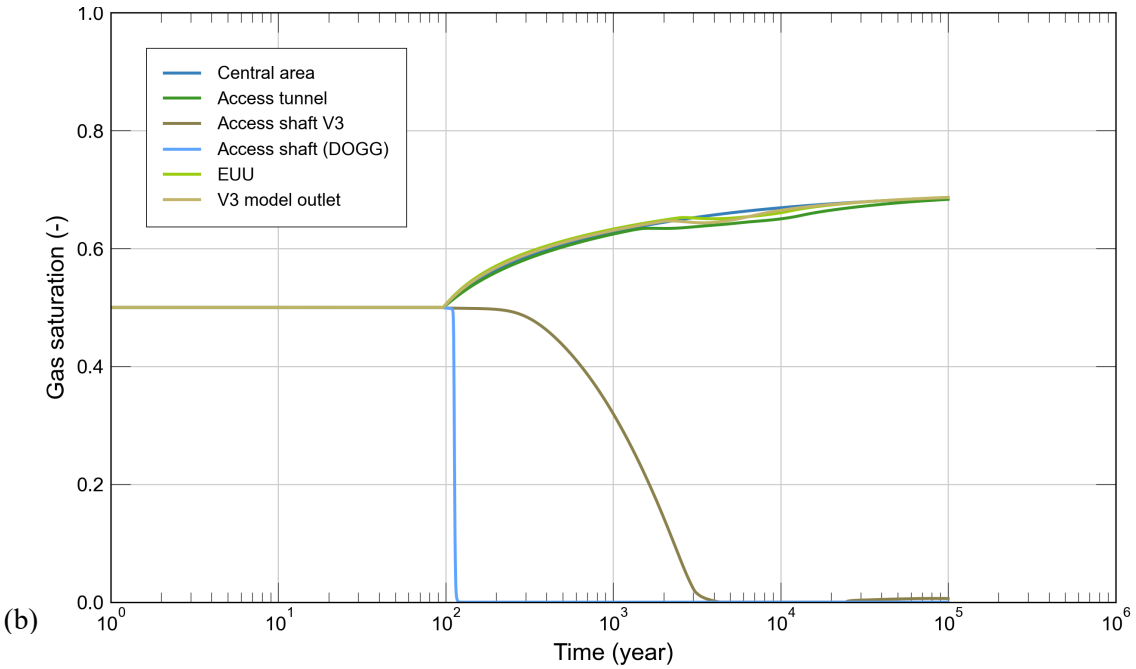

Fig. 6-31: Deviations scenario *"high-permeable V2 and V1 seals"*: (a) pressure and (b) gas saturation in the central area of the repository

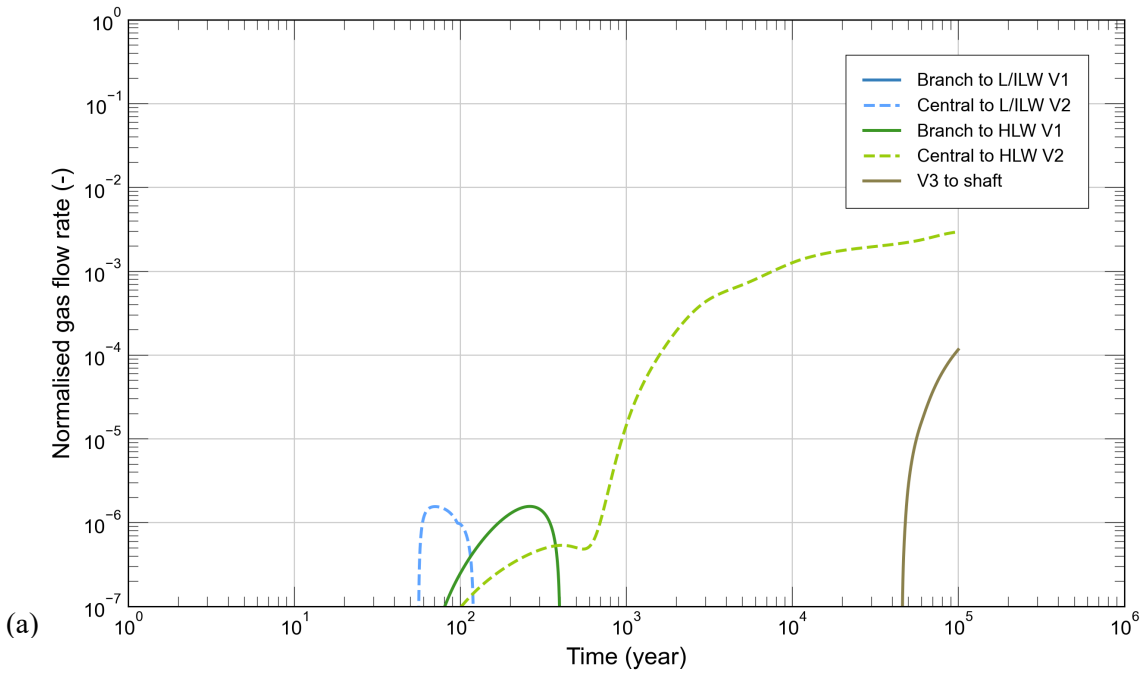

(a)

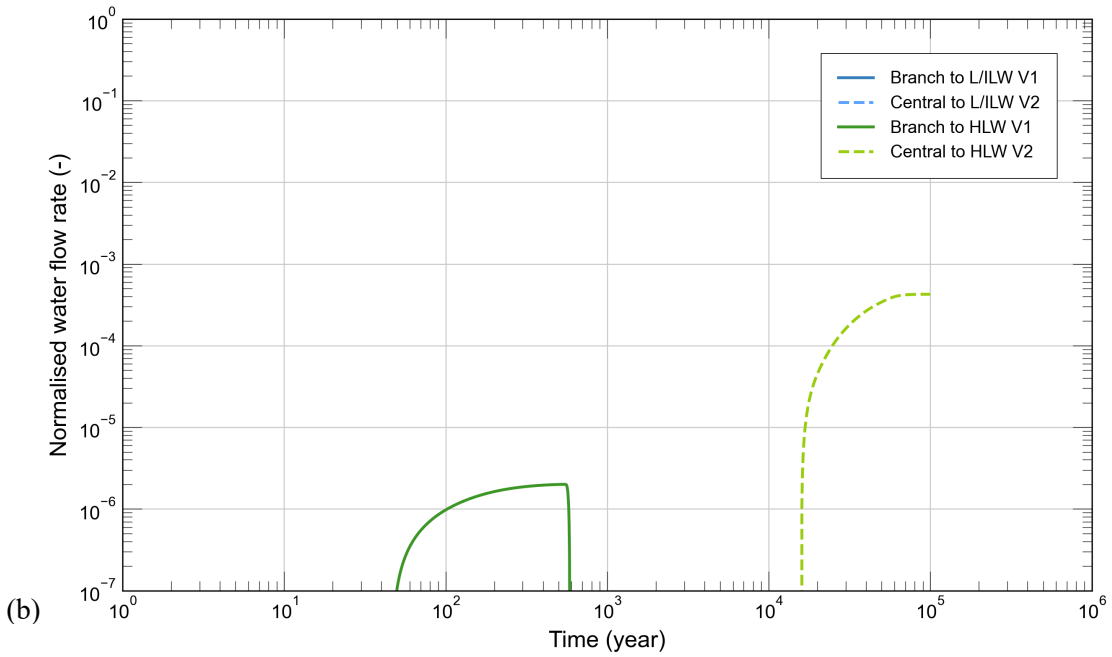

(b)

Fig. 6-32: Deviations scenario *"high-permeable V2 and V1 seals"*: normalised cumulative flows of (a) gas and (b) liquid

7 Probabilistic model-based analyses – HLW

7.1 Expected performance

The probabilistic analysis for the HLW disposal area is based on a sample set of 1,000 simulations using the 2D component model described in Section 3.4. The expected performance is simulated with model *2D-HLWx20*. The perturbed parameters and sampling procedure are those described in Section 3.4.6. Four indicators are evaluated for the quantitative assessment for HLW, namely the average temperature in the bentonite, thermally induced overpressures at a distance of 20 m above the disposal area, gas induced overpressures in the HLW nearfield, and normalised tracer fluxes through the CRZ (I-129). The effects of gas and heat are simulated for a period that corresponds to 1,000,000 years after emplacement. The solute source term is based on an instantaneous release $IRF_{I\text{-}129}$ (10% of initial activity of ^{129}I) from the HLW repository (Nagra 2024j). The tracer fluxes are shown in terms of release from OPA, release to Keuper and Malm, and release to Muschelkalk and Malm over a time scale which exceeds by a factor of 10 the period of assessment (10 million years). A biosphere dose conversion factor ($BDCF_{I\text{-}129}$) of 6.32E-13 Sv/Bq corresponding to present-day climate is used to convert the activity of I-129 into dose and subsequently normalise with the regulatory limit. The simulated transients are shown in Fig. 7-1 (temperatures and pressures) and Fig. 7-2 (tracer fluxes). In each sub-figure, the so-called reference case depicting the expected evolution for the best estimates of input parameters is shown with a blue line. The bandwidth around the reference case corresponds to the 1,000 samples of input parameters illustrating the parametric uncertainty range. In addition, the pressure lines corresponding to the magnitudes of the principal components of minimum and maximum horizontal strength at the respective observation point are shown for comparison to the simulated nearfield pressures. The failure criteria used for gas- and thermally-induced effects in the PA and resulting performance margins are documented in Nagra (2024j).

The average temperature in the bentonite (Fig. 7-1a) increases directly after emplacing the canister (at t = 2 years) and reaches a maximum of ~95 °C between 10 and 20 years in the reference case. Maximum average temperatures in the probabilistic simulations vary between ~85 °C and ~108 °C. After 10,000 years and until the end of the simulations, the temperature deviations from the reference case are practically negligible.

Thermally induced overpressure at 20 m above the disposal area (Fig. 7-1b) reaches a peak of ~12.6 MPa after ~100 years and then gradually decreases to reach hydrostatic pressure after ~10,000 years. The probabilistic simulations result in an overall larger spread in the transients compared to temperature. Most realisations considering parametric uncertainty for the expected evolution result in peak pressure in the range between 11 MPa and 15 MPa reached within the first 600 years. About twenty realisations result in peak pressure between 15 MPa and 16.5 MPa. Deviations from the reference case decrease as the thermal pulse dissipates and are less than 1 MPa after 10,000 years.

Gas induced overpressure in the HLW nearfield (Fig. 7-1c) correlates with the assumed time of canister breaching and subsequent increase in corrosion rate until the canister corrodes entirely (Nagra 2024g, see also Section 6.1). This results in two distinct peaks of ~11.3 MPa after ~15,000 years and 11.6 MPa after ~115,000 years, respectively. The probabilistic simulations result in peak pressures between 10 MPa and 13.5 MPa. Deviations from the reference case decrease with time and are less than 0.5 MPa after 1 million years.

The normalised tracer flux released from the OPA (Fig. 7-2a) reaches a peak of release equivalent to ~3E-03 (-) of the dose limit after ~120,000 years. The corresponding maximum release reached in the probabilistic simulations is ~5E-03 (-) of the dose limit after ~60,000 years. The normalised tracer flux released into the Keuper and Malm aquifers (Fig. 7-2b) reaches ~5E-04 (-) of the dose limit after ~500,000 years in the reference case and reaches a slightly higher value, namely ~7E-04 (-), in the probabilistic simulations. The maximum release into Muschelkalk and Malm (Fig. 7-2c) is even lower, namely ~3E-04 and 4E-04 (-) in the reference case and in the probabilistic simulations, respectively.

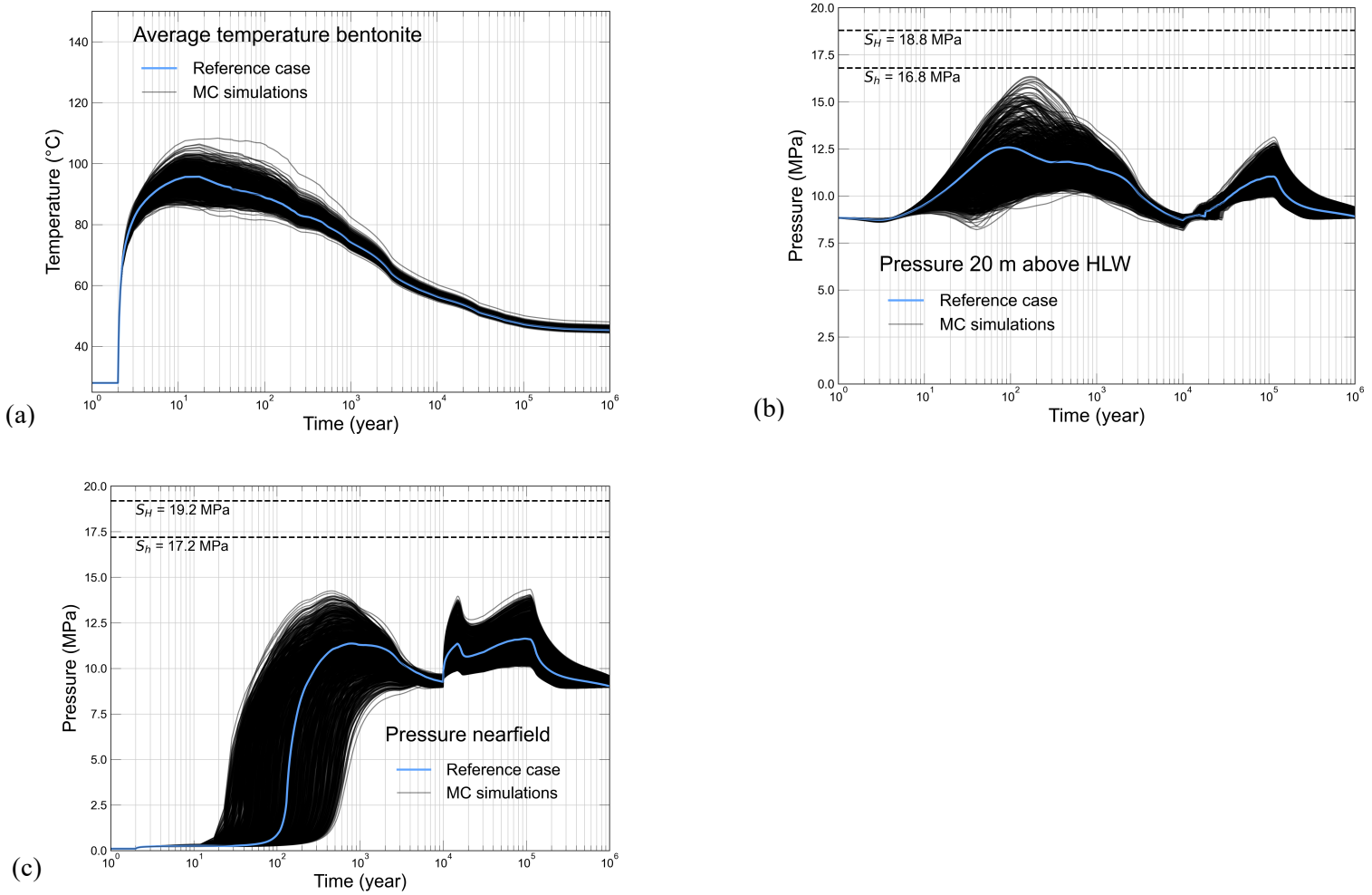

Fig. 7-1: Expected barrier performance HLW: best estimate and uncertainty ranges

(a) Average temperature of the bentonite buffer; (b) thermally induced overpressures at a distance of 20 m above the disposal area; (c) gas induced overpressures in the HLW nearfield.

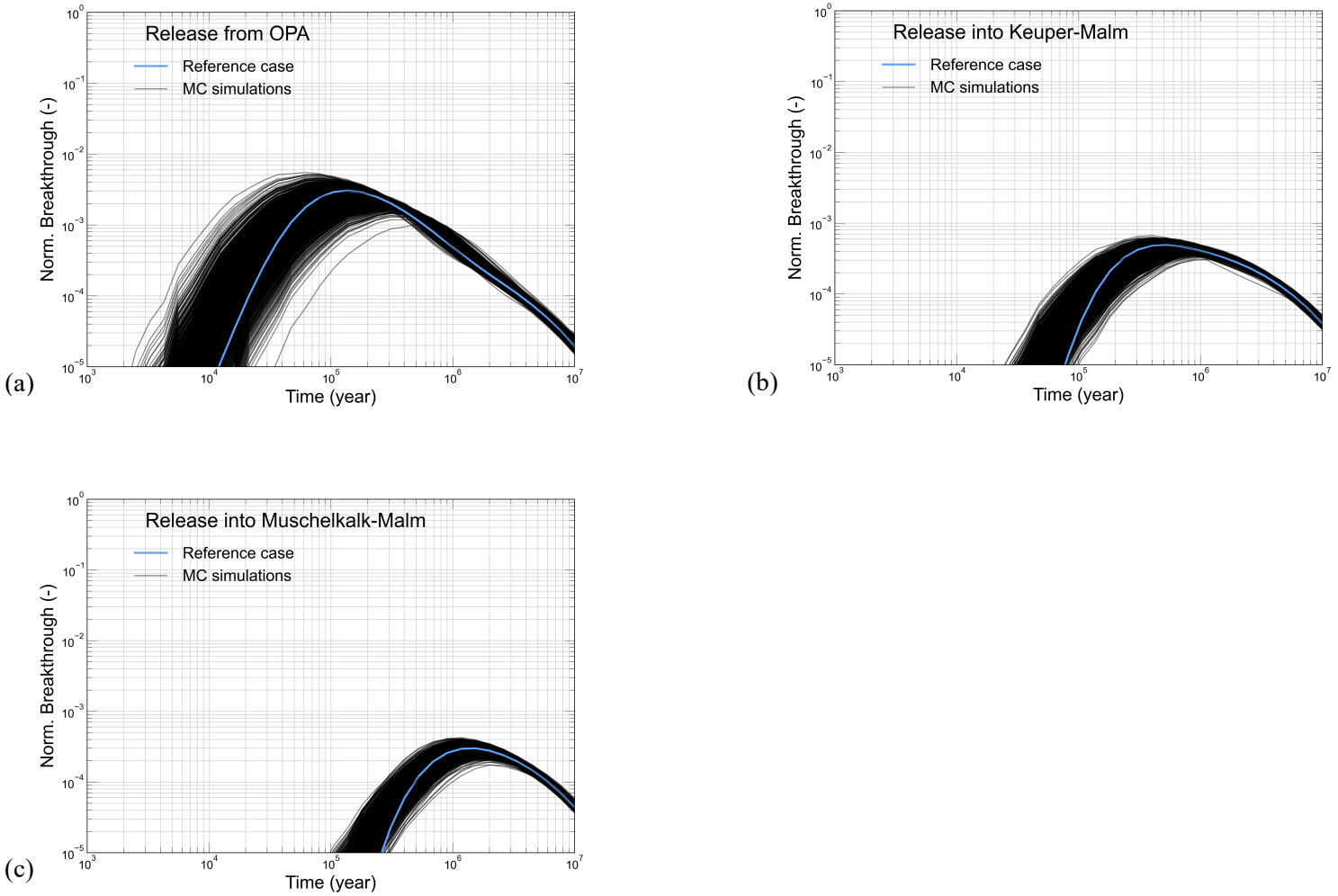

Fig. 7-2: Expected barrier performance HLW: best estimate and uncertainty ranges of solute tracer (I-129) release

(a) From OPA, (b) into the Keuper and Malm aquifers, (c) into the Muschelkalk and Malm aquifers.

7.2 Deviations

PA scenarios are specified for each barrier component to evaluate the impact of a reduced performance of the single component on the safety margins of the entire multi-barrier system. Tab. 7-1 presents a survey of the addressed PA scenarios for HLW with the associated barrier components. The model results of the respective assessments are discussed in the subsequent paragraphs.

Immobilisation, retention and retarded release of radionuclides is the primary safety function of the HLW waste matrix (Nagra 2024j). After canister failure, water will come in contact with the SF cladding and pellets, resulting in *instantaneous release* of a few percent of the total radionuclide inventory. The rest of the inventory, termed as *congruent release*, dissolved at low rates in porewater which slowly seeps into the canister. The PA scenarios formulated for the waste matrix relate to the release rate of activity. The first scenario assumes an instant release fraction of 6.5% and congruent release of the remaining activity (CONGRUENT). The second scenario assumes that the entire of I-129 inventory is released instantaneously and can be seen as a hypothetical deviation of performance of the SF pellets, presuming instantaneous dissolution of the UO_2 pellets after canister failure and porewater ingress.

The HLW disposal canisters are designed such that they provide full containment of the waste during the early post closure phase. The PA modelling is based on an assumed lifetime, according to their provisional design and on the expected source terms for heat emission of the waste (called "representative averages" in Nagra 2024g) and gas release associated with anaerobic canister corrosion (called "best estimate" in Nagra 2024g). Three PA scenarios are formulated as shown in Tab. 7-1, namely the early on-set of radionuclide release due to early canister breaching (WPFAIL), the enhanced heat emission (UBHEAT), and the enhanced gas generation (UBGAS).

A number of PA scenarios are dedicated to the CRZ (Tab. 7-1). Five scenarios are specified to evaluate possible deviations from the diffusion dominated transport namely scenarios UPFLOW, DOWNFLOW, HRDBED, HERWIS, MKALK, FLTHLWN, FLTHLWP, RIEHLW, and LOSSOB (Tab. 7-1). These are discussed in the respective sections.

Tab. 7-1: Deviations from expected performance HLW at level of components

PA scenario description (HLW)	Scenario code	Relevant barrier component
Instant release fraction 6.5% and congruent release of activity	CONGRUENT	HLW waste matrix
Instant release of entire activity	IRMAX	
Canister fail at time of repository closure	WPFAIL	HLW disposal canister
Pessimistic heat source term	UBHEAT	
Pessimistic gas source term	UBGAS	
Upflow with artesian pressure in Keuper	UPFLOW	CRZ
Downflow with artesian pressure in Malm	DOWNFLOW	
Hardbeds acting as release paths	HRDBDS	
Herrenwis unit acting as release path	HERWIS	
Fault normal to HLW drifts	FLTHLWN	
Fault parallel to HLW drifts (var1, var2)	FLTHLWP[1]	
Thermally or gas induced fracture	RIEHLW	
Loss of overburden	LOSSOB	

[1] Two variants with low and high fault transmissivity, respectively.

7.2.1 Instant release fraction and congruent release of activity (CONGRUENT)

The first scenario assumes 6.5% IRF and congruent release of the remaining activity. This scenario is simulated with model *2D-HLW×20* (see also Chapter 3). The normalised tracer flux released from the OPA is shown in Fig. 7-3a. The peak release in the reference case is equivalent to ~2E-04 (-) of the regulatory limit after ~200,000 years, which is one order of magnitude lower compared to the simulation assuming instantaneous release of the entire activity (here conservatively implemented in the expected evolution). The probabilistic simulations result in somewhat higher peaks of up to ~3E-04 (-), after ~90,000 years. The normalised tracer flux released into the Keuper and Malm aquifers is shown in Fig. 7-3b. The maximum release is reached after ~5 million years and corresponds to ~1E-04 (-) with a very small uncertainty envelope around that value. The maximum release into the Muschelkalk and Malm (Fig. 7-3c) is slightly decreased to below that value.

7.2.2 Instant release of activity entire activity (IRMAX)

This scenario assumes that the entire activity is released as IRF (after canister failure), which corresponds to a 10-fold increase of the IRF release compared to the expected evolution (from 10% to 100%, see Section 7.1). The scenario is simulated with model *2D-HLW×20.* The normalised tracer fluxes from scenario IRMAX are shown in Fig. 7-4. These are essentially 10 times higher compared to the expected evolution (see also Fig. 7-2).

7.2.3 Canister failure at time of repository closure (WPFAIL)

The first scenario aims to assess the impact of early canister failure on the performance of the CRZ as a transport barrier. This PA scenario is formulated as instantaneous release of the same activity as that used in the expected performance, however taking place as soon as the HLW nearfield is emplaced (instead of at the time of canister failure). It is simulated with model *2D-HLW×20.*

The normalised tracer flux released from the OPA is shown in Fig. 7-5a. The peak release occurs after 600,000 years and equals ~2E-03 (-) of the regulatory limit. The corresponding peak release to the Keuper and Malm aquifers is ~4E-04 (-) after 700,000 years (Fig. 7-5b). The peak release to the Muschelkalk aquifers, which occurs after ~2 million years, is slightly reduced to ~3E-04 (-) of the regulatory dose limit (Fig. 7-5c).

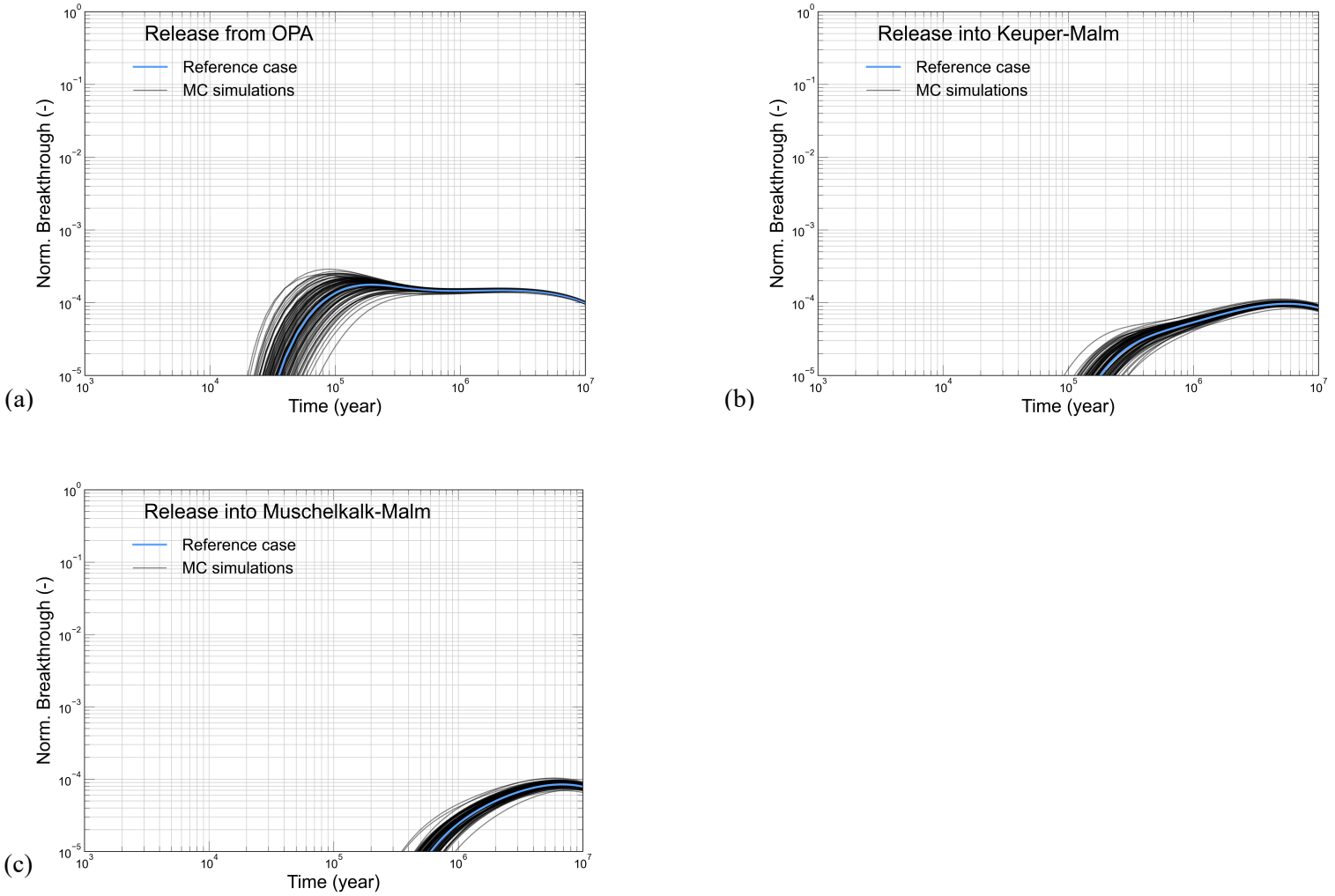

Fig. 7-3: CONGRUENT scenario: best estimate and uncertainty ranges of solute tracer (I-129) release
(a) From OPA, (b) into the Keuper and Malm aquifers, (c) into the Muschelkalk and Malm aquifers.

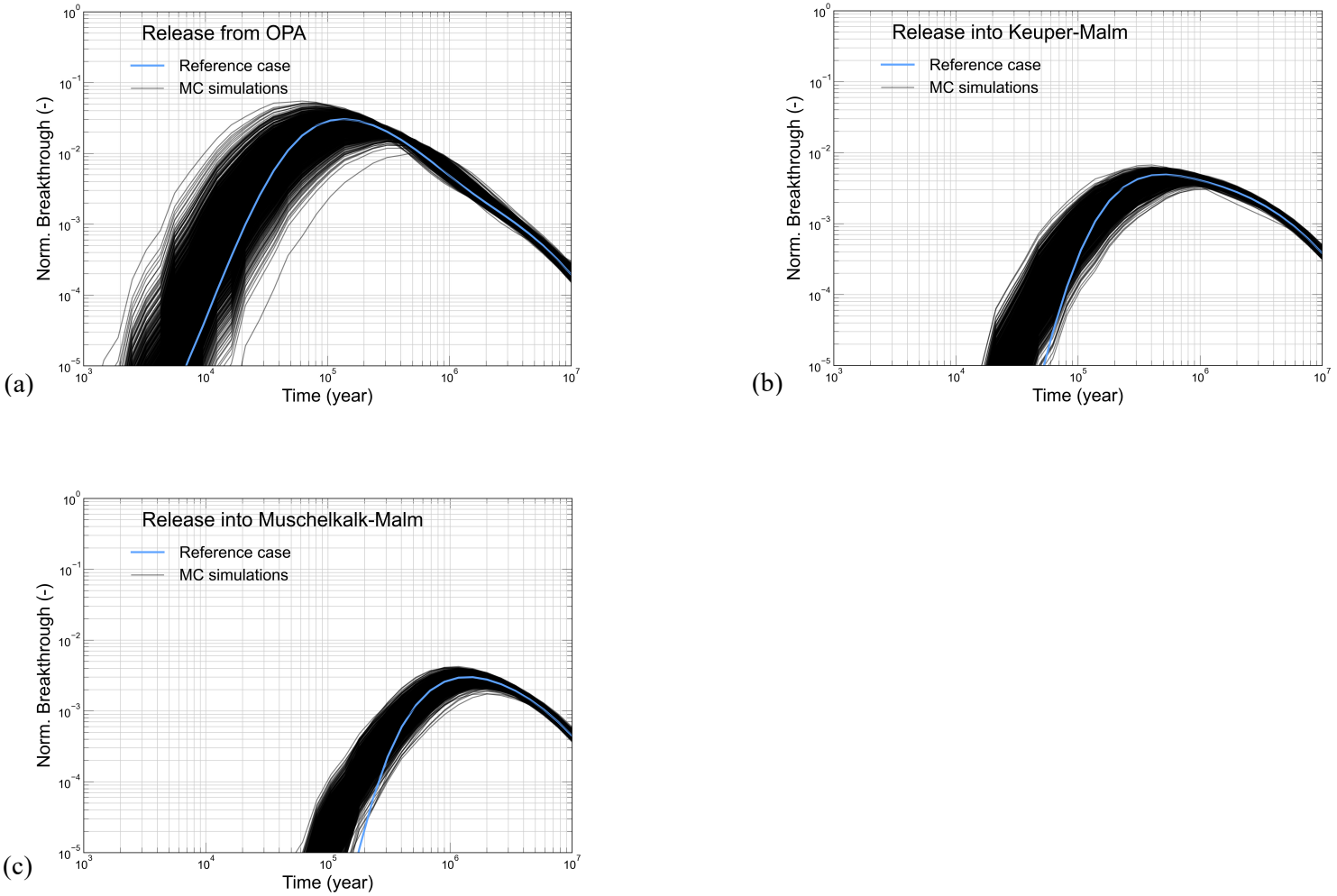

Fig. 7-4: IRMAX scenario: best estimate and uncertainty ranges of solute tracer (I-129) release

(a) From OPA, (b) into the Keuper and Malm aquifers, (c) into the Muschelkalk and Malm aquifers.

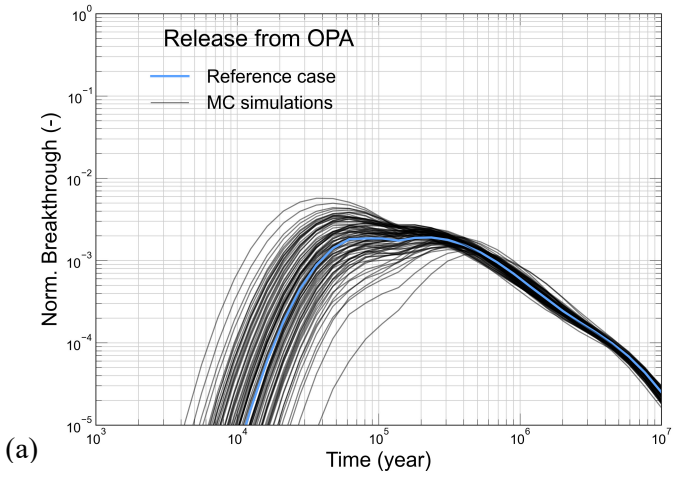

(a)

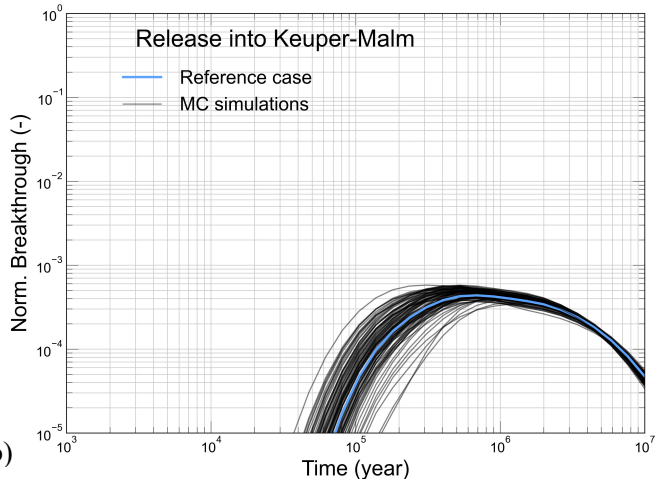

(b)

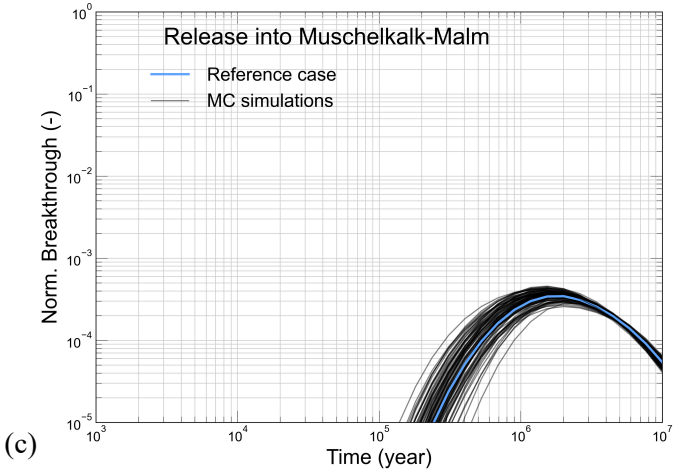

(c)

Fig. 7-5: WPFAIL scenario: best estimate and uncertainty ranges of solute tracer (I-129) release

(a) From OPA, (b) into the Keuper and Malm aquifers, (c) into the Muschelkalk and Malm aquifers.

7.2.4 Pessimistic heat source term (UBHEAT)

The second PA scenario associated with reduced canister performance addresses unexpectedly high thermal loads. For this, it is assumed that all canisters in the repository emit the amount of heat corresponding to the representative average of PWR-MOX (Fig. 3-7). Note that this does not depict a higher peak in heat output but a higher thermal load cumulatively, which affects the thermally-induced overpressures in the rock (see also Fig. 3-7). The scenario is simulated with model *2D-HLW×20.* The performance indicators for this scenario are the average temperature in the bentonite, the overpressures in the host rock 20 m above the canister, and the overpressures in the HLW drift.

The peak average temperatures in the bentonite, shown in Fig. 7-6a, are overall similar to those in the expected evolution (Fig. 7-1a). The decline in temperature is somewhat slower in this scenario owing to the pessimistic heat source term at the canisters.

The thermally induced overpressure at 20 m above the disposal area, shown in Fig. 7-6b, reaches a peak of ~13.5 MPa after ~700 years when the pessimistic heat source term is combined with the best estimate parameters. The probabilistic simulations perturbing parameters result in peak pressures reached within the first 800 years. One realisation results in peak pressure of 17.5 MPa which exceeds the magnitude of local minimum stress (16.8 MPa). Note that not all combinations of parameters have the same probability of occurrence as this depends on the parameter distributions discussed in Chapter 3. The assessment of the likelihood of such occurrences and the relevance to safety is discussed in Nagra (2024j).

The gas induced overpressures in the HLW tunnel are shown in Fig. 7-6c. Similar to the expected evolution, two peaks of 11.3 and 11.6 MPa are discerned after ~15,000 and ~115,000 years, respectively. The envelope of pressures resulting from parametric uncertainty is similar to that of the expected evolution.

7.2.5 Pessimistic gas source term (UBGAS)

In this scenario for the HLW disposal canister, it is assumed that the prevailing chemical conditions in the bentonite buffer give rise to enhanced corrosion rates. In the PA model, the upper bound gas generation rate is implemented (Nagra 2024g). The scenario is simulated with model *2D-HLW×20.*

The transients of average bentonite temperature, shown in Fig. 7-7a, do not show any appreciable differences from those in the expected evolution (Fig. 7-1a). Similarly, the thermally induced overpressures at a distance of 20 m above the disposal area, shown in Fig. 7-7b, show the same peak values and envelopes as in the expected evolution (Fig. 7-1b).

The gas induced overpressures in the HLW drift are shown in Fig. 7-7c. Due to the higher gas generation, the magnitude of peak pressures in this scenario increases to 14.0 MPa and 14.3 MPa after 15,000 years and 115,000 years, respectively. Five realisations result in peak pressures that exceed the magnitude of local minimum stress (16.8 MPa). Note that not all combinations of parameters have the same probability of occurrence as this depends on the parameter distributions discussed in Chapter 3. Furthermore, the pressures shown in Fig. 7-7c are obtained under very conservative assumptions in the model discussed in Chapter 4 (no consumption of water, no molecular diffusion, simultaneous breaching of all canisters). Accordingly, the assessment of the likelihood of such occurrences and the relevance to safety is discussed in Nagra (2024j).

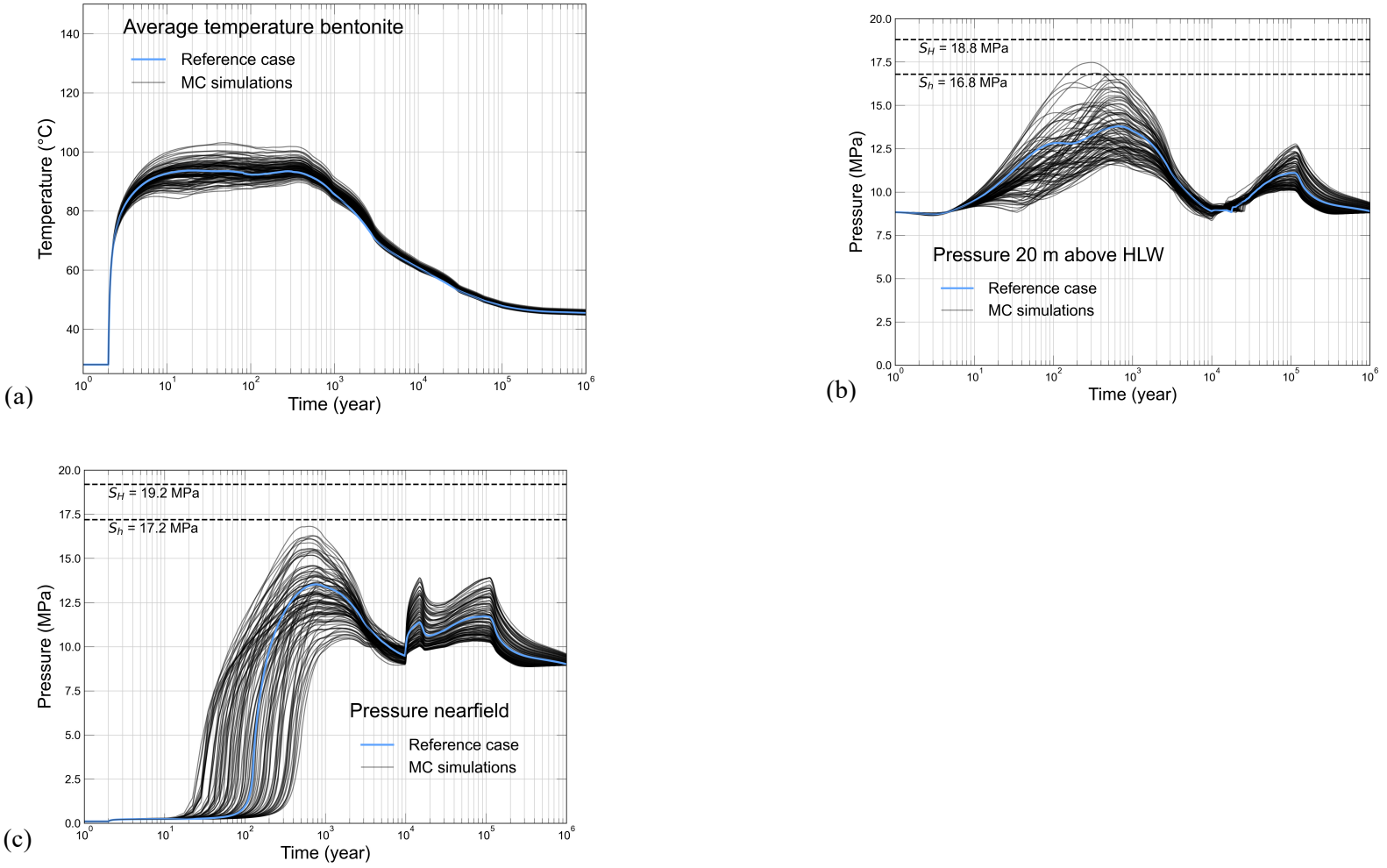

Fig. 7-6: UBHEAT scenario: best estimate and uncertainty ranges

(a) Average temperature of the bentonite buffer, (b) thermally induced overpressures at a distance of 20 m above the disposal area, (c) gas induced overpressures in the HLW nearfield.

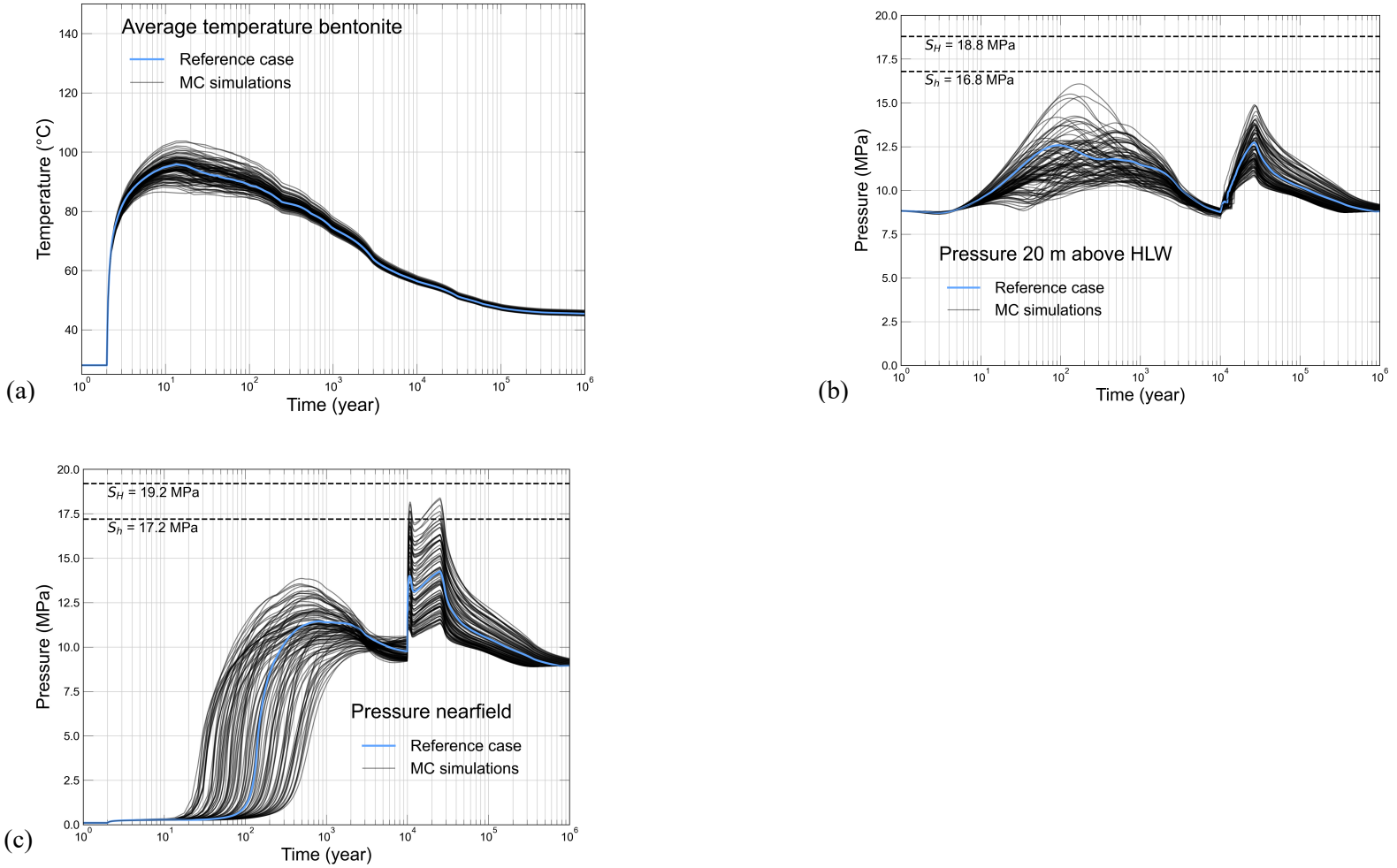

Fig. 7-7: UBGAS scenario: best estimate and uncertainty ranges

(a) Average temperature of the bentonite buffer, (b) thermally induced overpressures at a distance of 20 m above the disposal area, (c) gas induced overpressures in the HLW nearfield.

7.2.6 Upflow with artesian pressure in Keuper (UPFLOW)

The first scenario for the CRZ corresponds to artesian conditions in the Keuper aquifer, resulting in hydraulic head higher than that of the lithostratigraphic layer stack above. A head difference of 1 MPa between the Keuper and Malm aquifers is assumed. Furthermore, the upper bound hydraulic conductivity is adopted for the Keuper aquifer (see also Tab. 3-3). This scenario is simulated with model *2D-HLW×20.*

The normalised tracer flux released from the OPA is shown in Fig. 7-8a. A peak corresponding to ~3E-03 (-) of the dose limit is reached after ~120,000 years in the base case, which is the same as in the expected evolution (Fig. 7-2a). The normalised tracer flux released into the Keuper and Malm aquifers reaches ~8E-04 (-) of the dose limit after ~600,000 years (Fig. 7-8b), which is slightly higher compared to that observed in the expected evolution (Fig. 7-2b). The peak release into the Muschelkalk and Malm aquifers corresponds to ~2E-04 (-) of the dose limit after ~1.5 million years (Fig. 7-8c).

7.2.7 Downflow with artesian pressure in Malm (DOWNFLOW)

The second scenario related to the CRZ assumes downwards directed porewater flow with a head difference of 1 MPa between the Malm and Keuper aquifer. It is simulated with model *2D-HLW×20.*

The normalised tracer flux released from the OPA (Fig. 7-9a) is very similar to that observed in the expected evolution (Fig. 7-2a). A maximum that corresponds to ~3E-03 (-) of the dose limit is reached after ~120,000 years. The normalised tracer flux into the Keuper and Malm aquifers reaches a maximum corresponding to ~9E-04 (-) of the dose limit after ~500,000 years (Fig. 7-9b). The maximum release into the Muschelkalk and Malm aquifers is less than 2E-04 (-) of the dose limit, reached after nearly 2 million years (Fig. 7-9c).

7.2.8 Hardbeds as release path (HRDBDS)

This scenario considers the upper bound value for hydraulic conductivity of the hardbeds of the SCD units above the host rock (see also Tab. 3-1) combined with the upper bound hydraulic conductivity assigned to the SCAD units (see Tab. 3-3). Furthermore, a lateral hydraulic gradient of 0.1 m/m is assumed in the hardbeds. A hypothetical transmissive vertical fault at a distance of 200 m from the edge of the HLW disposal area is implemented and serves as a potential release path. The scenario is simulated with model *2D-HLW×20.*

The normalised tracer flux released from the OPA is shown in Fig. 7-10a. Similar to the result of the expected evolution (Fig. 7-2a), the peak is equivalent to ~3E-03 (-) of the dose limit and occurs after ~120,000 years. The normalised tracer flux into the Keuper and Malm aquifers peaks at ~1E-03 (-) of the dose limit after ~800,000 years (Fig. 7-10b). The maximum release into the Muschelkalk and Malm aquifers is ~5E-04 (-) of the dose limit and occurs after 1 million years (Fig. 7-10c).

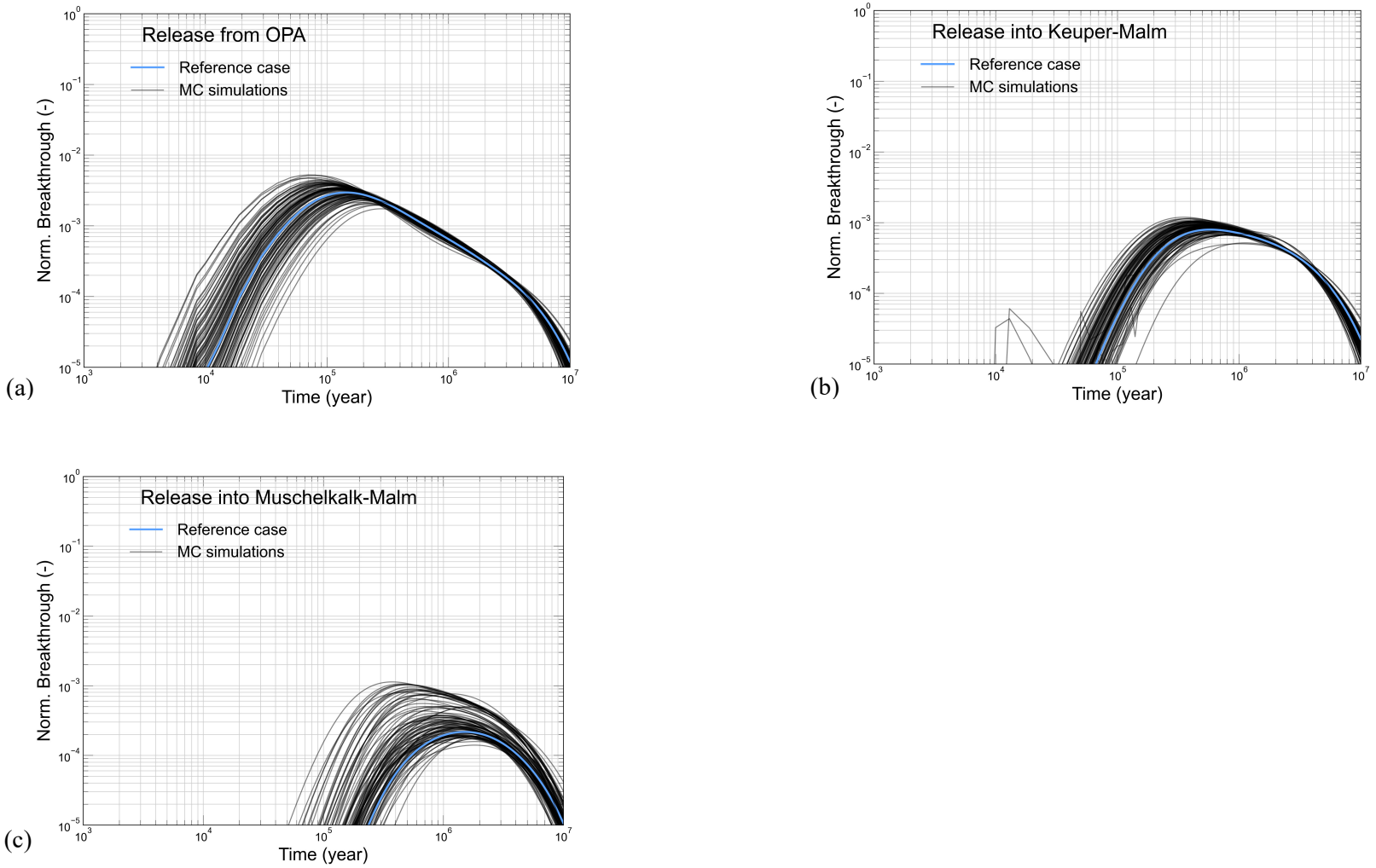

Fig. 7-8: UPFLOW scenario: best estimate and uncertainty ranges of solute tracer (I-129) release

(a) From OPA, (b) into the Keuper and Malm aquifers, (c) into the Muschelkalk and Malm aquifers.

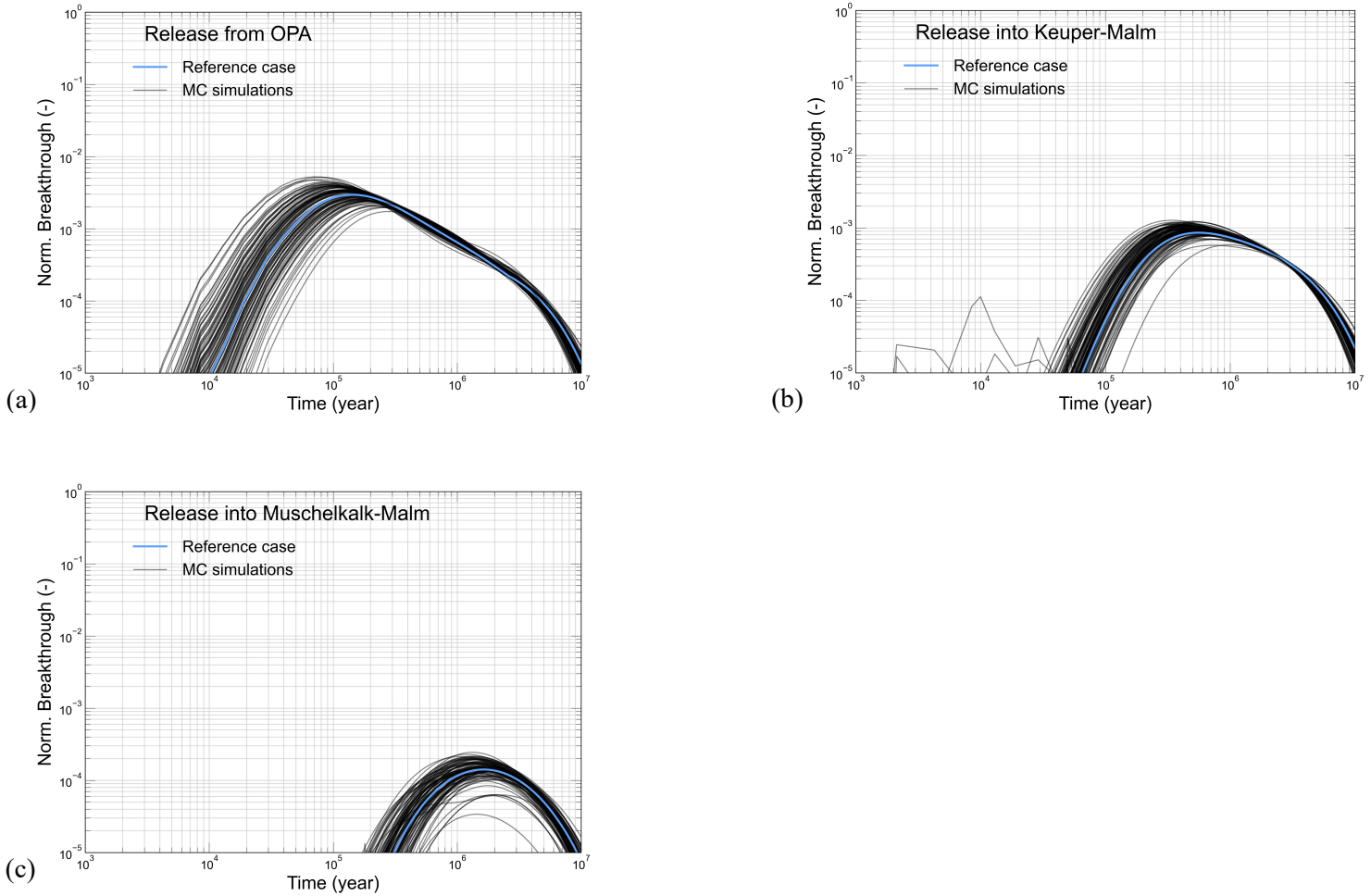

Fig. 7-9: DOWNFLOW scenario: best estimate and uncertainty ranges of solute tracer (I-129) release
(a) From OPA, (b) into the Keuper and Malm aquifers, (c) into the Muschelkalk and Malm aquifers.

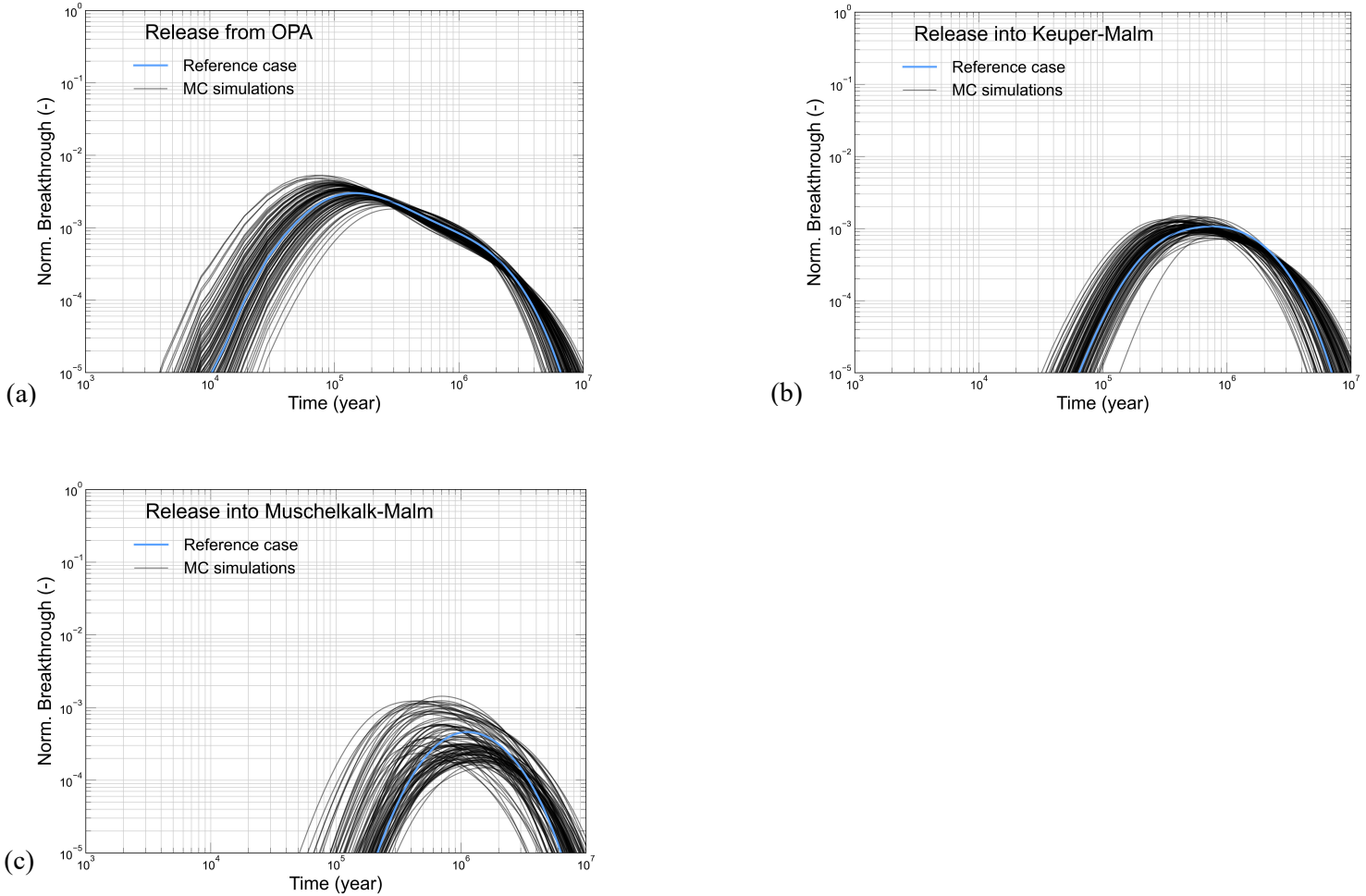

Fig. 7-10: HRDBDS scenario: best estimate and uncertainty ranges of solute tracer (I-129) release

(a) From OPA, (b) into the Keuper and Malm aquifers, (c) into the Muschelkalk and Malm aquifers.

7.2.9 Herrenwis as release path (HERWIS)

This scenario considers the Herrenwis unit as a heterogeneous carbonate formation with high permeability features. The unit is represented with a generic facies model with high permeability subfacies embedded in the heterogeneous carbonate formation sequence (for details see Nagra 2024j). All other formations are considered homogeneous with the best estimate values of transport parameters given in Chapter 3. Similar to the HRDBDS scenario, a lateral hydraulic gradient of 0.1 m/m is assumed, in this case in the Herrenwis unit, and a hypothetical transmissive vertical fault is placed at a distance of 200 m from the edge of the HLW disposal area. This scenario is simulated with model *2D-HLW×20.*

The normalised tracer fluxes, shown in Fig. 7-11, are very similar to those from scenario HRDBDS. The peak tracer flux released from the OPA (Fig. 7-11a) corresponds to ~3E-03 (-) of the dose limit and occurs after ~120,000 years. The normalised tracer flux into the Keuper and Malm aquifers reach a peak of ~1E-03 (-) of the dose limit after ~800,000 years (Fig. 7-11b). The maximum release into the Muschelkalk and Malm aquifers is less than 5E-04 (-) of the dose limit (Fig. 7-11c).

7.2.10 Fault normal to HLW drifts (FLTHLWN)

In this scenario it is assumed that a transmissive fault intersects the 20 HLW drifts at the centre of the HLW disposal area. The fault is placed perpendicular to the axes of the drifts. The fault transmissivity is sampled probabilistically from a uniform distribution with maximum and minimum values of 1.E-10 and 1.E-12 m^2/s, respectively. The fault thickness is assumed equal to 1 m. Input parameters of the geological formations are sampled in the same way as in the previous scenarios (see also Chapter 3). Furthermore, a vertical hydraulic gradient is applied between the Keuper and Malm aquifers, assuming cartesian conditions in the Keuper aquifer (1 MPa above hydrostatic). This results in advective flow of porewater through the fault towards the Malm aquifer. This scenario is simulated with model *2.5D-HLW×20*.

The normalised tracer flux released from the OPA is shown in Fig. 7-12a. The flux in the reference case does not show any significant differences to that of the expected evolution (Fig. 7-2a), with a peak of ~3E-03 (-) of the dose limit reached after ~120,000 years. The normalised tracer flux into the Keuper and Malm aquifers (Fig. 7-12b) is somewhat higher compared to the expected evolution, reaching ~9E-04 (-) of the dose limit after 600,000 years. The maximum release into the Muschelkalk and Malm aquifers (Fig. 7-12c), observed after ~1.5 million years, is less than 2E-04 (-) of the dose limit.

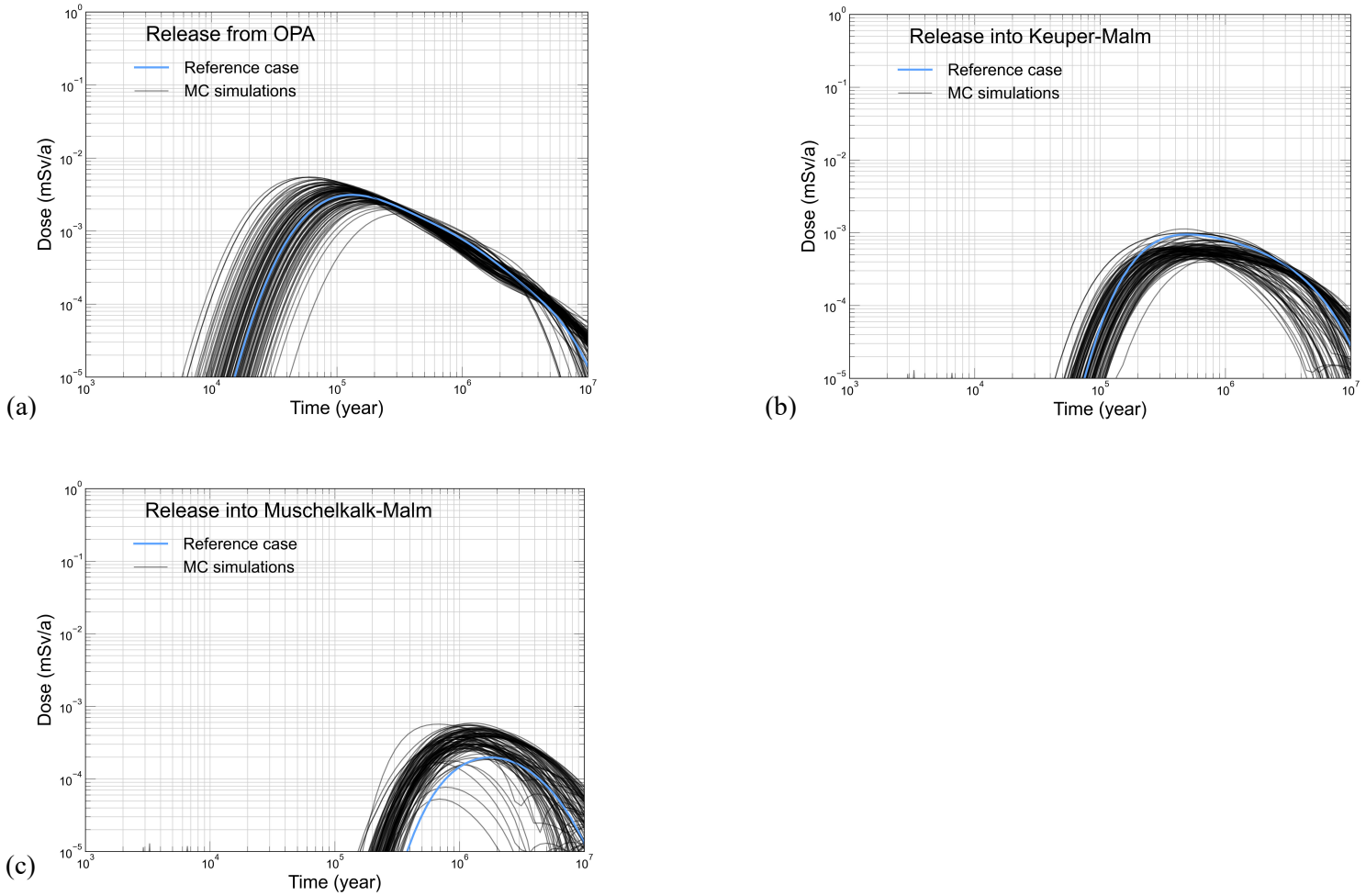

Fig. 7-11: HERWIS scenario: best estimate and uncertainty ranges of solute tracer (I-129) release

(a) From OPA, (b) into the Keuper and Malm aquifers, (c) into the Muschelkalk and Malm aquifers.

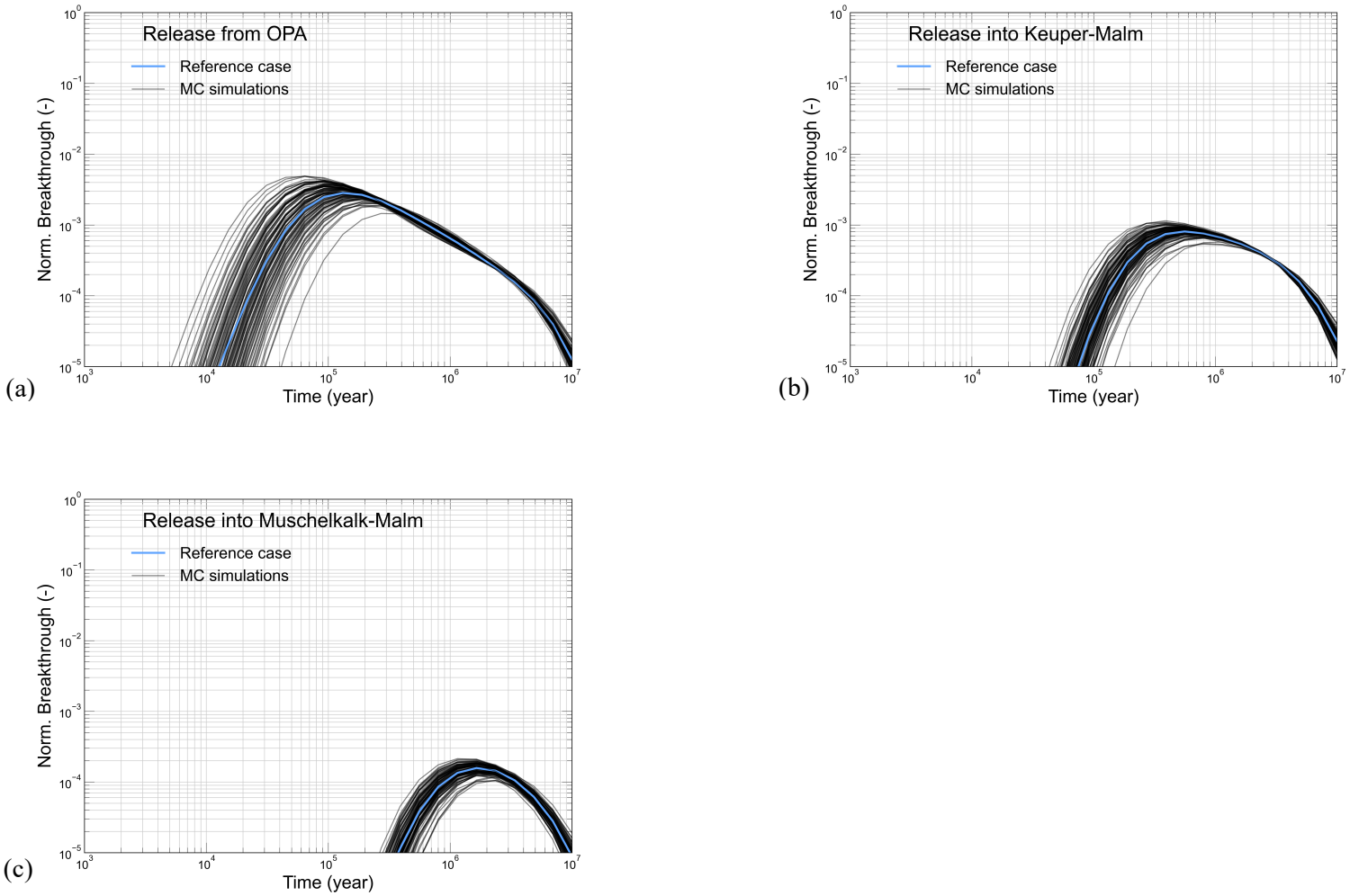

Fig. 7-12: FLTHLWN scenario: best estimate and uncertainty ranges of solute tracer (I-129) release
(a) From OPA, (b) into the Keuper and Malm aquifers, (c) into the Muschelkalk and Malm aquifers.

7.2.11 Fault parallel to HLW drifts (FLTHLWP)

In this scenario the transmissive fault is assumed to be parallel to the HLW drifts, at the middle between two HLW drifts at the centre of the disposal area. Two variants are implemented for this scenario. In the first variant the fault properties and probabilistic sampling are identical to scenario FLTHLWN (see Section 7.2.9, fault transmissivity sampled between 1.E-10 and 1.E-12 m^2/s). In the second variant the fault transmissivity is sampled between 1.E-08 and 1.E-10 m^2/s. Both variants are simulated with model *2D-HLW×20*.

The normalised tracer fluxes from the first variant (low fault transmissivity) are shown in Fig. 7-13. The normalised tracer flux released from the OPA (Fig. 7-13a) is similar to that of the expected evolution (Fig. 7-2a), reaching a peak that is equivalent to ~3E-03 (-) of the dose limit after ~120,000 years. The normalised tracer flux into the Keuper and Malm aquifers shows somewhat elevated peak compared to the expected evolution, reaching ~1E-03 (-) of the dose limit after ~500,000 years (Fig. 7-13b). The maximum release into the Muschelkalk and Malm aquifers is ~2E-04 (-) of the dose limit and occurs after ~1.5 million years (Fig. 7-13c).

The normalised tracer fluxes from the second variant (high fault transmissivity) are shown in Fig. 7-14. The normalised tracer flux released from the OPA (Fig. 7-14a) does not show any appreciable differences from the low fault transmissivity variant (Fig. 7-14a) and the expected evolution (Fig. 7-2a). The releases into the Keuper and Malm and into the Muschelkalk and Malm aquifers are overall similar to the low transmissivity variant.

7.2.12 Thermally or gas induced fracture (RIEHLW)

This scenario evaluates the impact of thermally- or gas-induced fractures on the barrier performance of the HLW disposal system with focus on transport of dissolved radionuclides through the CRZ. It is assumed that a thermally induced vertical fracture develops along the axis of a HLW emplacement drift at the centre of the HLW disposal area. The fracture transmissivity is 1E-10 m^2/s. The fracture intersects the middle of the emplacement drift and extends to the Malm and Keuper aquifers. This scenario is simulated with model *2D-HLW×20*.

The normalised tracer fluxes are shown in Fig. 7-15. These do not show any significant increase in tracer releases compared to the expected evolution (Fig. 7-2).

7.2.13 Loss of overburden (LOSSOB)

This scenario evaluates the effect of mechanical unloading of the host rock on its hydraulic conductivity, which is caused by the loss of overburden due to erosion processes. The loss of overburden is described by a functional relationship with a probability density function provided in Nagra (2024c) (for more details on the implementation see Nagra 2024j). As a proxy to overburden stress, depth is used to scale hydraulic conductivity of the OPA based on power law relationship provided in Nagra (2024j). In addition, a hydraulic head difference equivalent to 1 MPa is applied between the Keuper and Malm aquifers, resulting in upwards directed flow of porewater through the repository and the CRZ, similar to the UPFLOW scenario. In total, 100 realisations of time-dependent loss of overburden are generated based on the probability density function and accordingly 100 realisations of a time-dependent hydraulic conductivity are implemented in the Monte Carlo transport simulations. The scenario is simulated with model *2D-HLW×20*.

The normalised tracer fluxes are shown in Fig. 7-16. These do not show any appreciable differences to the expected evolution (Fig. 7-2). Notably, the probabilistic simulations associated with the samples of overburden loss do not introduce any deviations in the tracer fluxes.

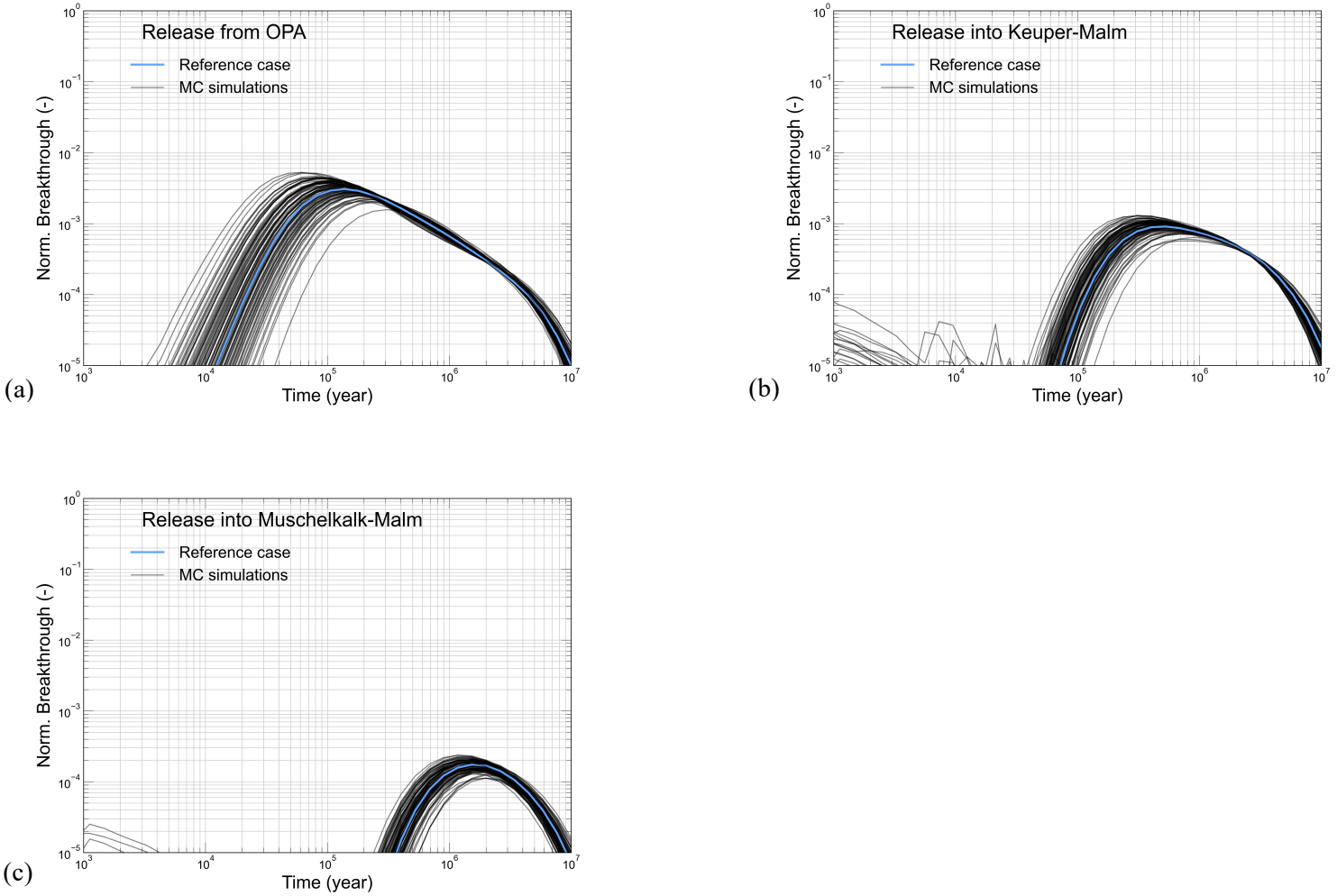

Fig. 7-13: FLTHLWP scenario (var. 1): best estimate and uncertainty ranges of solute tracer (I-129) release
(a) From OPA, (b) into the Keuper and Malm aquifers, (c) into the Muschelkalk and Malm aquifers.

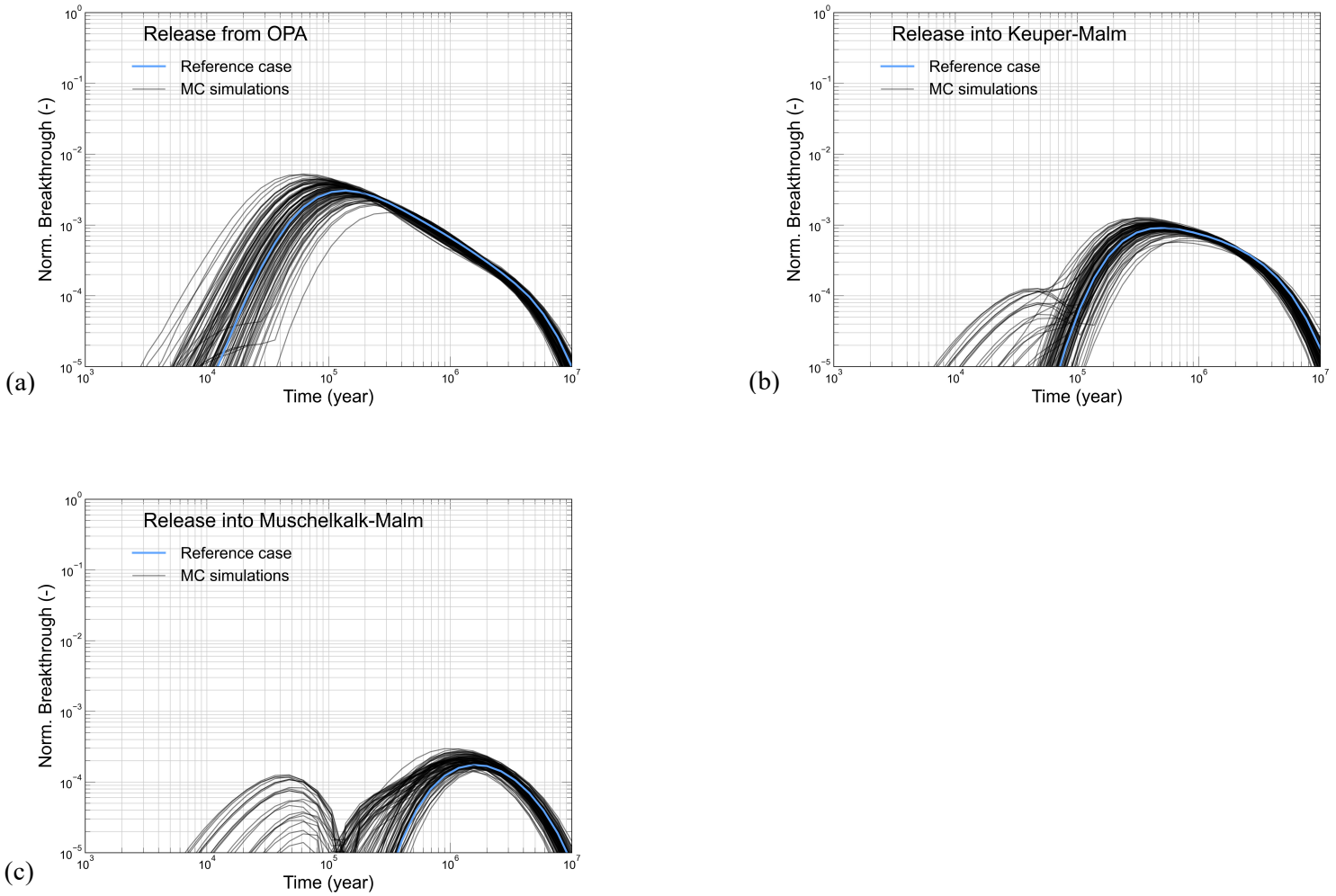

Fig. 7-14: FLTHLWP scenario (var. 2): best estimate and uncertainty ranges of solute tracer (I-129) release
(a) From OPA, (b) into the Keuper and Malm aquifers, (c) into the Muschelkalk and Malm aquifers.

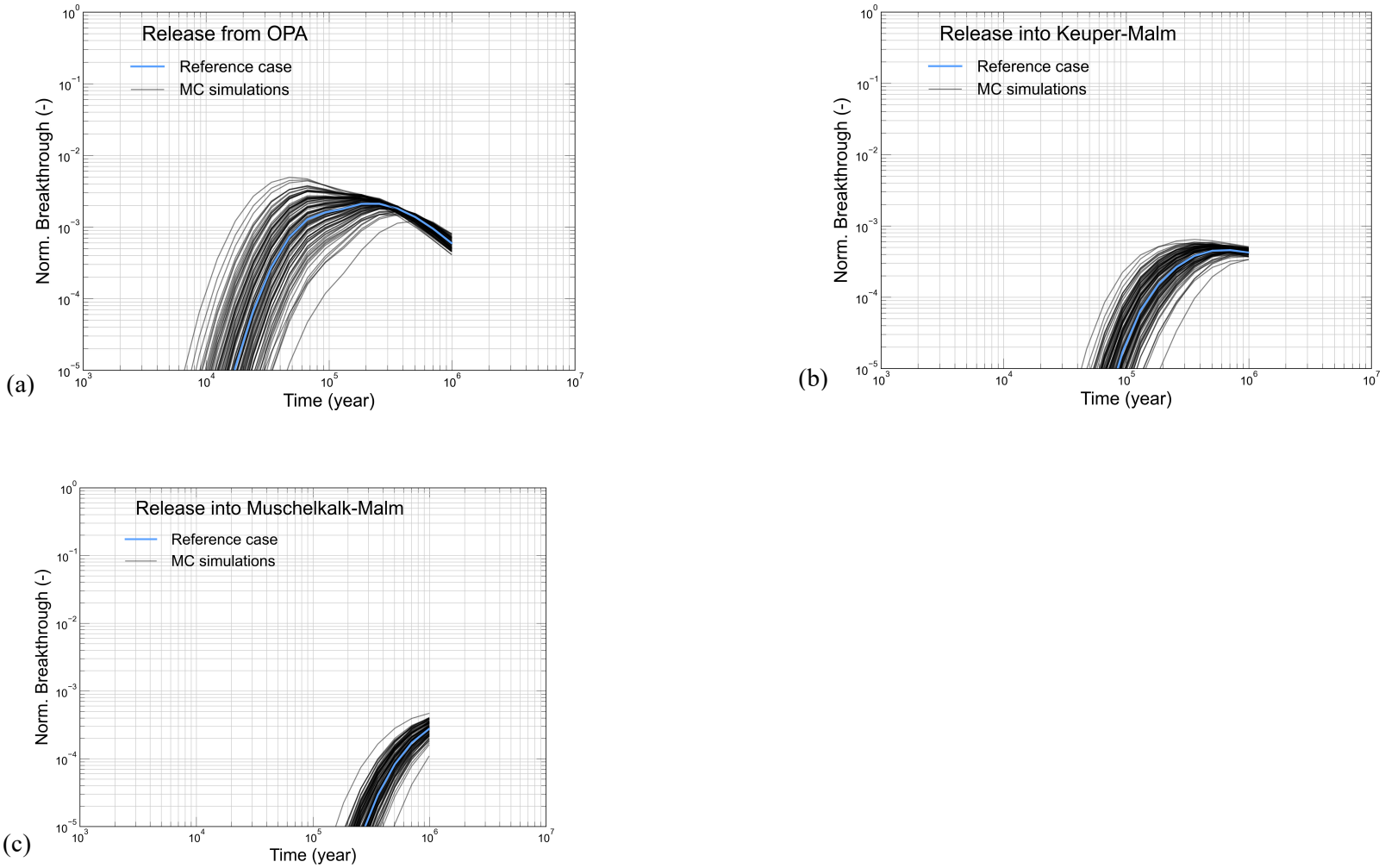

Fig. 7-15: RIEHLW scenario: best estimate and uncertainty ranges of solute tracer (I-129) release
(a) From OPA, (b) into the Keuper and Malm aquifers, (c) into the Muschelkalk and Malm aquifers.

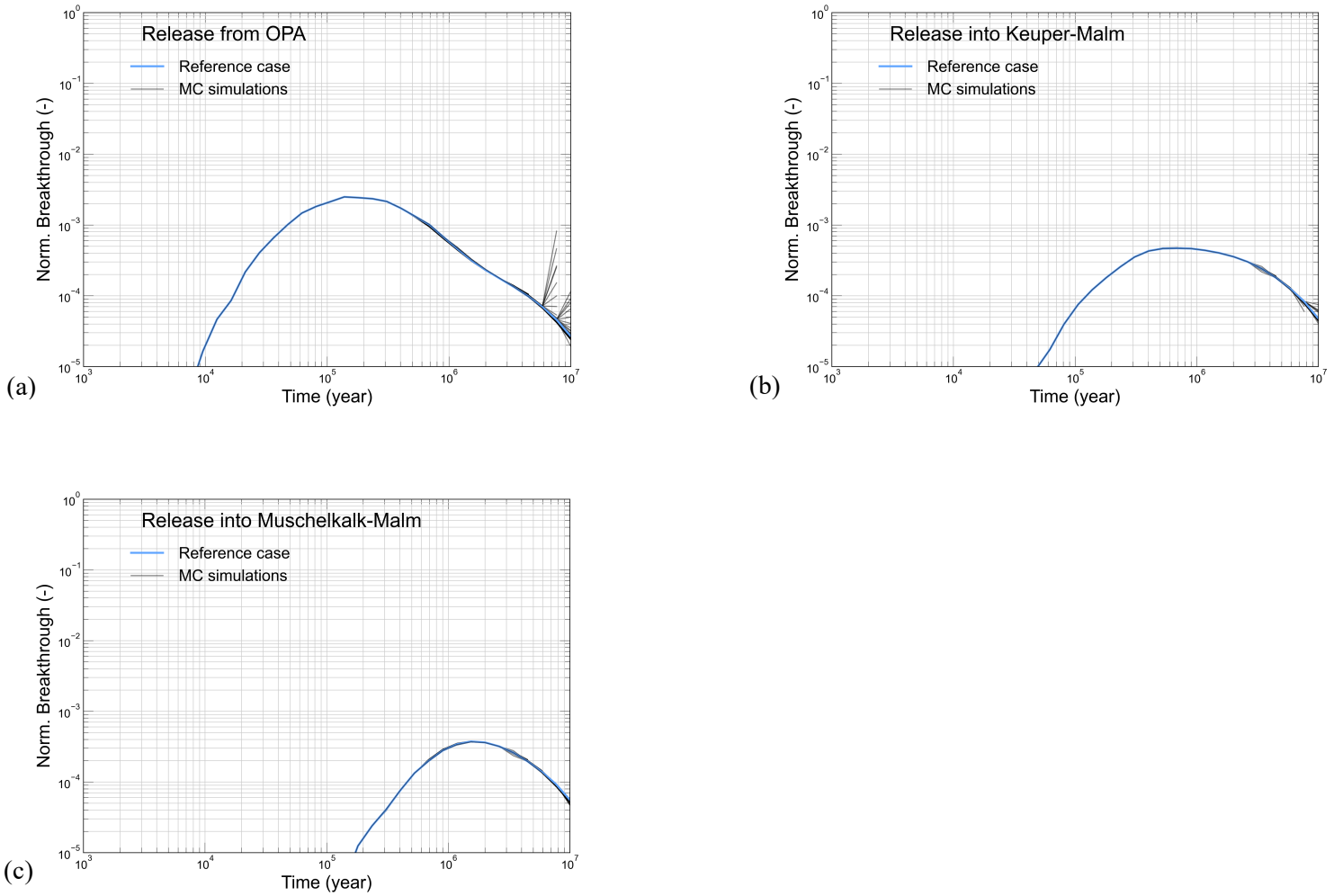

Fig. 7-16: LOSSOB scenario: best estimate and uncertainty ranges of solute tracer (I-129) release
(a) From OPA, (b) into the Keuper and Malm aquifers, (c) into the Muschelkalk and Malm aquifers.

8 Probabilistic model-based analyses – L/ILW

8.1 Expected performance

The probabilistic analysis for the L/ILW disposal area is based on a sample set of 100 simulations using the 2.5D component models described in Section 3.5. The expected performance is simulated with models *2.5D-LILWx1* and *2.5D-V3*. The perturbed parameters and sampling procedure are those described in Section 3.5.6. Three indicators are evaluated for the quantitative assessment for L/ILW, namely gas induced overpressures in the L/ILW nearfield, gas flow rates through the V3, and solute tracer (Cl-36) fluxes through CRZ. The latter is shown in terms of release from OPA, release to Keuper and Malm, and release to Muschelkalk and Malm. The simulated period for gas simulations corresponds to 100,000 years after emplacement. The solute tracer simulations are performed until 1 million years after emplacement. Note that the *2.5D-LILWx1* model version extending to V2-HLW is used for gas simulations, whereas the model version extending to V2-L/ILW is used for solute tracer simulations. The simulated transients are shown in Fig. 8-1 (gas pressures and gas flow rates) and Fig. 8-2 (solute fluxes). In each sub-figure, the so-called base case depicting the expected evolution for the best estimates of input parameters is shown with a blue line. The bandwidth around the reference case corresponds to the 100 samples of input parameters illustrating the parametric uncertainty range. In addition, the pressure lines corresponding to the magnitudes of the principal components of minimum and maximum horizontal strength at the respective observation point are shown for comparison to the simulated nearfield pressures. The failure criteria used for gas-induced effects in the PA and resulting performance margins are documented in Nagra (2024j).

Gas induced overpressure in the L/ILW nearfield (Fig. 8-1a) reaches a peak of ~9.6 MPa after ~70,000 years in the reference case. The probabilistic simulations result in peak pressures between 9 MPa and 10.5 MPa.

The gas fluxes through the V3 and into the shaft (Fig. 8-1a) show gas breakthrough time of ~23,000 years in the reference case and an envelope of breakthrough times between ~6,000 years and 55,000 years in the probabilistic simulations. The maximum rate of gas release corresponds to 5E-03 (kg/a) after 80,000 years in the reference case and remains below 2E-02 (kg/a) in all probabilistic simulations. Note that molecular diffusion, which is not included in this case, would reduce pressure buildup and increase the time until gas breakthrough times from the V3 (see also App. B and App. D).

The normalised solute tracer flux released from the OPA is shown in Fig. 8-2a. The breakthrough reaches after 100,000 years a value that is equivalent to less than 1E-06 of the dose limit. The corresponding release reached after 100,000 years in the probabilistic simulations is below 1E-05. The maximum tracer flux is reached after 400,000 years and corresponds to ~2E-06 of the dose limit. In all probabilistic simulations, the normalised tracer flux released into the Keuper and Malm aquifers (Fig. 8-2b) remains below 1E-08 and 1E-06 of the dose limit after 100,000 and 1 million years, respectively. Finally, the maximum release into the Muschelkalk and Malm (Fig. 8-2c) is practically negligible in comparison to the regulatory limit after 100,000 years and reaches up to 1E-07 after 1 million years.

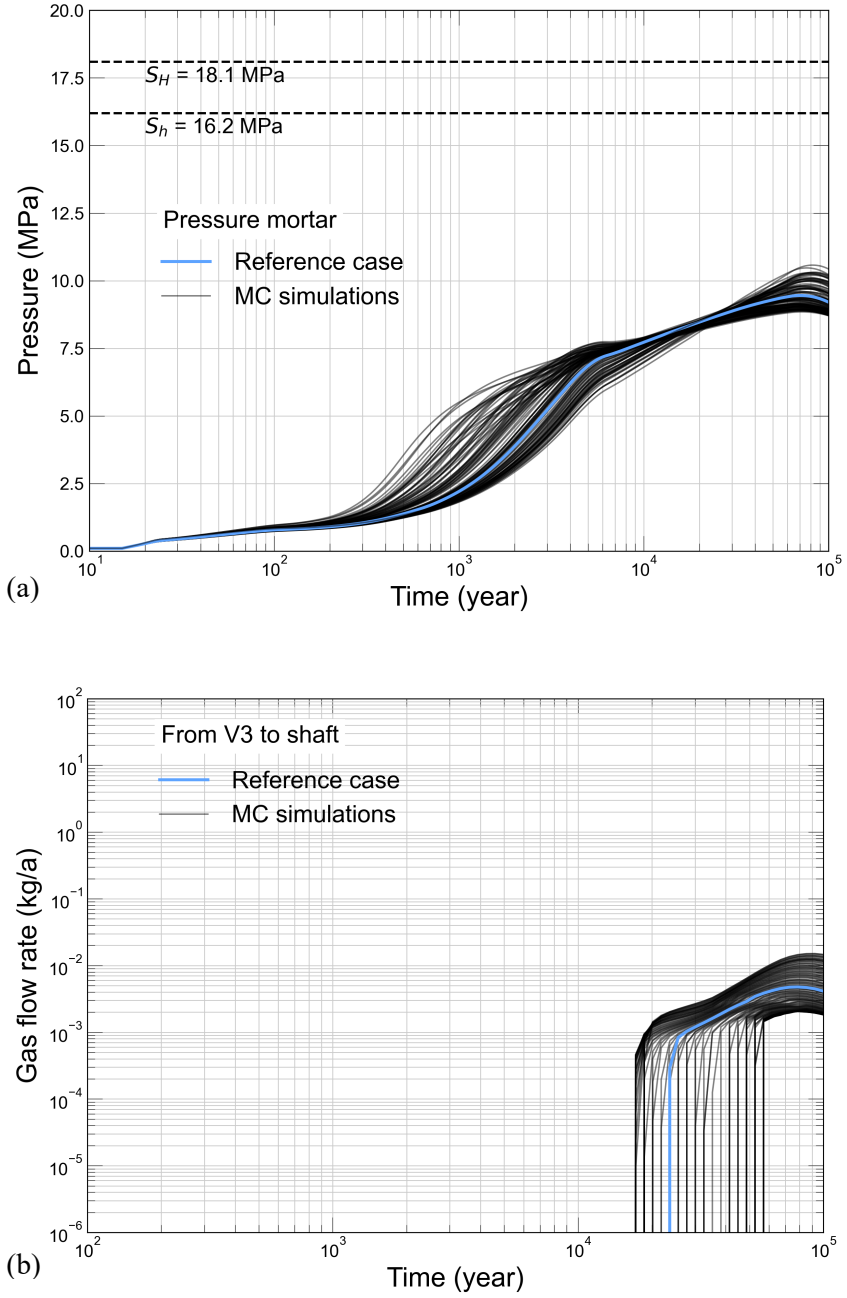

Fig. 8-1: Expected barrier performance L/ILW: best estimate and uncertainty ranges

(a) Gas induced overpressures in the L/ILW nearfield, (b) gas release through the V3 seal.

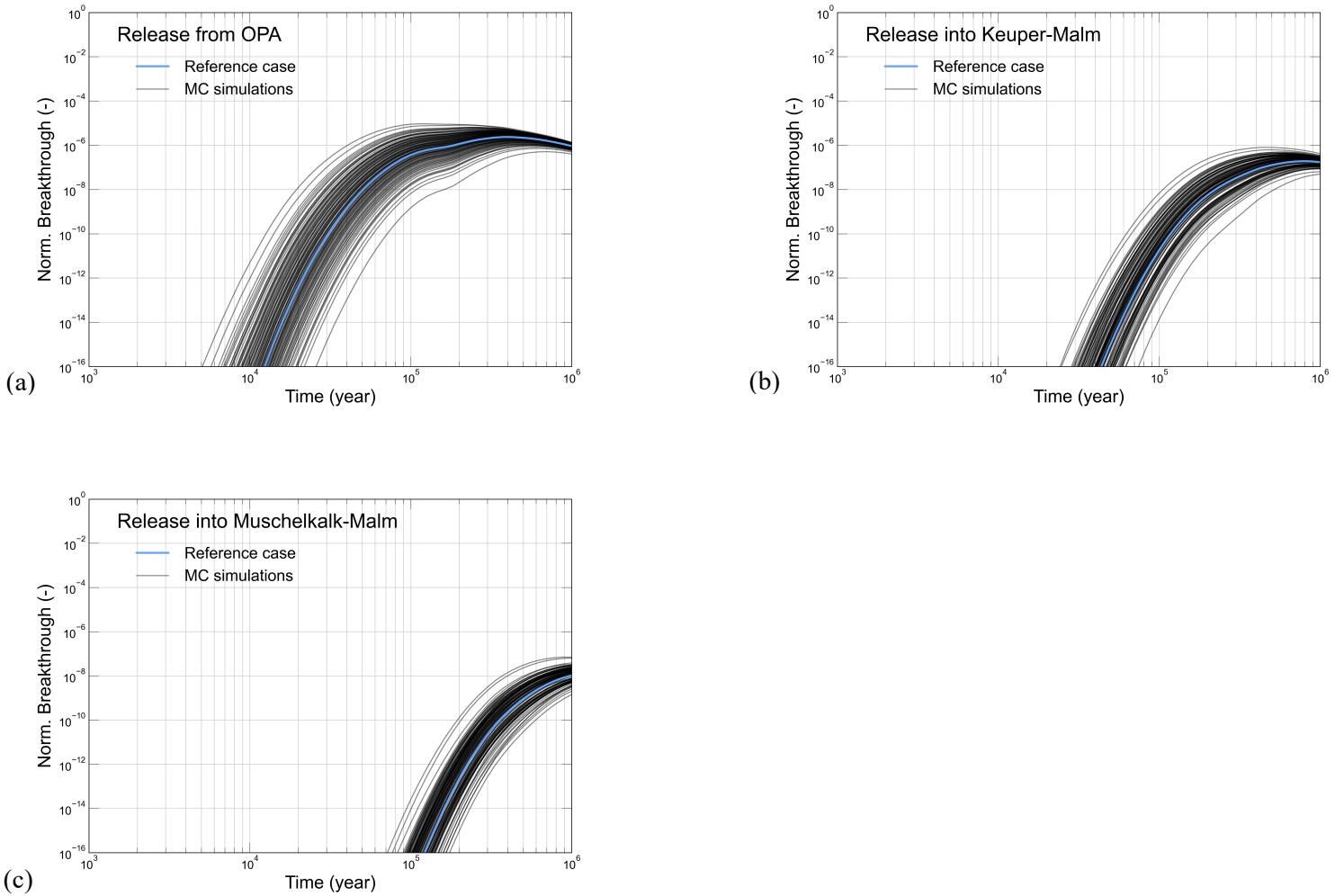

Fig. 8-2: Expected barrier performance L/ILW: best estimate and uncertainty ranges of solute tracer (Cl-36) release
(a) From OPA, (b) into the Keuper and Malm aquifers, (c) into the Muschelkalk and Malm aquifers.

8.2 Deviations

PA scenarios are specified for each barrier component relevant to the L/ILW to evaluate the impact of a reduced performance of the single component on the safety margins of the entire multi-barrier system. Tab. 8-1 presents a set of selected PA scenarios with the associated barrier components. The model results of the respective assessments are discussed in the subsequent paragraphs.

The sealing system comprising the V1-L/ILW, V2-L/ILW and V3 seals is currently designed to mitigate the buildup of gas pressure in the repository (see Chapter 6 and Nagra 2024g) and at the same time retard the release of dissolved and volatile radionuclides along the backfilled repository structures. In particular, the V1-L/ILW and V2-L/ILW seals are gas permeable to allow gas transport from the L/ILW emplacement caverns to the operations tunnels of the L/ILW section and the central area, whereas the V3 seal is gas-tight to limit the release of gas to the overlying shafts (see Chapter 6 and Nagra 2024g). Deterministic cases with deviations from expected performance of the sealing system are provided at the total system level in Chapter 6 and at the component level in Nagra (2024g). The PA scenario V3PERM is examined here to evaluate in a probabilistic manner the impact of a very permeable V3 seal on gas pressure buildup and on gas release to the overlying shaft.

The L/ILW is emplaced within a cement-based nearfield that provides favourable chemical conditions within the L/ILW caverns that retard radionuclides and reduce the gas generation rates from corrosion of metals and degradation of organics. Two PA scenarios, ZEROGAS and PESSGAS, are specified to evaluate deviations from the expected performance of the L/ILW cementitious nearfield as shown in Tab. 8-1. In ZEROGAS it is assumed that gas generation in the L/ILW caverns is negligible. In PESSGAS it is assumed that gas generation in the L/ILW caverns corresponds to the upper bound estimates (see also Fig. 3-12).

The presence of a transmissive fault intersecting the L/ILW repository nearfield can impact the hydraulic evolution of the repository (see Chapter 6) and change the functionality of the multi-barrier system. This is evaluated with the PA scenario FLTLILW that assumes there is a transmissive fault intersecting all L/ILW emplacement caverns near their mouth.

Tab. 8-1: Deviations from expected performance L/ILW – by barrier (component level)

PA scenario description (L/ILW)	Scenario code	Relevant barrier component
Permeable V3	V3PERM	Sealing system
Zero gas generation	ZEROGAS	Cementitious nearfield
Pessimistic gas generation	PESSGAS	
Transmissive fault through L/ILW caverns	FLTLILW	CRZ

8.2.1 Permeable V3 (V3PERM)

In this scenario, the log permeability of the V3 seal is sampled probabilistically from a uniform distribution between -20 (corresponding to value of 1.E-20 m^2 used in the expected performance) and -16 (corresponding to value of 1.E-16 m^2). The capillary strength parameter P_0 is scaled accordingly (see also Nagra 2024g). The rest of the parameters are unchanged from the expected evolution. The results from 100 probabilistic simulations are shown in Fig. 8-3. This scenario is simulated with model *2.5D-V3*. Two indicators are evaluated, namely gas pressure in the L/ILW nearfield and gas flow rates from the V3 to the shaft.

The highest peak pressure in the L/ILW nearfield (Fig. 8-3a) corresponds to the base case (which is the same as the expected evolution, see Fig. 8-1) as it is the simulation with the lowest permeability for the V3. In the probabilistic simulations, that adopt higher permeability values for the V3, lower peak pressures are overall combined with higher pressures between ~1,000 and ~40,000 years owing to porewater inflow through the permeable V3 that limits the amount of pore volumes available for gas storage (see also scenarios “high-permeable V3” and “high-permeable V3 and V2-L/ILW seals” in Section 6.2.2).

The gas flow rates through the V3, shown in (Fig. 8-3b), show gas breakthrough after ~23,000 years in the reference case (as in the expected evolution) with a range between ~6,000 years and 30,000 years in the probabilistic simulations associated with the increased permeability of the V3. The maximum rate of gas release in the probabilistic simulations reaches up to 2E+01 (kg/a).

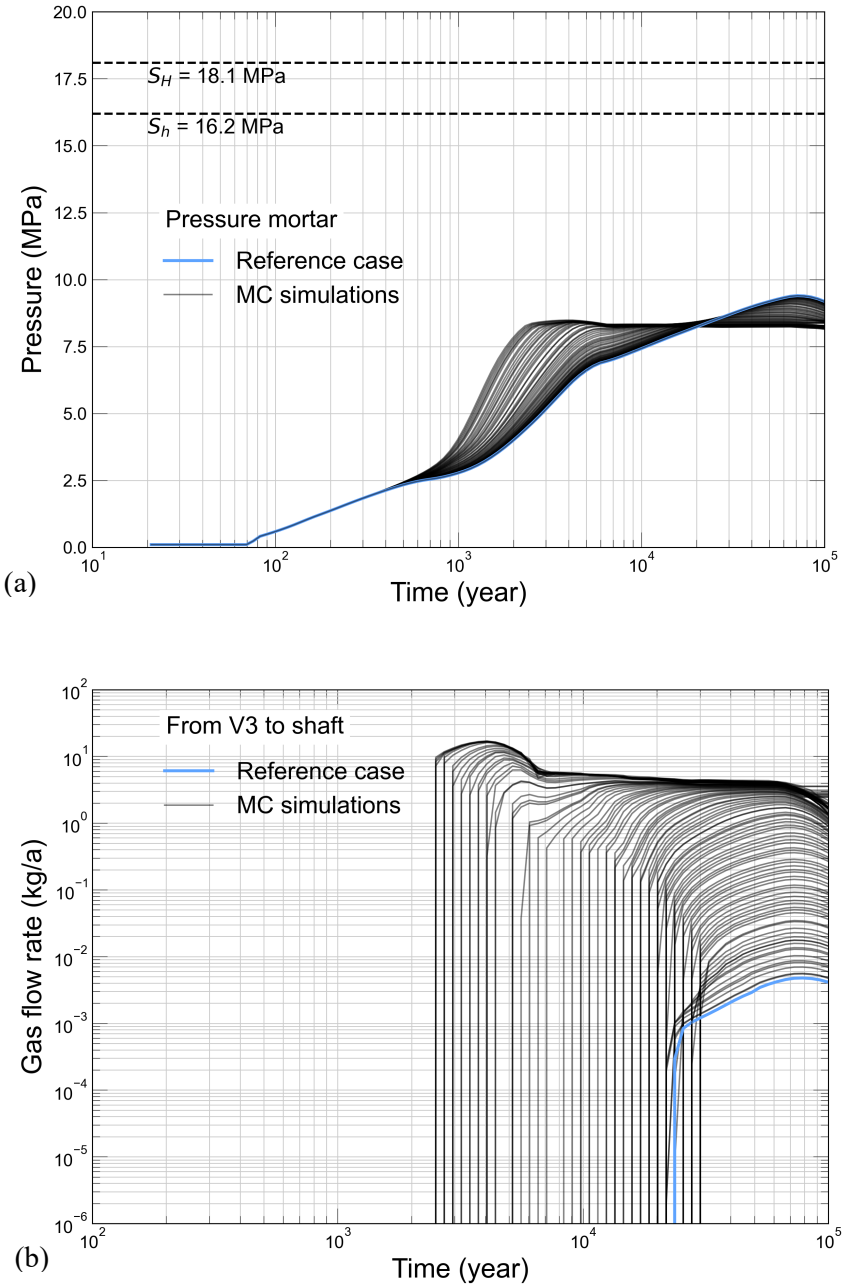

Fig. 8-3: V3PERM scenario: best estimate and uncertainty ranges

(a) Gas induced overpressures in the L/ILW nearfield, (b) gas release through the V3 seal.

8.2.2 No gas generation (ZEROGAS)

If there is no gas generated in the L/ILW caverns, or if the rate of gas generation is very low and all gas is dissolved in porewater, the impact on the nearfield evolution is twofold. First, there are no gas-induced overpressures in the L/ILW section, or they are negligible. This effect is discussed in detail in Nagra (2024g). Second, the water saturation in the L/ILW nearfield increases, which may impact the transport of soluble radionuclides to the surrounding rock. This is evaluated with a probabilistic simulation of solute tracer transport through the CRZ. The scenario is simulated with model *2.5D-LILWx1*.

The normalised solute tracer flux released from the OPA is shown in Fig. 8-4a. The fluxes reached in the reference case correspond to ~1E-06 (-) and ~1E-05 (-) of the dose limit after 100,000 and 300,000 years, respectively. These are slightly higher than in the expected performance (shown in Fig. 8-2a). The normalised tracer releases into the Keuper and Malm aquifers (Fig. 8-4b) and into the Muschelkalk and Malm aquifers (Fig. 8-4c) do not show any appreciable changes from the expected evolution (Fig. 8-2a;b).

8.2.3 Pessimistic gas generation (PESSGAS)

In this scenario gas generation rates in the L/ILW caverns are set equal to the upper bound values (see Fig. 3-12). The probabilistic simulations are used to evaluate the impact on gas-induced over-pressures and solute tracer release. This scenario is simulated with model *2.5D-LILWx1*.

Gas induced pressures in the L/ILW nearfield, shown in Fig. 8-5a, reach a peak of ~10 MPa after ~20,000 years in the reference case. The probabilistic simulations result in a range of peak pressures between 9 MPa and 11.3 MPa.

The normalised solute tracer fluxed released from the OPA, shown in Fig. 8-6a, reach a maximum of less than 1E-07 (-) and 1E-05 (-) of the dose limit after 100,000 and 400,000 years, respectively. These lie approximately 1 order of magnitude below the maximum reached in the expected performance (shown in Fig. 8-2a). The normalised tracer releases into the Keuper and Malm aquifers (Fig. 8-6b) and into the Muschelkalk and Malm aquifers (Fig. 8-6c) are somewhat decreased compared to the expected performance (Fig. 8-2a;b) and remain several orders of magnitude below the regulatory limit.

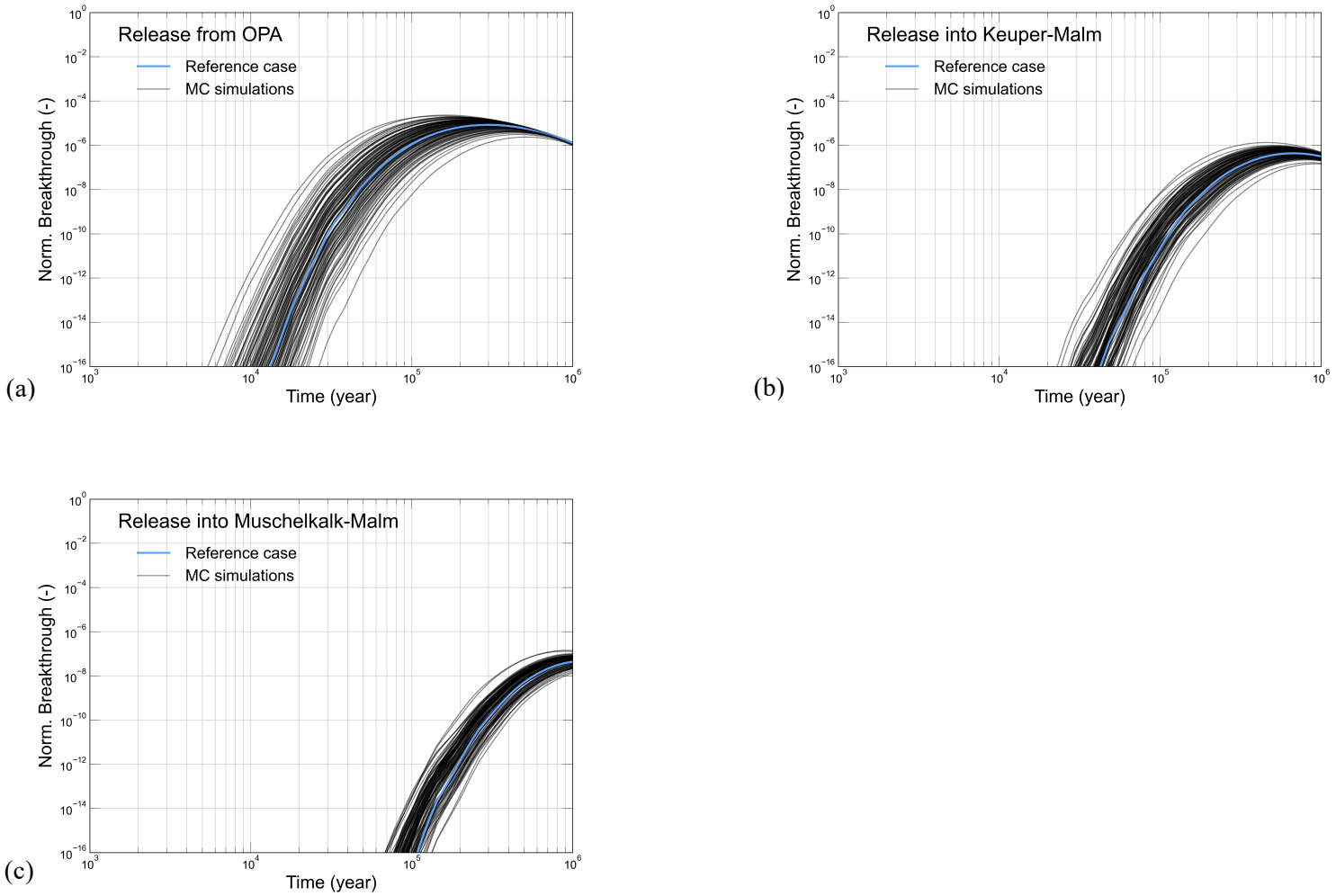

Fig. 8-4: ZEROGAS scenario: best estimate and uncertainty ranges of solute tracer (Cl-36) release
(a) From OPA, (b) into the Keuper and Malm aquifers, (c) into the Muschelkalk and Malm aquifers.

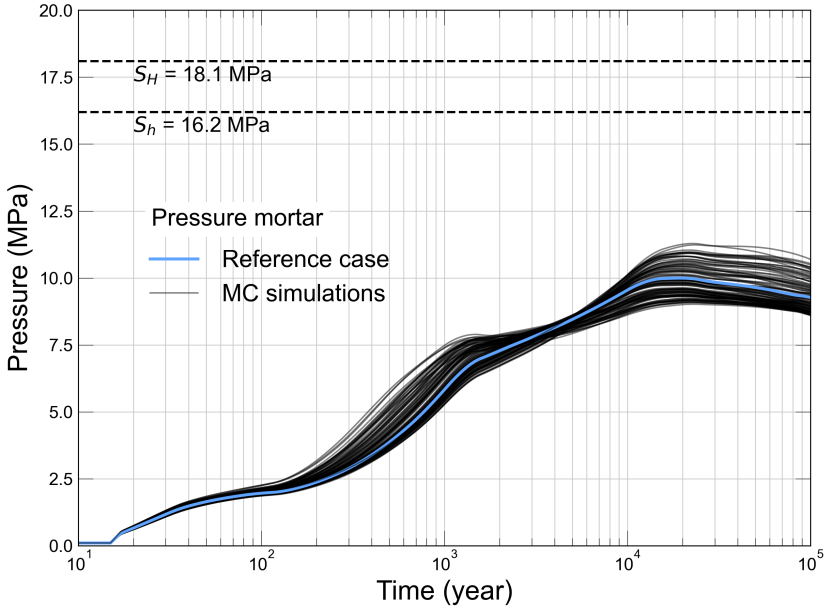

Fig. 8-5: PESSGAS scenario: best estimate and uncertainty ranges of gas induced pressures in the L/ILW nearfield

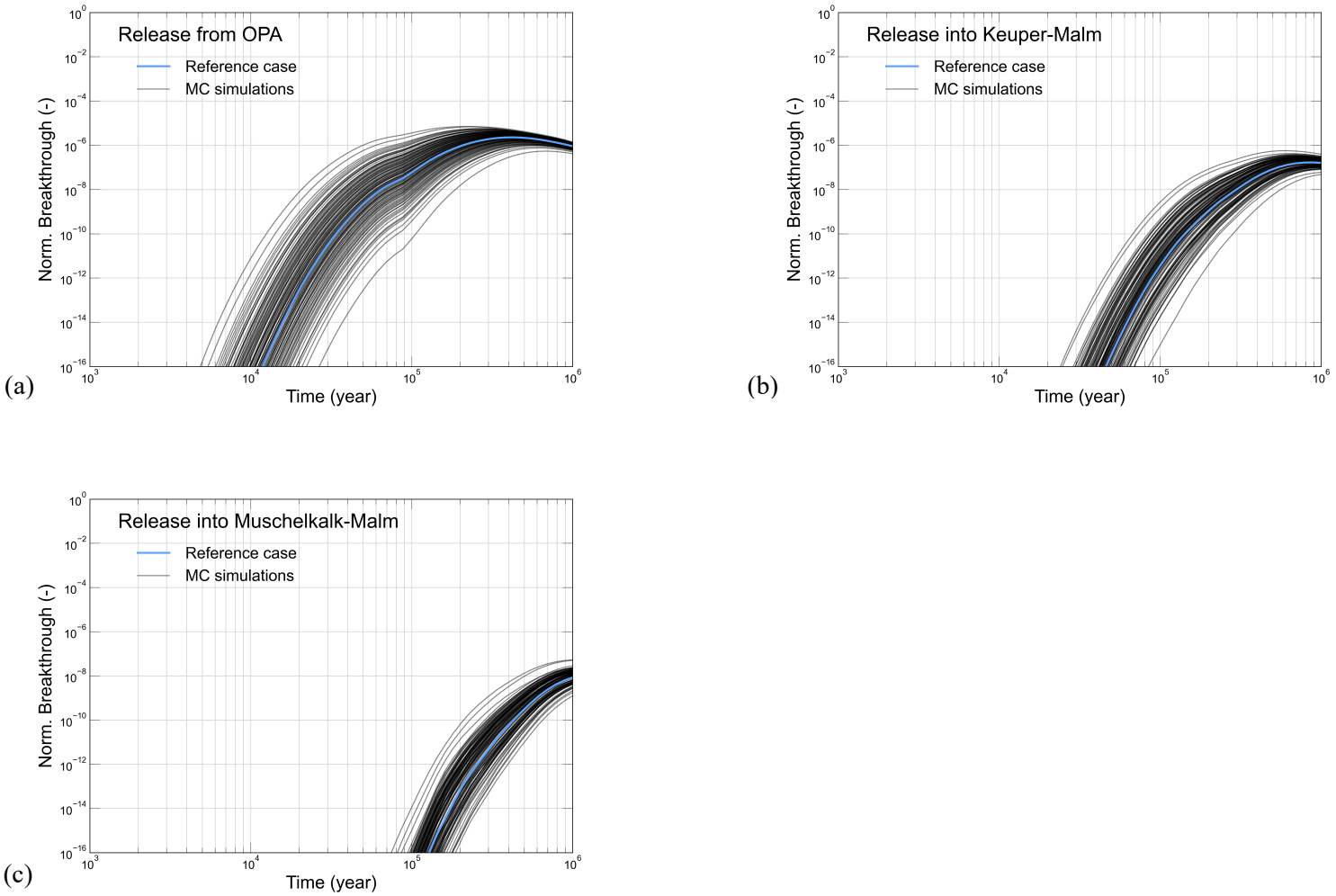

Fig. 8-6: PESSGAS scenario: best estimate and uncertainty ranges of solute tracer (Cl-36) release
(a) From OPA, (b) into the Keuper and Malm aquifers, (c) into the Muschelkalk and Malm aquifers.

8.2.4 Fault through L/ILW caverns (FLTILW)

This scenario assumes that the fault intersecting the L/ILW caverns has a transmissivity of 1.E-10 m^2/s. The best estimate gas generation rates are applied to the caverns (Fig. 3-12). Pore pressure conditions in the regional aquifer systems (Malm and Muschelkalk aquifers) are hydrostatic. In general, the presence of the transmissive fault can impact gas pressure buildup and radionuclide transport through the CRZ. Regarding the first, gas overpressures are mitigated due to depressurisation through the fault when a pressure gradient develops from the repository to the confining units, as shown in the simulations discussed in Section 6.2. The impact on solutes transport through the CRZ is evaluated here with a probabilistic simulation. This scenario is simulated with model *2.5D-LILWx1*. Note that the model version that accounts for operations tunnel up to the V2-L/ILW seal is used here. In comparison to the 3D repository model, or the 2.5D model extending to the V2-HLW seal, this introduces faster resaturation of the L/ILW caverns (see also Chapter 4).

The normalised solute tracer flux released from the OPA is shown in Fig. 8-7a. Tracer fluxes in the early post-closure phase (e.g., first 10,000 years) are overall increased compared to those in the expected performance (Fig. 8-2a) due to the more transmissive path for tracer transport provided by the fault. The fluxes, however, remain several orders of magnitude below the regulatory limit and the maximum values reached after 100,000 years are similar to those in the expected performance (Fig. 8-2a). Notably, the added release through the fault is insignificant after near-hydrostatic conditions are reached in the repository (see also Section 6.2). The effect on normalised tracer flux released into the Keuper and Malm aquifers (Fig. 8-7b) is similar, with increased values obtained in the first few tens of thousands of years that, however, do not exceed the maximum fluxes of the expected performance (Fig. 8-2b). The normalised tracer flux released into the Muschelkalk and Malm aquifers (Fig. 8-7c) is higher compared to the expected performance but remains practically negligible in comparison to the regulatory limit.

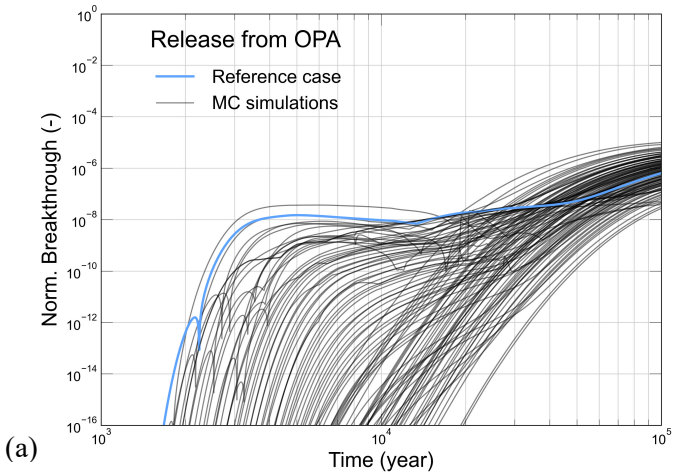

(a)

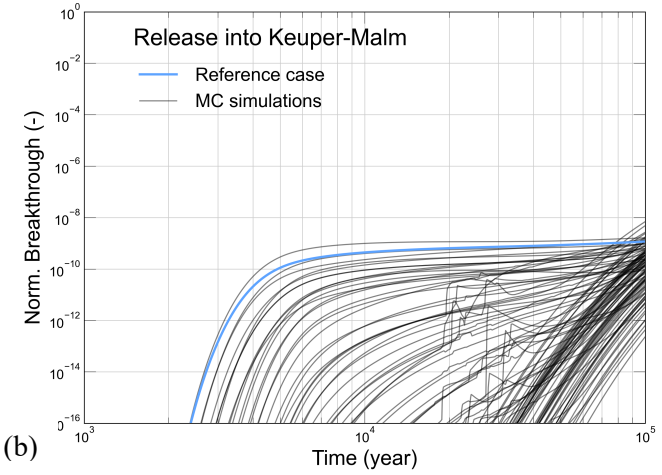

(b)

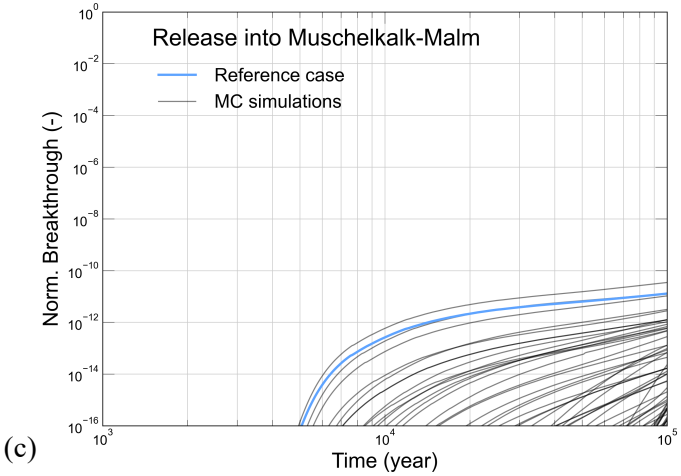

(c)

Fig. 8-7: FLTLILW scenario: best estimate and uncertainty ranges of solute tracer (Cl-36) release

(a) From OPA, (b) into the Keuper and Malm aquifers, (c) into the Muschelkalk and Malm aquifers.

9 Summary and conclusions

The present report builds upon the understanding of the thermo-hydraulic evolution of the repository, elaborated in Nagra (2024g), to take the next step in the PA: the implementation of a robust modelling workflow and the delivery of model-based analyses to the PA synthesis. This is done for the repository as a total system, which includes the disposal areas, access structures, sealing sections, and surrounding rock, as well as focused on HLW and L/ILW, respectively. In particular, this report aims to accomplish four objectives:

- *Obj1*: provide a comprehensive outline of numerical models used in the PA, including the input data, the configuration of each model, the model outputs evaluated in each model, and the links between models in the modelling chain.
- *Obj2*: describe in a comprehensive manner the abstraction methodology that encompasses the treatment of conceptual uncertainty, the justification of choices and conservatism in model implementations, and model benchmarking.
- *Obj3*: give an overview of the modelling workflow implemented for the model-based assessments including the role of each model.
- *Obj4*: provide documentation and comprehensive overview of the deterministic modelling performed for the total system as well as the probabilistic modelling performed for HLW and L/ILW, respectively.

The report structure follows these objectives accordingly: Chapter 3 gives the portfolio of models used in the PA; Chapter 4 presents the model abstraction methodology; Chapter 5 describes the modelling workflow implementation for the PA; and finally Chapters 6, 7, and 8 the model-based assessments performed for the total system, the HLW, and the L/ILW, respectively. The modelling results presented here feed into Nagra (2024j) which provides the quantitative synthesis and assessment with regards to safety functions and the associated performance margins.

The PA model chain encompasses models with different levels of detail, implemented on different spatial scales of interest (Chapter 3). Based on this, the numerical models are categorised into (i) 3D site models, (ii) 3D repository and component models for deterministic assessments, (iii) 2D/2.5D component models for probabilistic assessments, and (iv) 2D process models. The latter category supports the model validation and verification (Nagra 2024j) but is not used directly for the indicator-based assessments and is therefore not addressed in detail in this report. Each model of the first three categories, and the indicators it associates with, is tailored based on its intended use in the PA modelling workflow. The top to bottom implementation of the model chain provides consistency across scales with increasing level of detail as needed. A summary of the numerical models used for the assessments is given in Tab. 9-1.

A key objective therein is to disregard unnecessary detail without impairing the appropriateness of the model (Chapter 4). This involves making assumptions and approximations in terms of (i) geometrical representations, (ii) phenomena and processes, (iii) averaging and homogenising of material properties, and (iv) boundary conditions, initial conditions and source terms. In the PA framework, these are treated as sources of conceptual uncertainty (Nagra 2024j). Extensive benchmarking within the model chain is performed to evaluate these uncertainties and make reasonably conservative choices in the PA model implementation. A summary of selected benchmarking examples within the PA model chain is shown in Tab. 9-2, namely for the expected performance and for scenarios of UB gas generation, impermeable V2-L/ILW seals, and UB heat generation. Differences in model results are therein acceptable and shown to be traceable and justifiable with the abstractions adopted in each case. On the other hand, parametric uncertainty is accounted for by means of deterministic and probabilistic sampling of material parameters used as model input at the respective level of abstraction.

Tab. 9-1: Overview of chain of numerical models used in the model-based assessments

Model	**Emplacement rooms represented**	**Stratigraphy considered**	**Model size (# elements)**	**Transport problem**	**Type of assessment**
3D site	None	Permo-Carboniferous to Tertiary	77,000	Water, heat	Deterministic
3D repository	7×L/ILW 20×HLW 1×Pilot L/ILW 1×Pilot HLW	Permo-Carboniferous to Tertiary	437,000	Water, gas, volatile tracer, heat	Deterministic
3D L/ILW cavern & V1-L/ILW[1]	1×L/ILW	Opalinus Clay	189,000	Water, gas	Deterministic
3D HLW drift & V1-HLW	1×HLW	Opalinus Clay (Permo-Carboniferous to Tertiary in 1D)	154,000	Water, gas, heat	Deterministic
3D V2-L/ILW	None	Argillaceous Lias to Malm	51,000	Water, gas	Deterministic
3D V3	None	Argillaceous Lias to Malm	134,000	Water, gas	Deterministic
2.5D L/ILW caverns[1] *[2.5D-L/ILW×7]*	7×L/ILW	Permo-Carboniferous to Tertiary	39,000	Water, solute tracer, gas	Probabilistic
2.5D L/ILW cavern[1] *[2.5D-L/ILW×1]*	1×L/ILW	Permo-Carboniferous to Tertiary	6,000	Water, solute tracer, gas	Probabilistic
2.5D L/ILW cavern & V3 *[2.5D V3]*	1×L/ILW	Permo-Carboniferous to Tertiary	10,000	Water, solute tracer, gas	Probabilistic
2.5D HLW drifts *[2D-HLW×20]*	20×HLW	Permo-Carboniferous to Tertiary	66,000	Water, solute tracer, gas, heat	Probabilistic
2D HLW drifts *[2.5D-HLW×20]*	20×HLW	Permo-Carboniferous to Tertiary	28,000	Water, solute tracer, gas, heat	Probabilistic

[1] Two model variants with operations tunnel extending to V2-L/ILW and V2-HLW, respectively. Variant up to V2-L/ILW shown here.

Tab. 9-2: Selected examples of benchmarking within the PA model chain

Indicator	3D repository	3D L/ILW	2.5D L/ILW, L/ILW & V3	3D HLW	2D, 2.5D HLW
Expected performance					
$t_{hydrostatic}$ (ka)	L/ILW: 20 HLW: 2	20	20	0.7[5]	0.2
$t_{Pmax, heat}$ (ka)[1]	HLW: 0.2	-	-	0.15[5]	0.1
$t_{Pmax, gas}$ (ka)	L/ILW: 70 HLW: 115	70	70	115[5]	115
$t_{gas\ V3\ to\ shaft}$	L/ILW: 42[6] >100[7]	-	23[6]	-	-
$P_{max, heat}$ (MPa)[1]	HLW: 13	-	-	12.3[5]	12.6
$P_{max, gas}$ (MPa)	L/ILW: 9.3 HLW: 11.8	8.9	9.6	12.0[5]	11.6
UB gas generation					
$t_{hydrostatic}$ (ka)	L/ILW: 12 HLW: 2	1[2]	7	0.3[3,4]	0.25
$t_{Pmax, gas}$ (ka)	L/ILW: 70 HLW: 25	12[2]	20	25[3,4]	25
$t_{gas\ V3\ to\ shaft}$	L/ILW: 16[6]	-	-	-	-
$P_{max, gas}$ (MPa)	L/ILW: 9.7 HLW: 14.4[3]	11.7[2]	10.0	15.0[3,4]	14.2[3]
Impermeable V2-L/ILW					
$t_{hydrostatic}$ (ka)	L/ILW: 4	4	3	-	-
$t_{Pmax, gas}$ (ka)	L/ILW: 70	70	70	-	-
$P_{max, gas}$ (MPa)	L/ILW: 10.5	10.1	11	-	-
UB heat generation					
$t_{hydrostatic}$ (ka)	-	-	-	0.2	0.2
$t_{Pmax, heat}$ (ka)[1]	-	-	-	0.2	0.7
$P_{max, heat}$ (MPa)[1]	-	-	-	13.5	13.5

[1] In the OPA at 20 – 30 m above the HLW disposal area (depending on discretisation).
[2] Combined with impermeable V2-L/ILW seal.
[3] Pressure at the time when all canisters corrode entirely and simultaneously.
[4] Combined with UB heat generation (PWR-MOX).
[5] Only BWR canisters.
[6] Not taking account the diffusion of gas.
[7] Taking into account the diffusion of gas.

Modelling of the total system is performed deterministically using the 3D model of the entire repository (Chapter 6). Preceding this is the quantitative description of the hydraulic evolution, including more detailed appraisals of individual repository components, namely emplacement rooms and sealing sections, provided in Nagra (2024g). The expected performance corresponds to the evolution of the “as-designed” repository based on the current exemplified repository

project and associated provisional design. Two distinct phases are discerned after closure of the repository. The first phase coincides with the early-post closure phase (hundreds of years) and is marked by the development of a thermal pulse around the HLW disposal area from the heat released by the waste. The second phase coincides with the late post-closure phase (thousands to tens of thousands of years) and is marked by the accumulation of gas in the L/ILW and HLW repository sections. The associated transport regimes and key mechanisms are described in detail in Nagra (2024g). The total system analysis in the present report shows that pressure perturbations and water expulsion in the rest of the repository (i.e., outside the HLW disposal area) due to thermal effects in the HLW nearfield is very limited. Similarly, axial gas transport through the tunnels in the HLW section is very limited due to the low permeability of the bentonite buffer, and gas generated by the HLW dissipates through radial transport and dissolution (see also Nagra 2024g and Nagra 2024j). On the other hand, a key feature of the provisional design in the L/ILW repository section is the axial transport of gas along the repository structures which provides more storage volume for gas and, accordingly, more interface for gas dissolution to the surrounding rock (see also Nagra 2024g and Nagra 2024j). In Nagra (2024g) it is demonstrated that a connected path for gas transport along the roof of the repository tunnels and sealing sections in the L/ILW section is maintained for several tens of thousands of years. At the same time, expulsion of water along the tunnels in the L/ILW repository section is limited, and its cumulative effect is negligible in comparison to the storage volume available in the access and operation structures of the repository.

The analysis of the total system expected performance with regards to gas (for refined description of the TH behaviour see Nagra 2024g and Section 6.1 of this report) is summarised in the pie charts of Fig. 9-1. The distribution of gas generated by HLW and L/ILW, whether in gaseous or liquid form, is illustrated in terms of percentage stored in different domains of the repository nearfield at selected times in the post-closure phase. Each slice in the pie charts depicts percentage in a domain, namely (i) OPA (including EDZ), (ii) aquifers and shafts (excluding V3), (iii) confining units (CRZ excluding OPA), (iv) L/ILW section up to V2-L/ILW seal (including pilot), (v) HLW section up to V2-HLW seal (including pilot), and (vi) tunnels between V2-L/ILW and V2-HLW (excluding shafts above V3). Slices measuring less than 0.1% are omitted from the pie charts for practical reasons. The results show that gas generated by HLW is initially stored within the HLW section of the repository (mostly dissolved in the bentonite of the HLW drifts) but then dissipates in the OPA porewater so that gradually the percentage of gas stored in the host rock exceeds significantly that stored in the repository structures. After 50,000 years almost all the HLW-generated gas (~98%) is stored within the host rock. After 100,000 years, a small amount of the HLW-generated gas (~3%) has reached the upper confining unit, dissolved in porewater (see also App. B). On the other hand, gas generated by the L/ILW is predominantly stored within the repository in the first few thousands of years (namely ~85% of L/ILW-generated gas during the first 10,000 years). After an initial phase of gas storage in the L/ILW section of the repository, gas is increasingly stored in the central area of the repository up to the V2-HLW seal (~46% and 71% after 1,000 and 10,000 years, respectively). At later times, this percentage reduces as more gas is gradually dissolved and stored in the OPA (~32% and 44% after 50,000 and 100,000 years, respectively).

The mass balance of gas generated and stored in the repository nearfield after 100,000 years is shown in Fig. 9-2. The inner circle shows the amount of gas generated by HLW (~1.9E06 kg respectively ~2.3E07 m^3[SATP]) and by L/ILW (~1.2E06 kg respectively ~1.5E07 m^3[SATP]), respectively. The outer circle shows that ~2.4E06 kg, or ~77% of total gas generated in the repository, is stored in the geological barriers (which includes the EDZ) whereas ~0.7E06 kg, or ~23% of total gas generated in the repository, is stored in the engineered barriers. The middle circle shows a breakdown of HLW-generated and L/ILW-generated gas in engineered and geological barriers, respectively. Out of the ~2.4E06 kg that is stored in the geological barriers ~60% comes from HLW and 17% comes from L/ILW. The ~0.7E06 kg remaining in the

engineered barriers after 100,000 years mostly comes from L/ILW. Roughly 80% of the ~2.4E06 kg stored in the geological barriers is dissolved in porewater with the remaining 20% in gaseous phase (not shown in the figure).

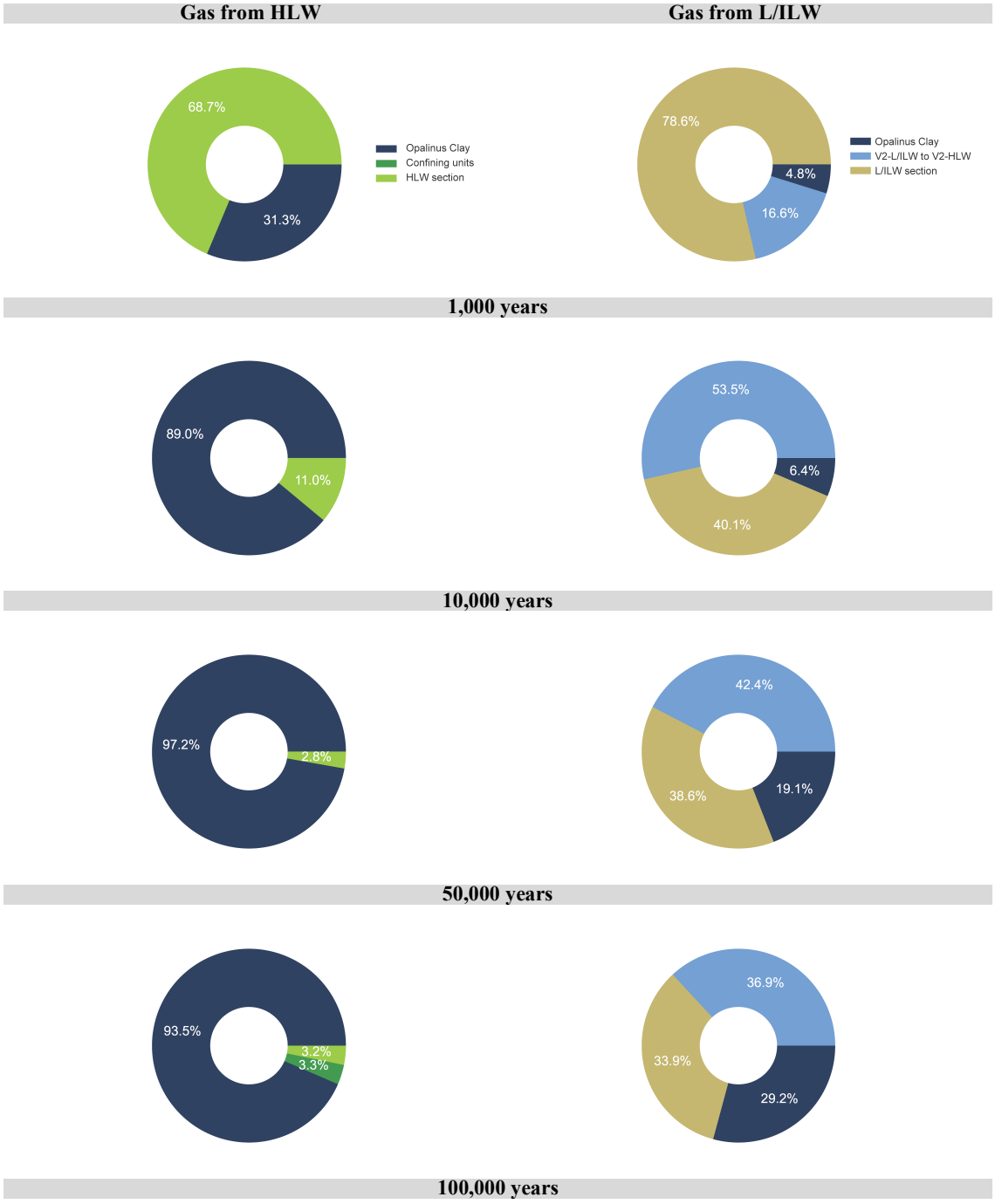

Fig. 9-1: Total system, expected evolution: distribution of gas generated from HLW (left) and from L/ILW (right) at different times

% of H_2 generated until the respective time, stored in gas phase or dissolved in OPA (including EDZ); aquifers and shafts (excluding V3); confining units (CRZ excluding OPA); L/ILW section up to V2-L/ILW seal (including pilot); HLW section up to V2-HLW seal (including pilot); tunnels between V2-L/ILW and V2-HLW (excluding shafts above V3).

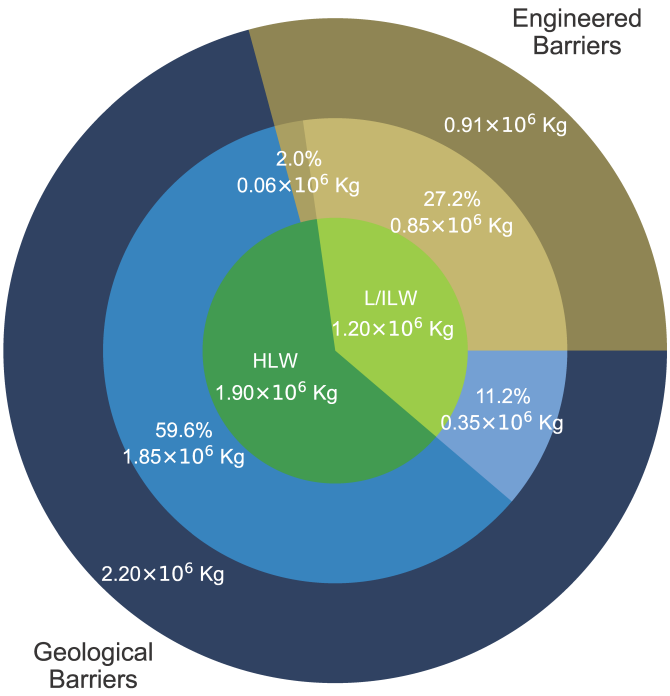

Fig. 9-2: Total system, expected evolution: storage of waste-generated gas mass after 100,000 years

Inner circle: amount of gas generated from HLW (1.90E6 kg) and L/ILW (1.20E6 kg); Middle circle: amount of gas generated from HLW stored in geological barriers (1.86E6 kg) and in engineered barriers 0.05E6 kg); amount of gas generated from L/ILW stored in geological barriers (0.53E6 kg) and in engineered barriers (0.67E6 kg); Outer circle: amount of gas generated in the repository (HLW and L/ILW) stored in geological barriers (2.39E6 kg) and in engineered barriers (0.72E6 kg).

For the total system analysis, deviations from expected performance are formulated in terms of deterministic scenarios. These include two scenarios related to thermal effects associated with the heat source of the HLW, two scenarios related to the gas generation rates, two scenarios with faults through the L/ILW caverns and through the central area, one scenario related to the initial saturation state of the repository, and nine scenarios related to the properties of the seals. Refined perspectives on the scale of individual components and additional scenarios are presented in Nagra (2024g). Both scenarios examined here related to thermal effects show that there are no thermal interactions between the HLW and L/ILW repository sections even for extremely conservative assumptions related to the heat source from HLW. Similarly, all scenarios result in negligible flows into the disposal areas, moderate overpressures in the central area of the repository, and accordingly no hydraulic interactions were identified between the HLW and L/ILW disposal areas.

The permeabilities of the seals determine how fast gas and water can migrate from one repository section to another. All variants with increased permeabilities compared to the expected performance result in a very effective transport path for gas from the L/ILW caverns to the adjacent repository structures. On the other hand, low seal permeabilities may limit the volume that is readily available for gas storage and therefore increase gas pressure (Nagra 2024g). Note that the capillary strength assigned to the sealing sections is scaled with their permeability in all scenarios. A cross-plot comparing the maximum overpressures (calculated as peak pressure minus hydrostatic pressure) observed in the repository to permeabilities assigned to the V2-L/ILW and the V3

seals is shown in Fig. 9-3. Note that only cases with the same rate of gas generation (e.g., the best estimate rates) are shown in the comparison. The expected evolution and four additional cases (two cases with faults, one case without V1 seals, and one case with low-permeable V1-L/ILW seals) with the reference permeability value of 5.E-18 m^2 for the V2-L/ILW seal result in similar overpressures in the range of ~0.7 to 1.2 MPa. Further increase of the permeability of the V2-L/ILW (including a case where the V2-L/ILW seals are replaced by the same backfill material used for the rest of the operation tunnels) does not result in lower overpressures, indicating that this is the range of overpressures reached when the central area is accessible to gas generated by the L/ILW. Notably, the scenarios with porewater ingress from faults into the repository structures do not compromise this functionality of the repository in the cases examined in the present report, and no additional overpressure was observed. Decreasing the permeability of the V2-L/ILW below 1.E-18 m^2 results in increasing overpressures, namely to 1.3 MPa and 2.1 MPa for permeability of 1.E-19 m^2 and 1.E-22 m^2, respectively (the latter being regarded as impermeable V2-L/ILW seals). The opposite effect is observed with regards to the permeability of the V3 seal. All cases with V3 permeabilities lower than 1.E-18 m^2 (including the expected evolution) do not have any appreciable effect on gas pressure in the repository. Reducing the V3 permeability to 1.E-22 m^2 (regarded as impermeable V3 seals) did not introduce additional overpressure in the repository. This indicates that the overpressure of 0.8 MPa is associated with an effective sealing function of the V3 for gas; in other words, gas release through the shaft is not required to limit gas pressure to that level. The overpressure of 0.8 MPa in the repository is reduced once the shaft permeability increases above ~1.E-18 m^2 and therewith releases gas to the shaft.

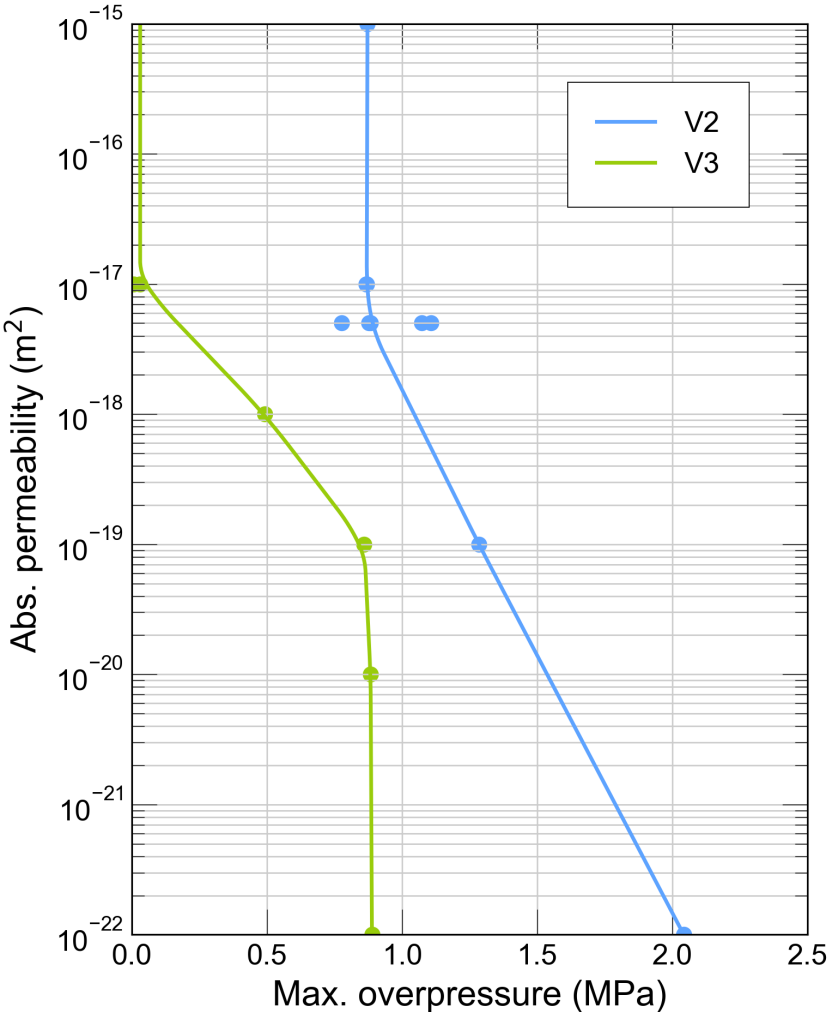

Fig. 9-3: Total system, deviation scenarios: correlation between maximum overpressure (calculated as peak pressure minus hydrostatic pressure) and permeability of V2-L/ILW seals (blue) and V3 seals (green)

Following scenarios are shown as V2-L/ILW variants:
K = 1E-15 m^2: "no V2 seals" (App. B);
K = 1E-17 m^2: "permeable V2 seals", "permeable V2, V1 seals" (Chapter 6);
K = 5E-18 m^2: EXPERF, "fault through EUU", "fault through L/ILW", "no V1 seals", "low-permeable V1-L/ILW seals" (Chapter 6, App. B);
K = 1E-19 m^2: "low-permeable V2 seals" (Chapter 6, also discussed in Nagra (2024g);
K = 1E-22 m^2: "impermeable V2-L/ILW seals" (App. B).

Following scenarios are shown as V3 variants:

K = 1E-17 m^2: "high-permeable V3 seals (var. 2)", "high-permeable V3 and V2-L/ILW seals" (Chapter 6);
K=1E-18 m^2: not documented in this report;
K=1E-19 m^2: "high-permeable V3 seals (var. 1)" (Chapter 6, also discussed in Nagra (2024g);
K=1E-20 m^2: expected performance (Chapter 6);
K=1E-22 m^2: "impermeable V3 seals" (App. B).

Dedicated modelling for the HLW disposal area is performed probabilistically in 2D (Chapter 7). The assessment for HLW is based on four indicators, namely average temperature in the bentonite, thermally induced overpressure at a distance of 20 m above the disposal area, gas induced overpressures in the HLW nearfield, and normalised tracer flux through the CRZ (I-129).

The results of the respective reference case in the expected performance and the scenarios relevant to gas- and thermally-induced effects are summarised in Tab. 9-2. Gas-induced pressures increase from 11.6 MPa in the expected performance to 14.2 MPa when the UB gas rates are combined with the assumption that all HLW canisters breach simultaneously. Similarly, thermally-induced pressures increase from 12.6 MPa in the expected performance to 13.5 MPa when the PWR-MOX heat output is assumed for all HLW canisters. The same scenario does not result in any considerable increase in average bentonite temperature compared to the 95 °C observed in the expected performance. Under the conservative assumptions adopted in this scenario (no consumption of water, no molecular diffusion, simultaneous breaching of all canisters and accordingly simultaneous increase in corrosion rate for all canisters), a small number of probabilistic simulations of gas and heat transport result in pressures that exceed the magnitude of local minimum stress (16.8 MPa), which is used here for comparison (for definition of failure criteria in the PA see Nagra 2024j). The probabilistic analysis considering the likelihood of combinations of parameter samples and the associated probability of failure with regards to safety criteria is discussed in Nagra (2024j). The reference case of the expected evolution results in normalised tracer flux released into the Keuper and Malm aquifers that reaches a maximum equal to ~5E-04 of the regulatory limit. In the probabilistic simulations that value increases only slightly, to ~7E-04. The results of the respective reference cases from the scenarios relevant to the release of I-129 through the CRZ are summarised in Fig. 9-4. Note that only scenarios with the same source term, corresponding to 10% IRF, are shown in the figure. The bar chart shows the % change in retention of I-129 in the CRZ in each of the scenarios compared to the expected performance (EXPERF). In all scenarios, the retention of I-129 in the CRZ remains above 75% of that observed in the expected performance, corresponding to I-129 fluxes into the Keuper and Malm aquifers that remain orders of magnitude below the regulatory limit.

Dedicated modelling for the L/ILW disposal area is performed probabilistically in 2.5D (Chapter 8). The assessment for L/ILW is based on three indicators, namely gas induced overpressures in the L/ILW nearfield, gas flow rates through the V3, and solute tracer fluxes through the CRZ (Cl-36).

The results of the respective reference case in the expected performance and the scenarios relevant to gas-induced effects are summarised in Tab. 9-2. Gas-induced pressures increase from 9.7 MPa in the expected performance to 10 MPa when the UB gas rates are conservatively adopted for all L/ILW. The expected performance results in breakthrough of gas to the shafts after ~23,000 years in the abstracted 2.5D model, which is a conservative estimate compared to ~42,000 years shown in the total system analysis (Tab. 9-2). Including the molecular diffusion of gas in the calculation further increases the breakthrough time to more than 100,000 years. A probabilistic scenario with increased permeabilities of the V3 seal results practically negligible overpressures in the repository, however combined with increased gas release to the shaft, with the magnitude of the increase depending on the seal permeability value. The probabilistic analysis considering the seal permeabilities and the associated probability of failure with regards to safety criteria is discussed in Nagra (2024j). The findings are consistent with the total system analyses discussed in the present report, wherein the V3 seal provides effective sealing with regards to gas transport to the shaft for permeabilities below 1.0E-18 m^2. All probabilistic simulations of gas transport in the L/ILW nearfield discussed in the present report result in pressures below the magnitude of local minimum stress (16.2 MPa), which is used here for comparison to the simulated nearfield pressures (for definition of failure criteria in the PA see Nagra 2024j). This is consistent with all deterministic scenarios evaluated in the total system analysis presented in this report as well as those discussed in the context of the hydraulic evolution of the repository in Nagra (2024g).

Similarly, all probabilistic simulations performed for the expected evolution and all scenarios relevant to the release of Cl-36 from the CRZ result in fluxes to the Keuper and Malm aquifers that are several orders of magnitude below the regulatory limit.

The workflow implementation and results documented in the present report serve two main purposes. First, confidence in the PA model chain is confirmed with a structured approach and comprehensive benchmarking within the multitude of numerical tools developed to support the analyses. Second, the robustness of the barrier system in the provisional repository implementation is demonstrated from the perspectives of the total system as well as of barrier components for HLW and L/ILW, respectively. These results feed into the PA synthesis presented in Nagra (2024j) which provides the quantitative assessment with regards to safety functions and the associated performance margins. The synthesis of the PA presented in Nagra (2024j) is the first stage of the SA.

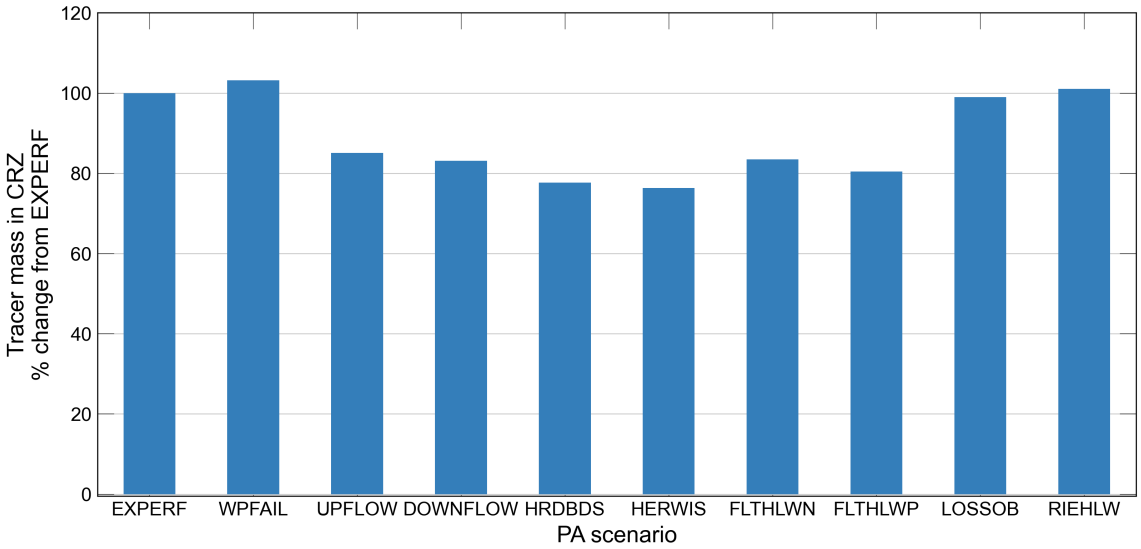

Fig. 9-4: PA scenarios HLW: percentage of tracer mass (I-129) retained in the CRZ compared to that in the expected performance (EXPERF)

10 References

Alcolea, A., Marschall, P., Damians, I.P., Olivella, S., Gens, A., Madaschi, A., Bosch, J., Laloui, L., Shao, H., Wang, W., Kolditz O. & Nagel, T. (2021): FE-Modelling Task Force / Task 1: Validation of thermally induced THM effects in the rock around the FE-tunnel. Subtask 1.1: Code and calculation verification. Subtask 1.2: Back-analyses. Nagra Arbeitsbericht NAB 19-40.

Bear, J. (1972): Dynamics of fluids in porous media. American Elsevier Publisher, New-York.

BFE (2008): Sachplan Geologische Tiefenlager: Konzeptteil. BFE 2. April 2008 (Revision vom 30. November 2011). Departement für Umwelt, Verkehr, Energie und Kommunikation UVEK, Bern.

Buchwald, J., Grunwald, N., Wang, W., Shao, H., Kolditz, O. & Nagel, T. (in prep.): Comparison between two-phase flow and Richards flow-based approaches and their implementation schemes on the evolution of the thermo-hydro-mechanical response of heat-emitting waste in clay-stone formations. Rock Mechanics and Rock Engineering.

Diomidis, N., Guillemot, T. & King, F. (2023): Definition of Reference Corrosion Rates for Performance and Safety Assessments. Nagra Arbeitsbericht NAB 23-22.

EDF (2016): Code_Aster Open Source - General FEA Software. EDF, Paris, France, available online at www.code-aster.org.

EDF (2021): Modélisation THHM: Généralités et algorithmes. EDF, Paris, France, available online at www.code-aster.org.

ENSI (2018): Präzisierungen der sicherheitstechnischen Vorgaben für Etappe 3 des Sachplans geologische Tiefenlager. Sachplan geologische Tiefenlager, Etappe 3. ENSI 33/649. Eidgenössisches Nuklearsicherheitsinspektorat ENSI, Brugg.

ENSI (2020): Geologische Tiefenlager. Erläuterungsbericht zur Richtlinie ENSI-G03/d. Eidgenössisches Nuklearsicherheitsinspektorat ENSI, Brugg.

ENSI (2023): Geologische Tiefenlager. Ausgabe Dezember 2020 (Änderung vom 1. November 2023). Richtlinie für die schweizerischen Kernanlagen ENSI-G03/d. Eidgenössisches Nuklearsicherheitsinspektorat ENSI, Brugg.

Finsterle, S. (2007): ITOUGH2 User's Guide. LBNL-40040, updated reprint. Lawrence Berkeley National Laboratory.

Geuzaine, C., Remacle, J.-F. &. (2009): Gmsh: A 3-D finite element mesh generator with built-in pre-and post-processing facilities. International Journal for Numerical Methods in Engineering 79/11, 1309-1331. DOI: 10.1002/nme.2579.

Glaus, M.A., Kulik, D.A., Miron, G.D., Van Loon, L.R., Wüst, R., Becker, J. & Li, X. (2024): Diffusion Databases for Opalinus Clay, Confining Geological Units, and Bentonite: Methods, Concepts, and Upscaling of Data. Nagra Technical Report NTB 23-08.

Grant, M.A. (1978): Permeability reduction factors at Wairakei. Paper 77-HT-52. Proceedings of the AIChe-ASME Heat Transfer Conference, Salt Lake City, Utah, August 15-17, 1977.

Guillemot, T., Wieland, E., Mosberger, L. & Warthmann, R. (2023): Degradation of Organic Materials in a L/ILW Repository. Nagra Technical Report NTB 23-11.

Hornung, U. (1997): Homogenization and Porous Media. Interdisciplinary Applied Mathematics (IAM, volume 6). Springer, New-York.

Jacops, E. & Kolditz, O. (2024): Gas transport mechanisms: diffusion, retention and advection processes. Task 2. Final technical report: EURAD-GAS Deliverable 6.7, available online at https://researchportal.sckcen.be/en/publications/gas-transport-mechanisms-diffusion-retention-and-advection-proces, status as of 24-09.2024.

Jung, Y., Pau, G.S.H., Finsterle, S. & Doughty, C. (2018): TOUGH3 User's Guide. Version 1.0 LBNL 2001093. Energy Geosciences Division, Lawrence Berkeley National Laboratory, University of California.

KEG (2003): Kernenergiegesetz (KEG) of March 21, 2003, status as of January 1, 2024. Systematische Sammlung des Bundesrechts SR 732.1, Schweiz.

KEV (2004): Kernenergieverordnung (KEV) of December 10, 2004, status as of January 1, 2024. Systematische Sammlung des Bundesrechts SR 732.11, Schweiz.

Luckner, L., van Genuchten, M.T. & Nielsen, D. (1989): A consistent set of parametric models for two-phase flow of immisable fluids in the subsurface. Water Ressources Research 25/10, 2187-2193. DOI: 10.1029/WR025i010p02187.

Luu, K. (2020): toughio: Pre-and post-processing Python Library for TOUGH. The Journal of Open Source Software 5/51, 2412. DOI: 10.21105/joss.02412.

Madaschi, A. & Laloui, L. (2019): EBS – Task Force / Task 7: Gas Transport in Bentonite - Modelling activities of LMS-EPFL (Final Report - October 2019). Nagra Arbeitsbericht NAB 19-37.

Marschall, P., Talandier, J., Kolditz, O., Kucerova, M., Mokni, N., Grgic, D., Agboli, D., Zhang C.-L., Cuss, R., Wiseall, A., Gonzales-Blanco, L., Romero, E., Llabjani, Q., Ferrari, A. & Keller, L. (2024): Barrier integrity: gas-induced impacts and model-based interpretation. EURAD-GAS: Work Package GAS (Mechanical understanding of gas transport in clay-based materials) of the HORIZON 2020 project EURAD. EC Grant agreement N°847593. Task 3. Final Technical Report. Deliverable 6.8 (D6.8).

Martin, L., Kosakowski, G., Papafotiou, A. & Smith, P.A. (2023): Evolution of the sealing system porosity and its impact on performance. Nagra Arbeitsbericht NAB 23-21.

Mualem, Y. (1976): A new model for predicting the hydraulic conductivity of unsaturated porous media. Water Ressources Research 12, 513-522.

Nagra (1985): Project Gewähr 1985: Nuclear Waste Management in Switzerland: Feasibility Studies and Safety Analyses. Nagra Project Report NGB 85-09.

Nagra (2002): Project Opalinus Clay: Safety report: Demonstration of disposal feasibility for spent fuel, vitrified high-level waste and long-lived intermediate-level waste (Entsorgungsnachweis). Nagra Technical Report NTB 02-05.

Nagra (2021): Entsorgungsprogramm 2021 der Entsorgungspflichtigen. Nagra Technischer Bericht NTB 21-01.

Nagra (2023a): Bautechnisches Dossier. Nagra Arbeitsbericht NAB 23-01 Band 1-9.

Nagra (2023b): Modellhaftes Inventar für radioaktive Materialien MIRAM-RBG. Nagra Technischer Bericht NTB 22-05.

Nagra (2024a): Abfallzuteilung und Betrachtungszeitraum für den Standortvergleich und Nachweiszeitraum für den Sicherheitsnachweis für das geologische Tiefenlager. Nagra Arbeitsbericht NAB 24-05.

Nagra (2024b): Anlagen- und Betriebskonzept für das geologische Tiefenlager. Nagra Technischer Bericht NTB 24-11.

Nagra (2024c): Geosynthesis of Northern Switzerland. Nagra Technischer Bericht NTB 24-17.

Nagra (2024) (*in prep.*): Depth Conversion of the 3D Seismic Interpretation for the Area of Interest in the Jura Ost, Nördlich Lägern and Zürich Nordost Siting Regions. Nagra Arbeitsbericht NAB 24-49.

Nagra (2024d): Model Supported Assessment of the Containment-Providing Rock Zone in Support of the Site Selection. Nagra Arbeitsbericht NAB 24-26.

Nagra (2024e): Phenomenological Description of the Evolution of a Geological Repository for Radioactive Waste in Opalinus Clay. Nagra Arbeitsbericht NAB 24-20 Rev. 1.

Nagra (2024f): Post-Closure Safety Report. Nagra Technical Report NTB 24-10.

Nagra (2024g): Production and Fate of Gases in the Geological Repository. Nagra Technical Report NTB 24-23.

Nagra (2024h): Safety and Repository Concept and Provisional Design. Nagra Arbeitsbericht NAB 24-18 Rev. 1.

Nagra (2024i): Safety Assessment Methodology. Nagra Technical Report NTB 24-19.

Nagra (2024j): Synthesis of the Performance Assessment for a Deep Geological Repository for Radioactive Waste. Nagra Technical Report NTB 24-22.

Nagra (2024k): Thermo-hydraulic modelling of the temperature distribution in the siting regions JO, NL and ZNO. Nagra Arbeitsbericht NAB 24-24.

Nagra (2025a): Rahmenbewilligungsgesuch für das geologische Tiefenlager – Begründung der Standortwahl. Nagra Technischer Bericht NTB 24-03.

Nagra (2025b): Rahmenbewilligungsgesuch für das geologische Tiefenlager – Sicherheitsbericht. Nagra Technischer Bericht NTB 24-01.

Papafotiou, A., Namhata, A., Singh, A., Williams, M., Jigmond, M. & Marschall, P. (2016): Parametric sensitivity analysis of heat and gas release for a geological repository for SF/HLW in Northern Switzerland. Nagra Arbeitsbericht NAB 17-05.

Pinder, G.F. & Gray, W.G. (2008): Essentials of multiphase flow and transport in porous media. (ISBN 978-0-470-31762-4). John Wiley & Sons, Inc., New Jersey.

Quintard, M. & Whitaker, S. (1994a): Transport in ordered and disordered porous media, (I): The cellular average and the use of weighting functions. Transport in Porous Media 14, 163-177. DOI: 10.1007/BF00615199.

Quintard, M. & Whitaker, S. (1994b): Transport in ordered and disordered porous media, (II): Generalized volume averaging. Transport in Porous Media 14, 179-206. DOI: 10.1007/BF00615199.

Romero, E. & Gonzalez-Blanco, L. (2019): Hydro-mechanical processes associated with gas transport in MX-80 Bentonite in the context of Nagra's RD&D programme (results by May 2019). Nagra Arbeitsbericht NAB 19-16.

Senger, R., Lanyon, B., Marschall, P., Vomvoris, S. & Fujiwara, A. (2008): Numerical modelling of the gas migration test at the Grimsel Test Site (Switzerland). Nuclear Technology 164/2, 155-168. DOI: 10.13182/NT08-A4016.

Thacker, B.H., Doebling, S.W., Hemez, F.M., Anderson, M.C., Pepin, J.E. & Rodriguez, E.A. (2004): Concepts of Model Verification and Validation. Report LA-14167-MS. Los Alamos National Laboratory, Los Alamos, NM, USA.

Wendling, J., Norris, S. & editors (2024): Modelling of a generic geological disposal: evaluation of various approaches to model gas transport through geological disposal systems. EURAD-GAS: Work Package Gas (Mechanical understanding of gas transport in clay-based materials) of the HORIZON 2020 project EURAD. EC Grant agreement no: 847593. Task 4. Final technical report. Deliverable 6.9 (D6.9).

Whitaker, S. (1986): Flow in porous media, (I): A theoretical derivation of Darcy's law. Transport in Porous Media 1, 3-25. DOI: 10.1007/BF01036523.

Wojnarowicz, M., Madaschi, A. & Laloui, L. (2024): A methodology to optimize complex models in the context of nuclear waste repositories. Computers and Geotechnics 173. DOI: 10.1016/j.compgeo.2024.106579.

App. A Complementary information on model conceptualisation

A.1 Two phase flow and transport - mathematical formulations

The following subdivision of basic transport mechanisms is considered for gas transport in porous media (Nagra 2024g):

- advective-diffusive transport of gas dissolved in porewater;
- visco-capillary two-phase flow;
- dilatancy-controlled gas flow; and
- gas transport along macroscopic tensile fractures (hydro- and gas-fracturing).

A comprehensive description of each transport mechanism, with references to additional literature, is provided in Nagra (2024g). In the following, some technical aspects are elaborated related to the formulations used in the PA modelling.

Diffusive flux is calculated as the product of the effective diffusion coefficient (in L^2/T) and the gradient of mass fraction of each component in a fluid phase (in 1/L). For the solution of mass balance in the finite differences discretisation scheme, this volumetric flux of component κ in phase β is calculated as specific mass flux ($M/L^2/T$) by multiplying with the density ρ of the fluid phase:

$$\vec{F}_\beta^\kappa = -\rho_\beta \underbrace{\phi \tau D}_{D_e} \nabla X_\beta^\kappa \tag{14}$$

The effective diffusion coefficient corresponds to a product of porosity, tortuosity, and the molecular diffusion coefficient. The tortuosity is considered as a product of a porous medium dependent factor, τ_0, and a coefficient that depends on phase saturation, τ_β.

In the Millington-Quirk model, tortuosity is assumed to be a product of porosity and phase saturation:

$$\tau = \phi^{1/3} S_\beta^{10/3} \tag{15}$$

An alternative formulation that explicitly accounts for (material-specific) tortuosity in the diffusion coefficient is described in the TOUGH3 manual (Jung et al. 2018).

For visco-capillary flow, the van Genuchten parametric relationship between water saturation and capillary pressure is used:

$$P_c = P_0 \cdot \left(S_e^{n/(1-n)} - 1 \right)^{1/n} \tag{16}$$

where P_0 is the capillary strength parameter, n is the shape factor and S_e is the effective saturation derived through normalisation of the liquid saturation S_l with the liquid residual saturation S_{lr} as:

$$S_e = \frac{S_l - S_{lr}}{1 - S_{lr} - S_{gr}} \tag{17}$$

The capillary pressure depends on the surface tension of water σ (ca. 0.073 N m^{-1} at 20 °C), which is a function of temperature. In TOUGH3, the functional relationship is given as:

$$P_c' = P_c \cdot \left[\sigma / \sigma_0 - 0.0017 \cdot (T - T_0) \right] \tag{18}$$

where σ is the surface tension at a given temperature T and σ_0 is the surface tension at a reference temperature T_0.

For relative gas and water permeability ($k_{r,g}$ and $k_{r,l}$) the formulation of Mualem (1976) is used:

$$k_{r,l} = S_e^{\gamma} \cdot \left[1 - \left(1 - S_e^{\frac{n}{n-1}} \right)^{\frac{n-1}{n}} \right]^2 \tag{19}$$

$$k_{r,g} = (1 - S_e)^{\varepsilon} \cdot \left(1 - S_e^{\frac{n}{n-1}} \right)^{2\left(1-\frac{1}{n}\right)} \tag{20}$$

where ε and γ are empirical shape factors, describing the pore connectivity of the medium which are typically set to ε = 1/3 and γ = 1/2 (Luckner et al. 1989). Note that slightly modified expressions of this general formulation may be used in different models, with different effective saturations used for capillary pressure and relative permeabilities (see, for example, TOUGH3 manual – Jung et al. 2018).

Enhanced gas mobility is described by the Grant model (Grant 1978), where the relative permeability of the gas phase is given by:

$$k_{r,g} = 1 - k_{r,l} \tag{21}$$

With the Grant model, the gas and liquid phases tend to move independently of each other, which is typical for fracture-porous rocks where liquid tend to migrate primarily through the matrix due to higher capillary pressures, and gas migrates through the higher-permeable fractures characterised by lower capillary pressures. This has been used for upscaling a discrete-fracture network (DFN) model of the fractured EDZ to a homogeneous continuous porous media (CPM) model with effective two-phase flow parameters based on the Grant model for the gas relative permeability (Senger et al. 2008).

In case of heterogeneous distributions of intrinsic permeability k_i, the corresponding distribution of the capillary strength $P_{o,i}$ is generated based on the average value P_o, assuming Leverett scaling of the permeability field k_i normalised by its harmonic mean k_{harm}:

$$\eta_i = \frac{k_i}{k_{harm}} \quad \Rightarrow P_{o,i} = \frac{P_o}{\sqrt{\eta_i}} \tag{22}$$

Pore compressibility of the rock matrix is derived from Young's modulus and Poison ratio based on the assumption of oedometric stress conditions:

$$c_p = \frac{1}{n} \cdot \frac{3 \cdot (1 - 2 \cdot \upsilon)}{E} \tag{23}$$

Pathway dilation, when activated, is implemented with an enhanced permeability that depends on pressure as follows:

$$\mathrm{k}' = \mathrm{k}\left[1 + (\mathrm{k}_{\mathrm{factor}} - 1)\frac{\mathrm{P} - \mathrm{P}_1}{\mathrm{P}_2 - \mathrm{P}_1}\right] \tag{24}$$

where k_{factor} is a scaling factor, P_1 is the characteristic pressure for the onset of dilation and P_2 is the maximum pressure corresponding to the maximum enhanced permeability. Capillary strength is accordingly changed by Leverett scaling.

A.2 Geometric abstractions in repository modelling

A.2.1 Model geometry of entire repository

Geometric data of the individual repository components as described in the engineering dossier are given in Tab. A-1. Geometric data of their representation 3D repository model is provided in Tab. A-3 and Tab. A-4. A comparison of the cross-sections implemented with the model grid (Tab. A-3 and Tab. A-4) to the cross-sections specified in the engineering dossier (Tab. A-1) indicates the required scaling of the different repository elements through an effective porosity and specific heat that comprises both the porosity of the material and a cross-sectional scaling factor. The resulting scaled porosity and specific heat capacity values are given in Tab. A-3 and Tab. A-4.

Tab. A-1: Geometric data of repository sections

Adapted from Nagra (2023a).

Repository tunnel[1,2]	**Average cross-section for storage[1]** [m^2]	**Length[1]** [m]	**Volume imple-mented** [m^3]	**Porosity[2]** [-]	**Specific heat[2]** [J/kg/°C]	**Void space volume[3] imple-mented** [m^3]
HLW drifts	6.605	17,997.2	118,875.1	0.25	964	29,718.8
HLW V1 seals (incl. pilot)	6.605	230.0	1,519.2	0.30	964	455.8
HLW branching tunnels (incl. pilot repository)	52.688	1,870.9	98,576.4	0.35	920	34,501.7
HLW operations tunnel (incl. V2[4])	49.185	2,947.4	144,967.8	0.35	920	50,738.7
HLW ventilation tunnel (incl. V2[4])	49.514	2,504.3	123,998.7	0.35	920	43,400.0
HLW construction tunnel (incl. V2[4])	49.625	3,008.2	149,281.4	0.35	920	52,248.5
HLW connecting tunnels	48.585	720.0	34,981.1	0.35	920	12,243.4
HLW operations tunnel for pilot repository (incl. V2[4])	49.514	322.1	15,946.1	0.35	920	5,581.1
HLW observation drift	43.008	516.8	22,228.5	0.35	920	7,780.0
HLW pilot repository drift	6.605	603.8	3,988.3	0.30	964	997.1
L/ILW caverns	152.184	1,640.0	249,581.4	0.20	920	49,916.3
L/ILW caverns V1 seals (incl. pilot repository)	48.275	240.0	11,586.0	0.30	920	3,475.8
L/ILW branching tunnels (excl. pilot repository)	53.635	1,216.9	65,271.2	0.35	920	22,844.9
L/ILW operations tunnel (incl. V2[4])	49.072	1,166.9	57,260.4	0.35	920	20,041.1
L/ILW ventilation tunnel (incl. V2[4])	48.275	2,119.1	102,299.5	0.35	920	35,804.8
L/ILW connecting tunnels	48.275	180.0	8,689.5	0.35	920	3,041.3

Tab. A-1: Cont.

Repository tunnel[1,2]	**Average cross-section for storage[1]** [m²]	**Length[1]** [m]	**Volume imple-mented** [m³]	**Porosity[2]** [-]	**Specific heat[2]** [J/kg/°C]	**Void space volume[3] imple-mented** [m³]
L/ILW operations tunnel for pilot repository (incl. V2[4])	49.514	107.1	5,303.0	0.35	920	1,856.0
L/ILW observation drift	43.008	467.5	20,107.7	0.35	920	7,037.7
L/ILW pilot repository cavern	152.184	85.0	12,935.6	0.20	920	2,587.1
Central area	42.919	2,122.1	112,297.3	0.35	920	39,304.1
Access tunnel	63.588	87.7	5,574.1	0.35	920	1,951.0
Facilities for EUU	47.897	795.4	38,094.8	0.35	920	12,776.1
Total below V3	**-**	**40,984.4**	**1,403,363**	**-**	**-**	**438,301.3**
V3 (access)	91.609	82.0	7,511.9	0.30	964	2,253.6
V3 (ventilation)	54.106	47.0	2,543.0	0.30	964	762.9
V3 (construction)	109.359	50.0	5,467.9	0.30	964	1,640.4
Access shaft (excl. V3)	102.429	758.0	77,641.0	0.35	920	27,174.4
Ventilation shaft (excl. V3)	51.614	762.0	39,329.9	0.35	920	13,765.5
Construction shaft (excl. V3)	123.200	757.0	93,262.1	0.35	920	32,641.7

1 Extracted from Nagra (2023a).
2 From Nagra (2024g).
3 Product of porosity and volume.
4 Porosity of V2 seals is 0.3, specific heat of V2-HLW is 964 J/kg/°C.

Tab. A-2: Geometry of repository components in the L/ILW section and central area implemented in the 3D repository model grid and scaling of effective porosity to adjust void space volumes

	Cross-section [m^2]	**Length** [m]	**Volume** [m^3]	**Porosity conversion factor**[1] [-]	**Scaled porosity**[2] [-]	**Scaled specific heat**[3] [J/kg/°C]
L/ILW caverns	100	1,650 *(2 × 250 m + 5 × 230 m)*	165,000	1.522	0.3044	1,610.15
V1 seals (incl. pilot)	50	240 *(8 × 30 m)*	12,000	0.965	0.2896	875.32
Branch tunnels (incl. pilot)	50	1,200 *(8 × 150 m)*	60,000	1.073	0.3754	1,027.11
Operation tunnel (incl. V2[4])	50	1,290	64,500	0.981	0.3435	893.98
Ventilation tunnel (incl. V2[4] and connection tunnels)	50	2,020	101,000	0.965	0.3379	872.06
Pilot cavern	100	90	9,000	1.522	0.3044	1,610.15
Pilot operation tunnel (incl. V2[4])	50	100	5,000	0.990	0.3466	906.32
Control tunnel	50	505	25,250	0.860	0.3011	735.94
Central area	50	2,105	105,250	1.058	0.3704	1,005.30
Access tunnel	50	85	4,250	1.272	0.4451	1,370.59
EUU	50	675	33,750	0.958	0.3213	862.99
Access shaft V3[5]	100	60.52	6,052	0.916	0.3664	852.45
Access shaft (excl. V3)	100	792.75	79,275	1.024	0.3585	954.83
Ventilation shaft V3[5]	50	53.33	2,666	1.082	0.4328	1,081.22
Ventilation shaft (excl. V3)	50	768.55	38,427	1.032	0.3613	966.50
Construction shaft V3[5]	100	54.85	5,485	1.094	0.4374	1,098.27
Construction shaft (excl. V3)	100	760.48	76,048	1.232	0.4312	1,295.24

1 Calculated as ratio between cross-section in model and repository layout.
2 Porosities of backfilling materials scaled by porosity conversion factor.
3 Specific heat scaled by porosity conversion factor times (1-porosity)/(1-porosity_scaled).
4 Porosity and specific heat of V2 seals are different from tunnels (see Tab. A-1).
5 Porosity of 0.4 used for scaling to account for pore volume between V3 and repository level.

Tab. A-3: Geometry of repository components in the HLW section implemented in the 3D repository model grid and scaling of effective porosity to adjust void space volumes

	Cross-section [m^2]	**Length** [m]	**Volume** [m^3]	**Porosity conversion factor**[1] [-]	**Scaled porosity**[2] [-]	**Scaled specific heat**[3] [J/kg/°C]
HLW drifts	12.5	17,200 *(20 × 860 m)*	215,000	0.528	0.1321	440.20
V1 seals (incl.pilot)	12.5	230 *(23 × 10 m)*	2,875	0.528	0.1585	423.75
Branch tunnels (incl. pilot)	50	2,300 *(23 × 100 m)*	115,000	1.054	0.3688	998.37
Operation tunnel (incl. V2[4])	50	2,995	149,750	0.984	0.3443	897.14
Ventilation tunnel (incl. V2[4])	50	2,525	126,250	0.990	0.3466	906.32
Construction tunnel (incl. V2[4])	50	2,635	131,750	0.993	0.3474	909.43
Connection tunnels	50	600	30,000	0.972	0.3401	880.54
Pilot tunnels	12.5	480 *(3 × 160 m)*	6,000	0.528	0.1321	440.20
Pilot operation tunnel (incl. V2[4])	50	350	17,500	0.990	0.3466	906.32
Control tunnel	50	540	27,000	0.860	0.3011	735.94

1 Calculated as ratio between cross-section in model and repository layout.
2 Porosities of backfilling materials scaled by porosity conversion factor.
3 Specific heat scaled by porosity conversion factor times (1-porosity)/(1-porosity_scaled).
4 Porosity and specific heat of V2 seals are different from tunnels (see Tab. A-1).

A.2.2 Model geometry of a L/ILW emplacement cavern

Geometric data of the L/ILW emplacement caverns and adjacent tunnels based on the engineering dossier are given in Tab. A-4. Geometric data of the representation in the 3D component model (see Section 3.3.2 and Nagra 2024g) is provided in Tab. A-5.

Tab. A-4: Geometric data of L/ILW section

Adapted from Nagra (2023a).

Tunnel	**Excavation support** [m]	**Inner shell (lining)** [m]	**Deformation space** [m]	**Inner diameter** [m]	**3D lengths** [m]
L/ILW caverns 1 – 5	0.25	0.4	0.2	12.22	230
L/ILW caverns 6 – 7	0.25	0.4	0.2	12.22	245
Transfer area L/ILW	0.25	0.5	0.2	9.8	11
Unloading area L/ILW	0.25	0.5	0.2	7.30	9.0
L/ILW branching tunnels	0.25	0.5	0.15	6.04	115.0

Tab. A-5: Geometry of L/ILW emplacement cavern and adjacent tunnels implemented in the 3D component model grid

Tunnel	**Liner thickness top/bottom** [m]	**Inner diameter** [m]	**Length** [m]	
L/ILW cavern	-	12.2	230	
Transfer area	0.4 / 1.2	~10.5	11	
Unload area	0.4 / 1.2	~8.2	9.0	
V1-L/ILW	0	~7.7	20	115.0
Abutment V1	0	~7.7	7.5	
Branching tunnel	0.4 / 1.2	~6.0	83	

A.2.3 Model geometry of a HLW emplacement drift

Geometric data of the HLW emplacement drifts and adjacent tunnels based on the engineering dossier are given in Tab. A-6. Geometric data of the representation in the 3D component model (see Section 3.3.2 and Nagra 2024g) is provided in Tab. A-7.

Tab. A-6: Geometric data of HLW section

Adapted from Nagra (2023a).

Tunnel		**Excava-tion support** [m]	**Inner shell (lining)** [m]	**Tubbing** [m]	**Defor-mation space** [m]	**Inner diameter** [m]	**3D lengths** [m]
HLW drifts 1-20				0.4	0.05	2.80	909.86
Transfer area HLW 1 – 20	HLW unloading area	0.25	0.50	-	0.20	6.55	20.00
	HLW handover area	0.25	0.50	-	0.20	6.55	26.00
HLW branching tunnels 1 – 20		0.25	0.50	-	0.15	6.04	35.35

Tab. A-7: Geometry of HLW emplacement drift implemented in the 3D component model grid

Tunnel	**Liner / tubbing** [m]	**Inner diameter** [m]	**Length** [m]
HLW emplacement drift	0.5	2.85	886.77
V1-HLW	-	3.85	10
Abutments V1	-	3.85	4

A.2.4 3D component model of a V2-L/ILW seal

Geometric data of the V2-L/ILW seal and adjacent tunnels based on the engineering dossier are given in Tab. A-8. Geometric data of the representation in the 3D component model (see Section 3.3.2 and Nagra 2024g) is provided in Tab. A-9.

Tab. A-8: Geometric data of a V2-L/ILW sealing section

Based on Nagra (2023a).

Tunnel	**Excavation support** [m]	**Inner shell (lining)** [m]	**Deformation space** [m]	**Inner diameter** [m]
L/ILW operations tunnel Sector B - ND 50	0.25	0.5	0.15	6.04

Tab. A-9: Geometry of V2-L/ILW seal implemented in the 3D component model grid

Tunnel	**Outer liner** [m]	**Inner liner** [m]	**Inner diameter** [m]
Operations tunnel	0.356	0.52	6.0

A.2.5 3D component model of a V3 seal

Geometric data of the V3 seal and access shaft based on the engineering dossier are given in Tab. A-10. Geometric data of the representation in the 3D component model (see Section 3.3.2 and Nagra 2024g) is provided in Tab. A-11.

Tab. A-10: Geometric data of a V3 seal and access shaft

Based on Nagra (2023a).

Tunnel	**Excavation support** [m]	**Inner shell (lining)** [m]	**Deformation space** [m]	**Inner diameter** [m]	**3D lengths** [m]
Access shaft Section 2	0.36	1.10	-	8.50	758.00
Access shaft Section 3	0.25	0.70	0.20	8.50	82.00
Operations tunnel HLW / Allotment tunnel (connecting tunnel) ND 40	0.25	0.50	0.15	6.04	37.66

Tab. A-11: Geometry of V3 seal and shaft implemented in the 3D component model grid

Tunnel	**Diameter** [m]	**Length** [m]
Shaft in confining units	11.42[1]	~145[2]
Shaft in OPA	10.80[3]	82[4]
Access tunnel to shaft	7.84[5]	26

[1] Calculated as 8.5 + 2 × 1.1 + 2 × 0.36
[2] Up to base Malm (30 m in confining unit BD)
[3] Calculated as 8.5 + 2 × 0.2 + 2 × 0.70
[4] Including shaft sump
[5] Calculated as 6.04 + 2 × 0.15 + 2 × 0.50 + 2 × 0.25

App. B Complementary results: total system analysis

Complementary simulation results contributing to the total system analysis are provided in this appendix.

B.1 Expected performance

The transients provided in Section 6.1 are complemented in the following with plots of spatial distributions in the repository nearfield for the expected performance.

Distributions of temperature, gas saturation, and pressure obtained with the 3D repository model are shown in Fig. B-1, Fig. B-2, Fig. B-3, respectively. This simulation corresponds to the base case simulation presented in Section 6.1 and in Nagra (2024g).

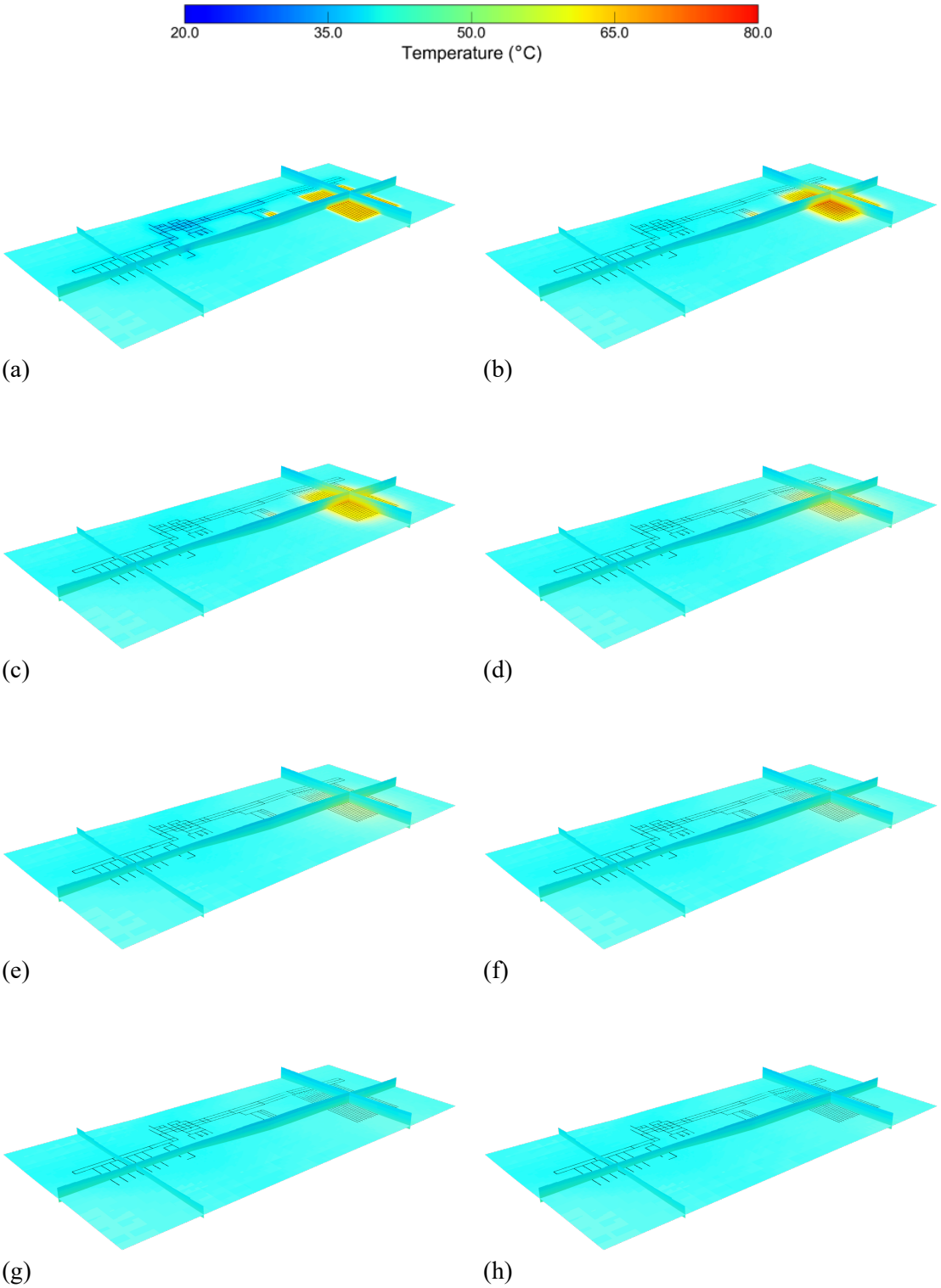

Fig. B-1: Expected performance total system (3D repository model): Spatial distribution of temperature after (a) 100 years, (b) 500 years, (c) 1,000 years, (d) 5,000 years, (e) 10,000 years, (f) 20,000 years, (g) 50,000 years, and (h) 100,000 years

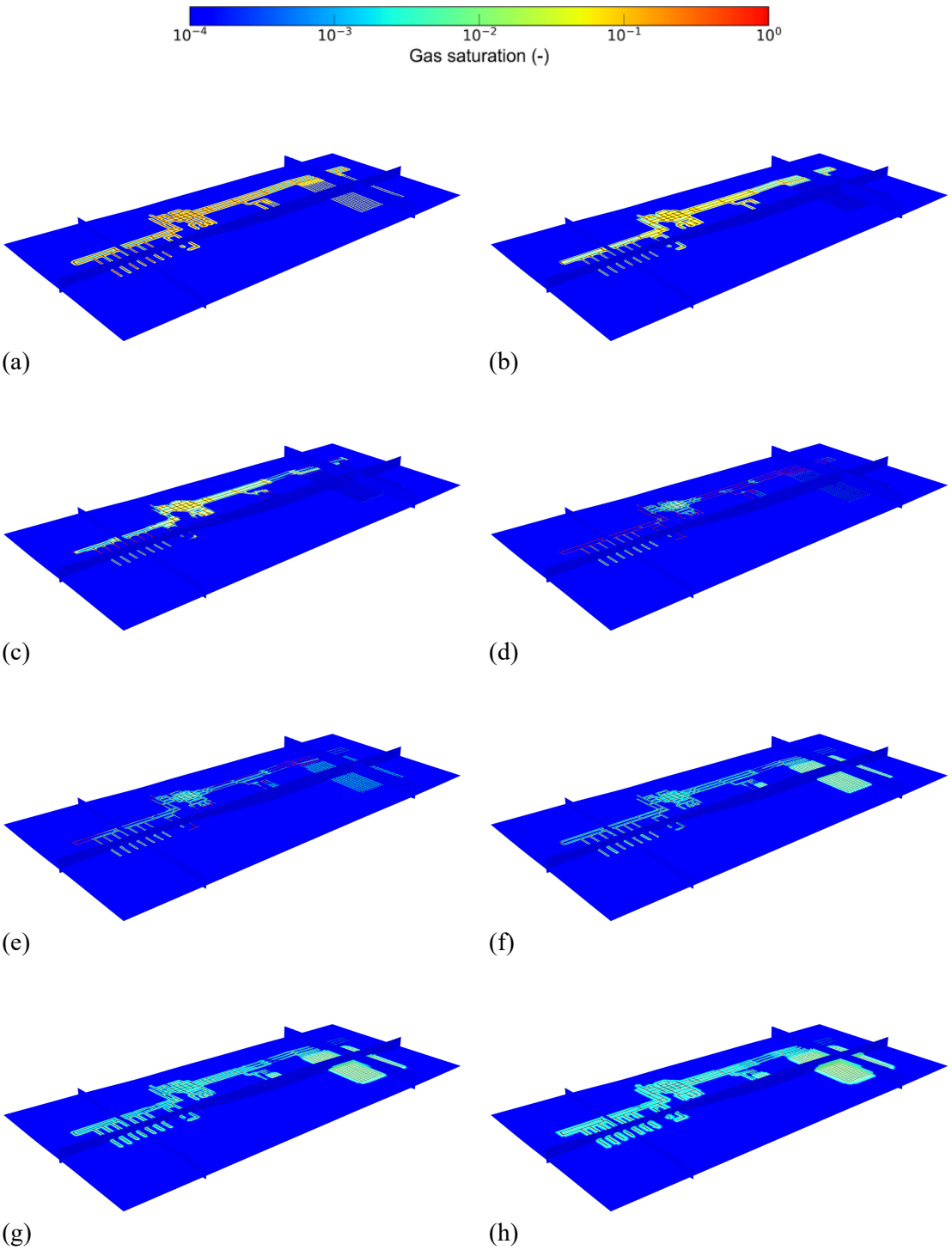

Fig. B-2: Expected performance total system (3D repository model): Spatial distribution of gas saturation after (a) 100 years, (b) 500 years, (c) 1,000 years, (d) 5,000 years, (e) 10,000 years, (f) 20,000 years, (g) 50,000 years, and (h) 100,000 years

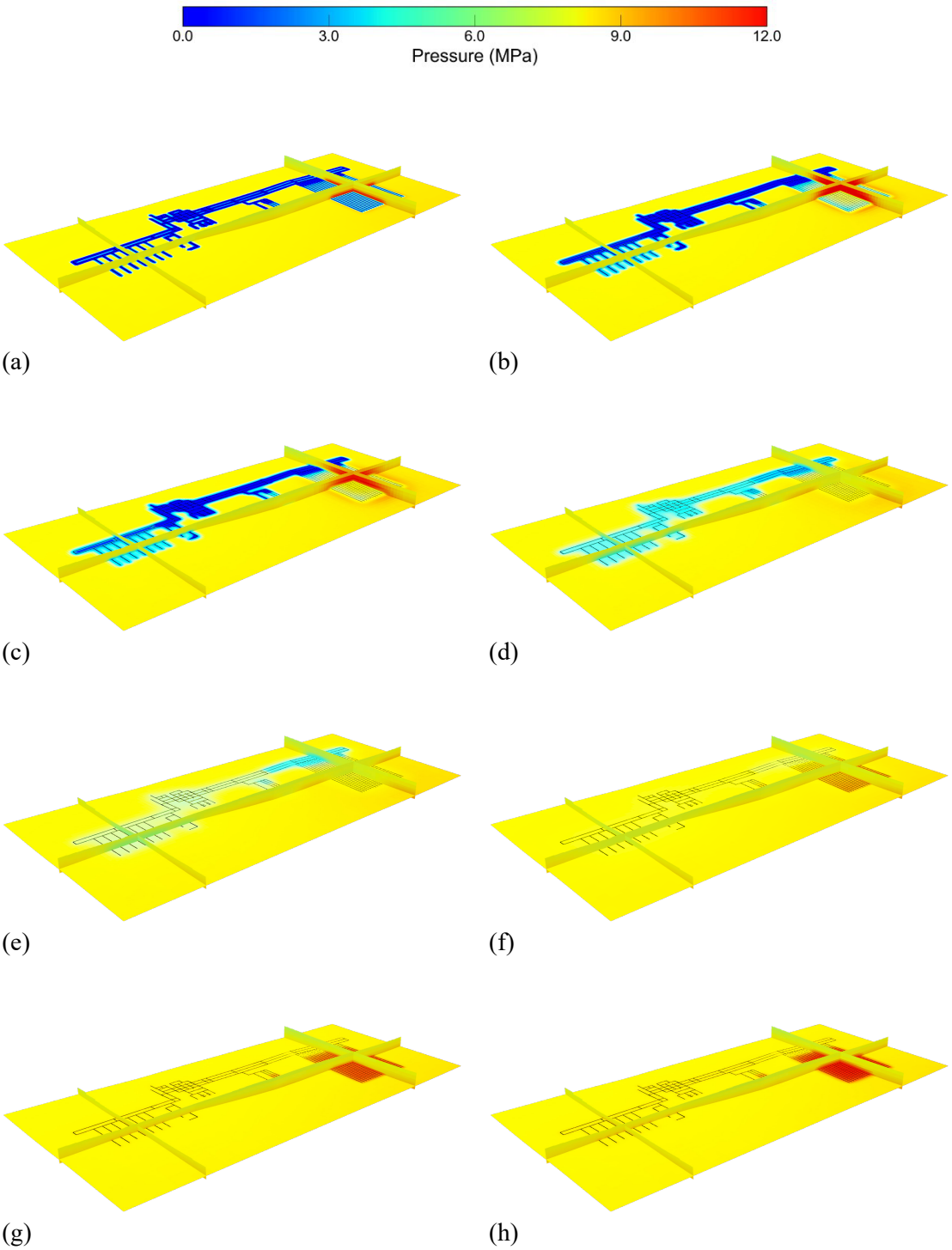

Fig. B-3: Expected performance total system (3D repository model): Spatial distribution of pressure after (a) 100 years, (b) 500 years, (c) 1,000 years, (d) 5,000 years, (e) 10,000 years, (f) 20,000 years, (g) 50,000 years, and (h) 100,000 years

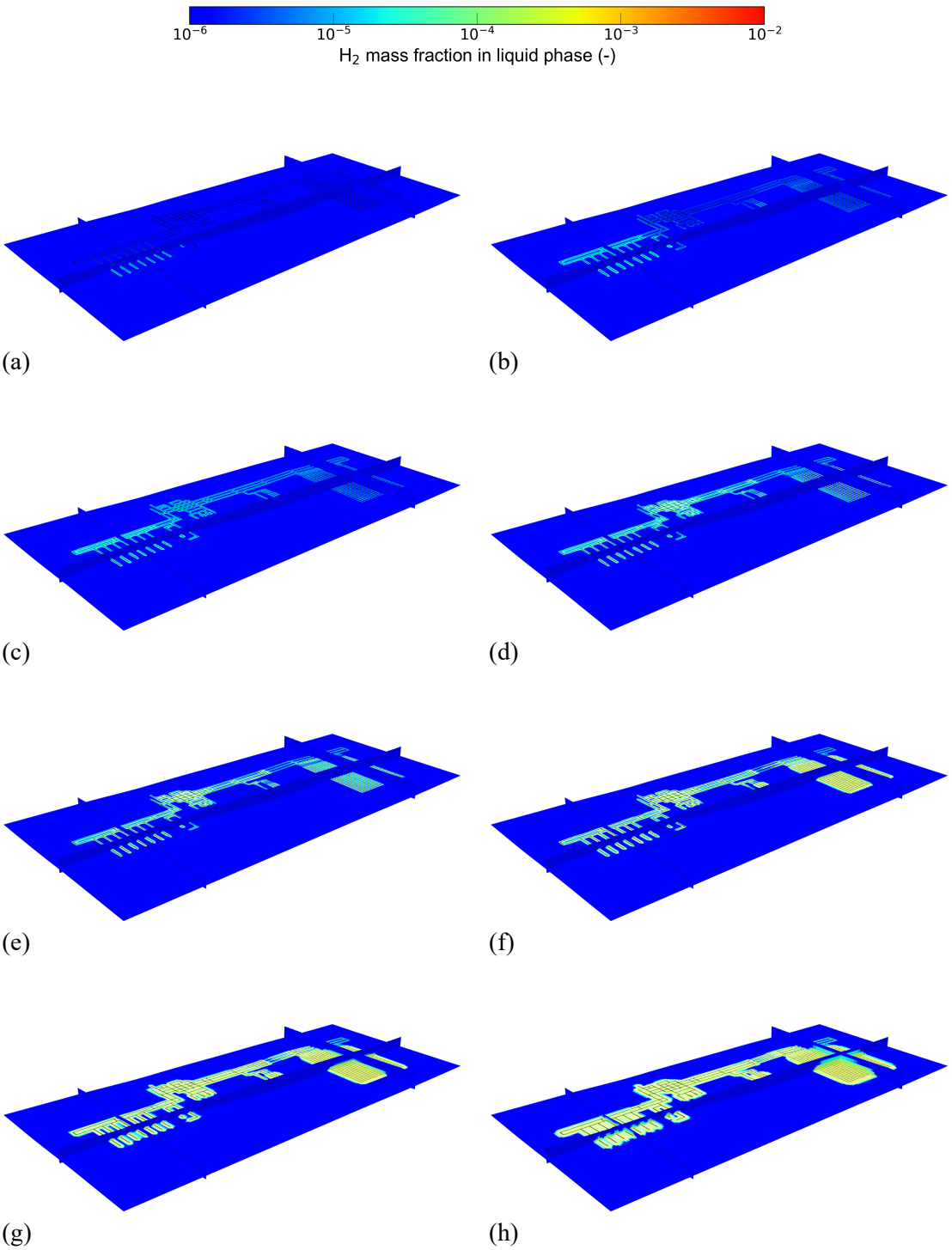

Fig. B-4: Expected performance total system (3D repository model): Spatial distribution of H_2 mass fraction in liquid after (a) 100 years, (b) 500 years, (c) 1,000 years, (d) 5,000 years, (e) 10,000 years, (f) 20,000 years, (g) 50,000 years, and (h) 100,000 years

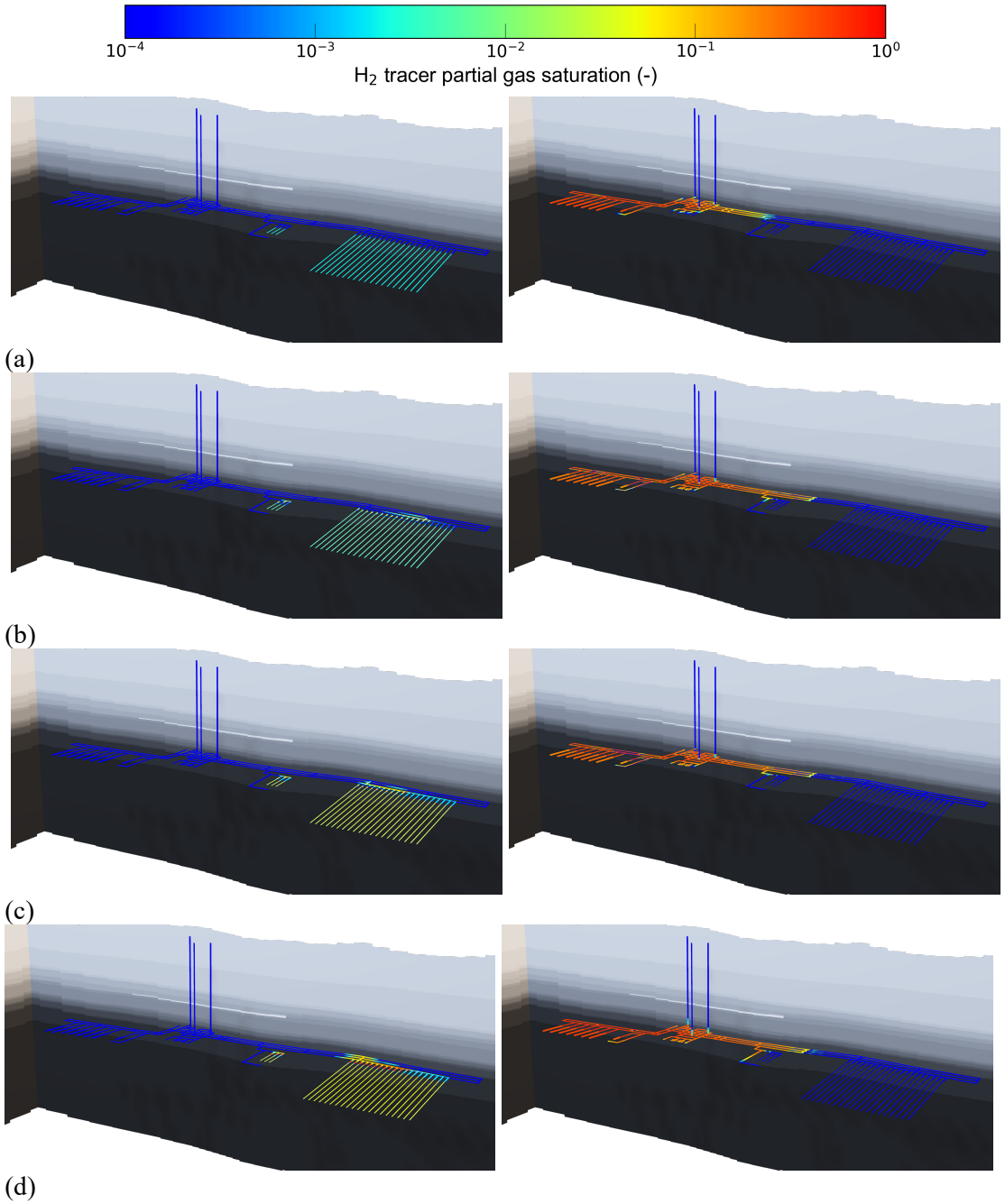

Fig. B-5: Expected performance total system (3D repository model): Spatial distribution of partial gas saturation of H_2 released in the HLW drifts (left) and in the L/ILW caverns (right) after (a) 1,000 years, (b) 10,000 years, (c) 20,000 years, and (d) 100,000 years

B.2 Expected performance with H_2 molecular diffusion

When using the Millington-Quirk model (see App. A) the approximation of two-phase diffusion coefficients is simplified and porosity is the only material-specific parameter. The molecular diffusion coefficient is material-independent and depends on the fluid phase and the component diffusing through it. In the two-phase models used in this report the components are water and hydrogen. The corresponding molecular diffusion coefficients are given in Tab. B-1. Note that in the repository system diffusion in gas phase occurs mainly within the partially saturated repository structures. The magnitude of gas diffusion in liquid phase is mainly relevant in the OPA.

Tab. B-1: Two-phase molecular diffusion coefficients[1]

Component	Unit	Liquid	Gas
H_2O	[m^2/s]	-	2.1E-05
H_2		2.0E-09[2] 5.1E-09[3] 4.5E-09[4]	2.1E-05

[1] Isotropic diffusion coefficients assumed for two-phase transport.
[2] Value used in SGT-E2 (self-diffusion coefficient of water).
[3] PSI report TM-44-21-12.
[4] Wikipedia (water at 25°C).

The simulation with the 3D repository model for the expected evolution is repeated, this time including molecular diffusion with H_2 molecular diffusion coefficient of 2.0E-09 m^2/s. The transients of temperature, gas saturation, and pressure are shown in Fig. B-6, Fig. B-7, and Fig. B-8, respectively. Temperatures in the repository are identical to the simulation without diffusion (shown in Fig. 6-1). On the other hand, gas saturations are overall lower due to the enhanced dissolution of gas associated with the additional gradient in concentration from the diffusion of dissolved gas into the surrounding rock. Accordingly, gas pressures in the repository are also lower compared to the expected evolution without diffusion (shown in Fig. 6-3). Notably, the transients of gas flow rate through the sealing sections, shown in Fig. B-9, show that there is no gas release from the V3 to the shaft in the first 100,000 years (in comparison, in the case without diffusion gas breaks through the V3 seal after 42,000 years, as shown in Fig. 6-4). This relates to two aspects of the hydraulic evolution when molecular diffusion is activated. First, the decrease in gas pressure, which results in decrease of pressure gradient from the repository tunnels to the shaft. Second, the enhanced dissolution of gas in porewater in the V3 and surrounding rock (note that some gas saturation is observed in the V3 when diffusion is not accounted for, as shown in Fig. 6-2). The transients of water flow rate through the sealing sections, shown in Fig. B-10, show somewhat lower flow rates compared the simulation without diffusion (shown in Fig. 6-5) due to the decrease in pressure buildup. In the entire simulated period of 100,000 years, there is no liquid flow from the V3 to the shaft. The normalised gas and water flow rates (Fig. B-11) show some small flows from the central area into the V2-HLW seals.

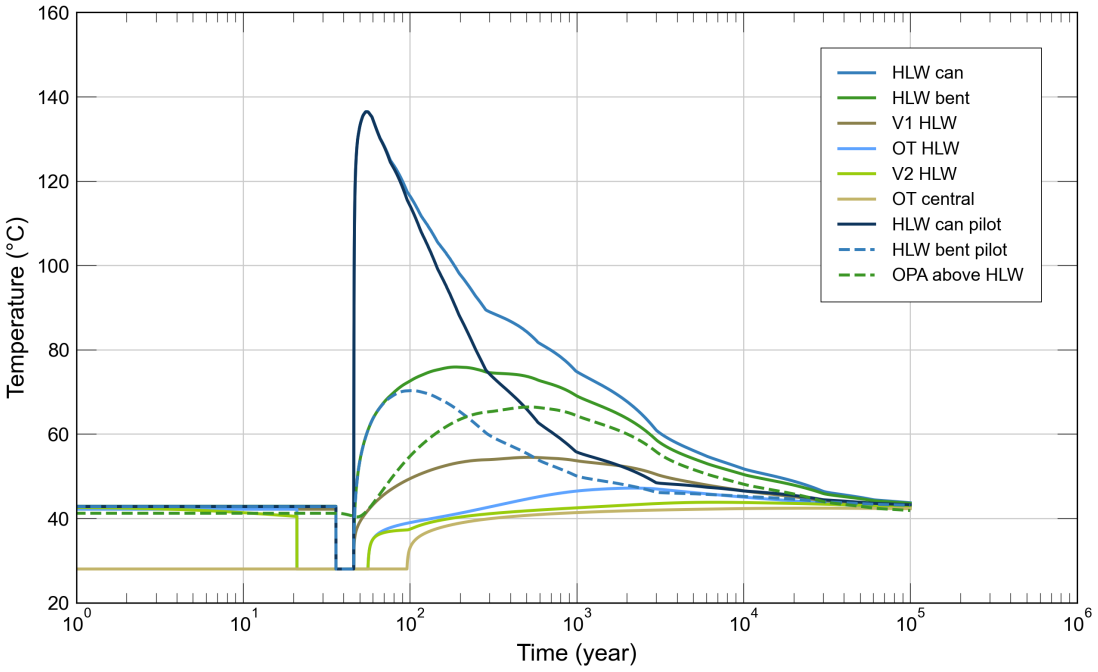
Temperature (°C)
Time (year)
HLW can
HLW bent
V1 HLW
OT HLW
V2 HLW
OT central
HLW can pilot
HLW bent pilot
OPA above HLW

(a)

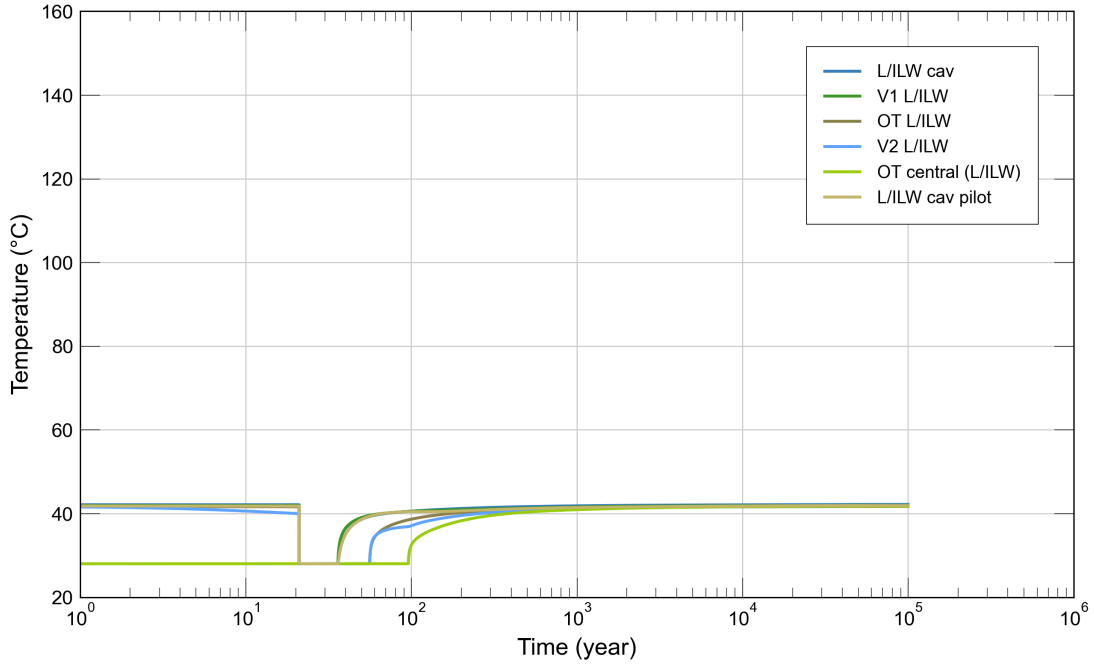
Temperature (°C)
Time (year)
L/ILW cav
V1 L/ILW
OT L/ILW
V2 L/ILW
OT central (L/ILW)
L/ILW cav pilot

(b)

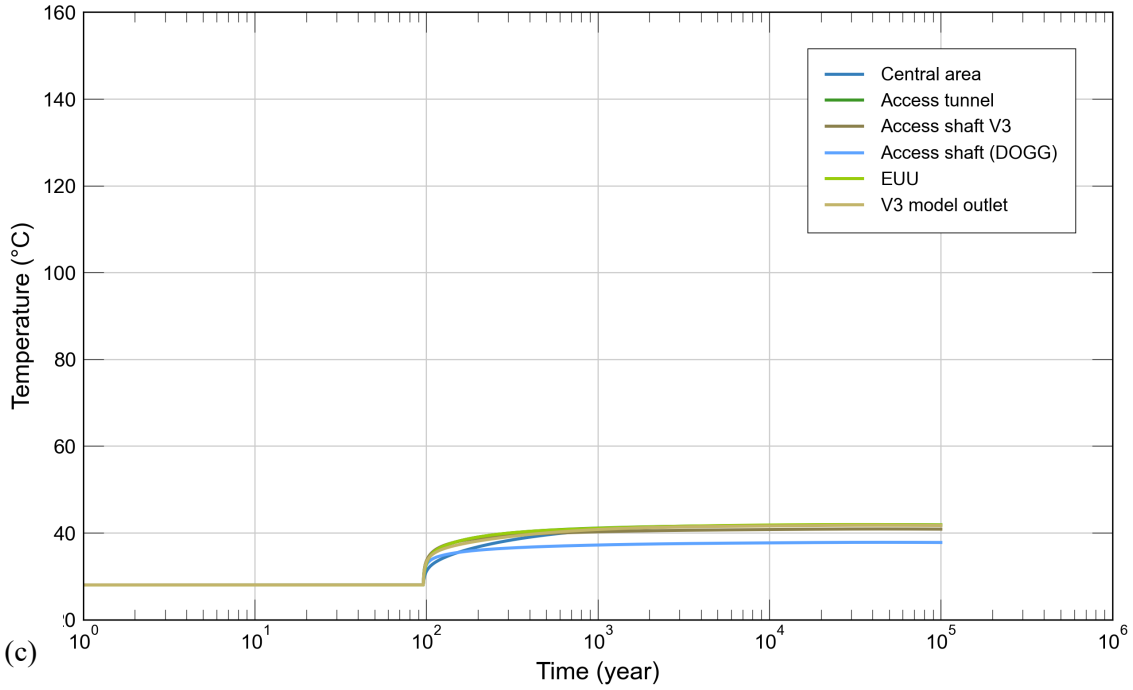

(c)

Fig. B-6: Expected performance total system with H_2 molecular diffusion: Transients of temperature

(a) HLW section, (b) L/ILW section and (c) Central area.

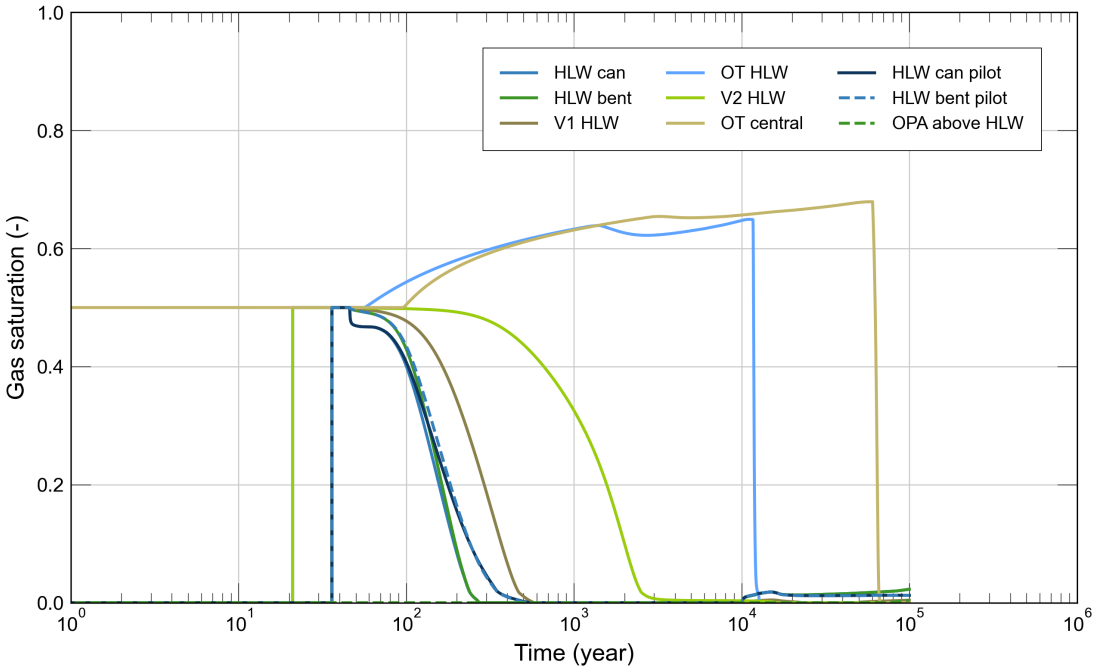
HLW can
HLW bent
V1 HLW
OT HLW
V2 HLW
OT central
HLW can pilot
HLW bent pilot
OPA above HLW
Gas saturation (-)
Time (year)

(a)

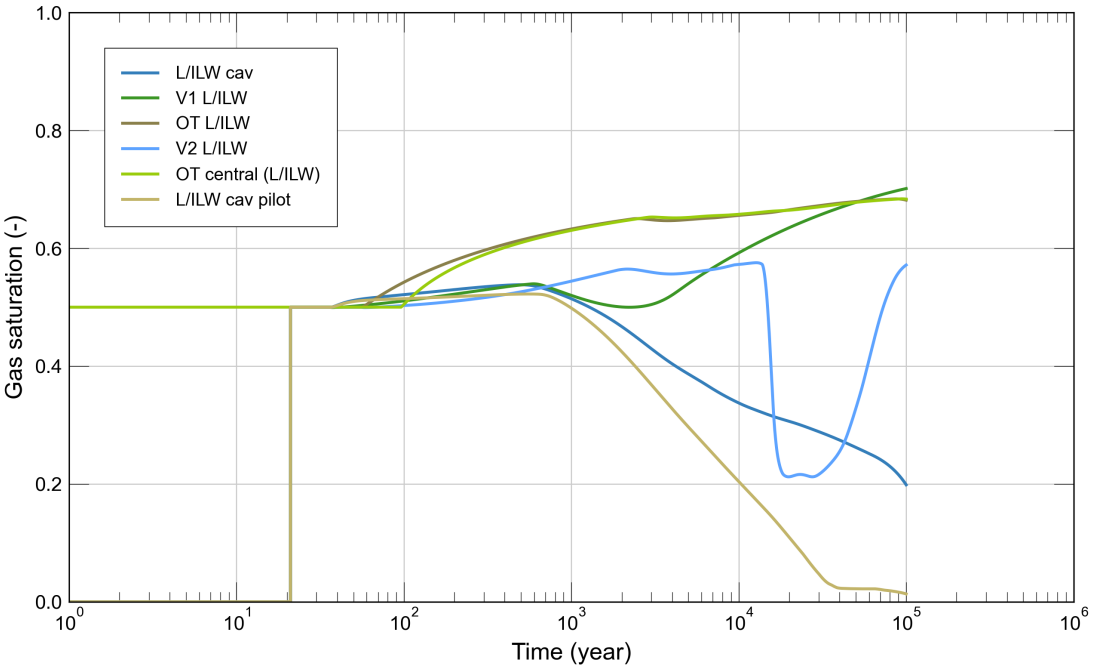
L/ILW cav
V1 L/ILW
OT L/ILW
V2 L/ILW
OT central (L/ILW)
L/ILW cav pilot
Gas saturation (-)
Time (year)

(b)

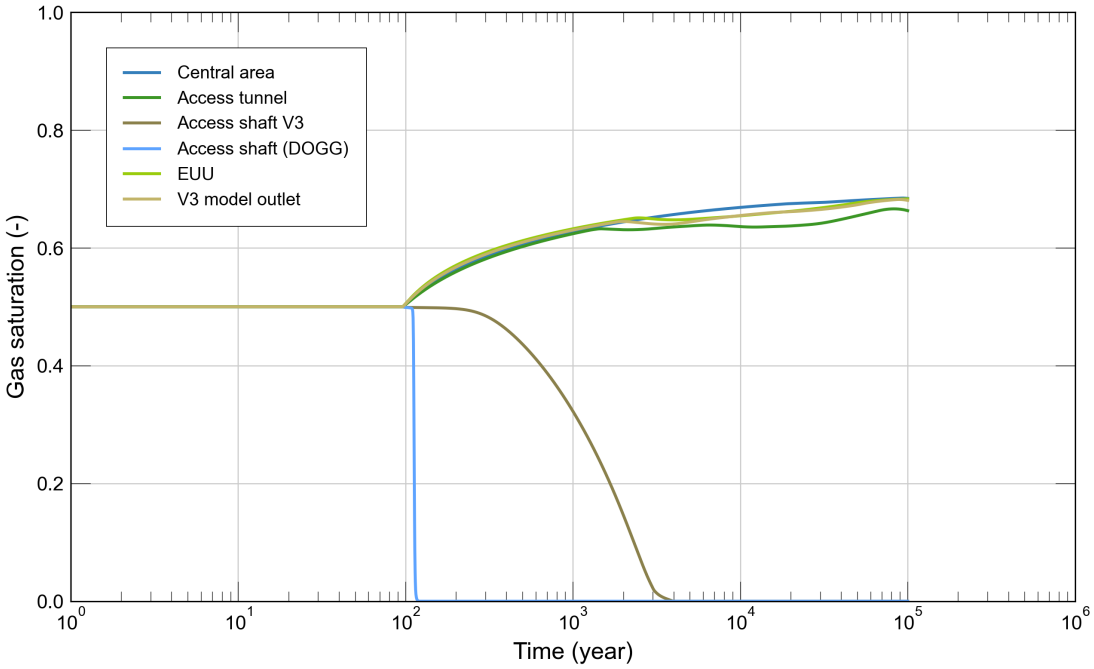

(c)

Fig. B-7: Expected performance total system with H_2 molecular diffusion: Transients of gas saturation

(a) HLW section, (b) L/ILW section and (c) Central area.

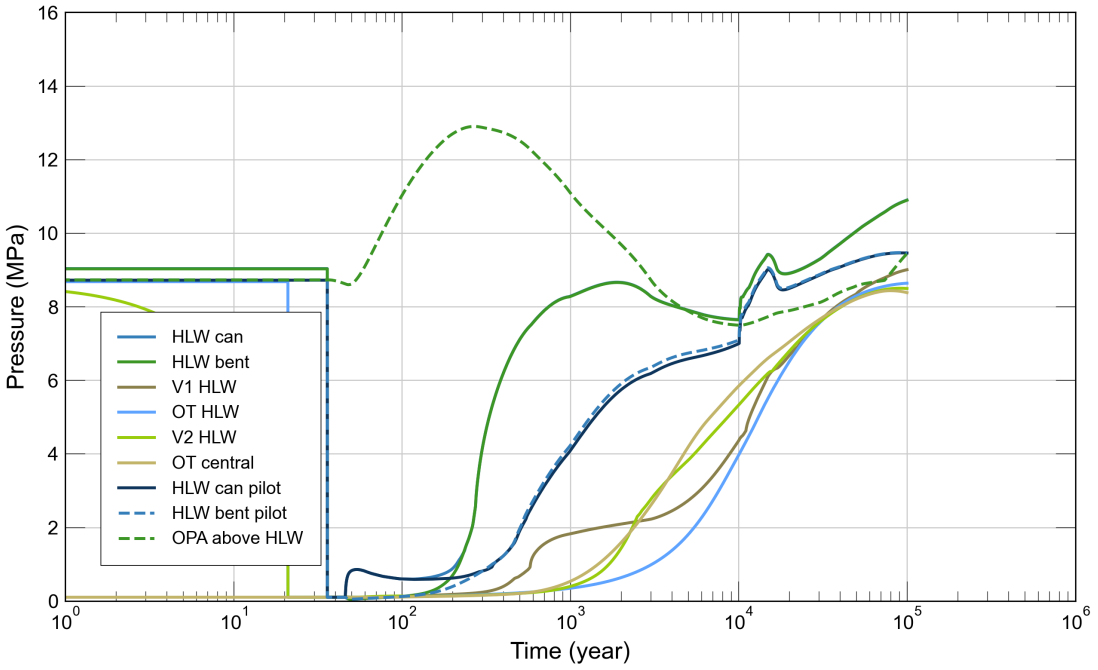
Pressure (MPa)
Time (year)
HLW can
HLW bent
V1 HLW
OT HLW
V2 HLW
OT central
HLW can pilot
HLW bent pilot
OPA above HLW

(a)

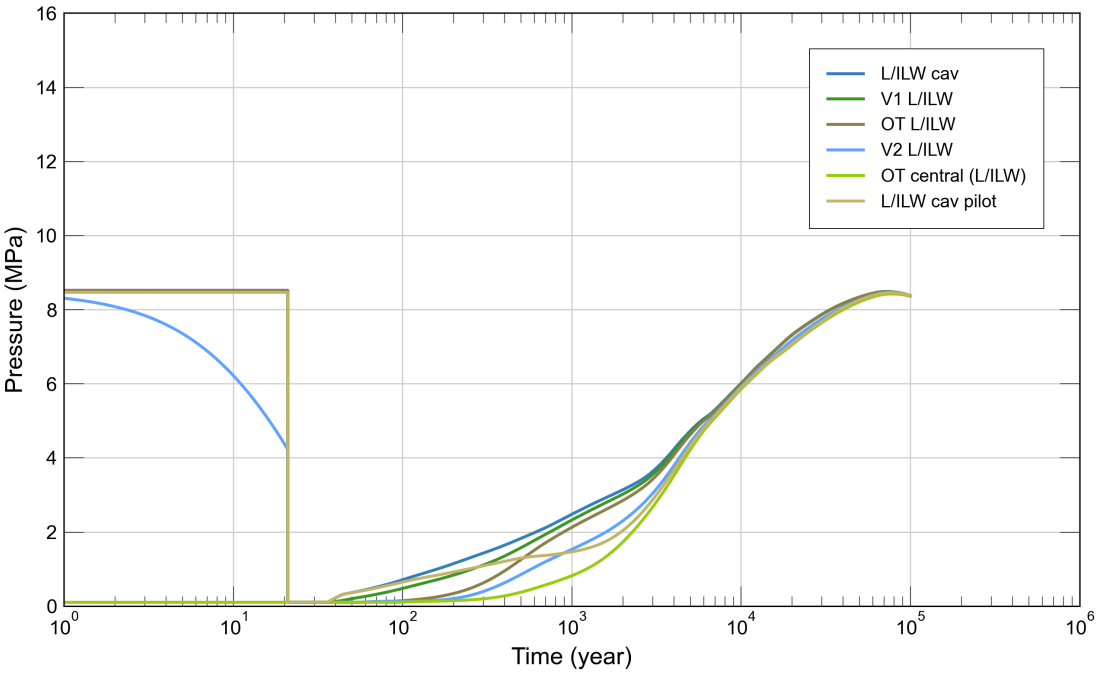
Pressure (MPa)
Time (year)
L/ILW cav
V1 L/ILW
OT L/ILW
V2 L/ILW
OT central (L/ILW)
L/ILW cav pilot

(b)

(c)

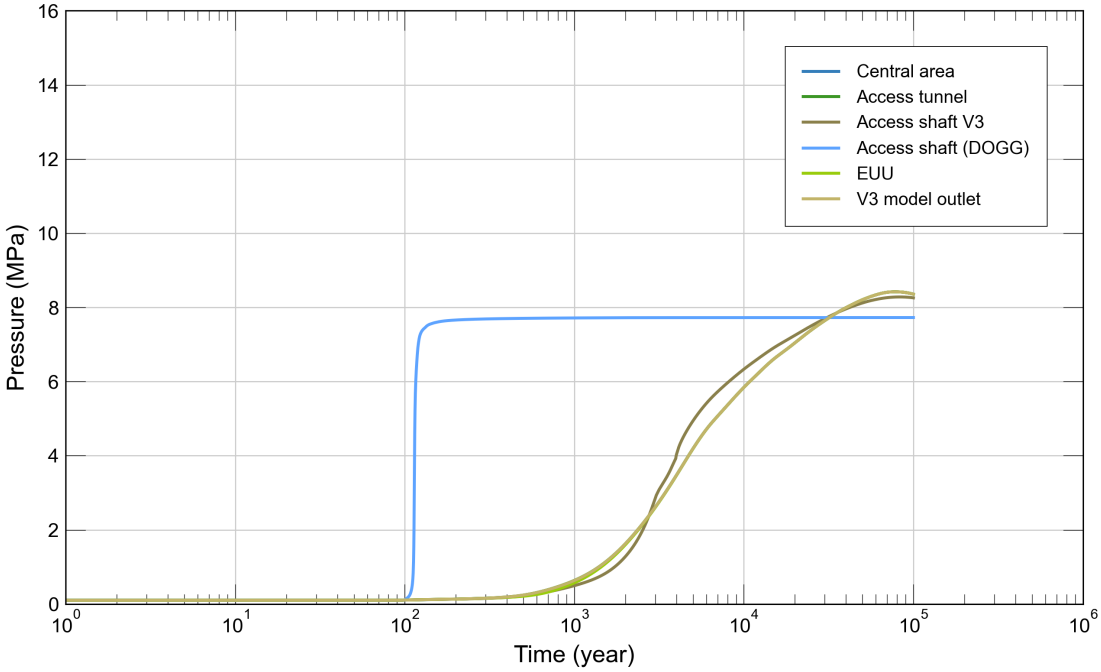

Fig. B-8: Expected performance total system with H_2 molecular diffusion: Transients of pressure

(a) HLW section, (b) L/ILW section and (c) Central area.

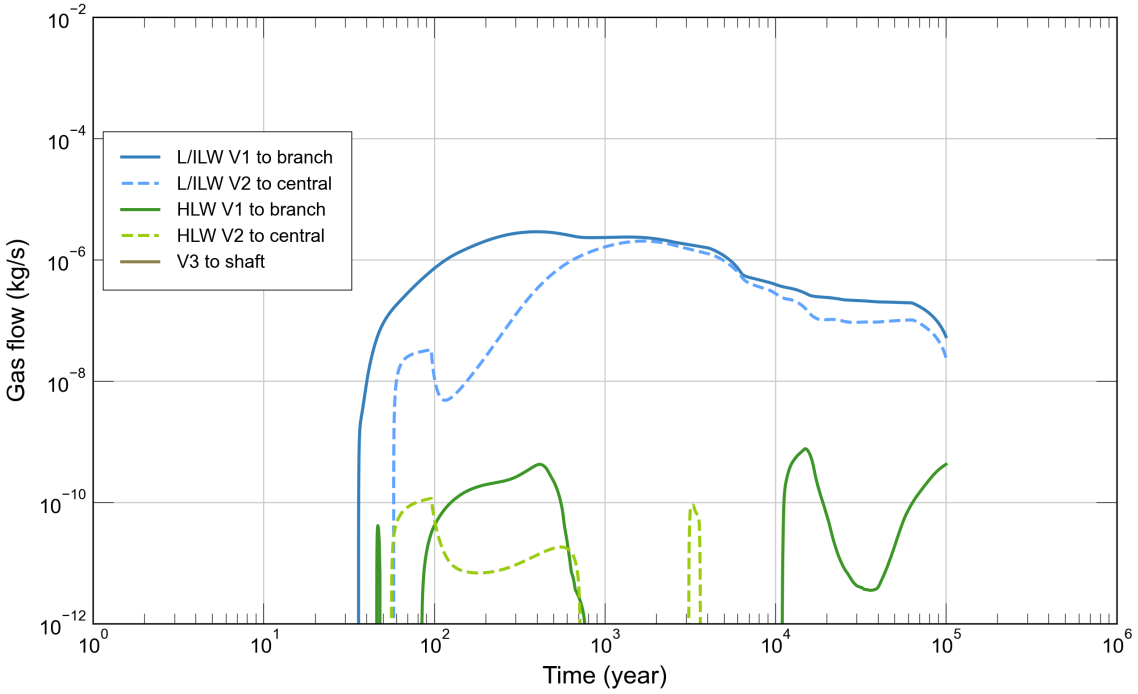

Fig. B-9: Expected performance total system with H_2 molecular diffusion: Transients of gas flow rate through the sealing sections of the repository (towards shafts)

Note: no gas flow through the V3-seal into the shaft within the first 100,000 years.

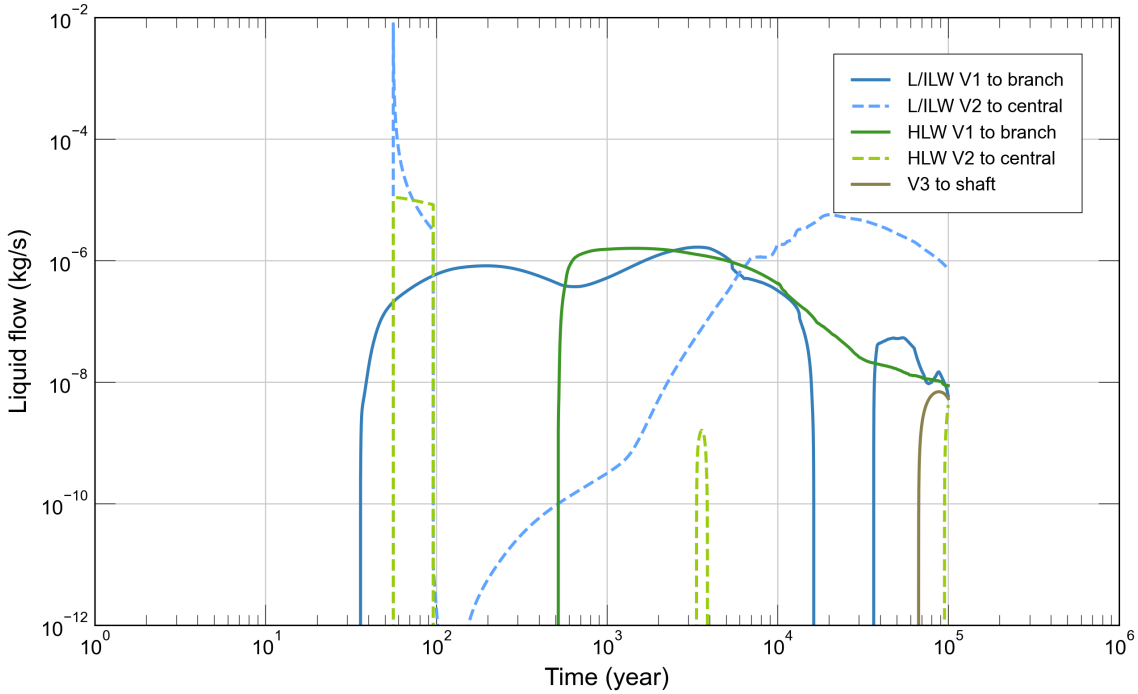

Fig. B-10: Expected performance total system with H_2 molecular diffusion: Transients of liquid flow rate through the sealing sections of the repository (towards shafts)

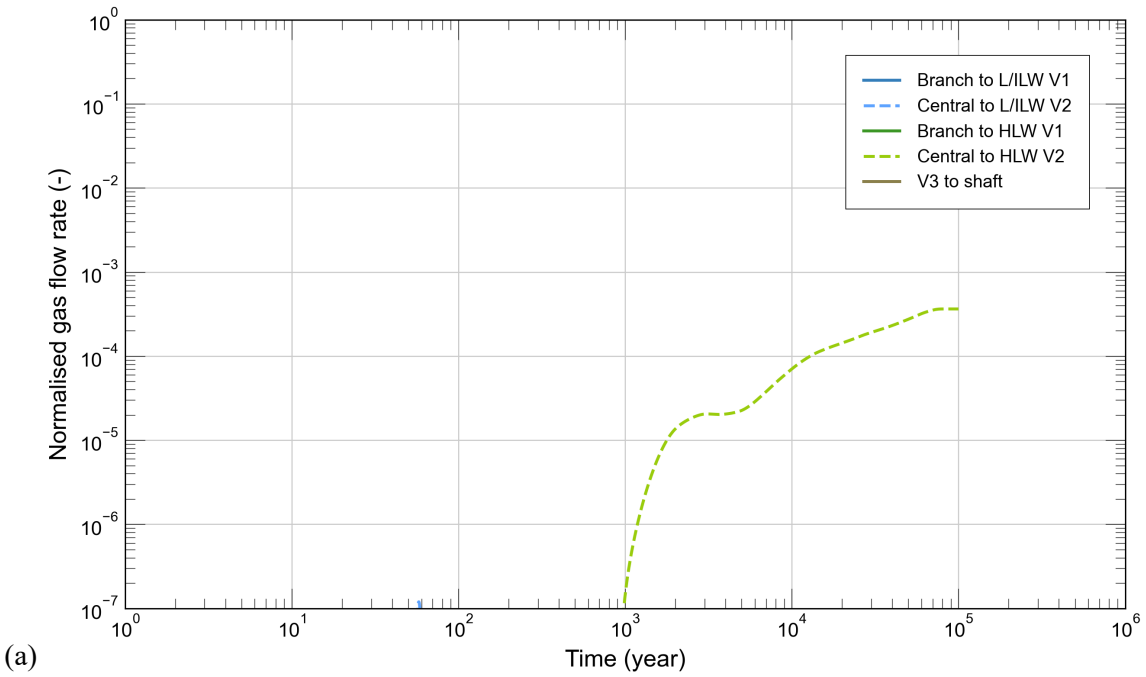

(a)

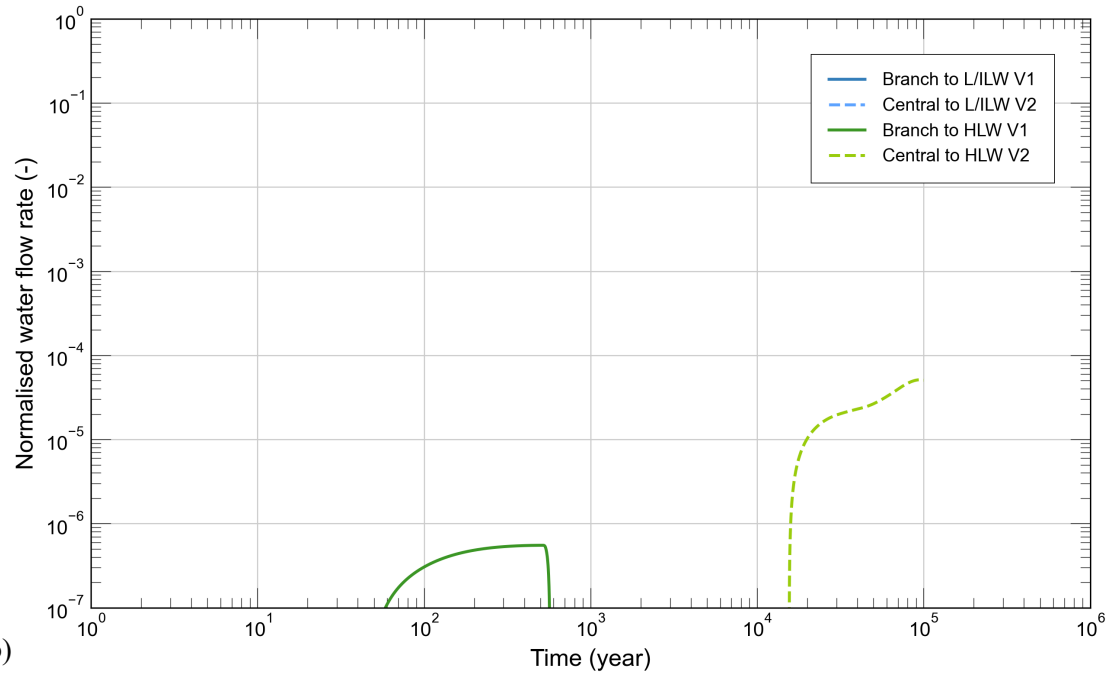

(b)

Fig. B-11: Expected performance total system with H_2 molecular diffusion: Transients of normalised flow rates of (a) gas and (b) liquid through the sealing sections of the repository (towards disposal areas)

B.3 Deviation: no V1 seals *[TSD14]*

This simulation assumes that there are no V1 seals in the repository. This is implemented in the repository model by replacing the V1 seals with VF1 backfill. The resulting transients of temperature, gas saturation, and pressure are shown in Fig. B-12, Fig. B-13, and Fig. B-14, respectively. The transients of gas and liquid flow rates through the sealing sections are shown in Fig. B-15 and Fig. B-16, respectively. The normalised gas and water flows are shown in Fig. B-17.

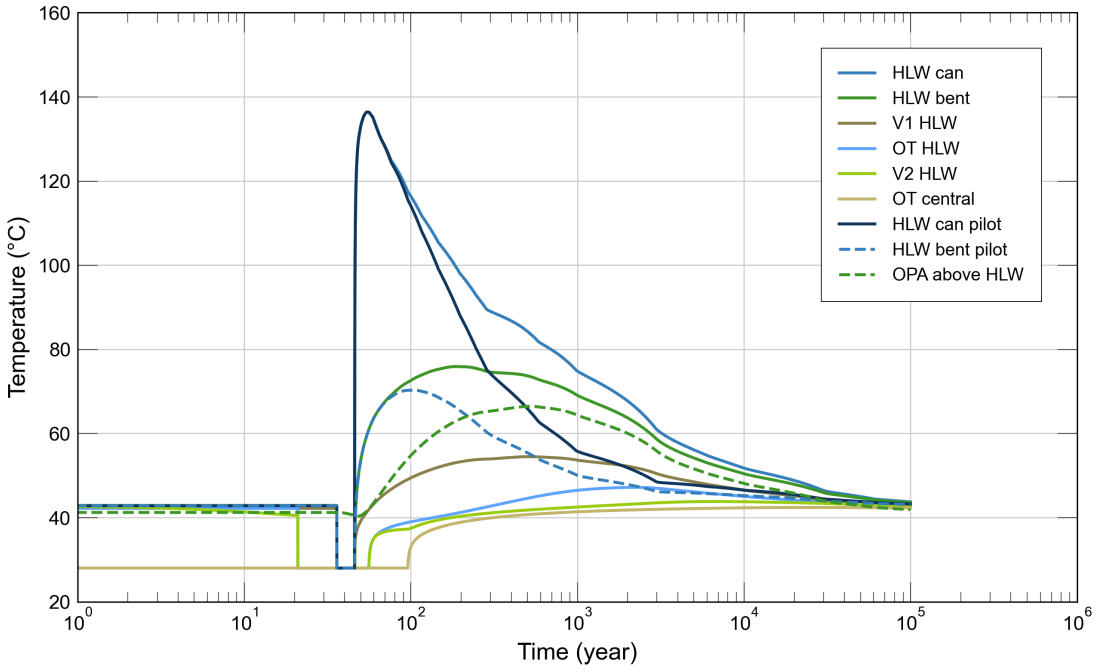

(a)

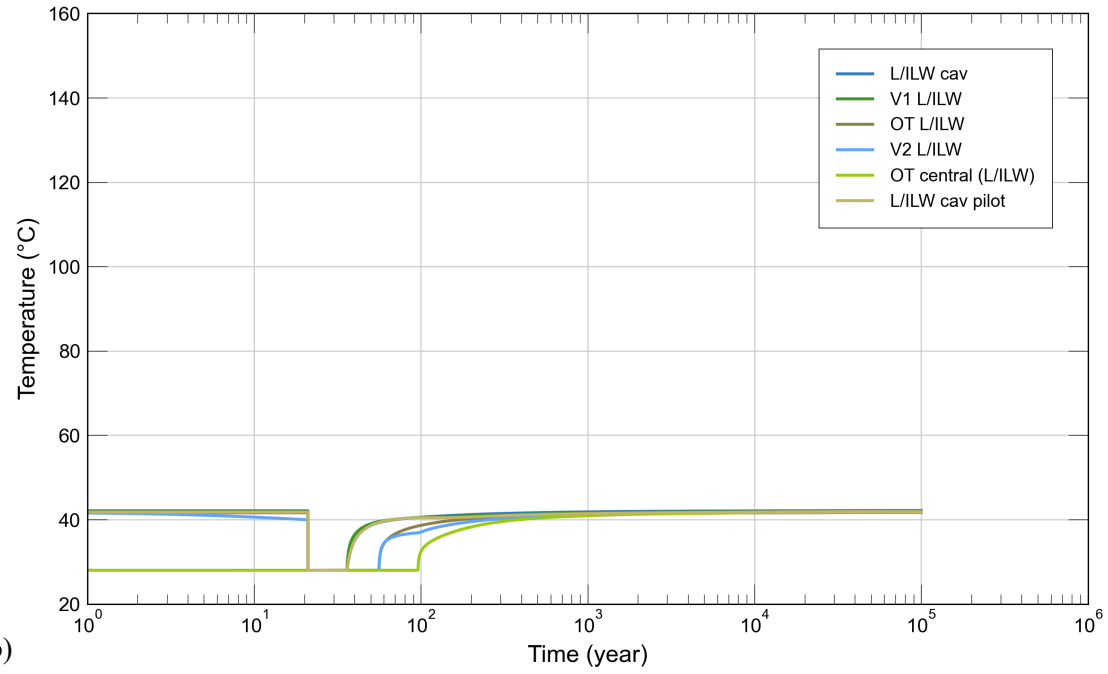

(b)

(c)

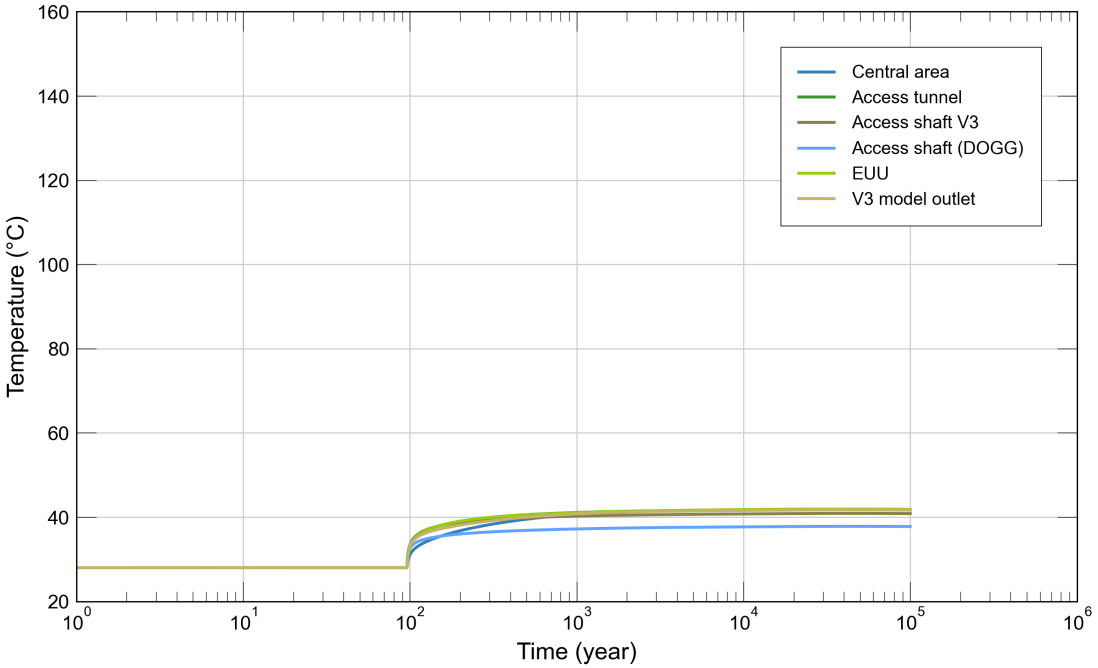

Fig. B-12: Deviations scenario *"no V1 seals"*: Transients of temperature
(a) HLW section, (b) L/ILW section and (c) Central area.

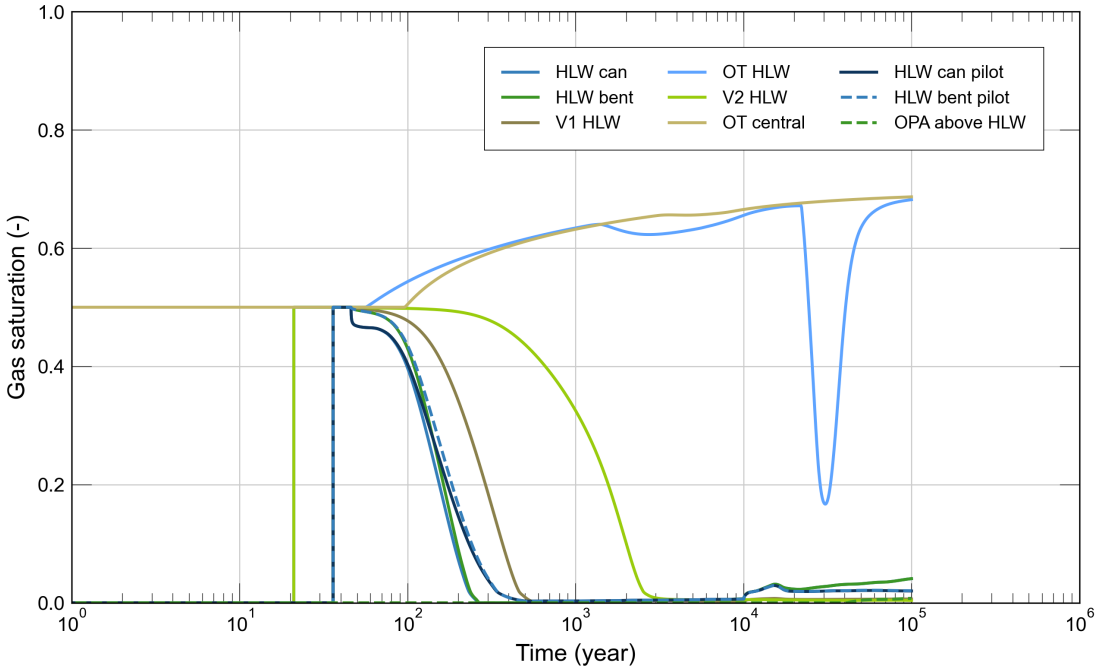
HLW can
HLW bent
V1 HLW
OT HLW
V2 HLW
OT central
HLW can pilot
HLW bent pilot
OPA above HLW
Gas saturation (-)
Time (year)

(a)

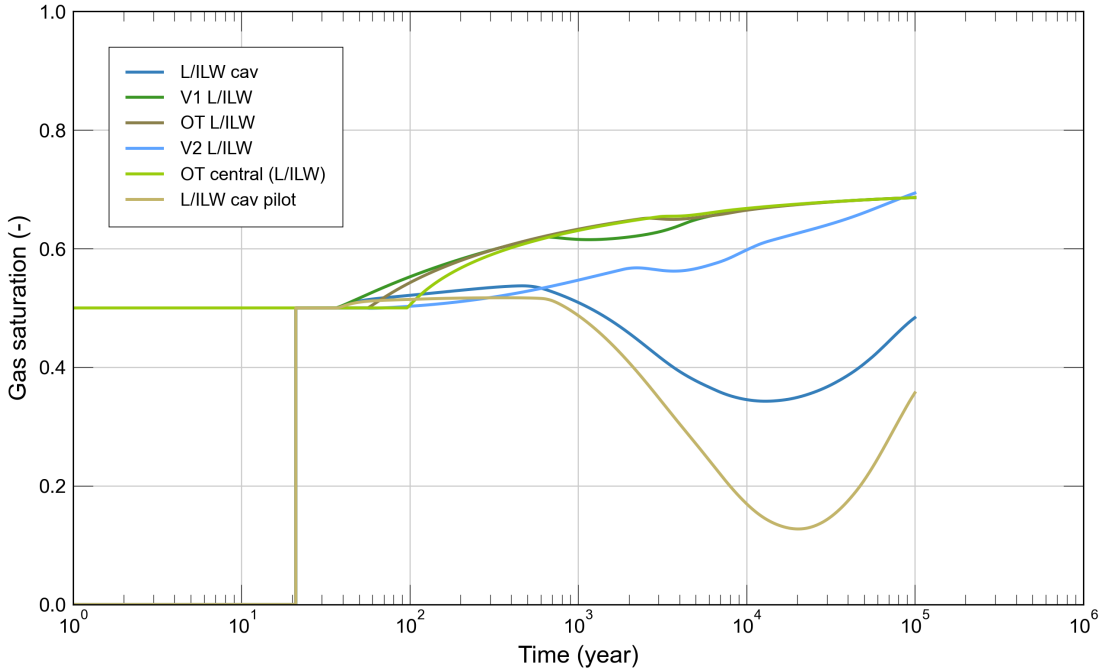
L/ILW cav
V1 L/ILW
OT L/ILW
V2 L/ILW
OT central (L/ILW)
L/ILW cav pilot
Gas saturation (-)
Time (year)

(b)

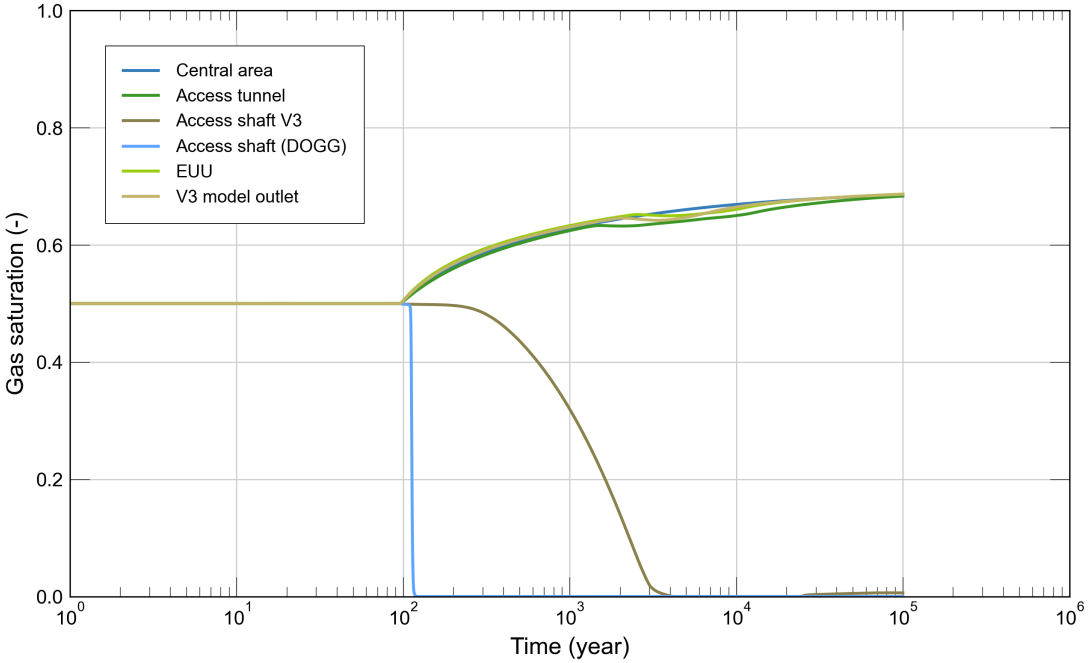

(c)

Fig. B-13: Deviations scenario *"no V1 seals"*: Transients of gas saturation
(a) HLW section, (b) L/ILW section and (c) Central area.

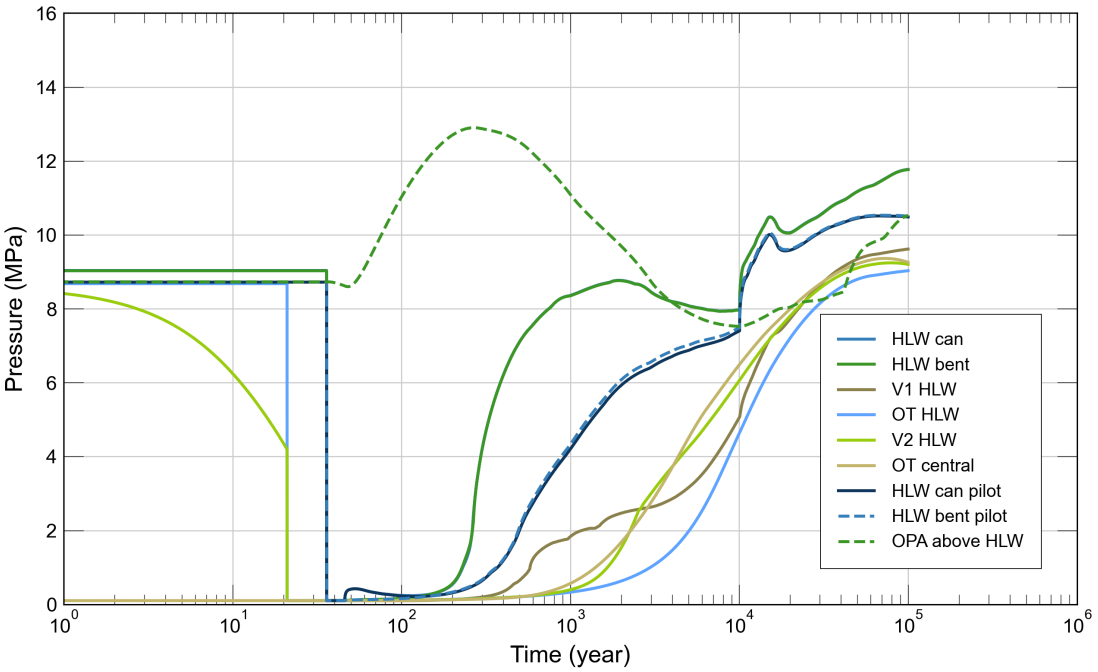
Pressure (MPa)
Time (year)
HLW can
HLW bent
V1 HLW
OT HLW
V2 HLW
OT central
HLW can pilot
HLW bent pilot
OPA above HLW

(a)

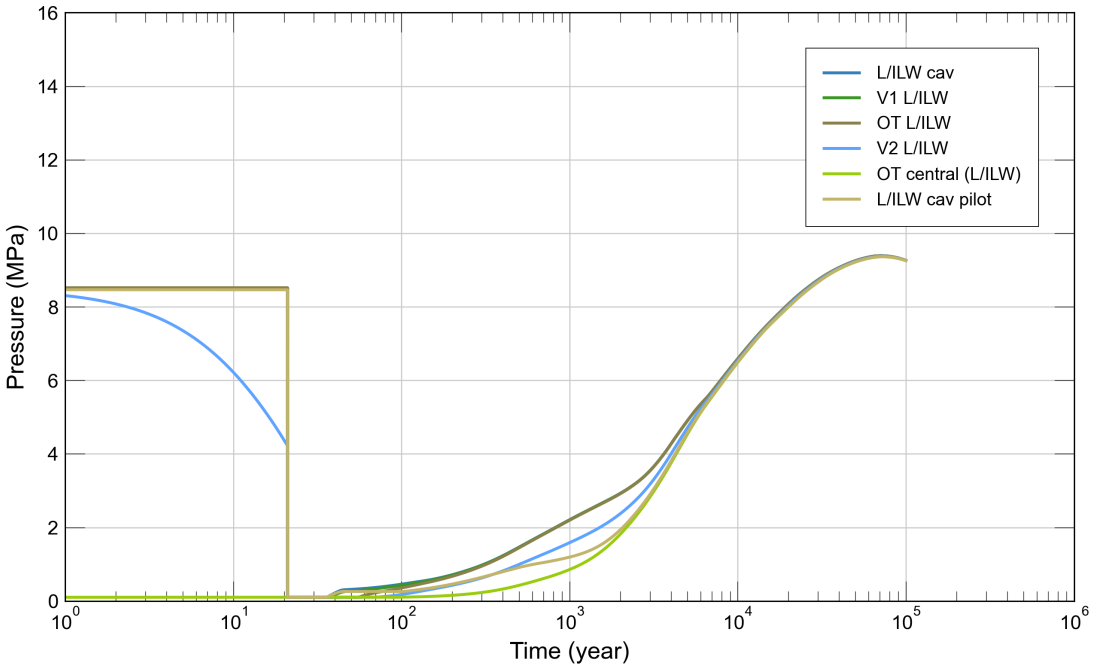
Pressure (MPa)
Time (year)
L/ILW cav
V1 L/ILW
OT L/ILW
V2 L/ILW
OT central (L/ILW)
L/ILW cav pilot

(b)

(c)

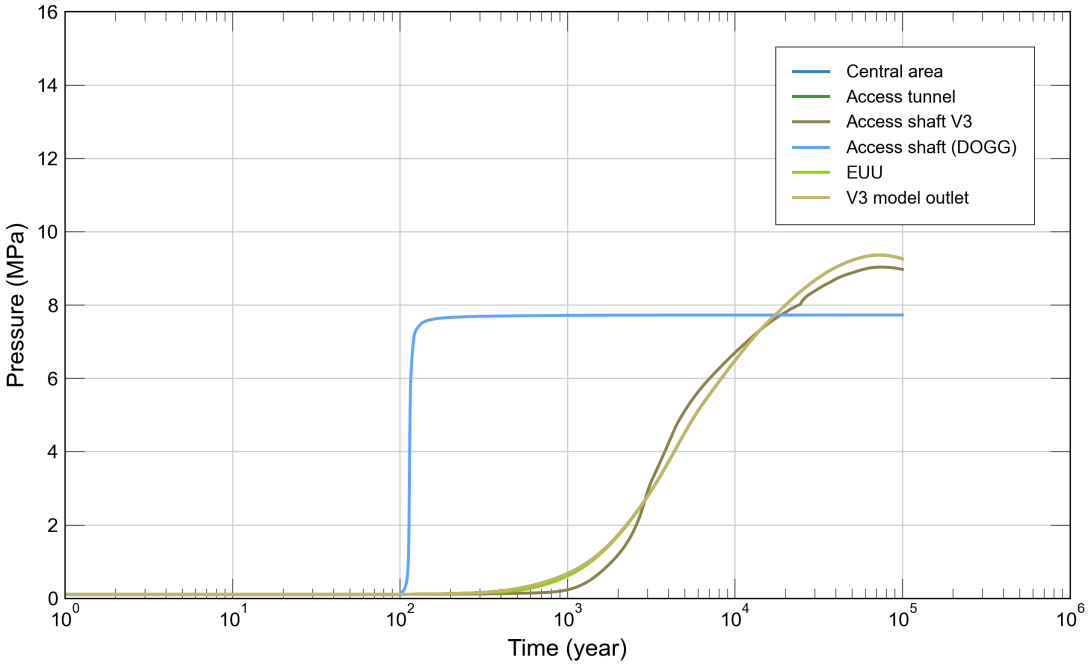

Fig. B-14: Deviations scenario “no V1 seals”: Transients of pressure
(a) HLW section, (b) L/ILW section and (c) Central area.

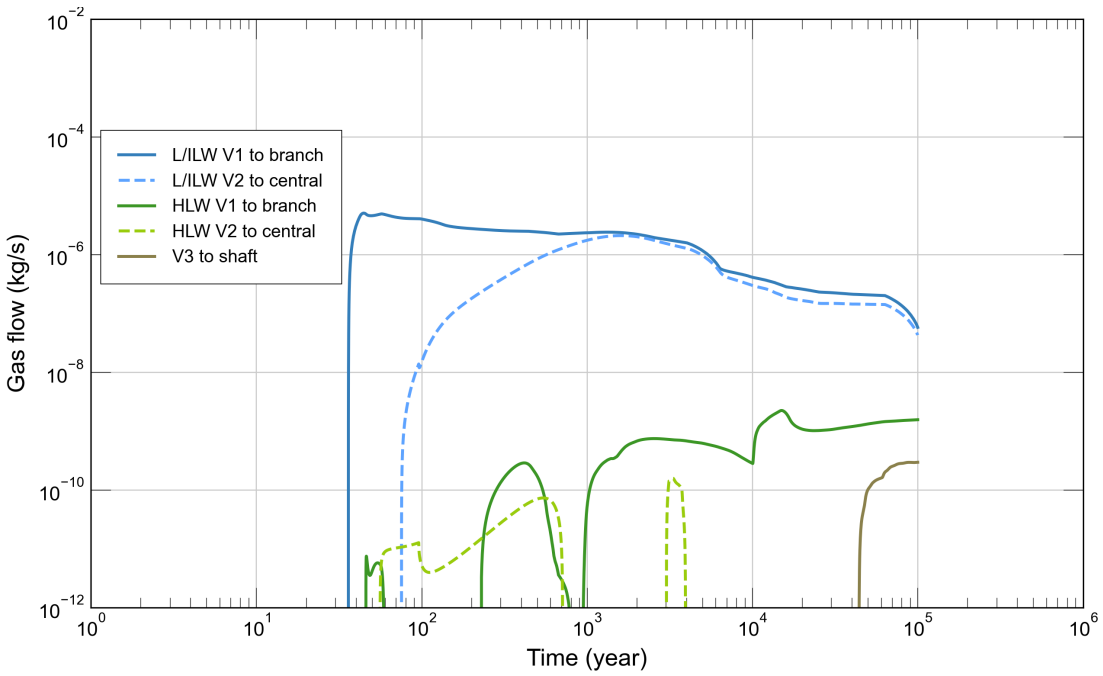

Fig. B-15: Deviations scenario *"no V1 seals"*: Transients of gas flow rate through the sealing sections of the repository (towards shafts)

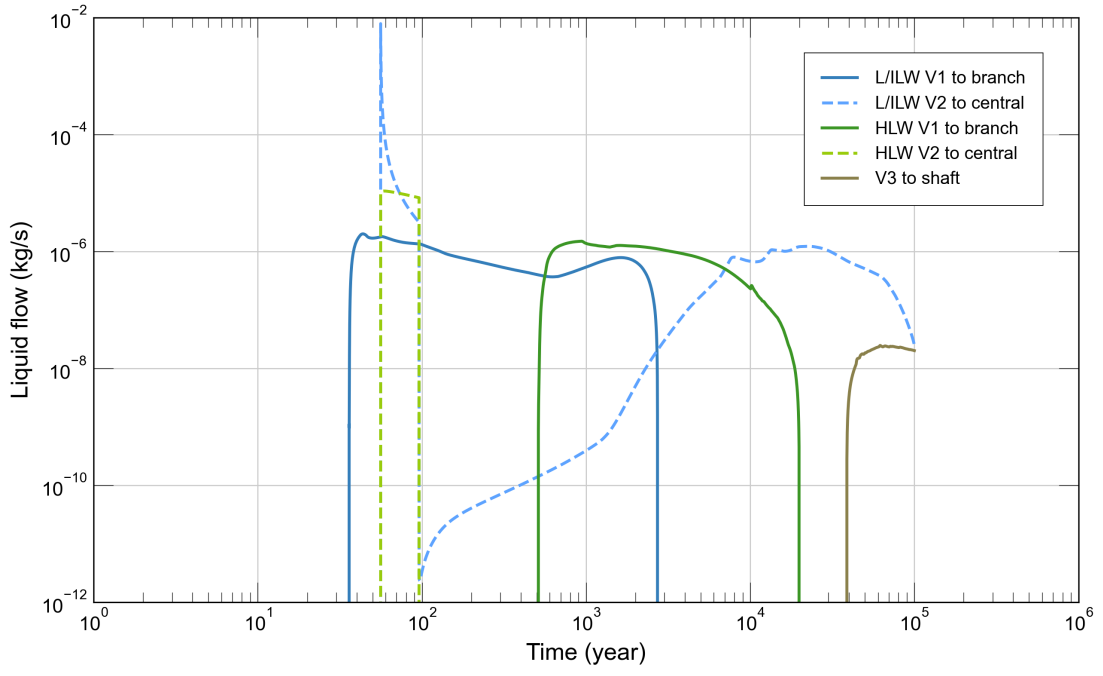

Fig. B-16: Deviations scenario *"no V1 seals"*: Transients of liquid flow rate through the sealing sections of the repository (towards shafts)

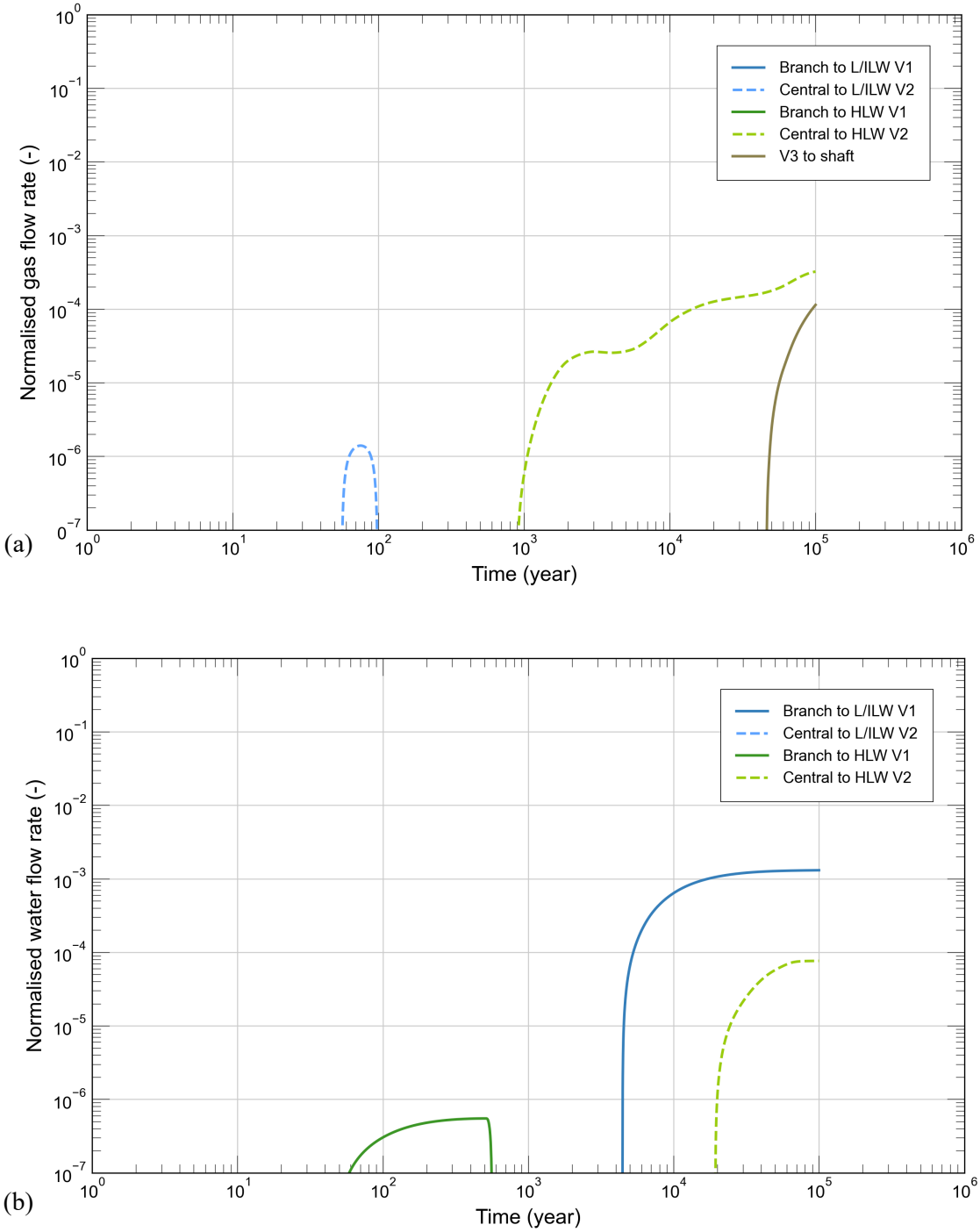

Fig. B-17: Deviations scenario *"no V1 seals"*: Transients of normalised flow rates of (a) gas and (b) liquid through the sealing sections of the repository (towards disposal areas)

B.4 Deviation: no V2 seals *[TSD15]*

This simulation assumes that there are no V2 seals in the repository. This is implemented in the repository model by replacing the V2 materials with backfill VF2 material. The resulting transients of temperature, gas saturation, and pressure are shown in Fig. B-18, Fig. B-19, and Fig. B-20, respectively. The transients of gas and liquid flow rates through the sealing sections are shown in Fig. B-21 and Fig. B-22, respectively. The normalised gas and water flows are shown in Fig. B-23.

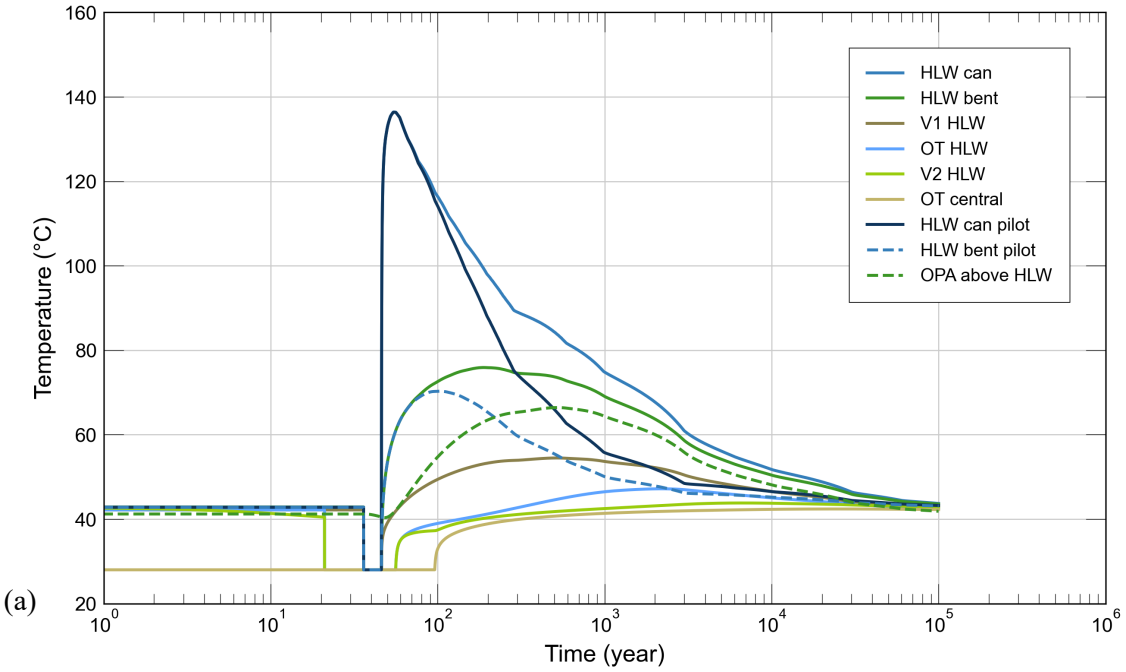

(a)

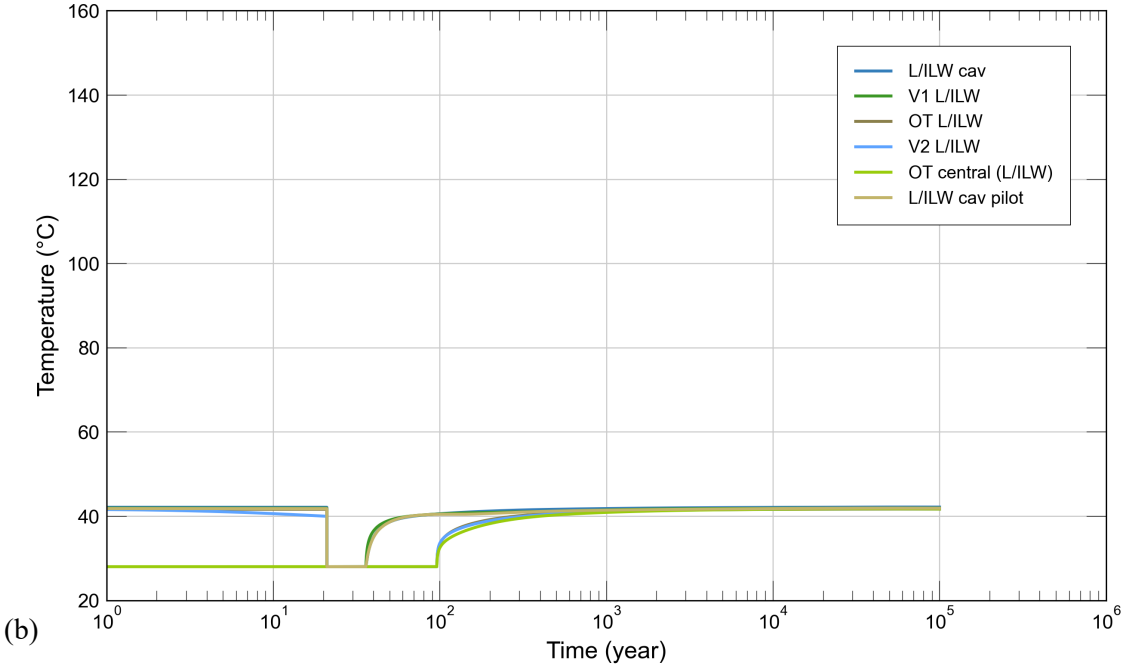

(b)

(c)

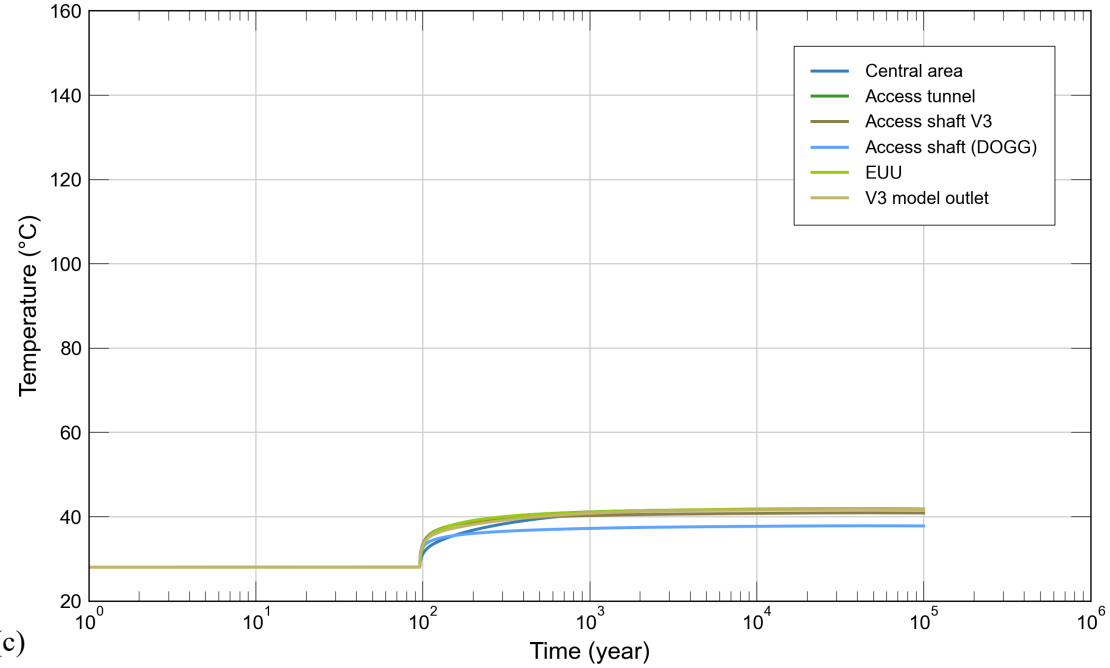

Fig. B-18: Deviations scenario *"no V2 seals"*: Transients of temperature
(a) HLW section, (b) L/ILW section and (c) Central area.

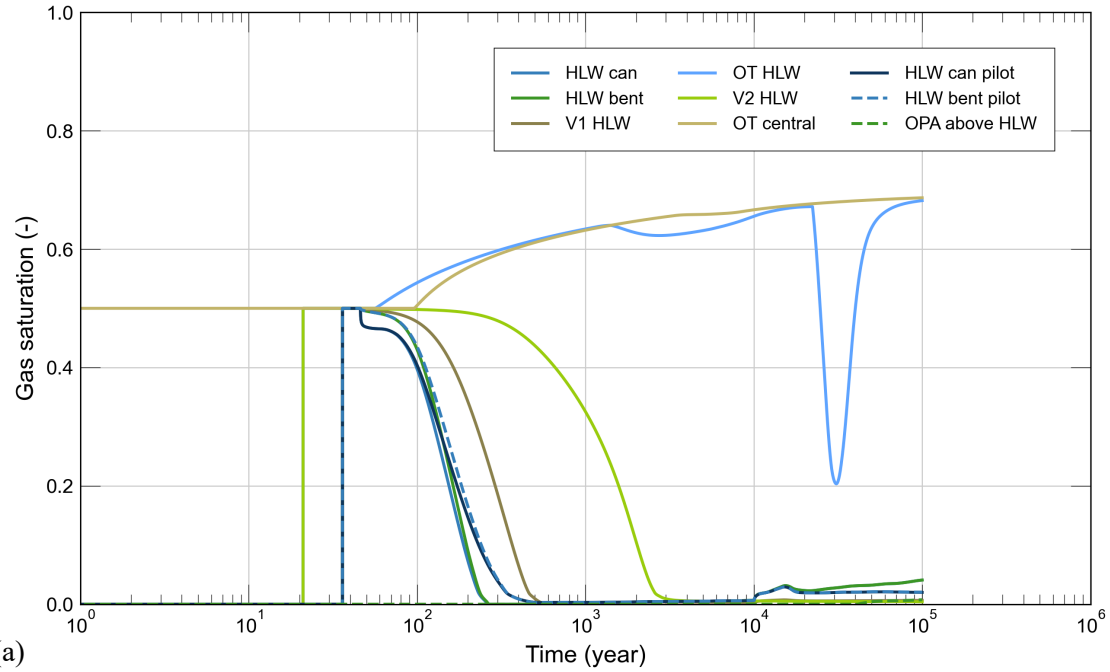
HLW can
HLW bent
V1 HLW
OT HLW
V2 HLW
OT central
HLW can pilot
HLW bent pilot
OPA above HLW
Gas saturation (-)
Time (year)

(a)

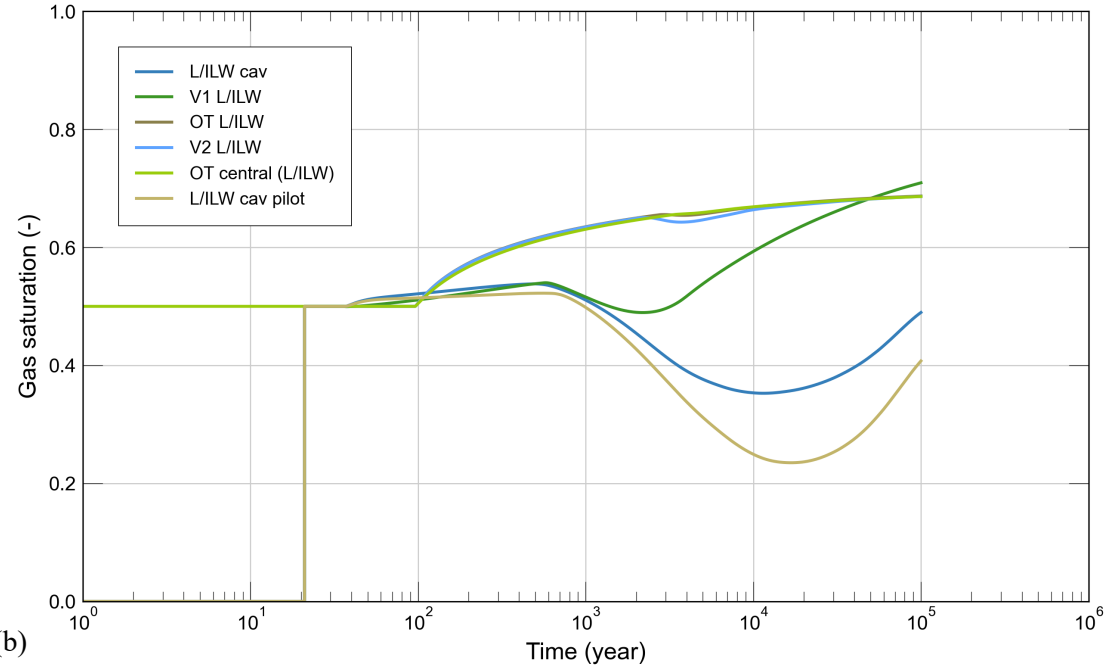
L/ILW cav
V1 L/ILW
OT L/ILW
V2 L/ILW
OT central (L/ILW)
L/ILW cav pilot
Gas saturation (-)
Time (year)

(b)

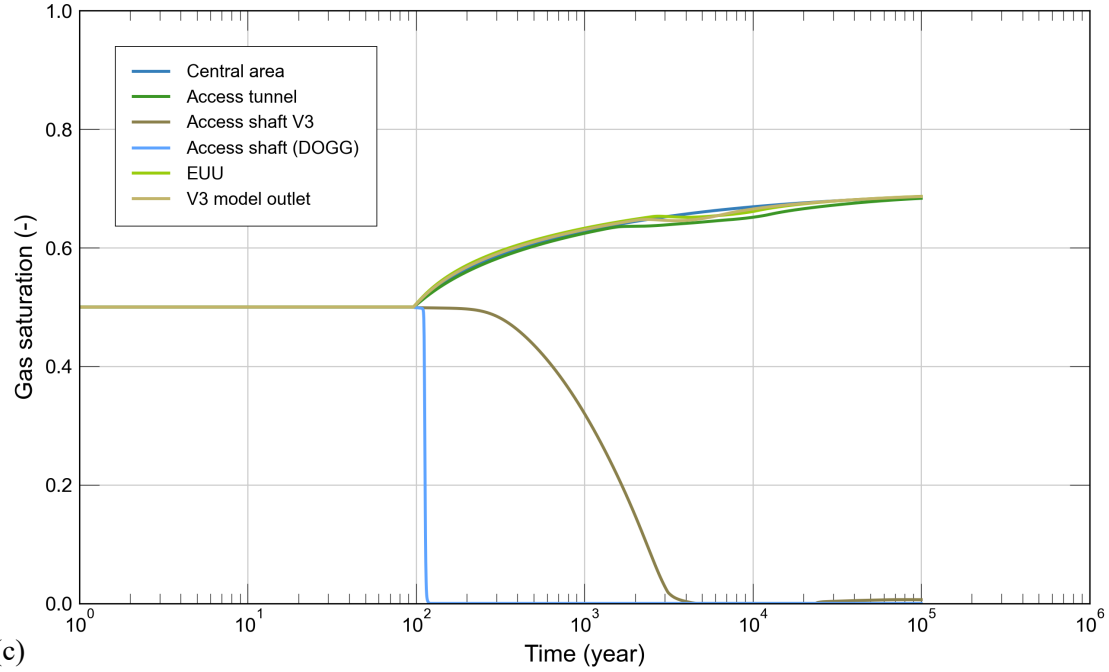

(c)

Fig. B-19: Deviations scenario *"no V2 seals"*: Transients of gas saturation
(a) HLW section, (b) L/ILW section and (c) Central area.

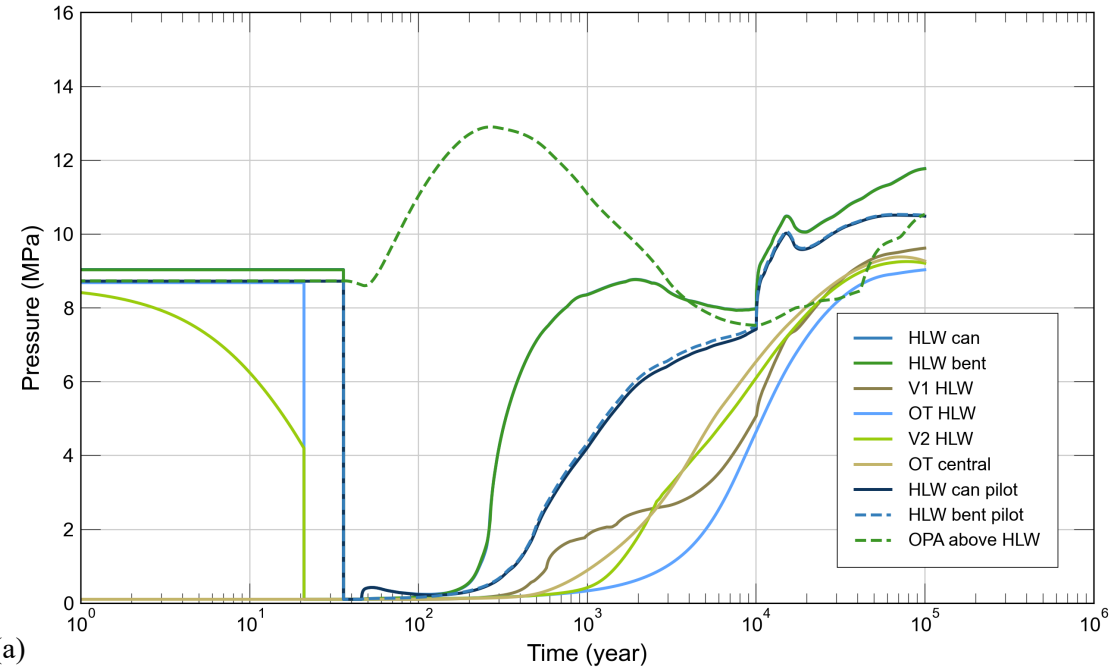
Pressure (MPa)
Time (year)
HLW can
HLW bent
V1 HLW
OT HLW
V2 HLW
OT central
HLW can pilot
HLW bent pilot
OPA above HLW

(a)

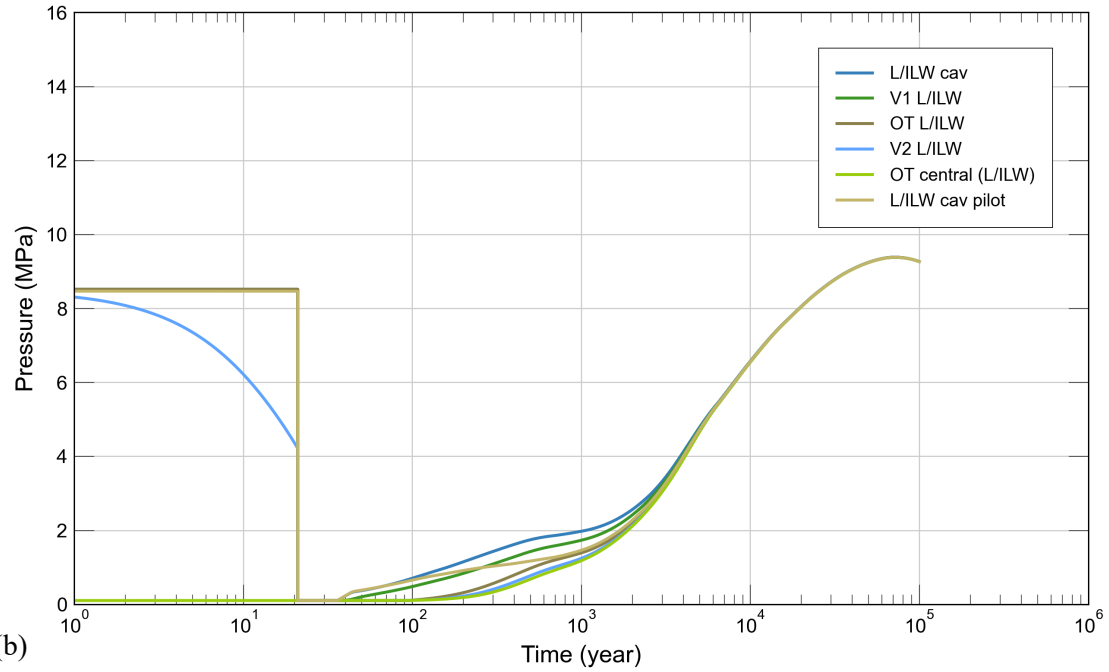
Pressure (MPa)
Time (year)
L/ILW cav
V1 L/ILW
OT L/ILW
V2 L/ILW
OT central (L/ILW)
L/ILW cav pilot

(b)

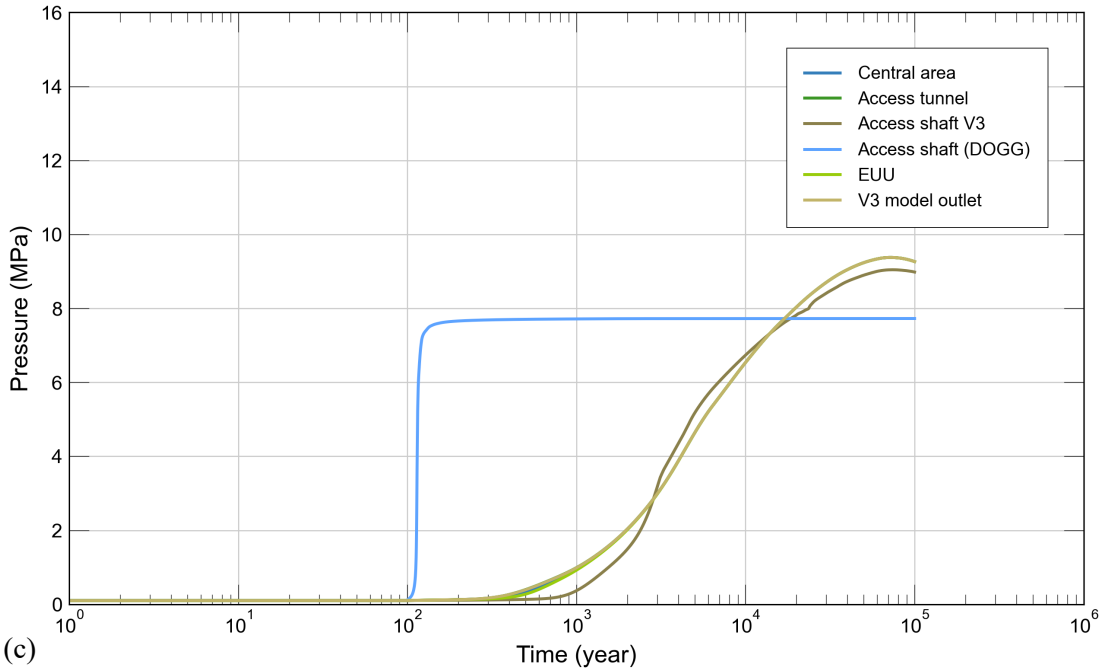

(c)

Fig. B-20: Deviations scenario *"no V2 seals"*: Transients of pressure
(a) HLW section, (b) L/ILW section and (c) Central area.

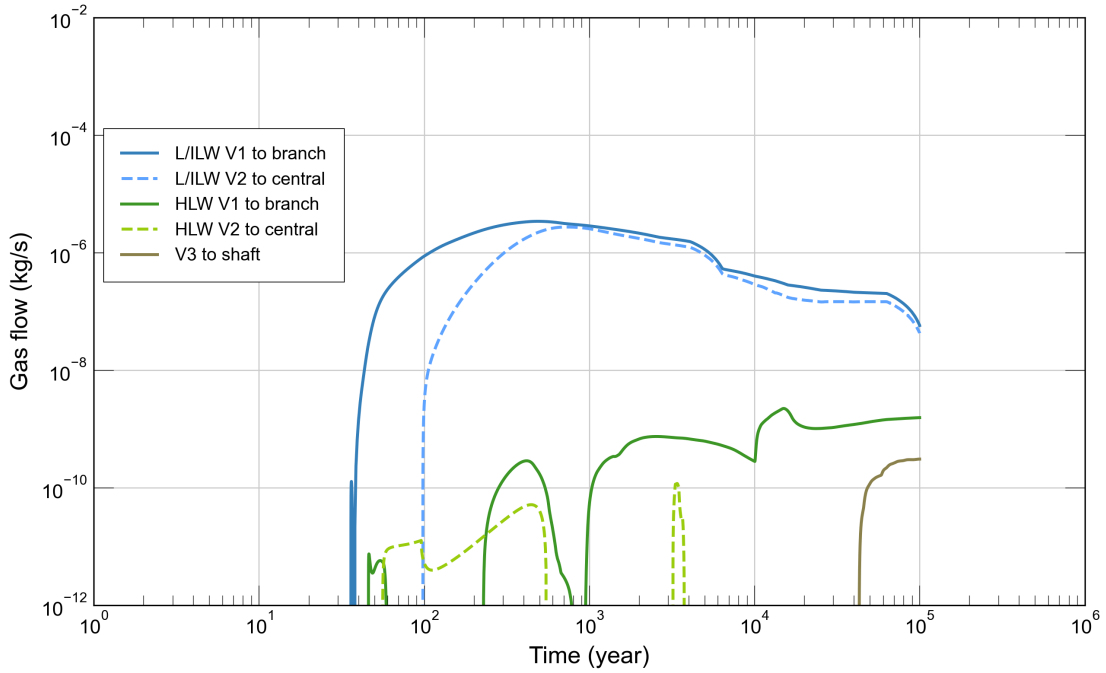

Fig. B-21: Deviations scenario *"no V2 seals"*: Transients of gas flow rate through the sealing sections of the repository (towards shafts)

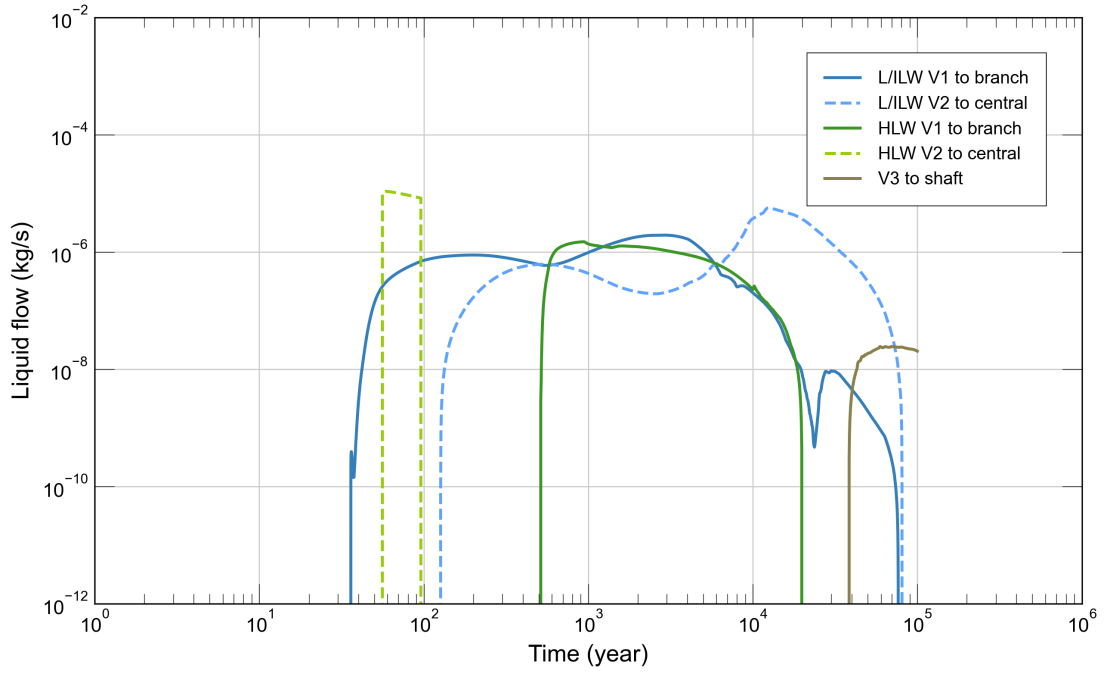

Fig. B-22: Deviations scenario *"no V2 seals"*: Transients of liquid flow rate through the sealing sections of the repository (towards shafts)

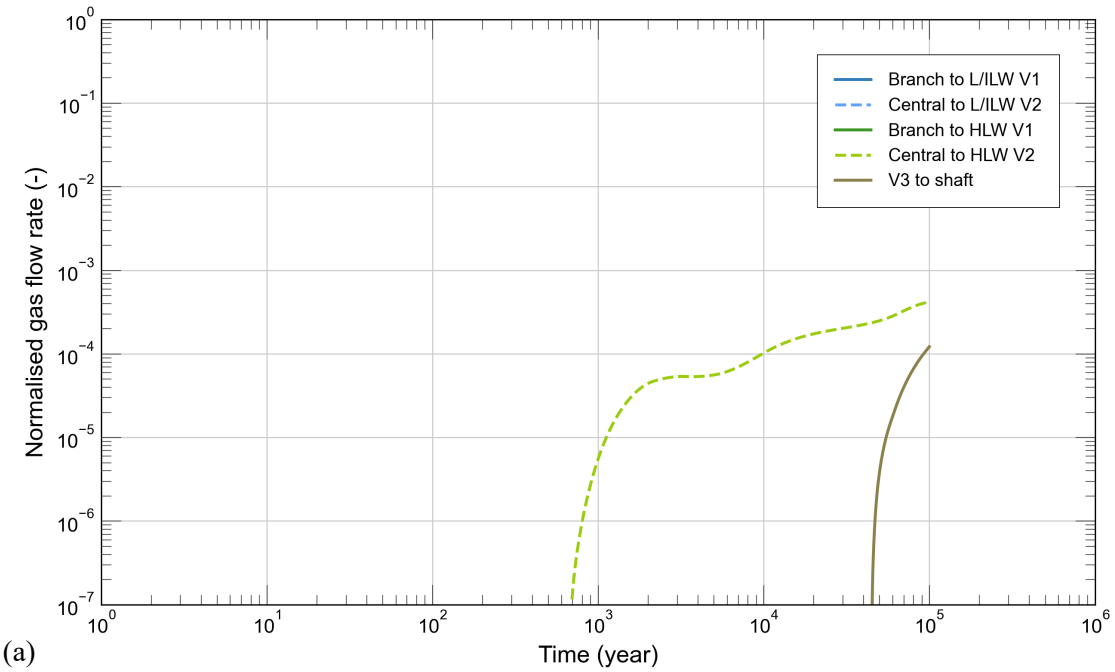

(a)

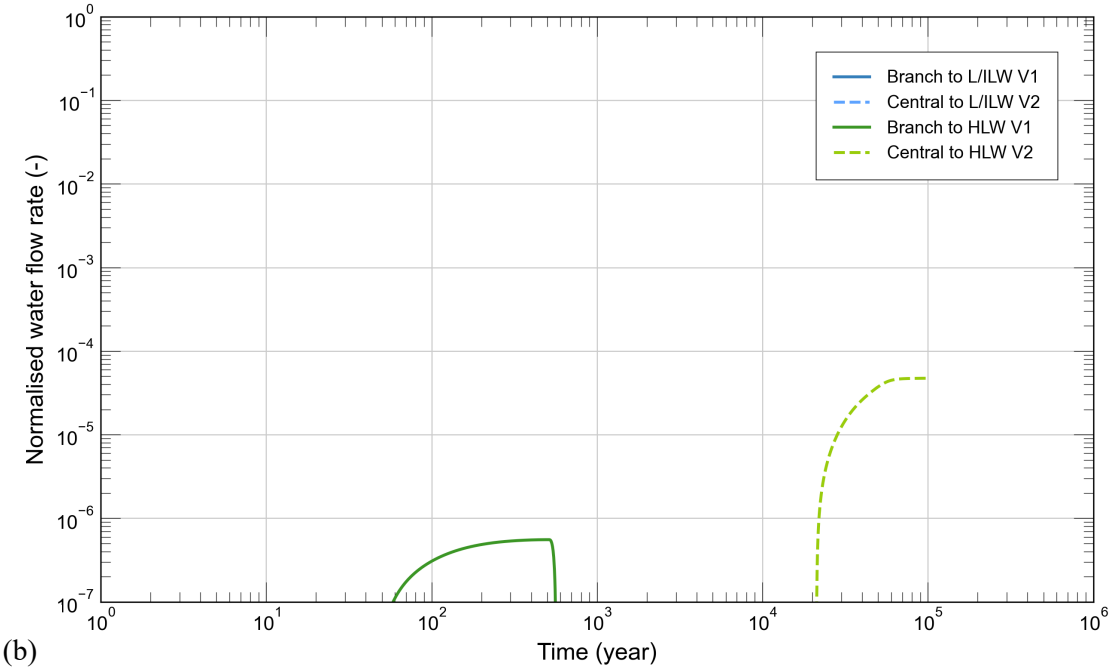

(b)

Fig. B-23: Deviations scenario *"no V2 seals"*: Transients of normalised flow rates of (a) gas and (b) liquid through the sealing sections of the repository (towards disposal areas)

B.5 Deviation: impermeable V3 seals *[TSD16]*

In this simulation, the intrinsic permeability of the sealing element of the V3 seals is set to 1.0E-22 m^2. The capillary strength parameter, P_0, is scaled accordingly to 76 MPa. The properties of the EDZ surrounding the V3 seal are assumed to be identical to those of the undisturbed OPA.

The transients of temperature, gas saturation, and pressure are shown in Fig. B-24, Fig. B-25, and Fig. B-26, respectively. The transients of gas and liquid flow rates through the sealing sections are shown in Fig. B-27 and Fig. B-28, respectively. The normalised gas and water flows are shown in Fig. B-28. The results show that a peak pressure of ~9.4 MPa is reached in the repository associated with gas generation from the L/ILW without any appreciable release of gas or water from the V3 seal to the shafts within 100,000 years.

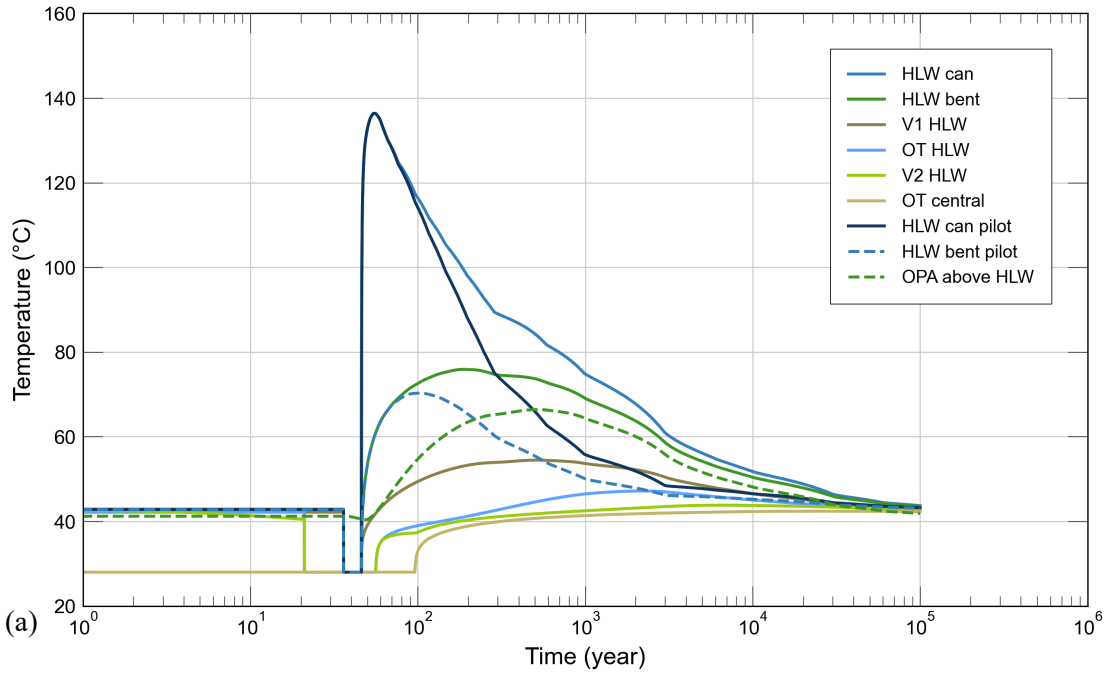

(a)

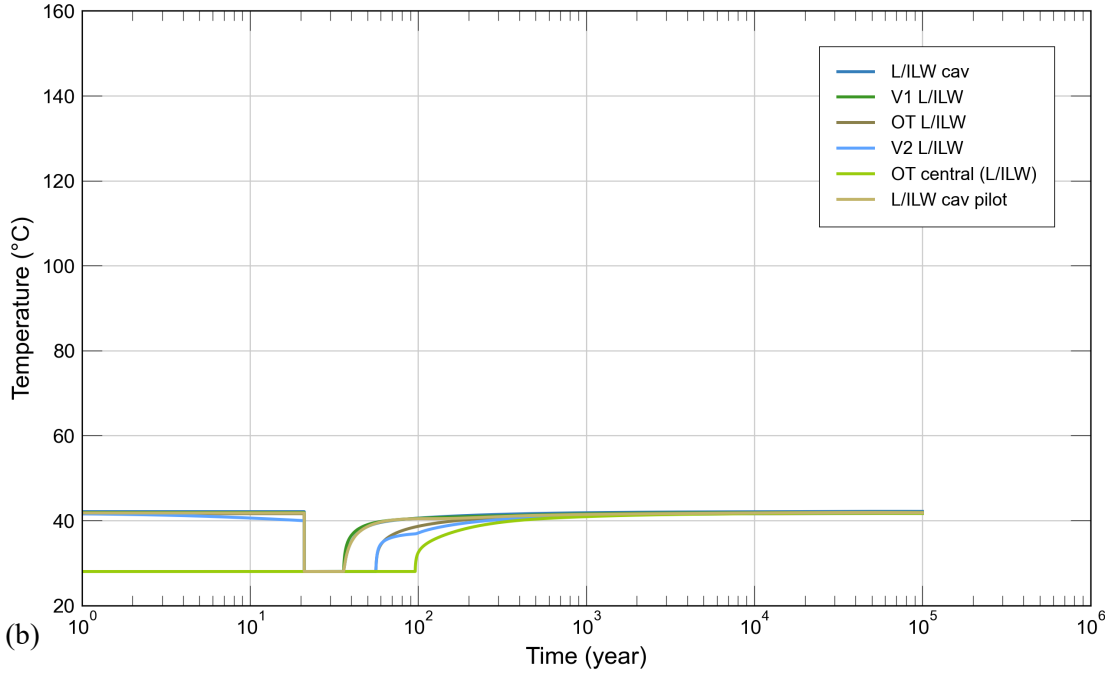

(b)

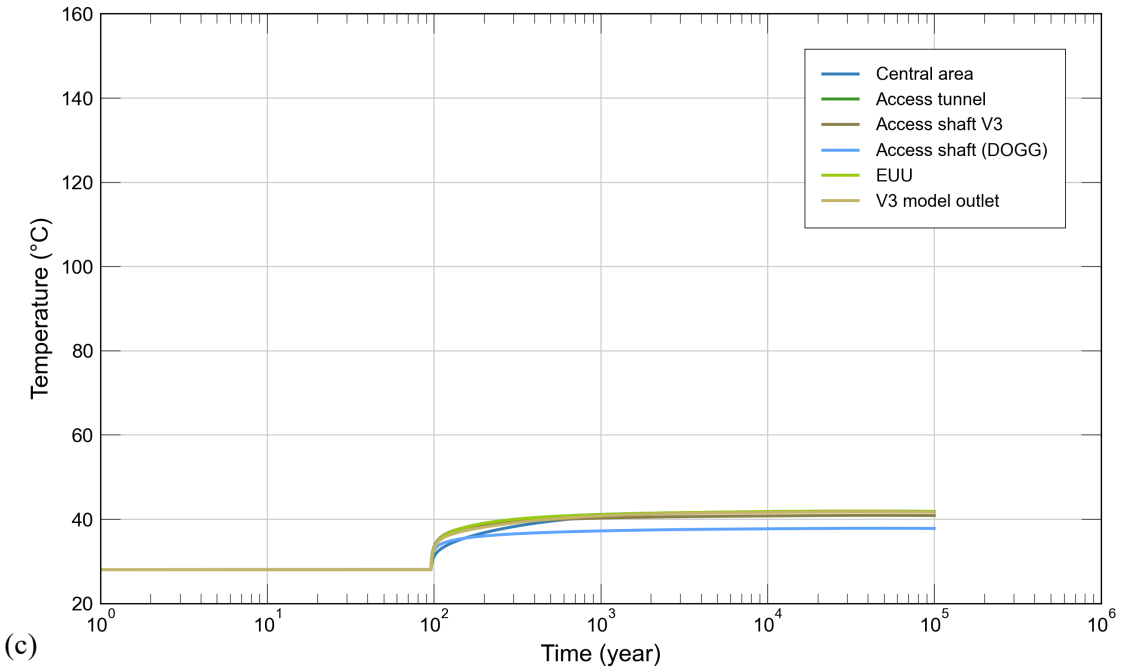

(c)

Fig. B-24: Deviations scenario *"impermeable V3 seals"*: Transients of temperature
(a) HLW section, (b) L/ILW section and (c) Central area.

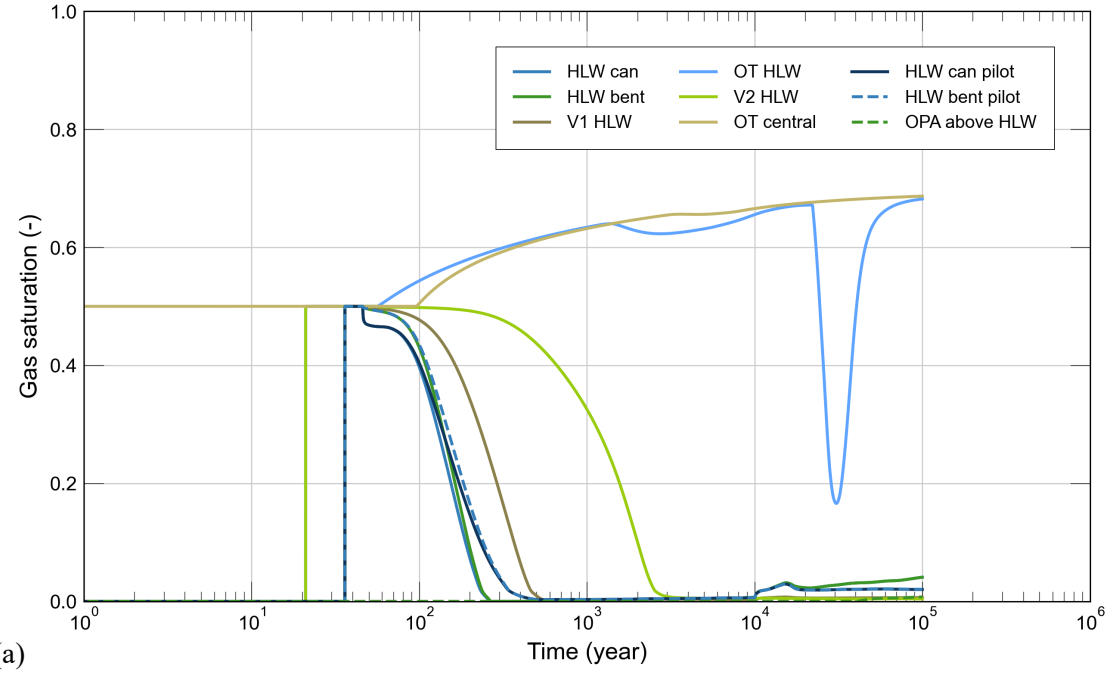
HLW can
HLW bent
V1 HLW
OT HLW
V2 HLW
OT central
HLW can pilot
HLW bent pilot
OPA above HLW
Gas saturation (-)
Time (year)

(a)

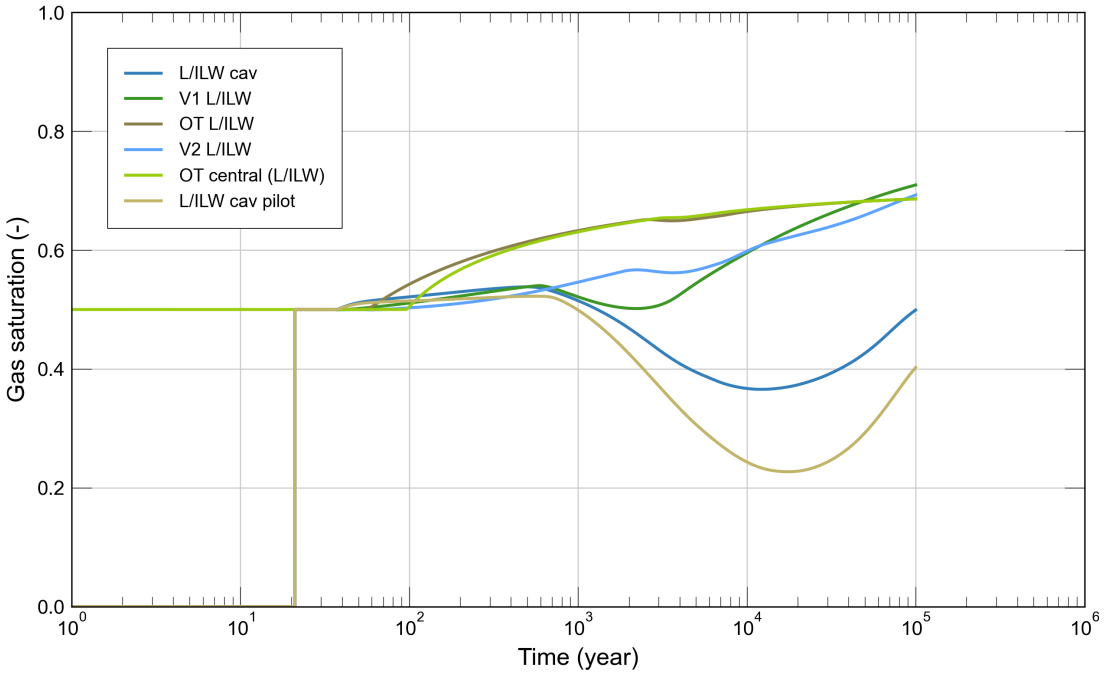
L/ILW cav
V1 L/ILW
OT L/ILW
V2 L/ILW
OT central (L/ILW)
L/ILW cav pilot
Gas saturation (-)
Time (year)

(b)

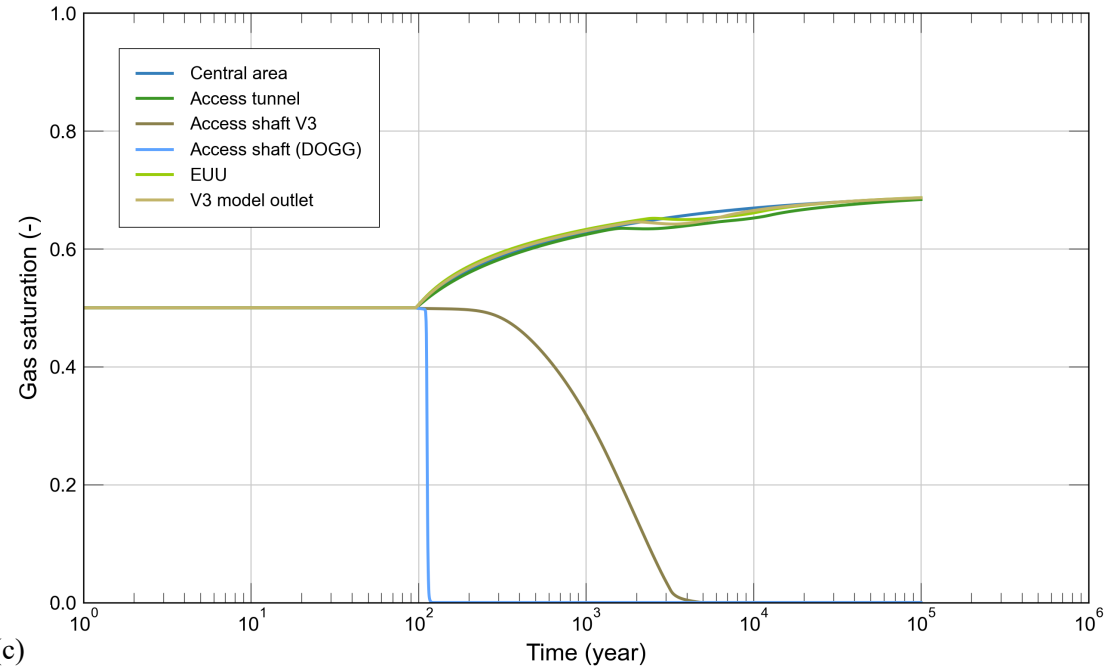

(c)

Fig. B-25: Deviations scenario *"impermeable V3 seals"*: Transients of gas saturation (a) HLW section, (b) L/ILW section and (c) Central area.

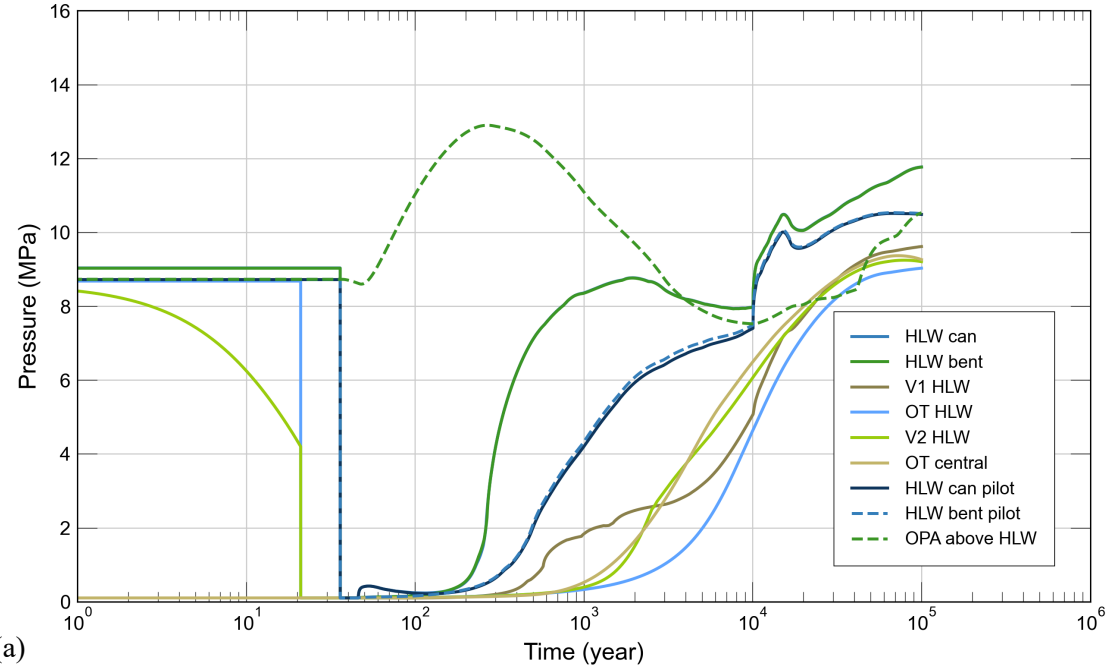
Pressure (MPa)
Time (year)
HLW can
HLW bent
V1 HLW
OT HLW
V2 HLW
OT central
HLW can pilot
HLW bent pilot
OPA above HLW

(a)

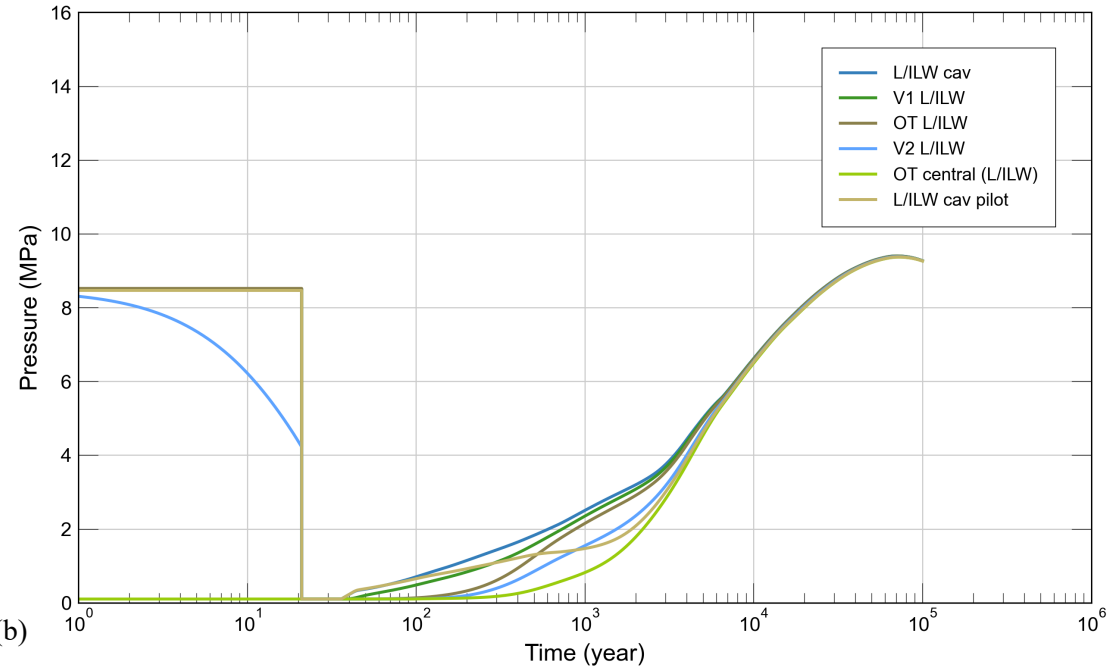
Pressure (MPa)
Time (year)
L/ILW cav
V1 L/ILW
OT L/ILW
V2 L/ILW
OT central (L/ILW)
L/ILW cav pilot

(b)

(c)

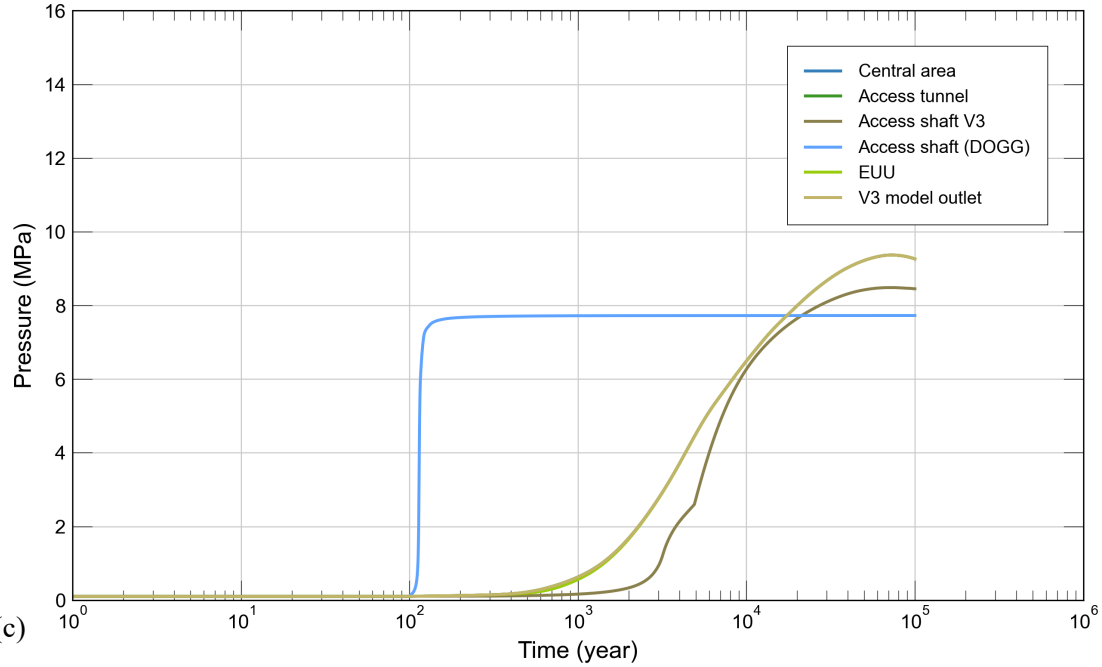

Fig. B-26: Deviations scenario *"impermeable V3 seals"*: Transients of pressure
(a) HLW section, (b) L/ILW section and (c) Central area.

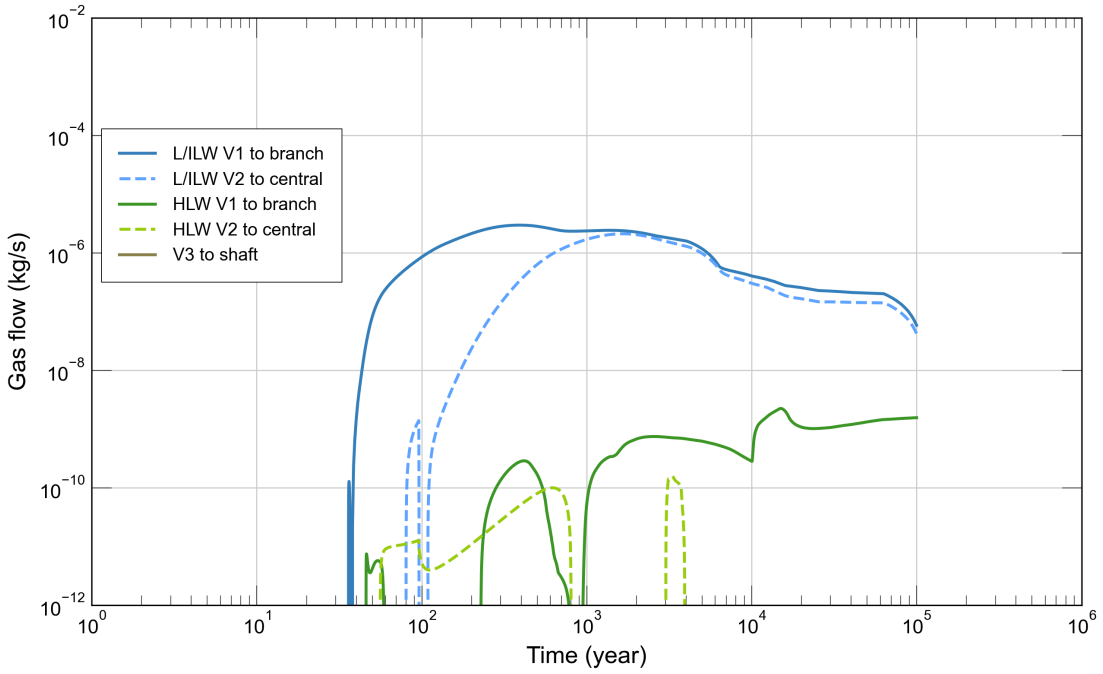

Fig. B-27: Deviations scenario *"impermeable V3 seals"*: Transients of gas flow rate through the sealing sections of the repository (towards shafts)

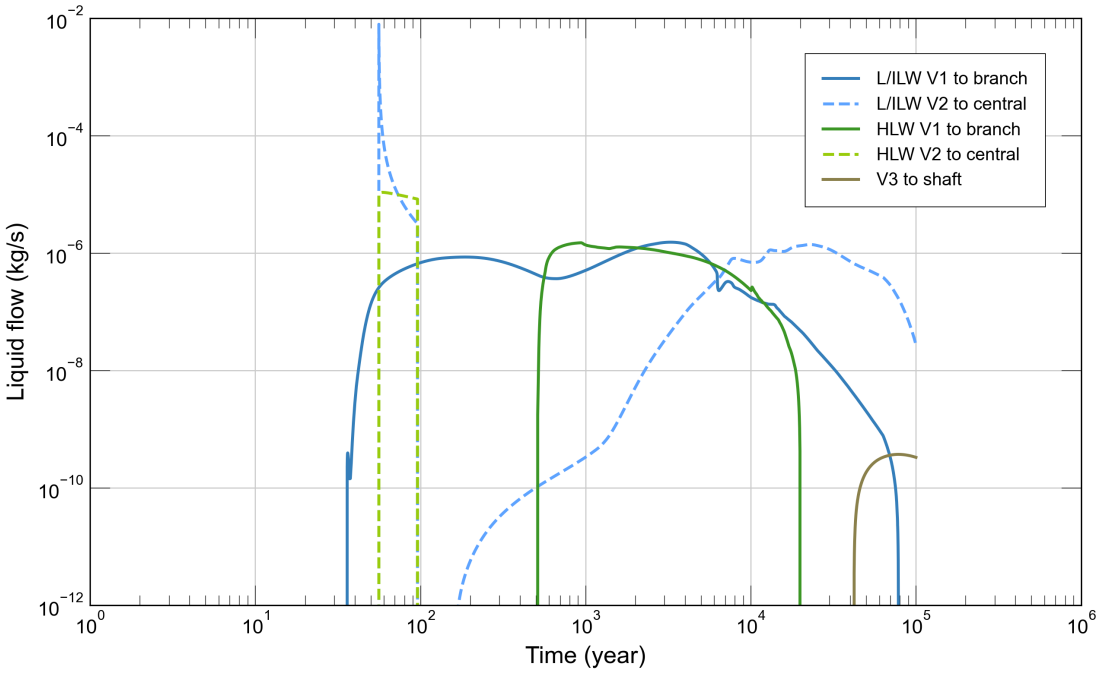

Fig. B-28: Deviations scenario *"impermeable V3 seals"*: Transients of liquid flow rate through the sealing sections of the repository (towards shafts)

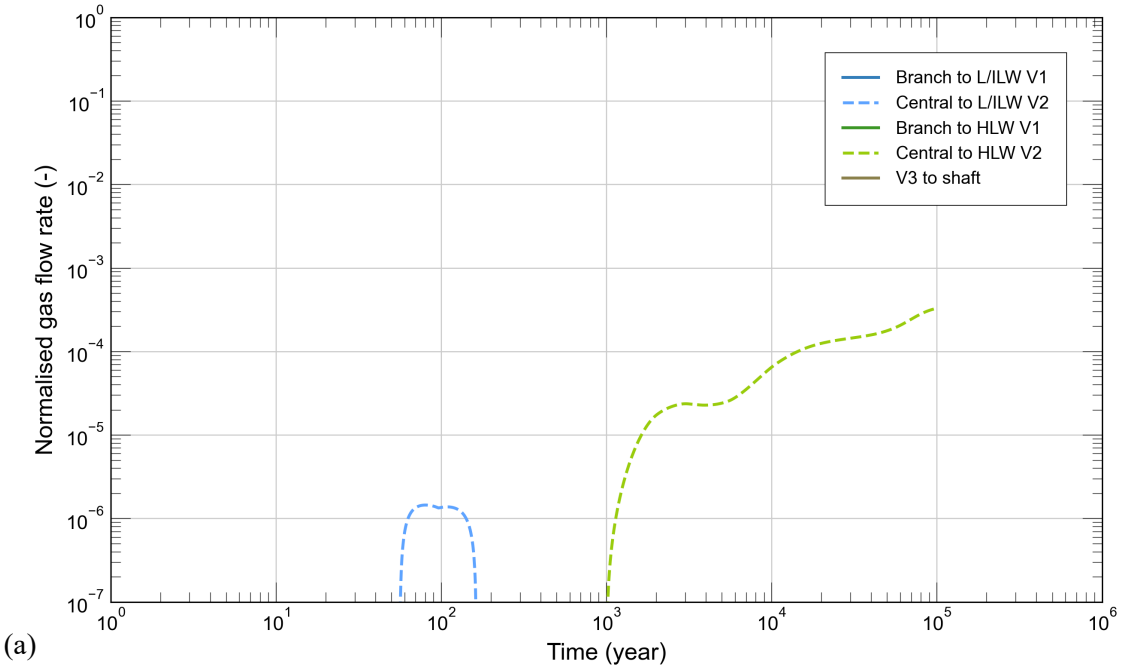

(a)

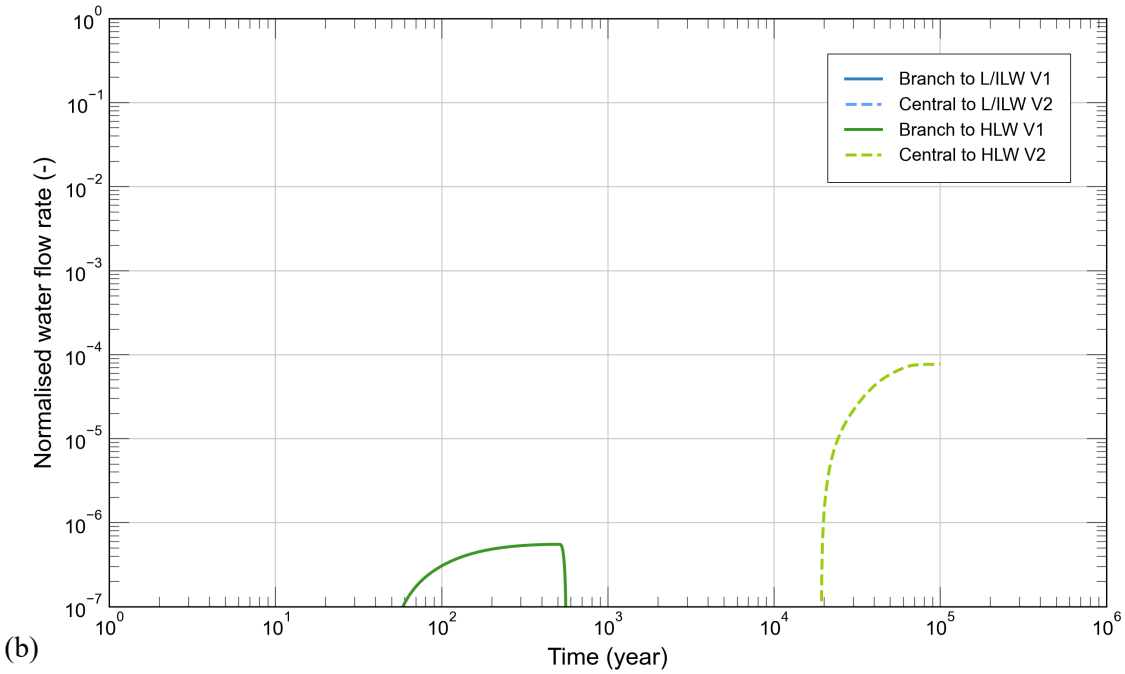

(b)

Fig. B-29: Deviations scenario *"impermeable V3 seals"*: Transients of normalised flow rates of (a) gas and (b) liquid through the sealing sections of the repository (towards disposal areas)

B.6 Deviation: impermeable V2-L/ILW seals *[TSD21]*

In this simulation, the intrinsic permeability of the sealing element of the V2-L/ILW seals is set to 1.0E-22 m^2. The capillary strength parameter, P_0, is increased to 76 MPa. The properties of the EDZ surrounding the V2-L/ILW seal are not changed.

The transients of temperature, gas saturation, and pressure are shown in Fig. B-30, Fig. B-31, and Fig. B-32, respectively. The transients of gas and liquid flow rates through the sealing sections are shown in Fig. B-33 and Fig. B-34, respectively. The normalised gas and water flows are shown in Fig. B-35. The results show that a peak pressure of ~10.5 MPa is reached in the repository associated with gas generation from the L/ILW.

(a)

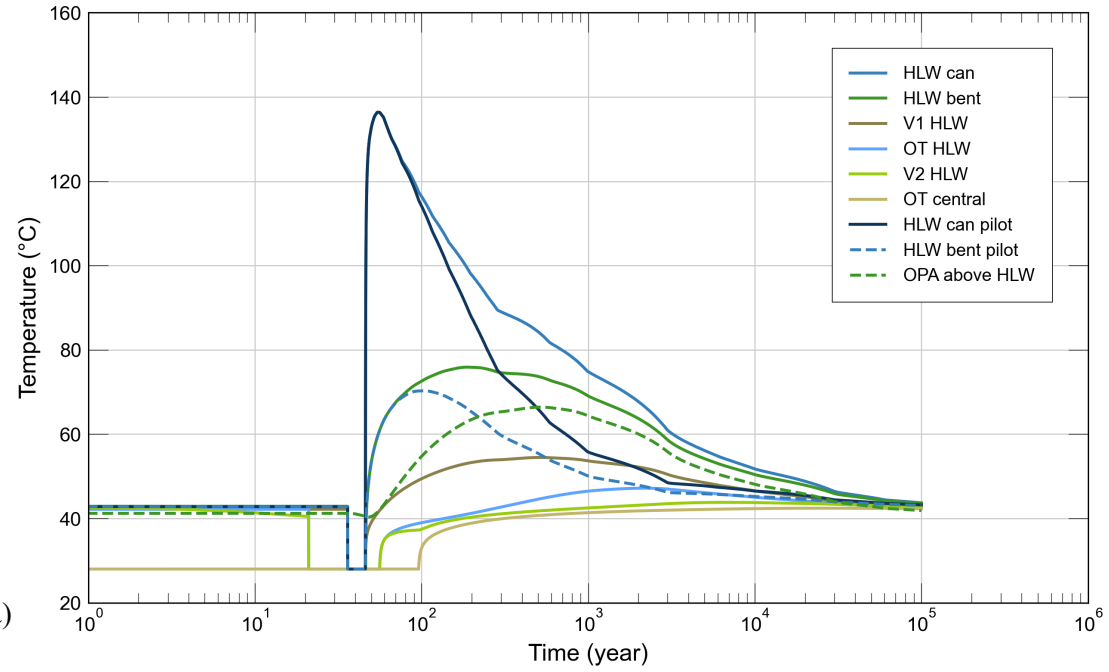

(b)

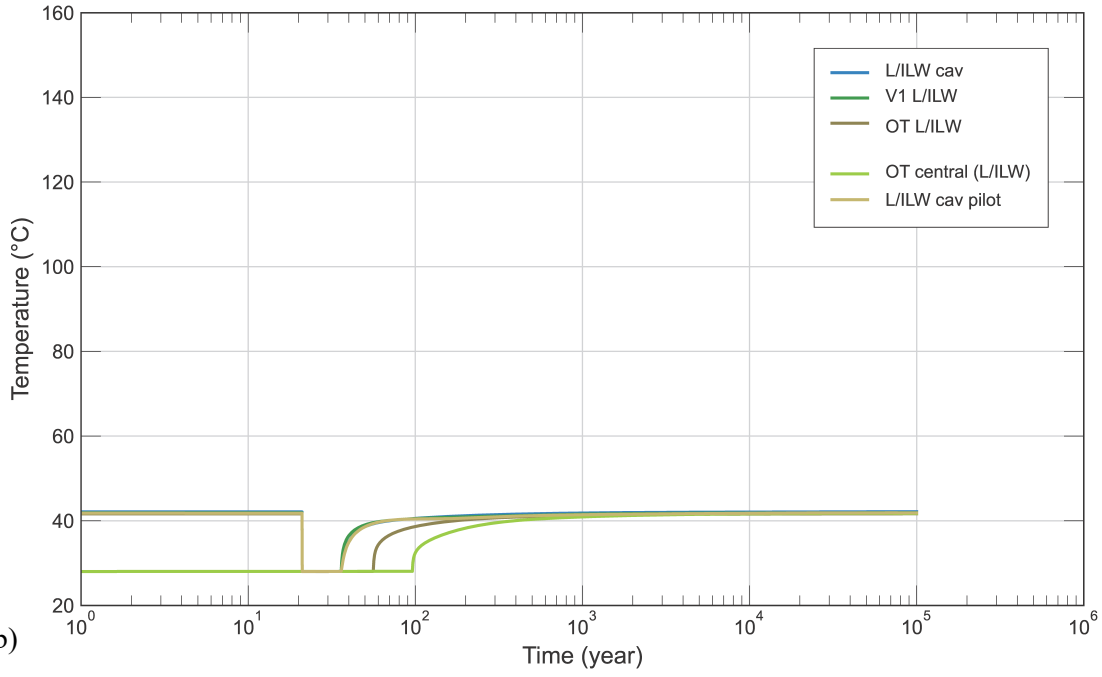

(c)

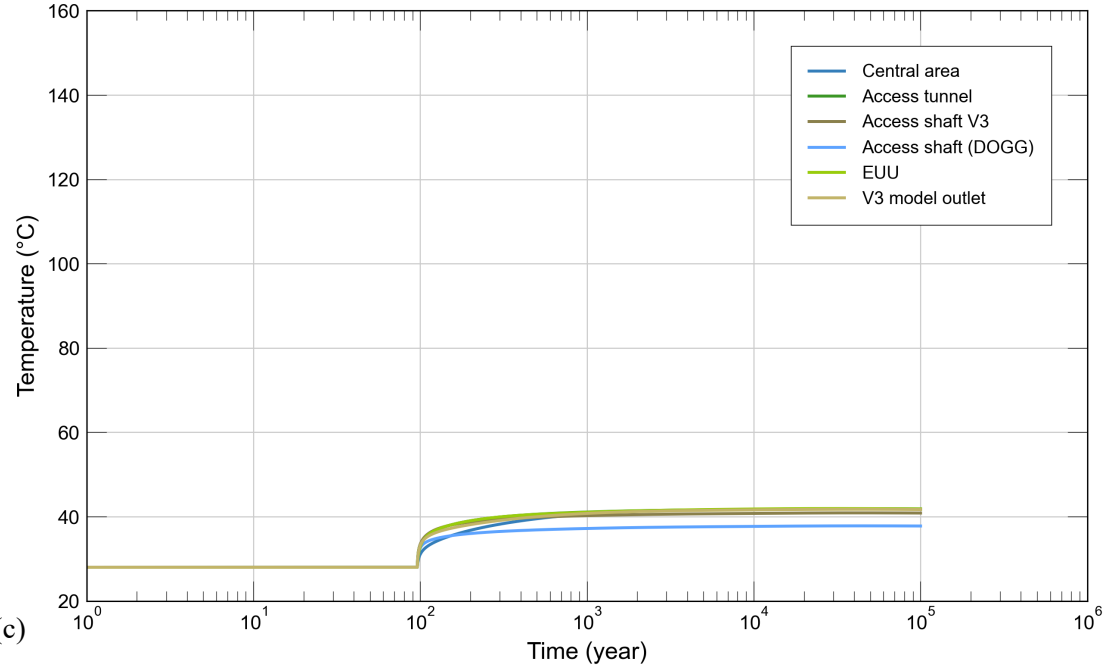

Fig. B-30: Deviations scenario *"impermeable V2-L/ILW seals"*: Transients of temperature (a) HLW section, (b) L/ILW section. And (c) Central area.

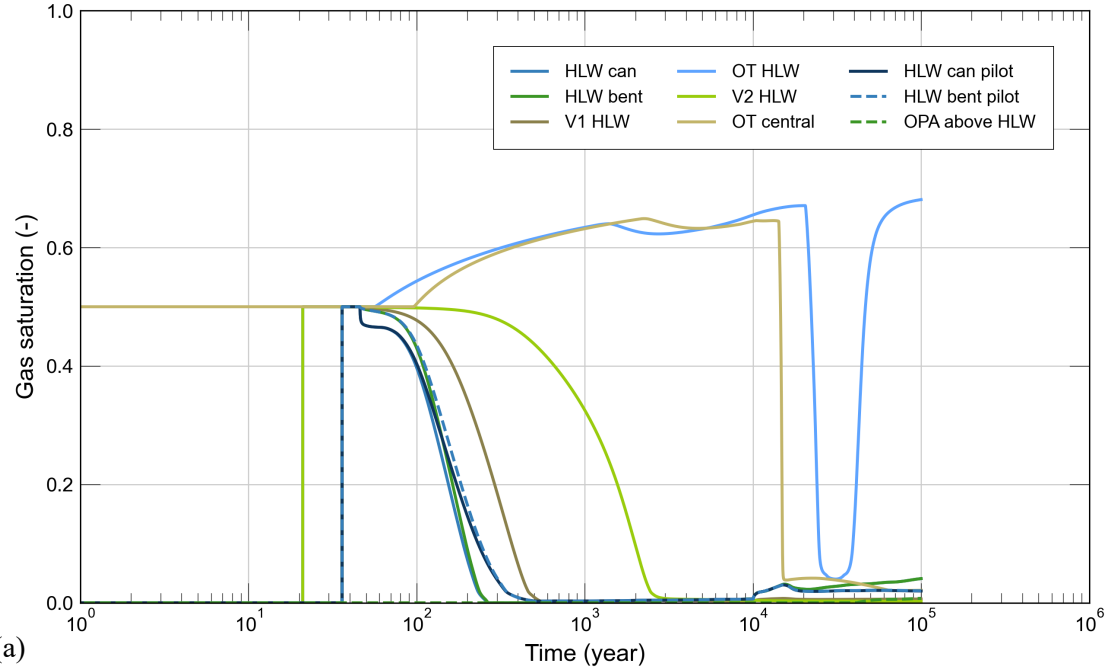
HLW can
HLW bent
V1 HLW
OT HLW
V2 HLW
OT central
HLW can pilot
HLW bent pilot
OPA above HLW
Gas saturation (-)
Time (year)

(a)

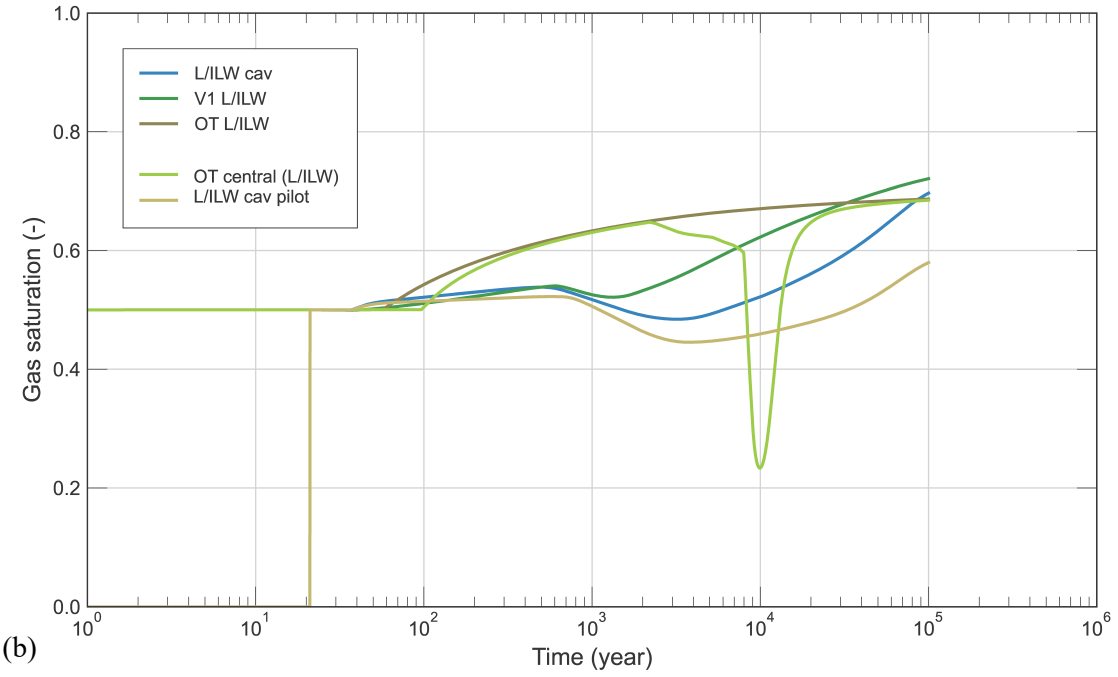
L/ILW cav
V1 L/ILW
OT L/ILW
OT central (L/ILW)
L/ILW cav pilot
Gas saturation (-)
Time (year)

(b)

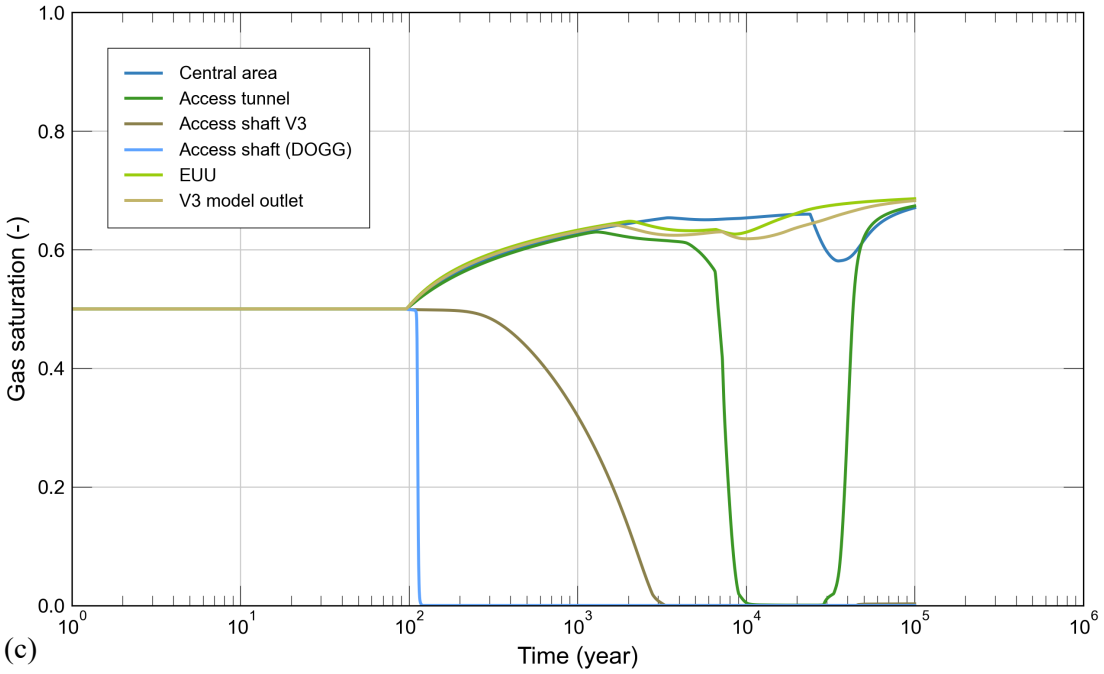

(c)

Fig. B-31: Deviations scenario *"impermeable V2-L/ILW seals"*: Transients of gas saturation (a) HLW section, (b) L/ILW section and (c) Central area.

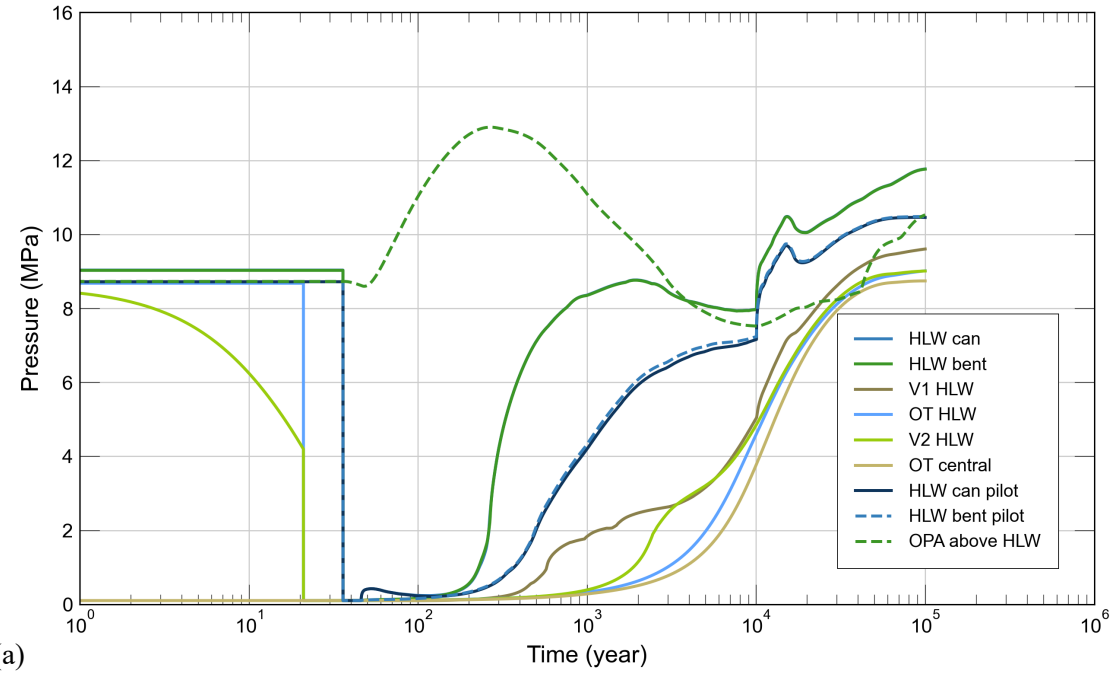
Pressure (MPa)
Time (year)
HLW can
HLW bent
V1 HLW
OT HLW
V2 HLW
OT central
HLW can pilot
HLW bent pilot
OPA above HLW

(a)

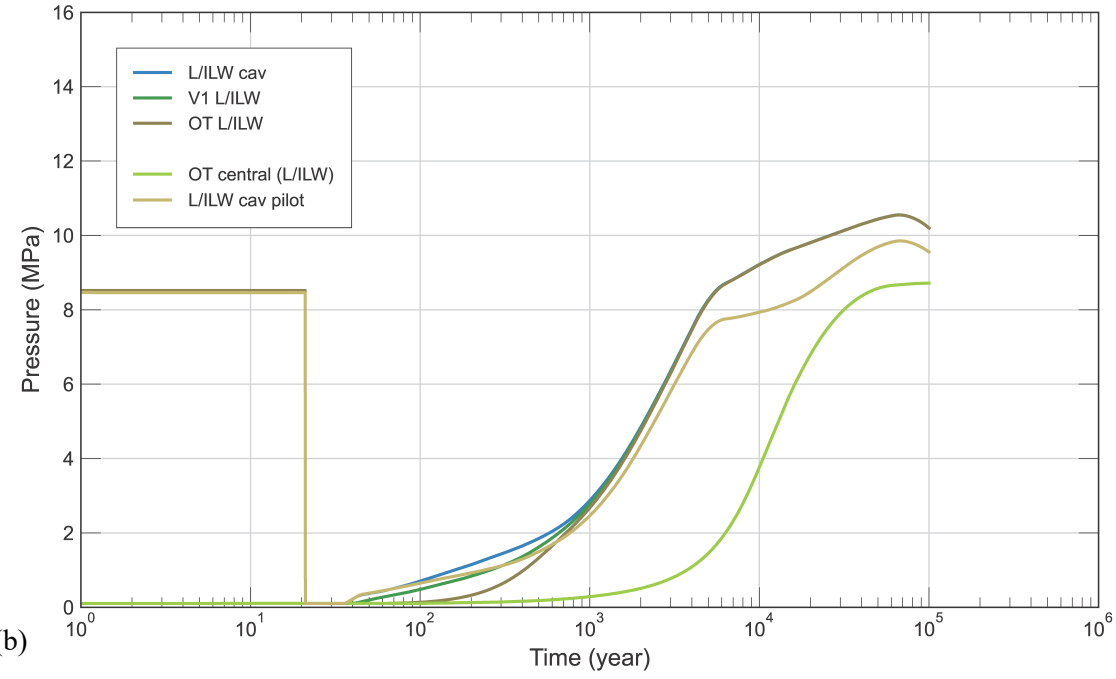
Pressure (MPa)
Time (year)
L/ILW cav
V1 L/ILW
OT L/ILW
OT central (L/ILW)
L/ILW cav pilot

(b)

(c)

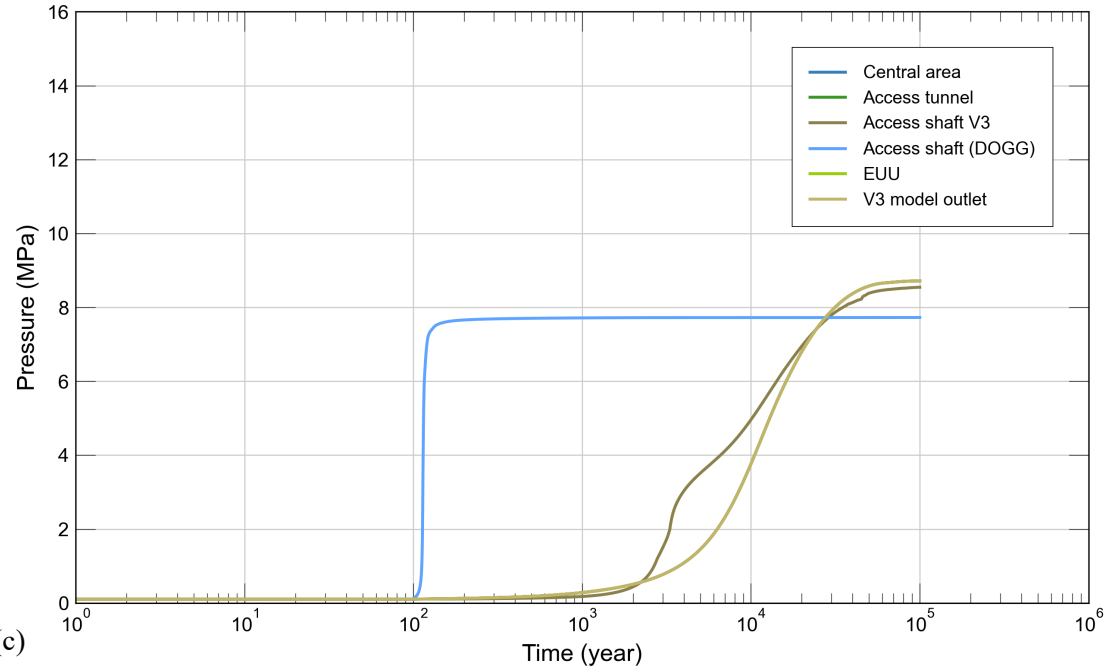

Fig. B-32: Deviations scenario *"impermeable V2-L/ILW seals"*: Transients of pressure (a) HLW section, (b) L/ILW section and (c) Central area.

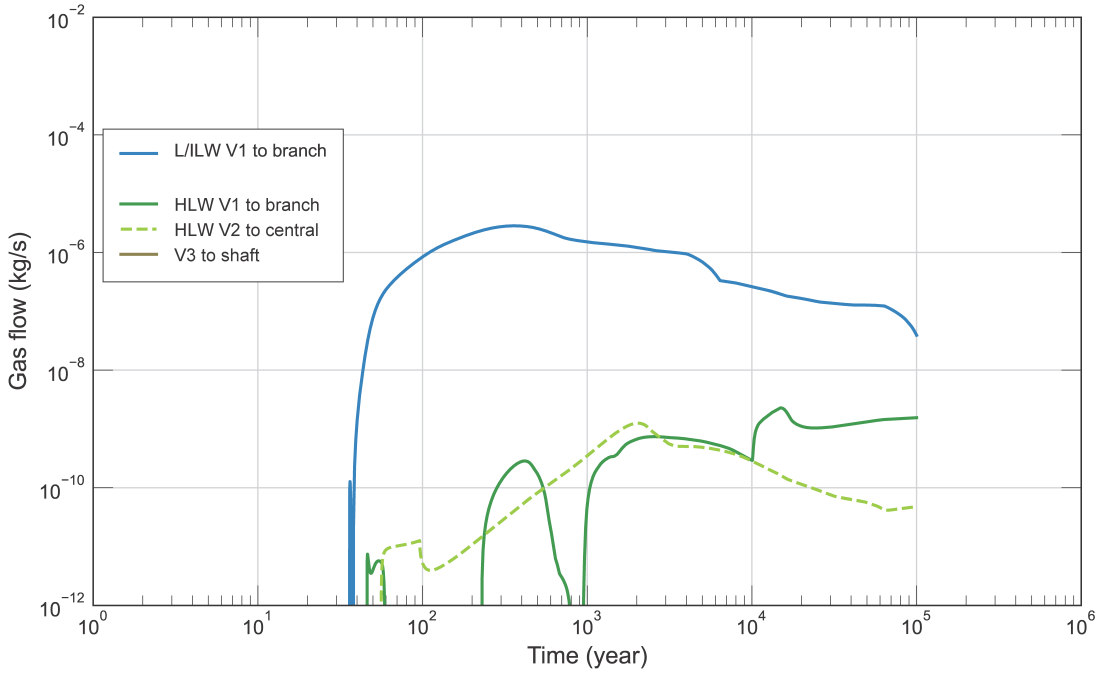

Fig. B-33: Deviations scenario *"impermeable V2-L/ILW seals"*: Transients of gas flow rate through the sealing sections of the repository (towards shafts)

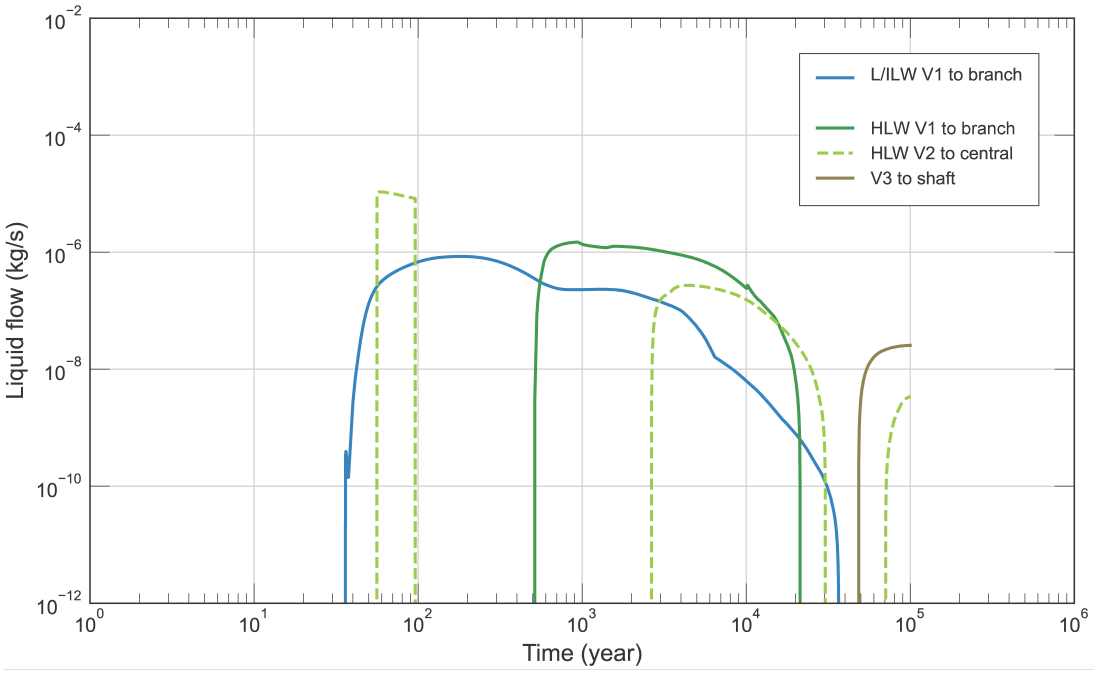

Fig. B-34: Deviations scenario *"impermeable V2-L/ILW seals"*: Transients of liquid flow rate through the sealing sections of the repository (towards shafts)

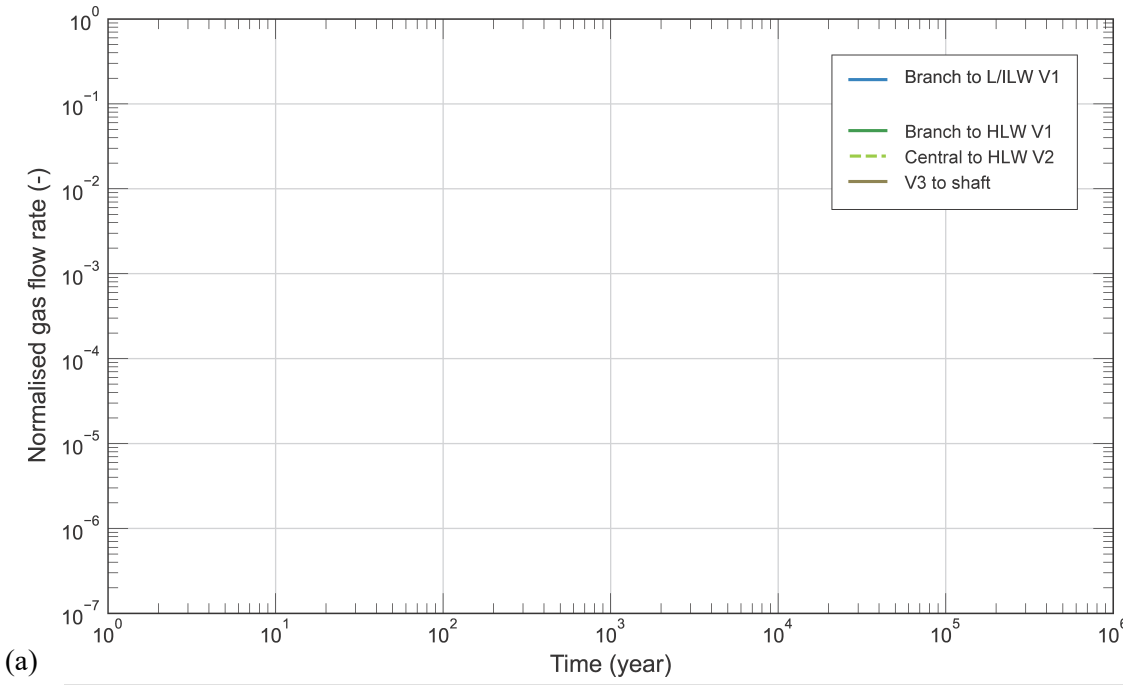

(a)

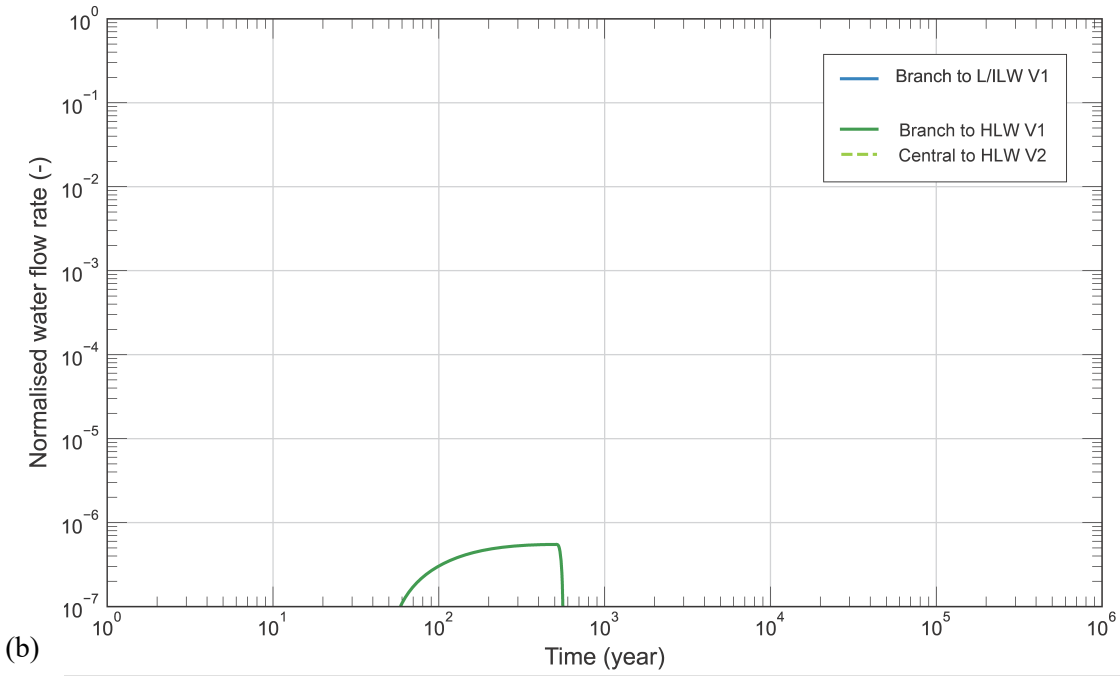

(b)

Fig. B-35: Deviations scenario *"impermeable V2-L/ILW seals"*: Transients of normalised flow rates of (a) gas and (b) liquid through the sealing sections of the repository (towards disposal areas)

B.7 Deviation: low-permeable V1-L/ILW seals *[TSD20]*

In this simulation, the intrinsic permeability of the sealing element of the V1-L/ILW seals is set to 1.0E-19 m^2.

The transients of temperature, gas saturation, and pressure are shown in Fig. B-36, Fig. B-37, and Fig. B-38, respectively. The transients of gas and liquid flow rates through the sealing sections are shown in Fig. B-39 and Fig. B-40, respectively. The normalised gas and water flows are shown in Fig. B-41. The peak pressure in the L/ILW section of the repository corresponds to ~9.6 MPa after ~70,000 years.

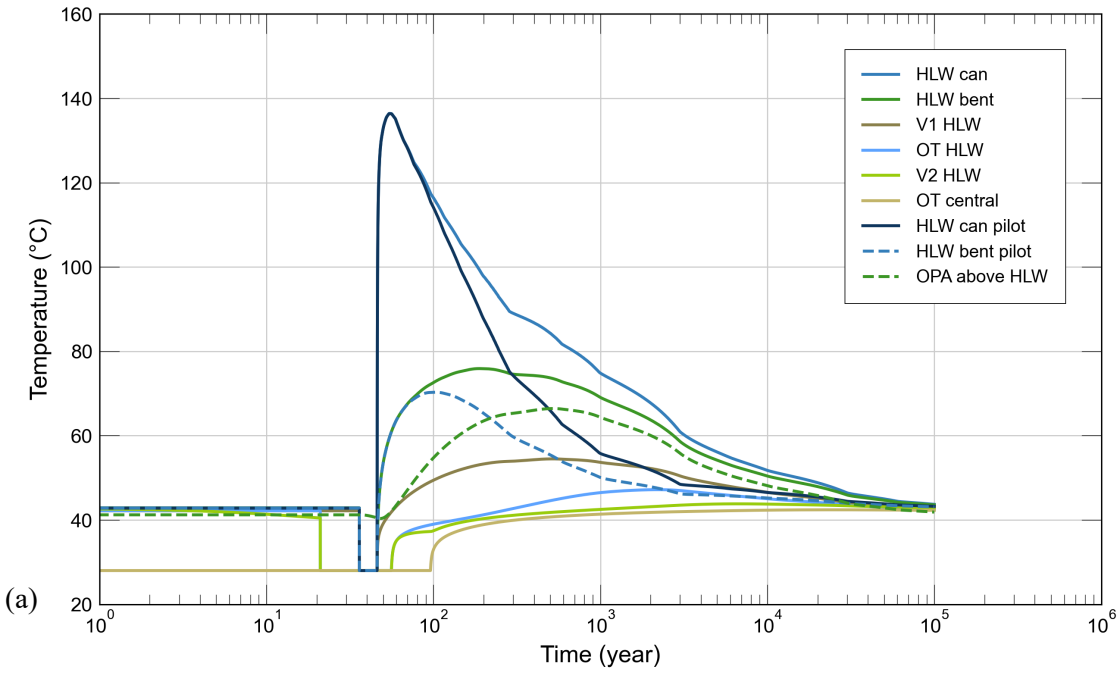

(a)

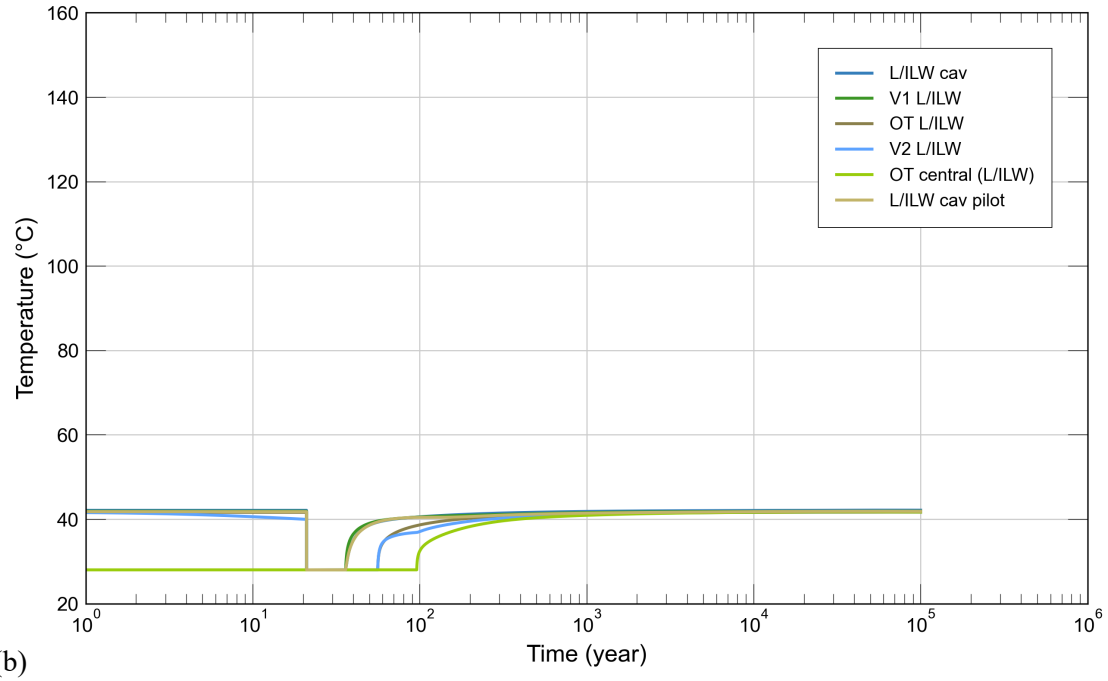

(b)

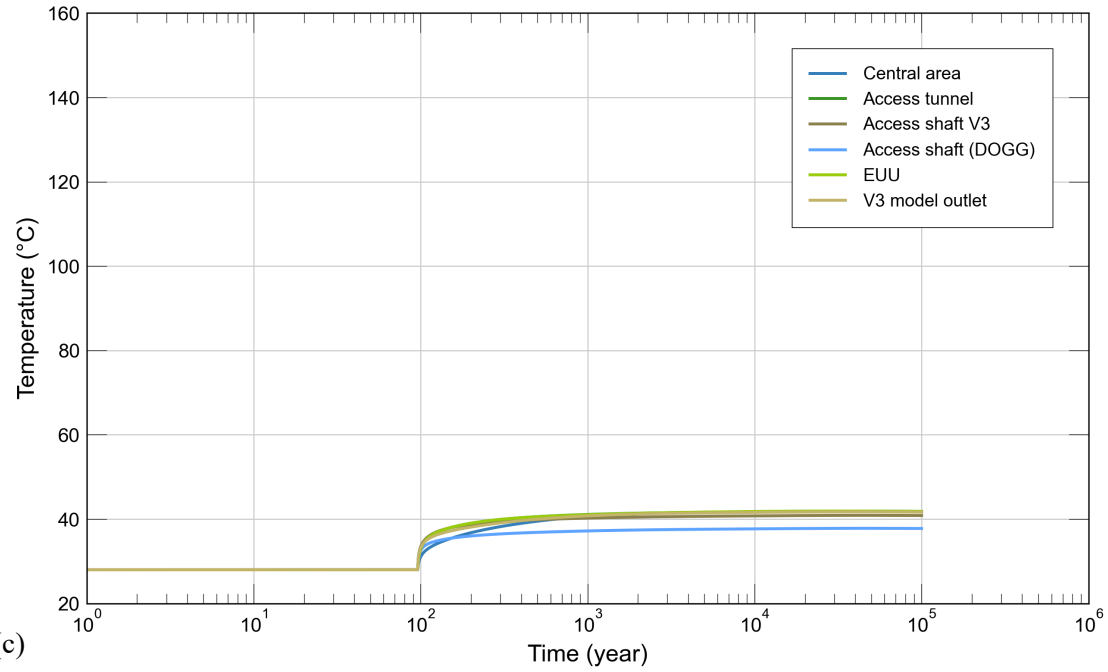

(c)

Fig. B-36: Deviations scenario *"low-permeable V1-L/ILW seals"*: Transients of temperature (a) HLW section, (b) L/ILW section and (c) Central area.

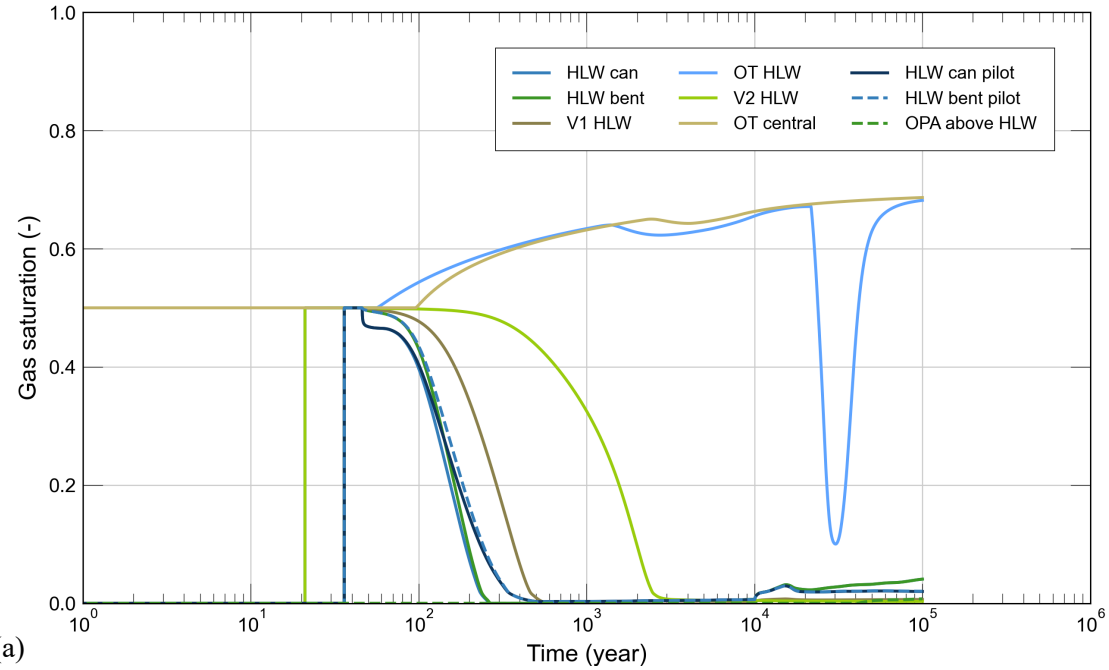
HLW can
HLW bent
V1 HLW
OT HLW
V2 HLW
OT central
HLW can pilot
HLW bent pilot
OPA above HLW
Gas saturation (-)
Time (year)

(a)

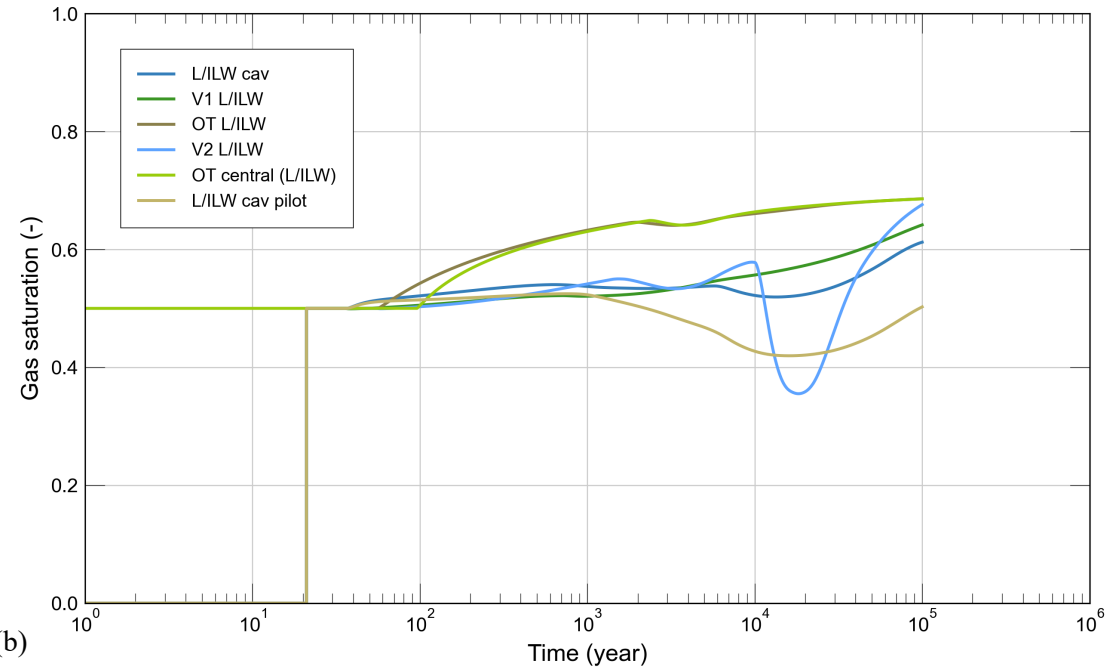
L/ILW cav
V1 L/ILW
OT L/ILW
V2 L/ILW
OT central (L/ILW)
L/ILW cav pilot
Gas saturation (-)
Time (year)

(b)

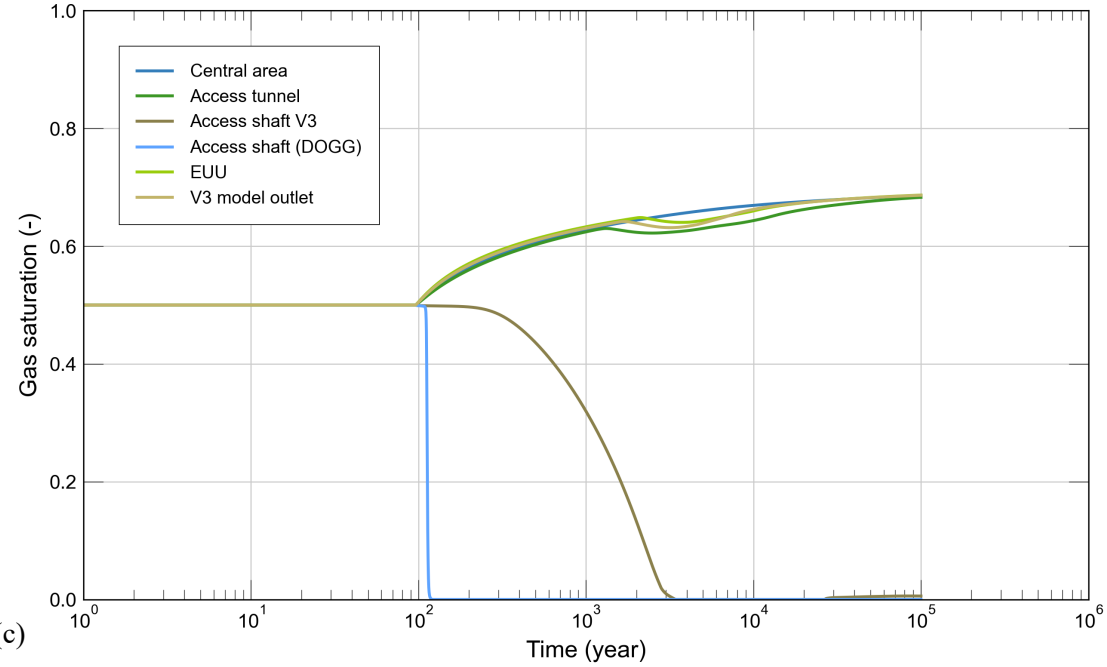

(c)

Fig. B-37: Deviations scenario *"low-permeable V1-L/ILW seals"*: Transients of gas saturation (a) HLW section, (b) L/ILW section and (c) Central area.

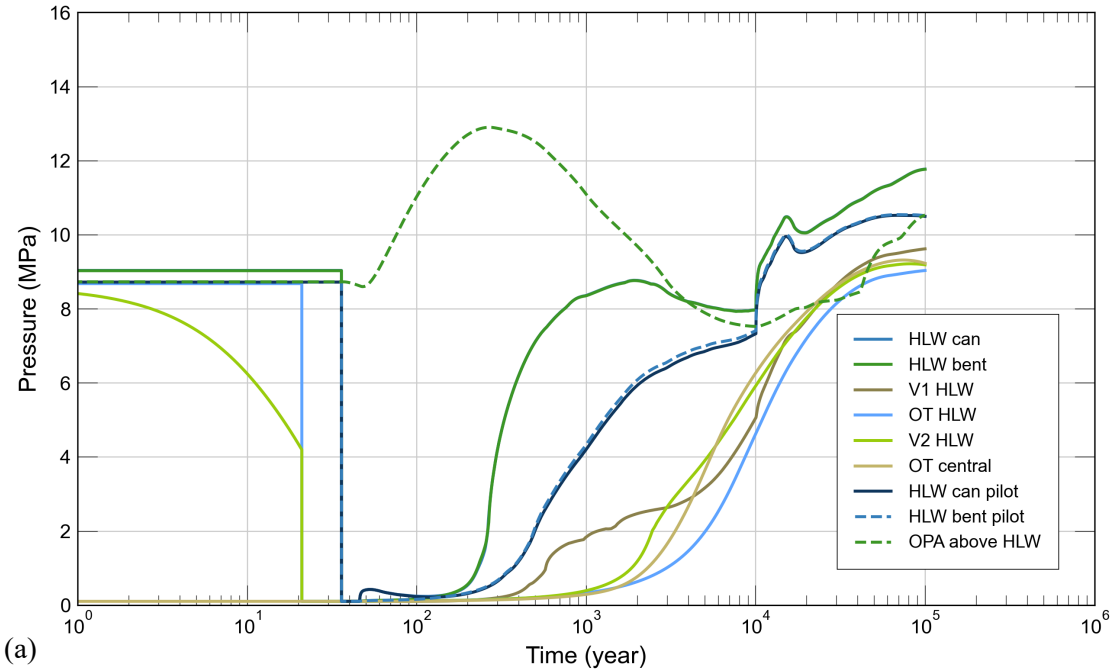
Pressure (MPa)
Time (year)
HLW can
HLW bent
V1 HLW
OT HLW
V2 HLW
OT central
HLW can pilot
HLW bent pilot
OPA above HLW

(a)

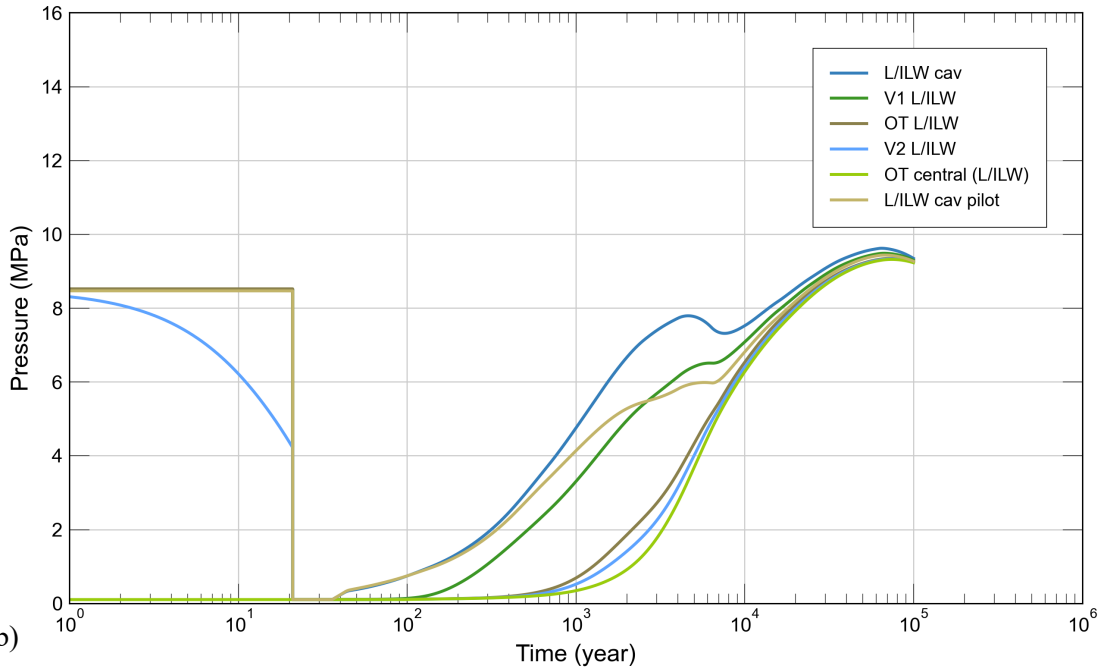
Pressure (MPa)
Time (year)
L/ILW cav
V1 L/ILW
OT L/ILW
V2 L/ILW
OT central (L/ILW)
L/ILW cav pilot

(b)

(c)

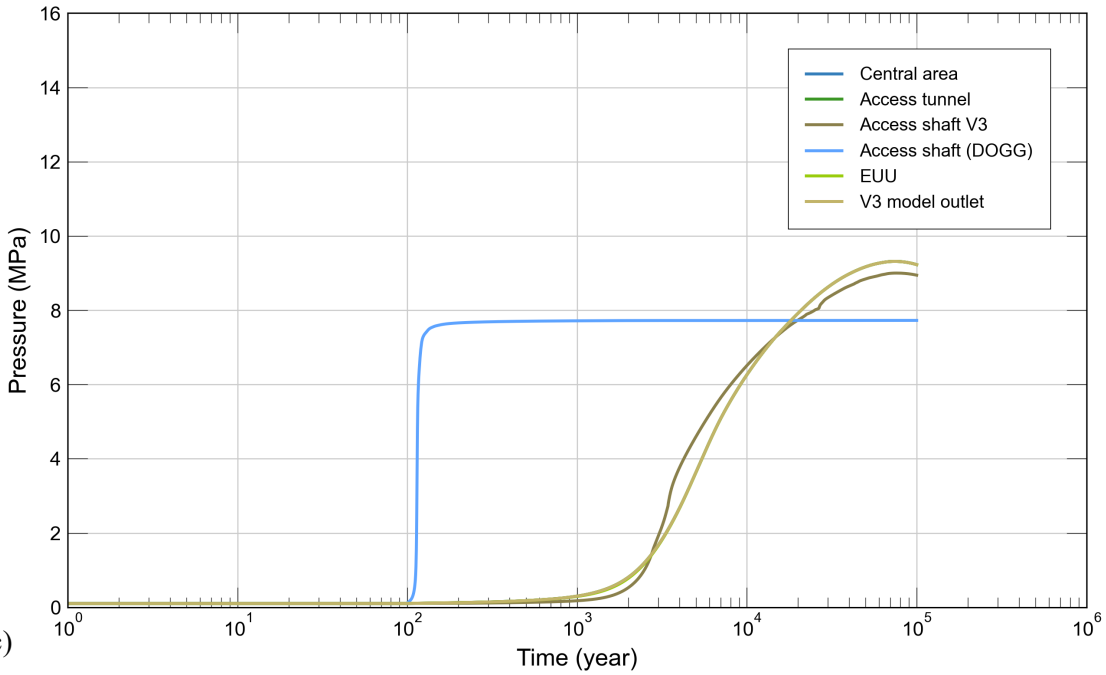

Fig. B-38: Deviations scenario *"low-permeable V1-L/ILW seals"*: Transients of pressure (a) HLW section, (b) L/ILW section and (c) Central area.

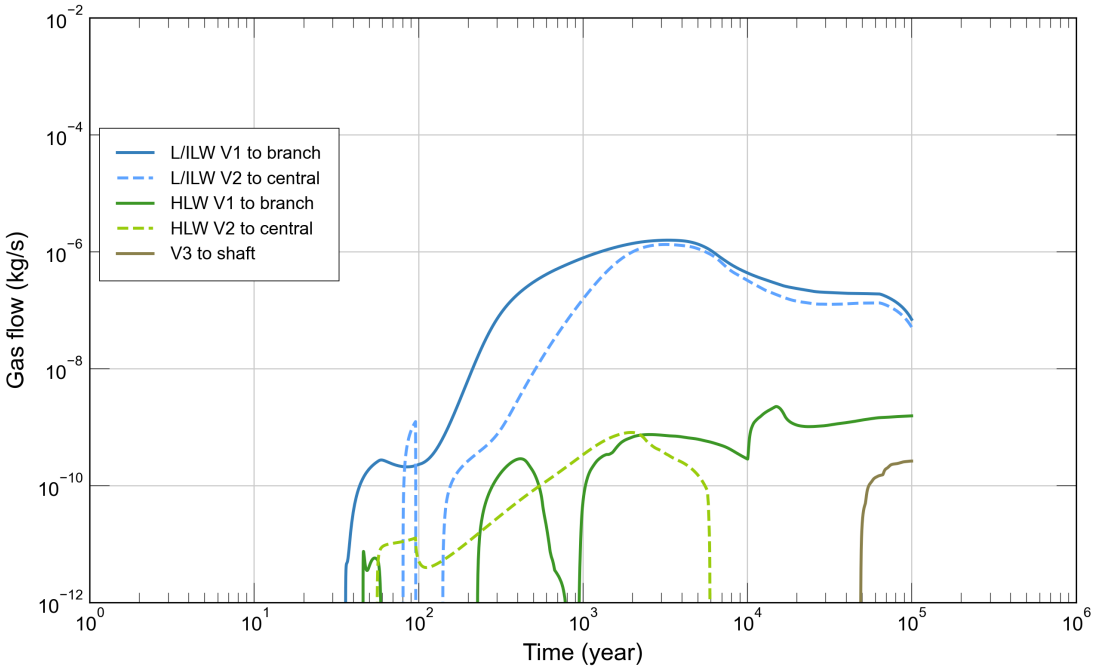

Fig. B-39: Deviations scenario *"low-permeable V1-L/ILW seals"*: Transients of gas flow rate through the sealing sections of the repository (towards shafts)

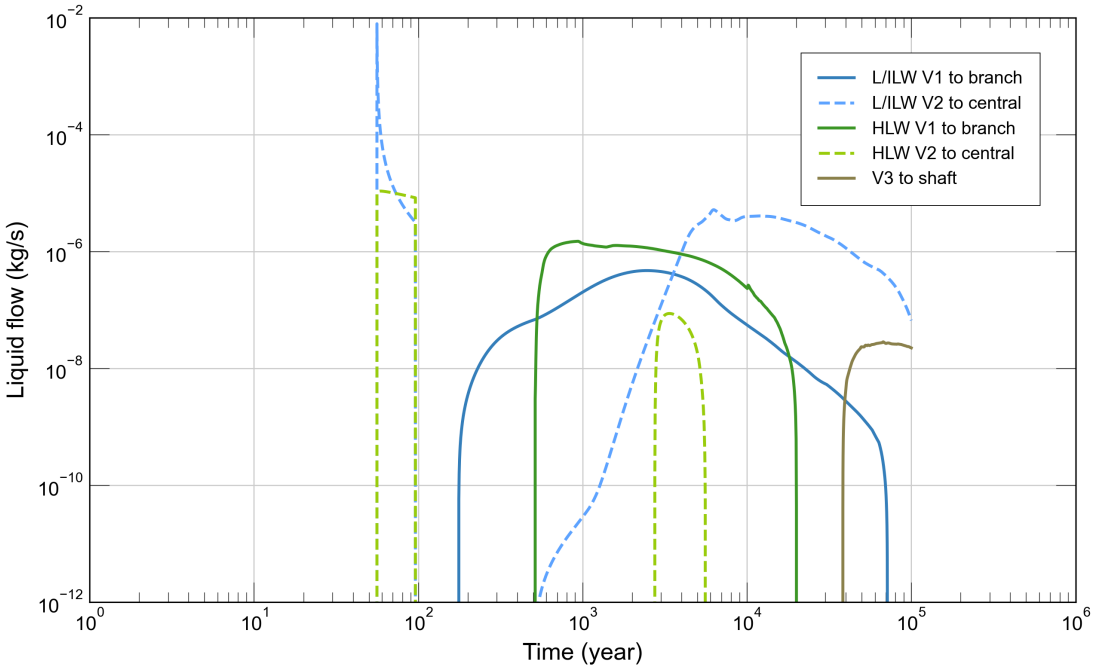

Fig. B-40: Deviations scenario *"low-permeable V1-L/ILW seals"*: Transients of liquid flow rate through the sealing sections of the repository (towards shafts)

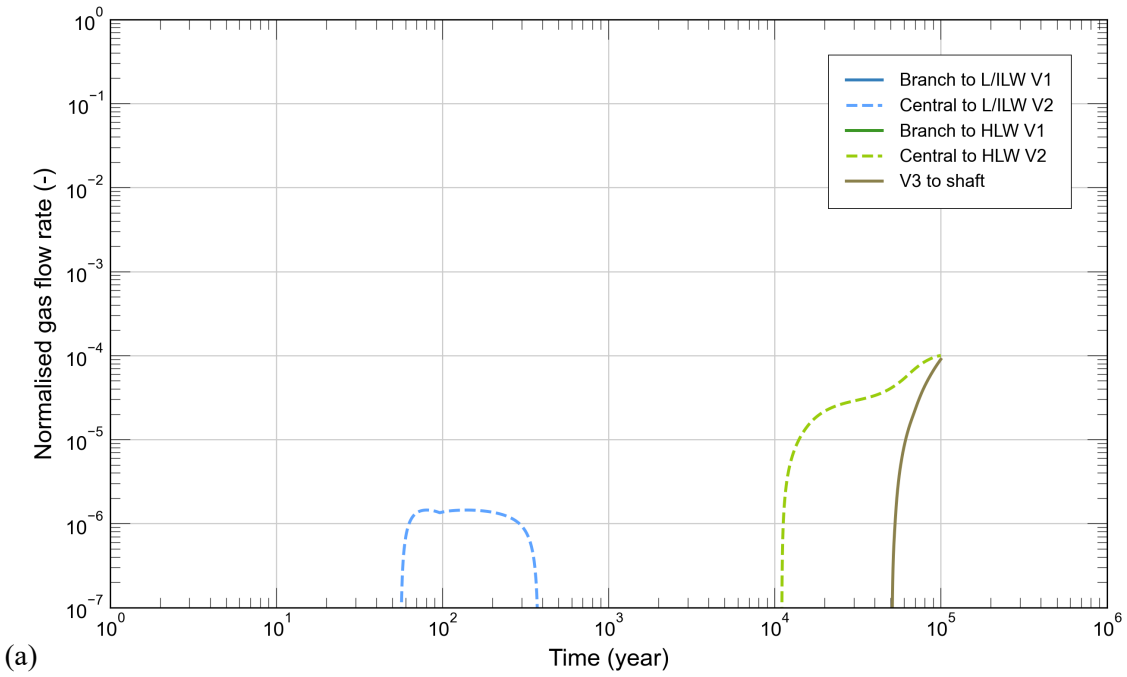

(a)

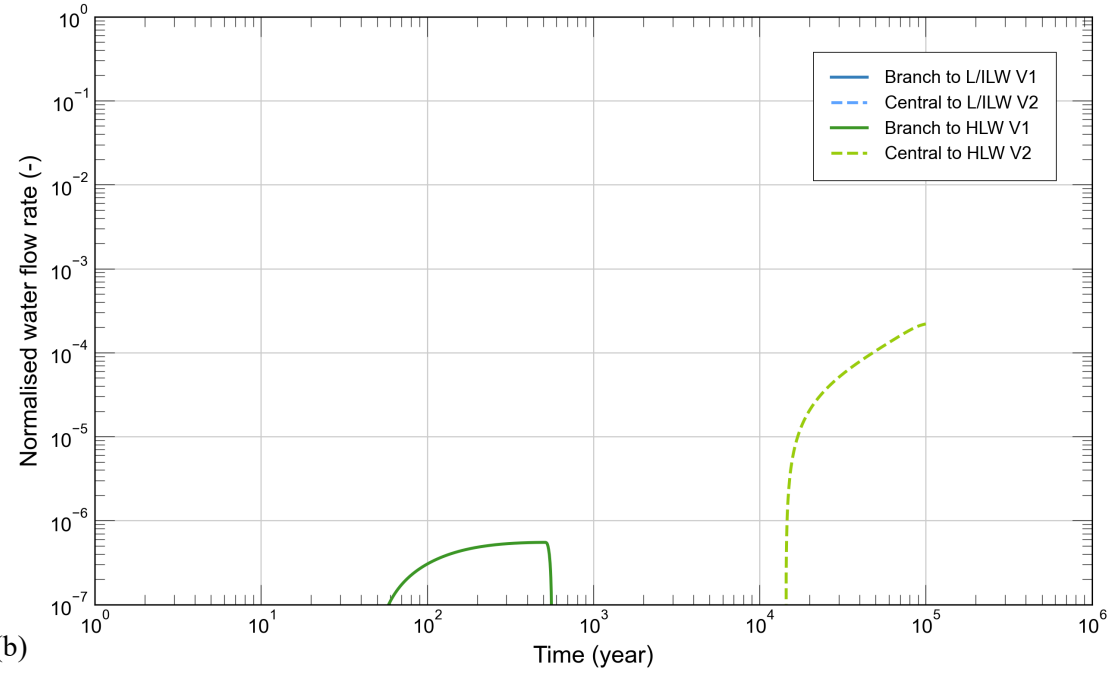

(b)

Fig. B-41: Deviations scenario *"low-permeable V1-L/ILW seals"*: Transients of normalised flow rates of (a) gas and (b) liquid through the sealing sections of the repository (towards disposal areas)

B.8 Deviation: instant repository resaturation *[TSD4]*

In this simulation, the initial water saturation of the repository tunnels is set to 95%. The properties of the materials emplaced in the repository are not changed.

The transients of temperature, gas saturation, and pressure are shown in Fig. B-42, Fig. B-43, and Fig. B-44, respectively. The transients of gas and liquid flow rates through the sealing sections are shown in Fig. B-45 and Fig. B-46, respectively. The normalised gas and water flows are shown in Fig. B-47. Similar to the expected evolution, a peak pressure of ~9.5 MPa is reached in the L/ILW section and central area of the repository after ~60,000 years.

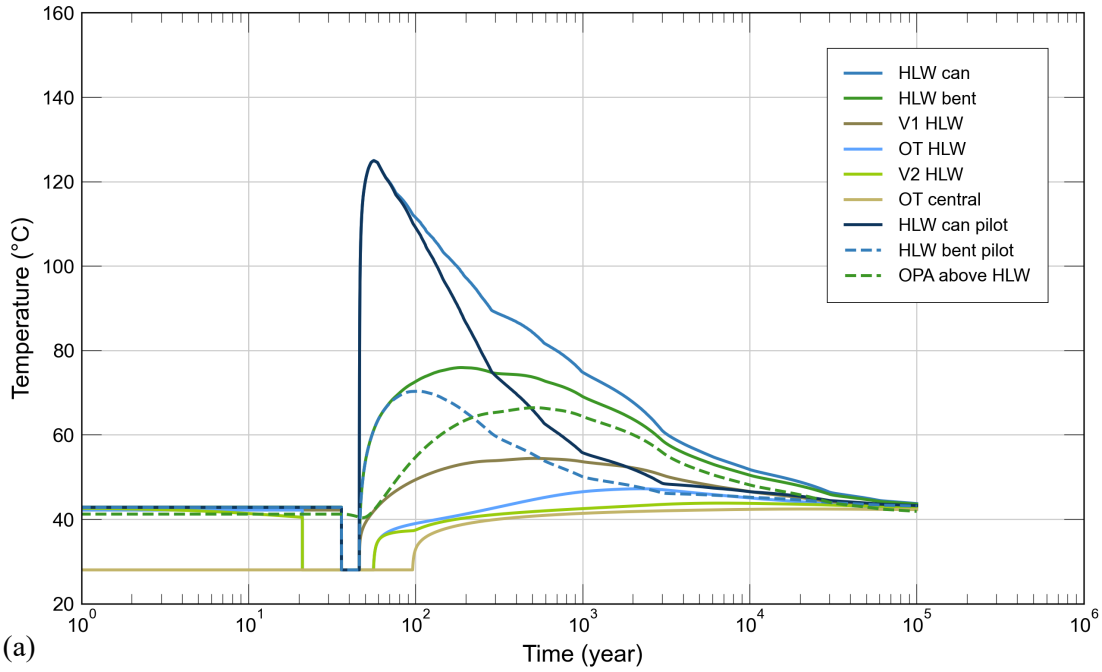

(a)

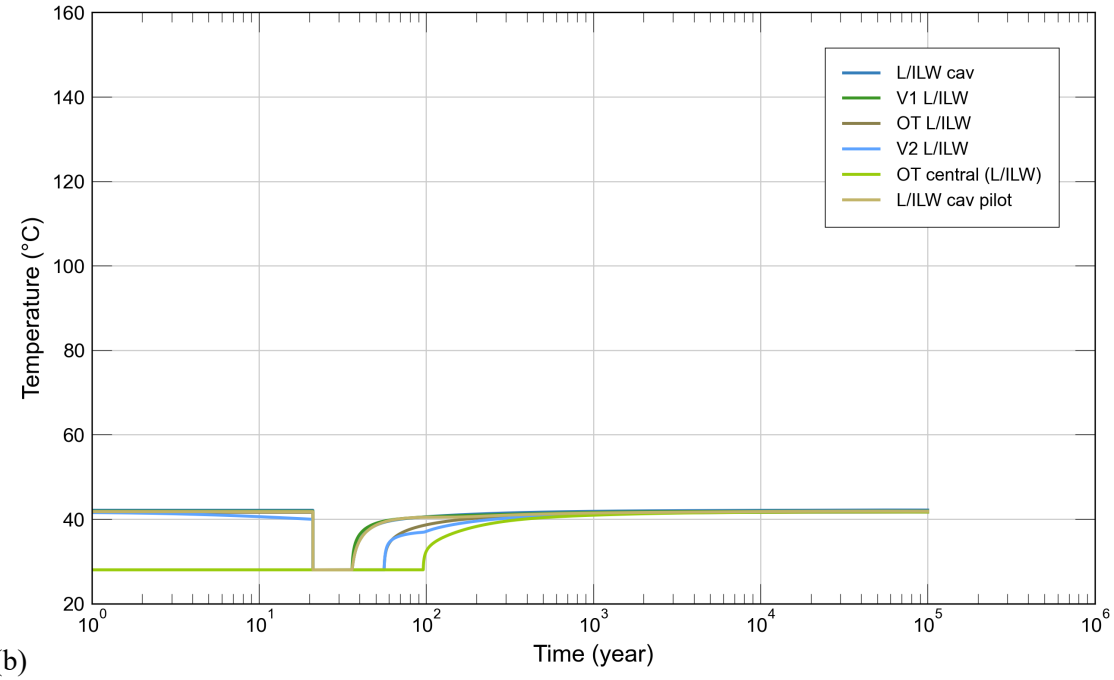

(b)

(c)

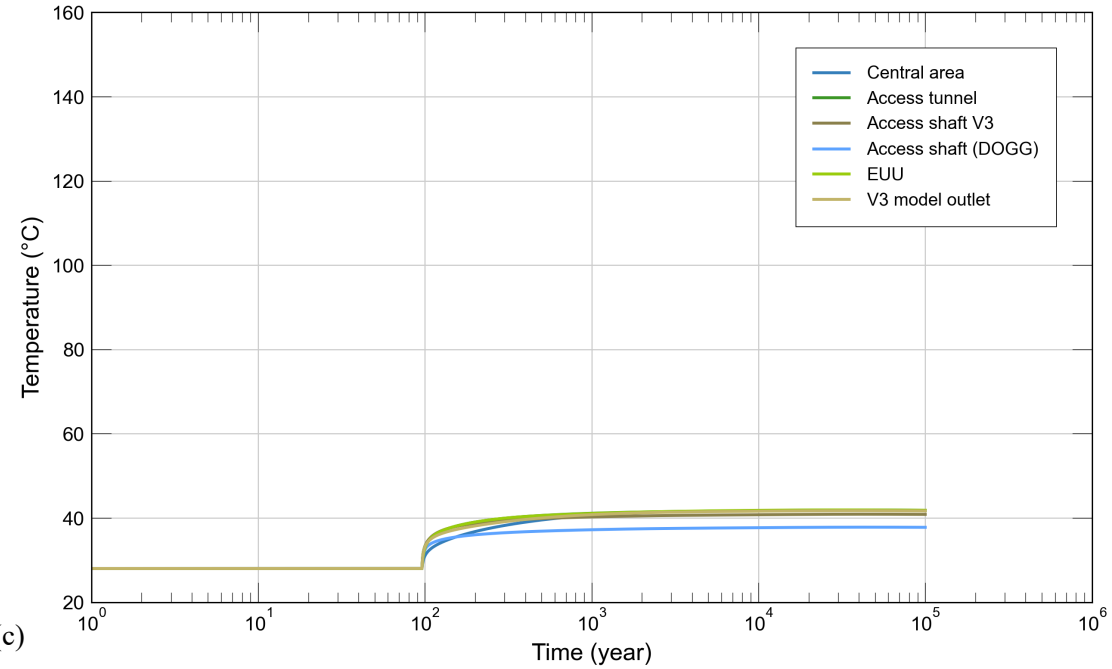

Fig. B-42: Deviations scenario *"instant repository resaturation"*: Transients of temperature (a) HLW section, (b) L/ILW section and (c) Central area.

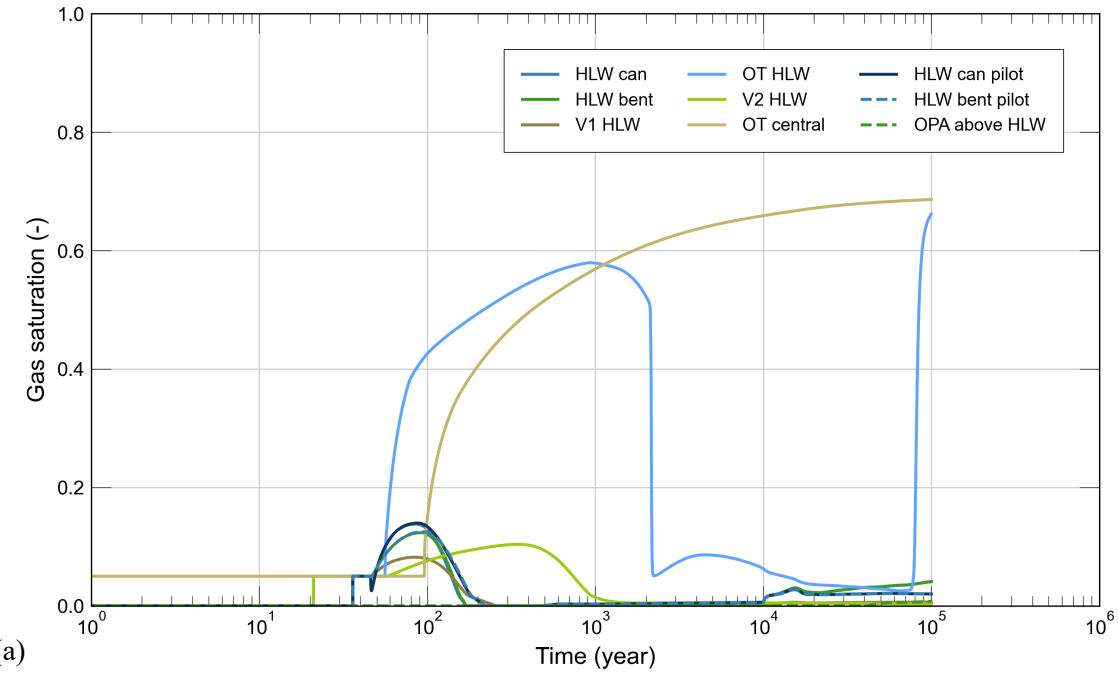
HLW can
HLW bent
V1 HLW
OT HLW
V2 HLW
OT central
HLW can pilot
HLW bent pilot
OPA above HLW
Gas saturation (-)
Time (year)

(a)

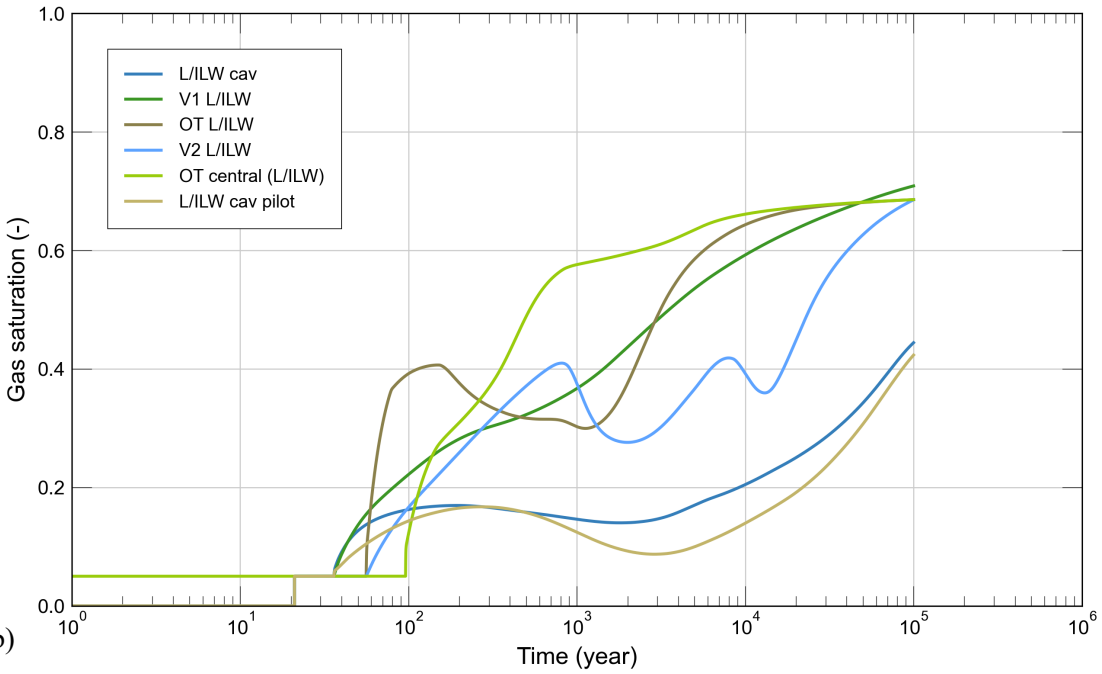
L/ILW cav
V1 L/ILW
OT L/ILW
V2 L/ILW
OT central (L/ILW)
L/ILW cav pilot
Gas saturation (-)
Time (year)

(b)

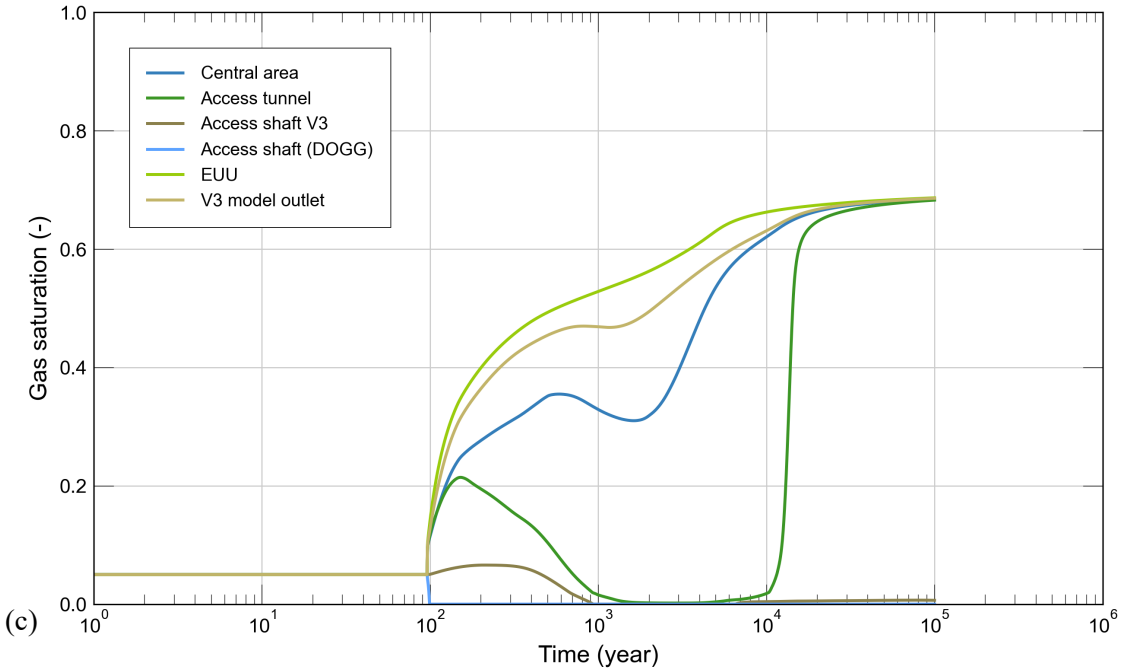

(c)

Fig. B-43: Deviations scenario *"instant repository resaturation"*: Transients of gas saturation (a) HLW section, (b) L/ILW section and (c) Central area.

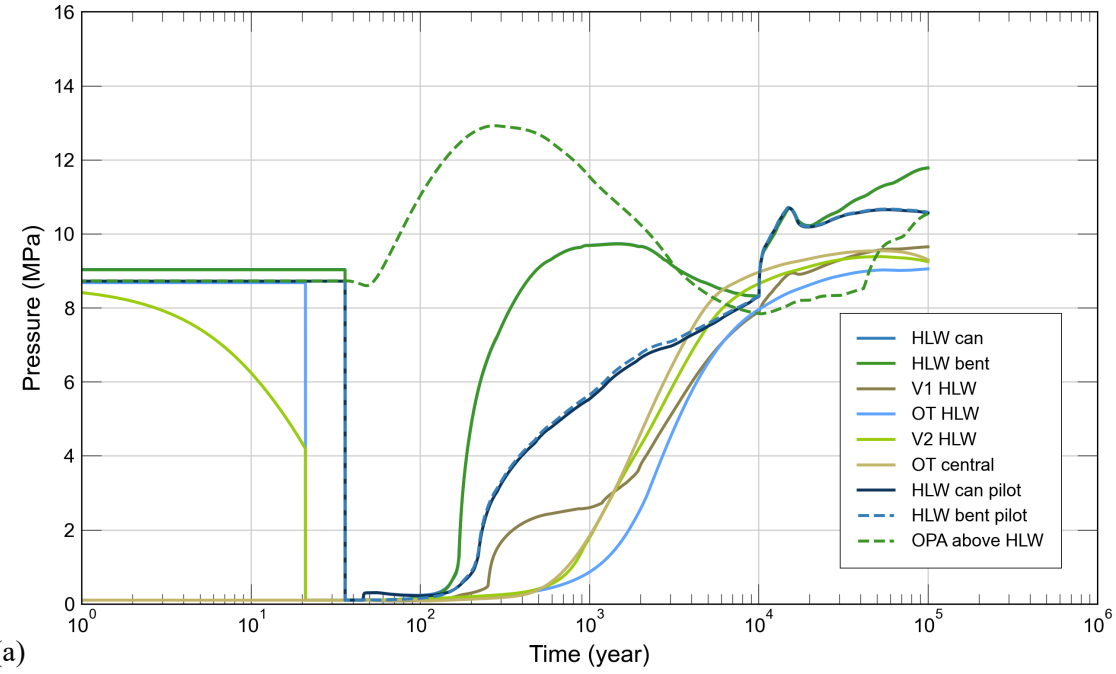
Pressure (MPa)
Time (year)
HLW can
HLW bent
V1 HLW
OT HLW
V2 HLW
OT central
HLW can pilot
HLW bent pilot
OPA above HLW

(a)

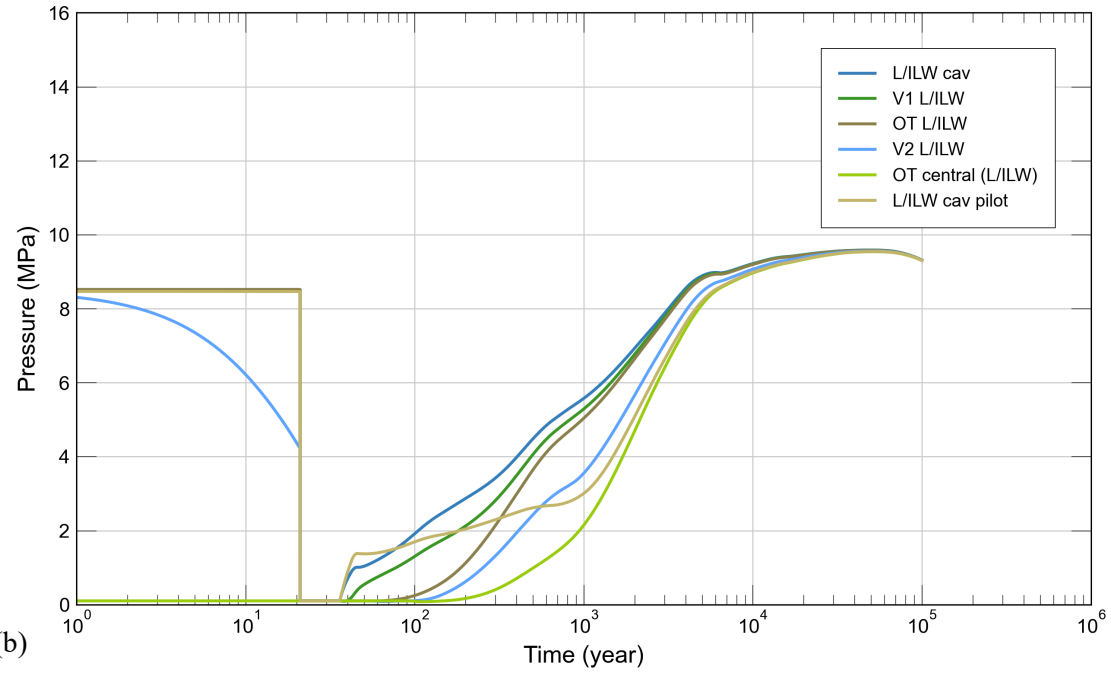
Pressure (MPa)
Time (year)
L/ILW cav
V1 L/ILW
OT L/ILW
V2 L/ILW
OT central (L/ILW)
L/ILW cav pilot

(b)

(c)

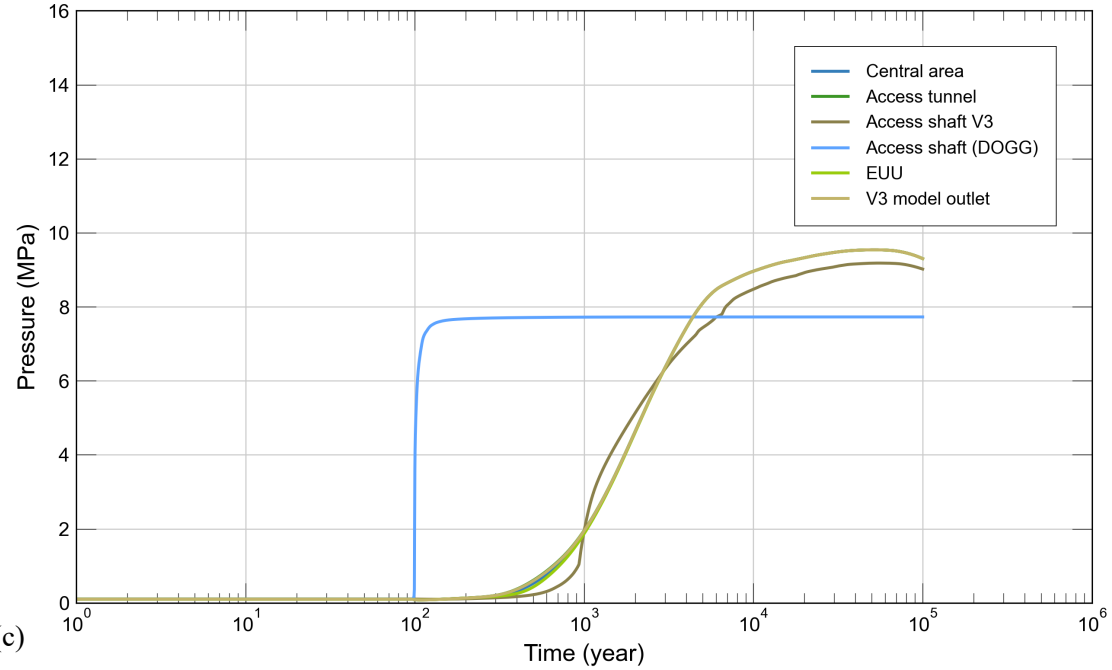

Fig. B-44: Deviations scenario *"instant repository resaturation"*: Transients of pressure (a) HLW section, (b) L/ILW section and (c) Central area.

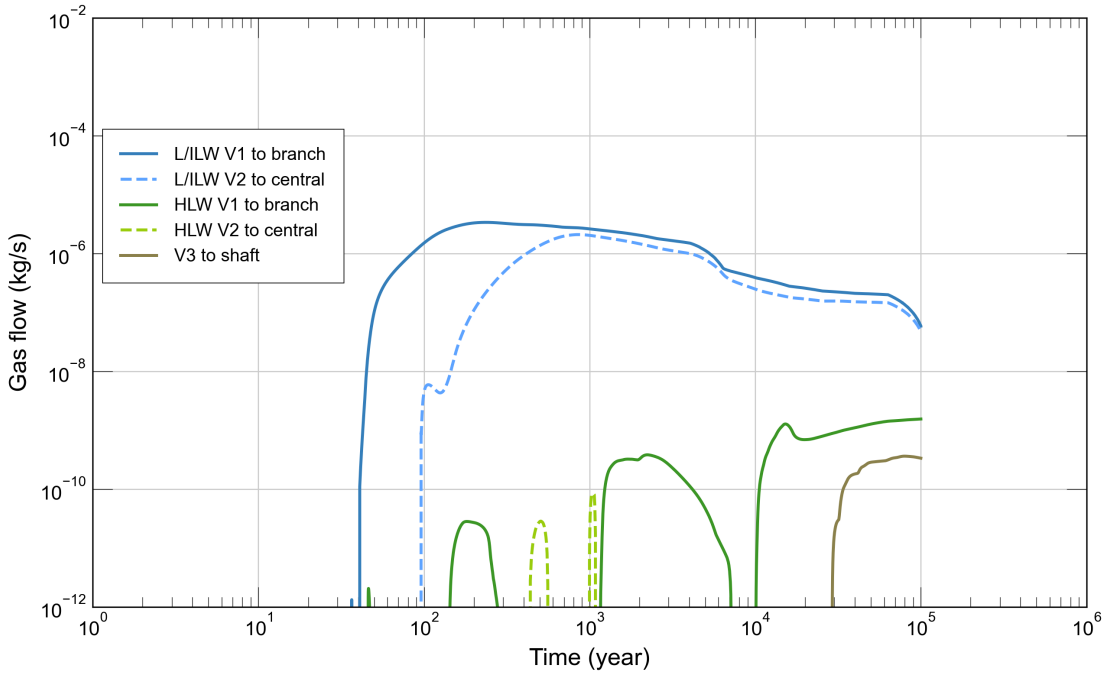

Fig. B-45: Deviations scenario *"instant repository resaturation"*: Transients of gas flow rate through the sealing sections of the repository (towards shafts)

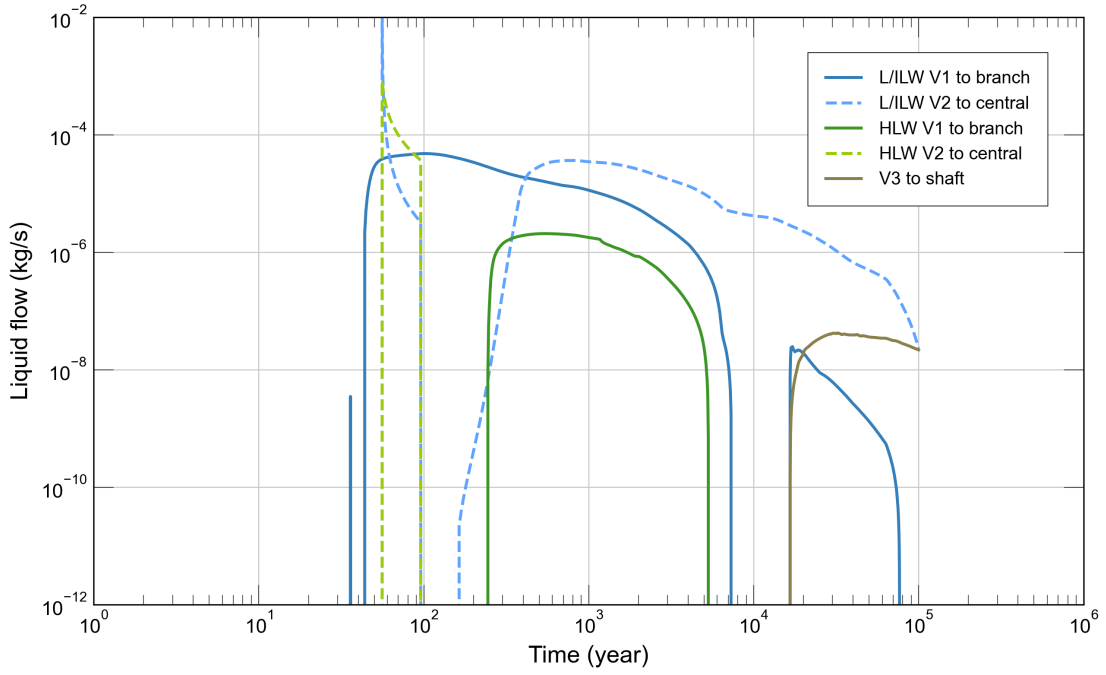

Fig. B-46: Deviations scenario *"instant repository resaturation"*: Transients of liquid flow rate through the sealing sections of the repository (towards shafts)

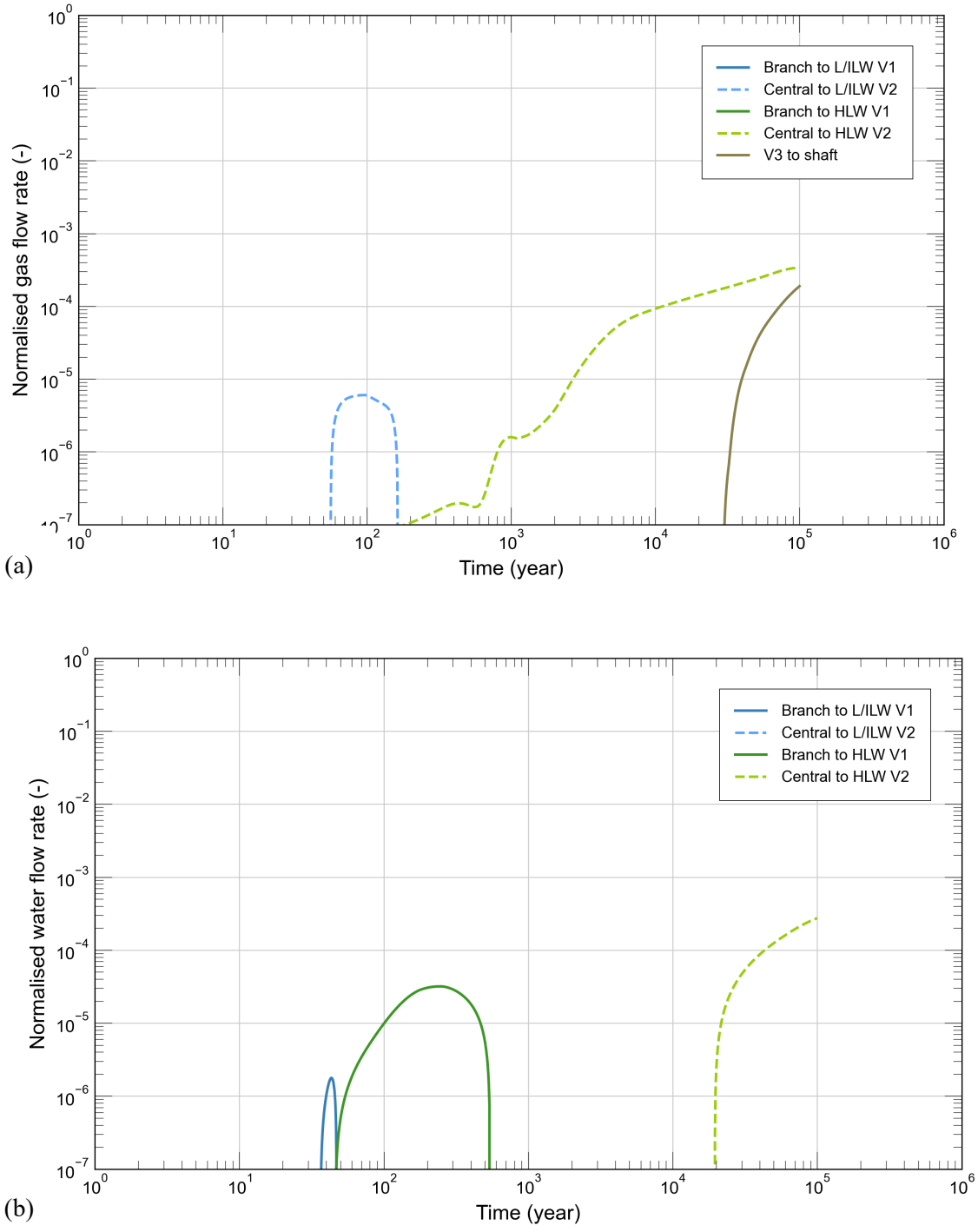

Fig. B-47: Deviations scenario *"instant repository resaturation"*: Transients of normalised flow rates of (a) gas and (b) liquid through the sealing sections of the repository (towards disposal areas)

B.9 Deviation: fault through L/ILW caverns

In addition to the transients provided in Section 6.2 for deviations scenario "*fault through L/ILW*", distributions of gas saturation in the fault and the L/ILW section are shown in Fig. B-48, transients of gas flow rate and cumulative gas flow are shown in Fig. B-49, and transients of liquid flow are shown in Fig. B-50.

The flow transients show gas breakthrough from the fault to the Malm aquifer after 9,000 years. The rate of gas release is approximately one order of magnitude below the rate of gas generation in the caverns. On the other hand, water flow occurs in the direction from Malm into the repository through the fault, starting shortly after backfilling of the L/ILW section and continuing until the end of the simulation.

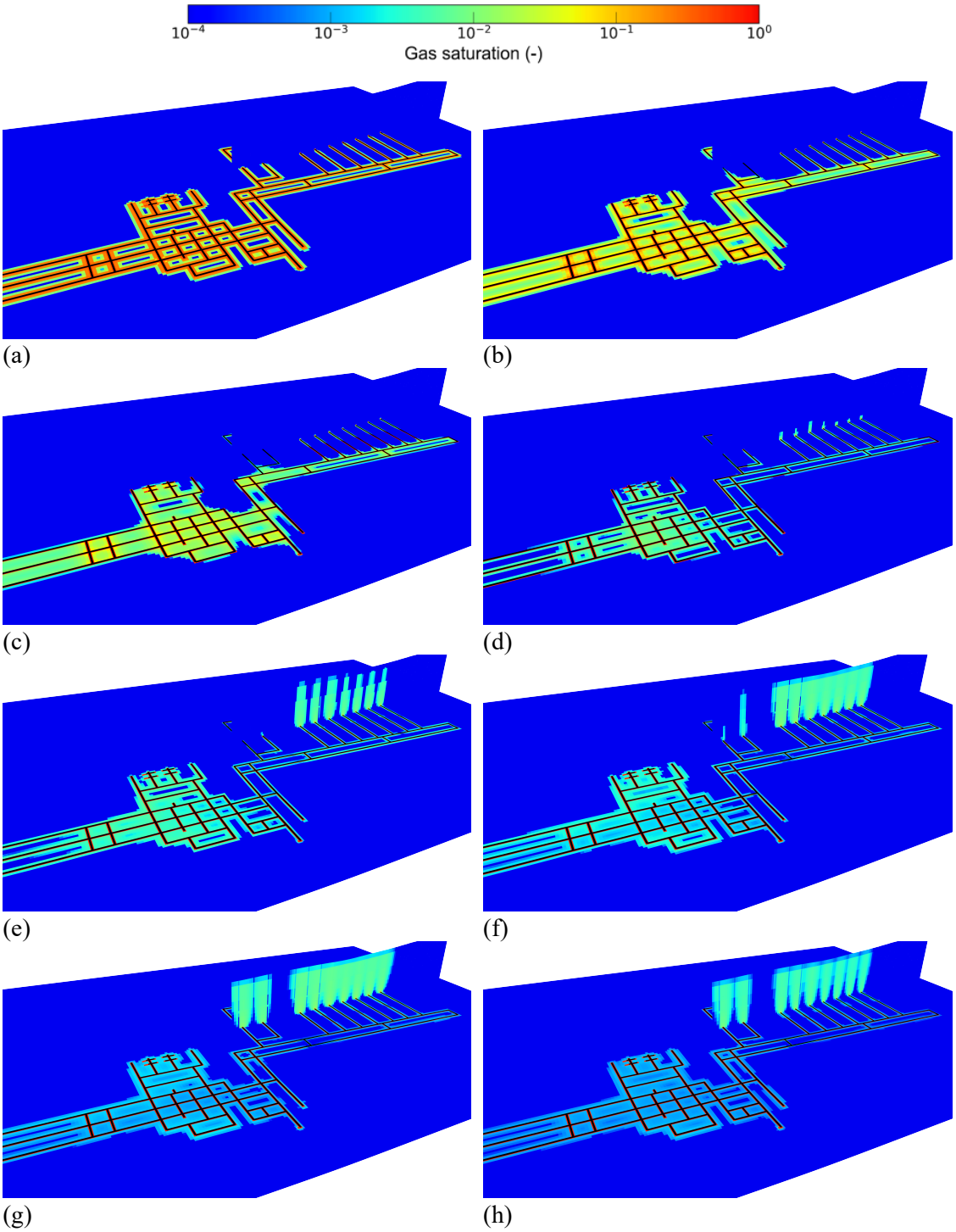

Fig. B-48: Deviations scenario *"fault through L/ILW"*: Spatial distribution of gas saturation in the repository and the fault after (a) 100 years, (b) 500 years, (c) 1,000 years, (d) 5,000 years, (e) 10,000 years, (f) 20,000 years, (g) 50,000 years, and (h) 100,000 years

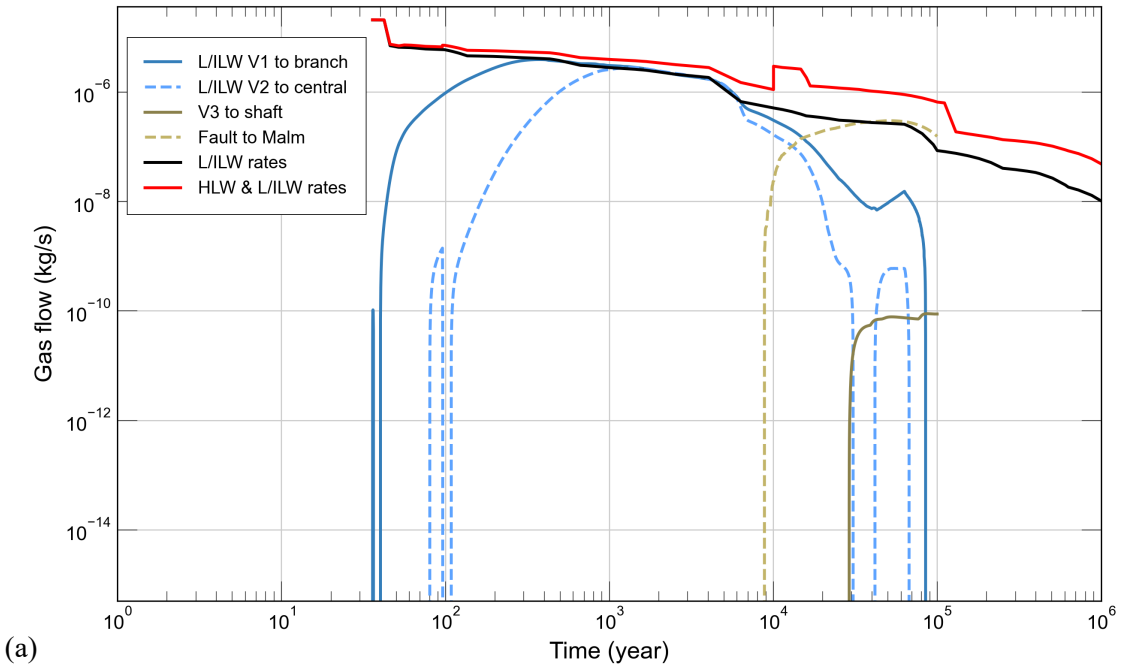

(a)

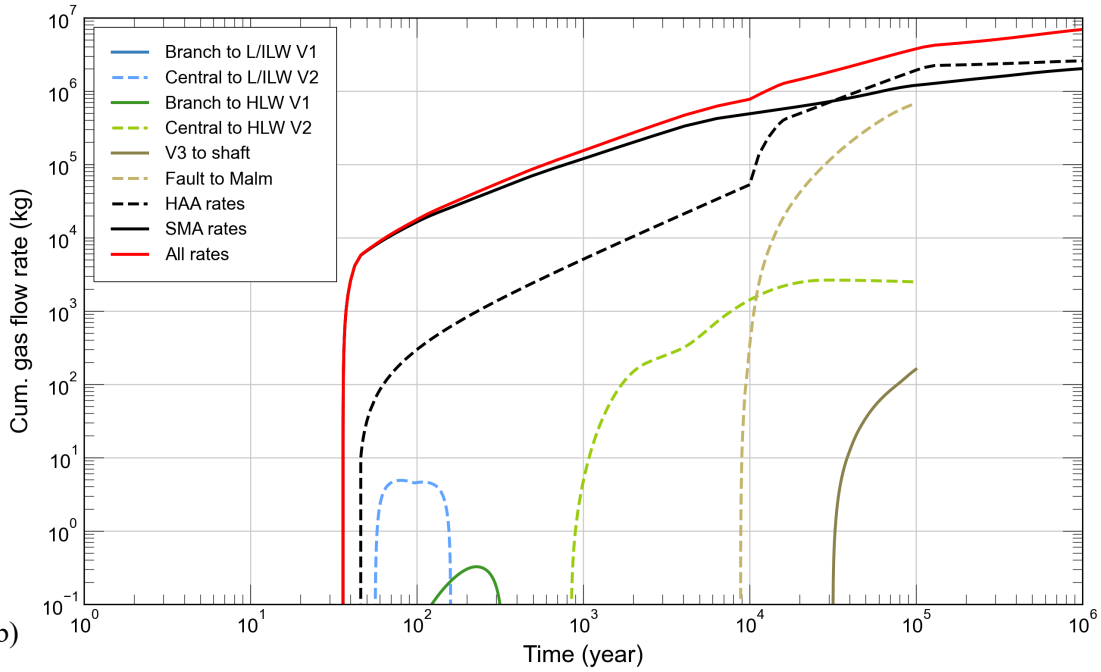

(b)

Fig. B-49: Deviations scenario *"fault through L/ILW"*: Transients of (a) gas flow rate and (b) cumulative gas flow through the sealing sections of the repository (towards shafts) and through the fault

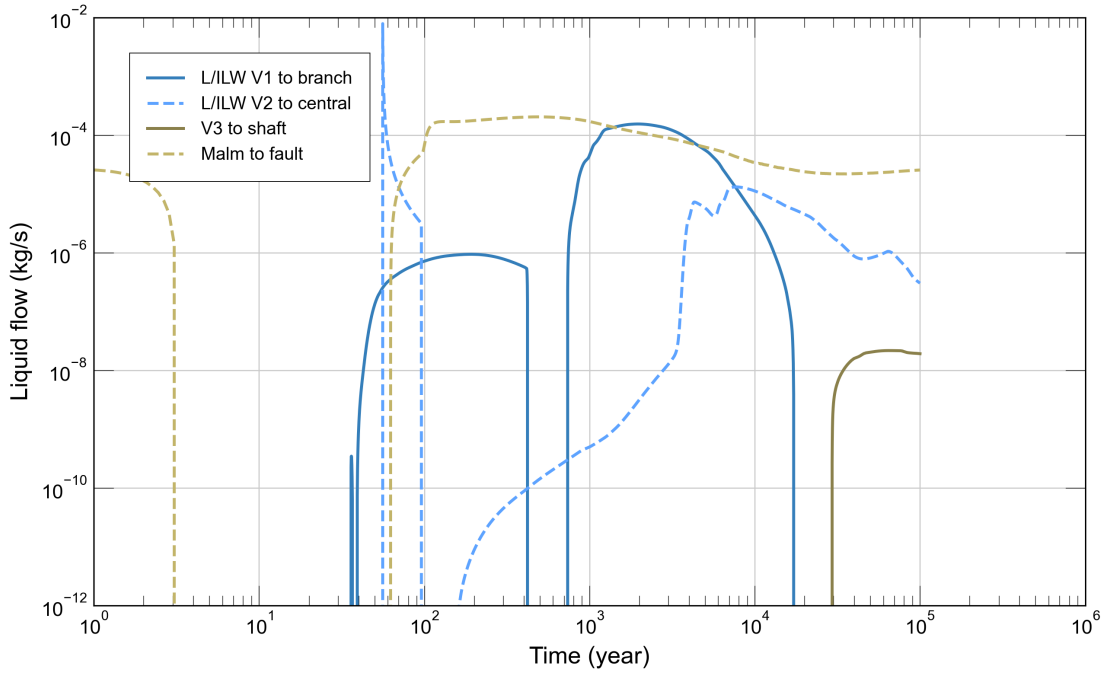

Fig. B-50: Deviations scenario *"fault through L/ILW"*: Transients of liquid flow rate through the sealing sections of the repository (towards shafts) and through the fault

App. C Complementary results: HLW

Complementary simulation results contributing to the HLW analysis are provided in this appendix.

C.1 Expected performance

The transient plots provided in Section 7.1 are complemented with plots of spatial distributions in the HLW nearfield for the expected performance.

Distributions of temperature, gas saturation, and pressure obtained with the 3D component model of a single HLW emplacement drift are shown in Fig. C-1, Fig. C-2, and Fig. C-3, respectively. This corresponds to the base case simulation presented in Nagra (2024g).

Distributions of temperature, gas saturation, and pressure obtained with the 2D component model of 20 HLW emplacement drifts are shown in Fig. C-4, Fig. C-5, and Fig. C-6, respectively. Distributions of tracer mass fraction in water (I-129 liquid saturation) are shown in Fig. C-7. This simulation corresponds to the base case simulation presented in Section 7.1.

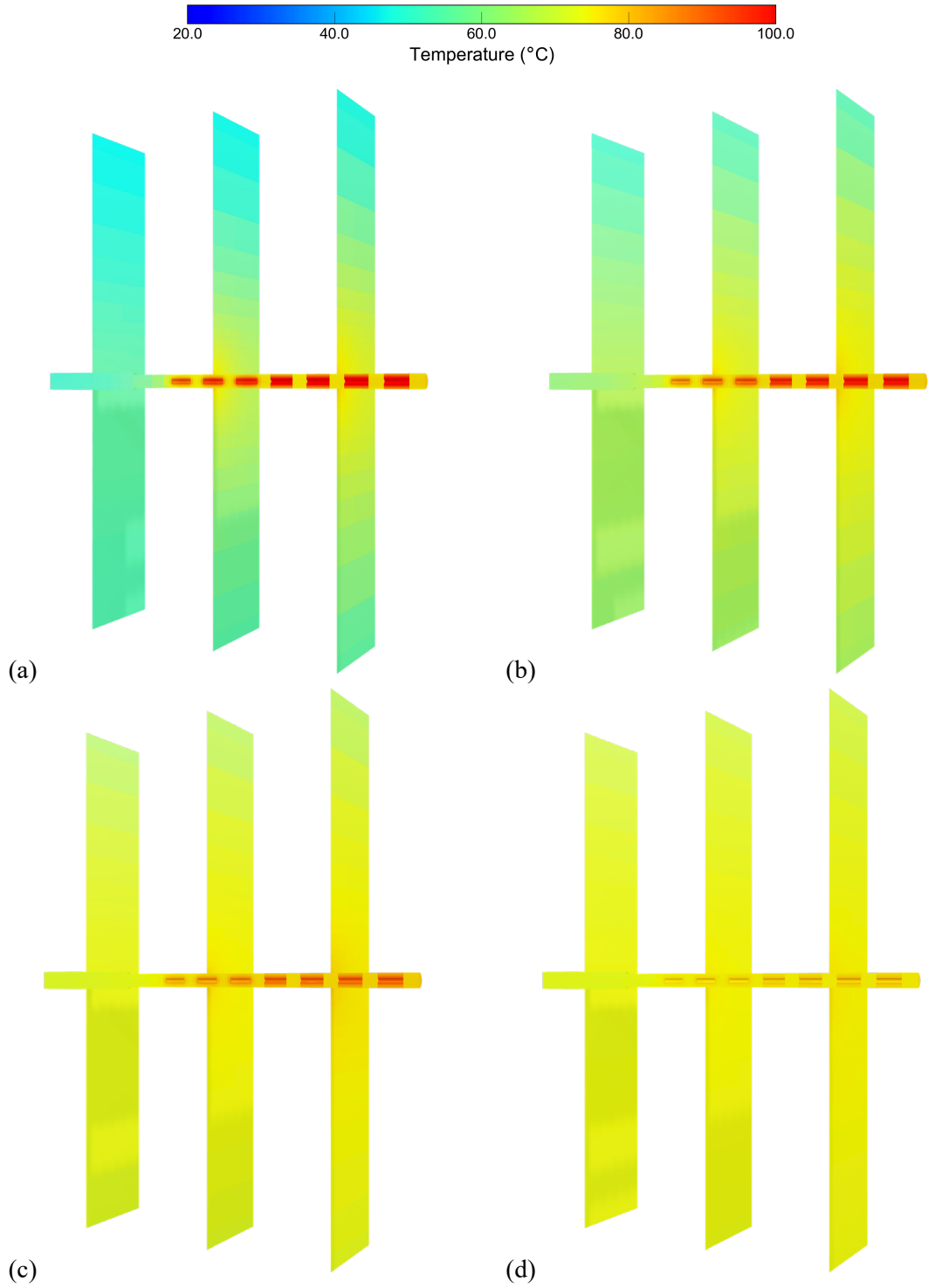

Fig. C-1: Expected performance HLW (3D component model): Spatial distribution of temperature after (a) 100 years, (b) 200 years, (c) 500 years, and (d) 1,000 years

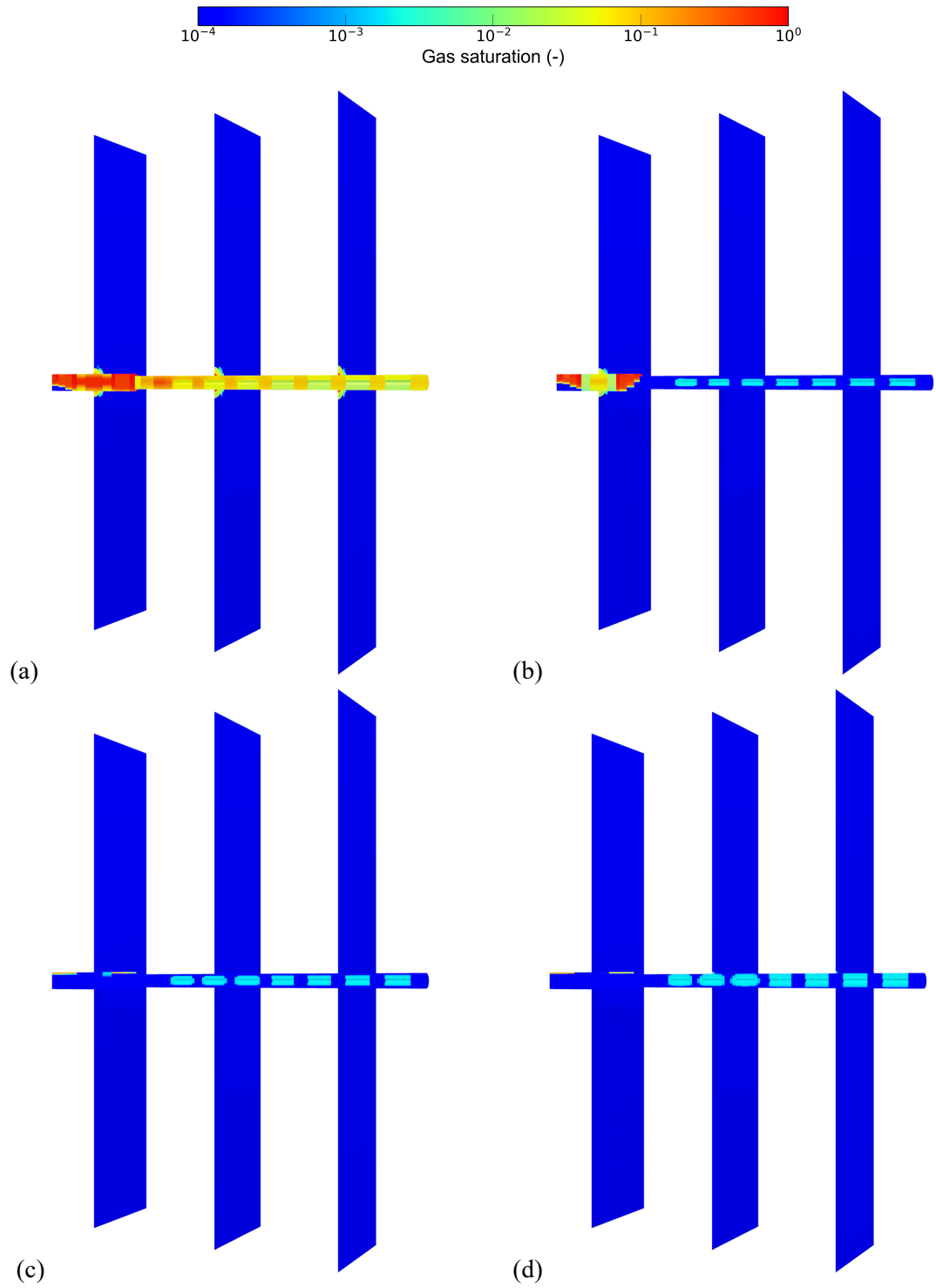

Fig. C-2: Expected performance HLW (3D component model): Spatial distribution of gas saturation after (a) 100 years, (b) 200 years, (c) 500 years, and (d) 1,000 years

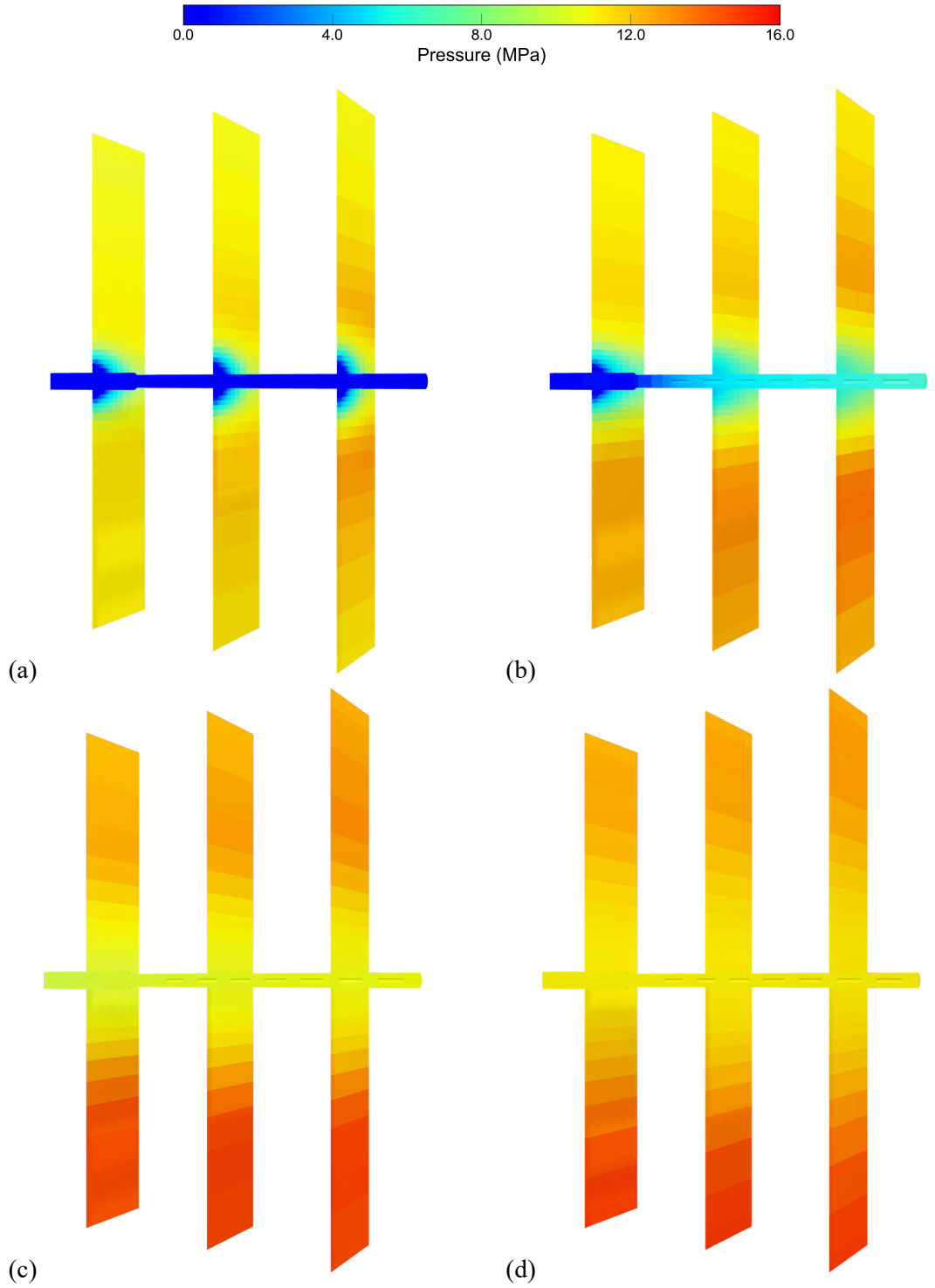

Fig. C-3: Expected performance HLW (3D component model): Spatial distribution of pressure after (a) 100 years, (b) 200 years, (c) 500 years, and (d) 1,000 years

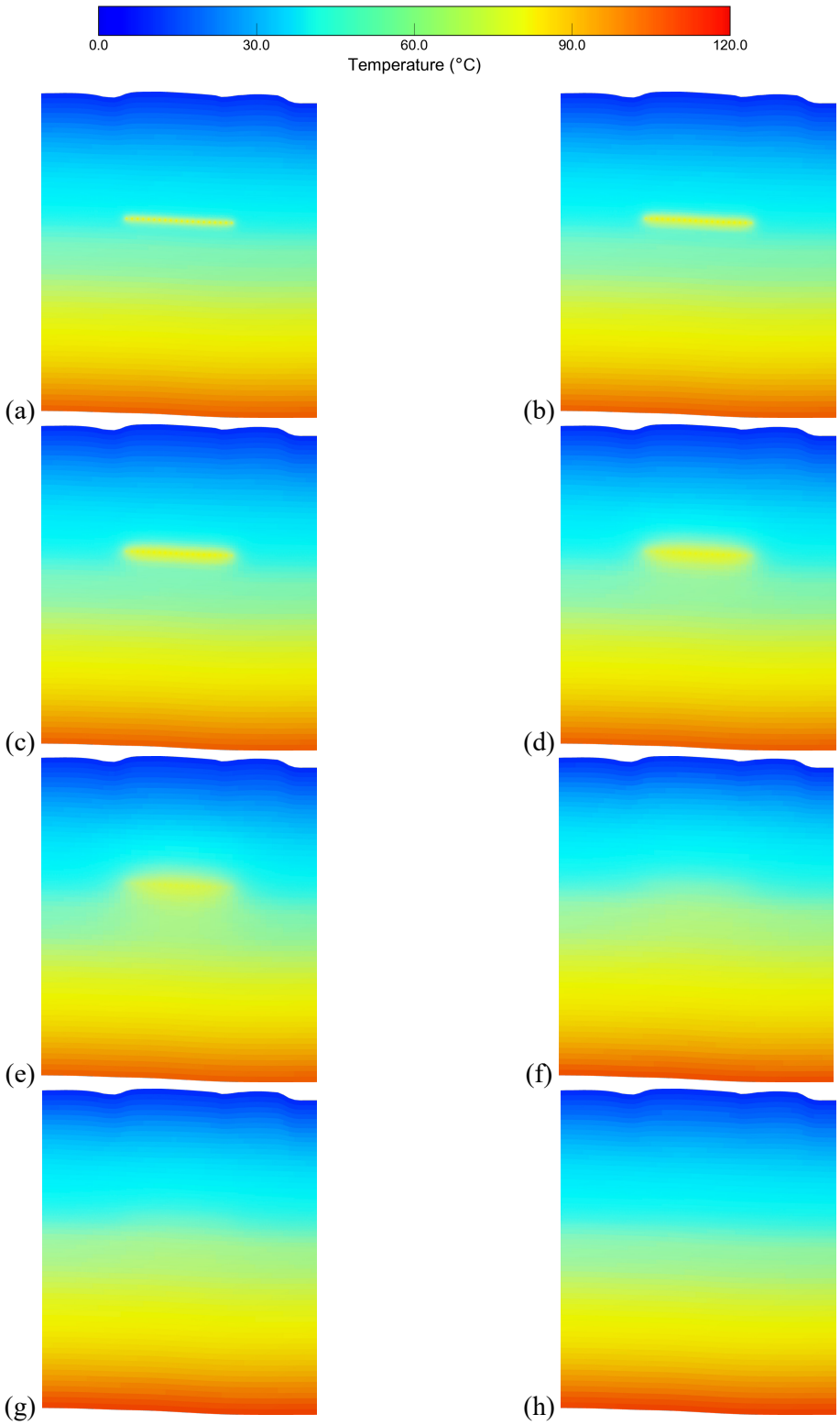

Fig. C-4: Expected performance HLW (2D component model): Spatial distribution of temperature after (a) 50 years, (b) 100 years, (c) 200 years, (d) 500 years, (e) 1,000 years, (f) 10,000 years, (g) 20,000 years, and (h) 100,000 years

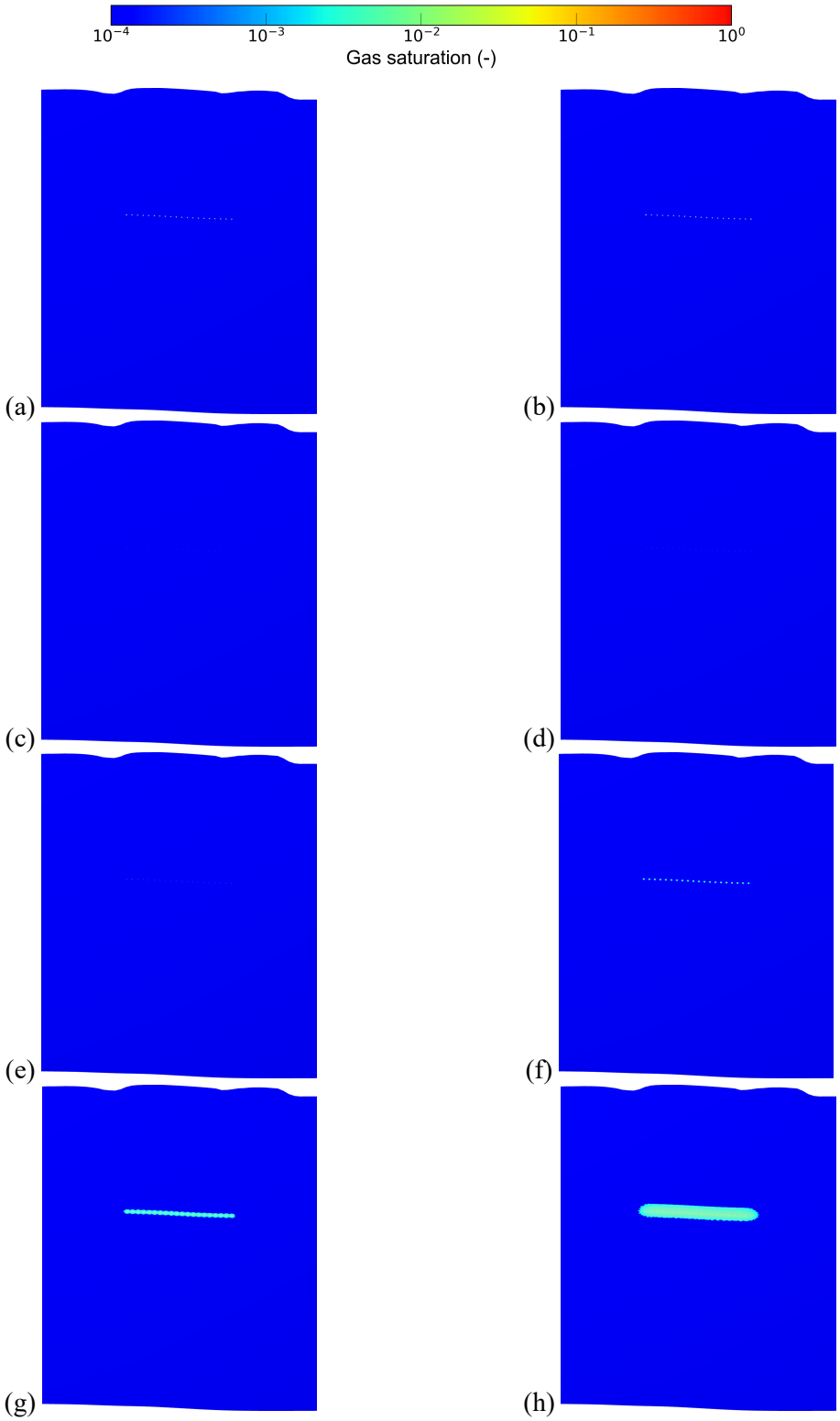

Fig. C-5: Expected performance HLW (2D component model): Spatial distribution of gas saturation after (a) 50 years, (b) 100 years, (c) 200 years, (d) 500 years, (e) 1,000 years, (f) 10,000 years, (g) 20,000 years, and (h) 100,000 years

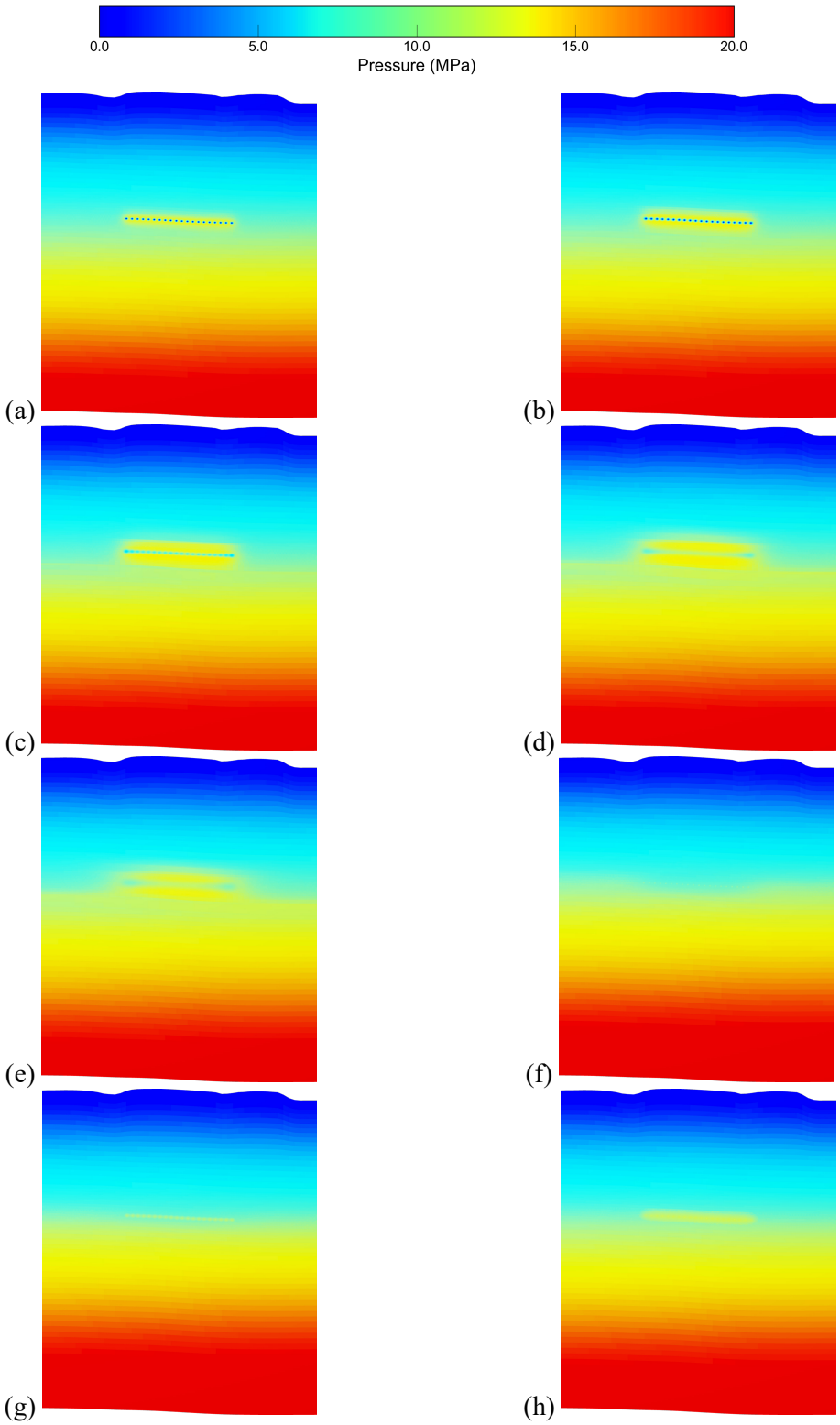

Fig. C-6: Expected performance HLW (2D component model): Spatial distribution of pressure after (a) 50 years, (b) 100 years, (c) 200 years, (d) 500 years, (e) 1,000 years, (f) 10,000 years, (g) 20,000 years, and (h) 100,000 years

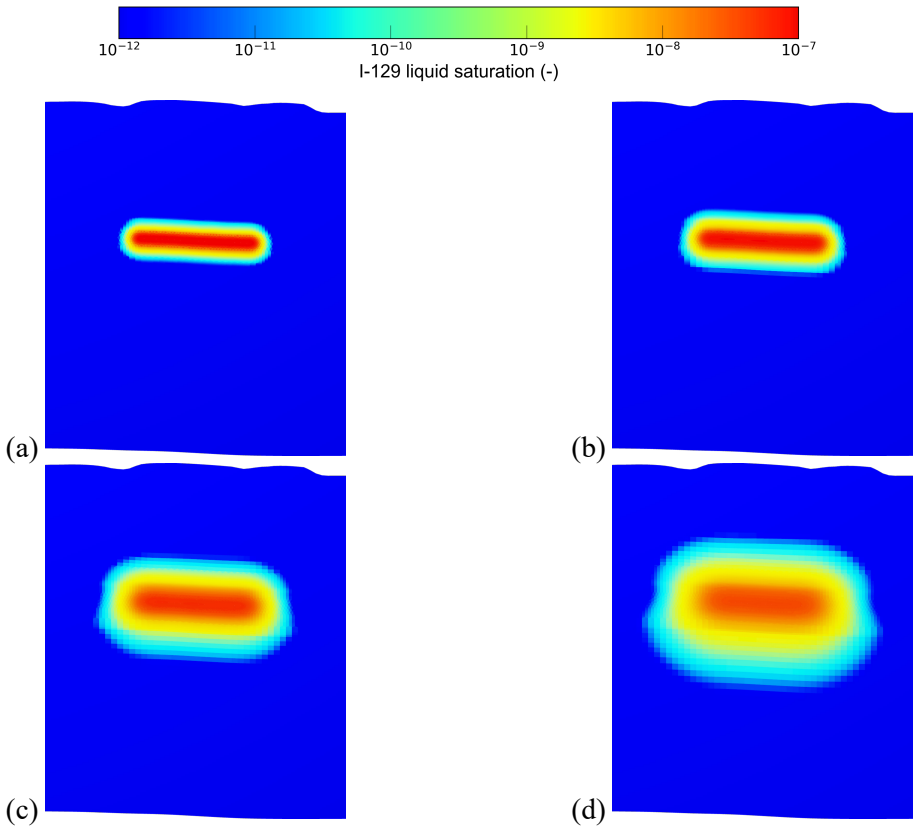

Fig. C-7: Expected performance HLW (2D component model): Spatial distribution of I-129 liquid saturation after (a) 100,000 years, (b) 200,000 years, (c) 500,000 years, and (d) 1,000,000 years

C.2 Expected performance with H_2 molecular diffusion

The simulation with the 2D component model of 20 HLW emplacement drifts is repeated for the expected performance, this time including molecular diffusion with H_2 molecular diffusion coefficient of 2.0E-09 m^2/s (see also Tab. B-1). The transients of average bentonite temperature, thermally induced overpressures 20 m above the disposal area, and gas induced overpressures in the nearfield are shown in Fig. C-8.

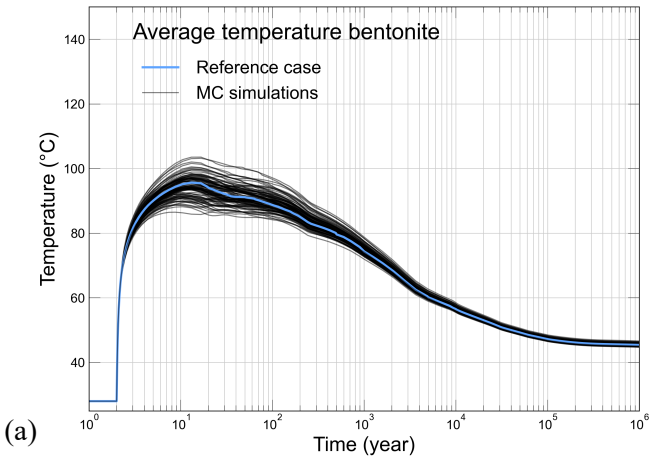

(a)

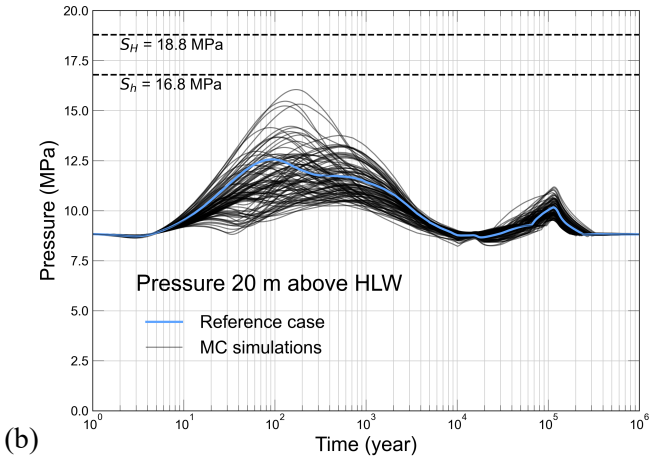

(b)

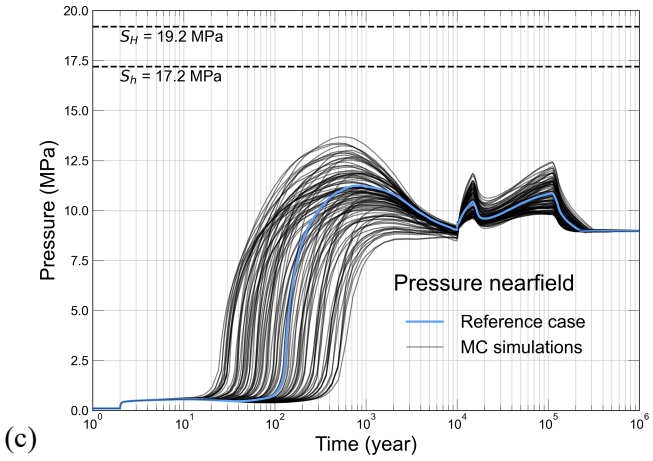

(c)

Fig. C-8: Expected performance HLW with H_2 molecular diffusion (2D component model): best estimate and uncertainty ranges

(a) Average temperature in the bentonite buffer, (b) thermally induced overpressures at a distance of 20 m above the disposal area, (c) gas induced overpressures in the HLW nearfield.

C.3 Expected performance with H_2O consumption

The simulation with the 2D component model of 20 HLW emplacement drifts is repeated for the expected performance, this time including water consumption associated with the corrosion of metals (for reactions and stoichiometries see Nagra 2024g). The transients of average bentonite temperature, thermally induced overpressures 20 m above the disposal area, and gas induced overpressures in the nearfield are shown in Fig. C-9.

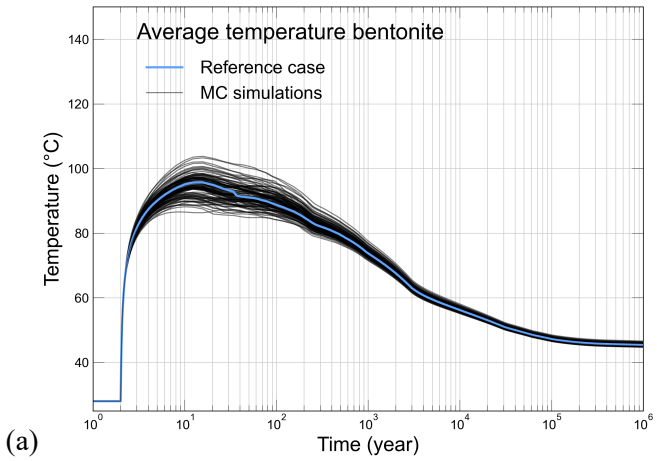

(a)

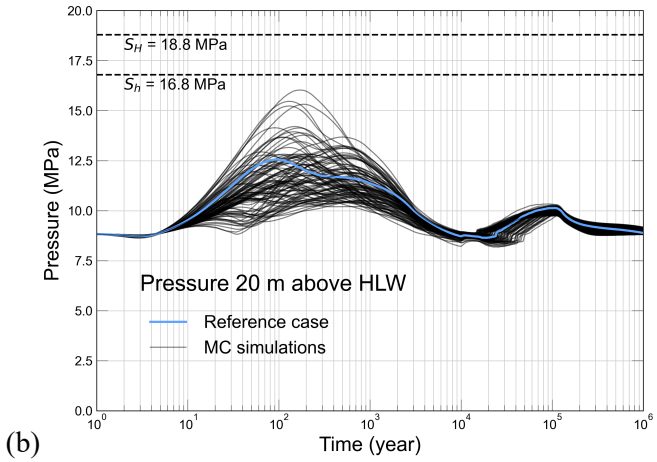

(b)

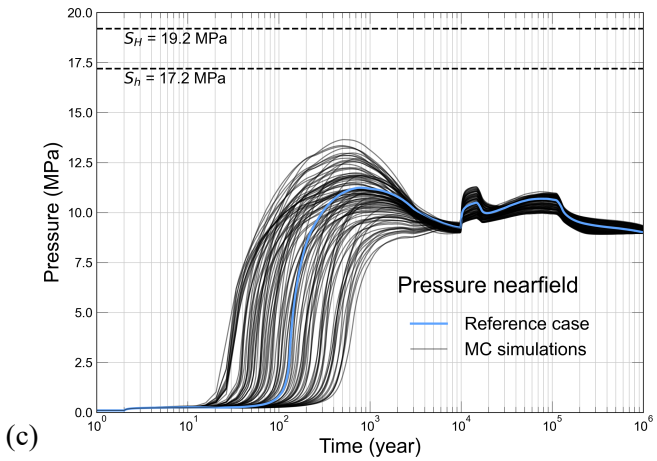

(c)

Fig. C-9: Expected performance HLW with water consumption (2D component model): best estimate and uncertainty ranges

(a) Average temperature in the bentonite buffer, (b) thermally induced overpressures at a distance of 20 m above the disposal area, (c) gas induced overpressures in the HLW nearfield.

App. D Complementary results: L/ILW

Complementary simulation results contributing to the L/ILW analysis are provided in this appendix.

D.1 Expected performance

The transients provided in Section 8.1 are complemented in the following with plots of spatial distributions in the L/ILW nearfield for the expected performance.

Distributions of gas saturation and pressure obtained with the 3D component model of a single L/ILW emplacement cavern are shown in Fig. D-1 and Fig. D-2, respectively. This simulation corresponds to the base case simulation presented in Nagra (2024g). Note that the model version with operations tunnel extending only up to the V2-L/ILW is shown here, which is conservative for pressure buildup (see also Chapter 4).

Distributions of gas saturation and pressure obtained with the 2.5D component model of a single L/ILW emplacement cavern are shown in Fig. D-3 and Fig. D-4, respectively. Distributions of tracer mass fraction in water (Cl-36 liquid saturation) are shown in Fig. D-5. For comparison to the 3D model, the model version with operations tunnel extending only up to the V2-L/ILW is shown here.

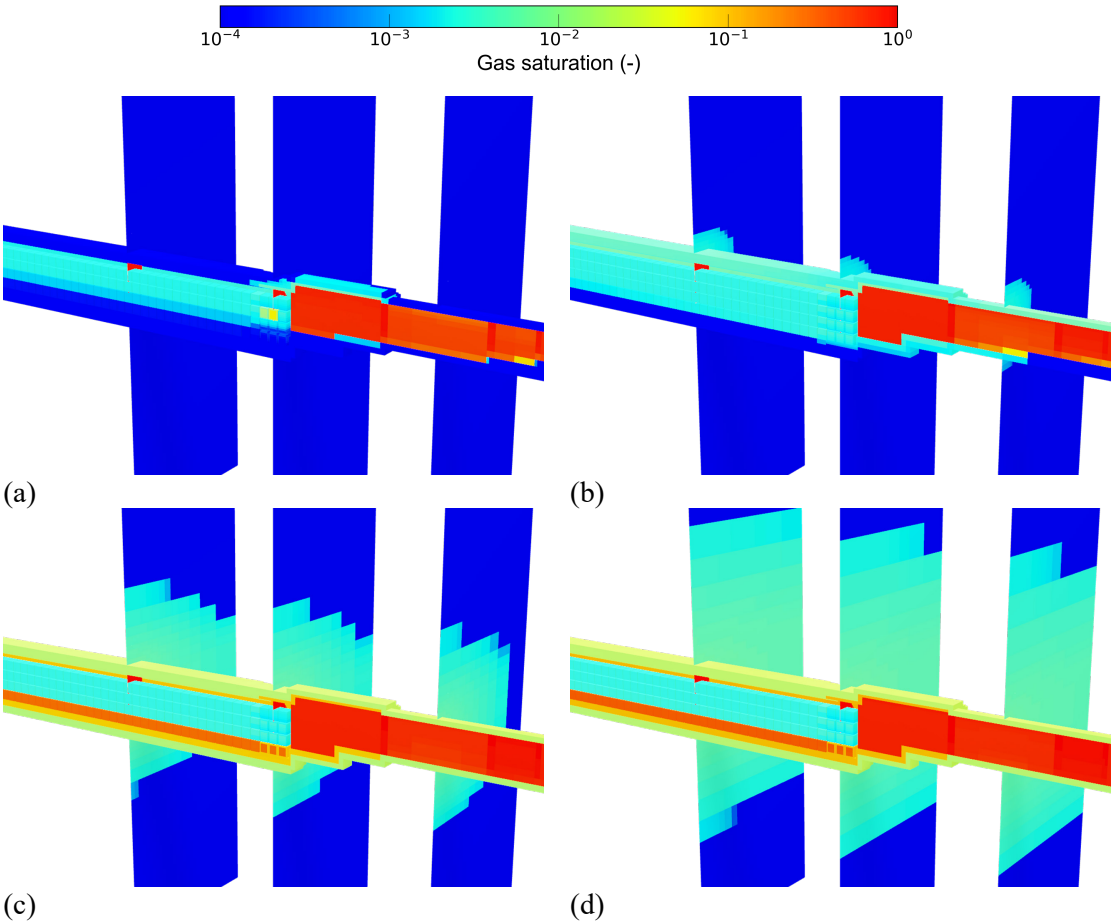

Fig. D-1: Expected performance L/ILW (3D component model up to V2-L/ILW): Spatial distribution of gas saturation after (a) 1,000 years, (b) 10,000 years, (c) 50,000 years, and (d) 100,000 years

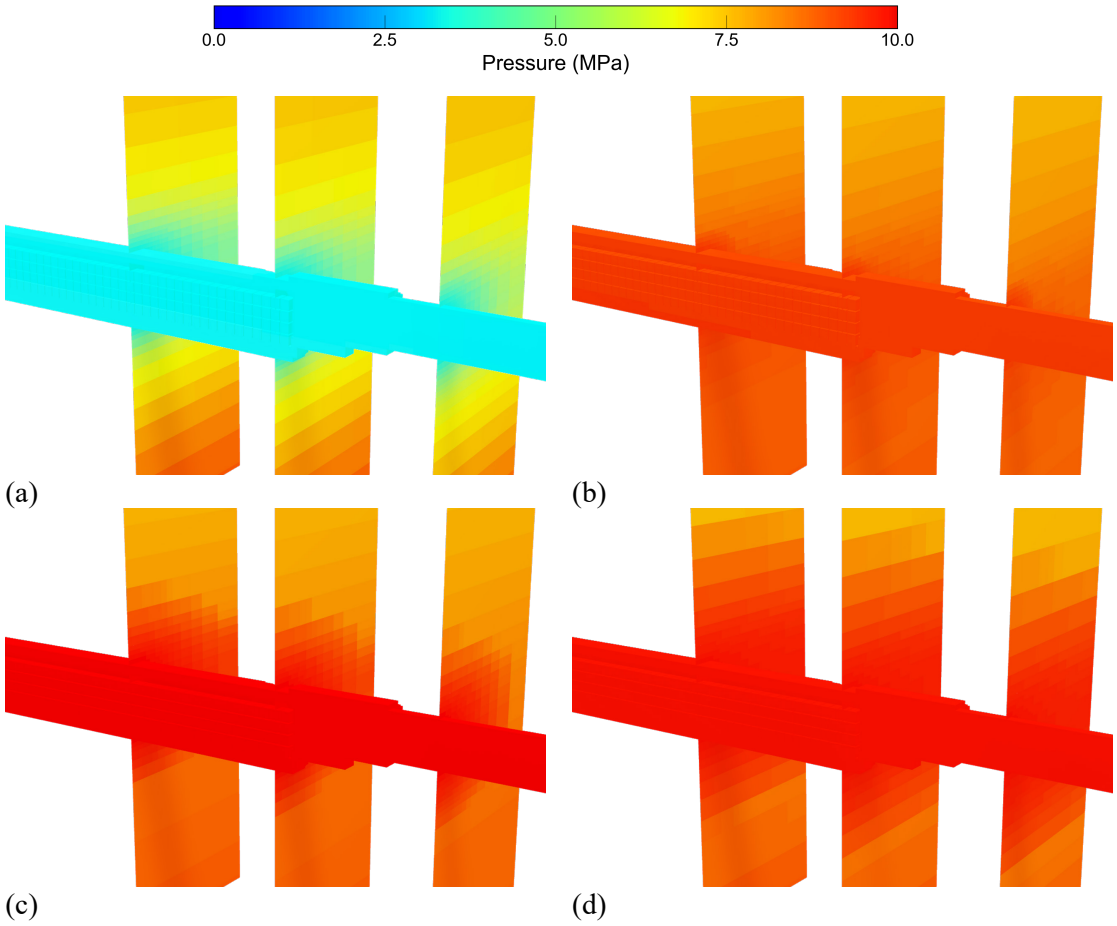

Fig. D-2: Expected performance L/ILW (3D component model up to V2-L/ILW): Spatial distribution of pressure after (a) 1,000 years, (b) 10,000 years, (c) 50,000 years, and (d) 100,000 years

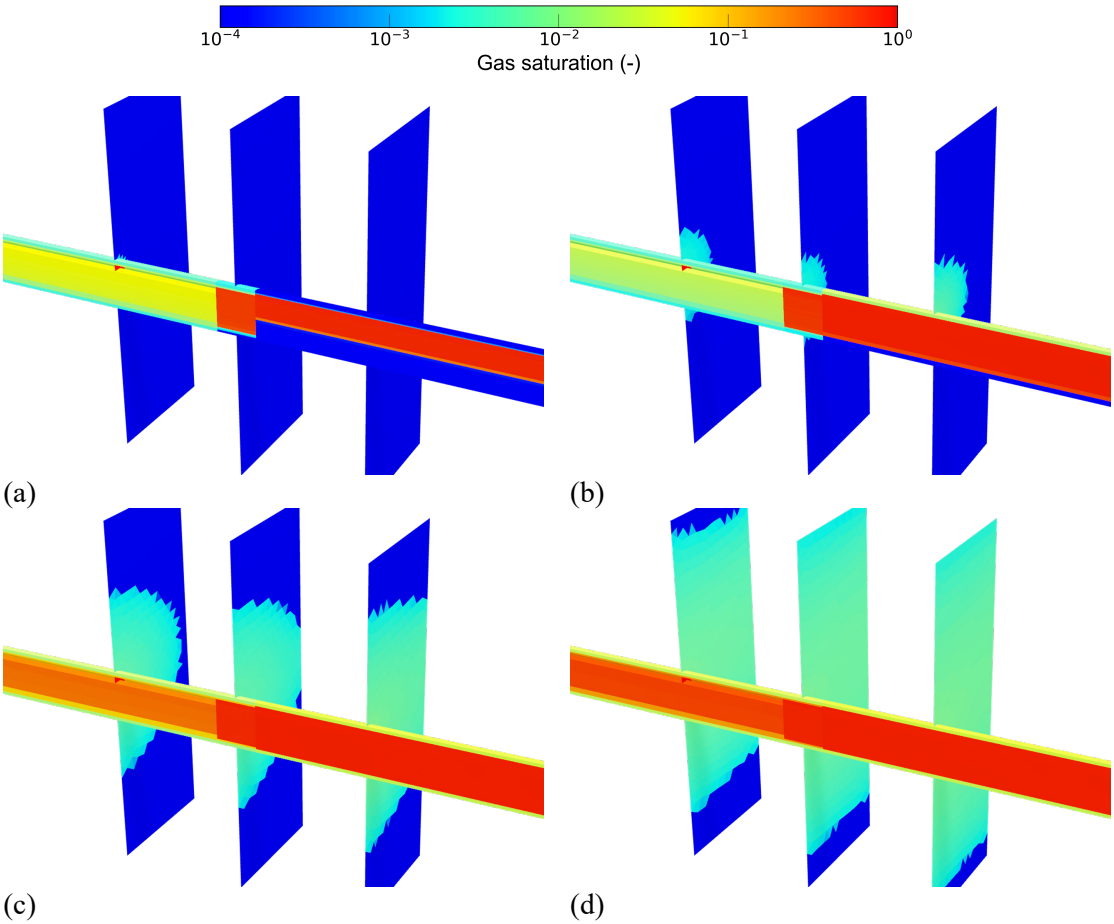

Fig. D-3: Expected performance L/ILW (2.5D component model up to V2-L/ILW): Spatial distribution of gas saturation after (a) 1,000 years, (b) 10,000 years, (c) 50,000 years, and (d) 100,000 years

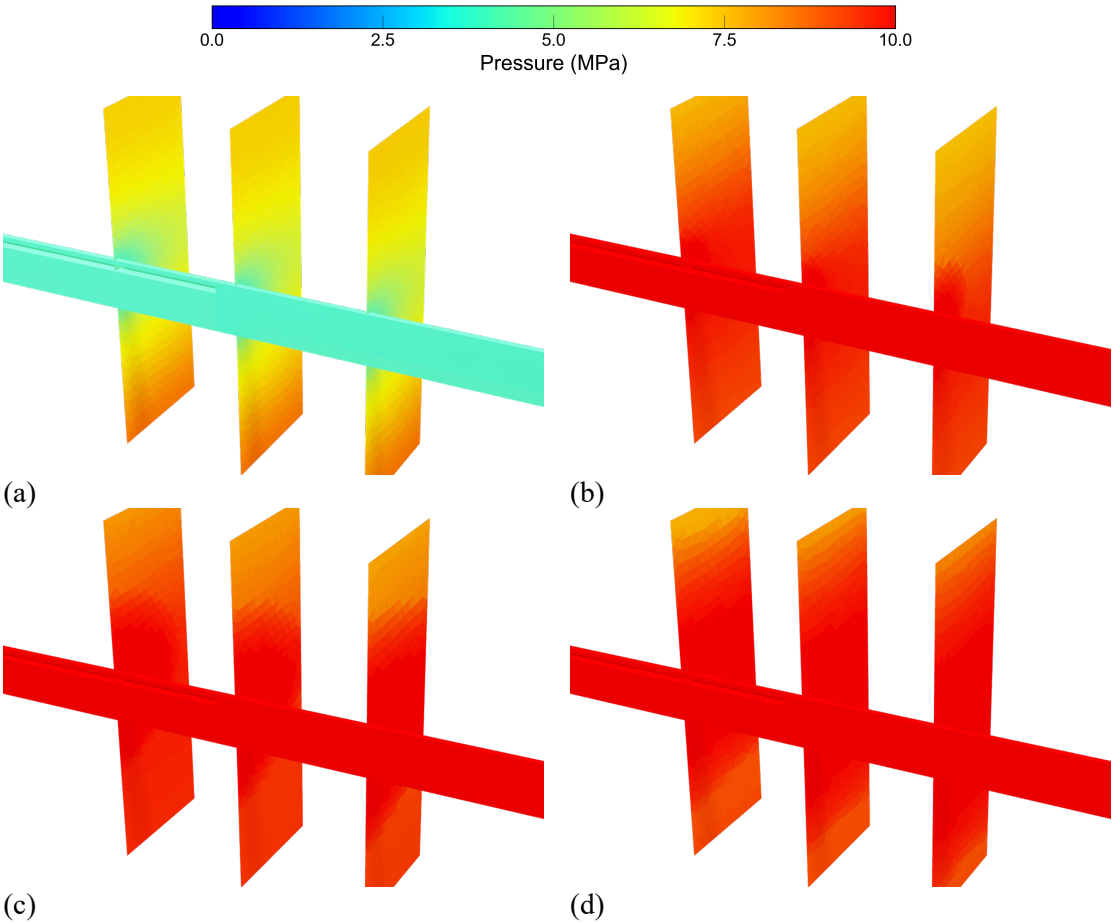

Fig. D-4: Expected performance L/ILW (2.5D component model up to V2-L/ILW): Spatial distribution of pressure after (a) 1,000 years, (b) 10,000 years, (c) 50,000 years, and (d) 100,000 years

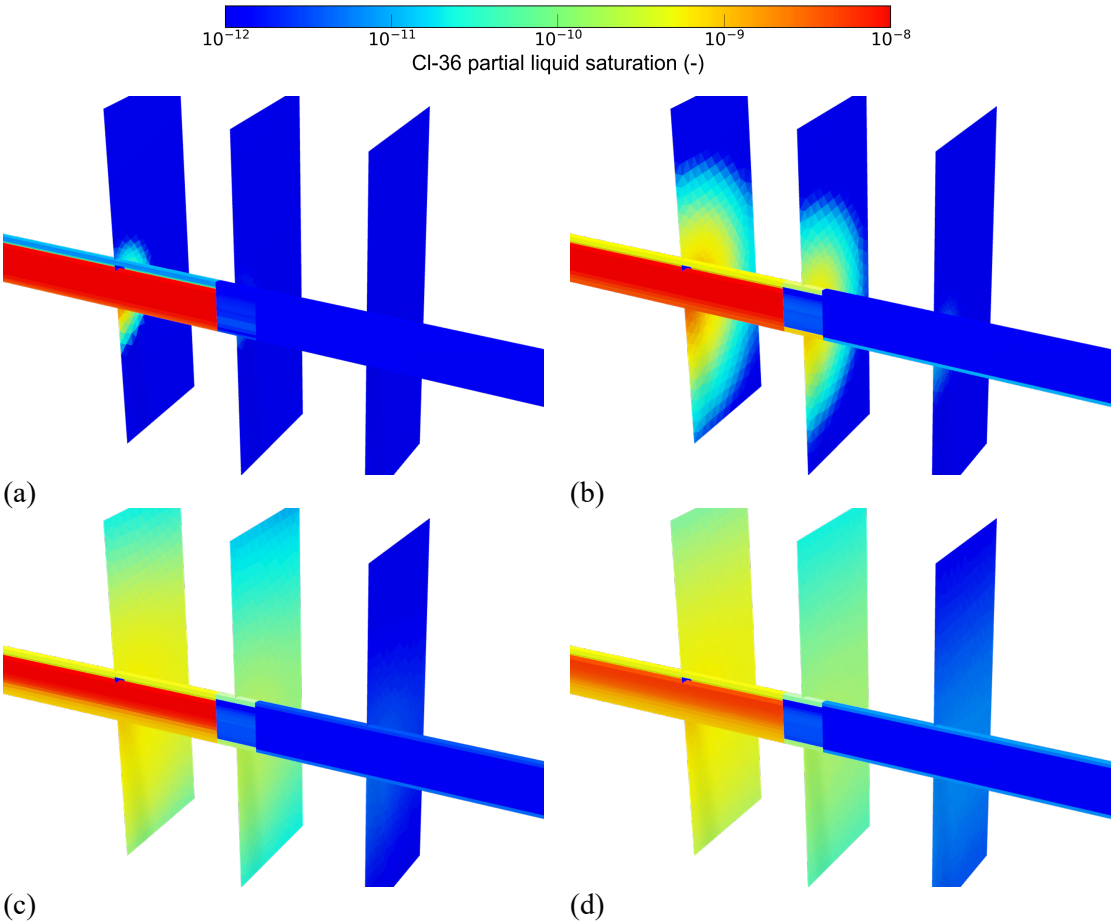

Fig. D-5: Expected performance L/ILW (2.5D component model up to V2-L/ILW): Spatial distribution of Cl-36 liquid saturation after (a) 100,000 years, (b) 200,000 years, (c) 500,000 years, and (d) 1,000,000 years

D.2 Expected evolution with H_2 molecular diffusion and H_2O consumption

A deterministic simulation of the expected evolution including the molecular diffusion of hydrogen and the consumption of water associated with the corrosion of metals is carried out with the 3D component model of an L/ILW emplacement cavern presented in Nagra (2024g). Note that the model version with operations tunnel extending only up to the V2-L/ILW is shown here, which is conservative for pressure buildup (see also Chapter 4). Spatial distributions of gas saturation and pressure are given in Fig. D-6 and Fig. D-7, respectively.

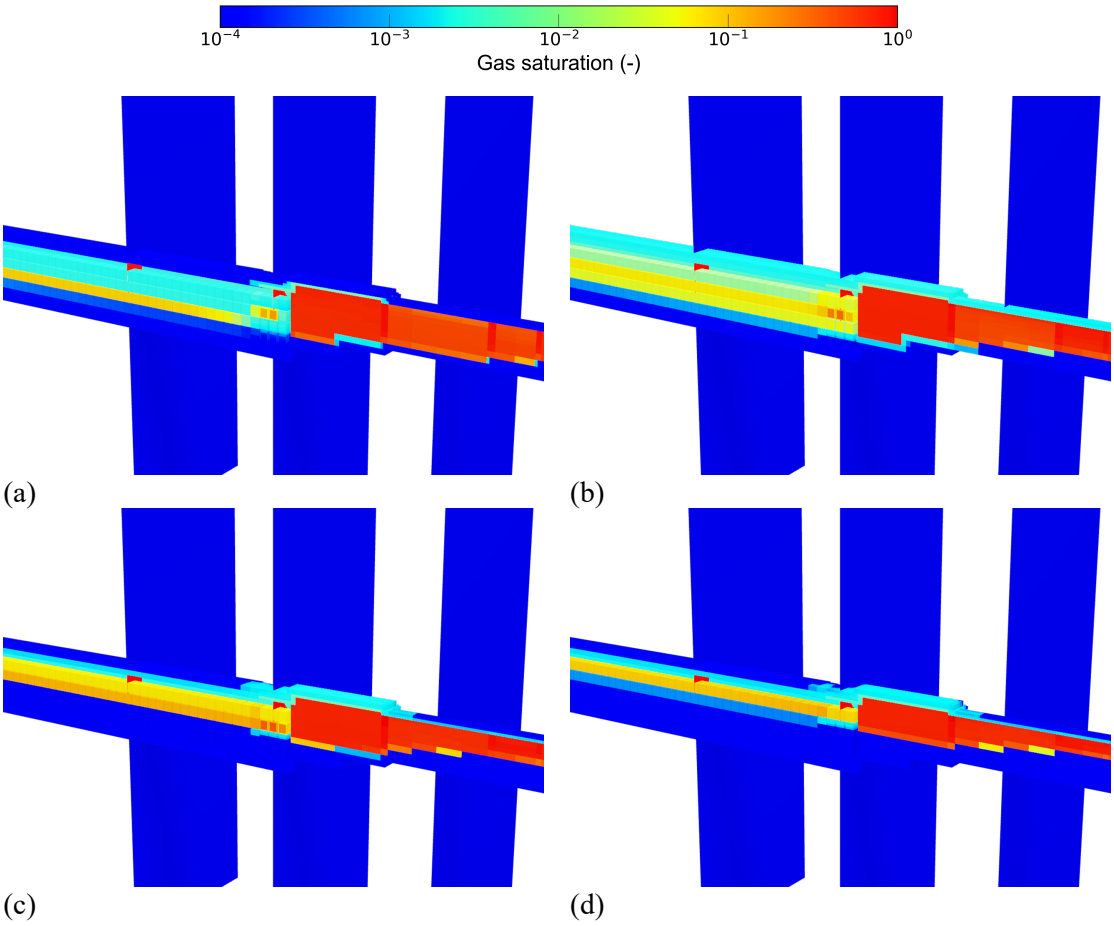

Fig. D-6: Expected performance L/ILW with water consumption and H_2 molecular diffusion (3D component model): Spatial distribution of gas saturation after (a) 1,000 years, (b) 10,000 years, (c) 50,000 years, and (d) 100,000 years

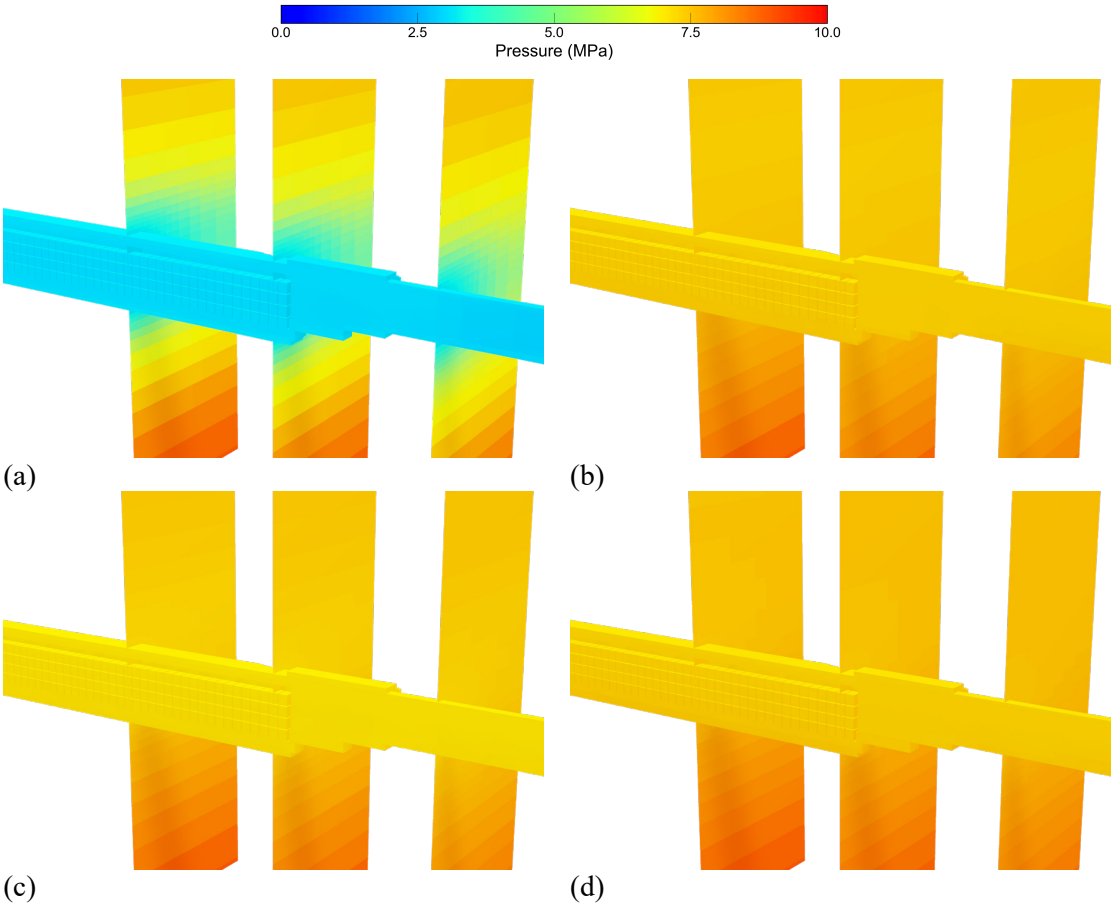

Fig. D-7: Expected performance L/ILW with water consumption and H_2 molecular diffusion (3D component model): Spatial distribution of pressure after (a) 1,000 years, (b) 10,000 years, (c) 50,000 years, and (d) 100,000 years

D.3 Expected evolution with H_2 molecular diffusion (probabilistic)

The simulation with the 2D component model of 7 L/ILW emplacement drifts is repeated for the expected performance, this time including molecular diffusion with H_2 molecular diffusion coefficient of 2.0E-09 m^2/s (see also Tab. B-1). The transients of gas induced overpressures in the nearfield and volatile tracer normalised flux through the V3 are shown in Fig. D-8.

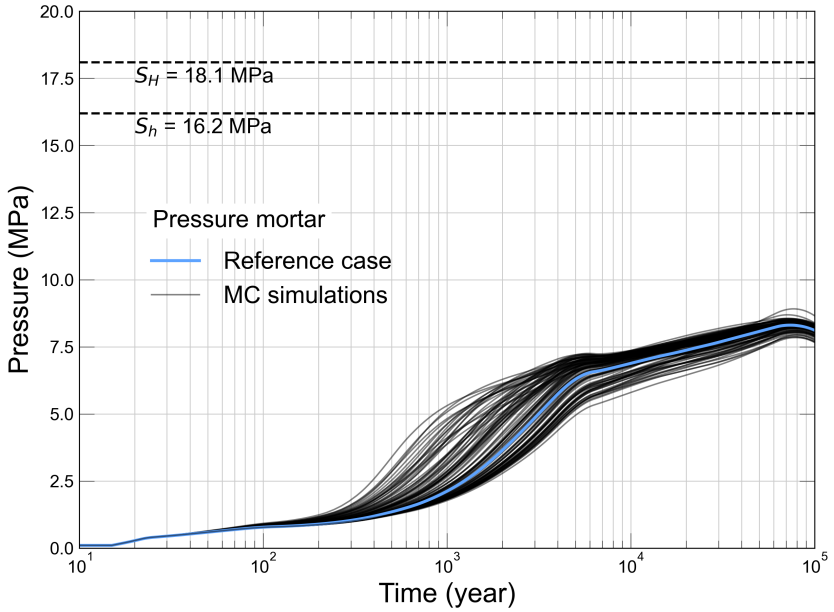

Fig. D-8: Expected barrier performance L/ILW with H_2 molecular diffusion (2.5D component model): best estimate and uncertainty range of gas induced overpressures in the L/ILW nearfield

D.4 Expected evolution with H_2O consumption (probabilistic)

A deterministic simulation of the expected evolution including the consumption of water associated with the corrosion of metals in the 3D component model of an L/ILW emplacement cavern is presented in Nagra (2024g).

Here, the probabilistic simulation of the expected performance with the 2D component model of 7 L/ILW emplacement caverns presented in Section 8.1 is repeated, this time including water consumption associated with the corrosion of metals (for reactions and stoichiometries see Nagra 2024g). The transients of gas induced overpressures in the nearfield are shown in Fig. D-9. In comparison to the 3D simulation discussed in Nagra (2024g), the 2D model used here is based on a more homogenised representation of the nearfield (i.e., no gaps filled with mortar between the waste packages) and results in more conservative pressure estimates.

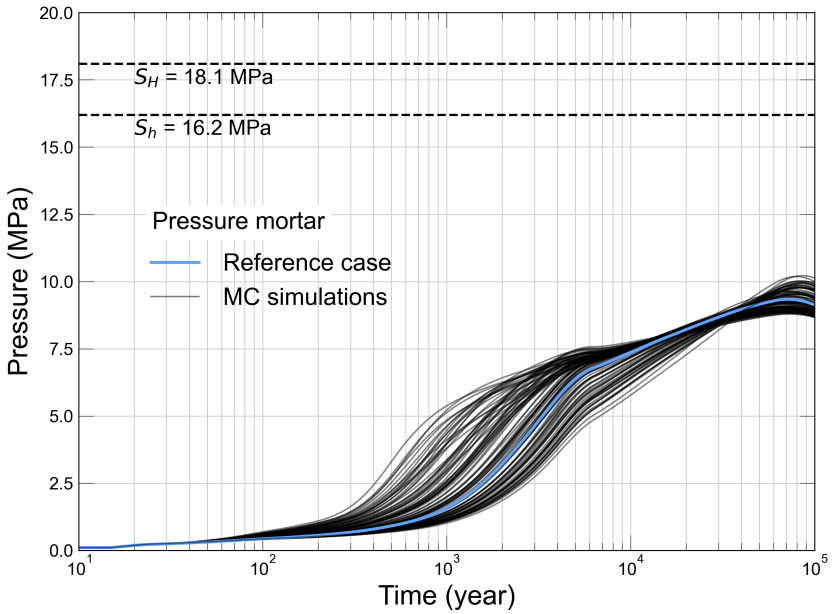

Fig. D-9: Expected barrier performance L/ILW with water consumption (2.5D component model): Best estimate and uncertainty range of gas induced overpressures in the L/ILW nearfield

App. E Benchmarking between PA and safety analysis

Extensive benchmarking between modelling approaches used by the PA and safety analysis, respectively, has allowed to quantify abstraction errors associated with (i) the geometric simplification of transport processes (e.g., representation of 3D and 2D transport geometries by a simplified 1D scheme), and (ii) the mathematical and numerical representations of the transport problem with different codes. For this, results of solute tracer transport simulations have been compared when obtained in 2D with TOUGH and in 1D with PICNIC. The simulations represent tracer transport through the OPA by either diffusion only or by diffusion and advection. Variants of diffusion coefficients (with and without anisotropy) and Darcy velocity are implemented as part of the benchmarking exercise.

An exemplary quantitative comparison performed for the benchmarking is illustrated in Fig. E-1. It shows breakthrough and normalised breakthrough curves of tracer diffusion from an HLW emplacement drift to the top of the OPA, respectively. The normalisation is obtained by scaling with the injected mass flux at the HLW emplacement drift. The mass flux leaving the OPA is very similar in both models, with slightly higher values obtained with the 2D TOUGH2 model.

An additional comparison is illustrated in Fig. E-2 for tracer diffusion and advection assuming an upwards Darcy velocity of 2E-14 m/s in the OPA. The breakthrough curves from the 1D PICNIC model, that do not account for any lateral transport in the nearfield, result in earlier breakthrough and accordingly higher fluxes at early times. After the transient phase (~200,000 years) the results in 1D and 2D are very similar.

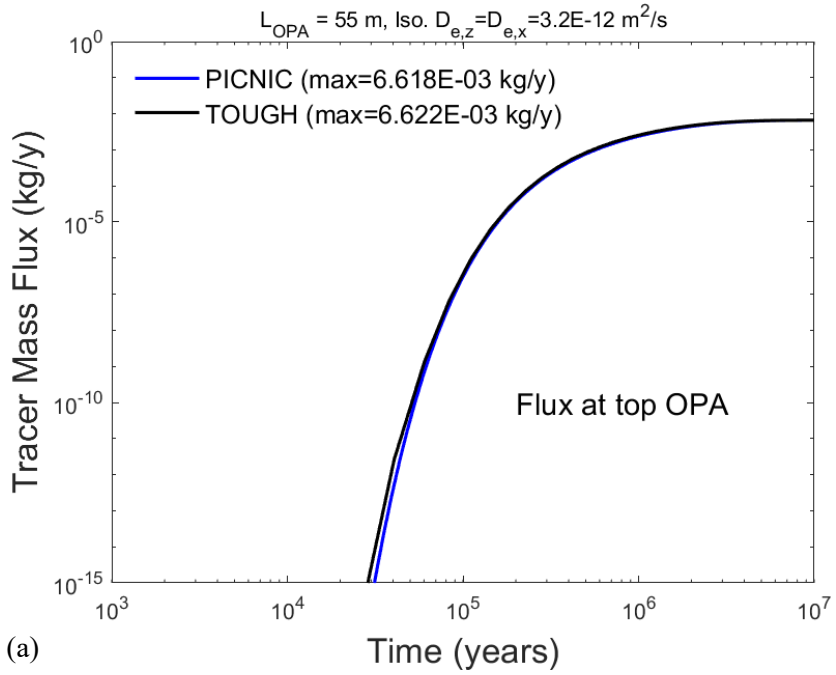

(a)

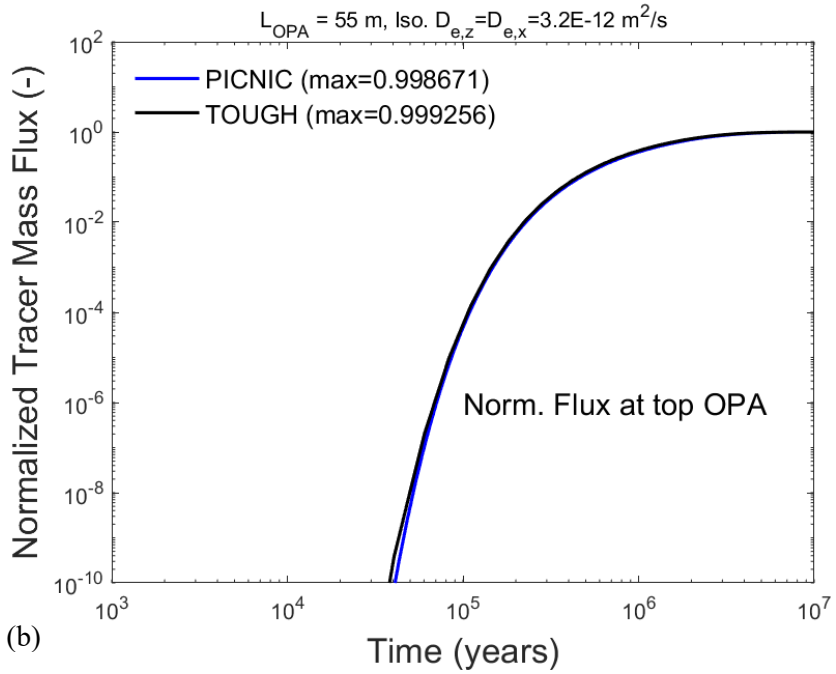

(b)

Fig. E-1: Comparison between (a) tracer mass fluxes and (b) normalised tracer mass fluxes at top-OPA obtained in 1D with PICNIC and in 2D with TOUGH2, for the case of tracer transport by diffusion only

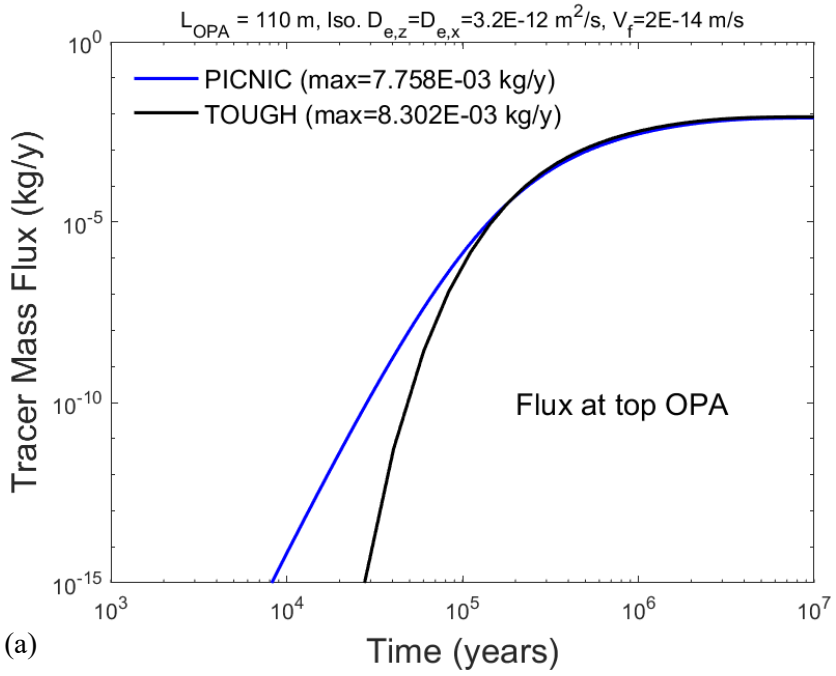

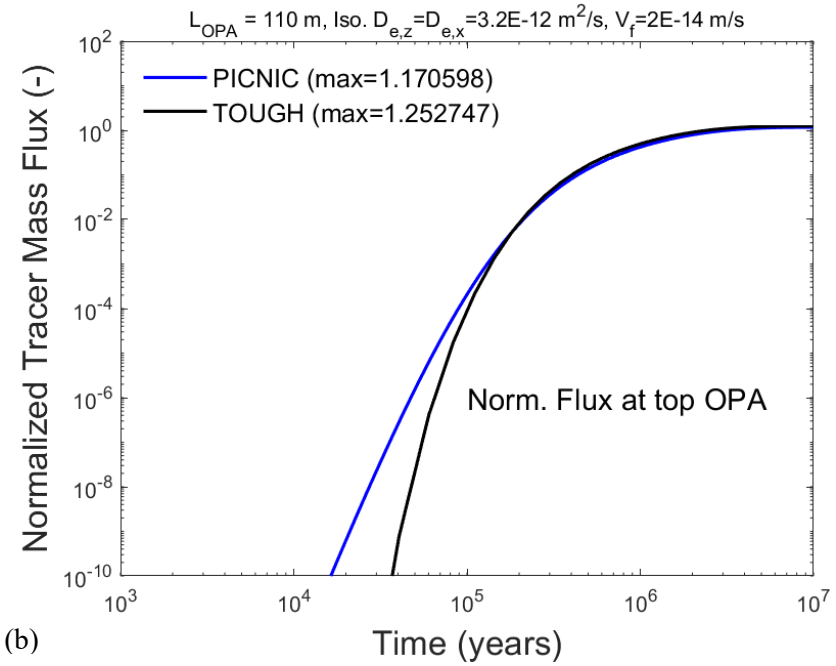

Fig. E-2: Comparison between (a) tracer mass fluxes and (b) normalised tracer mass fluxes (right) at top-OPA obtained in 1D with PICNIC and in 2D with TOUGH2, for the case of tracer transport by diffusion and advection with v_f = 2E-14 m/s (Pe = 0.344)